Developments in Microdosimetry and Nanodosimetry for Space and Therapeutic Applications

A thesis submitted in fulfilment of the requirements
for the award of the degree

Doctor of Philosophy

from

University of Wollongong

by

Andrew James Wroe,
B. Med. Rad. Phys., 1st Class Honours, UoW

Department of Engineering Physics
2007

For my family

Certificate of Originality

I hereby declare that this submission is my own work and that, to the best of my knowledge and belief, it contains no material previously published or written by another person.

I also declare that the intellectual content of this thesis is the product of my own work, even though I may have received assistance from others on style, presentation and language expression.

(Signed).....

Acknowledgements

Firstly, I would like to extend my sincerest thanks to my mentor of eight years, Professor Anatoly Rosenfeld. He provided the initial direction of my project and gave me the ability to peruse the research independently. He always provided a scientific sounding board for ideas, questions, developments or problems no matter what the time, or where I was in the world. Professor Rosenfeld's support in allowing me to complete research at a number of different international facilities and present this work at multiple international conferences was invaluable for my professional and personal development. These opportunities have allowed me to develop into the scientist I am today.

Dr Reinhard Schulte at Loma Linda Medical Center in the US was another major influence in my PhD completion. For the two years I completed research at this facility Dr Schulte was a constant source of scientific support in developing my knowledge of nanodosimetry and radiobiology. Without his direction, my achievements in these fields would not have been possible. Further, the support he and his family provided while I was away from my own family was also very much appreciated.

A PhD program requires funding and this was especially true in my case with experiments at various institutions worldwide. I would like to acknowledge the following funding agencies for their support:

- The Australian government through an Australian Postgraduate Award for the duration of my PhD program.
- The Australian Institute for Nuclear Science and Engineering (AINSE) provided a corner stone of support through a Postgraduate Award that provided not only financial benefit but also access to facilities and personnel at the Australian Nuclear Science and Technology Organisation (ANSTO). This ongoing support was invaluable to my work. AINSE also provided funding for me to attend a 2004 IEEE NSS meeting in Italy and the Radiation 2006 meeting in Sydney which was also greatly appreciated.

- A Fulbright Scholarship awarded by the Australian–American Fulbright Commission allowed my research at Loma Linda and other US institutions to take place over a period of 12 months in 2005-2006.
- Dr James Slater and Loma Linda University have supported this work through extensive financial funding of radiobiology supplies and equipment for cell survival work, use of irradiation facilities, as well as through the purchasing a computer cluster to enhance my ability to complete Monte Carlo simulations for my thesis.
- The National Space and Biomedical Research Institute (NSBRI) also provided support in allowing me to complete research at the United States Naval Academy (USNA) and the NASA Space Radiation Laboratory (NSRL) at Brookhaven National Laboratory.

Dr Vladimir Bashkirov's support in nanodosimetry, collection of experimental nanodosimetric data and advice on proton dosimetry was invaluable for the completion of this work.

The staff at Loma Linda University Medical Center within the department of Radiation Therapy was extremely supportive in all aspects of experimental research completed at this institution. Whilst all staff was exceptional in providing their time and expertise, Dr George Coutrakon, Peter Koss, Robert Simpson, Franko Piskulich, Eric Ramirez, Dr Abiel Ghebremedhin, Ed Schultz and Dr Baldev Patyal were exceptionally gracious with their time and expertise.

Staff at the Australian Nuclear Science and Technology Organisation including my AINSE supervisor A/Prof Dimitri Alexiev, Prof. David Cohen, Dr Mark Reinhard, Dale Prokopovich, Mark Hurry, Adam Sarbutt and Dr Reiner Siegele was most helpful in providing their time and expertise for various projects. This included Ion Beam Induced Charge Collection experiments, GEANT4 simulations, SOI system development and was also supported by Dr Iwan Cornelius from the Centre for Medical Radiation Physics.

Dr Carl Rossi and Dr Ryan Grover were always forthcoming in providing information on the clinical aspects of proton therapy both at Loma Linda and on our various cycling expeditions. These discussions were greatly appreciated.

Radiobiology and experimental cell survival work was a new field which I had limited practical experience. To this end the support and advice provided by Dr Diala Gridley and Melba Andres from Loma Linda University was invaluable for the success of this work. Further, the radiobiology protocol developed in this work required a large team of volunteers. I was fortunate enough to have support from Birgit Schulte, Chad Sila, Ying Nie and Chandima Ratnayake who gave up many nights and weekends to enable this data to be obtained. Their sacrifice is greatly appreciated.

Dr Alberto Fazzi and Dr Andrea Pola from Politecnico di Milano were of great support as part of the collaboration to evaluate the charge collection properties of the ΔE-E telescope with IBICC and obtain experimental results in hadron therapy.

Professor John Dicello and Professor Vince Pisacane were supportive in the development of SOI technology for space flight and assisted greatly in the acquisition of data both at USNA and NSRL. Their support in collaboration with Professor Anatoly Rosenfeld allowed this facet of the research to take place.

Adam Rusek and Mike Sivertz provided invaluable support during experiments at NSRL, and were largely responsible for the quantity and quality of the data obtained.

Bing Frazer, her colleagues at Loma Linda University and her family made my time in the US enjoyable through their assistance in making sure I not only succeeded professionally but experienced the culture of the US. For this I am thankful.

Finally to my family without whose constant support this thesis would not be completed today.

Abstract

This thesis further applies solid-state microdosimetry and low-pressure gas nanodosimetry to both radiation therapy and radiation protection. A number of unique applications have been identified where considerable advancements could be made with current technology and consequently have a significant bearing on developments in these fields.

Silicon-on-Insulator (SOI) microdosimetry technology was utilised to provide a complete and detailed analysis of out-of-field dose equivalents for proton therapy. The superior device spatial resolution and established quality factors of the microdosimetry method allowed for a new perspective on this issue. Microdosimetric measurements within heterogeneous tissue equivalent phantoms were also completed to discern measurable changes in radiation field as a function of preceding phantom material and if such changes should be included in treatment planning calculations. These measurements were correlated with Monte Carlo simulations for experimental validation and further analysis of treatment planning parameters.

The application of SOI microdosimetry to space radiation was also tested with an experimental and theoretical analysis. Experimentally the devices were tested within homogeneous Perspex phantoms irradiated with a range of heavy ions including iron, titanium and oxygen. The microdosimetric parameters of these fields and the ability of the SOI microdosimeter to be applied in such fields was evaluated and established. This was further supported through theoretical simulations of the SOI microdosimeters response to solar protons prior to their deployment aboard the MidSTAR-I satellite. It is expected that such devices will make a valuable contribution evaluating the complex radiation field in space while at the same time establishing improvements for the next generation of devices.

A new monolithic silicon ΔE-E telescope was evaluated in hadron therapy applications, obtaining data for both modulated and un-modulated therapeutic proton beams. This detector system provides two-dimensional information on LET and particle

identification that is based on energy depositions, collected in coincidence, within the ΔE and E stages of the detector. This apparatus is advantageous over existing systems, that provide one-dimensional information on the lineal energy or LET spectra, as it allows for particles of differing type yet the same LET to be identified separately and the corresponding difference in both energy deposition properties and biological effect accounted for. To achieve this, a correlation matrix based on established in-vitro biology data was developed and verified to link the output of such a device directly to in-vitro radiobiological effect. This system has great application to both hadron therapy and radiation protection as it may provide a means for accurate real time analysis of the radiobiological properties of a complex mixed radiation field. It could be expected that such a system may form the basis of radiobiological treatment planning in hadron therapy.

Nanodosimetry is the next logical extension from microdosimetry, providing information on radiation track structure at a DNA or nanometre level which is dependant on particle type and energy. Experimental results were obtained for a range of proton energies and the results compared with Monte Carlo simulation codes in an effort to both validate these codes and evaluate the performance of the low-pressure gas nanodosimeter. The initial development of a biophysical model in nanodosimetry was also presented, which will be further developed in future work. A requirement for such development is accurate biological data for low energy ion radiations. To this end cell survival work was completed on a human glioma cell line for a range of proton energies and Co-60 control with the development of a thin-film cell survival protocol. It is expected that the expansion of this radiobiology protocol will allow for the further correlation of cell survival with ΔE-E telescope and nanodosimetry output. Such correlation and biophysical model development is useful in hadron therapy treatment planning and radiation protection applications as it directly links a measured physical quantity to biological effect through models that are based on accurate experimental data.

Contents

List of Publications

The author contributed to the following papers that have been published in peer reviewed journals:

1. A.Rosenfeld, **A.Wroe**, I.Cornelius, D.Alexiev, M.Reinhard "Analysis of inelastic interactions for therapeutic proton beam using Monte Carlo simulations", IEEE Trans. on Nucl. Sci , 51, 6, pp. 319-325, 2004

2. **A. J. Wroe**, I. M. Cornelius, A. B. Rosenfeld, V. L. Pisacane, J. F. Ziegler, M. E. Nelson, F. Cucinotta, M. Zaider, J. F. Dicello, "Microdosimetry simulations of solar protons within a spacecraft," IEEE Transactions on Nuclear Science, Volume 52, Issue 6, Part 1, pp. 2591 – 2596, 2005

3. **A. J. Wroe**, I. M. Cornelius, A. B. Rosenfeld, "Role of inelastic reactions in absorbed dose distribution from proton therapeutic beam in different medium," Med Phys. 32, pp. 37-41, 2005

4. Reinhard W. Schulte, Vladimir Bashkirov, Márgio C. Loss Klock, Tianfang Li, **Andrew J. Wroe**, Ivan Evseev, David C. Williams, Todd Satogata, "Density resolution of proton computed tomography: Results of a Monte Carlo simulation study," Med Phys. 32, pp. 1035-46, 2005.

5. **A.J. Wroe**, R. Schulte, V. Bashkirov, A.B. Rosenfeld, B. Keeney, P. Spraldin, H.F.W. Sadrozinski, B. Grosswendt, "Nanodosimetric Cluster Size Distributions of Therapeutic Proton Beams", IEEE Transactions on Nuclear Science, Volume 53, Issue 2, pp. 532 – 538, 2006

6. Reinhard Schultę, Vladimir Bashkirov, Sergei Shchemelinin, Amos Breskin, Rachel Chechik, Guy Garty, **Andrew Wroe**, Bernd Grosswendt, "Mapping the Sensitive Volume of an Ion-Counting Nanodosimeter," Journal of Instrumentation, Vol. 1, P04004, April 2006.

7. **A. J. Wroe**, A. B. Rosenfeld, I. M. Cornelius, D. Prokopovich, M. Reinhard, R. Schulte, V. Bashkirov, "Silicon Microdosimetry in Heterogeneous Materials:

Simulation & Experiment," IEEE Transactions on Nuclear Science, Volume 53, Issue 6, pp. 3738 – 3744, 2006

8. Anatoly Rosenfeld, **Andrew Wroe**, Martin Carolan, Iwan Cornelius, "Method of Monte Carlo verification in Hadron Therapy with non-tissue equivalent detectors," SSD 2004 Special Issue Article, Radiation Protection Dosimetry, Volume 116, Issue 1-4, pp. 487-490, 2006.
9. V. Bashkirov, R. Schulte, A. Breskin, R. Chechik, S. Schemelinin, G. Garty, **A.Wroe**, H. Sadrozinski, B. Grosswendt, "Ion-counting nanodosimeter with particle tracking capabilities," Radiation Protection Dosimetry, Volume 122, pp. 415-419, 2006
10. V. L. Pisacane, Q. E. Dolecek, F. Maas, M. E. Nelson, P. J. Taddei, Z. Zhao, J. F. Ziegler, P. C. Acox, M. Bender, J. D. Brown, T. Garritsen, C. Gaughan, A. Hough, B. Kolb, J. Langlois, J. Ross, M. Sheggeby, D. Thomas, J. F. Dicello, F. A. Cucinotta, M. Zaider, A. B. Rosenfeld, and **A. Wroe**, "MIcroDosimeter iNstrument (MIDN) on MidSTAR-I," SAE Transactions Journal of Aerospace, vol. 2006-01-2146, 2006.
11. I. Cornelius, A. Rosenfeld, M. Reinhard, A. Fazzi, D. Prokopovich, **A. Wroe,** R. Siegele, A. Pola, S. Agosteo; "Charge collection imaging of a monolithic ΔE-E telescope for radiation protection applications," Radiation Protection Dosimetry, Volume 122, pp. 387-389, 2006
12. **A. J. Wroe**, A. B. Rosenfeld, R. W. Schulte; "Out-Of-Field Dose Equivalents Delivered by Proton Therapy of Prostate Cancer," Medical Physics, Vol. 34, Issue 9, pp. 3449-3456, 2007.
13. **A. Wroe**, A. Rosenfeld, M. Reinhard, V. Pisacane, J. Ziegler, M. Nelson, F. Cucinotta, M. Zaider, J. Dicello, "Solid State Microdosimetry with Heavy Ions for Space Applications," IEEE Transactions on Nuclear Science, in print 2007.

List of Conferences

The author's research was presented at the following conferences:

2007:

- **IEEE National Space and Radiation Effects Conference, Hawaii USA**
  - Solid State Microdosimetry with Heavy Ions for Space Applications (oral)

- **IEEE Nuclear Science Symposium and Medical Imaging Conference, Hawaii USA**
  - Test of Silicon Microdosimeters on a 100 MeV Proton Therapy Beam
  - Silicon detector telescope for radiobiological efficiency and Monte Carlo verifications in ion therapy (poster)

- **Image Guided Radiotherapy Conference, University of Wollongong, Wollongong Australia**
  - Comparison of Measured Neutron Doses delivered by Proton Treatments (oral)

2006:

- **Radiation 2006: Sydney University, Sydney Australia**
  - Nanodosimetric cluster size distributions of a 250MeV therapeutic proton beam (poster/oral).
  - Ion-counting Nanodosimeter with Particle Tracking Capabilities (poster).
  - Investigation of microdosimetric spectra within heterogeneous structures (oral).
  - Preliminary investigation of a Test Strip for Low-Energy Ion Radiobiology (poster).
  - Microdosimetry simulations of solar protons within a spacecraft (poster).
  - Suitability of a SOI microdosimeter for personal monitoring in mixed gamma neutron fields (oral)
  - The use of the GEANT4 toolkit at the CMRP: application to radiation protection, oncology and medical imaging (poster)
  - Monolithic silicon ΔE-E telescope for heavy ions and microdosimetry: IBIC characterization (poster)

- **International Conference On Environmental Systems, Virginia USA**
  - MIDN, A MIcroDosimeter iNstrument for Space Exploration (poster)

- **IEEE National Space and Radiation Effects Conference, Florida USA**
  - Microdosimetric Spectra within Heterogeneous Tissue Equivalent Structures (poster)

- **Australian High Energy Physics Meeting, Melbourne Australia**
  - Microdosimetry in Space and Proton Therapy: GEANT4 simulations and experimental results Exploration (oral)
  - Ion Beam Induced Imaging of a Monolithic Silicon Telescope (oral)

- **Loma Linda University Annual Postgraduate Conference, California USA**
  - Preliminary investigation of a Test Strip for Low-Energy Ion Radiobiology (poster)

- **Engineering and Physical Sciences in Medicine 2006: Noosa, Australia**
  - Validation and Verification of techniques in low-pressure gas nanodosimetry (oral).

- **PTCOG 2006: MD Anderson, Houston TX USA**
  - Secondary Neutron Doses delivered by Proton Treatments (oral).
  - Investigation of the Suitability of Tissue Equivalent Materials for Proton Therapy Treatment Planning (poster)

- **IEEE Nuclear Science Symposium and Hadron Therapy Workshop 2006: San Diego, CA USA**
  - Microdosimetry within Heterogeneous Tissue-Equivalent Structures (oral)
  - Investigation of the Suitability of Tissue Equivalent Materials for Proton Therapy Treatment Planning (oral)

- **International Symposium on Developing and Understanding a Hospital Based Proton Therapy Facility: Palm Springs, CA USA**
  - Neutron Dose delivered by Proton Treatments (oral).

- **Radiation Research Conference: Philadelphia, PA USA**
  - The Frequency of Ionisation Clusters produced by Protons in the Therapeutic Energy Range (poster).

2005:

- **International Workshop on Micro- and Mini-Dosimetry, University of Wollongong, Wollongong Australia**
  - Ion-counting Nanodosimeter with Particle Tracking Capabilities (oral).
  - Investigation of microdosimetric spectra within heterogeneous structures (oral).
  - Microdosimetry simulations of solar protons within a spacecraft (poster).
  - Nanodosimetric cluster size distributions of a 250MeV therapeutic proton beam (poster).

- **Radiation Research Society, Colorado USA**
  - Investigation of microdosimetric spectra within heterogeneous structures (oral).

- **IEEE National Space and Radiation Effects Conference, Seattle USA**
  - Microdosimetry simulations of solar protons within a spacecraft (poster).

- **14th International Symposium on Microdosimetry, Venezia Italy**
  - Ion-counting Nanodosimeter with Particle Tracking Capabilities (oral).
  - MIcroDosimeter iNstrument (MIDN) for Space Flight (poster).

- **Young Australian Researchers Forum, Australian Institute of Physics Congress, Canberra Australia**
  - A new millennia of Medical Physics Research at CMRP (oral).
  - Nanodosimetric cluster size distributions of a 250MeV therapeutic proton beam (poster).

- **GEANT4 10th user conference and collaboration workshop, Bordeaux France**
  - Use of the GEANT4 Toolkit at the CMRP: Application to Radiation Protection, Radiation Oncology, and Medical Imaging (poster).

- **IEEE Nuclear Science Symposium and Medical Imaging Conference, Puerto Rico**
  - Response of a SOI Microdosimeter to a 238PuBe Neutron Source (oral).
  - Ion beam induced charge imaging of a monolithic silicon telescope. (oral).

- **University of Wollongong Careers Fair, University of Wollongong, Wollongong Australia**
  - Microdosimetry and Nanodosimetry in Proton Therapy (oral).

2004:

- **IEEE Nuclear Science Symposium, Medical Imaging Conference, Symposium on Nuclear Power Systems and the 14th International Workshop on Room Temperature Semiconductor X- and Gamma- Ray Detectors, Rome Italy**
  - Nanodosimetric cluster size distributions of a 250MeV therapeutic proton beam (poster).

- **14th International Conference on Solid State Dosimetry, Connecticut USA**
  - Method of Monte Carlo Simulation Verification in Hadron Therapy with Non-tissue Equivalent Detectors (poster).

- **Health Week, Wollongong Hospital, Wollongong Australia**
  - Medical Microdosimetry & Nanodosimetry. Measuring Radiation Interactions on the Cellular and DNA Level (poster).

- **Australian High Energy Physics Meeting, Wollongong Australia**
  - Nanodosimetric Cluster Size Distributions from 250MeV Protons (oral)

- **Experimental Radiation Oncology Conference, Newcastle Australia**
  - Nanodosimetric Cluster Size Distributions from 250MeV Protons (oral).

- **University of Wollongong Physics Information Seminars, University of Wollongong, Wollongong Australia**
  - Proton Therapy and Dosimetry (oral)

- **Insight Oceania Curie Prize, St Vincents Hospital Sydney Australia**
  - Nanodosimetric Cluster Size Distributions from 250MeV Protons (oral).

- **Physics in Industry Day, University of Western Sydney, Sydney Australia**
  - Measuring Radiation Interactions on the Cellular and DNA Level (poster/oral).

2003:

- **IEEE Nuclear Science Symposium, Medical Imaging Conference, Portland USA**
  - Towards RBE Based Treatment Planning in Proton Therapy (poster).

- **Australian High Energy Physics Meeting, Wollongong Australia**
  - Simulation of Dose from Primary and Secondary Particles in a Proton Therapy Beam using the GEANT4 Monte Carlo Toolkit (oral)

- **Experimental Radiation Oncology Conference, St George Hospital Australia**
  - Simulation of Dose from Primary and Secondary Particles in a Proton Therapy Beam using the GEANT4 Monte Carlo Toolkit (oral).

List of Figures

List of Tables

List of Equations

Glossary of Abbreviations

ANSTO.....	Australian Nuclear Science and Technology Organisation
BNCT.....	Boron Neutron Capture Therapy
BNL.....	Brookhaven National Laboratory
BP.....	Bragg Peak
BREP.....	Boundary-Represented
CCE.....	Charge Collection Efficiency
CMRP.....	Centre for Medical Radiation Physics
CRO.....	Cathode Ray Oscilloscope
CSD….....	Cluster Size Distribution
CSG.....	Constructed Solid Geometry
DAQ.....	Data Acquisition System
DMEM.....	Dulbecco's Modified Eagle's Medium
DSB….....	Double Strand Break
FBS.....	Foetal Bovine Serum
FNT.....	Fast Neutron Therapy
FWHM.....	Full Width at Half Maximum
HCL.....	Harvard Cyclotron Laboratory
HIT.....	Heavy Ion Therapy
IBICC.....	Ion Beam Induced Charge Collection
IC….....	Ionisation Chamber
ICRP.....	International Commission on Radiological Protection
ICRU.....	International Commission on Radiation Units
IMRT.....	Intensity Modulated Radiation Therapy
IMXRT.....	Intensity Modulated X-Ray Radiation Therapy
ISS.....	International Space Station
LET.....	Linear Energy Transfer
LLUMC.....	Loma, Linda University Medical Center
MC.....	Monte Carlo

MCS….....	Mean Cluster Size
MD.....	Microdosimeter
MPRI.....	Midwest Proton Radiotherapy Institute
NCD.....	Nanodosimetric Cluster Distribution
ND.....	Nanodosimeter
NSRL.....	NASA Space Radiation Laboratory
OD.....	Optical Density
PE……....	Plating Efficiency
PEDR.....	Peak to Entrance Dose Ratio
PET.....	Positron Emission Tomography
PSI.....	Paul Scherrer Institute
PT.....	Proton Therapy
PTB….....	Physikalisch-Technische Bundesanstalt
QA.....	Quality Assurance
RBE.....	Radiobiological Effect
RI….....	Recycling Integrator
RPP.....	Right-Angled Parallelepiped
SEM….....	Secondary Electron Emission Module
SEP.....	Solar Energetic Particle
SOBP.....	Spread Out Bragg Peak
SOI.....	Silicon on Insulator
SSB….....	Single Strand Break
SV.....	Sensitive Volume
TE.....	Tissue Equivalent
TEPC.....	Tissue Equivalent Proportional Counter
UoW.....	University of Wollongong

1 Thesis Outline

This section provides a summary of the individual research components making up this thesis.

Chapter 1: Thesis outline, identifying and describing major research components.

Chapter 2: Literature review of areas of research and concepts introduced and discussed within the scope of this work. Concepts discussed include radiation interactions, hadron therapy, microdosimetry, nanodosimetry, Monte Carlo simulations and radiobiology.

Chapter 3: Outlines the process used in benchmark testing of the SOI microdosimeters used in this work. The SOI experimental system is also described with emphasis on noise levels and energy calibration.

Chapter 4: Describes an area of work where the SOI microdosimeter was used to evaluate the dose equivalent external to a typical radiation field used in proton therapy of prostate cancer. The results provide a through three-dimensional analysis of the dose equivalent with appropriate benchmarking to existing data.

Chapter 5: The SOI microdosimeter is used to validate a GEANT4 based application that simulates the response of the device within heterogeneous tissue equivalent phantoms irradiated with therapeutic protons. The change in microdosimetry spectra as a function of preceding material is investigated and reported with relation to treatment planning in proton therapy.

Chapter 6: A GEANT4 based investigation into the effect of tissue equivalent material composition on the transport of therapeutic protons. ICRP, commercially available and water equivalent materials of the same tissue type were comparatively tested using depth dose profile, lateral beam profile and microdosimetry.

Chapter 7: Testing of the SOI microdosimeter to radiation fields that will be encountered in a space deployment is presented. GEANT4 simulations exhibit the response of the SOI microdosimeter to solar protons within various conditions encountered in orbital space deployment. Experimental measurements have been completed to assess the performance of the SOI microdosimeter to heavy ion radiation fields and determine its applicability to deep space deployment. Monte Carlo simulations are also presented that assess the effect of silicon sensitive volume size on detector performance.

Chapter 8: Investigation of the response of a new ΔE-E telescope to therapeutic proton radiation. Comparative SOI microdosimetry measurements were also completed to assess the performance of the new detector apparatus. In parallel, a radiobiological effect matrix has been developed that directly links the output of the ΔE-E telescope to in-vitro biological effect.

Chapter 9: Presents an analysis of low-pressure gas nanodosimetry to various proton energies and benchmarking with existing Monte Carlo simulation systems. Further directions including detector, biological model and Monte Carlo simulation system development are also addressed.

Chapter 10: Describes the development of a thin-film cell survival protocol for use with high-LET, low energy charged hadrons. This protocol has been tested using a human glioma cell line and evaluated for further work in obtaining radiobiological data for micro- and nanodosimetric model development.

Chapter 11: Overall conclusions of the thesis. This is in addition to the concluding remarks and recommendations for future work contained within each chapter.

Note that the language used in this thesis is Australian English, while the referencing system employed corresponds to the IEEE standard.

2 Introduction

2.1 Purpose of Work

The purpose of this work was to further apply solid state microdosimetry and low-pressure gas nanodosimetry to radiation therapy and radiation protection applications. This involved experimental measurements for a range of radiation species and energies typically encountered both in radiation therapy and the space environment. Measurements were made in free air and within homogeneous and heterogeneous phantoms of both the primary and secondary radiation spectra to assess both the performance of the devices and the applied radiation field. In addition to testing the output and applicability of these devices, measurements allowed for the validation of Monte Carlo systems developed to theoretically simulate device response. Once verified these simulations will provide powerful tools that can be applied to a wide range of applications and remove some of the burden placed on experimental measurements.

One of the main advantages of these detector systems is that they have the ability to measure radiation events on the cellular and DNA level. In conjunction with an appropriate biological model it is possible to convert the measured physical quantity to actual in-vitro or in-vivo biological effect of the applied radiation field. Such models were developed and tested in this work to provide in-vitro biological effect from a measured physical quantity, further expanding the use of these technologies in radiation therapy and radiation protection. To further ensure the continued development of the biological modelling to other mammalian cell lines and incident radiation species a thin-film cell survival protocol was developed and tested.

The overall goal of this work was to provide further testing of micro- and nanodosimetry, develop Monte Carlo simulation systems to investigate their performance, link the output of such detectors to biological effect and put in place procedures and protocols to further the development of these technologies.

2.2 Radiation Interactions

Understanding radiation interactions in matter is essential to assess the impact of such interactions at a biological level and simulate these interactions within a Monte Carlo framework. Within this thesis the primary radiations to be investigated are hadrons including protons and heavy ions. However, such particles produce secondaries including neutrons, heavy charged particles, fragments, electrons and photons the associated interactions must be understood and accounted for correctly and accurately. This section will provide an in depth analysis of charged hadron interactions, with an overview of secondary particle interaction mechanisms.

2.2.1 Charged Hadron Interactions

Charged hadrons, including protons, have various mechanisms through which they can interact as they traverse through a material. Due to the charged nature of such particles, interactions occur primarily with the electrons and electric field surrounding the target nucleus, however, it is also possible for the particle to interact directly with the nucleus in what is termed a nuclear interaction. The main classes of interactions for protons and charged hadrons are:

- Electronic Interactions with Individual Electrons
- Multiple Coulomb Scattering at Small Angles
- Elastic Nuclear Interactions
- Inelastic Nuclear Reactions

2.2.1.1 Electronic Interactions with Individual Electrons

As the name suggests, in this interaction the charged hadron will interact with a single bound electron of the target nucleus and either excite the electron and/or ionise the target atom or molecule. This type of interaction forms a bulk of the charged hadron's energy loss as it traverses a medium. Electronic interactions with individual electrons can be classed as being either inelastic or elastic in nature depending on the following factors:

- The collision is considered to be **inelastic** if the electron receives enough energy to either excite it to a higher energy level within the shell structure of the target atom, OR if the electron receives enough energy to eject it into an unbound state. A

diagram indicating the ionisation of an atom through the ejection of an electron is illustrated in Figure 2-1.

- If the amount of energy transferred to the electron is insufficient to either eject it to an unbound state or excite it to a higher energy level (this is known as a sub-excitation collision) then the collision is considered **elastic** where both energy and momentum are conserved.

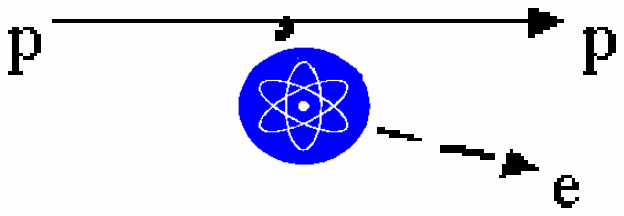

Figure 2-1: An electronic interaction between an incident proton and a single bound electron. Note how the electron is ejected from the shell structure of the target atom, ionising the atom.

It is only the inelastic interactions between the charged hadron and the electron that contribute to dose within the patient, as the unbound electrons deposit energy at target sites away from the point off interaction.

2.2.1.2 Multiple Coulomb Scattering at small angles

In Multiple Coulomb Scattering at small angles the incident hadron approaches the target nucleus and it is the interaction of their electric fields that produces the scattering. The interaction between the electric fields of both the hadron and target nucleus can cause either the hadron to be scattered with a reduced energy or both the nucleus and hadron to be scattered at angles to one another. In this case only glancing interactions between the hadron and the target nucleus are considered, where the hadron is deflected by a small angle θ from its original track with reduced energy P' which is depicted in Figure 2-2.

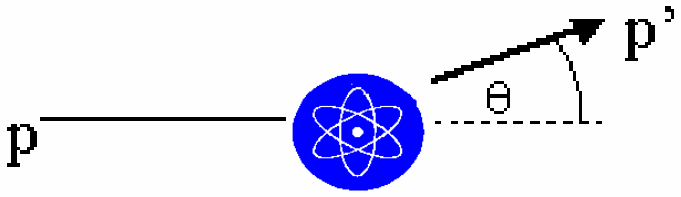

Figure 2-2: A multiple Coulomb scattering event at a small angle. Note how the proton is scattered at an angle θ with a reduced energy P'.

The fact that this is a glancing interaction, and the mass of the target nucleus can be many times that of the hadron, the nucleus itself does not recoil and as such no secondary particles such as neutrons, recoil protons or alpha particles are produced. As a result of this interaction no high LET secondary radiations are produced. Also, as the interaction only results in a small scattering angle, the energy of the hadron is not changed dramatically and as a consequence this is not a significant form of energy loss. What this interaction does do is cause the track of the hadron to be altered resulting in a spread of the hadron beam at depth, which is important in hadron therapy applications. When many of these interactions occur the hadron beam's collimation can be effected resulting in a widening of the penumbra as it moves through the medium.

2.2.1.3 Elastic Nuclear Reactions

Elastic nuclear interactions are also an interaction between the electric field of both the hadron and the target nucleus, however, unlike the instance of small angle scattering that was discussed previously, the scattering that takes place in an elastic collision is not a glancing one. Rather it results in a large scatter of the hadron with greater energy loss, and also in the target nucleus itself being scattered. As the name suggests the elastic nature of this reaction means that the total energy and thus momentum of the incident hadron and nucleus is conserved. An artist's representation of the process of elastic nuclear scattering is illustrated in Figure 2-3.

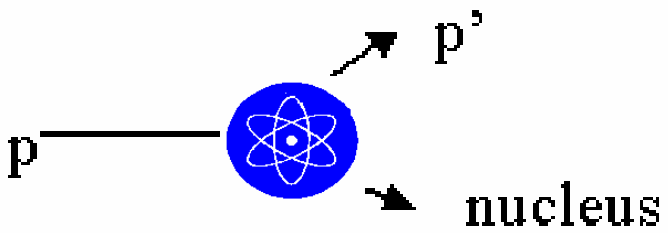

Figure 2-3: An elastic nuclear interaction. Note how in this interaction both the proton and nucleus are scattered.

The size of the target nucleus and the incoming hadron determines the extent of the scatter, as does the energy of the hadron. This type of scattering is more prevalent with lighter targets, lighter and more energetic hadrons (this is opposed to small angle scatter which occurs for larger target atoms). Once again in this interaction no high LET particles are produced from the nucleus. However, the scatter of the hadron, especially lighter species such as protons can be significant. It should be noted that as this interaction is considered elastic, both energy and momentum are conserved and no other particles are produced.

2.2.1.4 Inelastic Nuclear Reactions

The inelastic nuclear interaction is a case where the hadron interacts directly with the target nucleus. However, unlike the previous cases where only the hadron and possibly the nucleus were scattered, this form of interaction produces secondary particles (other than electrons) that are important to consider when determining the RBE. This is caused by the hadron overcoming the coulomb barrier and interacting directly with the nucleus resulting in a transfer of energy. This interaction has the ability to not only vary the hadron's energy and direction markedly, but also cause the nucleus to be elevated into an excited state. In order to move to a stable state, particles are ejected from the nucleus including recoil protons, neutrons, photons and alpha particles which is illustrated in Figure 2-4.

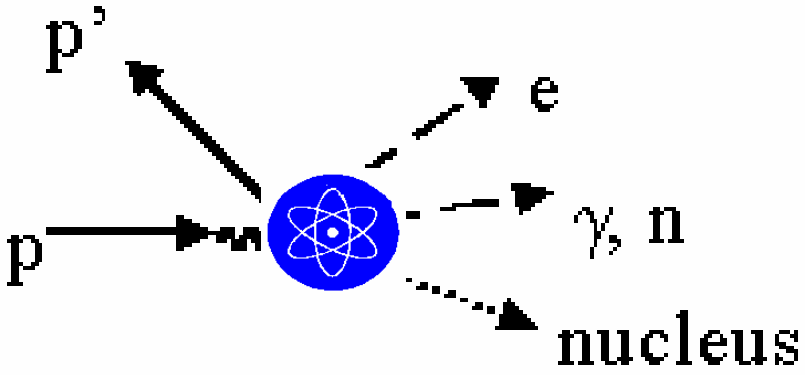

Figure 2-4: An inelastic nuclear reaction. Note how not only is the proton and target nucleus scattered but secondary particles such as neutrons, electrons and photons are also produced. Note that heavier particles can also be produced through such interactions including charged hadrons.

In the case of suitably large incident hadrons, fragmentation of the incident ion can also occur with the production of 2 or more products through direct interaction with the target nucleus. The products (whether components of the incident ion or fragments of the target nuclei) are generally of higher LET than the incident particle. These high LET particles can cause significant biological damage. However, neutrons and gamma photons produced in such interactions are also a concern as they can deposit dose past the Bragg peak (or at a depth greater than the range of the primary particle) due to their long path lengths.

2.2.2 Neutron Interactions

As neutrally charged hadrons, the interaction parameters for neutrons are very different from charged hadrons. While neutrons are electrically neutral, they do have magnetic moment, spin and a non-zero distribution of charge within them. It is these properties that allow the neutron to interact with the spin and charge of an electron giving rise to electromagnetic forces between electrons and neutrons. As these forces are extremely weak, interactions between electrons and neutrons can be considered negligible [1]. It is the absence of direct interaction between neutrons and electrons which contribute to the neutrons large path length through matter.

The predominant neutron interactions with matter occur when the neutron interacts directly with the nucleus of an atom. These interactions occur along three distinct

interaction pathways. The first is elastic scattering where the energy and momentum of the system is conserved. In this case the neutron will interact either with the nuclear field (shape elastic scattering) or overcome this field and be absorbed by the target nucleus and then re-emitted (compound elastic scattering). In this instance part of the neutrons energy may be transferred to the nucleus with the amount determined by the energy of the neutron, recoil angles and relative size of the ion. The energy lost by the neutron in this case is equal to the kinetic energy of the recoil nucleus. The second interaction pathway is in-elastic scattering. In this case the neutron interacts with the target nucleus depositing energy and causing it to move to an excited state. The nucleus can then return to a natural state through the emission of photons, neutrons and charged particles. Both inelastic and elastic scattering are the predominant sources for interaction at high neutron energies. However, as the neutron energy decreases the instance of neutron capture increases. Neutron capture occurs when the neutron is absorbed by the nucleus elevating the nucleus to an excited state. Again the nucleus can return to a relaxed state through the emission of photons, neutrons and charged particles. In both the case of inelastic scattering and neutron capture, the neutrons energy is transferred indirectly to the surrounding media via the secondary particles generated by these interactions.

2.2.3 Electron Interactions

As electrons are the predominant secondary particle species produced as charged hadrons traverse matter, their interaction properties are important to understand and consider. As negatively charged particles they can excite and ionise atoms in a similar fashion as charged hadrons. However, as electrons are considerably lighter than hadrons ($9.1x10^{-31}$kg) they can be deflected through interaction with the Coulomb force surrounding the atom. This deflection results in the emission of a photon to conserve the systems momentum. This process is known as Bremsstrahlung. Finally, in the presence of a positron (positively charged particle of the same mass of an electron), annihilation may occur with the emission of two 511 keV photons in opposite directions. This interaction is the basis for position emission tomography (PET) imaging in diagnostic studies.

2.2.4 Photon Interactions

Photons are uncharged and as such do not continually lose energy as they traverse matter. Rather they interact discreetly and rely on particles generated through excitation interactions to deposit energy in matter. There are four distinct pathways of interaction for photons that are governed through the photons energy and material being traversed [2]. The photoelectric effect occurs when a photon interacts directly with a bound electron. The photon is completely absorbed ejecting the electron, with the total kinetic energy of the electron equal to the energy of the photon minus the initial electron binding energy. In this interaction the photon is not re-emitted. As a general rule the photoelectric effect is dominant at low photon energies.

Compton scattering is similar to the photoelectric effect in that the photon interacts with a bound electron resulting in ionisation. However, in this case the photon transfers only part of its energy to the electron and is scattered with a reduced energy that is dependant on the final kinetic energy of the photon, kinetic energy of the electron, binding energy of the electron and relative scattering angles of the two particles.

Pair production is possible when the energy of the photon reaches twice the rest energy of an electron (i.e. 1.022 MeV) and increases in probability with increasing photon energy. In the presence of the Coulomb field of a nucleus the photon may disappear and be replaced with an electron-positron pair. The excess photon energy above 1.022 MeV will be shared by the two particles as kinetic energy. As the positron will normally annihilate after slowing, a pair of annihilation photons will also be produced by this interaction.

Finally, Coherent or Rayleigh scattering occurs when the photon interacts coherently with all the electrons of the atom transferring no energy and hence neither exciting nor ionising the atom. The result is a scattering of the photon with a change in direction but no change in energy. The probability of this interaction increases at low photon energies and in high-Z materials. Also the deflection angle of the photon decreases as the photon energy increases.

2.3 Proton & Heavy Ion Therapy

Presently one of the major health risks mankind faces is cancer. One in three people will suffer from this disease or side effects of its treatment at some stage in their life [3]. Because of the deleterious effects that cancer and often current treatment forms are having on the human population, better treatment techniques are constantly being sought. Besides surgery, external beam radiation therapy is a mainstay of cancer treatment and cure. High energy protons and hadrons such as carbon ions are an important innovation in external beam radiation therapy, providing highly conformal dose distributions, thus sparing normal tissues through the benefits afforded by the Bragg peak.

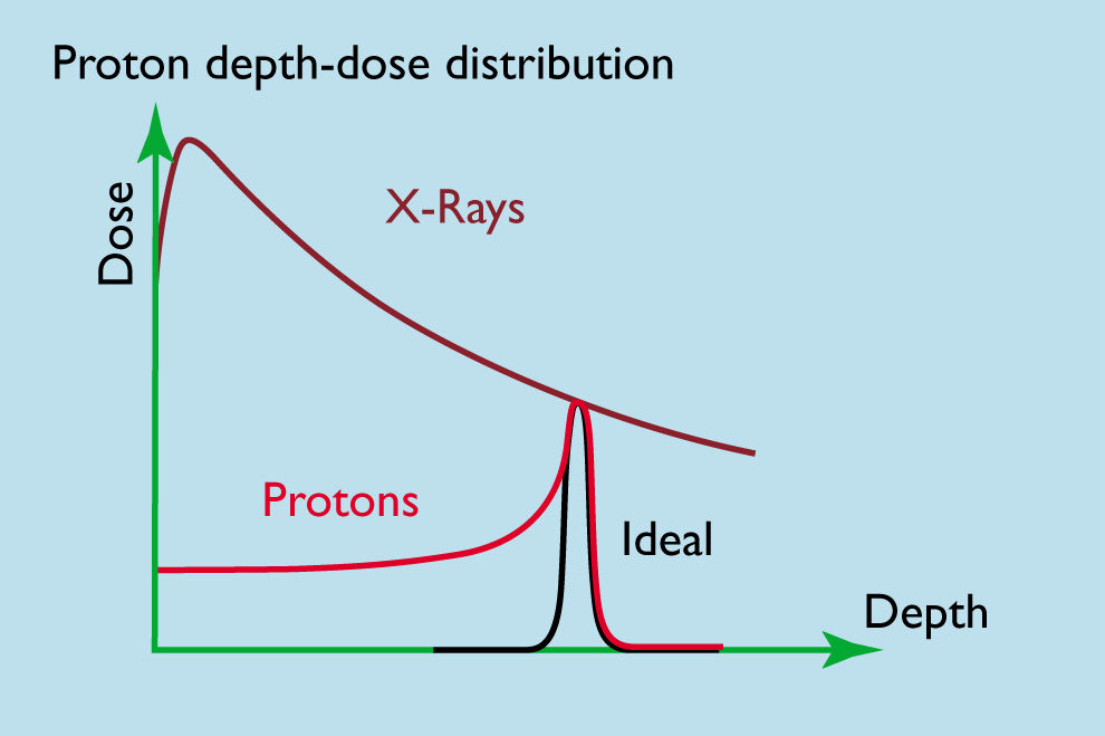

Figure 2-5: Depth dose distributions for X-rays, protons and the ideal distribution [4].

In radiation therapy it is desirable to maximise dose delivered to the tumour volume whilst minimising dose to surrounding normal structures. By varying the hadrons energy it is possible to place the Bragg peak at any point within the patient and hence within the tumour volume. Through the use of multiple convergent beams it is possible to magnify the dose to the tumour volume through superposition of multiple Bragg peaks. The depth dose profile of charged hadrons is in stark contrast to X-rays (considered as a standard

radiation modality), which achieve maximum dose either at or just below the surface of the patient. It is only through the superposition of multiple treatment fields that an elevated radiation dose to the target volume is achievable. However, the use of multiple fields results in a situation of large volumes of normal tissues receiving low doses of radiation, the effects of which are still unclear. Comparative plans for both Intensity Modulated X-Ray Radiotherapy (IMXRT) and proton therapy are displayed in Figure 2-6 and clearly indicate how protons have the potential to minimise dose to the surrounding structures.

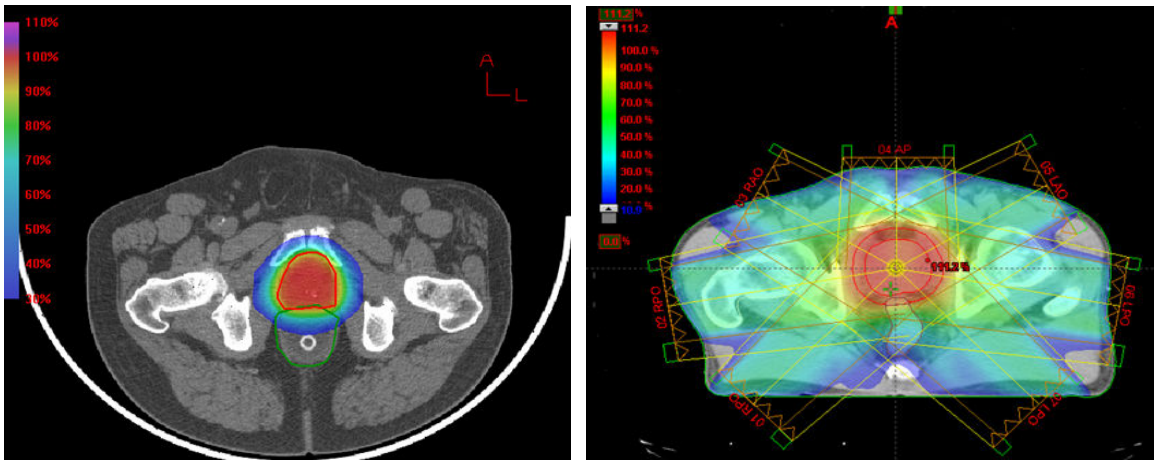

Figure 2-6: Comparative 7-field treatment plans for protons (left) and X-rays (right). Images provided courtesy of Dr C. Rossi.

A further advantage of protons is that past the Bragg peak no dose is delivered from the primary radiation field (some dose is delivered by secondary particles and nuclear fragments which will be discussed further in Section 4). This is a distinct advantage over X-rays as it allows for the sparing of sensitive structures such as the brainstem and bladder which may lie in close proximity to the tumour volume.

The use of fast protons as a clinical tool was first suggested by Wilson in 1946 [5] and was first used clinically in 1954 [4]. Since its inception, there have been many advances in areas including accelerator, focussing technologies and treatment planning. A typical proton therapy department is based around a single accelerator with multiple treatment rooms making it more complex and expensive than X-ray therapy which exists as "stand alone" modules. Proton delivery techniques can be categorized as passive or active in the

delivery of a uniform dose to the treatment volume. Passive techniques, which have been most commonly used in the clinical setting [6, 7] spread the beam laterally using a combination of gold and Lexan foils [8]. The combination of two materials, one of low and the other of high atomic number produces a flat beam of constant flux and a constant range. Typically a dual scattering foil arrangement [9] is utilised that is optimised to deliver a flat field of the cross sectional area required for treatment. The beam is then modulated in depth using a rotating plastic wheel [5, 10] that effectively allows for the superposition of multiple Bragg peaks of varying intensity to create a region of uniform high dose called the Spread-Out Bragg Peak (SOBP) [9]. The beam is then collimated by brass or Cerrobend® apertures and its penetration depth is varied by means of a wax bolus. Such an arrangement creates a uniform dose across the treatment volume as displayed in Figure 2-7.

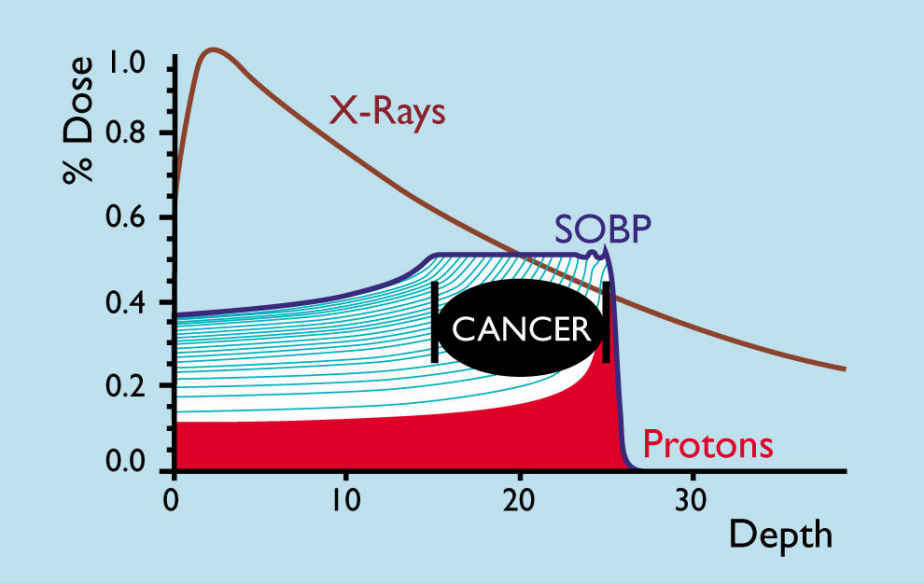

Figure 2-7: Comparison of the X-ray depth dose curve with the SOBP used in passive proton beam delivery for clinical treatment [4].

Active techniques [11-14], currently only practiced in a clinical situation at the Paul Scherrer Institute (PSI), employ a magnetically guided proton pencil beam in combination with dynamic changes of beam energy and beam intensity during treatment. One advantage of the active system is that it minimises interaction between the primary beam and beam modifying devices, in-turn minimising the production of secondary

particles. Further, it has the potential to treat complex tumour volumes with greater precision and improved normal tissue sparing. However, the dosimetry and beam delivery is also more complex and problematic as errors in this regard can lead to high and low dose regions and an incomplete treatment of the tumour volume. Organ motion during treatment is another complicating factor which also needs to be considered for effective and accurate treatment of the tumour volume.

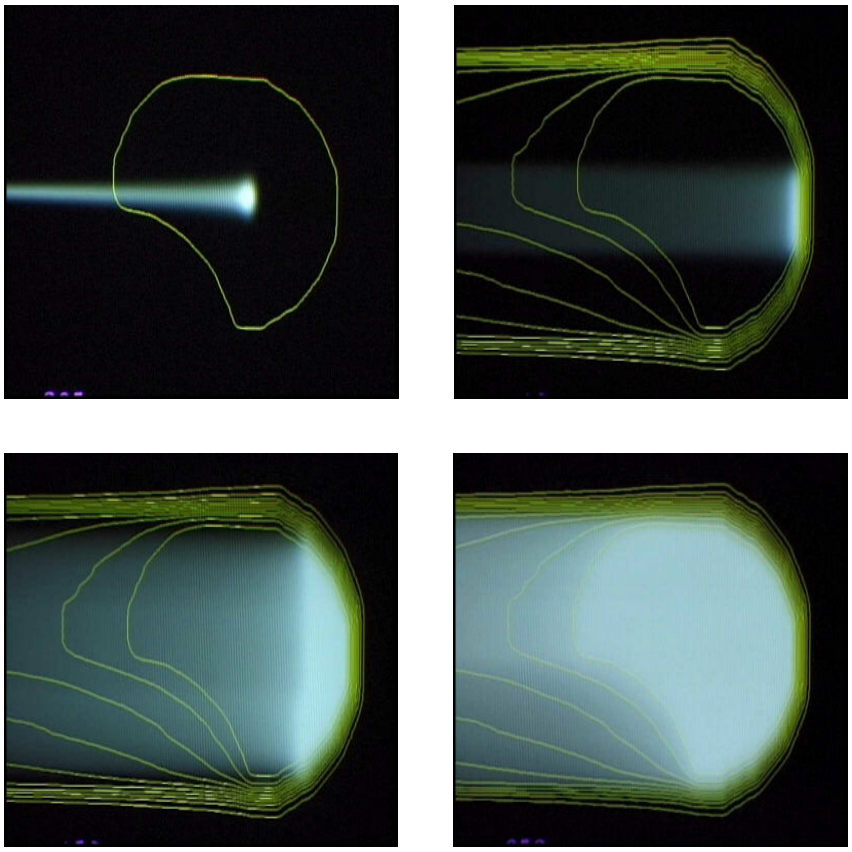

Figure 2-8: A representation of active scanning, illustrating how the superposition of multiple Bragg peaks or hot spots can be used to create a uniform dose across a desired volume of irregular shape [15].

Hadron therapy and its clinical applications have expanded over the last two decades. Currently there are approximately 20 proton therapy treatment sites worldwide with plans in progress to construct a further 20 [4]. Currently over 45,000 people have been treated using protons since 1954 with approximately 12,000 treated at Loma Linda University Medical Center (LLUMC) since 1990 [16]. With further developments in technology it is expected that proton and heavy ion therapy will continue to expand and develop.

2.4 Microdosimetry

Microdosimetry involves measuring the energy deposited within a micron ($1x10^{-6}$ m) scale. As radiation deposits energy in stochastic events the measurement of such depositions on a micron level may provide a more accurate analysis on the effect of such interactions on biologically important structures including cells (typically micrometres in size). Microdosimetry also has applications to single event upset (SEU) rates in space deployments of electronic systems [17], as junction sizes in electronic circuits are typically of the order of microns or smaller in size.

The standard measurement device for microdosimetry has been tissue equivalent proportional counters (TEPC) which have allowed for the effective measurement of energy depositions within an equivalent-micron sized volume. Typically such detectors are spherical in shape with an A-150 outer shell and tissue equivalent (TE) gas sensitive volume (SV). Such devices have an established track record in radiation protection and therapeutic applications [18-20] and are generally considered the standard detector modality for microdosimetry. The advantages of TEPC's for microdosimetry is that they provide an equivalent micron sized volume that is TE through the use of A-150 chamber walls and a TE gas SV. Further, as the SV is spherical in shape, the average chord length is well known and does not depend on incident field direction.

TEPC's do have disadvantages that are largely dependant on the field of application. Firstly, the device does not provide a truly microscopic SV, but rather achieves this through the scaling of the TE SV density. For quality assurance (QA) applications in hadron therapy a large TEPC is unsuitable for in-phantom measurements of radiation fields as they exhibit poor spatial resolution. In space deployments, TEPC's are less than ideal due to their large size, high power requirements and delicate construction. The advantages and disadvantages of TEPC's have been discussed in greater detail in [21].

Solid-state detectors providing a true microscopically small SV's are another option for microdosimetry. The first comparison of microdosimetric measurements between a spherical proportional counter and a single junction solid-state detector were made by Dicello [20]. In this case, a silicon detector of a large area with 7 μm thickness was used.

A new approach for silicon microdosimetry based on arrays of silicon SV's (pn-junctions) was proposed by McNulty and Roth [22, 23] for separation of gamma and neutron fields (no microdosimetric spectra was produced) and later an SOI microdosimeter was developed and applied to hadron therapy by Rosenfeld [24].

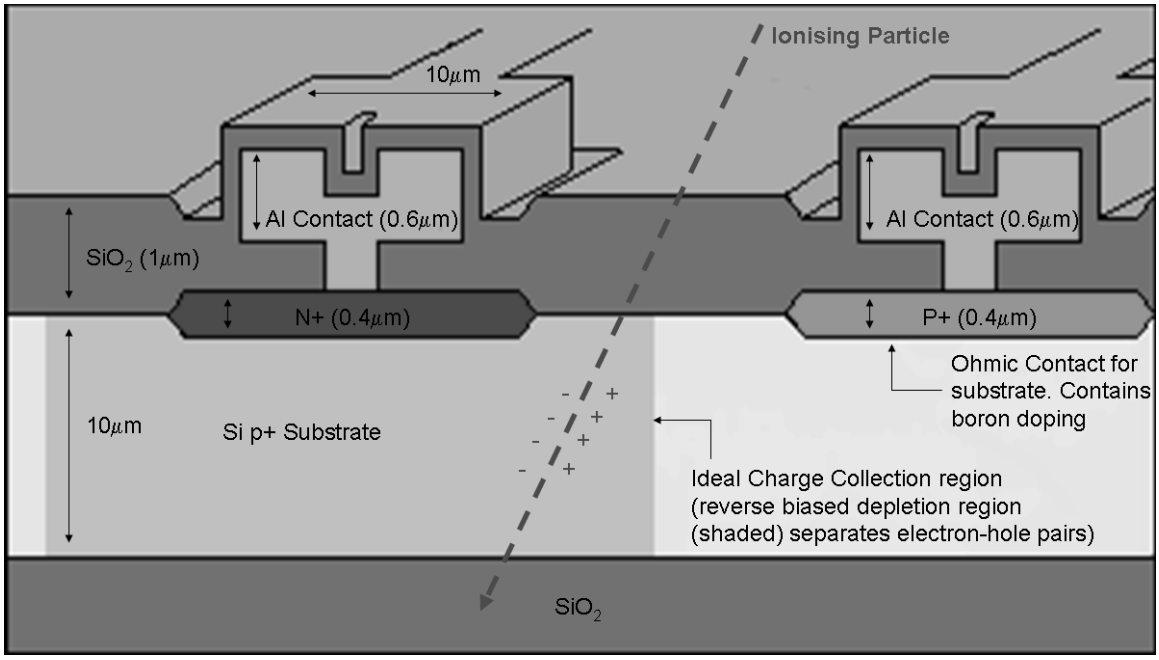

Figure 2-9: Schematic diagram of the SOI structure.

The main advantage of silicon microdosimeters is their compact size and low voltage for operation. However, previously they have suffered the drawback of the lack of a well-defined SV. A new approach to microdosimetry using Silicon-On-Insulator (SOI) technology has been developed at the Centre for Medical Radiation Physics (CMRP) at the University of Wollongong (Figure 2-9) and produced by Fujitsu. It comprises a 2D-diode array providing well-defined SV's and as such this microdosimeter has significantly improved performance [25] over previous attempts at solid state microdosimetry. Si substrate thicknesses of 2, 5 and 10 μm have been manufactured on a SiO_2 substrate with n+ and p+ regions formed through arsenic and boron implantation. The impurity concentration of the p-type Si is $1.5x10^{15}$ cm^3 [26].

Each Si cell is connected in parallel within the given array structure for signal collection. On each chip there are three functioning arrays each with different numbers of cells and cross sectional areas. This information is summarised in Table 2-1. The advantage of this system is that it allows arrays to be selected based on the application. For example, in the case of high flux radiation fields, a small array would be advantageous to minimise pileup in the detector.

Array	Cross Section (μm^2)	Detector Elements
1	120x120	150
2	120x120	50
4	30x30	4800

Table 2-1: Description of cross sectional area and number of sensitive detector elements which make up the three functioning arrays on each SOI microdosimetry chip [21].

There are some important considerations when using solid-state microdosimeters in dosimetry applications. Firstly, unlike the TEPC which is constructed of TE material, the tissue equivalence (or lack thereof) of a solid-state Si device needed to be considered and corrected for in generation of the microdosimetry spectra. This was addressed through experimental comparisons with TEPC chambers for neutrons and charged hadrons [25]. Through the use of a uniform scaling factor, based on the ratio of Si and TE stopping powers, applied to the average chord length it was possible to demonstrate the accuracy of the SOI device in producing reliable microdosimetry spectra. It should be noted that such a conversion factor is dependant on the induced radiation field and should be studied further for heavy ion radiation fields using comparative measurements and Monte Carlo simulations.

Secondly, the charge collection properties of the individual detection elements needed to be investigated and benchmarked. Artefacts within the energy deposition spectra can be attributed to variations in charge collection and were extensively tested through the use of Ion Beam Induced Charge (IBIC) imaging [27]. Finally, the performance of the device can be altered through exposure to radiation and the introduction of defects into the lattice structure of the semiconductor material. Such a change in performance is not experienced by gas counters (although the gas volume needs regular inspection for out-

gassing) and may have an impact on the long-term deployment of SOI microdosimeters into high radiation fields. The radiation hardness of these devices has been previously studied [28] and will be further considered in this work.

The SOI microdosimeter has been extensively tested in a wide range of radiation fields including those used in fast neutron therapy (FNT) [29], proton therapy within homogeneous phantoms [30] and boron neutron capture therapy [31] with microdosimetric spectra produced for analysis. It will be the work of this thesis to expand on previous studies and test the SOI microdosimeter in heavy ion radiation fields associated with space deployment, within heterogeneous phantoms for hadron therapy treatment planning applications and further extend the output of the device to include dose equivalent and average quality factor, complimenting microdosimetry spectra which has been generated in previous work.

2.5 Microdosimetric Quantities

Collection of raw data using a microdosimeter takes the form of energy deposition events within a micron sized SV. These single energy deposition events are collected to form a spectra (i.e. $f(E)$ Vs E). This spectra needs to be corrected for charge collection efficiency (CCE) of the device and converted to tissue equivalent material in the case of a Si device. For an SOI microdosimeter the CCE has been established as 0.8 [26, 27], which expresses how 80% of all charge deposited within the SV is collected and registered in the energy deposition spectra. This correction factor will be applied to all experimental SOI microdosimetry measurements made unless otherwise stated.

The quantity of interest in microdosimetry is lineal energy (y), which is a measure of the stochastic energy depositions along a given chord length in tissue. In this instance the lineal energy spectra ($f(y)$ Vs y) is obtained by dividing the energy spectra by the average chord length in tissue. The average chord length of any concave shape can be approximated using the relationship described in Equation 2-1. In the case of a spherical SV, typical in TEPC measurements, the average chord length is the 2d/3 where d is the diameter of the sphere.

$$< l >= \frac{4V}{A\zeta}$$

Equation 2-1: Expression to determine the average chord length, where V is the volume, A the surface area of the SV and ζ a TE conversion factor [32].

The TE conversion factor is used to determine the microdosimetry spectra in tissue from that which is detected in the silicon SV. From previous research [30] and comparisons with TEPC's the most appropriate value of ζ was determined to be ζ=0.63 which has been obtained through the ratio of ranges of charged particle relevant to radiotherapy applications in tissue and silicon. For the 30x30x10μm^3 sensitive volume typically used in this work the average chord length is 19.05μm.

More typically the lineal energy spectra is weighted by the lineal energy to give the dose weighted lineal energy spectra, which simply indicates how higher lineal energy events deposit more dose within the SV. The dose weighted lineal energy distribution is given by the relationship in Equation 2-2.

$$d(y) = \frac{yf(y)}{y_f} = \frac{yf(y)}{\int_0^\infty yf(y)dy}$$

Equation 2-2: *d(y)* relationship as used in microdosimetry work [32, 33].

The *y* Vs *d(y)* distribution gives the fraction of total absorbed dose in the interval $y \rightarrow y+dy$. By definition this distribution is normalised to unity and typically plotted as *yd(y)* Vs *log y*. Examples of experimentally obtained *f(E)* Vs *E*, *f(y)* Vs *y* and *yd(y)* Vs *y* distributions in a proton radiation field are provided in Figure 2-10.

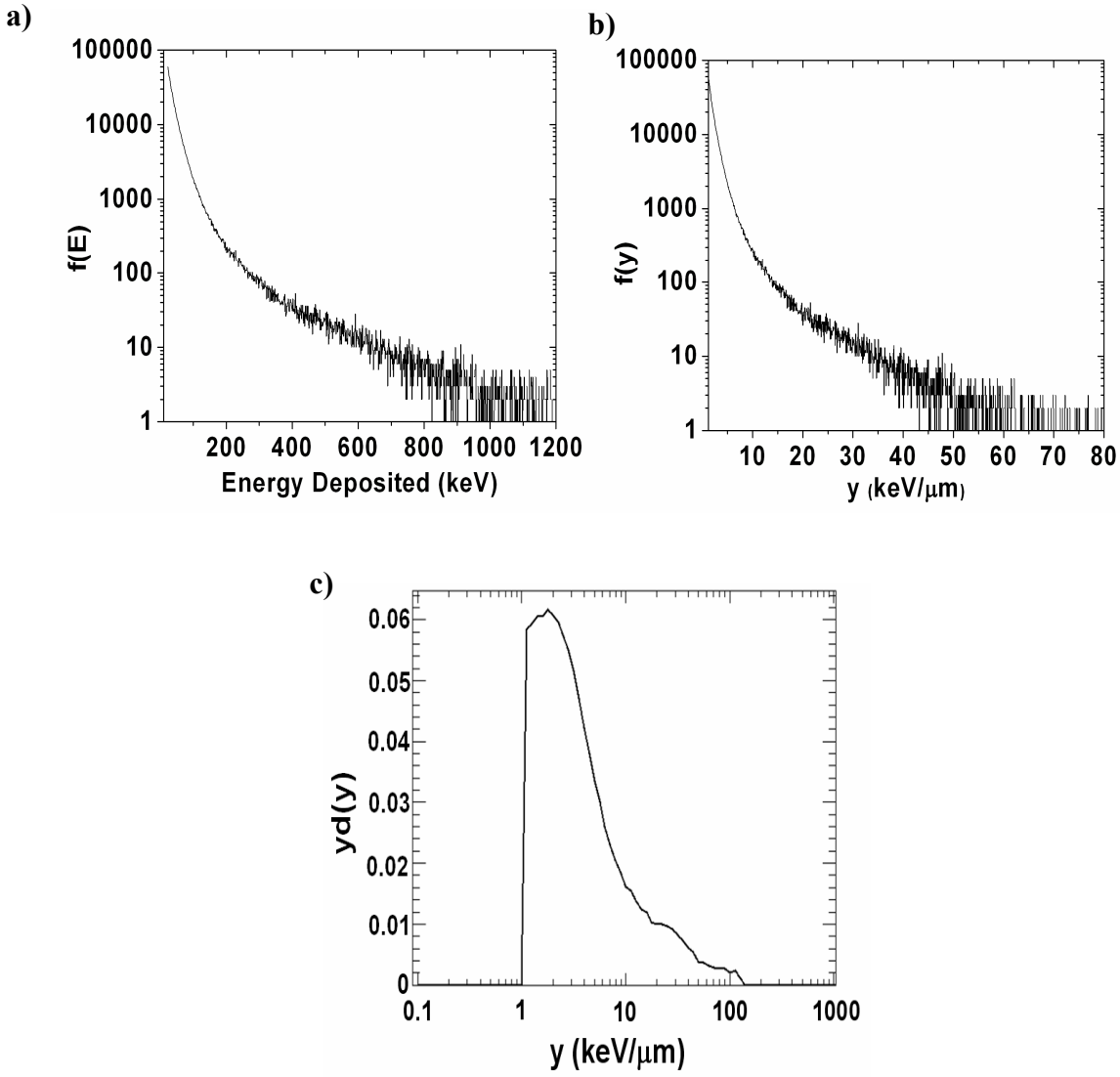

Figure 2-10: Examples of distributions obtained using the SOI microdosimeter including a) *f(E)* Vs *E* distribution; b) *f(y)* Vs *y* distribution; c) *yd(y)* Vs *y* distribution

From a microdosimetry distribution there are two quantities which may be observed that are of interest in determining the quality of the radiation field. These quantities are the frequency mean lineal energy ($\bar{y}_f$) and dose weighted mean lineal energy ($\bar{y}_d$) and are described in Equation 2-3.

$$\bar{y}_f = \frac{\int_0^\infty y f(y)dy}{\int_0^\infty f(y)dy} \qquad \bar{y}_d = \int_0^\infty y d(y)dy = \frac{1}{\bar{y}_f}\int_0^\infty y^2 f(y)dy$$

Equation 2-3: Relationship describing the frequency mean lineal energy ($\bar{y}_f$) and dose weighted mean lineal energy ($\bar{y}_d$)

The dose equivalent (*H*) was defined in [32] as a measure of radiation to identify and quantify the effects of ionizing radiation on health at a point in space. The unit of dose equivalent is the Sievert (Sv) with *Q* specified by the ICRU [34]. In this study, the method outlined in [32, 33] was used in the determination of *H* from measured microdosimetry spectra with specified *Q* values, that are dependant on lineal energy. The conversion of measured microdosimetry spectra to dose equivalent proceeds in two steps: (1) calculation of absorbed dose to tissue at each point of measurement, (2) calculation of the dose-averaged quality factor at that point.

$$H = QD$$

Equation 2-4: Definition of dose equivalent where *Q* is the average quality factor of the radiation field and *D* is absorbed dose in tissue at a given point of interest.

Microdosimetric data acquired as energy deposition spectrum *f*(*E*) Vs *E* when corrected for CCE can be used to calculate the absorbed dose to silicon by integrating over the spectrum (Equation 2-5).

$$D_{Si} = \frac{\int_0^\infty f(E)EdE}{\rho_{Si} V n_{cells}}$$

Equation 2-5: Determination of the absorbed dose in silicon, where n_{cells} is the number of SV's in a given array used (4800) [25], *V* is the volume of a 30x30x10μm^3 individual detection element, and the ρ_{Si} the density of silicon [35].

The tissue-equivalent (TE) dose D_{TE} can then be determined using Bragg-Gray cavity theory from the ratio of total stopping powers of protons for silicon S_{Si} and tissue S_{TE} assuming that all charged particles measured by SOI microdosimeter are crossers [35] (referred to in this document as TE conversion factor ζ). This is an advantage of the truly microscopically small SV available in SOI microdosimetry.

$$\frac{D_{Si}}{D_{TE}} = \frac{S_{Si}}{S_{TE}} = \zeta$$

Equation 2-6: Definition of the tissue equivalent conversion factor based on the ratio of relative stopping powers.

In order to determine dose equivalent a y-dependent quality factor $Q(y)$ is introduced [34] as shown in Figure 2-11.

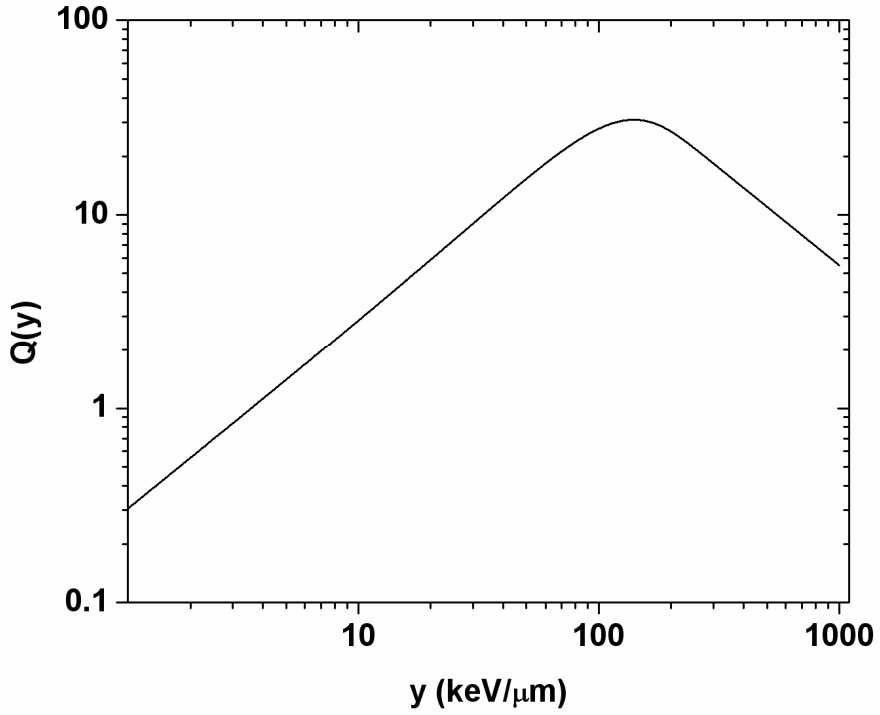

Figure 2-11: $Q(y)$ distribution as published within [34].

From the *d(y)* distribution, the dose equivalent at that point in space can be determined using the relationship in Equation 2-7.

$$H = D_{TE} \int_0^\infty Q(y) d(y) dy = Q_{avg} D_{TE}$$

Equation 2-7: Definition of dose equivalent using the microdosimetry method. Note that Q_{avg} is the average quality factor.

The ability of microdosimetry to determine average quality factor and dose equivalent makes it a very useful tool in a wide range of radiation fields for both radiation therapy and radiation protection. The methods outlined above will be used in analysis of both experimentally and theoretically obtained microdosimetric spectra.

2.6 Nanodosimetry

Presently the standard for measuring radiation is absorbed dose, which provides a macroscopic value for the energy deposited by radiation within a volume of a given mass (Equation 2-8). However, as understanding of cellular function and DNA develops it is desirable to measure the effects of radiation on a DNA level, as this could provide a more accurate assessment of the biological effect of various radiation fields.

$$Dose(Gy) = \frac{Energy(Joules)}{Mass(kg)}$$

Equation 2-8: Equation of Absorbed dose within a volume of a given mass.

Experimental nanodosimetry provides a means for determining the distribution of radiation-induced ionisations on a nanoscopic or DNA level [36-39]. Such a device would be useful in radiation therapy applications in determining the quality of the radiation at different levels within a patient and hence could be utilised in QA applications for treatment planning verification. Radiation protection is another field that would benefit from the development of nanodosimetry, including space travel and the deployment of electronic systems into this hazardous radiation environment. As in radiation therapy, nanodosimetry could be used to provide scientists with an improved understanding of the effects which space radiation (comprising of protons, photons,

electrons, neutrons and heavy ions) could have on personnel exposed to such conditions. In turn it could be used to optimise shielding structures that would limit the production of high LET secondary particles therefore minimising nanoscopic damage from stochastic events.

There is also another area where nanodosimetry could be applied within the radiation protection field. Before electronics can be deployed to a radiation environment they must be rigorously tested under the radiation conditions which they will experience during their operational lifetime. With electronics and particularly microchips becoming smaller and smaller, a device that can measure stochastic events at the sub micron level will be of use in predicting SEU rates and also in devising new shielding structures for such electronics in an effort to extend deployment lifetimes. In this case the nanodosimeter could be utilised in accelerator experiments to assess such radiation fields prior to radiation hardness testing. This will allow for the configuration and shielding of such electronics to be optimised prior to testing, which in turn may minimise costs incurred by such testing procedures and result in a longer deployment lifespan.

The measurement quantity in nanodosimetry is the frequency of radiation induced ionisation events within a low pressure gas volume. Per incident particle entering the SV there will be a certain number of ionisation events or cluster of events occurring within a nanometric sized SV which provides an indication of the ability of the radiation to damage biological and electronic systems. This leads to the two current forms of nanodosimetry that are based on counting the individual ionisation induced electrons or positive ions produced through radiation interaction within the SV.

2.6.1 Electron Based Nanodosimetry

Electron based nanodosimetry involves collecting free electrons from delta ray transport into a wall-less nanometric sized SV (see Figure 2-12) defined using electric fields. In this mode of detection the ion beam passes in close proximity to the SV and ionised electrons can be transported into the SV and counted to determine the properties of the radiation field. The species and energy of ion studied will have a unique electron distribution that can be used to determine biological effect. Such devices have been built,

tested and discussed previously [40, 41]. Electrons that enter the wall-less SV (defined by electric fields) are transported into a drift column to allow for separation of individual electrons. The individual electrons are then multiplied and counted to provide an assessment of the stochastic ionisation density of the radiation on a nanometric volume.

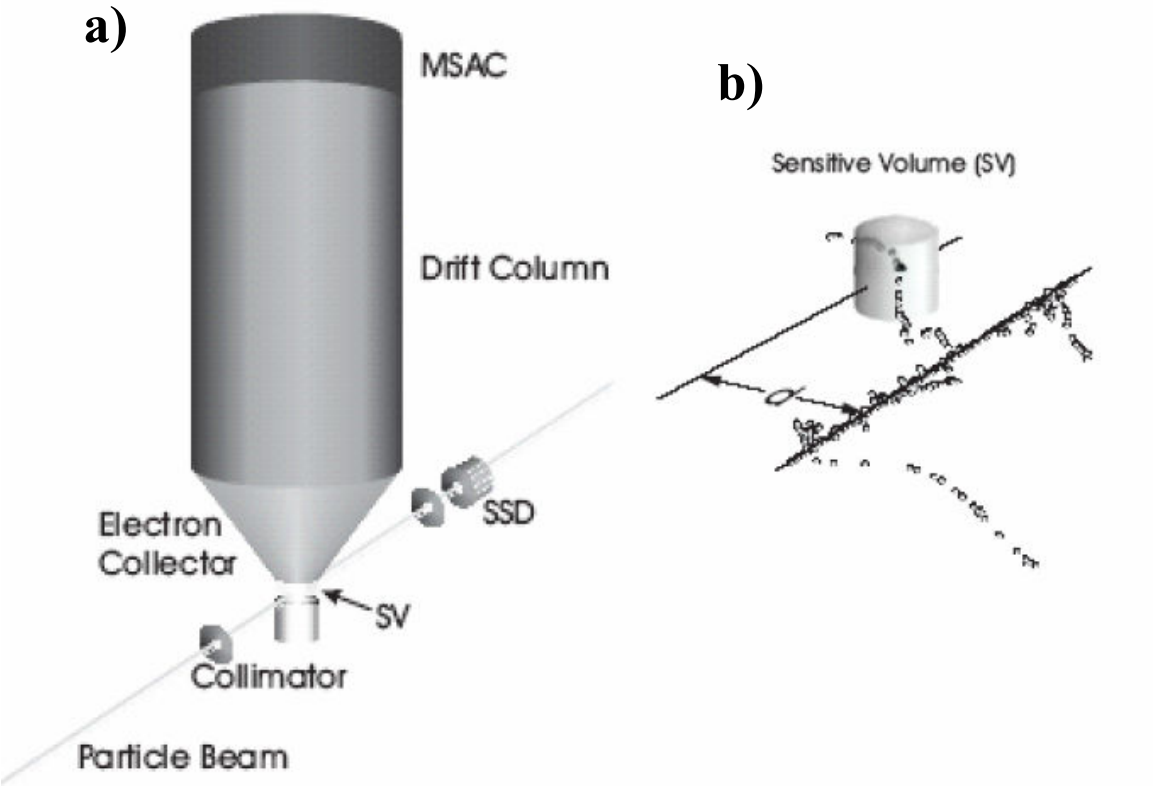

Figure 2-12: Schematic of a single electron counter [40]. Figure a) provides a schematic of the entire experimental assembly including collimators, SV, electron collector, drift chamber and multi-stage avalanche counter (MSAC). Figure b) provides a magnified view of the particle track in relation to the SV. Note how the particle track is external to the SV and the delta ray is transported into the SV for detection.

This device is a useful tool in providing information on the electron track density of various radiation fields. However, it does suffer some drawbacks that make it a less than ideal nanodosimeter in practical application. Firstly, there is a limitation on the diameter at which the SV can be constructed (20 nm lower limit). This is almost an order of magnitude higher than the diameter of a DNA strand. Further, the efficiency of this instrument is quite low (10-20%) requiring long acquisition times. Finally, this device requires a precisely controlled radiation field (i.e. collimated and aligned in close proximity to the SV) in a laboratory environment and consists of multiple support

systems such as high voltage, vacuum pumps etc. As a result, it is not suited to practical deployments in radiation protection and QA applications.

2.6.2 Ion Based Nanodosimetry

Ion based nanodosimetry involves the collection of radiation induced ions within a wall-less SV. The investigators at LLUMC, in collaboration with the Weizmann Institute of Science and the Santa Cruz Institute of Particle Physics, have built and optimized two ion counting nanodosimeters (ND). One of these nanodosimeters is situated on a research beam line at LLUMC and has been utilised in this research.

The design of the LLUMC nanodosimeter is shown in Figure 2-13. The nanodosimeter detects positive ions which are induced by the protons (or other charged particles) in a low-pressure propane gas. The use of the low gas pressure (1 Torr or 133.32 Pa) allows scaling down a millimetre-size gas volume from which ions are collected to an equivalent tissue density volume of nanometre size (i.e., by a factor 10^6). The exact scaling factor also depends on mean free path length between ionisations, and for propane of 1 Torr (133.32 Pa), 1 mm in the lab system corresponds to approximately 3 nm in the tissue-equivalent unit-density system.

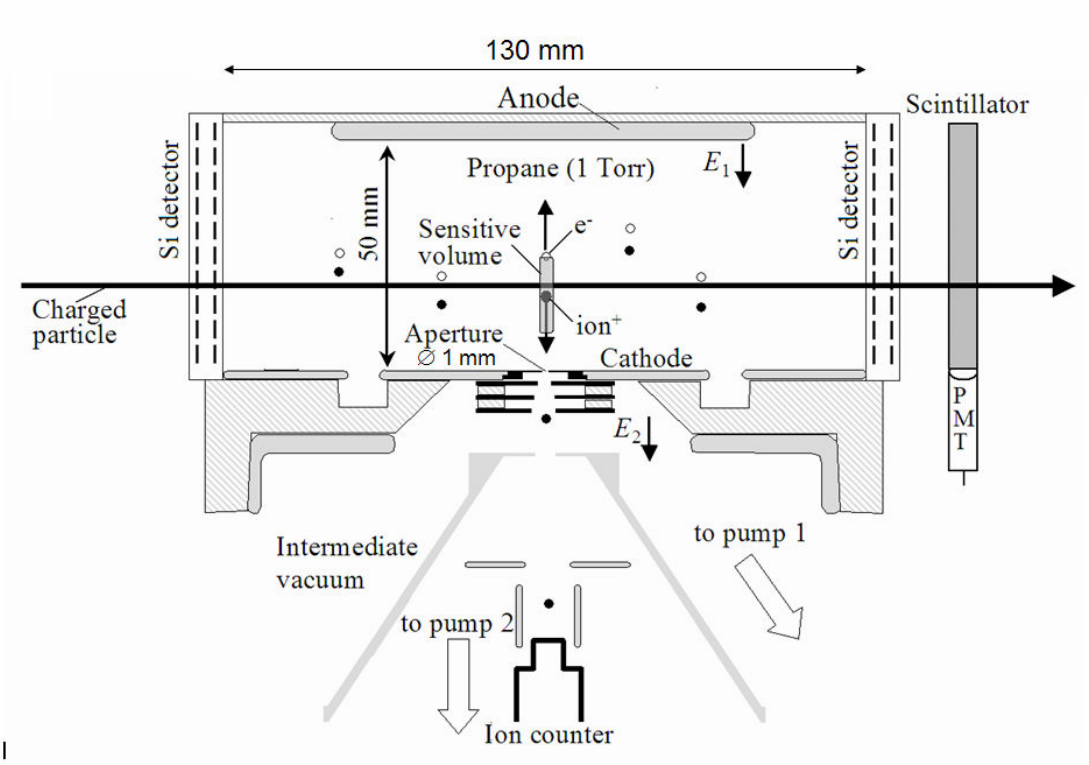

Figure 2-13: Cross-section of the ion-counting ND at LLUMC. The sensitive volume (SV) from which ionisation ions are collected is shown as a shaded cylinder above the ND aperture. The field E1 is defined by the voltage at the anode with respect to the cathode (ground). The field E2 is defined by the voltages on the three electrodes below the ND aperture, the cone voltage, and the voltage on the first dynode of the ion counter. Pumps 1 and 2 (not shown) are turbumolecular pumps (VT 250 and VT 550, Varian) that generate the pressure gradient between the 1 Torr (133.32Pa) gas volume and the 5x10-5 Torr pressure (6.7x10-3 Pa) required for the ion counter (low noise electron multiplier SGE model AF180HIG).

The nanodosimeter is equipped with a silicon tracking system consisting of four planes of single-sided silicon strip detectors, one X- and Y-plane located at the entrance of the gas volume and the other at its exit. The tracking system has several functions. One is to measure ion cluster size distributions as a function of the primary particle's distance from the sensitive volume. In this case, cluster size is the number of ionisations detected or simulated within a SV representative of a segment of double-stranded DNA. Another function is to adjust for spatially inhomogeneous particle fluence rates or to create a desired beam profile using offline data cuts. A detailed description of the tracking system and its performance can be found elsewhere [42].

Inside the nanodosimeter, a wall-less needle-shaped sensitive volume (SV) is formed by means of an electric field E_1 that drifts the radiation-induced positive ions toward a 1 mm diameter aperture at the bottom of the gas volume. An acceleration field E_2 below the aperture accelerates the collected ions toward an ion counter, which is operated in vacuum. The SV is defined by the 3D distribution of ion collection efficiency. Based on measured ion transport parameters in propane and the electric field distribution inside the gas volume, the SV efficiency map can be calculated [37] and is seen in Figure 2-14 and Figure 2-15.

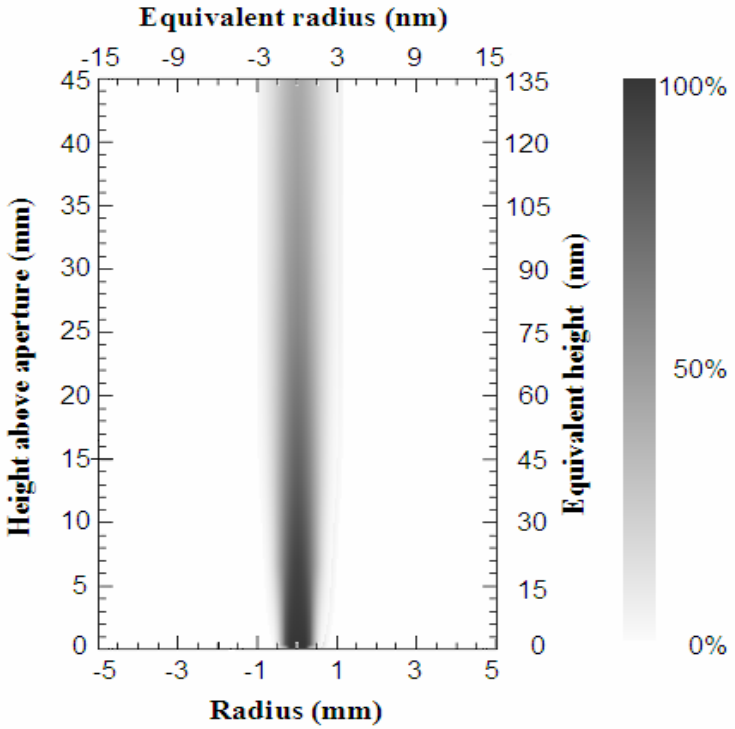

Figure 2-14: Greyscale representation of the ion collection efficiency map representing the SV in the cross-sectional plane shown in Figure 2-13. The map was calculated for an electric field of E_1 = 60 V/cm. The left scale specifies height above aperture in millimetres and the right scale in tissue-equivalent nanometres.

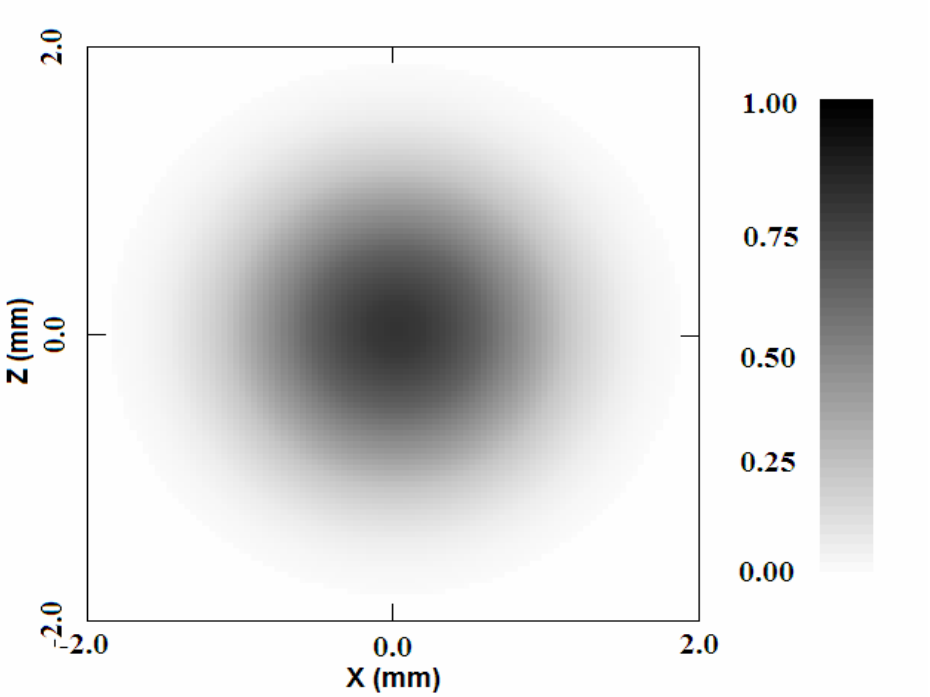

Figure 2-15: Greyscale representation of the ion collection efficiency map in a horizontal plane at 15mm above the collection aperture. The mm scale in gas can be converted to nm in tissue using a $3x10^{-6}$ scaling factor.

The nanodosimeter thus measures the number of ions induced per particle in an approximately cylindrical, wall-less sensitive volume simulating a segment of DNA. The accuracy of this technique is influenced by several factors which need to be considered when comparing experimental with simulated data. The ion collection efficiency at any given location within the SV equals the product of the probability that the ion drifts through the aperture and the efficiency of ion detection at the ion counter. For the former only a calculated efficiency map is presently available [37] and this was used in the simulation. The accuracy of the calculated map depends on the accuracy of measured ion drift parameters, which is of the order of 10% [36]. The ion detection efficiency of the ion counter in use has been measured to be close to 100% [43], and this value was also assumed for the simulation. A surplus of ions in the measurements can be caused by (1) ion multiplication in gas and/or (2) noise in the ion channel. Gas multiplication due to ionisation electrons has been observed in the LLUMC device but can be suppressed effectively by using a pulsed mode of ion extraction [37]. The noise of the ion channel is

approximately 5 Hz, which indicates that the probability of registering at least one extra ion during the 100μs readout time window is of the order of $5x10^{-4}$.

The length of the SV can be selected during offline analysis by using appropriate cuts on ion drift time. Ion drift time is defined as the time between the primary proton trigger and the registration of the ion at the ion counter. The mean drift time of ions is linearly related to the drift length y in propane. Thus, a symmetric time window placed around an arrival time t_0 corresponds to a spatial window symmetrically placed around a location y_0. The centre of the SV is typically placed at 15 mm height above aperture. In this case, one can operate with sensitive volume segments of ~5-100 nm length that are completely wall-less and sufficiently distant from the influence of the bottom and top walls of the ND chamber.

The quantity of interest for applications in radiation therapy and radiation protection is the frequency distribution of ion clusters formed in the DNA-like SV. It has been hypothesized that large clusters, despite being quite rare, are mainly responsible for irreparable DNA damage in a living cell and, therefore, determine the biological effectiveness of the radiation [44].

Nanodosimetry, which has been developed over the last 10 years, would benefit from support of Monte Carlo (MC) track structure simulations, accurately reflecting the experimental radiation conditions. It will be the goal of this work to develop and verify such a system. Once the Monte Carlo simulation system has been developed and verified, it will be possible to include more complex homogeneous and heterogeneous structures into the theoretical model. This may then provide a means for better predicting radiation effects in radiation therapy or assess radiation risks in radiation protection applications in cases where experimental data are not available.

2.7 Introduction to Monte Carlo

The Monte Carlo method is a numerical solution to a problem that models objects interacting with objects or their environment based upon object-object or object-environment relationships. It is an attempt to model nature based upon a simulation of the dynamics of the system. This technique is used extensively in radiation research because it allows the operator to accurately simulate results for a given set of input parameters such as particle energy, phantom material etc.

Monte Carlo techniques are based on selections that are made by random number generation, similar to rolling dice. There are many types of Monte Carlo codes that are used which range from those that are widely available such as GEANT4 and MCNPX to those that have been constructed for a specific purpose or experimental system. Monte Carlo codes differ from other treatment planning algorithms in that they track individual particles through the treatment medium. In most codes the operator stipulates the geometry, incident particles, incident energies and interactions to consider. The program will then use a random number generator to produce a particle of given energy and direction, and track this through the medium. Interaction cross-sections and interaction models that are contained within the program itself will determine interactions of the particle. The incident particles angle and the angles of any secondary particles that are created will be determined once again by the random number generator. There are a number of ways in which the Monte Carlo code can treat secondary particles. In some cases the secondary particles may not be tracked at all, and are assumed to deposit all their energy locally. Often this is used to speed up simulation times. Another method is to track the secondary particles when they are created before continuing to track the incident particle. Finally, the program can completely transport the incident particle and then transport the secondary particles.

The user can determine the size, shape and number of sensitive volumes within the simulation geometry. These sensitive volumes are known as voxels. Within the voxel a great deal of information can be ascertained on either the primary or secondary particle that is traversing the volume. This information can include:

- The energy deposited

- The charge of the particle
- Whether the particle crosses, interacts, or stops within the volume.
- The mass of the particle
- The atomic number of the particle

The operator sets the information that is collected and output by these sensitive volumes.

2.8 GEANT4 - A Monte Carlo Toolkit

GEANT4 is the Monte Carlo toolkit that was selected for radiation transport simulations within the scope of this thesis. It is an object orientated toolkit written in C++ that is available as open source from the GEANT4 website [45]. It was originally developed by the GEANT4 collaboration as a high energy physics simulation tool. However, with low energy extensions to physics models it has become widely used within the medical [46-48] and radiation protection [49-51] fields. The main advantage of this toolkit in its current form is that it allows for simulations of a wide range of particles and energies. Particles that may be simulated within the framework of a GEANT4 based application include leptons, photons, hadrons and ions. With the current physics models and low energy extensions it is possible to simulate many of these particles from energies as low as 250 eV extending into the TeV range.

The physics models incorporated within GEANT4 allow simulation of all particles considered within the framework of the simulation and may be completely customized by the operator. Electromagnetic physics processes which are considered within GEANT4 are extensive [49, 52]. Electron/positron transport processes include ionisation, multiple scattering, Bremsstrahlung and annihilation. Photon processes considered include pair production, the photoelectric effect, Compton scattering and Rayleigh scattering. Low energy extensions down to 250 eV have been included as well as the Penelope [53] electron, photon and positron transport models which may be selected by the operator. Ionisation and scattering of hadrons are also considered within GEANT4 with verification comparisons [49] with NIST databases [35]. The energy ranges of electromagnetic processes contained within the GEANT4 toolkit are displayed in Figure 2-16. The low threshold energy for electron transport is useful in micro- and nanodosimetry applications with further improvements in low energy electron transport

through the GEANT4-DNA Project [47]. GEANT4 also allows for the transport of optical photons, which is valuable in simulating scintillator response to radiation fields.

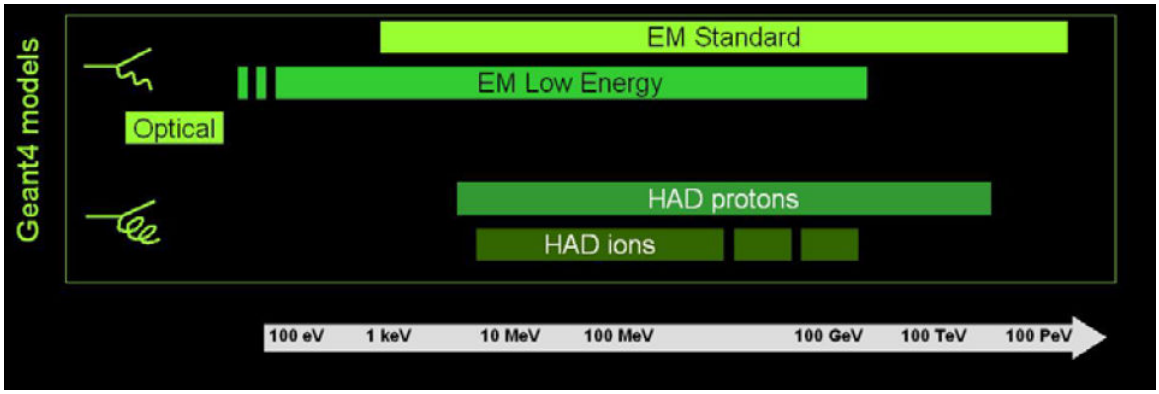

Figure 2-16: Schematic representation of the energy range covered by GEANT4 physics processes [54].

GEANT4 provides for weak and electromagnetic decays of long-lived, unstable particles either at rest or in flight. A range of hadronic processes are also considered through the use of data driven, parameterisation driven, and theory driven models. The use of such models allow for optimal accuracy and efficiency in radiation simulations. Data driven modelling is known to provide the most accurate approach to low energy neutron transport, while parameterisation models are widely used for calorimeter simulations. Multiple hadron interaction models are available for selection and allows for seamless transport of hadrons over a wide energy range. Continual advances in model development and validation are being conducted to remove any gaps in the physics models (Figure 2-16).

Operators of GEANT4 based applications have the ability to construct complex geometries through the use of an extensive collection of solid volumes. Such Constructed Solid Geometry (CSG) shapes can be simple including boxes, spheres and cylinders to more complex CSG shapes such as twisted trapezoids and tori. Boundary-Represented (BREP) solids are also contained within GEANT4 such that the user can create shapes with arbitrary surfaces including planar, 2nd or higher order, Spline, B-Spline and NURBS (Non-Uniform B-Spline). The ability to create complex shapes within GEANT4 allows it to complete modelling of complex structures such as the International Space Station, High Energy Physics Calorimeters and human DNA. The materials

comprising solids can again be stipulated from GEANT4 files, or input by the operator using isotopic and elemental abundances. This further increases the ability for GEANT4 applications to be customised to any application.

To allow for accurate construction of complex geometries GEANT4 can output a wide range of visualization files including openGL, VRML (Virtual Reality Markup Language) and HepRep files. These can be viewed through a number of plug-in viewers including openGL viewers, VRMLVIEW and Wired3. Visualisation is essential in creating complex structures and was used extensively in all GEANT4 simulations within this thesis. It was found that VRML files produced the more accurate images and were most useful for debugging processes. It was also useful to complete simulations and view openGL and HepRep files to ascertain the radiation spectra at different levels within the simulation as such files could be viewed for large numbers of incident particle histories.

Previously Monte Carlo simulations have suffered from long computation times limiting the use of such a valuable tool. GEANT4 has allowed for various optimisation features within its construction to minimise simulation times. Such features include range cuts for electrons/photons/positrons, tracking optimisation through the use of smart voxels, and parameterisation. Further, the use of parallel and cluster computing allows for improved simulation times. In this thesis both the Barossa Cluster (as part of AC3) and the Loma Linda University Medical Center Cluster Computing Facility were utilised to achieve useful simulation times. As this technology improves and becomes more cost-effective Monte Carlo simulations will become more time-efficient and may even be incorporated into treatment planning applications in radiation therapy.

GEANT4 is a useful tool that can be applied to a number of different applications in medicine, radiation protection and high energy physics. Within the scope of this thesis it will be used to simulate the response of solid state microdosimeters to various radiation fields, the radiation spectra for various particles within an experimental environment and to test new radiobiological protocols. Further work is currently underway in other applications utilising GEANT4 across a wide range of fields including simulations of

human DNA and other biological systems [47], simulations to optimise spacecraft shielding [50, 51, 55], simulations to develop and optimise medical imaging such as proton CT [48] and Positron Emission Tomography (PET) using GATE [56-58], simulations hadron therapy [59] and incorporation of Monte Carlo into treatment planning [60, 61]. It is expected that as parallel and cluster computing becomes more readily available such simulation studies will continue to increase in importance for physics applications.

2.9 Radiobiology

Radiobiology is the practical study of the effects of ionising radiation on biological systems. The biological systems can take the form of DNA, cells, tissues or complete systems such as mice and humans. These studies provide important information that can be used to establish safe working limits, or treatment parameters. As such this is a very broad and diverse field with many aspects that are outside the scope of this study. The work presented in this thesis will centre on the development of in-vitro cell survival protocols and the use of in-vitro cell survival data in the development of biological models to link detector output to biological effect. As such this section will limit its discussion to this facet of radiobiology. Further information on radiobiology can be found in [62].

Cell survival studies in-vitro are based on the surviving fraction of cells as a function of absorbed dose. This is typically referred to as colonogenic cell survival as the number of colonies present in a given sample provides an indication of the surviving fraction of cells. However, the term of survival is very broad and needs further clarification. In the case of differentiated cells that do not proliferate, it may be appropriate to study the loss of a specific function or induction of senescence. However, in the case of proliferating cells, such as tumour cells, the loss of reproductive capacity leads to cell death. This is termed **reproductive death**, and is the end point used in colonogenic cell survival.

This definition is understandable in the context of radiation therapy. In order to treat the tumour volume, the tumour itself does not need to be destroyed, but rather its ability to proliferate and reproduce needs to be removed. This does not have to occur at the time

of irradiation, but can occur at some time in the future (i.e. after a number of divisions). The mode of cell death is unimportant in this case and can take a number of pathways. Two major pathways of cell death include **mitotic death**, where the cell dies during reproduction from un-repaired chromosome damage, or **apoptosis**, which is a pre-programmed cell death in response to an environmental factor (such as radiation-induced damage) without the attempt of repair. In the case of a large biological system, such as a tumour, the loss of reproductive integrity will cause the tumour to cease expansion and be absorbed by the system as the cells die. In a colonogenic cell experiment the loss of reproductive ability prevents the formation of a colony, which is typically classed as a grouping of 50 or more cells [63] created over a period of incubation (typically 1-2 weeks). If the cells are in a truly single cell suspension, a single cell and its daughters needs to complete at least 6 divisions to create a colony which is not possible with the loss of reproductive integrity.

Colonogenic cell survival techniques are a mainstay of radiobiology since their first use in the 1950's [63]. Typically these use an established mammalian cell line that has been generated from a tissue culture. The cells are then suspended into a single cell suspension using Trypsin and divided into samples. The first test to complete is to determine the **plating efficiency (PE)** of the experimental procedure. The plating efficiency is a measure of the surviving fraction of cells (represented by colonies) for each sample in the absence of radiation. It is determined by the relationship described in Equation 2-9. Typically in cell survival experiments a PE of 50-90% is acceptable as some cells may undergo mitotic death or apoptosis as a result of the cell stress in the plating procedure, errors in counting and less than ideal growth conditions etc. The PE will then be considered in all subsequent experiments with radiation.

$$PE = \frac{\#Colonies}{\#Cells} \times 100$$

Equation 2-9: Relationship for plating efficiency, where *#Colonies* is the number of colonies counted in the sample after a predetermined period of time, and *#Cells* is the incident number of cells seeded into the cell culture dish.

The PE is generally re-established using a no-radiation control sample for each experimental series (this allows for any changes in experimental conditions to be observed and considered). To establish an experimental cell survival curve multiple samples of a given cell concentration are irradiated to differing levels of absorbed dose. The samples are then seeded into a cell culture dish and left for an incubation period of 1-2 weeks to allow for colony formation (i.e. to determine the number of cells which have lost the ability to replicate). After the pre-determined incubation time the cells are stained and the number of colonies counted. The number of colonies can be related to the surviving fraction of cells using the relationship described in Equation 2-10. Typically this is plotted on a semi-log plot of surviving fraction (SF) versus absorbed dose.

$$SF = \frac{\#Colonies}{\#Cells \times \frac{PE}{100}}$$

Equation 2-10: Relationship determining the surviving fraction of cells in a colonogenic cell survival experiment. Note that SF is the surviving fraction, *#Colonies* is the number of counted colonies, *#Cells* is the number of seeded cells and *PE* is the plating efficiency.

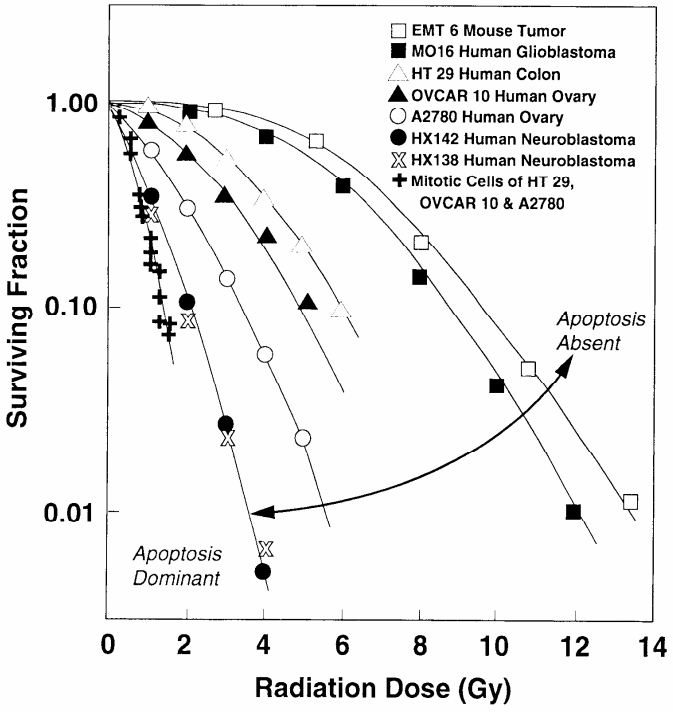

Figure 2-17: Compilation of cell survival curves of different cell lines exposed to a common low-LET radiation field [62].

The cell survival curve can provide a great deal of information regarding the cells response to a given form of radiation. For high-LET radiations a cell survival curve typically appears linear, which indicates the presence of complex double strand DNA breaks that are difficult to repair. For lower-LET radiation the cell survival curve typically has a large shoulder which indicates the cells ability to repair damage at low doses. However, as the dose increases the cell survival curve takes a downward trend as the damage from low-LET particles overwhelms the repair mechanisms of the cell and sub-lethal damage can combine to form lethal lesions.

Comparing cell survival curves for differing cell lines for a given reference radiation (typically X-rays or gamma radiation) can provide an indication of the intrinsic radiosensitivity of the cell line. An example of such a comparison is displayed in Figure 2-17. It is clear from this figure that radioresistant cell lines such as glioblastoma and various other cell lines exhibit a large shoulder and are generally devoid of apoptosis. As a result, mitotic cell death is the primary mechanism for cell inactivation. Radiosensitive cell lines such as neuroblastoma and certain human ovary cell lines exhibit a more linear relationship to induced radiation whilst exhibiting a small shoulder indicating apoptosis as the dominant mechanism for cell death.

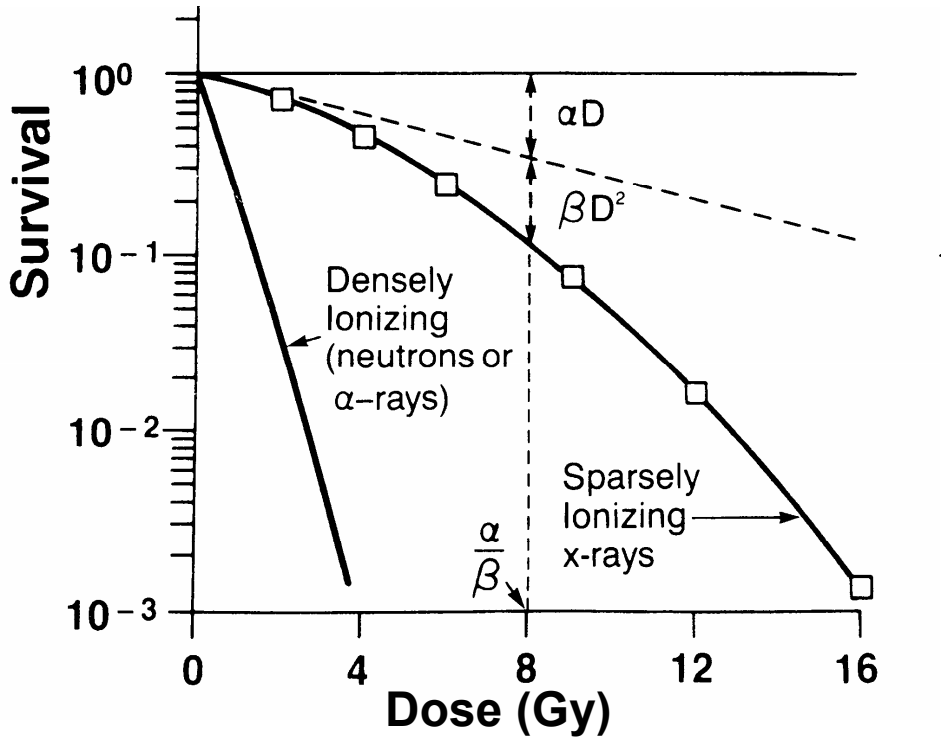

Figure 2-18: Example of high and low-LET survival curves with associated linear-quadratic modelling [62]. Note that the dose point at which the linear and quadratic components of the model are equal in cell kill is defined as α/β.

The nature of cell survival curves lends to the development of models to describe the response of cells to radiation. The most widely used of these is the **linear-quadratic model**. This model assumes two parts to the cell survival curve and hence two components to radiation induced cell death. The first is proportional to the dose delivered and is the initial slope of the cell survival curve which has a gradient defined as α. The second component is proportional to the square of the dose and becomes increasingly dominant at higher doses as damage becomes irreparable. This component causes the cell survival curve to bend downwards as the quadratic component dominates with increasing dose. In the case of high-LET radiation, only a linear component is present indicating the irreparable nature of the radiation damage even at low doses. The linear-quadratic model is defined by the expression described in Equation 2-11, where α and β are cell specific components that are dependant on the applied radiation. In the linear-quadratic model the point at which the linear and quadratic modes of cell kill are equal occurs at a dose which is prescribed by α/β.

$$SF = \exp\left(-\alpha D - \beta D^2\right)$$

Equation 2-11: Expression for the surviving fraction of cells (*SF*) using the linear-quadratic model. In this case α and β are constants, while *D* is the delivered dose.

It should be noted that the linear-quadratic model does not describe the cell survival curve ideally. Rather, as the experimental cell-survival curve is followed through many decades, it is observed to straighten and become linear. However, in the linear-quadratic model the quadratic component is dominant in this region which results in a continued downward curvature that is usually not observed experimentally. It should be noted that often cell survival experiments do not extend to these high dose levels and as a consequence the linear-quadratic model provides an acceptable means of modelling colonogenic cell survival. It has the added advantage of having two parameters which are clearly defined.

The relative biological effectiveness (RBE) is another parameter that is used extensively when linking an applied radiation field to biological effect. It was defined to provide a reference as to the potential for cell kill of a given radiation field to a reference radiation. It is determined by the ratio of absorbed dose of a test radiation to that of a reference radiation (typically X-Rays or gamma photons) to achieve a certain endpoint, which may correspond to a given cell survival or cell inactivation (Equation 2-12). The RBE is thus dependant on the radiation quality or LET, delivered radiation dose, dose rate, number of fractions, and the chosen endpoint. It is important that when comparing or determining RBE values the same endpoint is observed as this can have a dramatic effect on RBE.

$$RBE = \frac{D_{250}}{D_X}$$

Equation 2-12: Definition of RBE as the ratio of dose delivered by 250-kV X-rays (D_{250}) and the dose delivered from another radiation field (D_X) to achieve the same biological endpoint.

3 SOI Microdosimeter Testing

3.1 Introduction

SOI microdosimeters have been experimentally tested in a number of different radiation environments, including those produced in proton therapy (PT) [64, 65], fast neutron therapy (FNT) [21, 29], ion-beam induced charge collection studies (IBICC) [26, 27] and various irradiations with radioactive sources including Am-241 and PuBe-238 [66]. Such experiments have the potential to change the response of these devices to radiation induced signal. The SOI devices needed to undergo benchmark testing before the commencement of experimental studies to ensure stable and reproducible performance. Tests included Current-Voltage (I-V) characterisation and alpha particle irradiation that were completed using facilities at the Australian Nuclear Science and Technology Organisation (ANSTO). In addition the devices were calibrated to enable accurate determination of the lineal energy spectra. Finally, systematic studies on the systems electronic noise and shielding properties of the experimental probe assembly were completed. Such tests were important as this system was a prototype having undergone a number of changes from the original system proposed in [21, 25].

3.2 IV Testing & Characterisation

Measurements of the I-V characteristics of both 5 and 10 μm SOI microdosimeters were completed to assess diode integrity and provide initial information on the device performance and noise characteristics. Such information enabled unsuitable devices to be initially tested and discounted from further testing or experimental use. These measurements were completed using a Keithley 237 high voltage measurement unit which is situated at ANSTO and is dedicated to the measurement of I-V characteristics. The accuracy of the meter is within 0.3% in the 10 nA range. Measurements were completed for all devices and arrays in 1 V incremental measurements from 0-20 V reverse bias. As the purpose of these measurements was to identify functioning devices these tests were performed at atmosphere with a temperature of 22±2^{o}C. For each measurement a 1-2 second settling time was employed.

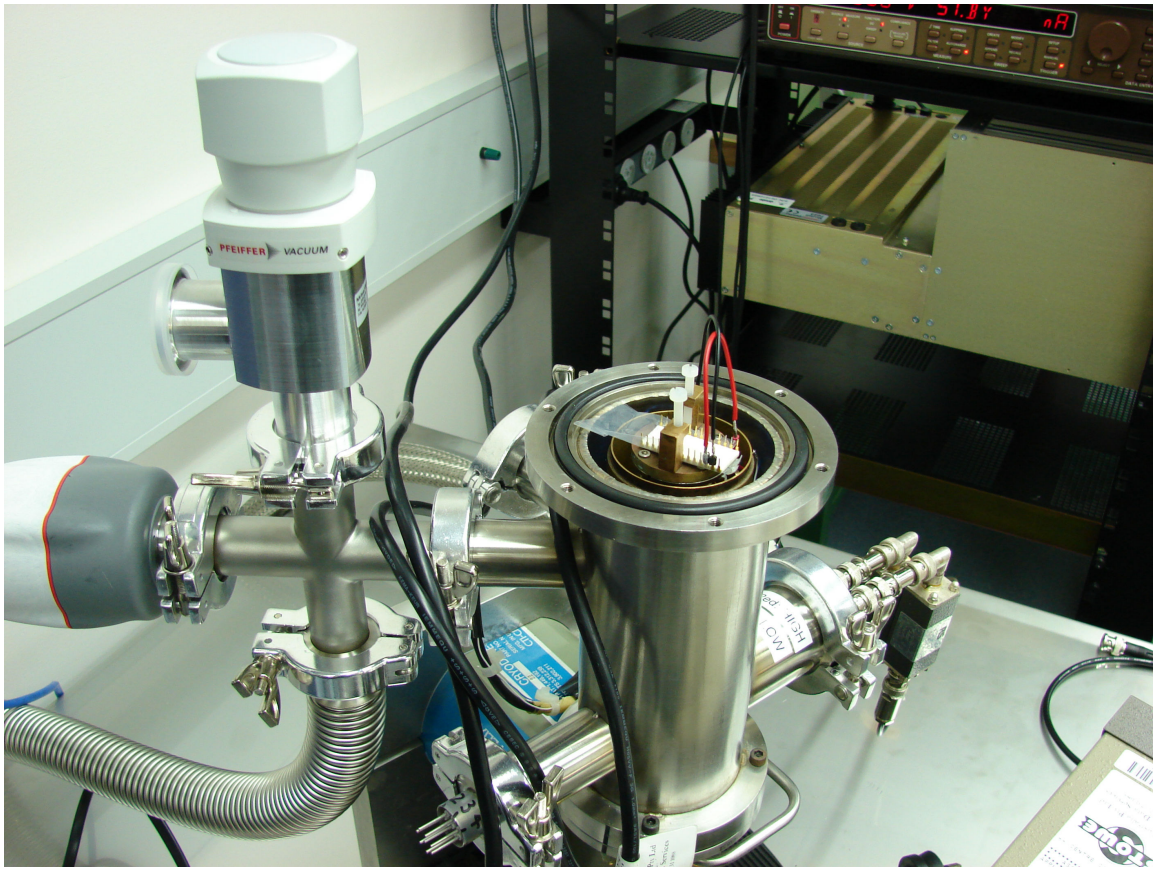

Figure 3-1: Picture of the experimental set-up used for I-V characterisation of the SOI microdosimeters. Note that during measurements a cover was placed over the vacuum chamber to shield the device from light. The stage assembly was also wrapped in polyethylene to ensure sufficient electrical insulation.

Using the protocol outlined in [21] functioning devices were selected using the following criteria:

- The I-V should be linear with a positive slope
- At 0 V have a nominal current range of $-0.25 \leq I \leq 0.25$ nA
- At 10 V reverse bias have a nominal current range of $0 \leq I \leq 200$ nA

Characteristic I-V curves for the 10 μm devices are displayed in Figure 3-2, with each array structure contained within a separate graph. Note that the arrays are named as follows:

Array 1 (A1): 120x120x10μm^3 with 150 detector elements

Array 2 (A2): 120x120x10μm^3 with 50 detector elements

Array 4 (A4): 30x30x10μm^3 with 4800 detector elements

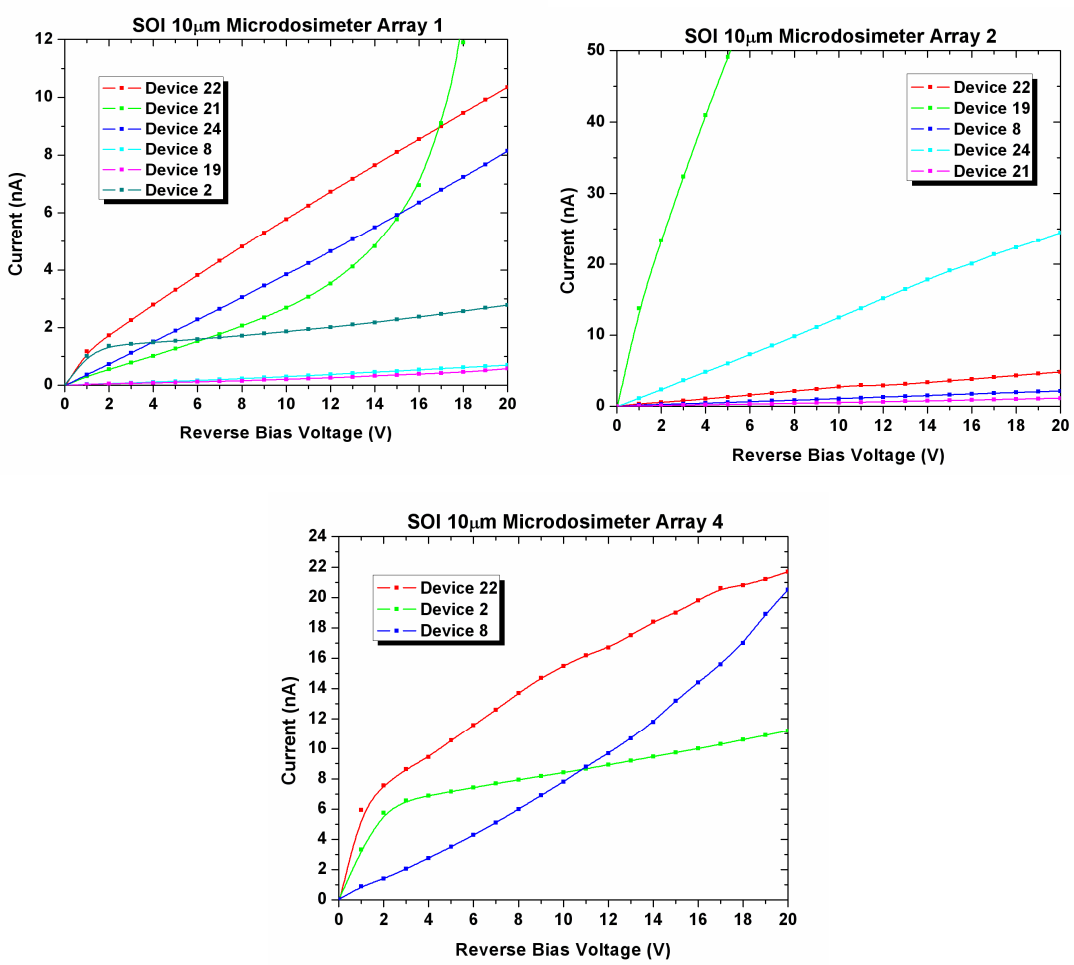

Figure 3-2: Characteristic I-V curves for 10 μm devices tested. Note how the 3 separate array structures are contained within separate graphs for easier identification.

It is clear from the I-V characteristics which devices meet the operational criteria for operating and those which should be rejected. For array A1, device 21 clearly displays an exponential rise in current with voltage making it unsuitable for radiation measurements. Furthermore, device 2 has a non-linear response for voltages below 2 V but in the region $2 \leq V \leq 20$ V a linear relationship between current and voltage is displayed. As the operating voltage for such devices is 10 V and the relationship is linear in this region such devices are deemed to be operational provided they successfully complete all other tests. For array A2 all devices meet the criteria, except device 19 which clearly encounters breakdown at very low reverse bias voltages and was rejected from further testing. The A4 devices have been used most extensively in previous work and the response of these devices indicates this. Both devices 22 and 2 display non-

linearity when the reverse bias voltage is leas than 2 V, however above this value all three curves appear linear. For this reason the three A4 devices were utilised in this work for comparative measurements with other microdosimetry systems and arrays. All 10 μm devices selected for further testing on the basis of linear response also met the current requirements at 0 and 10V.

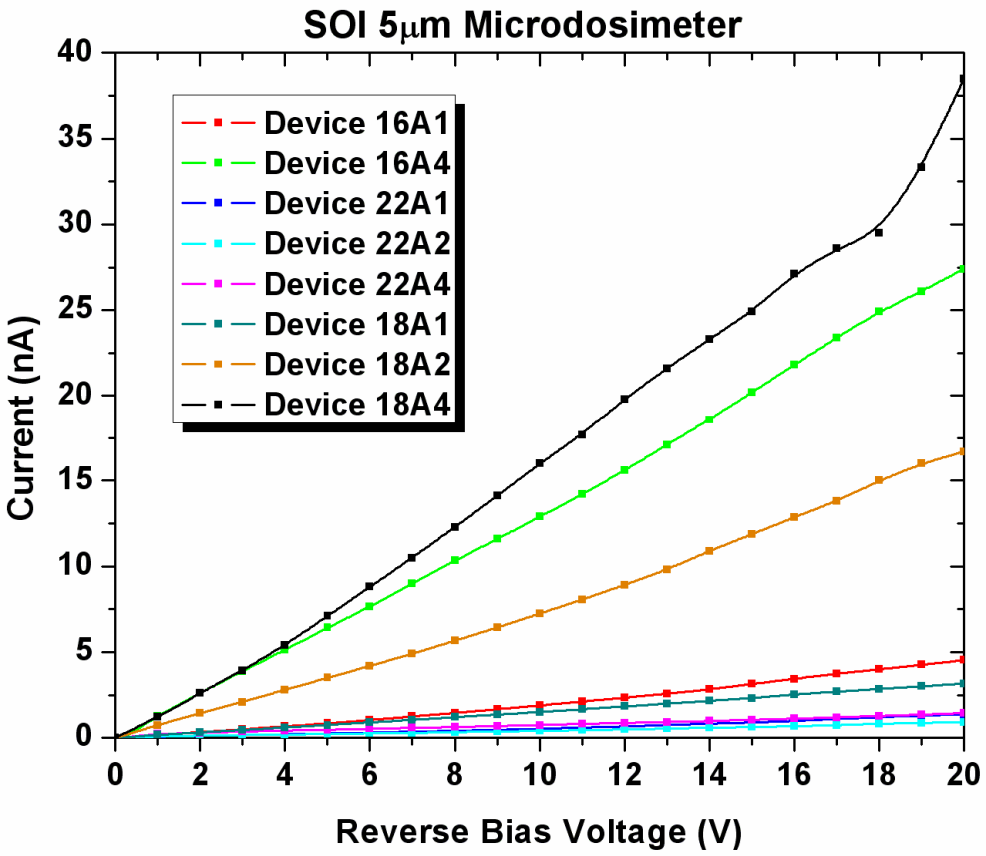

Figure 3-3: Characteristic I-V curves for 5 μm devices tested. Note how the 3 separate array structures are contained within a single graph for easier identification.

The 5 μm devices displayed a much more uniform response with all devices tested meeting criteria for further testing. Non-linearity at reverse bias voltages less than 2 V was not observed in 5 μm devices, with the only non linear response occurring with applied voltages larger than 18 V in the case of device 18 A4. This could be caused by device heating or breakdown. Due to the high reverse bias at which this occurs, it does not rule the device out for further electronic testing.

3.3 Alpha Source Testing

Alpha source testing using an Am-241 electroplated source provides a means for further testing of devices with an applied radiation field prior to deployment. Such measurements are useful as they provide a benchmark for chip performance to radiation by comparing the following parameters:

- Noise level
- Alpha Peak position
- Alpha Peak amplitude

These tests were completed at a dedicated radiation metrology laboratory at ANSTO and involved the use of an electroplated Am-241 source of approximately 5 mm in diameter. The entire experimental assembly was situated within a vacuum chamber to minimise attenuation of the incident radiation field in addition to shielding the device from light contamination. The source was situated parallel to the SOI microdosimeter chip separated by a distance (in vacuum) of approximately 1 cm with the centre of the Am-241 source corresponding to the centre of the SOI chip.

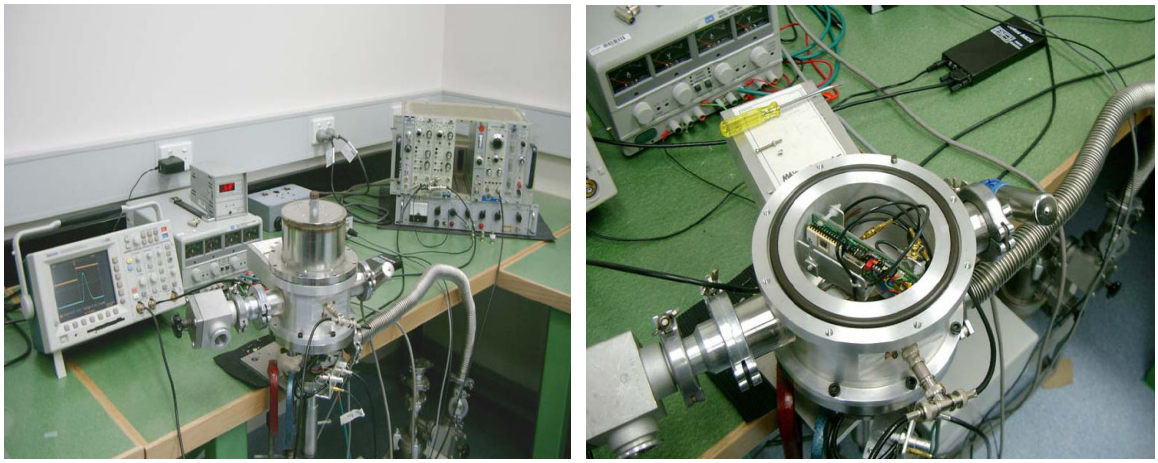

Figure 3-4: Pictures of the experimental set-up at ANSTO for alpha source irradiations of SOI microdosimeters. The picture on the left illustrates the complete experimental set-up including vacuum chamber, pulser, main amplifier, cathode ray oscilloscope (CRO) and power supplies. The picture on the right gives a view inside the vacuum chamber with a SOI microdosimeter and circuitry board mounted in the experimental measurement position.

All microdosimeter arrays which passed initial I-V testing were subjected to alpha irradiation to assess performance. Representative 5 and 10 μm device results are displayed in Figure 3-5 and Figure 3-6 for each of the three array structures. Spectra were collected for 5 and 10 minutes in the case of the 5 and 10 μm devices respectively. In addition a pulser with energy of 3 MeV (for 10 μm devices) and 2 MeV (for 5 μm devices) was applied to the spectra post-collection to give an indication of how the varying capacitance of the three arrays affected the energy calibration.

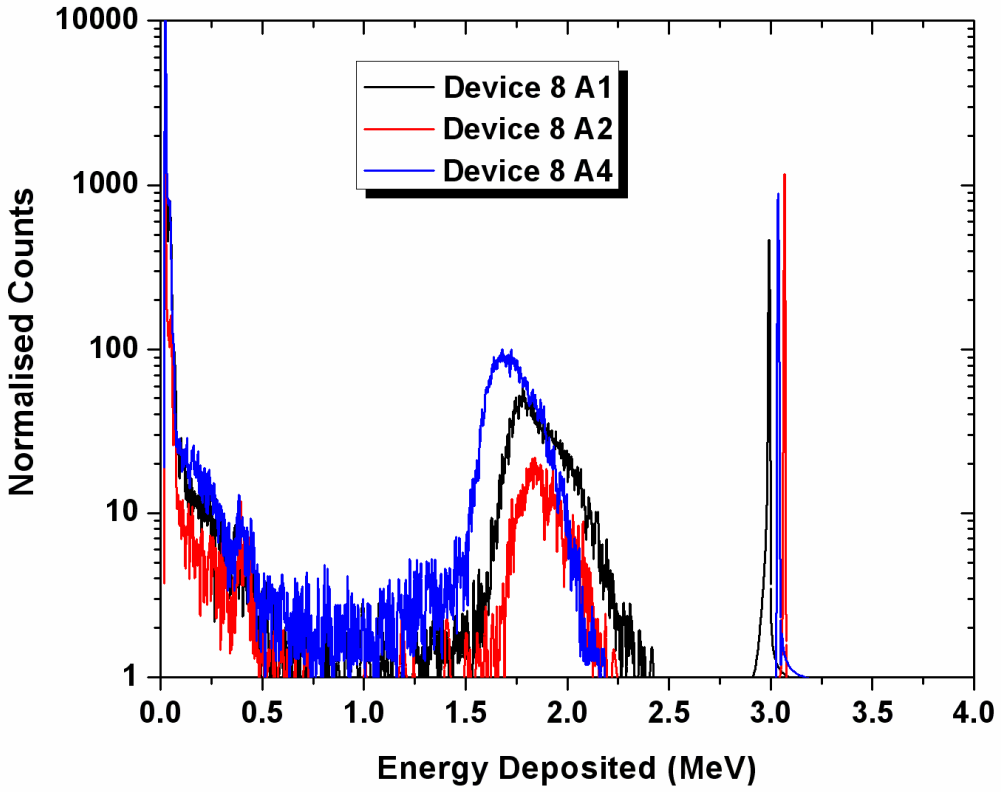

Figure 3-5: Normalised alpha spectra for 10 μm SOI microdosimeter 8 for the three working arrays.

Figure 3-5 provides the alpha spectra for a 10 μm SOI microdosimeter chip. It is clear from the results that this is a well performing chip which further supports the results from I-V testing. Firstly, the lower noise level remains constant for the three arrays. Further, the position of the pulser peak also remains relatively stable. Variation in position is inherent on the changes in capacitance between the three arrays, however, variation is only of the order of ±40 keV or approximately ±1% which is considered within the operational limits of the device. The alpha peak amplitude and position also

varies depending on the array selected. The amplitude depends on the cross sectional area of the given array and hence collected signal. The position of the alpha peak also varies as a function of chosen array for a number of reasons:

- The capacitance difference between the arrays causes a shift in energy calibration which can be quantified through comparisons with pulser measurements as being ±40 keV.
- The arrays vary in position on the chip and the radiation field may vary as a function of position relative to the radiation source. This could result in a small shift in the response of the device.
- As the source was not collimated onto the SV the radiation is not perpendicular to the array but has some divergence which is dependant on the position of the array relative to the source. Hence, the path length through the SV may vary depending on SV position.

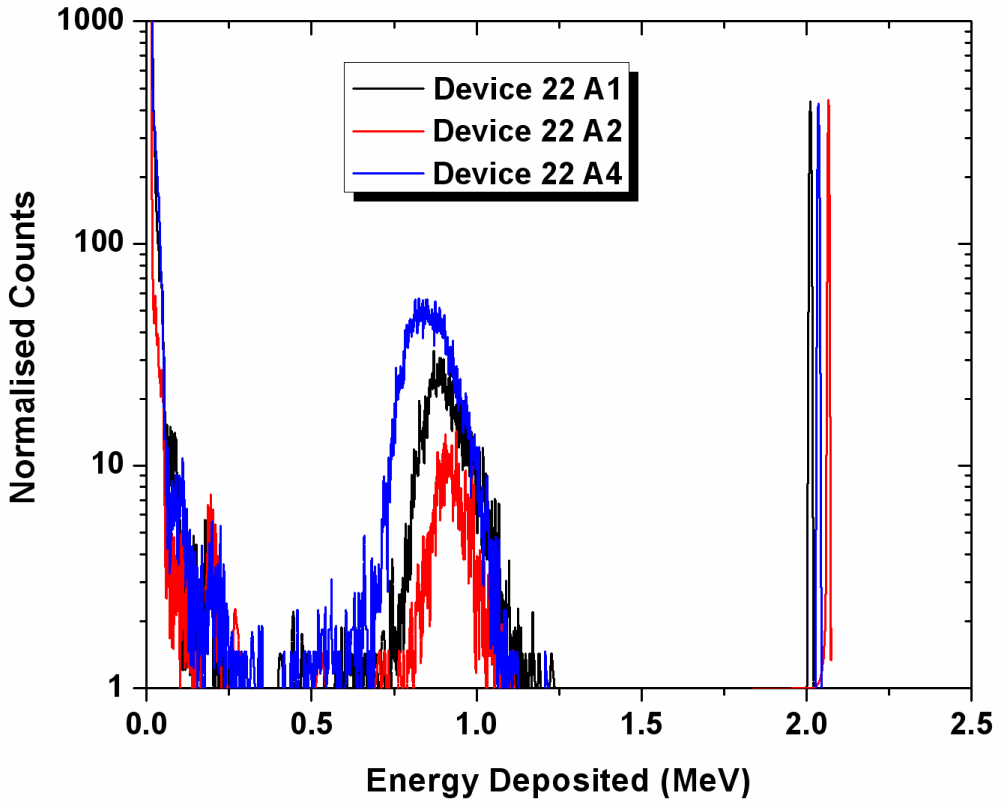

Figure 3-6: Normalised alpha spectra for 5 μm SOI microdosimeter 22 for the three working arrays.

Figure 3-6 illustrates the alpha spectra for a functional 5 μm device. The results are very similar to those reported in the 10 μm case with minimal variation in position of the pulser peak with differing array structure. Again the alpha amplitude and position varies depending on the selected array structure for the same reasons as described above. While such tests are important for determining the response of different array structures in relation to one another, this testing is also used to select functioning devices. As such tests are completed to compare all array structures of a given type, an example of which is displayed in Figure 3-7.

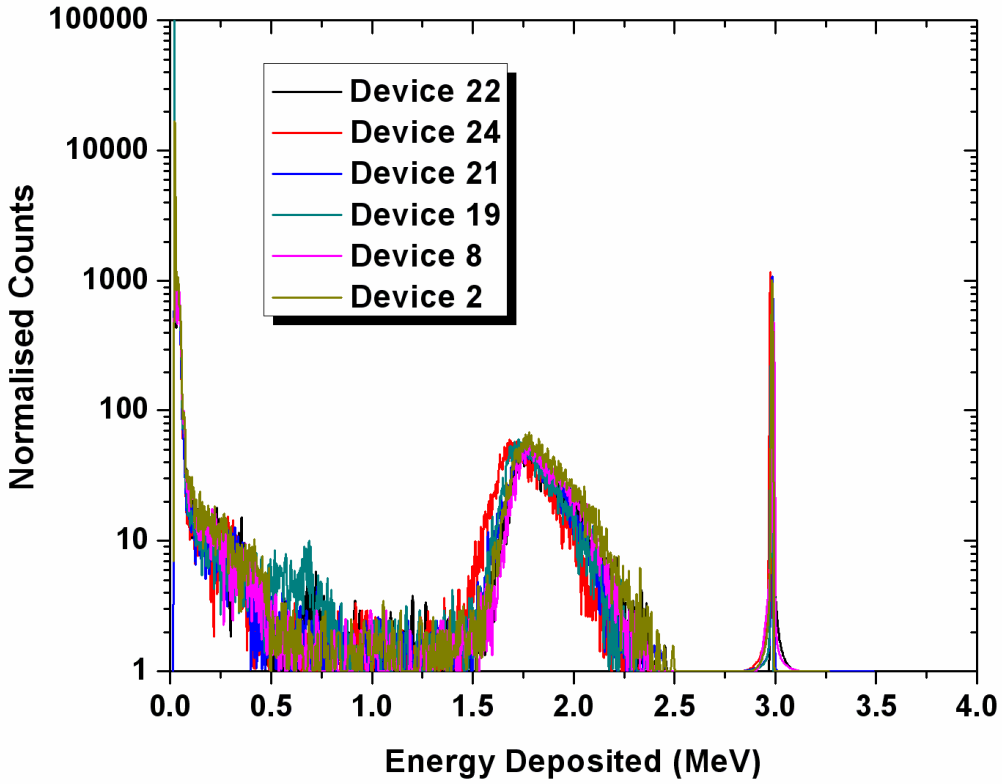

Figure 3-7: Normalised array A1 alpha spectra for all 10 μm SOI microdosimeter chips used in this experimental work.

Figure 3-7 provides a comparison for all the array A1 10 μm SOI microdosimeter arrays tested for use in radiation characterisation experiments. What is immediately apparent is that the alpha peak position and amplitude is uniform across the devices showing not only that they have comparable capacitance (one reason stated above for differences between array structures) but also that they are functioning correctly. This

conclusion is strengthened through the uniform position of the pulser peak in the spectra. What is also encouraging from these results is that the lower noise threshold is uniform across the devices. In this instance all chips displayed were selected for experimental use.

3.4 Final Chip Selection

Using the data from I-V and alpha particle testing it was possible to select suitable devices for further experiments both at Loma Linda University Medical Center, and the NASA Space Radiation Facility at Brookhaven National Laboratory. The devices selected for the experimental SOI microdosimetry portion of this work are contained within Table 3-1.

Device 10 μm	**Array 1**	**Array 2**	**Array 4**
2	Selected	Rejected	Selected
22	Selected	Selected	Selected
19	Selected	Rejected	Rejected
8	Selected	Selected	Selected
21	Rejected	Selected	Rejected
24	Selected	Selected	Rejected
Device 5 μm	**Array 1**	**Array 2**	**Array 4**
11	Selected	Rejected	Rejected
22	Selected	Selected	Selected
18	Rejected	Selected	Selected

Table 3-1: SOI microdosimeters selected for further experimental studies in proton and heavy ion fields.

3.5 Experimental Probe Design

For SOI microdosimetry studies of both proton and heavy ion radiation fields a new experimental probe assembly was designed and constructed. This system was a hybrid system incorporating the ideas and methods previously outlined in [21] with further improvements for both proton, heavy ion and mixed radiation field sampling. The basis of the system involved a probe which would hold the SOI microdosimeter, pre-amplifier, buffer-amplifier, and associated circuitry (see Figure 3-8). To allow for a low-noise environment this probe assembly was made out of 0.9 mm thick aluminium sheet that was folded and welded to create a light tight box with a removable end cap. This probe formed a Faraday cage for the device during experimental measurements, and further reduced noise by providing a dark environment devoid of external lighting. The end cap was machined from a piece of aluminium and was through drilled to allow for the installation of pass throughs for detector bias, pre-amplifier power, incident pulser and signal. Such an arrangement maintained the integrity of the Faraday cage whilst allowing the transfer of power and signal.

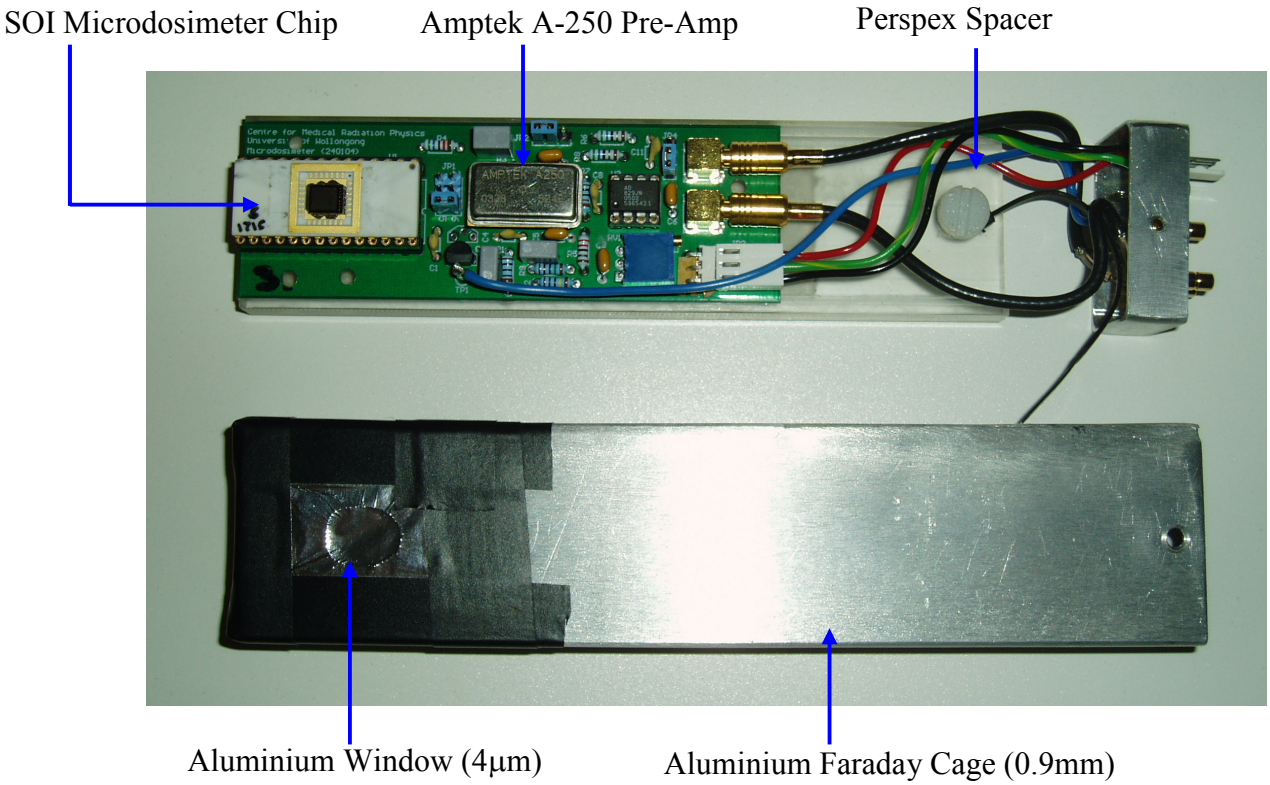

Figure 3-8: Picture of microdosimeter probe assembly developed for this study.

Situated inside the experimental probe assembly was a Perspex spacer, which allowed for reproducible placement of the SOI microdosimeter electronics board. This was achieved through the use of locator holes within the spacer that matched up with projections from the electronics board, locking it in place. In [21] the spacer assembly completely surrounded the SOI microdosimeter and electronics board with a given thickness of Perspex both in-front and behind electronic assembly. This meant that not only was the electronic assembly reproducibly placed within the aluminium experimental probe, but it also meant that a converter of a given thickness was situated at all times immediately anterior to the SOI microdosimeter array. The presence of a converter allows for the detection of neutrons in a free air environment, but in combination with a 0.9 mm thick aluminium probe wall thickness, can prevent low range secondaries produced within a phantom material from reaching the SV.

The spacer used in these studies is fundamentally different in that it was situated behind the electronics board only, and ensured not only reproducible placement of the SOI microdosimeter, but also ensured that the SV was immediately inside the anterior wall of the aluminium probe. In addition, a circular hole was cut in the aluminium probe immediately anterior to the SV location and replaced with an aluminium foil of 4 μm thickness. Such an arrangement allowed for the detection of low range secondaries by the SV as they need only traverse a 4 μm thick aluminium window. To allow for the detection of neutrons in a free air situation, provision was also made such that a 0.5 mm thick polyethylene converter could be affixed immediately anterior to the SV within the probe assembly.

As in previous work a CMRP circuitry board complete with Amptek A-250 and x10 (variable) buffer amplifier was utilised in this work. This was completely housed within the probe assembly. To enable reproducible placement within layered phantom structure a special Perspex probe holder was built. This consisted of a 20x20x3 cm^3 slab of Perspex with a channel machined along the central axis with the same dimensions as the Aluminium probe. A Perspex rod allowed for the microdosimetry assembly to be situated anywhere along this channel (typically with the SV at the central axis) allowing for central and off axis measurements to be completed.

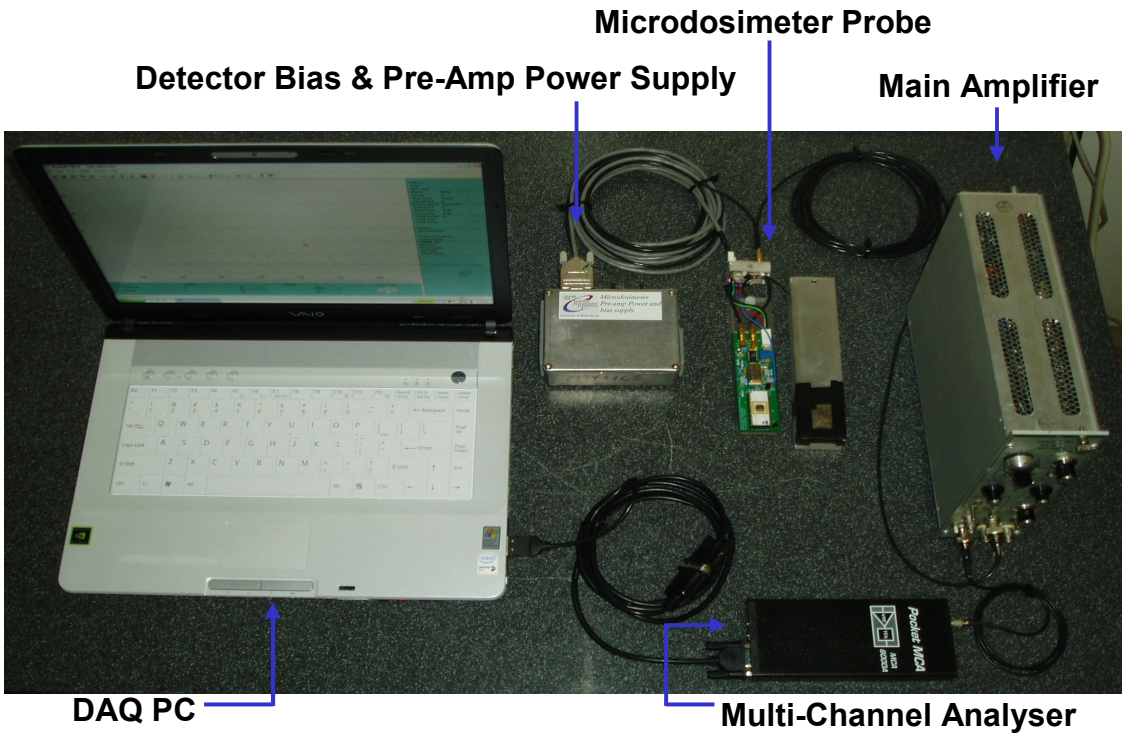

Figure 3-9: The complete data acquisition system (DAQ) used in SOI microdosimetry measurements both in proton, heavy ion, and mixed radiation fields.

The complete SOI experimental assembly was kept as simple and compact as possible to allow for a high level of portability and is displayed in Figure 3-9. It consists of a regulated battery pack which supplies 10V reverse bias to the SOI microdosimeter, and ±6 V power to the A-250 pre-amplifier. Signal from the device was transferred to a Tennelec TC244 Spectroscopy Amplifier. The amplified signal was then transferred to an Amptek Pocket MCA and the resulting signal displayed using the packaged MCA software on a laptop. This software allowed for real time analysis and visualisation of the acquired data with 0.5 second updates via a PC-card to RS-232 interface. The real advantage of this system was that it was highly portable being completely contained within a standard briefcase. The only limitation of this system was that it required NIM power supply for the amplifier. Future developments of this system should incorporate a stand alone amplifier that is either battery powered or has provision to be connected to filtered mains power (120-240 V).

3.6 Apparatus Calibration

The apparatus needed to be calibrated for all possible experimental configurations. As four circuitry boards and two Amptek A-250 pre-amplifiers would be utilised, it was important to determine an energy calibration curve for each combination. The same experimental set-up used for alpha particle irradiations (described in Section 3.3) was utilised in device calibration. For initial tests, the SOI microdosimeter was replaced with a 1 mm^2 silicon planar detector that was mounted on the SOI circuitry board. A reverse bias of 40 V was applied via a Fluke 415B GW power supply providing a situation of full depletion in the ion implanted detector. The advantage of this device was that it had a similar capacitance to the SOI microdosimeter and allowed for a spectroscopy measurement of the Am-241 alpha spectra. When mounted in the vacuum chamber and irradiated with the Am-241 electroplated alpha source, a spectra was measured (Figure 3-10) and correlated with established results.

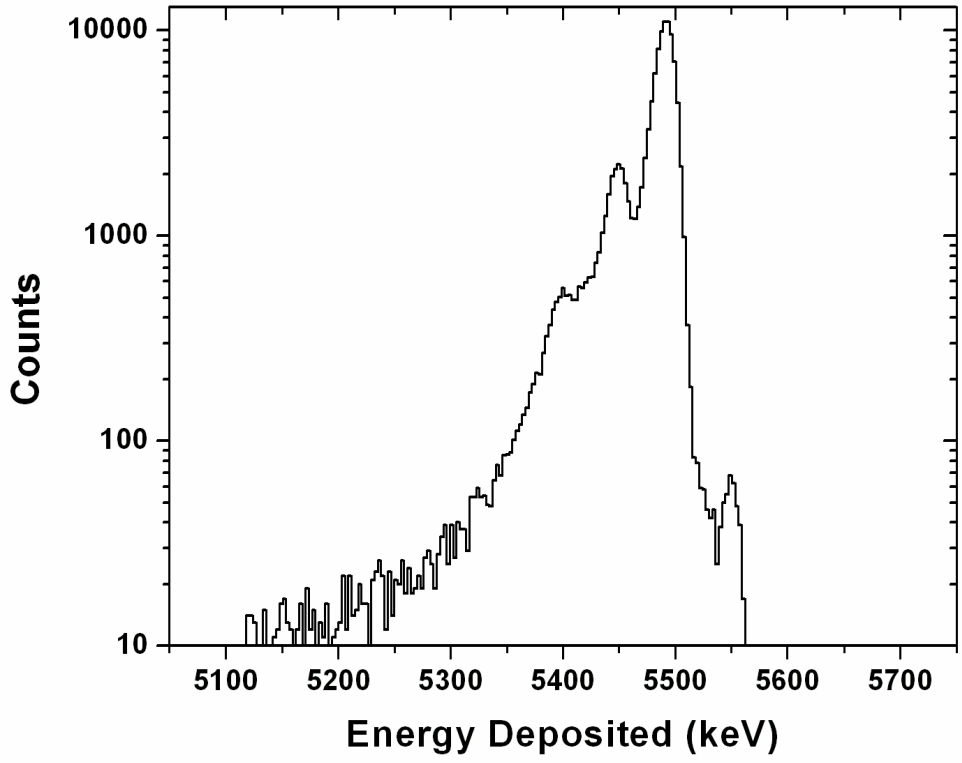

Figure 3-10: Alpha spectra as obtained using the 1 mm^2 silicon planar detector. Note, the four discernable characteristic peaks corresponding to 5.389 MeV (1.3% abundance), 5.443 MeV (12.8% abundance), 5.486 MeV (85.2% abundance) and 5.545 MeV (0.35% abundance). A fifth peak is also present at 5.513 MeV (0.12% abundance) but this is not discernable on the graph.

The main 5.486 MeV alpha peak of the spectra was used to normalise an Ortec Model 448 precision pulse generator. The silicon planar detector was then replaced with a 10 μm SOI microdosimeter with array 4 selected. Array 4 was utilised for all calibration work as this has the mean capacitance of the three useable arrays. For each perspective gain setting and pre-amplifier/circuitry board combination a range of pulser amplitudes (corresponding to calibrated input energies) were collected to provide a relationship between channel number and collected energy. From this relationship a calibration curve for each gain setting and pre-amplifier/circuitry board combination was established to provide accurate calibration of all experimental results.

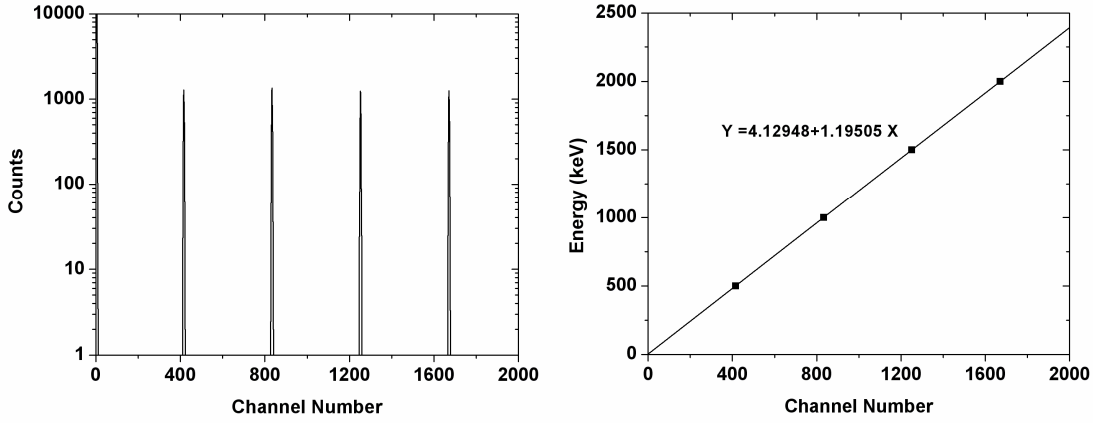

Figure 3-11: On the left is a pulser spectra collected for a coarse gain of 20 and with the buffer amplifier activated. Each pulse is calibrated to a given energy value. On the right, is a calibration curve created from the energy/channel relationship. Note the equation which is used for the calibration of all experimental spectra collected using this gain setting and device/pre-amplifier/circuitry board combination.

To ensure that the calibration remained constant, periodic checks with both pulse generators and alpha particle irradiation were also completed both pre and post experiment. This method of calibration ensured accurate results for each gain setting and device/pre-amplifier/circuitry board combination, which was especially important as variations in experimental setup (i.e. changing board and/or A-250) had a measurable effect on the energy calibration through variations in system capacitance. It should be noted that in order to obtain the correct energy scale for an experimentally obtained spectra using the SOI device a CCE of 0.8 [26] needs to be applied to the energy scale.

3.7 Experimental System Noise Assessment

The final test for the experimental probe assembly was to ensure that the noise limitations of the device were understood and could be accounted for when comparing to Monte Carlo simulations of the experimental system. To determine the intrinsic noise of the system, signal pulses from an Ortec Model 448 precision pulse generator was input into the system over a range of energies (0.1-8MeV using the calibrated energy scale) and main amplifier gain settings. Such measurements provided the intrinsic noise of the entire experimental system and determined if this changed with main amplifier gain. In each instance these measurements were made with a 10 μm SOI microdosimeter chip connected in the experimental assembly, as this was most representative of a typical experimental setup.

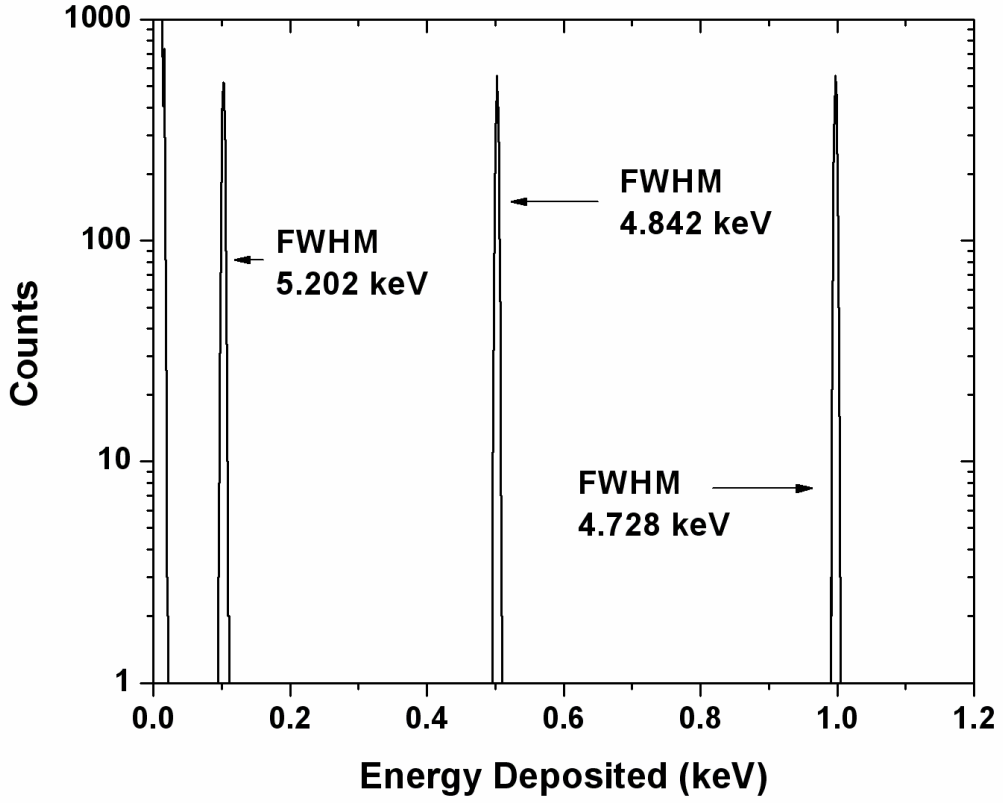

Figure 3-12: Incident pulser spectra collected using the experimental probe and amplifier assembly.

Figure 3-12 shows the incident pulser spectra collected using the experimental setup for 0.1-1 MeV. It is clear from these measured values that the full-width at half maximum (FWHM) ranges from approximately 4.7-5.2 keV. To illustrate this more

clearly, an expanded pulser spectra is displayed in Figure 3-13. Across all energy and gain settings tested an average value of approximately 5 keV at FWHM was measured which remained relatively constant. This value will be applied as a Gaussian distribution of σ=5 keV to Monte Carlo simulations to better reflect the intrinsic noise of the experimental system. This agrees well with what has been measured and used previously [26].

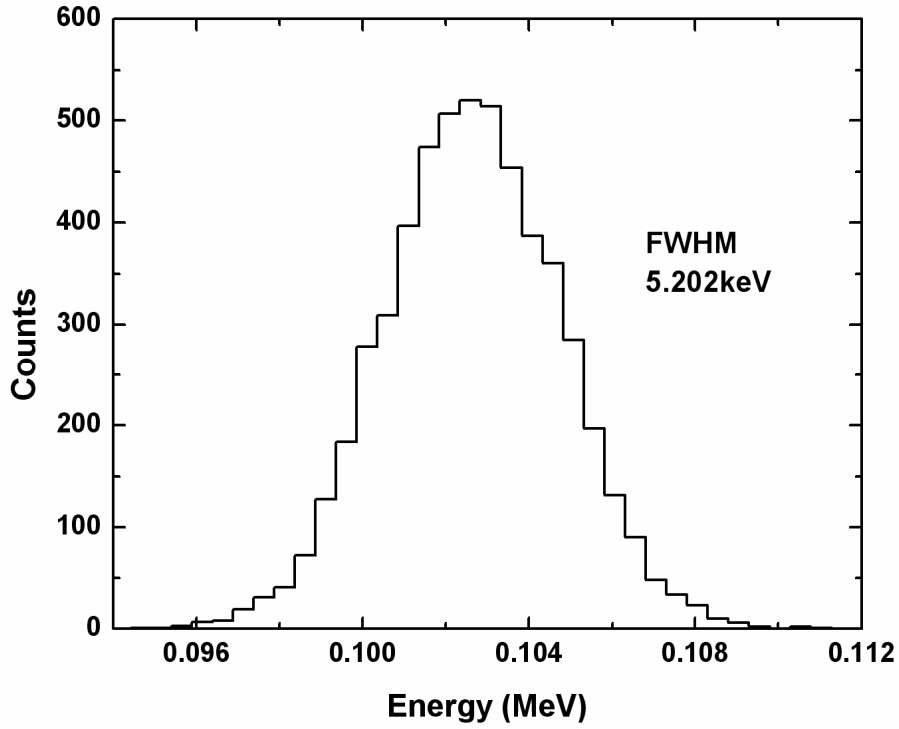

Figure 3-13: Magnified incident pulser spectra collected using the experimental probe and amplifier assembly.

The other important noise characteristic of the experimental system which needed to be quantified was the lower level noise threshold. This is extremely important, especially in low-LET radiation environments, as the noise level ultimately determines the sensitivity of the instrument. This was determined both with the pulser connected but turned off (as is typically the case in device testing), and then with the pulser disconnected completely from the system (typical for external beam radiation measurements) and the results are displayed in Figure 3-14. It was clear that the presence of the pulser did introduce some additional noise to the system. However, as this was not be the case in experimental studies it could largely be disregarded. With the pulser

removed from the system a lower level noise threshold of approximately 15 keV was measured for the 30x30x10 μm^3 microdosimetry array A4 which again compares favourably with what is published in [21]. This corresponds to a tissue equivalent (TE) lineal energy limit of approximately 0.8 keV/μm using a mean tissue equivalent chord length of 19.05 μm that was determined using the method outlined in [32] and Section 2.5.

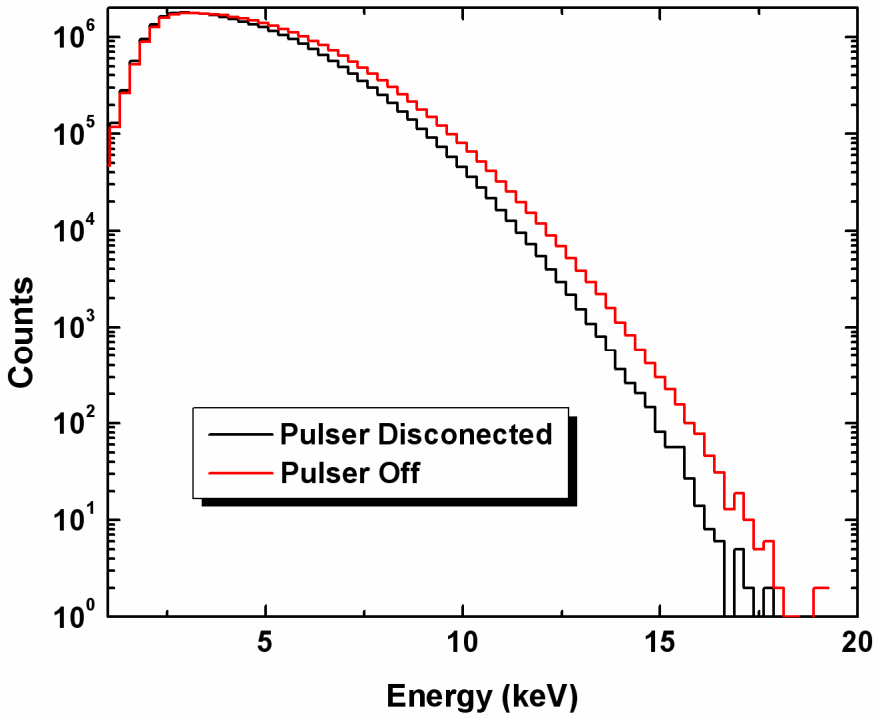

Figure 3-14: Lower noise threshold of the experimental microdosimetry system with a 10μm SOI microdosimeter.

The noise levels of the modified experimental assembly compare well with the previous published benchmark values of the SOI microdosimeter [21, 25]. As such the improvements that were made to the experimental probe assembly to enable the transport of low range secondaries into the SV did not have a detrimental effect of the noise characteristics of the system. The benchmarks established in this section of research will be utilised in subsequent SOI microdosimetry studies.

4 Measured Out-Of-Field Dose Equivalents in Proton Therapy

4.1 Introduction

Presently one of the major health risks mankind faces is cancer. Projections are that one in three people will suffer from this disease or side effects of its treatment at one stage in their life [3]. Because of the deleterious effects that cancer and current treatment forms are having on the human population, better treatment techniques are constantly being sought. Besides surgery external beam radiation therapy is a mainstay of cancer treatment and cure. Over the last two decades highly conformal radiation therapy techniques have been developed, including intensity modulated photon radiotherapy (IMRT) and radiotherapy utilising protons and carbon ions. One drawback of these techniques is that they may increase the contribution of lower doses to large volumes of normal tissues outside the target volume [67].

High energy protons are an important innovation in external beam radiation therapy, providing highly conformal dose distributions, thus sparing normal tissues through the benefits afforded by the Bragg peak. These dose distributions provide a smaller integral dose to surrounding normal tissues when compared with conventional X-ray treatments. Despite the dose sparing properties of protons and heavy ions, they do have the potential to produce unwanted dose outside the primary field due to secondary particles, such as neutrons, through inelastic nuclear interactions with the beam modifying devices and tissues traversed. This is of concern as neutrons are known to be more effective than photons and high energy protons at producing radiation induced cancers [67]. The primary beam is also scattered as it traverses the patient contributing additional unwanted dose outside the primary treatment field.

The production of secondary particles with therapeutic proton beams and the delivery of unwanted dose equivalent outside the treatment field is closely related to the delivery technique employed [67]. Proton delivery techniques can be categorized as passive or active in the delivery of a uniform dose to the treatment volume. Passive techniques,

which have been most commonly used in the clinical setting, including prostate cancer treatment, [6, 7] spread the beam laterally using a combination of gold and Lexan foils [8] and in depth by using a rotating plastic wheel [5]. The beam is then collimated by brass or Cerrobend® apertures and its penetration depth is varied by means of a wax or Perspex bolus. Active techniques [11-14], currently only practiced in a clinical situation at the Paul Scherrer Institute (PSI), employ a magnetically guided proton pencil beam in combination with dynamic changes of beam energy and beam intensity during treatment. Comparatively, passive beam delivery techniques provide a larger source of secondary neutrons due to the additional presence of scattering foils, modulator, aperture and bolus.

Measurements of out-of-field doses delivered in both active and passive clinical proton modalities are scarce [68-70] and have primarily concentrated on the measurement of neutrons with Bonner spheres and bubble detectors. Additional measurements are required and should be performed systematically for different beam delivery techniques utilising the same method of measurement. We have approached this problem utilising silicon-based microdosimetry, which is characterized by a superior spatial resolution and directly provides information on the dose equivalent using established quality factors [32]. The measurements reported here provide information on the depth and lateral distance dependence of the dose equivalent for a passively scattered proton beam used in a typical prostate cancer treatment. Silicon microdosimetry measurements were compared with published results obtained utilising different measurement techniques.

4.2 Experimental Method

This study utilised a solid-state microdosimeter with Silicon-On-Insulator (SOI) technology as illustrated in Figure 2-9 and described in Section 2.4. The large size of tissue equivalent proportional counters (TEPC), classically used in microdosimetry measurements [33], make them unsuitable for measurements of dose equivalent in small increments close to the primary proton treatment field edge and within a phantom structure. The SOI microdosimeter used for this work, presented in detail in [25] and Section 2.4, comprised an array of 4800 silicon cells, each with a physical size of 30x30 μm^2, on a single chip with a sensitive volume (SV) thickness of 10 microns. This small size allowed for accurate placement within the phantom structure and in close proximity

to the primary field edge. The application of SOI microdosimeters in therapeutic neutron radiation fields has been studied in detail and good agreement was observed between the derived microdosimetry spectra of both the SOI and TEPC devices [21, 29, 71]. The SOI microdosimeter has also been used extensively in hadron and proton therapy particularly in primary beam microdosimetry measurements [25, 29-31, 64]. This previous work supports the use of the SOI microdosimeter in this application.

In this experimental setup, the SOI microdosimeter, pre-amplifier, and accompanying electronics were situated within an Aluminium probe assembly to allow for a low noise environment to be achieved. The wall thickness of the probe was 900 μm, with a 4 μm Aluminium window immediately in-front of the microdosimeter to allow for the transport of low range secondaries into the SV. The microdosimeter probe was housed within a Perspex probe holder to enable accurate placement throughout the experiment. This set-up is described further in [64] and Section 3.5. A 0.5 mm thick polyethylene converter affixed immediately anterior to the SOI microdosimeter allowed for the conversion of neutrons to recoil protons at the surface of the phantom that could then be detected within the SV. Such converters have been employed in previous neutron and mixed field measurements with this device [29, 31].

All measurements were completed using a patient specific aperture-bolus combination, and proton energy of 225 MeV to simulate a typical radiation field delivered in a clinical prostate case. The maximum aperture dimension was 8 cm both in lateral and vertical direction. Additional measurements were also completed in some cases using a 13 cm diameter circular aperture (Quality Assurance or QA aperture) with no bolus present to demonstrate the effect of aperture size and bolus on the dose equivalent. To conduct a thorough study of the dose equivalent delivered outside the treatment field, four separate experimental configurations were used, each measuring a different aspect of the radiation field. In the first case, the patient was simulated with an anthropomorphic phantom (Rando® Phantom, The Phantom Laboratory, Salem, NY) housed within a regular patient immobilisation system (Figure 4-1). The microdosimeter (MD) was placed on the phantom surface at the height of the central axis, and

microdosimetry measurements were performed to measure change in dose equivalent as a function of increasing lateral distance from the field edge.

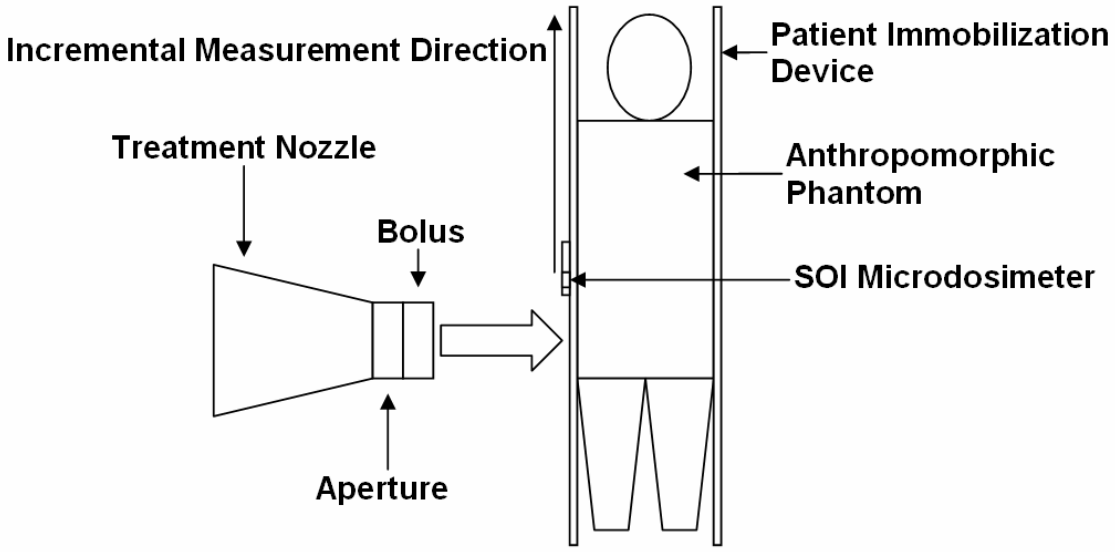

Figure 4-1: Experimental set-up for surface dose equivalent measurements as a function of distance from the field edge.

Additional measurements were conducted with the anthropomorphic phantom replaced with a stack of polystyrene blocks (Figure 4-2). Using this experimental set-up, three measurement series were completed. Firstly, the MD was placed at different depths within the polystyrene phantom at a distance of 5 cm from the field edge to estimate the change in dose equivalent as a function of depth within the patient (series M1). Measurements were also completed to assess the change in dose equivalent as a function of lateral distance from the field edge at different depths within the polystyrene phantom (series M2). Finally, measurements were completed to assess the dose equivalent beyond the distal edge of the SOBP (series M3), with the distal edge being defined as the point where the primary dose reached 50%. In all cases, dose equivalent was normalised to the proton dose delivered at isocenter.

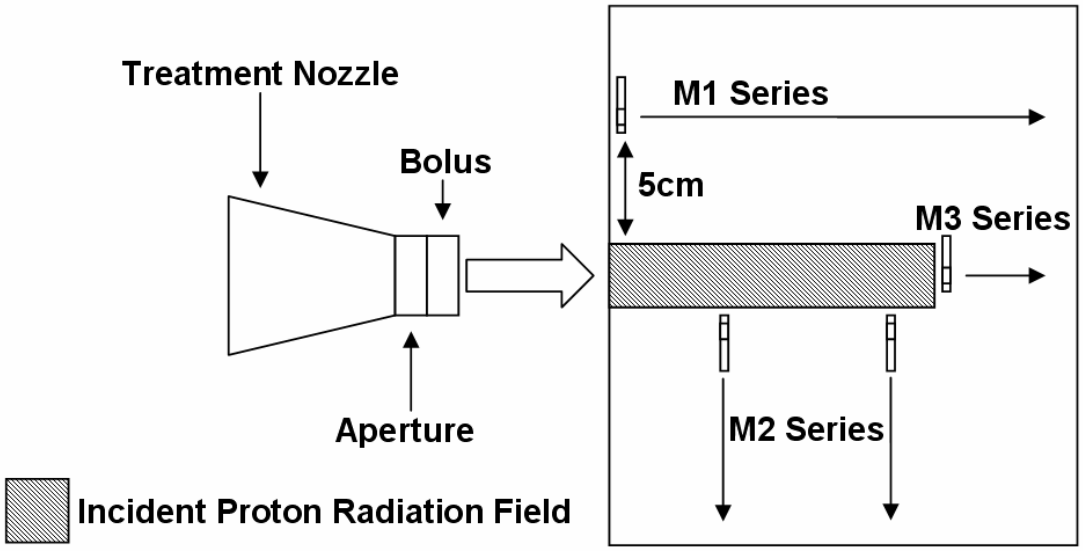

Figure 4-2: Experimental set-up for dose equivalent measurements within a polystyrene phantom. Note the 3 separate measurement series conducted with this experimental setup. M1 measured the change in dose equivalent as a function of depth 5 cm from the treatment field edge; M2 measured the change in dose equivalent as a function of distance from the field edge for 2 separate depths within the polystyrene phantom; and M3 measured the change in dose equivalent past the distal edge.

For each measurement position the dose equivalent and average quality factor was determined using the protocol outlined in [32, 33] and Section 2.5. Where possible, results were compared to existing data to determine the accuracy of this measurement technique.

4.3 Results & Discussion

Figure 4-3 presents the results of dose equivalent values on the surface of the anthropomorphic phantom as a function of distance from the incident proton field edge. It is evident from these results that the aperture and bolus used within a typical prostate cancer patient treatment increased the dose equivalent by a factor of 2-4 when compared to the 13 cm diameter circular QA aperture without bolus. The increased collimation present in the case of the patient specific aperture resulted in greater interaction of the primary proton beam with the collimation material, leading to elevated doses outside the treatment field. Dose equivalent values of approximately 4 and 2 mSv/Gy were measured at 2.5 cm from the edge of the primary beam for the patient specific aperture/bolus combination and the QA aperture respectively. Sub-mSv readings were detected at

distances greater than 10 cm and 20 cm from the field edge in the case of the QA aperture and patient specific combination respectively. At a distance of 60 cm from the field edge the dose equivalent for the patient specific setup was 0.176 mSv/Gy which would result in a total dose equivalent at this point of 14 mSv assuming a total dose delivery of 80 Gy to isocenter, which is the typical integral dose used in patient treatments.

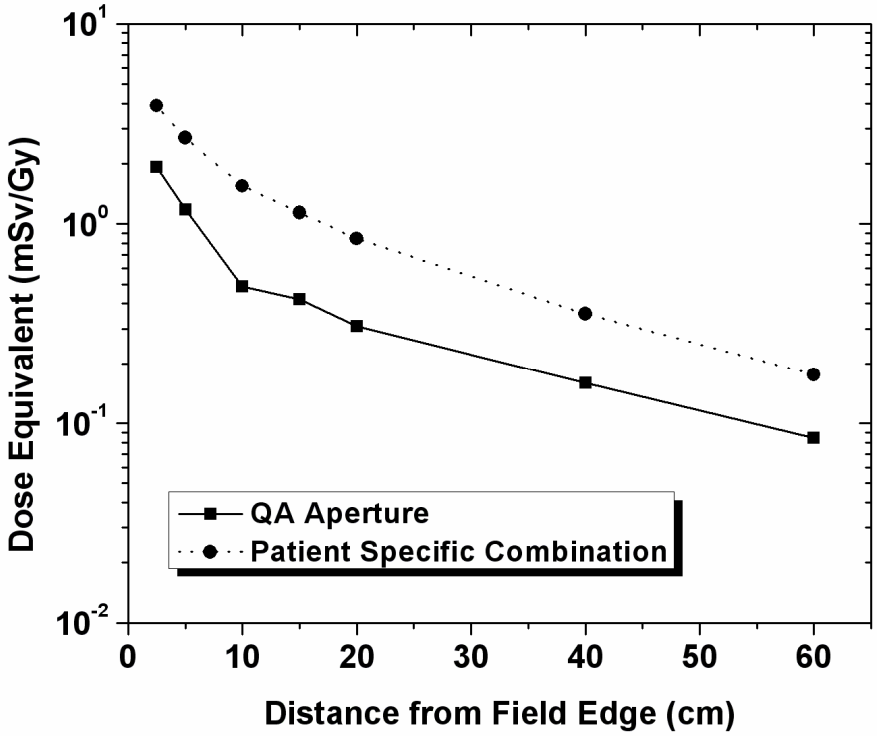

Figure 4-3: Results as measured with the SOI microdosimeter for both the patient specific aperture/bolus portal and the 13 cm circular QA aperture with no bolus present.

Figure 4-4 displays results of measurements that were completed to assess the change in dose equivalent as a function of depth in a polystyrene phantom at 5 cm lateral distance from the patient-specific proton field (series M1). For comparison, the central axis depth-dose distribution of the primary proton beam is also displayed and is normalised to the dose at isocenter (100%). Initial dose equivalent values at the surface of the phantom decreased by 38% after traversing 5 cm of phantom material. This leads to the conclusion that many secondary particles produced within the passive scattering and collimation system were of low penetrating power or "softer" and did not penetrate to a great depth within the phantom.

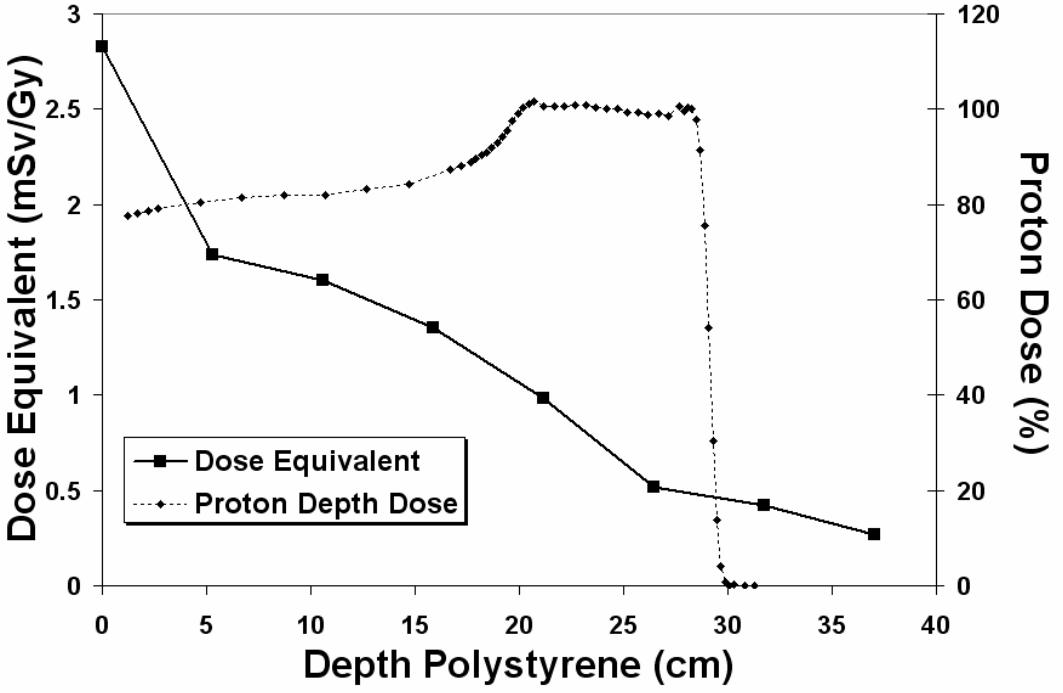

Figure 4-4: Dose equivalent measured at 5cm from the field edge compared with the depth dose distribution of the proton beam as measured along the central axis with a Markus chamber. The proton dose is expressed as a percentage with 100% dose delivered at isocenter.

Figure 4-5 displays the lateral distance dependence of dose equivalent at two different depths within the polystyrene phantom (measurement series M2). Measurements were completed at the plateau region (158 mm depth polystyrene) and the level of the SOBP (264.5 mm depth polystyrene). The dose equivalent decreased with increasing distance from the field edge, similarly to what was measured at the phantom surface (Figure 4-3) however with a more gradual fall off. Moreover, the fall off is less pronounced at the level of the SOBP compared to the shallower depth, which leads to a convergence of the two curves at a distance of about 20 cm from the field edge. This would indicate that secondaries produced inside the phantom contributed increasingly to the dose equivalent.

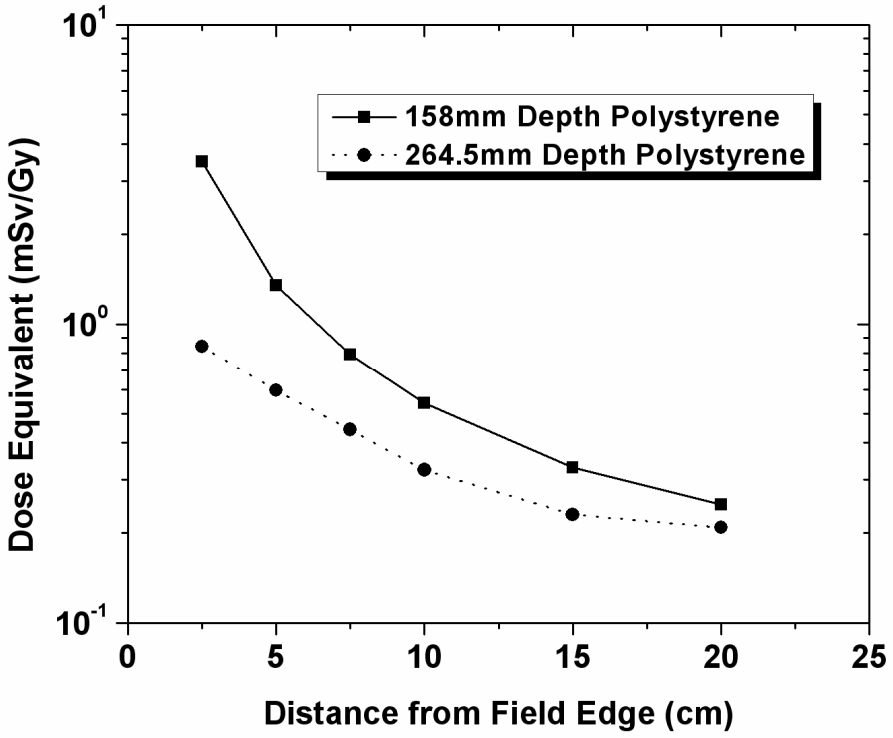

Figure 4-5: Assessment of the dose equivalent as a function of lateral distance from the field edge at different depths within the polystyrene phantom.

Figure 4-6 displays the measured dose equivalents past distal edge of the SOBP in the polystyrene phantom (measurement series M3). The dose equivalent in the case of the typical prostate treatment investigated here was 1.6 mSv/Gy at 0.6 cm from the distal edge and decreased exponentially with increasing distance from the distal edge. Fitting an exponential function to this trend resulted in the relationship described in Equation 4-1 for the dose equivalent in mSv/Gy:

$$H = 1.65e^{-0.1081x}$$

Equation 4-1: Relationship between dose equivalent (H) per unit absorbed dose and distance from the SOBP distal edge (x in cm) along the central axis.

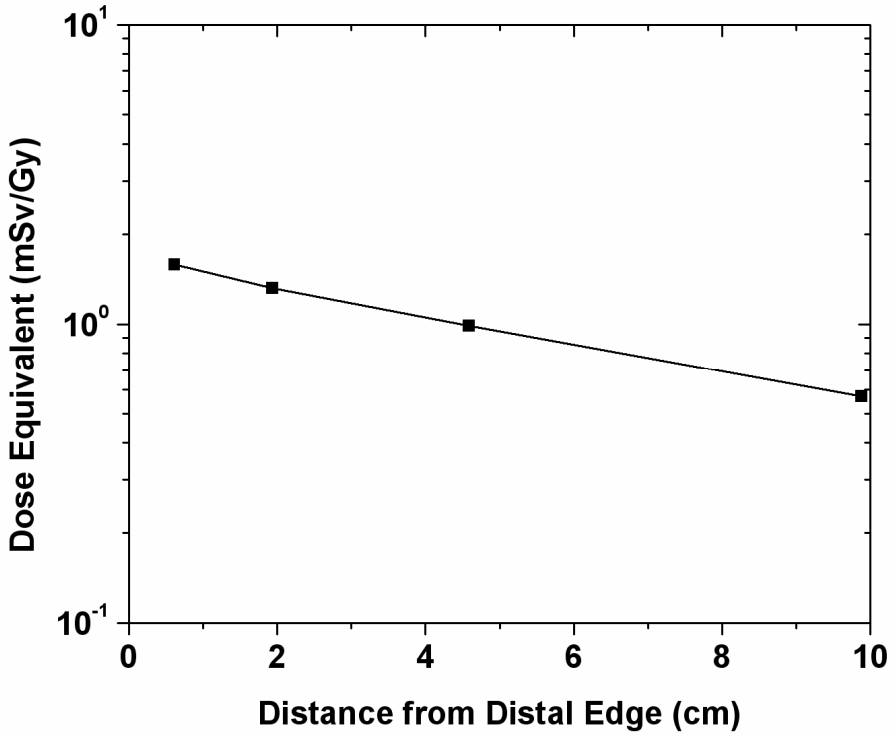

Figure 4-6: Dose equivalent measurements past the distal edge of the SOBP.

The average quality factor is valuable as it provides information on the types and abundances of radiation present. This information is presented in Figure 4-7 as a function of lateral distance from the treatment field edge measured at the surface of the anthropomorphic phantom and also past the distal edge of the SOBP in the homogeneous polystyrene phantom (measurement series M3). At the phantom surface the average quality factor increased from 2 to 7 at a distance of 2.5 and 60 cm from the field edge respectively. This indicates that close to the field edge scattered neutrons of higher energy and lower LET made up a substantial portion of the dose equivalent, however, further from the field edge lower energy neutrons predominated resulting in higher measured average quality factors. Figure 4-7b) shows that the average quality factor past the SOBP remained relatively constant at an approximate value of 6.5. In this region, high energy primary protons were not present and the radiation field comprised of relatively low-energy neutrons produced both from proton interactions with the beam-modifying/monitoring devices and within the phantom. The constant nature of the average quality factor indicates that the radiation field past the SOBP did not change markedly in composition nor energy.

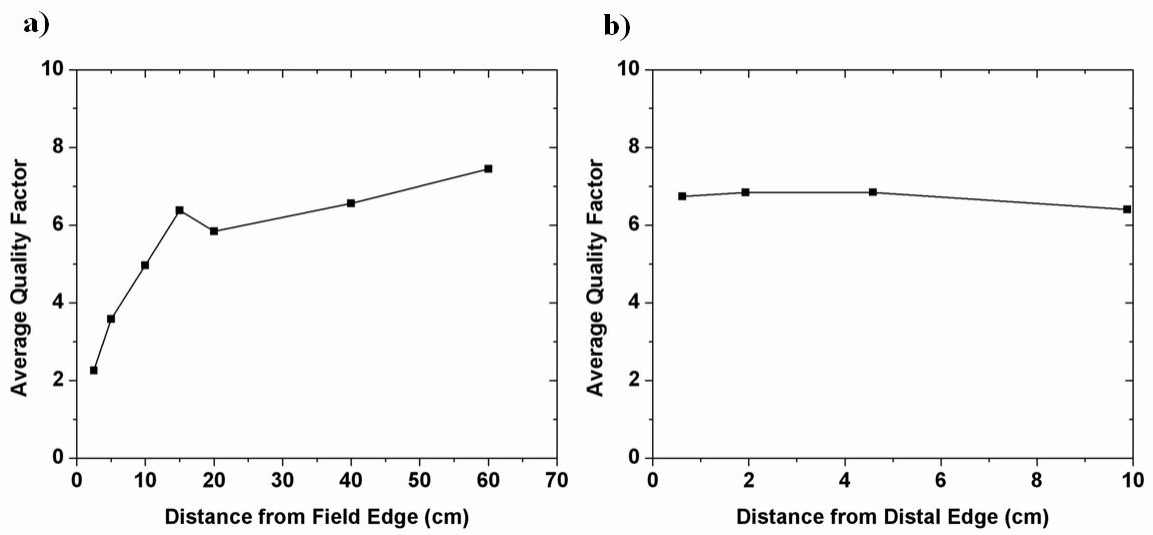

Figure 4-7: Average quality factor values for a) points lateral to the treatment field edge at the surface of the anthropomorphic phantom and b) points past the SOBP within the polystyrene phantom. In each case, the aperture and bolus combination was that for a typical prostate patient.

4.4 Accuracy of Results

In this work, we have utilised a microdosimeter based on SOI technology to measure the depth and lateral distance dependence of the dose equivalent for a passively scattered proton beam used in a typical prostate cancer treatment. Unlike conventional TEPC devices, the SOI microdosimeter comprises of an array of truly microscopic detection elements. This allows for faster data acquisition through the use of multiple SV's, good spatial resolution, and the ability to measure within phantoms. The microdosimetry method also provides a more accurate estimation of dose equivalent using an established relationship between lineal energy and quality factor. This is particularly advantageous in mixed radiation field measurements.

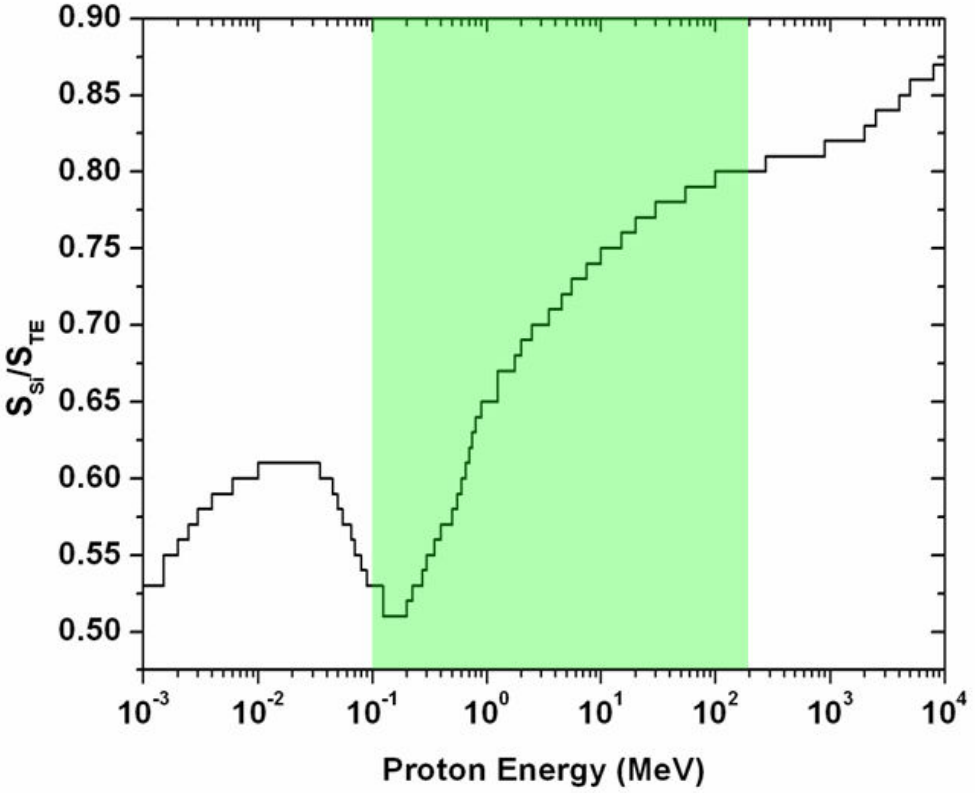

Figure 4-8: Ratio of proton stopping powers for silicon and tissue [35]. The region of interest in this case was approximately 0.1-200 MeV and is highlighted in green.

SOI microdosimetry has certain limitations that need to be considered when evaluating the uncertainty of the measurements presented in this work. The lower level detection limit of the SOI device is approximately 0.8-1 keV/μm, whereas the *y* values in the *Q(y)* distribution extend down to 0.1 keV/μm. This limitation does not produce a significant error in the dose equivalent because the *Q* value is less than 1 in this region (Figure 2-11). The main source of error in these measurements arises from the TE conversion factor, which is derived from the ratio of stopping powers. This factor covers a wide range of recoil proton energies from 0.1–200 MeV and hence the value for each individual particle can lie from 0.5 – 0.8 as shown in Figure 4-8. Previous work with protons and alpha particles has found best agreement using a value of 0.63 [21]. By using this value, the systematic error introduced in the data presented here may be up to approximately ±15%. Additional work, including Monte Carlo simulations, is necessary to further reduce and understand this uncertainty for proton therapy applications.

4.5 Comparison with Existing Data

It is important when applying existing technology to a new mode of measurement, to benchmark results against existing data in the field. Figure 4-9 illustrates the comparison of results from other centres using different measurement techniques.

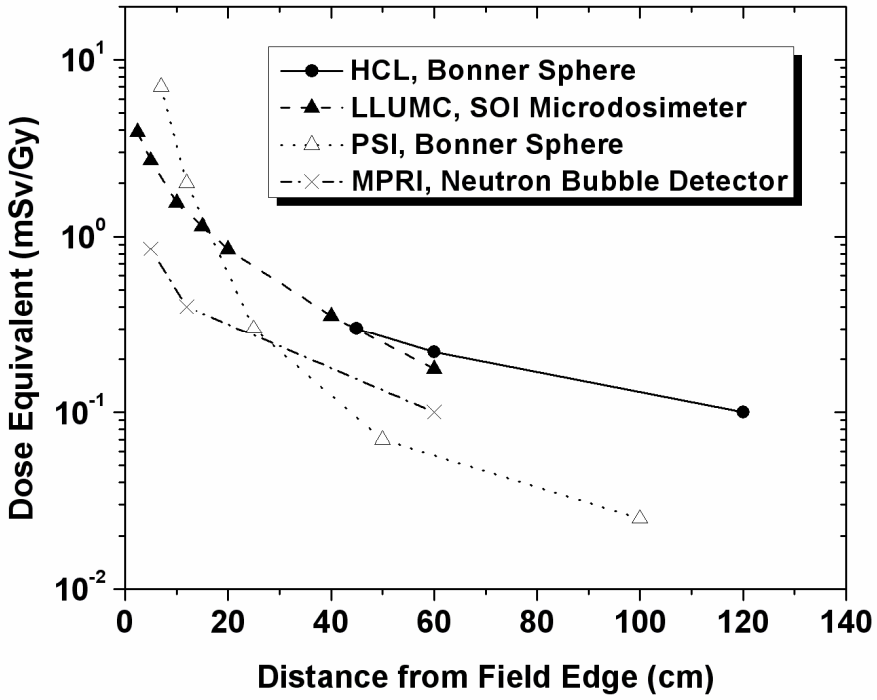

Figure 4-9: Comparison of dose equivalent values measured using different methods. In this figure results are presented from HCL [68], PSI [70] and MPRI [69] in comparison with results presented in this paper using the SOI microdosimeter and the patient specific aperture/bolus combination (Figure 4-3) at the surface of the anthropomorphic phantom.

At the Midwest Proton Radiotherapy Institute (MPRI), neutron doses were measured with a neutron bubble detector and a passively scattered and modulated proton beam of 12 cm range in water. The field size in this instance was 10 cm in diameter with an 8 cm modulation delivered to the midline of an anthropomorphic phantom. Measurements were made as a function of distance from the proton field edge within the phantom, with the detector situated within the abdomen to determine the scattered neutron dose at the location of a foetus. Measurements were completed for two snout sizes (10 and 20 cm) with the 20 cm results presented here. The Harvard Cyclotron Laboratory (HCL) data were derived on the 160 MeV beam line used for patient treatments, utilising Bonner spheres for the detection of neutrons. A Lucite phantom (26 cm in diameter and 24 cm in

length) represented the patient, while the primary proton radiation field had a cross sectional area of 5x5 cm^2 and a range of 16 cm with a modulation of 8.2 cm. The neutron dose equivalent per unit proton absorbed dose was measured as a function of vertical distance below isocenter. Finally, the data from the Paul Scherrer Institute (PSI) provides information on the secondary neutron dose delivered during a spot scanning treatment. Again this study utilised Bonner spheres as the radiation detection apparatus with an incident beam of 177 MeV and no range shifter plates in the beam path. A water phantom with 0.5 cm thick Lucite walls was used to simulate the patient. The values of effective neutron dose were measured laterally from the water phantom at the level of the treatment volume, not the surface of the phantom as in the case presented here.

Despite the difference in experimental conditions and measurement techniques, the agreement between the data is good. Of note, the equivalent doses measured with the spot-scanning beam were consistently lower than the other data, in particular at distances greater than 50 cm. This is consistent with the fact that the spot scanning system does not contain beam modifying devices such as apertures and scattering foils which contribute neutrons to the radiation field outside the primary treatment field. The results from PSI, HCL and MPRI consisted of lower energies than the measurements completed with the SOI microdosimeter, which may have a bearing on the results as lower incident proton energies have in-turn lower cross sections for inelastic reaction. Further the results from MPRI are also completed at the position of the foetus within the anthropomorphic phantom and hence a reduction in dose equivalent over measured surface values is expected which is illustrated in Figure 4-4 and Figure 4-5.

4.6 Conclusion & Future Recommendations

This study has shown the applicability of the SOI microdosimeter in measuring the dose equivalent outside proton treatment fields and has provided valuable information on the dose equivalent both at the surface and at depth experienced by prostate cancer patients treated with protons. They show that dose equivalent values are of the order of a few mSv/Gy within 10 cm of the treatment volume (Figure 4-3 and Figure 4-5) and appears to level off at about 0.2 mSv/Gy for larger distances from the treatment volume (Figure 4-5). These dose equivalent values compare favourably to those experienced by

patients from IMRT treatments [67] and cone beam CT imaging that is increasingly used for image guided radiation therapy [72].

It was clearly demonstrated in Figure 4-9 that SOI microdosimetry measurements compared favourably to those measured at other centres with Bonner spheres and bubble detectors. However, close comparisons are difficult due to the different measurement conditions and apparatus used. Further, this limits comparisons using the current data on the dose equivalents delivered by different proton therapy centres and delivery techniques. Such measurements in proton therapy are important and must be completed to ascertain where future improvements in beam delivery and patient treatment can be made.

To achieve this aim further studies utilising the SOI microdosimeter are currently being conducted with therapeutic proton fields generated with both passive and active beam delivery techniques under otherwise equivalent conditions and for different clinical treatment scenarios including paediatric cancers. Such studies will also compare the response of SOI detector to other microdosimetric and neutron measurement techniques, to provide a quantitative assessment of its accuracy in mixed radiation fields.

5 SOI Microdosimetry: TE Validation

5.1 Introduction

Microdosimetry has many applications both in radiation therapy and radiation protection. In radiation protection the determination of biological doses for astronauts and single event upset (SEU) rates in micro and nano electronics are important goals for world space organizations in the 21st century. Conversely, in radiation therapy a better understanding of the changes in therapeutic radiation spectra with tissues traversed will enable advances in treatment planning and possibly improved efficacy in treatment with reduced side effects. One method that can be employed in these studies is microdosimetry, especially the use of solid-state microdosimeters such as those that have been developed at the Centre for Medical Radiation Physics (CMRP) at the University of Wollongong (UoW) and which are described in Section 2.4.

The main advantage of solid-state microdosimeters for space and aircraft operation is their compact size and low voltage for operation. However, previously they have suffered the drawback of the lack of a well-defined sensitive volume (SV). This problem has been addressed using Silicon-On-Insulator (SOI) technology which results in well defined microscopically small SV's. Scaling of the mean chord length allows derivation of tissue-equivalent microdosimetric spectra. Equivalent dose and average quality factor of a radiation field can then be determined by convolution of the microdosimetric spectra with a spectra of quality coefficients [32]. The microscopically small cell size is also useful in determining SEU's in microelectronics, allowing sufficient shielding to be constructed and thus enabling extended deployments of electronic devices.

In radiation therapy, especially hadron therapy, microdosimetry provides a means for determining the dose equivalent of a wide range of therapeutic radiation fields and secondaries such as neutrons. Such abilities have been previously displayed in Section 4. SOI microdosimeters also have the added advantage of being able to be used within phantoms for measurements of changing microdosimetric spectra. This is important in hadron therapy applications as it allows the change in biological effect within a phantom

to be measured and a determination of whether this should be considered in treatment planning applications.

Previously SOI microdosimeters have undergone Monte Carlo simulation studies within homogeneous phantoms and the results compared with experimental data obtained in neutron and proton radiation fields [25, 26, 29, 30, 66, 73]. These studies have illustrated that such simulations yield useful and accurate information. However, in these cases experimental information has only been obtained for homogeneous Perspex and water phantoms. It is desirable to obtain information utilising more complex layered heterogeneous structures of biologically important materials for a number of disciplines such as radiation protection and radiation therapy. Such studies can better develop our understanding of radiation interactions within the body and the changes to the radiation spectra as it traverses biological structures. This in turn can then be utilised to more efficiently construct radiation shielding in radiation protection applications and also better consider changes in treatment radiation fields during the planning process for radiation therapy.

The aim of this work is to observe the changes in experimental microdosimetry spectra as proton radiation traverses biologically important structures such as the human head and chest. These results will be compared with simulation studies utilising the GEANT4.7.1p1 Monte Carlo toolkit [52] for validation. The experimental validation of the GEANT4 based application for heterogeneous commercial phantoms will allow for further simulation studies of the SOI microdosimeter without experimental noise limitations. These simulations will enable changes in microdosimetric parameters such as mean dose weighted lineal energy, average quality factor and dose equivalent to be observed as a function of preceding phantom material..

5.2 Experimental Method

For this study a tissue equivalent (TE) phantom was specially constructed. It consisted of 20x20x1cm^3 slices of adipose, lung, brain, bone and muscle that were layered in a given order such that it could be configured to represent the structure of the human head and chest. The structure of these phantoms is outlined below and in Figure

5-1. The compositions of these phantoms were provided by the manufacturer for simulation using GEANT4.

- **Head:** 10 mm muscle, 10mm bone, 10 mm brain (in the case of 250 MeV protons 25-50 mm Perspex is also added to simulate a greater depth in brain)
- **Chest:** 10 mm adipose, 10 mm bone, 10 mm muscle, 20 mm lung

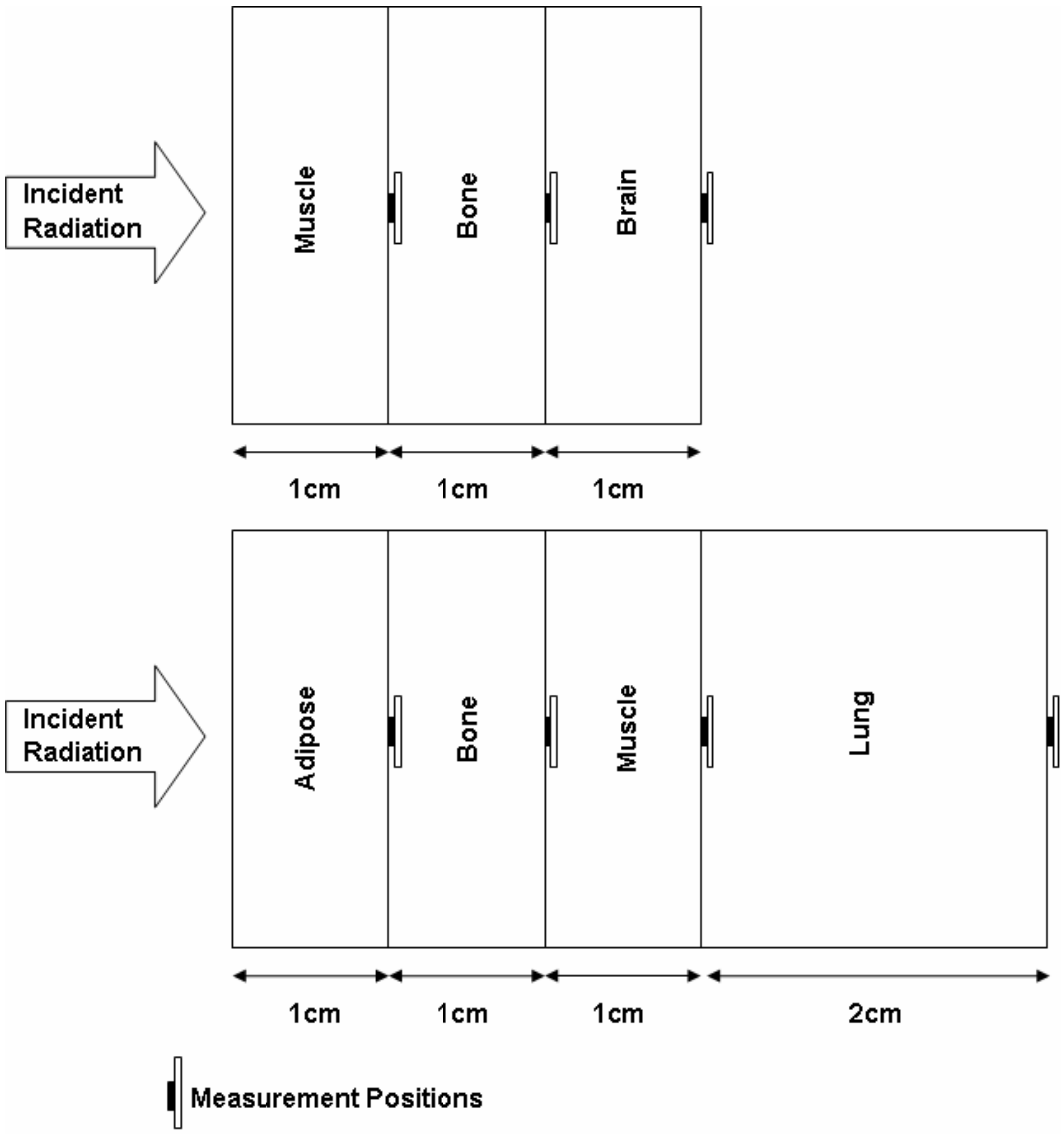

Figure 5-1: Schematic diagram of the phantom configuration as used within the experimental and theoretical portion of this work. Note the microdosimeter positions indicating the position of measurement (or simulated measurement). In the case of 250 MeV proton irradiations, 25 and 50 mm thicknesses of Perspex were also interspaced between the bone and brain layer (in the case of the head phantom) to provide additional measurement points at greater depths in brain.

A 10 μm thick SOI microdosimeter was used in this study. The array chosen in this experiment comprises of 4800 detector elements (40x120) with each cell having a physical size of 30x30 μm^2. The device was contained within a 0.9 mm thick probe holder of aluminium which would act as a Faraday cage. A 4 μm thick aluminium window was located immediately in front of the microdosimeter to allow for the transport of secondary particles into the SV. To enable reproducible placement of the microdosimeter probe on the central axis at tissue boundaries, it was housed within a purpose built Perspex probe holder. The probe was then placed at tissue boundaries within this phantom to ascertain the changes in microdosimetry spectra as a result of changing biological material.

The incident radiation field utilised in this study was 100 and 250 MeV protons with measurements completed on the central NASA research beam-line at Loma Linda University Medical Center (LLUMC). Experimental measurements were conducted with beam sizes of the order of 50 mm diameter at the point of entry into the phantom for 10 minutes. During this time the dead time was kept stable at 10% with a low noise threshold set on the Multi-Channel Analyser (MCA) of approximately 9 keV. Throughout the course of the experiment the device was irradiated with 0.2-0.35 cGy per spill (accelerator delivered radiation pulse of approximately 0.4 seconds duration with a total cycle time of 2.2 seconds [9]). The dose was monitored at regular intervals with a calibrated ion chamber, which has 12 μm Mylar entrance and exit windows, a 1.58 mm air SV thickness, and is described in [74] and Section 10.5.

5.3 Monte Carlo Method

The experimental setup was recreated within an application that was based on the GEANT4.7.1p1 Monte Carlo Toolkit. This included not only the SOI microdosimeter chip (as represented in Figure 5-2), but also the aluminium faraday cage, Perspex probe holder and layered phantom structure. The experimental setup in its entirety is displayed in Figure 5-3.

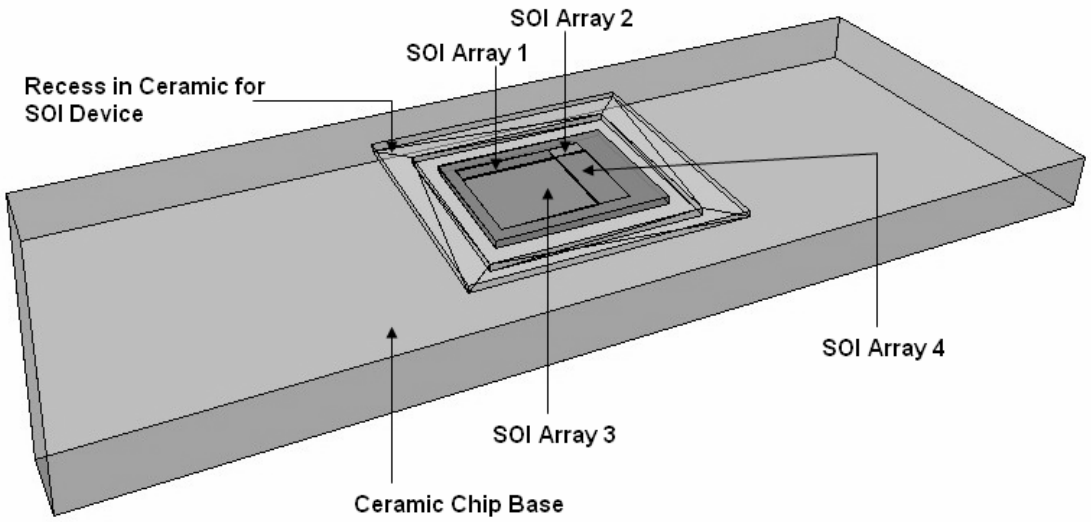

Figure 5-2: Schematic of the SOI microdosimeter chip as recreated within the GEANT4 based application. Note the four separate SOI microdosimetry arrays.

The SOI microdosimeter chip assembly was constructed within the GEANT4 based application from an arrangement of right angled parallelepiped volumes (RPP). Forming the body of the chip was the ceramic base layer with the dimensions of 35.4x14.6x2.0 mm^3 into which is formed a two stage recess with a total depth of 500 μm. Into this recess the Si substrate (279 μm thick), SiO_2 insulator (10 μm thick), Si SV (2, 5 or 10 μm thick depending on the device being simulated) and SiO_2 overlayer (1 μm thick) were defined as layered RPP volumes each with a cross sectional area of 5.5x6.5 mm^2. As such the Si detector was recessed into the ceramic chip with an approximate distance of 200 μm between the surface of the ceramic chip and the SiO_2 overlayer. Within the Si SV, four regions were defined as sensitive (i.e. energy depositions within these volumes were registered) which corresponded to the four detector arrays. The size and position of each individual array are described in [21] and were re-confirmed through microscopic analysis.

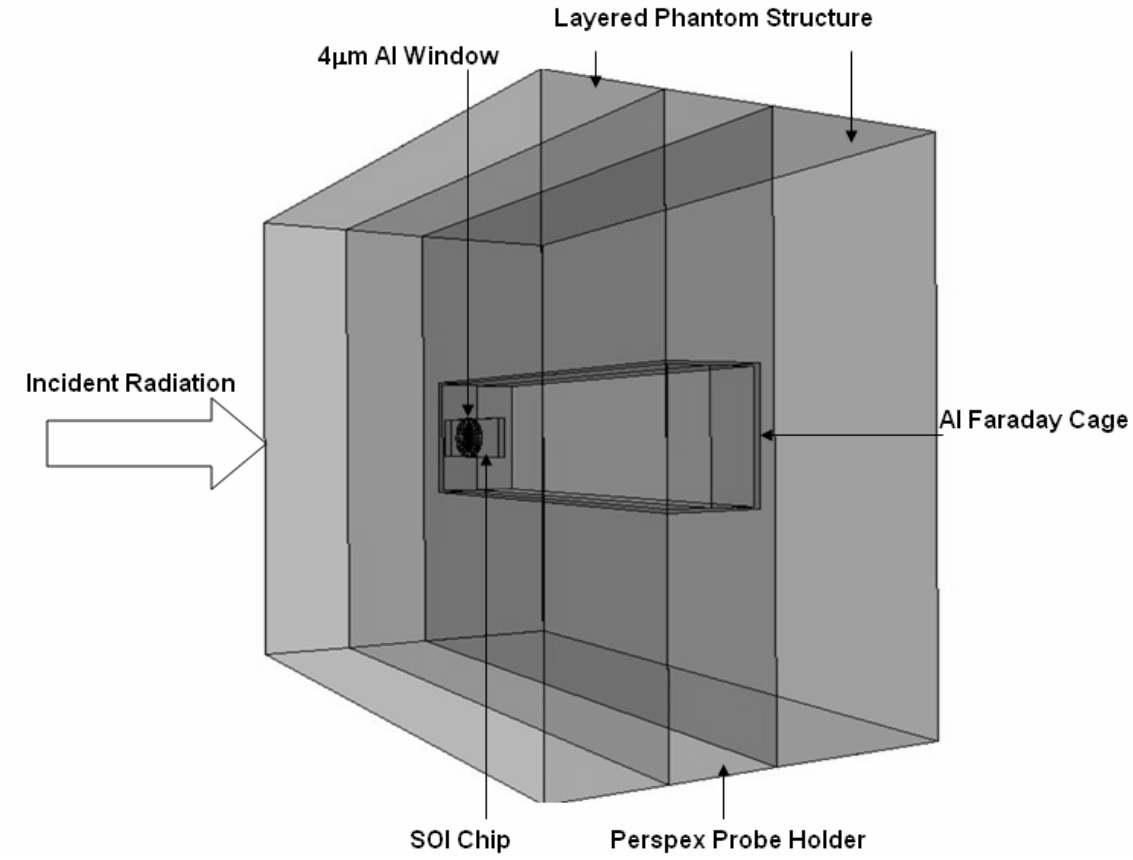

Figure 5-3: Schematic of the experimental setup as recreated within the GEANT4 based application.

The commercially available phantoms were reproduced within the simulation program according to the manufacturer's specifications. Energy depositions within the 10 μm SOI device were scored to create a spectrum of energy deposition events for comparison with the experimental results. This comparison was used to determine the accuracy of the GEANT4 based application in simulating the response of the microdosimeter within heterogeneous commercially available TE phantoms.

The Physics processes utilised for the transport of light ions (including protons) included low energy inelastic scattering (G4preCompound model), low energy ionisation (ICRU 49) and multiple scattering models. The physics of secondary particles including photons, electrons, neutrons and nuclear secondaries was also considered and accounted for using the appropriate models, with low energy extensions for electron and photon transport used where possible. Each simulation was carried out for $2x10^7$ normally incident protons transported along an evacuated beam pipe, beam exit window and across

a 3.5m air gap into the phantom and experimental probe assembly. The incident beam profile was approximated as circular with 10 mm diameter. In the case of the 250 MeV simulations, a 1.0 mm thick lead scattering foil was used to achieve a larger, more uniform field at the phantom. The advantage of completing experiments on a research beam-line was that there were minimal beam modifying structures in place which needed to be considered in the simulation. Regardless all beam-modifying devices were considered in GEANT4 simulations and were approximated using planar structures of a given thickness outlined in Table 5-1. As is the case with all Monte Carlo simulations in this study the compositions of which were defined isotopically from manufacturers specifications or from compositions sourced through NIST [35].

Beam Modifying Device	Material	Thickness (mm)
Beam Exit Window	titanium	0.025
Scattering Foil (250 MeV only)	Lead	1.0
Air	Air	3500

Table 5-1: Beam modifying devices considered in GEANT4 Monte Carlo simulations of the primary proton field present in the experimental case.

5.4 Result Normalisation

In comparing the simulated and experimental results for validation it is important that adequate and appropriate normalisation occurs. The experimental results were binned into 2048 channels by the MCA. An energy calibration was applied to the experimental results that in turn was derived using the method described in Section 3.6.

The simulated results were binned into 8000 bins spanning an energy range of 0-4MeV. The simulated results then had a charge collection efficiency (CCE) of 0.8 applied which has been previously determined and verified through ion beam induced charge collection studies (IBICC) [26, 27]. The simulated results were then convolved with a Gaussian of σ=5keV (measured experimentally in Section 3.7) to reflect the electronic noise present in the system.

$$f_j = \sum_{i=j-3\sigma}^{j+3\sigma} \frac{1}{\sqrt{2\sigma^2\pi}} f_i \exp - \frac{(\varepsilon_j - \varepsilon_i)^2}{2\sigma^2}$$

Equation 5-1: Gaussian which is convolved with simulated results to better reflect the experimental noise present in measurements. ε_i is the energy values corresponding to bin i of the frequency distribution.

Finally, both the simulated and experimental results were normalised to the total number of events present above twice the noise threshold of the experimental device. In this case the noise threshold of the experimental device was measured to be 15 keV. As such the results were normalised to total number of events higher than 30 keV.

5.5 Microdosimetry Spectra Generation

Once validation of the GEANT4 based application had occurred the raw simulated data was converted into microdosimetry spectra using the protocol outlined in [32] and described in Section 2.4. A mean chord length of $\langle l \rangle$ = 19.05 μm was used for these calculations. This value was calculated using Equation 2-1 based on a 30x30x10 μm^3 volume and a tissue equivalent scaling factor of ζ=0.63:

The spectra produced provide the fraction of the total dose occurring from lineal energy events in the interval $y \rightarrow y+dy$ where y is the lineal energy in keV/μm. The mean dose weighted lineal energy (Equation 2-3) was determined from the lineal energy spectra and used as an indicator of changes to incident radiation field as a function of preceding material. The dose equivalent and average quality factor was also be used as an indicator of changes in the incident radiation field and was determined using the methods described in Section 2.5.

5.6 Validation Results and Discussion

Experimental measurements were completed on the central NASA research beam-line at LLUMC. Experimental results for all energy/phantom combinations are unobtainable below 15keV due to the noise limit of the device. This lower level noise limit is clearly evident in all the graphs displayed.

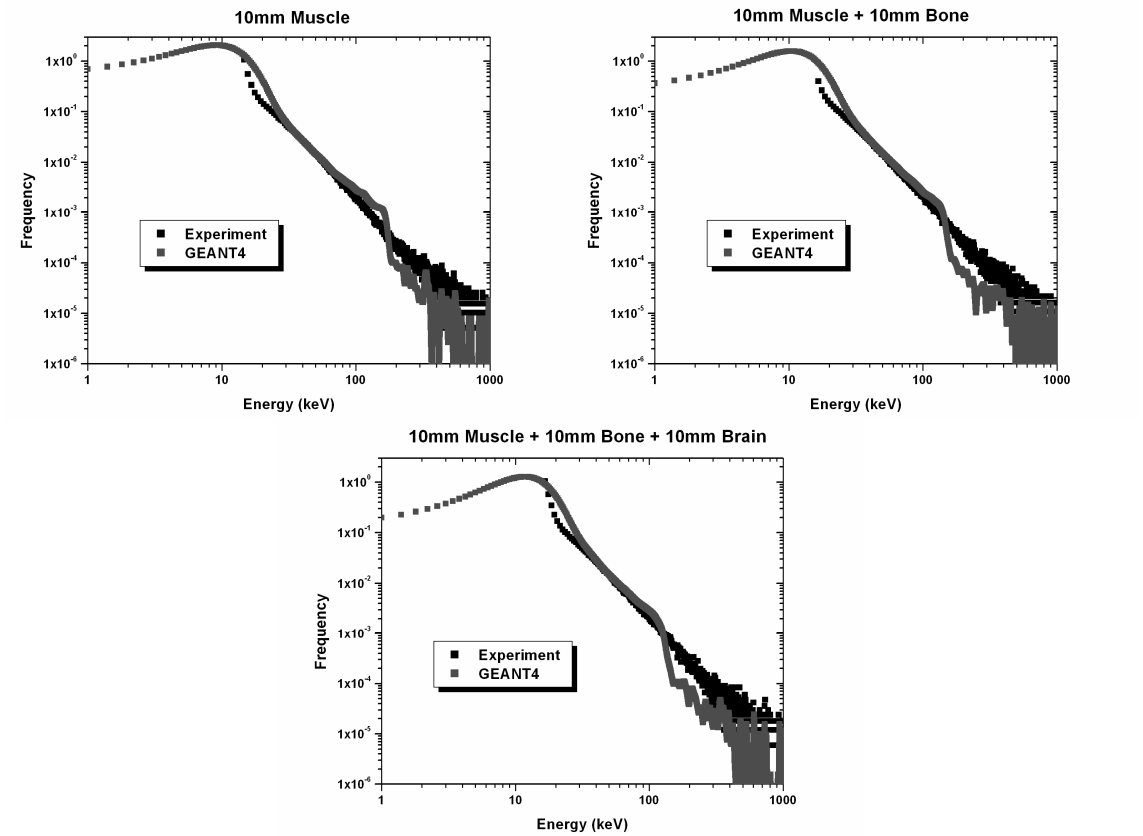

Figure 5-4: Comparative experimental and simulation results for the head phantom, when irradiated with 100 MeV protons.

Figure 5-4 shows a comparison between simulated and experimental results for 100 MeV protons within the head phantom. A discontinuity is observed in the simulated case at approximately 140 keV. The simulated case has a sharp drop before continuing parallel to the experimental trend at higher energy values. This is observed for all 100 MeV simulations, yet no discontinuity is observed for 250 MeV incident protons. Possible explanations for the discontinuity are:

a) A discontinuity in the physics models for lower proton energies regarding nuclear reactions. However, as the same models are used for the higher energy simulations with no discontinuity observed this seems unlikely.

b) The range cut in electron transport preventing low energy electrons for depositing energy in the device. However, as the same cut is used for the higher energy simulations with no discontinuity observed this seems unlikely.

c) An overestimation in the device overlayer in the simulated case. The simulated overlayer was constructed within the GEANT4 simulation to be a uniform layer of SiO_2 with a 1μm thickness. In actual fact it may have regions of varying thickness and possibly composition. Also, the aluminium contacts were not constructed within the simulation which could lead to errors in particle transport into the SV. Such errors could cause low energy protons to be prevented in reaching the SV. This would be seen causing a greater impact on 100 MeV results as nuclear secondaries (including recoil protons) produced would have a lower energy, which could be affected to a greater degree by inaccurate overlayer simulation.

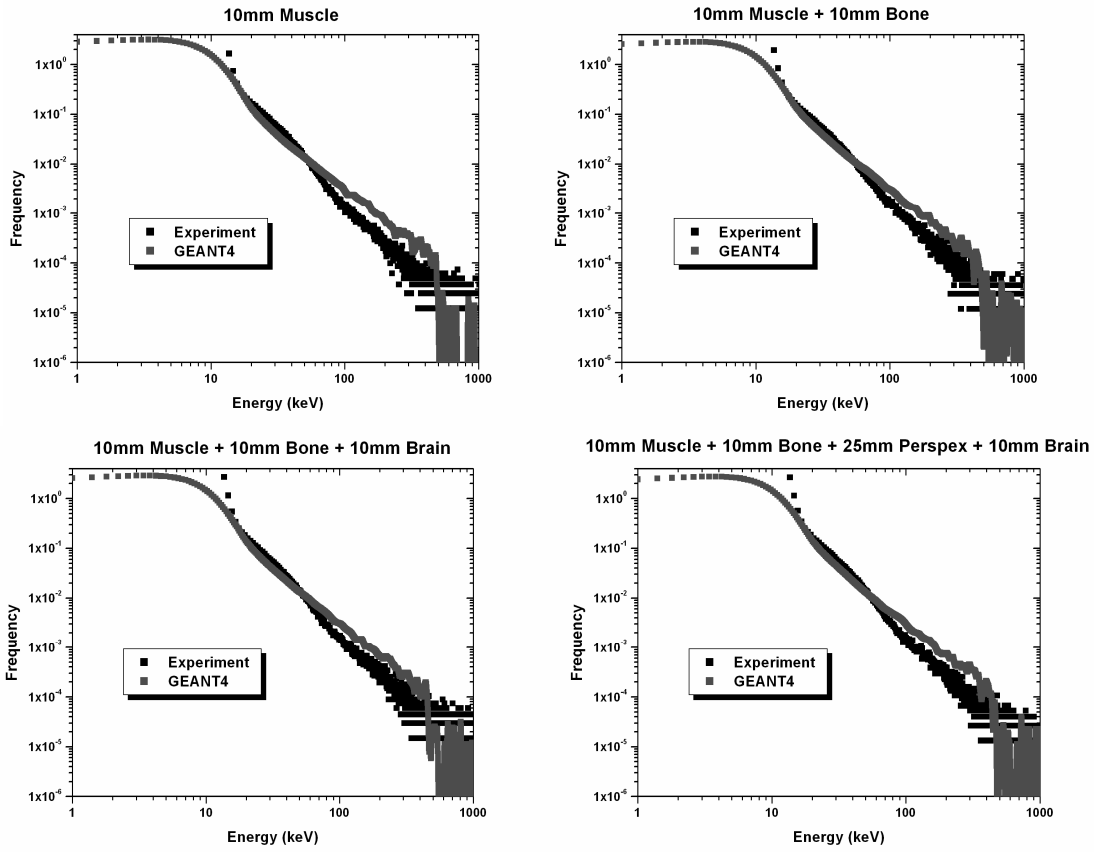

Figure 5-5: Comparative experimental and simulation results for the head phantom, when irradiated with 250MeV protons.

Figure 5-5 and Figure 5-6 show the comparison between experimental and simulated spectra for 250 MeV protons incident on the head and chest phantom, respectively. The agreement between the simulated and experimental cases is best in the region of 15-80 keV with almost no discrepancy. In the region of 80-500 keV there is some discrepancy between the simulated and experimental data, which can be as large as a factor of 2-3. This difference was most likely caused by an oversimplification in simulation of the device overlayer as for high linear energy transfer (LET)/low range secondaries an incorrectly simulated overlayer could result in error in their transport and hence energy deposition within the SV.

It is also important to note that this difference is most pronounced for the first 10 mm layer of each phantom structure. This amplification in discrepancy is most likely caused by an underestimation of the beam divergence as it travels along the beam pipe towards the experimental set-up. In the simulation, the beam was approximated as circular in profile travelling normally down an evacuated beam pipe, however, this may not be the case in practice. Such discrepancies are only observed in the first 10 mm of the phantom, as small initial beam divergence errors are nullified at depth within the phantom due to internal scatter of the incident protons. Despite this discrepancy the trend of the experimental results are well represented by the simulation for all phantom material configurations.

In the case of the head phantom for 250MeV incident protons a 25 mm thick Perspex slab was used to simulate a greater depth within the brain. However, in this case the brain slab was re-orientated to remain the last layer of the phantom immediately before the microdosimeter probe assembly. This would ensure that any short range secondaries produced by the brain phantom were transported and detected by the device, not attenuated by Perspex.

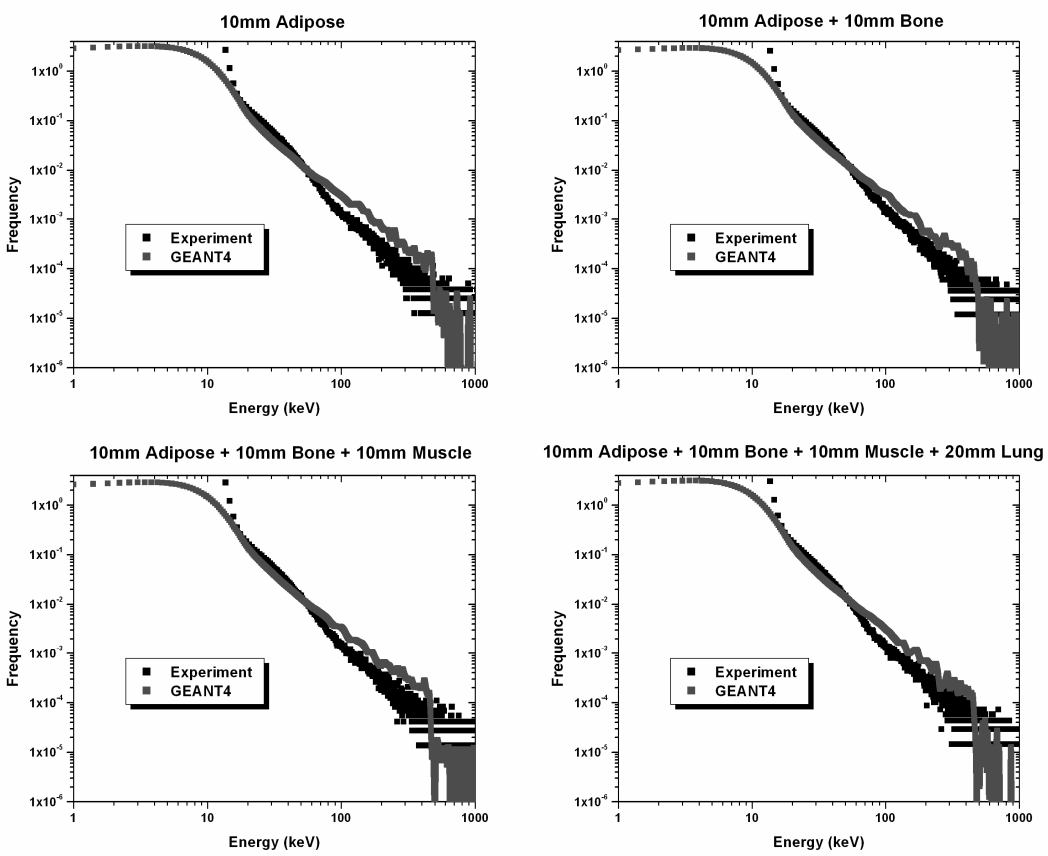

Figure 5-6: Comparative experimental and simulation results for the chest phantom, when irradiated with 250MeV protons.

5.7 Microdosimetry Results and Discussion

Although some discrepancy was observed between the simulated and experimental cases for higher energy deposition events, the experimental trend/response of the microdosimeter (a complex radiation metrology device) was well reflected in the simulation. The advantage which the simulation provides over the experimental device is that it is possible to simulate a device with no electronic noise and no lower level noise threshold, which may provide a better understanding of the radiation field at a given point.

The simulated results with no noise convolution or charge collection applied were converted into dose weighted lineal energy spectra according to the protocol outlined in [32, 33] and Section 2.5. Due to small variations in microdosimetry spectra as a function of phantom material upstream of the measurement position, the mean dose weighted

lineal energy, dose equivalent and average quality factor were used to discern changes in radiation field. Such measurement parameters provide information not only on changes in radiation field composition, but also possible variations in the radiobiological effect (RBE) for different regions in the heterogeneous phantom. These results are presented in Table 5-2 and Table 5-3 for the case of 250MeV protons irradiating the head and chest phantom. The advantage of using 250MeV protons for this study is that all simulated measurement positions took place within the plateau region, before the Bragg Peak. As such the changes in lineal energy are mostly caused by the changing phantom material rather than the slowing of the proton in the Bragg peak region.

Measurement Position	$\bar{y}_d$ (keV/μm)	Dose Equivalent (mSv)	Average Quality Factor
Phantom Surface	4.06	0.53	1.17
Muscle/Bone Interface	4.75	0.63	1.32
Bone/Brain Interface	5.85	0.80	1.58
10mm Depth Brain	5.65	0.75	1.51
35mm Depth Brain	4.46	0.61	1.25
60mm Depth Brain	4.79	0.63	1.31

Table 5-2: Mean dose weighted lineal energy values for simulated measurement positions within the head phantom when irradiated with 250MeV protons. Presented also is the corresponding dose equivalent measurement and average quality factor that was determined from the simulated response of the SOI microdosimeter.

In the case of the head phantom it is clear that there is a variation in the mean dose weighted lineal energy as a result of the preceding TE material. Measurements immediately behind the bone boundary result in an increase in mean dose weighted lineal energy of approximately 44%. An elevated value is also recorded at 10 mm depth within brain before returning to more stable values at greater depths within the TE brain phantom as simulated by additional layers of Perspex. The dose equivalent (for $2x10^7$ incident protons) and average quality factor also exhibit elevated values past the bone layer which is clearly evident in Figure 5-7. Immediately after the bone layer, the dose equivalent increases by a factor of approximately 50% while the average quality factor shows a similar increase of 35%. The dose equivalent and average quality factor

decrease to more stable values after traversing 35 mm of brain material. This would indicate that high LET low range secondaries are produced within the bone layer in turn increasing the mean dose weighted lineal energy, dose equivalent and average quality factor in the region immediately behind the bone boundary.

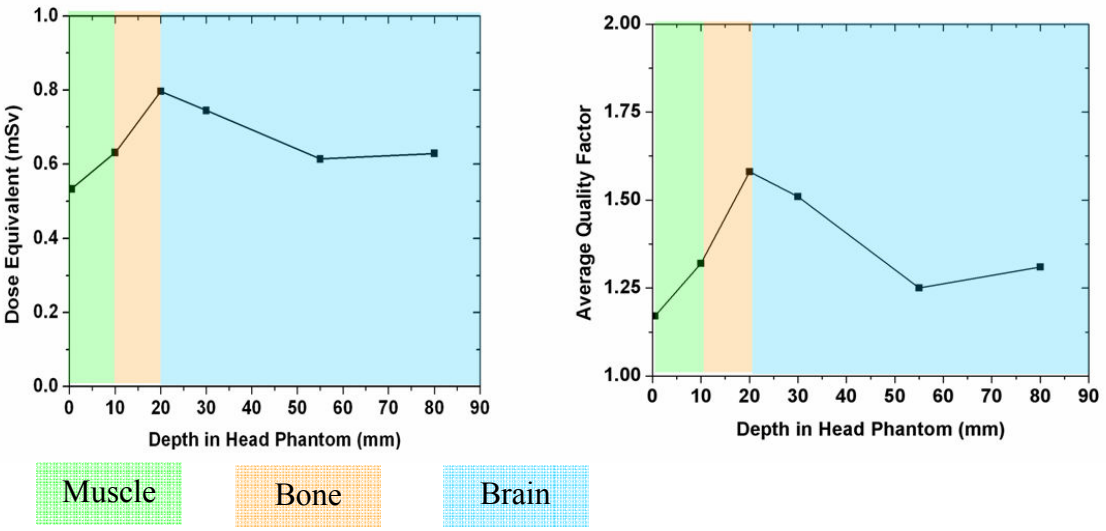

Figure 5-7: Graph of the variation in dose equivalent and average quality factor as a function of position within the head phantom.

It is clear from Table 5-2 and Figure 5-7 that the radiation quality has changed as a result of traversing a bone layer in the head phantom. The change in beam quality from the surface provides further information on the change in biological effectiveness as a function of preceding phantom material. In the case of the head phantom the dose equivalent increases by 50% after the proton beam traverses the bone layer. However, as current treatment planning relies on analytical simulation techniques and absorbed dose as the measurement parameter, such variations may not be considered and could have an adverse impact on sensitive normal structures in this region.

Measurement Position	$\bar{y}_d$ (keV/μm)	Dose Equivalent (mSv)	Average Quality Factor
Phantom Surface	4.05926	0.53	1.17
Adipose/Bone Interface	5.08208	0.69	1.44
Bone/Muscle Interface	5.70244	0.72	1.45
Muscle/Lung Interface	5.79357	0.78	1.57
20mm Depth Lung	5.38776	0.63	1.36

Table 5-3: Mean dose weighted lineal energy values for simulated measurement positions within the chest phantom when irradiated with 250MeV protons. Presented also is the corresponding dose equivalent measurement and average quality factor that was determined from the simulated response of the SOI microdosimeter.

Simulation of the microdosimetry spectra within the chest phantom (see Table 5-3 and Figure 5-8) reveals the same trends as is seen as in the head phantom. Immediately after the bone layer there is an increase in mean dose weighted lineal energy of 42% which continues to greater depth within the phantom. In this instance the elevated mean dose weighted lineal energy values traverse into the lung phantom which is an indication of higher LET secondaries being able to travel to greater depths within the lower density lung material. As in the head phantom the elevated dose equivalent and average quality factor occurs past the bone layer with increases of 34% in both parameters when compared with values measured at the surface. This further supports the trend of increasing biological effectiveness of therapeutic proton radiation as a direct result of traversing a hard boundary such as bone.

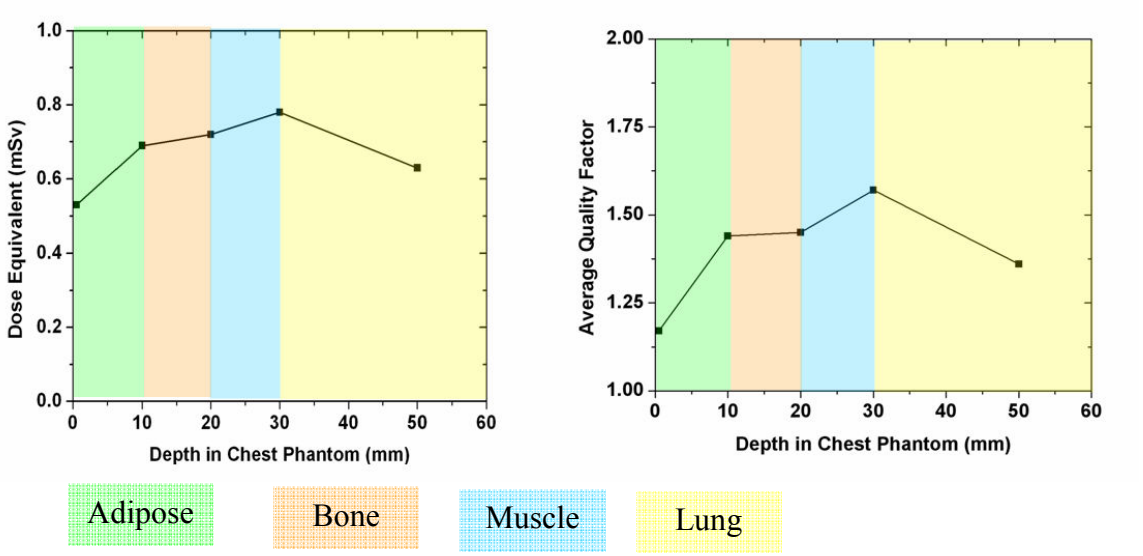

Figure 5-8: Graph of the variation in dose equivalent and average quality factor as a function of position within the chest phantom.

Another interesting trend observed in these results occurs in both phantoms after only 10 mm of material. In the case of the head phantom muscle is the most anterior (i.e. closest to the incident radiation) phantom layer, while in the case of the chest phantom this material is adipose. The differing composition of these two layers results in a clear variation in not only in the mean dose weighted lineal energy but also the dose equivalent and average quality factor. As the main variation of composition in these commercially available TE phantoms is that adipose contains approximately 5% more carbon, it could be concluded that these increased levels of carbon produced increased levels of inelastic and elastic scatter resulting in an increased dose weighted mean lineal energy, quality factor and dose equivalent.

5.8 Overall Conclusions & Recommendations

This study has highlighted the ability of GEANT4 in simulating therapeutic proton radiation. In this work the response of a relatively complex radiation detection structure was simulated with acceptable accuracy considering the complex nature of the incident beam, and heterogeneous phantom structure. Some discrepancies were observed which can be reduced through further improvements to the simulation program. In this case improvements could include:

- A better estimation of the initial beam size and divergence in both the vertical and lateral direction. In this instance the initial beam was approximated as a circular beam with 10 mm diameter and zero divergence. Such an approximation has lead to some level of error in surface measurements, however discrepancies were removed through in-phantom scattering for measurements at depth.
- A more complex model of the SOI microdosimeter including a more complex simulation of the device overlayer and contact structure.
- Testing with improved physics models released with the GEANT4.8.1 toolkit. Such physics models may explain the differences observed at 100MeV [75].

From the simulated response of the microdosimeter within commercially available TE phantoms it is clear that the quality of the proton radiation varies in different tissue substances. This has been established through the comparison of mean dose weighted lineal energy, dose equivalent and average quality factor obtained through the simulated response of an SOI microdosimeter situated at tissue boundaries within a head and chest phantom. Such variations in radiation quality were most prevalent immediately past the bone layer. In the head phantom this is evident with increases in mean dose weighted lineal energy of 44%, dose equivalent of 50% and average quality factor of 35%. These trends are also reflected in the chest phantom with increases in mean dose weighted lineal energy of 42%, dose equivalent and average quality factor of 34%. As all simulated responses were completed within the plateau region of the 250 MeV Bragg peak, changes in these parameters are most likely caused by changes in the proceeding phantom material and hence the spectra of secondary particles produced when the primary proton field traverses these materials.

While the biological effects of small variations in radiation quality and dose equivalent are unclear, it would be advisable that they be considered over the entire course of treatment as the summation of these effects may become clinically relevant. Such changes in radiation quality are not accounted for in current treatment planning systems which rely on analytical simulation techniques and the macroscopic quantity of absorbed dose as a planning parameter. Future advances in treatment planning may

utilise Monte Carlo methods, microdosimetry and dose equivalent as their basis to accurately plan for changes in radiation field composition.

To better understand the effect produced by actual tissue materials, simulation studies should be initiated using homogeneous phantoms of commercially available TE materials, ICRP/ICRU TE material compositions and water scaled to the physical and electron density of the TE material being simulated (typically done in treatment planning). In such simulations it is important to consider the changes in depth dose profile, lateral profile and microdosimetry spectra. Such simulations will illustrate how well commercially available TE materials and water scaled to the physical and electron density of the TE material reflect actual tissue compositions in proton therapy.

To compliment such simulations in a homogeneous phantom material, heterogeneous studies should also be completed. In this instance phantoms such as the ones presented in this section or anthropomorphic phantoms [76] should be recreated within the simulation program using commercially available TE materials, ICRP/ICRU TE material compositions and water scaled to the physical and electron density of the TE material being simulated. Again the response of the SOI microdosimeter should be simulated with mean dose weighted lineal energy, dose equivalent and average quality factor used to determine any change in the radiation quality as a function of preceding phantom material. Such simulations will again provide information on the effect of tissue boundary on therapeutic proton radiation spectra, but will also illustrate how accurately commercially available TE materials and water scaled to the electron/physical density to represent tissue, reflect actual tissue in the transport of proton radiation.

6 TE Material Comparison for Treatment Planning

6.1 Introduction

To gain maximum benefit from proton therapy, extensive treatment planning is required to determine the optimum aperture, energy, angle and bolus for each individual treatment. In existing treatment planning algorithms, CT number is converted to water equivalent material with the electron density varied to reflect changes in CT number. Using analytical methods the simulated absorbed dose distribution is then created to optimise the patient treatment. In many experiments commercially available tissue equivalent (TE) materials are used to verify the accuracy of proton therapy treatment planning algorithms and measure changes in radiation field.

In Section 5, the GEANT4 Monte Carlo toolkit was verified through simulations of experimental response of SOI microdosimeter within heterogeneous commercially available TE phantom. Further investigation of the simulated response of the SOI microdosimeter illustrated changes in therapeutic radiation quality as a function of preceding phantom material in a basic head and chest phantom configuration. Such results are of paramount importance to proton therapy treatment planning as improvements in simulated radiation transport will benefit the efficacy of treatment allowing for smaller tumour margins, improved normal tissue sparing and more uniform dose delivery to the target volume. However, questions remained as to the accuracy in which commercially available TE phantoms represent therapeutic proton radiation transport in actual tissue.

In order to investigate this, the GEANT4.7.1p1 Monte Carlo toolkit [52] was used to complete simulations in homogeneous TE phantoms. GEANT4 was utilised to provide information on dose, lateral scatter and microdosimetry spectra as a function of depth within different homogeneous TE materials. These materials will have three basic configurations:

- ICRP compositions as provided by NIST [35]. These were considered the "gold standard" in representing actual tissue compositions.
- Commercially available phantom materials with compositions defined by manufacturer specifications.
- Water scaled to the physical and electron density of the tissue material being simulated. Such simulations using Monte Carlo provided a good reference to what is currently the standard material in treatment planning.

Using these three different material categories four tissue materials were simulated as homogeneous phantoms, adipose, muscle, bone and brain. Such simulations of both the macro and microscopic radiation properties provided a further indication of the effectiveness of such materials in representing the transport of therapeutic protons in actual tissue.

6.2 GEANT4 Simulation Parameters

The GEANT4.7.1p1 Monte Carlo toolkit was used for all simulations in this work. Simulations utilised cluster computing technology to allow for realistic simulation times to be achieved, including the Barossa cluster as part of AC3 and the Loma Linda University Medical Center Cluster Computing Facility (LLUMC CCF). The Barossa cluster comprises of 304 3GHz Pentium4 processors with 2GB memory per node. The LLUMC CCF is a Beowulf cluster consisting of 7 dual AMD 64bit 2 GHz processors running Scyld Beowulf v30oz. Each node has 2 GB RAM while the system has common hard drive storage of 300 GB.

The broad nature of this study resulted in a number of simulations, each with varying geometry and data analysis methods. However, each simulation utilises the same physics processes and methods for radiation transport.

6.2.1 Physics Models

The Physics processes utilised in this work was based on the modular design of that used in the Hadron Therapy example supplied with the GEANT4 distribution. Inelastic scattering and nuclear interactions of protons and light ions were considered using the G4preCompound model. Ionisation interactions of charged hadrons was considered using low energy models based on ICRU Report 49 while multiple scattering models were also employed for the transport of protons and light ions through the geometry of the simulation. The physics of secondary particles including photons, electrons, neutrons and nuclear secondaries was also considered and accounted for using the appropriate models. The physics processes employed in this simulation were the same as those which had undergone validation in Section 5.

6.2.2 Material Definition

Material definition in this study is paramount as accurate definition is required to ascertain changes in radiation field as a function of phantom material. As has been outlined previously four tissue materials were utilised in homogeneous phantom studies: adipose, bone, brain and muscle. These materials were defined in three different configurations within the Monte Carlo simulation to ascertain the accuracy of commercially available phantoms and water equivalent materials in simulating the response of real tissue to proton radiation transport.

In this case ICRP compositions were used to represent real tissue and were considered the “gold standard” in this case. The compositions were provided by NIST [35] and are outlined in Table 6-1.

Element	Abundance Muscle (%)	Abundance Bone (%)	Abundance Brain (%)	Abundance Adipose (%)
H	10.064	4.7234	11.067	11.948
C	10.783	14.433	12.542	63.724
N	2.768	4.199	1.328	0.797
O	75.478	44.610	73.772	23.233
Na	0.075	N/A	0.184	0.050
Mg	0.019	0.22	0.015	0.002
P	0.180	10.497	0.354	0.016
S	0.241	0.315	0.177	0.073
Cl	0.079	N/A	0.236	0.119
K	0.302	N/A	0.310	0.032
Ca	0.003	20.993	0.009	0.002
Fe	0.004	N/A	0.005	0.002
Zn	0.005	0.01	0.001	0.002

Table 6-1: ICRP elemental compositions of adipose, brain, muscle, lung and bone tissues to be used in this work as provided by [35].

Commercially available phantoms were defined isotopically as per manufacturer's specifications. Due to commercial confidentiality constraints they are unable to be presented here for discussion. Water equivalent representations of ICRP tissues were constructed using water whose density (and hence electron density) had been scaled to that of the ICRP material. ICRP material densities were obtained using NIST and are contained in Table 6-2.

Muscle (gcm^{-3})	Bone (gcm^{-3})	Brain (gcm^{-3})	Lung (gcm^{-3})	Adipose (gcm^{-3})
1.04	1.85	1.03	0.30	0.92

Table 6-2: ICRP densities for adipose, brain, muscle, lung and bone tissues to be used in this work as provided by [35].

In all cases materials were defined at standard temperature and pressure within the Monte Carlo application.

6.2.3 Phantom Configuration

Two main phantom geometries were utilised within this research allowing the parameters of dose, lateral scatter and microdosimetry spectra as a function of depth to be observed and recorded.

The phantom geometry to provide depth dose and lateral scatter information consisted of a rectangular prism with sensitive slices covering the cross sectional area of the phantom and extending into the phantom (Figure 6-1). 1000 sensitive slices with a cross sectional area of 100x100 mm^2 were utilised in the simulation. Each slice was 5 μm thick separated by gaps of 500 μm to provide adequate resolution as a function of depth. Energy deposition events within the sensitive slices were scored to provide depth dose information, while the position of interaction was also registered at each depth to provide information on the changing beam profile as a function of depth. The primary beam in this case was a normally incident 250 MeV proton beam covering a cross sectional area of 20x20 mm^2, allowing sufficient sensitive volume coverage to detect any changes in beam profile as a function of depth.

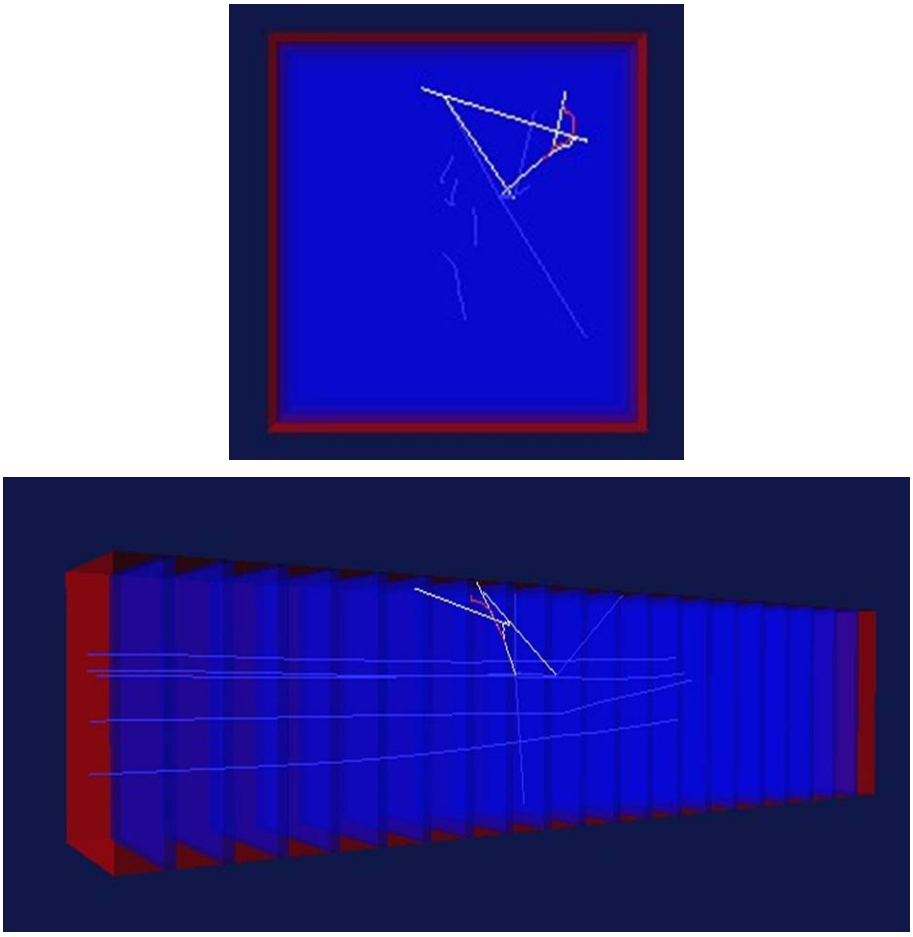

Figure 6-1: Schematic diagram of the layered phantom structure utilised within the GEANT4 based application to provide dose and lateral scatter profiles as a function of depth. The top diagram gives the cross sectional profile of the phantom, while below is the lateral profile which indicates the transport of protons as a function of depth in the phantom structure. The SV's are highlighted in blue and are situated within the homogeneous phantom (red), note that both are the same material within the phantom. Particle tracks can be seen in these diagrams as the primary protons (blue) are transported through the phantom geometry.

In order to provide microdosimetry information, the simulation was repeated with the sensitive slices replaced with an 800x800 cell array of 5 μm diameter sensitive spheres (Figure 6-2). Up to 5 SV arrays were placed in the phantom to sample the microdosimetry spectra at key points along the protons path such as the Bragg peak and distal edge. Energy deposition events in each SV were scored to produce a microdosimetry spectra for a given depth according to the protocol outlined in [32, 33]. The primary beam in this case was a normally incident 250MeV proton beam covering the entire cross sectional area of the phantom to allow for maximum statistical sampling of the beam as a function of depth.

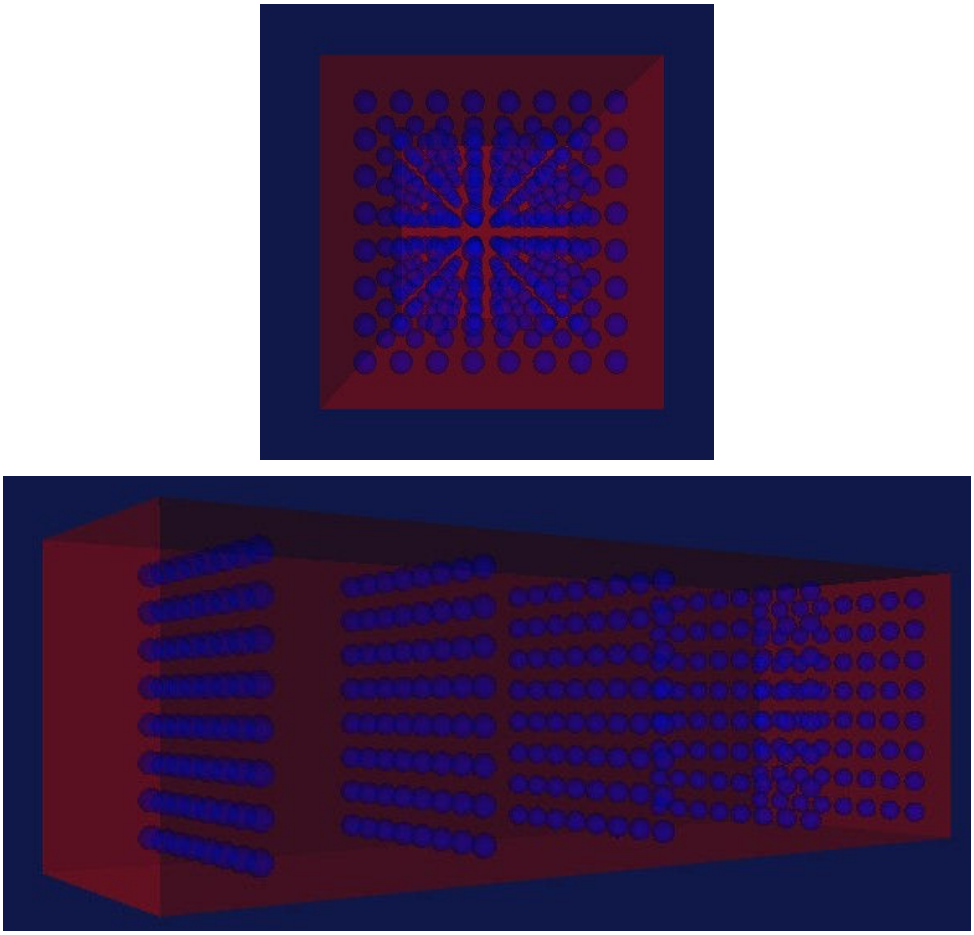

Figure 6-2: Schematic diagram of the cell array phantom structure utilised within the GEANT4 based application to provide microdosimetry spectra as a function of depth. The top diagram provides the cross sectional view, whilst the bottom illustrates the arrangement of SV's with depth in the phantom. The SV's are highlighted in blue and are situated within the homogeneous phantom (red), note that both are the same material within the phantom.

6.2.4 Incident Radiation Field

250MeV protons comprised the incident radiation field. Simulations of lateral scatter and depth dose profiles consisted of a normally incident beam of protons with a cross sectional area of 20x20 mm^2. This incident field ensured adequate beam profile size to quantify changes in penumbra, and also ensure that minimal numbers of protons are lost due to lateral scatter as the SV cross sectional area is a factor of 5 larger than the incident beam. For simulations of microdosimetry spectra within the homogeneous tissue equivalent phantoms the incident radiation field was again comprised of normally

incident 250MeV protons. However, in this case the incident radiation field covered the entire cross sectional area of the SV array ensuring maximum statistical sampling.

The number of histories simulated in each case depended on the statistics required and the simulation time available on the cluster computing facilities. For depth dose results $1.2x10^5$ incident protons were simulated, while determination of lateral scatter profiles required $3x10^5$ and microdosimetry information required $5x10^7$ incident histories.

6.2.5 Data Analysis

The data analysis differed depending on the parameter being displayed and investigated.

6.2.5.1 Depth Dose Profile

Within each SV slice the total number of energy deposition events was summed to give the total energy deposited for a given number of incident protons. As the volume and density of the SV is known it was then be possible to determine dose if required. As each SV was 5 μm in thickness with a separation of 500 μm adequate resolution of the Bragg peak was achieved.

6.2.5.2 Lateral Profile

The lateral profile simulations utilised the same geometry as that used in determining the depth dose profile of the beam. In this instance each particle (primary or secondary) interacting or crossing a SV had its vertical and horizontal position recorded as well the SV at which the event is taking place. From this a 2D matrix of the beam profile was created at each SV plane. As 1000 SV planes made up the entire homogeneous phantom it was possible to determine the beam profile at any point along the path of the primary proton beam.

6.2.5.3 Microdosimetry Spectra

Within the homogeneous phantom an array of 800x800 SV spheres at five different depths provided microdosimetry information as a function of depth. Each spherical SV within a given array acted separately measuring the total energy deposited within that given SV for each incident primary proton. At the end of the simulation the total number

of energy depositions events within all 640,000 SV's of the 800x800 SV array were utilised to create an energy deposition spectra at a given depth within the homogeneous phantom. Using an average chord length of 5 μm (i.e. the diameter of the sphere) and the techniques outlined in [32, 33] and Section 2.5, a microdosimetry spectra of lineal energy events was created. From this the mean lineal energy was determined to allow for a comparative analysis between phantom materials.

6.3 Depth Dose Results

These results show how well commercially available TE phantom materials and water equivalent materials reflect the depth dose profile of the actual ICRP material being simulated. Two parameters that were used in gauging this representation were the Bragg Peak position and the Peak to Entrance Dose Ratio (PEDR).

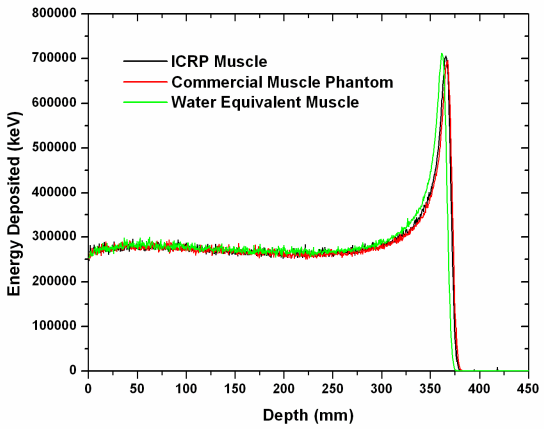

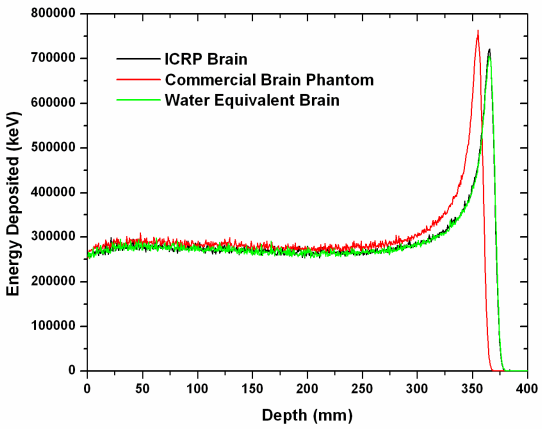

Material	Bragg Peak Depth (mm)	Difference in Range to ICRP (%)
ICRP	366.123	-
Commercial	367.637	0.41
Water Eq.	362.082	-1.10
Material	**Peak to Entrance Dose Ratio (PEDR)**	**Difference in PEDR to ICRP (%)**
ICRP	2.84	-
Commercial	2.76	-2.82
Water Eq.	2.79	-1.76

Material	Bragg Peak Depth (mm)	Difference in Range to ICRP (%)
ICRP	365.618	-
Commercial	355.012	-2.90
Water Eq.	365.618	0
Material	**Peak to Entrance Dose Ratio (PEDR)**	**Difference in PEDR to ICRP (%)**
ICRP	2.83	-
Commercial	3.01	6.36
Water Eq.	2.74	-3.18

Figure 6-3: Depth dose profile and tabulated information for ICRP, commercial and water equivalent muscle (left) and brain (right). Attached in tabulated form is the relevant data on Bragg peak position and peak to entrance dose ratio.

In the case of both the muscle and brain simulations the representation of the Bragg Peak position from both commercially available and water equivalent materials is within 2% of that for the ICRP phantom (Figure 6-3). There is a slight discrepancy for the commercial brain phantom with it overestimating the stopping power, resulting in a slightly shallower Bragg peak position differing from the ICRP case by approximately 3%. In the case of muscle, the PEDR for commercial and water equivalent phantoms is within 3% of ICRP value. However, in the case of the commercially available TE brain phantom the difference in PEDR when compared with the ICRP results is over 6%. This coupled with the elevated stopping power properties of this material means that further improvements could be made to this material to ensure a more accurate representation of the ICRP material it is emulating.

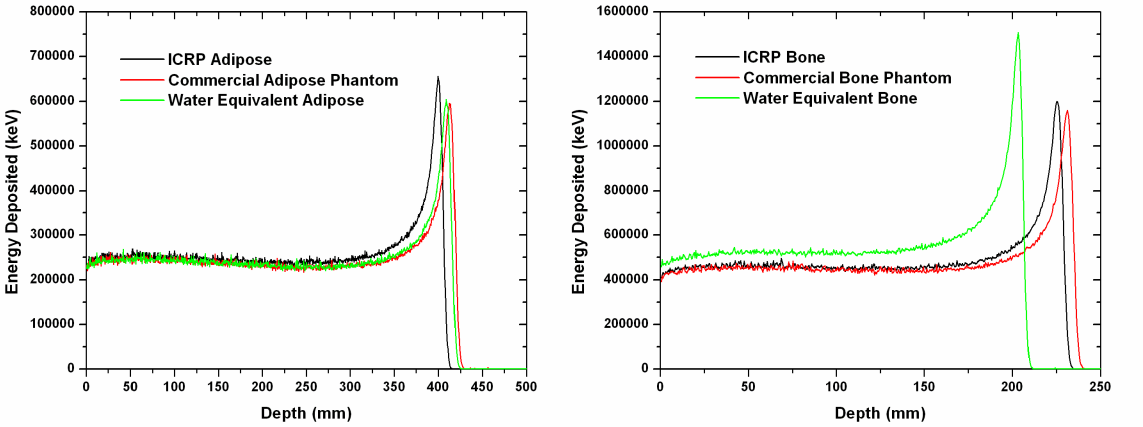

Material	Bragg Peak Depth (mm)	Difference in Range to ICRP (%)
ICRP	399.957	-
Commercial	410.058	2.50
Water Eq.	409.048	2.27
Material	**Peak to Entrance Dose Ratio (PEDR)**	**Difference in PEDR to ICRP (%)**
ICRP	2.86	-
Commercial	2.56	-10.49
Water Eq.	2.68	-6.29

Material	Bragg Peak Depth (mm)	Difference in Range to ICRP (%)
ICRP	225.732	-
Commercial	231.287	2.46
Water Eq.	203.512	-9.84
Material	**Peak to Entrance Dose Ratio (PEDR)**	**Difference in PEDR to ICRP (%)**
ICRP	2.92	-
Commercial	2.96	1.37
Water Eq.	3.30	13.01

Figure 6-4: Depth dose profile and tabulated information for ICRP, commercial and water equivalent adipose (left) and bone (right). Attached in tabulated form is the relevant data on Bragg peak position and peak to entrance dose ratio.

There is however, significant differences between the ICRP, commercially available and water equivalent phantom materials when comparing across bone and adipose (Figure 6-4). In the case of bone, while the commercial case reflects well both the Bragg peak position and the PEDR, being within 3% of the ICRP values, the water equivalent

material exhibits significant differences. Water equivalent bone (i.e. water scaled to the same physical density as ICRP bone) exhibits approximately a 10% underestimation of Bragg Peak position and a 13% overestimation in the PEDR. In the case of adipose, variation in Bragg peak position from that of the ICRP material is approximately 2.5%, with both the commercial and water equivalent materials over estimating the range of protons. The PEDR of ICRP adipose is underestimated rather significantly with a 10.5% underestimation in the case of the commercially available phantom, and 6.3% in the case of the water equivalent material.

	Water	Muscle	Bone	Brain	Adipose	A-150
Mean Ionisation Energy (eV)	75.0	75.3	106.4	73.3	63.2	65.1

Table 6-3: Mean ionisation energy of materials studies in this section as provided by [35].

As ionisation is the predominant mechanism for energy loss, small variations in mean ionisation energy can account for these differences in the depth dose curves. When water is scaled to reflect the electron density of a TE material, the mean ionisation energy is not changed and this results in error pertaining to the depth dose profile. This conclusion was evident in the bone and adipose simulations where a larger error is observed between the ICRP and water equivalent Bragg Peak position and PEDR, which corresponds to an increasing variation in the mean ionisation energy of water and the ICRP TE material being simulated. While on the other hand the agreement between ICRP and water equivalent muscle and brain materials was good as the mean ionisation energy of ICRP brain and muscle closely resembles that of water.

This explanation however, can not exclusively account for the variations in depth dose profile between the ICRP and commercially available materials. In this instance while differences in the mean ionisation energy is a possible factor there is no published data to make this conclusion. Also, as the compositions of these materials are commercially confidential, discussion of this parameter is also difficult. Suffice to say that in the case of commercial phantoms the material is constructed as a polymer to reflect the density and mean ionisation energy of the TE material in question, but the composition differs markedly from that of the ICRP tissues. While commercially available phantoms do a suitable job in reflecting ICRP muscle further work could be

made into optimizing other material compositions for the transport of protons as this is a growing radiotherapy modality.

Further, the difference in compositions between the materials will have an effect on the nuclear interactions present in the system. This has been investigated previously [73, 77] and has been shown to have an effect on the PEDR. Additionally the presence of such reactions and produced secondaries would be expected to have an effect on the microdosimetry spectra at different points along the protons path. This has been investigated and discussed in Section 6.5.

6.4 Lateral Profile Results

GEANT4 was used to create beam profiles as a function of depth within the various homogeneous phantoms. This provides information on the amount of lateral scatter and the size of the beam penumbra as a function of depth within the phantom. Comparisons between ICRP phantoms, commercially available phantoms and water scaled to specific tissue densities with lateral profile as the quantity of interest allowed for an assessment of how each material affects the lateral scatter properties of therapeutic protons

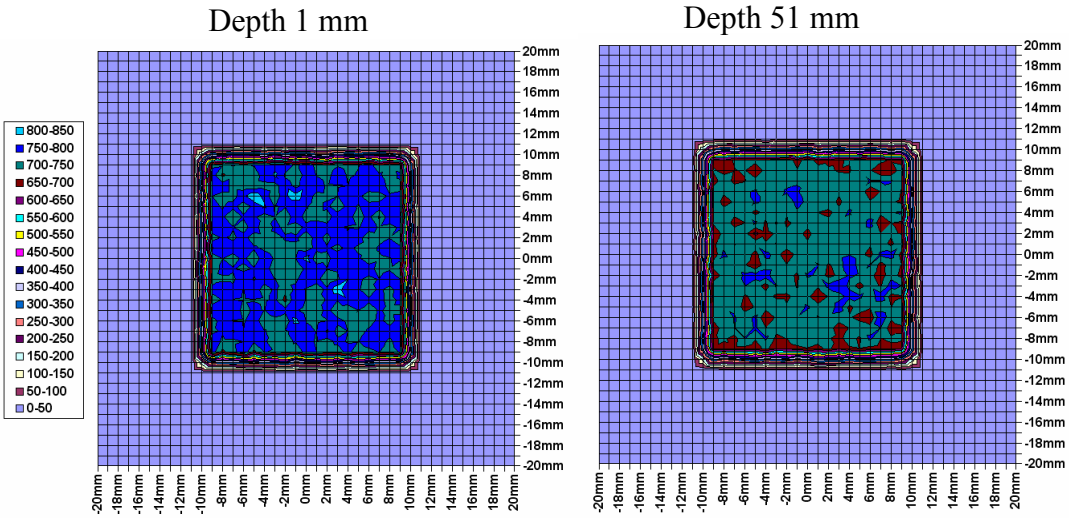

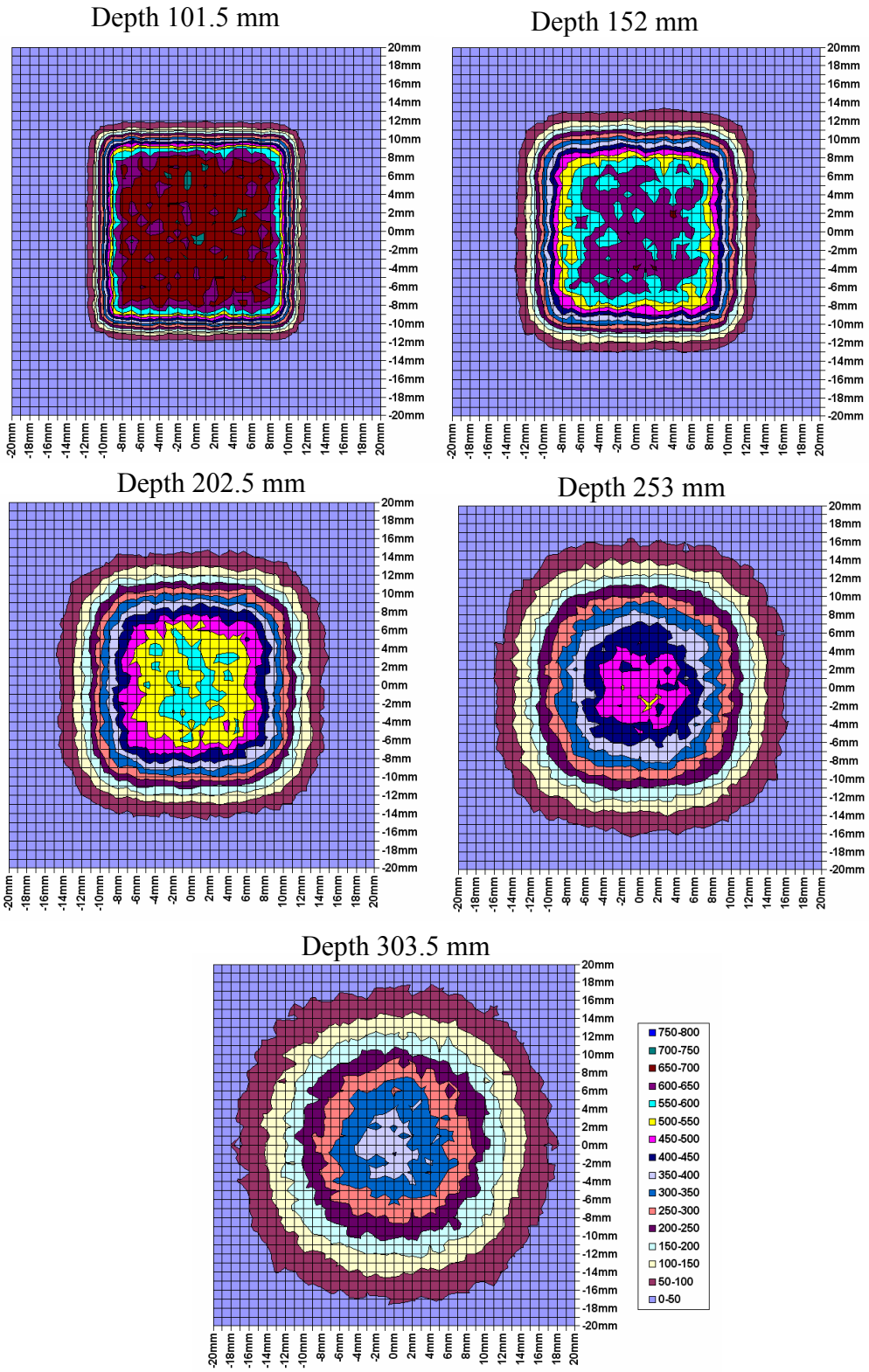

Figure 6-5: Two-dimensional dose profiles for an incident 20x20 mm^2 250 MeV proton beam traversing a homogeneous A-150 phantom.

It is clear from Figure 6-5 that the profile of the 250MeV proton beam does change significantly as a function of depth within the A-150 phantom. After 100 mm in A-150 the beam begins to lose its initial shape (i.e. 20x20 mm^2 square field) with the corners becoming rounded and the beam penumbra beginning to increase in size as the plateau region of the beam profile decreases. At depths of 250 and 300 mm the beam appears more circular in shape and has lost all resemblance of its initial square shape. These changes in beam profile indicate how important it is to account for lateral scatter accurately in treatment planning, as assumptions can result in an incorrect dose profile at the most important region, the tumour site.

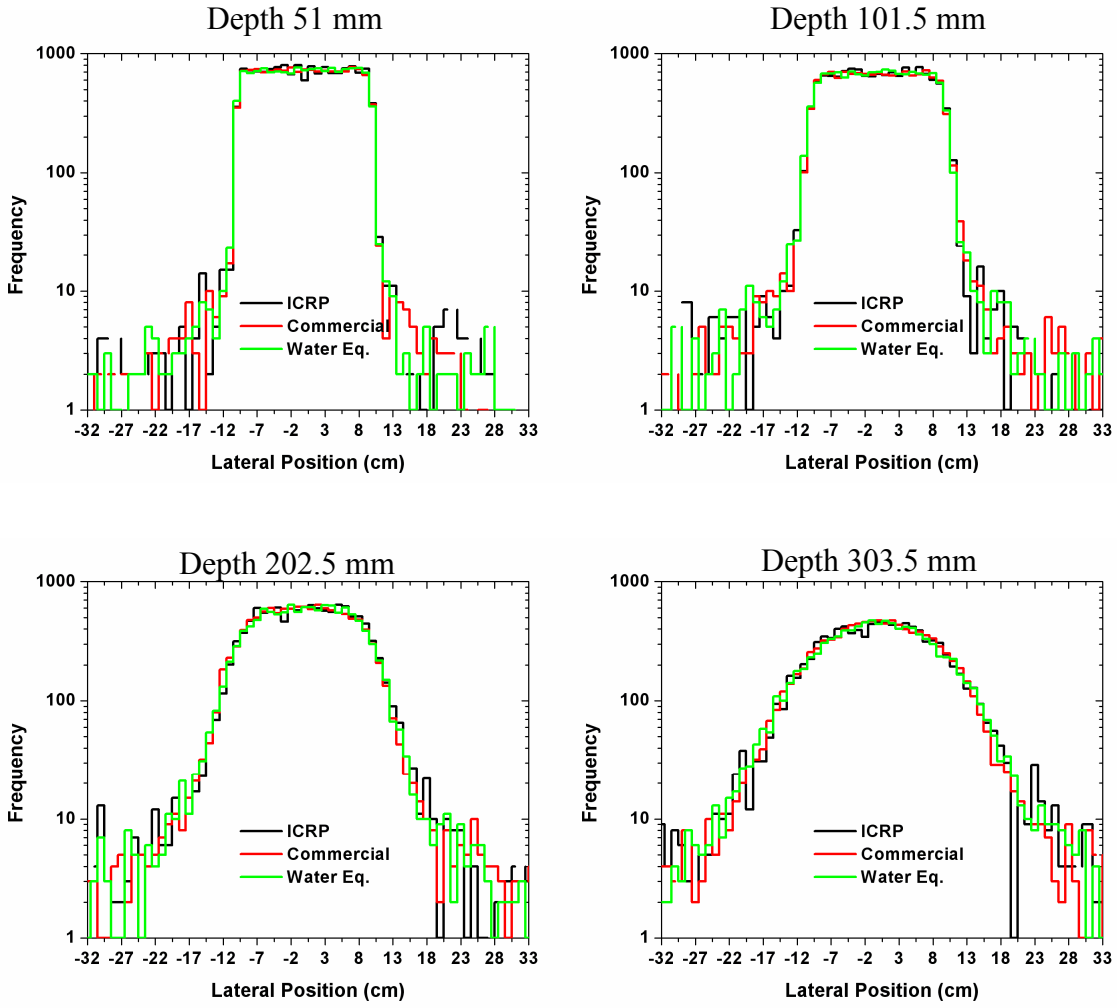

Figure 6-6: Lateral profile of 250MeV protons normally incident on a homogeneous adipose phantom using ICRP, commercial and water equivalent compositions.

The goal of this section was to compare the lateral dose profile of ICRP, commercially available and water equivalent (water scaled to the density of the material it is representing) phantoms of adipose, bone, brain and muscle, and observe if they are in good agreement as a function of depth along the protons path. To achieve this one-dimensional lateral profiles were created at the level of the central axis with millimetre resolution for a range of depths within the homogeneous phantoms.

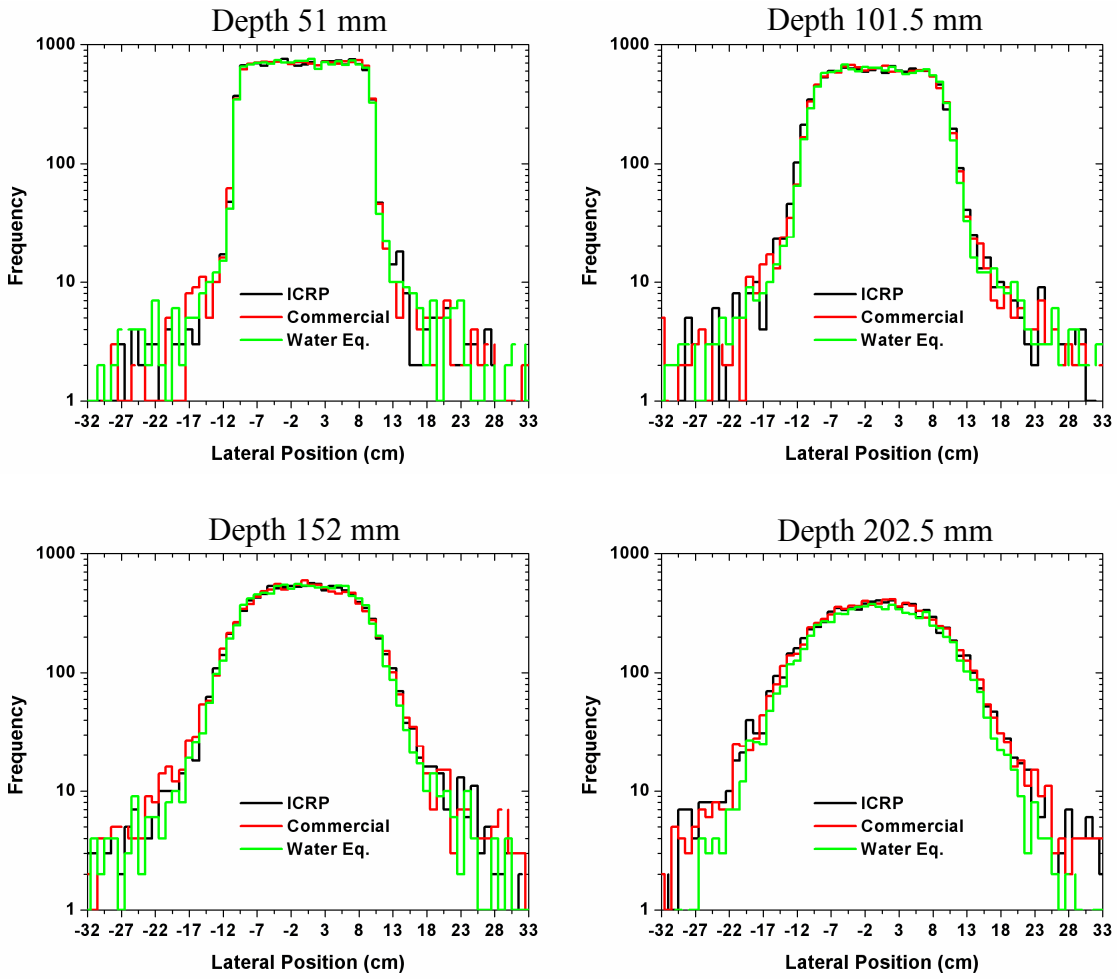

Figure 6-7: Lateral profile of 250MeV protons normally incident on a homogeneous bone phantom using ICRP, commercial and water equivalent compositions.

It is clear from these results that the lateral profiles produced using ICRP, commercially available and water equivalent phantoms of bone, brain, adipose and muscle agree very well (Figure 6-6 to Figure 6-9). In all cases commercially available and water equivalent phantoms reflect the lateral scatter profile of ICRP TE materials accurately over a range of depths. This would support the use of such materials both in

treatment planning (provided the treatment planning algorithm accurately reflects the lateral scatter of the proton) and also experiments utilising TE materials.

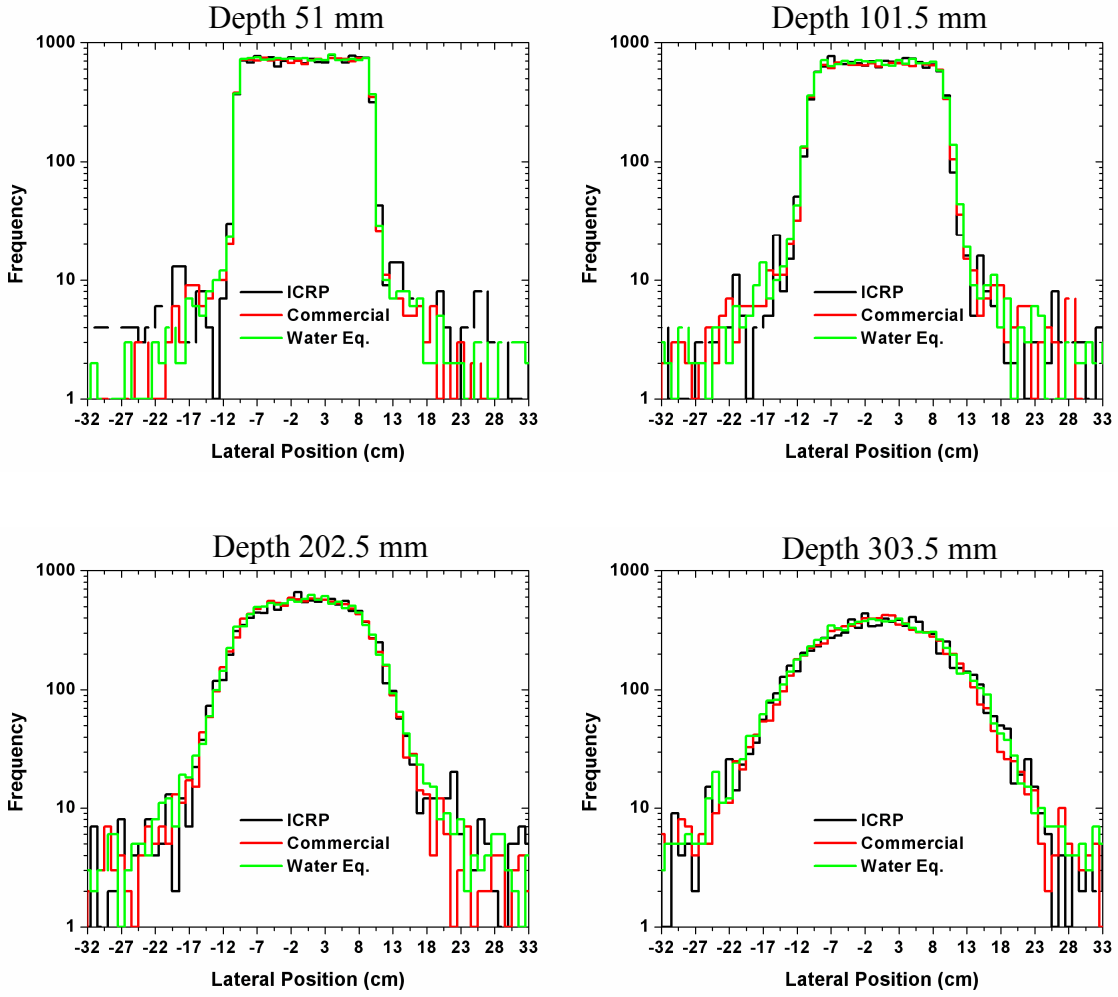

Figure 6-8: Lateral profile of 250MeV protons normally incident on a homogeneous brain phantom using ICRP, commercial and water equivalent compositions.

As in the previous 2D case outlined in Figure 6-5, the loss of beam profile shape as a function of depth is apparent. This does not seem to be more pronounced in one soft tissue over another, however in a heterogeneous system it could be expected that the inclusion of bone and other high density structures such as implants could increase the level of lateral scatter. These results further highlight the importance that treatment planning systems account for lateral scatter accurately as it is clear that transport through even soft tissues such as muscle and adipose cause significant changes in beam profile, especially near the Bragg Peak.

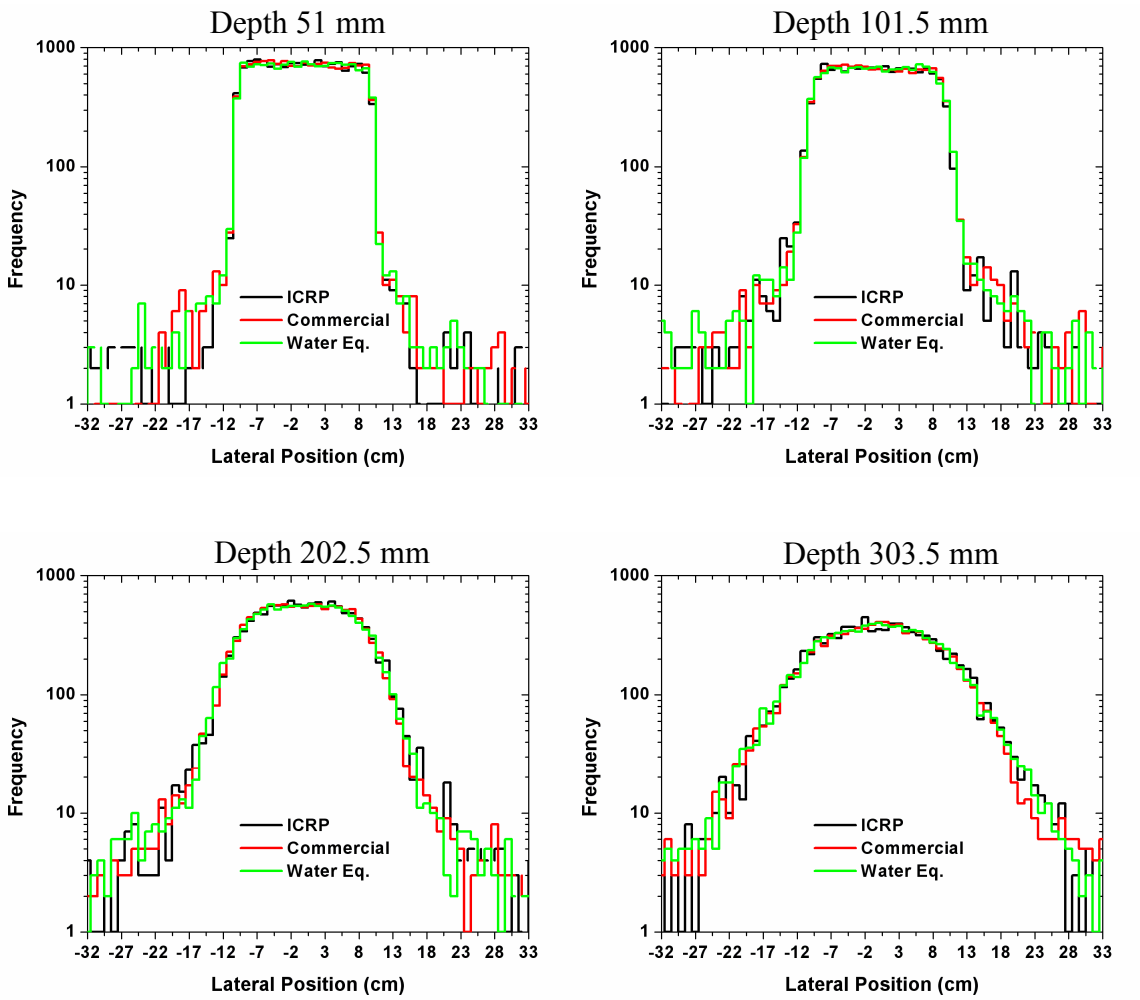

Figure 6-9: Lateral profile of 250MeV protons normally incident on a homogeneous muscle phantom using ICRP, commercial and water equivalent compositions.

6.5 Microdosimetry Results

Microdosimetry is another parameter for which the different TE phantoms may be compared and assessed. In this instance the mean lineal energy and dose weighted mean lineal energy was determined using at the surface of the phantom (i.e. 0.5 mm depth), at 50% Bragg Peak depth (i.e. in the plateau region before the Bragg Peak), and at 100% Bragg Peak depth (or at the height of the Bragg Peak) for all TE materials studied in this work. Such comparisons determined whether commercial and water equivalent materials accurately reflect the spectra of secondaries produced within ICRP tissues.

Material	Phantom Surface	50% Bragg Peak Depth	100% Bragg Peak Depth
ICRP Brain	0.285	0.384	3.584
Commercial Brain	0.289	0.413	3.645
Water Eq. Brain	0.277	0.414	3.501
ICRP Bone	0.455	0.622	5.080
Commercial Bone	0.467	0.618	5.406
Water Eq. Bone	0.505	0.735	6.145
ICRP Muscle	0.312	0.394	3.430
Commercial Muscle	0.288	0.404	3.415
Water Eq. Muscle	0.283	0.398	3.459
ICRP Adipose	0.259	0.375	3.254
Commercial Adipose	0.258	0.369	2.605
Water Eq. Adipose	0.253	0.363	3.045

Table 6-4: Comparison of mean lineal energy (keV/μm) values for ICRP, commercially available and water equivalent phantoms of muscle, bone, brain and adipose.

The mean lineal energy provides an indication of the ionisation density of the primary particle as it traverses the homogeneous phantom. What is immediately apparent is the factor of 8-10 increase in mean lineal energy between the surface/plateau region and the value determined at the Bragg Peak position (Table 6-4). This corresponds with the slowing of the primary proton and production of the Bragg peak through an increase in

the ionisation density. Those materials which have shallower and/or greater amplitude to their Bragg peak also have an elevated mean lineal energy at the level of the Bragg Peak. The lineal energy deposited is also dependant on the density of the material, with denser phantom materials resulting in a denser particle ionisation track per unit length and hence an elevated mean ionisation energy.

Comparing the mean lineal energy values across phantom materials supports the depth dose trends presented in Section 6.3. In materials such as muscle and brain, the agreement between ICRP, water equivalent and commercially available phantoms materials is very good. There is minimal variation in the mean lineal energy both at the surface, 50% Bragg peak depth and at the depth of the Bragg peak within the phantom structure. Variation of up to 21% is observed in the mean lineal energy for water equivalent bone and approximately 10% for commercially available bone when compared with ICRP values at the level of the Bragg peak. This trend is also observed in adipose with variation from ICRP mean lineal energies of up to 20%. In the case of adipose, this is most evident at the level of the Bragg peak with agreement at the surface and plateau region within 4%. For bone, however, mean lineal energy values for commercially available and water equivalent structures consistently vary from those of ICRP bone along the entire length of the protons track. Such variation in lineal energy support the depth dose results indicating that commercially available and water equivalent phantoms of adipose and bone do not accurately reflect the ICRP case.

Material	Phantom Surface	50% Bragg Peak Depth	100% Bragg Peak Depth
ICRP Brain	15.252	6.814	7.583
Commercial Brain	11.963	5.970	7.851
Water Eq. Brain	10.398	25.599	7.408
ICRP Bone	13.260	7.050	10.136
Commercial Bone	18.035	7.496	11.250
Water Eq. Bone	6.493	11.524	13.104
ICRP Muscle	38.906	14.399	7.159
Commercial Muscle	13.234	13.906	7.191
Water Eq. Muscle	11.481	10.285	7.562
ICRP Adipose	12.408	8.182	6.909
Commercial Adipose	17.603	17.881	6.230
Water Eq. Adipose	9.425	9.902	6.457

Table 6-5: Comparison of mean dose weighted lineal energy (keV/μm) values for ICRP, commercially available and water equivalent phantoms of muscle, bone, brain and adipose.

The mean dose weighted lineal energy provides information on the level of high LET particles present at a certain point within the phantom. This is because large energy deposition events (which are typically caused by high LET secondary particles induced by nuclear interactions) are weighted and greatly influence the results. In Table 6-5 it is clear that high mean dose weighted lineal energies are experienced at a depth of 0.5 mm in the phantom (labelled the phantom surface). This is directly caused by higher lineal energy deposition events caused through nuclear reactions and the resulting low range high LET particles. At the surface of the phantom such interactions are of higher probability due to the high energy (250 MeV) of the incident protons. In this region nuclear interactions can be responsible for 10-20% of the total energy loss of the proton in this region [78]. At the level of 50% the Bragg peak depth the trend across the phantom materials is for a decreased mean dose weighted lineal energy as the probability for nuclear interaction has decreased significantly through the resulting decrease in the incident proton energy. At the point of the Bragg peak, the mean dose weighted lineal

energy again increases as the ionisation density of the proton increases. This is further compounded by the fact that incident protons can stop within the microscopic SV depositing large amounts of energy.

It is difficult to draw comparative conclusions across phantom material categories (i.e. ICRP, commercially available and water equivalent) using mean dose weighted lineal energy, as the resultant effect is caused by fewer then ten energy deposition events over 200keV (or 40 keV/μm). While the probability of such particles is statistically very rare the weighting of such particles results in a large influence on the mean dose weighted lineal energy. Trends comparing mean dose weighted lineal energy along the protons path can certainly be identified, however, statistics need to be improved in order to come to an effective conclusion across phantom material categories. In this case simulations were completed for $5x10^7$ histories and information was gathered at each depth in the phantom from an 800x800 SV array. Such simulations typically took 120 hours of computer simulation time and using 5 arrays spaced at different depths (or $3.2x10^6$ SV's) used 1 Gb of RAM. Drastically increasing either the number of histories or the size of the SV array was unachievable in this case using the LLUMC CCF. It would be recommended however that such simulations be completed in order to make a through assessment of the microdosimetry performance of different phantom configurations and could possibly be achieved through the use of the AC3 Barossa cluster.

6.6 Conclusions & Future Recommendations

This work has tested the performance of commercially available and water equivalent phantom structures against ICRP compositions in therapeutic proton transport. It utilised the GEANT4.7.1p1 toolkit and assessed the performance of these different phantom configurations for adipose, brain, bone and muscle tissues utilising dose, range, lateral scatter, mean lineal energy and dose weighted mean lineal energy as parameters for comparison. This study has provided an assessment of such material configurations for proton therapy and identified areas of improvement to better reflect the response of ICRP materials.

The depth dose results provided information not only on the range of the particles, but also the peak to entrance dose ratio (PEDR). It is clear from such results that water equivalent materials reflected the transport of therapeutic protons in materials such as muscle and brain where the mean ionisation energy is similar to that of water. In materials such as adipose and bone where the mean ionisation energy differs markedly from that of water, variations of up to 10% are observed in the range and PEDR of water equivalent phantoms when compared with ICRP compositions. Commercial materials reflected the response of ICRP materials well for bone and muscle, however discrepancies of up to 10% are observed in the range and PEDR for adipose and brain.

As current treatment planning technologies rely on dose as the planning parameter it is imperative that accurate representation of radiation transport pertaining to the depth dose profile and range of primary protons in ICRP materials be reflected in water equivalent materials. These results would indicate that water equivalent materials used in treatment planning need to be altered to better reflect the mean ionisation energy of ICRP materials and hence return more accurate depth dose results. This can be achieved within treatment planning systems and may be supplemented with imaging information such as that which is supplied by proton CT [48]. It is imperative that such modifications be checked either through Monte Carlo studies and/or experimental measurements. Further, QA experiments using commercially available materials also need to be as accurate as possible for treatment planning verification. In this regard, modification to the response of commercially available adipose and brain can be further optimised for proton transport. This should be completed in close collaboration with material science departments and may be optimised with Monte Carlo studies prior to material casting and testing via experimental means.

Simulations of the lateral scatter of 250MeV protons in homogeneous TE materials indicated how the penumbra significantly increases in size with depth traversed. This highlighted the importance of scattering algorithms in treatment planning as the effect to the dose distribution can be marked. Comparing across the four materials (adipose, bone, brain and muscle) found excellent agreement across the three material classes (i.e. ICRP, water equivalent and commercially available). As the physical density (and hence

electron density) was comparable across the three material classes this can be seen as the determining factor in lateral scatter. On the other hand, composition and mean ionisation energy varied markedly across the three material classes and while this variation affected the depth dose distribution, the lack of effect on lateral scatter is apparent.

Microdosimetry provided another means for benchmarking the response of commercially available and water equivalent phantom materials to ICRP compositions. The simulated mean lineal energy values at the surface, plateau region and Bragg peak further supported the depth dose results. In materials such as muscle and brain, the agreement between ICRP, water equivalent and commercially available phantom materials is very good. Variation of up to 21% is observed for water equivalent bone and approximately 10% for commercially available bone when compared with ICRP values of mean lineal energy at the level of the Bragg peak. This trend is also observed in adipose with variation from ICRP mean lineal energies of up to 20%. In the case of adipose, this is most evident at the level of the Bragg peak with agreement at the surface and plateau region within 4%.

The mean dose weighted lineal energy was also obtained to provide an indication on the presence of nuclear secondaries. Elevated values were detected across all three material categories at the surface region, indicating the higher probability of nuclear interactions for high energy protons. An increase is also observed at the level of the Bragg peak which was caused by an increase in the ionizing density of the protons in this region. Unfortunately statistics were not satisfactory to draw suitable conclusions across the three material categories. It would be advisable that such simulations be continued with improved statistics to draw suitable conclusions for this parameter.

This study has shown that there is some possibility for improvement in the transport of therapeutic protons in water equivalent materials and commercially available phantoms to better reflect that of the ICRP case. Such improvements in radiation transport properties will improve the accuracy of treatment planning and quality assurance measurements. Further work should be completed in assessing the response of these material compositions for 2D dose distributions and microdosimetry spectra in

clinical situations. Such work can be completed using Monte Carlo techniques with comparisons to existing treatment planning software. This could provide an assessment on the effect that differences in material composition have in a clinical setting rather than a homogeneous phantom. In addition, microdosimetry simulations should be continued to assess the change in microdosimetry spectra as a function of depth along the path of the primary proton. Such simulations will allow for an assessment of any change in biological properties of the beam which could possibly be used in the future as a treatment planning parameter.

7 SOI Microdosimetry: Space Applications

7.1 Introduction

Space radiation is an important issue with an expanding human presence in space and through the further development of space for communication, commercial and defence purposes. As earth based technologies such as communication continue to expand and grow, there is a demand on a greater number of satellites in orbit and for deployed satellites to have longer service lives. Further, with plans for an increasing long term human presence in space such as returning to the moon and manned missions to mars, humans will be exposed to these radiation fields for longer periods of time than has ever been experienced. A radiation detector is required to not only monitor the doses received by personnel and electronics to establish safe working environments, but also provide an online means for measuring any change in the radiation field so that it may be possible for personnel to move to a shielded part of the facility/spacecraft that affords them greater protection.

Space radiation provides a great challenge as it comprises of a wide range of particles and energies, the composition of which can be effected by magnetic fields, stars and other planets. Humans and electronic systems exploring outer space are exposed to space radiation composed of high-energy protons and heavy ions. In deep space, the radiation environment consists mainly of galactic cosmic radiation (GCR). In the energy range from 100 MeV per nucleon to 10 GeV per nucleon, the GCR consists of 87 percent protons, 12 percent helium ions, and 1 percent heavier ions [79]. Protons are also the major component of solar particle events (SPE), with a smaller contribution from helium and heavier ions emitted from the Sun.

With such a wide range of particles (both charged and uncharged) and energies, radiation detection in this environment is difficult. Most current radiation detection systems provide absorbed dose as the measurement parameter, and are sensitive to a portion of the radiation spectra present and are as such often problematic in providing the

dose equivalent required in such a situation. Microdosimetry provides a means of measuring a wide range of particles and energies in real time, and utilising the techniques outlined in [32, 33] and Section 2.5, it is possible to determine the dose equivalent delivered to a point. Such advantages have seen the deployment of tissue equivalent proportional counters (TEPC's) on various missions including the space shuttle [80]. However, the operational constraints of such devices such as their high power consumption, relatively large size and weight, makes them less than ideal for long space deployments. Devices such as the SOI microdosimeter described in [25, 28-31, 55, 64, 71, 81] and Section 2.4 of this report meet such design characteristics for space deployment, and has lead to their inclusion as part of the dosimetry payload on the MidSTAR-1 satellite launched on 9th March 2007 [82].

Prior to deployment in space it was important to gain an understanding of the response of such devices to space radiation fields which are very different than those encountered in hadron therapy where such devices had been tested previously. As such, the following aims were completed as part of this thesis:

- Simulate the response of the SOI microdosimeter to solar protons both outside the spacecraft and within typical shielding structures utilised in space.
- Simulate the response of the SOI microdosimeter when packaged with converters of differing thickness to solar protons. This was important as the SOI microdosimeter is typically packaged with a polyethylene/Perspex converter of a given thickness to measure the neutron spectra. However, it was also important to determine how the inclusion of such a converter effected the response of the device to protons, the dominant particle in GCE and SPE [79].
- Simulate the response of the SOI microdosimeter when imbedded within a TE phantom and irradiated with solar protons. Such simulations provided information on the changing radiobiological effect of protons as they traversed the astronaut contained within the space capsule.
- Measure the response of the SOI microdosimeter to heavy ion fields including iron, oxygen and titanium. Utilising established techniques for determining the dose

weighted mean lineal energy [25] the results were compared with established TEPC data [83].

- Measure the response of the SOI microdosimeter at various positions along the Bragg peak of heavy ion fields such as iron, oxygen and titanium utilising a Perspex phantom. Such measurements provided important information on the changes in mean dose weighted lineal energy as a function of depth within tissue, which is of primary concern in manned space missions.
- Simulate the response of Si cells of varying dimensions to heavy ions. Through measuring the spectra of energy deposition events it is possible to discern if the production of long range delta rays affected the measured result. Such simulations are of great importance to future device development.

7.2 MiDN: First SOI microdosimeters in Space

The goal of the MIcroDosimeter iNstrument (MIDN) on MidSTAR-I [84] was to apply solid-state microdosimetry to a space environment and directly assess astronaut risk to an unknown mixed radiation field. The SOI microdosimeter in this instance was perfectly suited as it met the flight constraints of being rugged, having low power (< 1.25W), low mass, and utilises low voltages (± 5V). The SOI microdosimeter would be used to determine in real time the dose equivalent in Sieverts which is the regulatory quantity used to evaluate risk and limits of radiation exposure [32].

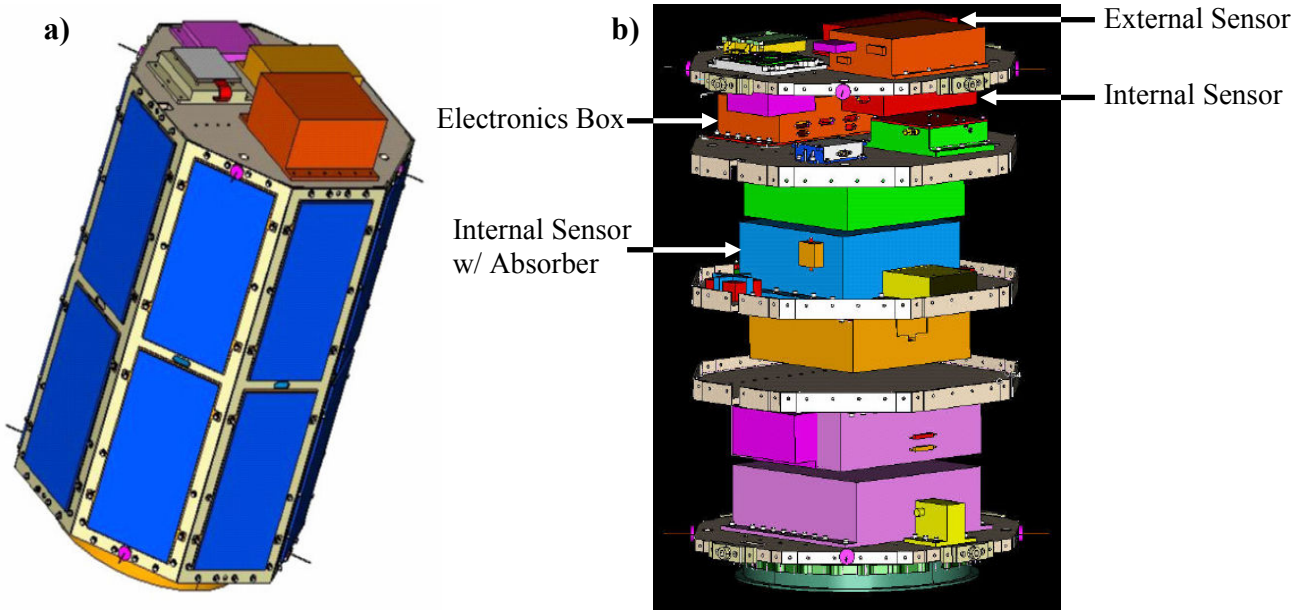

Figure 7-1: a) Schematic of the complete MidSTAR-1 satellite. b) Schematic of the MidSTAR-1 satellite with the external panels removed. Note the position of the 3 sensor arrays and electronics [82, 84, 85].

The MidSTAR (Midshipmen Space Technology Application Research) series of spacecraft have been developed as a low-cost, quick response platform, accommodating small payloads approved by the Space Test Program of the U.S. Department of Defence. MidSTAR-1 is the first of the MidSTAR series and was launched aboard a Lockheed-Martin Atlas V rocket on 9th March 2007. The satellite is 38 inches in length and 28 inches in diameter with a total payload mass of 80kg. Contained within the satellite are 3 SOI microdosimeters; one near the extremity of the spacecraft enclosed in an aluminium shield, one inside the spacecraft enclosed in an aluminium shield and one inside the spacecraft enclosed within a polyethylene converter (for the measurement of neutrons). In order to meet weight and power requirements, the three devices will utilise a common power supply, data acquisition and storage systems [84].

7.3 Incident Space Radiation Spectra

Information on the radiation spectra at different altitudes from earth can be obtained using specialised radiation codes. In this report both the SPENVIS (Solar Particle Environment Information System) [86] and CREME96 (Cosmic Ray Effects on Micro-Electronics) [87] codes were utilised in the generation of radiation fields for various incident ions to provide further information for both GEANT4 simulation studies and

experimental measurements. In each case the position of interest was modelled as the Internal Space Station (ISS).

7.3.1 SPENVIS

SPENVIS was utilised in the generation of solar proton fields. The incident radiation fields were obtained for a primarily circular orbit of altitude 360 km, an inclination of 51.6 degrees and 12 month mission duration. The JPL model was utilised in these calculations as it provided an improvement on the existing King models [86]. In each case a 95 percent confidence level in the JPL model was maintained.

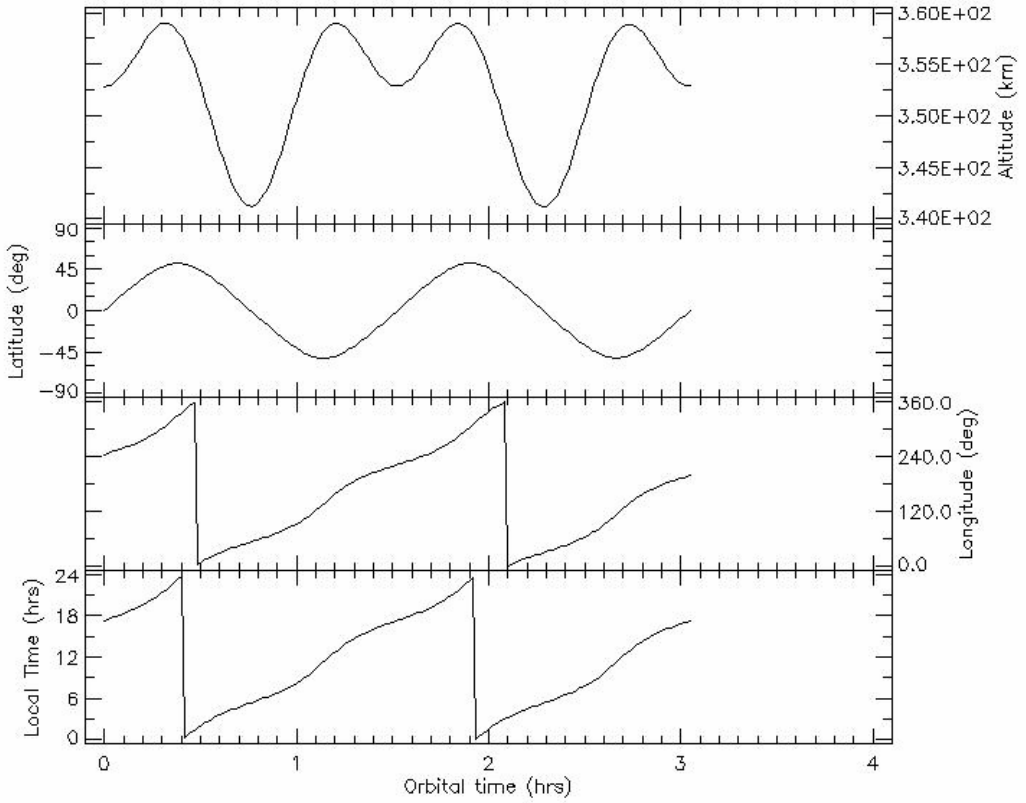

Figure 7-2: Orbit Parameters generated using SPENVIS for two complete orbits of Earth totalling 3 hours 16 minutes.

This model was employed for three conditions; without geomagnetic shielding, accounting for geomagnetic shielding within a stormy magnetosphere, and finally accounting for geomagnetic shielding within a quiet magnetosphere. From the results displayed in Figure 7-3 it was clear that the solar protons were predominantly below 10 MeV in energy, with the maximum energy supplied by the JPL model being 200 MeV. It

is well established [86] that solar protons can penetrate much deeper into the magnetosphere than predicted by the simple attenuation model. As the case ignoring geomagnetic shielding was considered a worse case scenario it was utilised as the incident proton radiation spectra for the GEANT4 simulations. It should be noted however, that as the shape of the spectra does not change significantly (only the radiation fluence) it was possible to theoretically compare results across geomagnetic conditions.

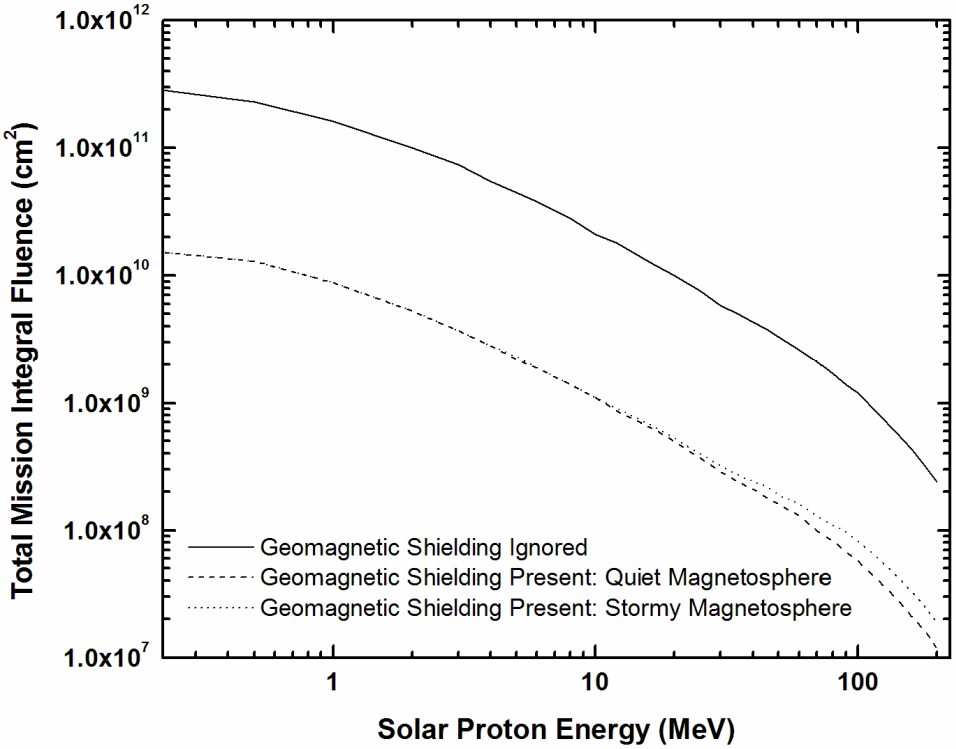

Figure 7-3: Total mission integral fluence of solar protons for the ISS during a 12 month period beginning the 1st January 2003. Note, the greater than order of magnitude increase when geomagnetic shielding is ignored, which in this simulation study is considered a "worst" case scenario.

7.3.2 CREME96

The CREME96 code was utilised to provide information on the radiation spectra at the ISS for a range of different ions including protons, helium, carbon, oxygen, silicon and iron. Using the default ISS orbital files contained within CREME96, radiation spectra were generated for a complete orbit of the ISS which was located at an altitude of 450 km and an inclination of 51.6 degrees. The model utilised for the generation of these incident radiation files was the Solar Energetic Particle (SEP) or Flare model, which is appropriate for evaluating "worst case" and "peak" particle fluxes and also single event

upset (SEU) rates. Within this model are three different levels of solar particle intensity. In this study it was decided to obtain spectra using the "Worst Day Model" which is based on SEP fluxes averaged over 18 hours beginning at 1300 UT on 20 October 1989. This period was the single largest flux enhancement in October 1989. It was caused by the arrival at Earth of a powerful interplanetary shock, which also produced a large geomagnetic storm. For these simulations the Earth's geomagnetic field was accounted for but considered "stormy", which is a situation of increased penetration of cosmic rays to near-Earth orbit altitudes. It is also important to note that the CREME96 code considers SEP charge states, which are important for accurate flux calculation in low inclination, low-Earth orbits.

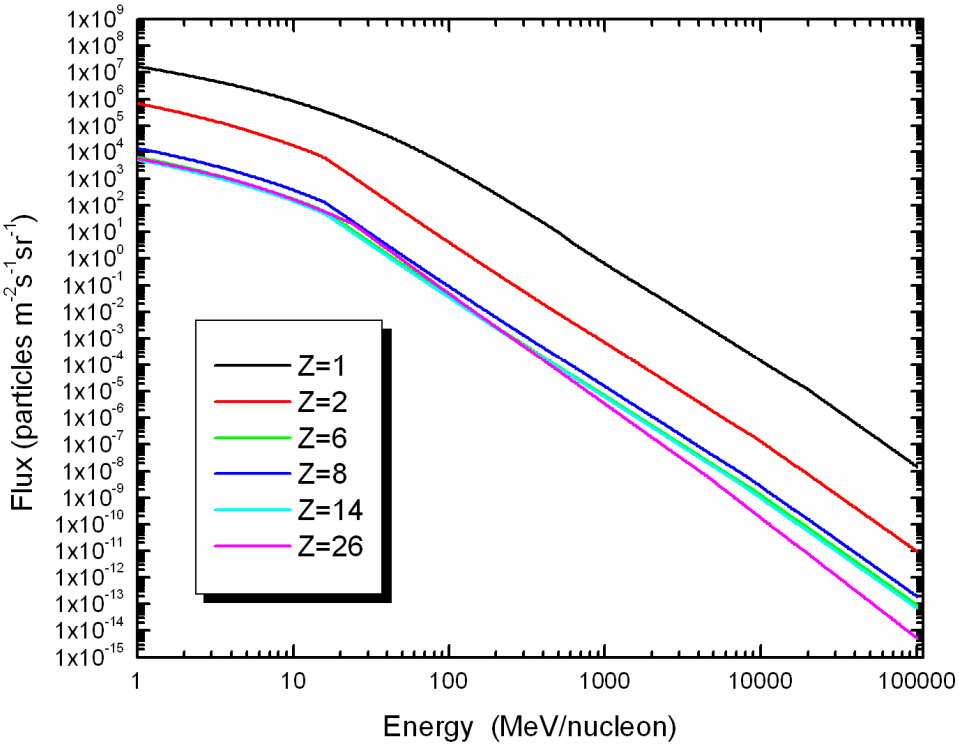

Figure 7-4: Particle radiation spectra generated using CREME96 for the ISS. It is clear from this that solar protons contribute greatly to the radiation spectra in the space environment with 1-2 orders of magnitude increase in flux over other ion species.

Figure 7-4 indicates how in near-Earth orbits, such as that of the ISS, protons are the primary radiation particle with a greater than order of magnitude increase in flux over any other particle for a given energy. It is also clear that the flux is highly dependant on the energy of the particle, with a significantly higher flux at lower particle energies. The flux

in Figure 7-4 ranges from 10^{9}-10^{-15} particles $m^{-2}s^{-1}sr^{-1}$ with the bulk of the particles having an energy of 10 MeV/nucleon or less. It is expected that such particles would be predominantly filtered out by the aircraft shielding or spacesuit material, however this hypothesis will be confirmed in this work. As the higher energy particles have the potential to cross shielding structures they are of continuing concern in radiation protection.

7.4 Solar proton simulations and results

GEANT4.7.1p1 was utilised to simulate the response of the SOI microdosimeter to a spectra of solar protons as generated using the SPENVIS program and which is illustrated in Figure 7-3. Simulation studies utilising GEANT4 have been proven effective in determining the response of the SOI microdosimeter for monoenergetic and therapeutic hadron radiation fields [64, 66, 71, 73] and this work is a logical extension of this. This work:

- Evaluated the response of the SOI microdosimeter to solar protons both outside the spacecraft and within typical shielding structures of varying thickness.
- Simulated the response of the SOI microdosimeter when packaged with converters of differing thickness.
- Simulated the response of the SOI microdosimeter within a TE phantom.

7.4.1 GEANT4 Simulation Parameters

The GEANT4.7.1p1 Monte Carlo Toolkit [52] was used to simulate the microdosimetry spectra obtained from an SOI microdosimeter irradiated with solar protons. There were three important components of this program:

- Phantom Construction and Definition
- Physics Process and Incident Particles
- Tracking of Events

7.4.1.1 Phantom Construction & Definition

Elements making up materials utilised within the phantom geometry were defined by isotropic abundance. This provided the most accurate composition available and was obtained from an ICRU based NIST database [35]. Many of these compositions have also been published elsewhere [73, 77]. The 10 μm thick SOI microdosimeter was simulated using the geometry outlined in Section 5.3 of this report. The simulated geometry is illustrated in Figure 7-5. The microdosimeter chip was not contained within a probe holder or assembly as in experimental validation simulations, but rather would stand alone either outside, or inside the spacecraft, or within the TE phantom structure. To simulate the presence of a probe assembly an aluminium window was situated immediately upstream of the microdosimeter chip. This was sufficient in this case as the incident proton field was to be considered as unidirectional. The cross-sectional area of the window was the same as that of the ceramic chip with a thickness of 40 μm. This is a thicker window than that used in land based experimental studies (generally 4 μm) as it is assumed that a more rugged window material will be needed for long space deployments, especially near the extremities of the satellite.

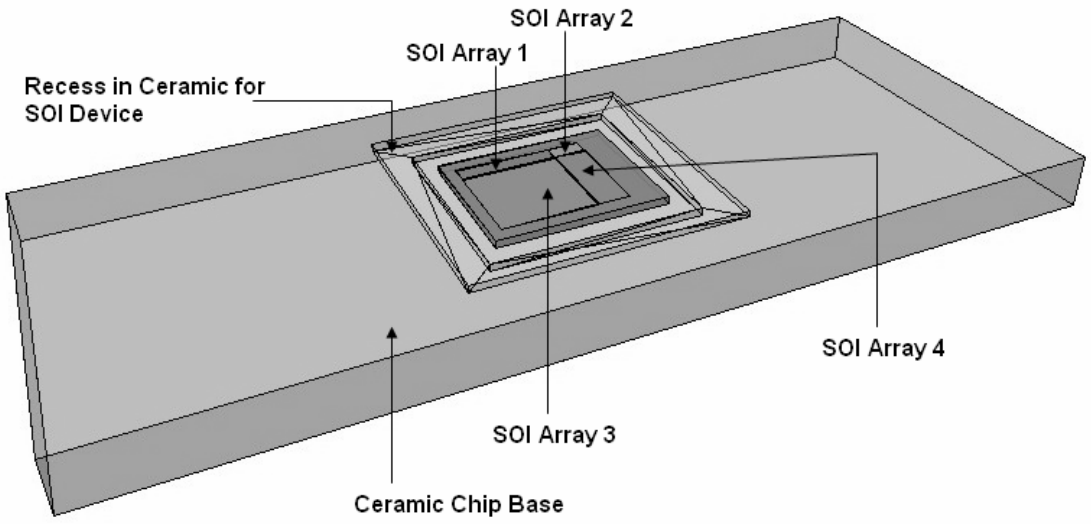

Figure 7-5: Schematic diagram of the simulated SOI microdosimeter geometry. Note the 4 separate arrays which were considered sensitive in this simulation study to improve statistics.

To determine the effect of converter thickness on microdosimetry spectra, a Perspex Right-angled Parallelepiped (RPP) volume was interspaced between the aluminium window and the chip assuming no spacing between structures. The converter in this case had the same cross sectional dimensions as the ceramic chip and Al window with a thickness of 0.5, 1, 3 and 5 mm. To ensure maximum registration of energy deposition events all four arrays were linked in series and considered as sensitive within the simulation. Thus a particle depositing energy in any of the four array structures was registered by the program, hence improving the statistics of the simulation study.

The geometry of the spacecraft shielding, polyethylene converter and TE phantoms were created utilising RPP volumes. Three different series of simulations were completed. In the first series of simulations the microdosimeter with the aluminium window present was situated both outside the spacecraft and inside the spacecraft shield, whose thickness was varied to determine the effect of shielding thickness on microdosimetric spectra. The thicknesses evaluated in this simulation study was 1, 2, 3, 4, 5, 10, 15, and 20 mm, while the cross sectional area of the RPP shielding volumes was 5x5 cm^2. A 300 cm air gap interspaced the 2 simulated walls of the spacecraft to represent the astronaut's environment.

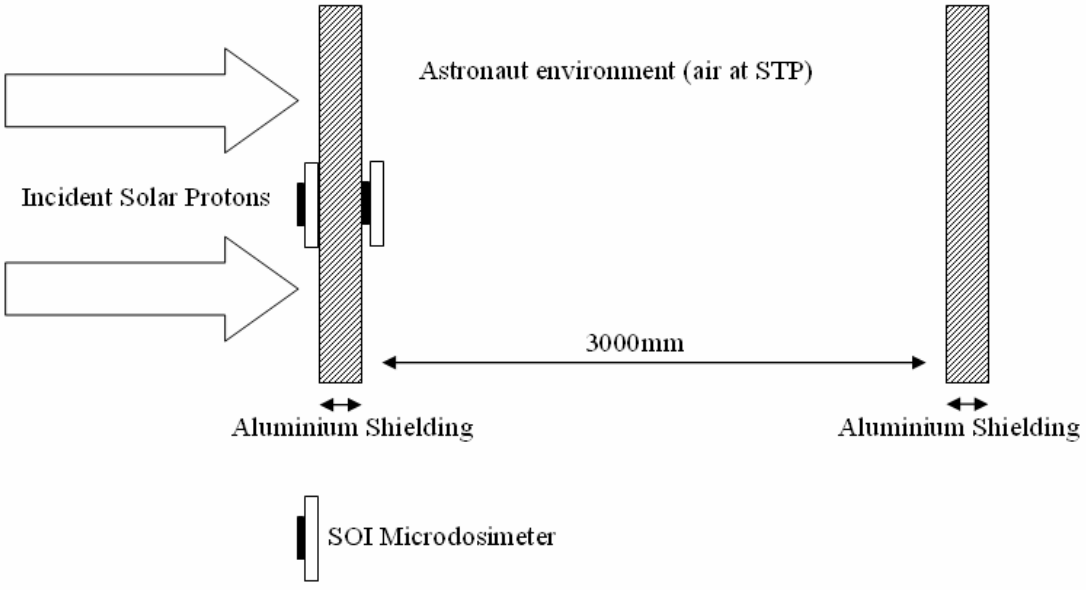

Figure 7-6: Schematic of simulation configuration determining the effect of shielding thickness on microdosimetry spectra generated by solar protons utilising the SOI microdosimeter. In these simulations the thickness of the aluminium shielding was varied with thicknesses of 1, 2, 3, 4, 5, 10, 15, and 20 mm.

In determining the effect of converter thickness (Figure 7-7) the simulation geometry remained largely the same as in the previous case. In this instance the spacecraft shielding had a fixed thickness of 5 mm and a converter of varying thickness was interspaced between the aluminium window and the SOI microdosimeter chip. Simulated data was then obtained both inside and outside the spacecrafts shield to complete a thorough evaluation on the effect converter thickness on the simulated microdosimetry spectra.

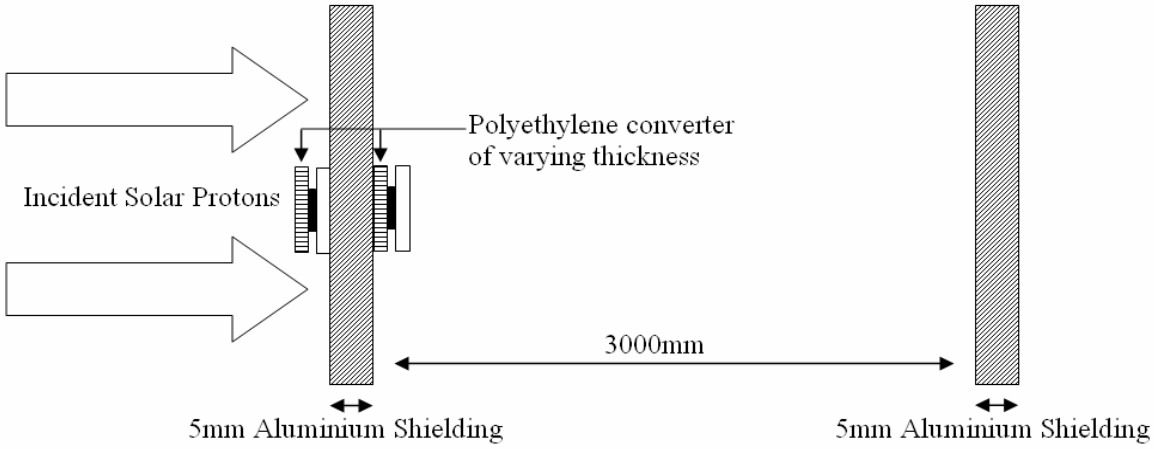

Figure 7-7: Schematic of simulation configuration determining the effect of converter thickness on microdosimetry spectra generated by solar protons utilising the SOI microdosimeter. In these simulations the thickness of the polyethylene converter was varied with thicknesses of 0.5, 1, 3 and 5mm.

The final simulation configuration involved simulating the change in microdosimetry spectra within a TE phantom contained inside the space capsule. This TE phantom was constructed to represent the chest of an astronaut, utilising three RPP volumes of ICRP muscle, bone and lung of thicknesses 10mm, 10mm and 200mm respectively. The spacecraft shield had a fixed thickness of 5 mm. The microdosimeter assembly (no converter present) was situated at the muscle/bone and bone/lung interfaces whilst also at a depth of 100 mm within the lung material. Such simulations illustrated the change in microdosimetry spectra within the astronaut and determined if there is a particular organ or region that has an elevated biological risk associated with solar proton irradiation.

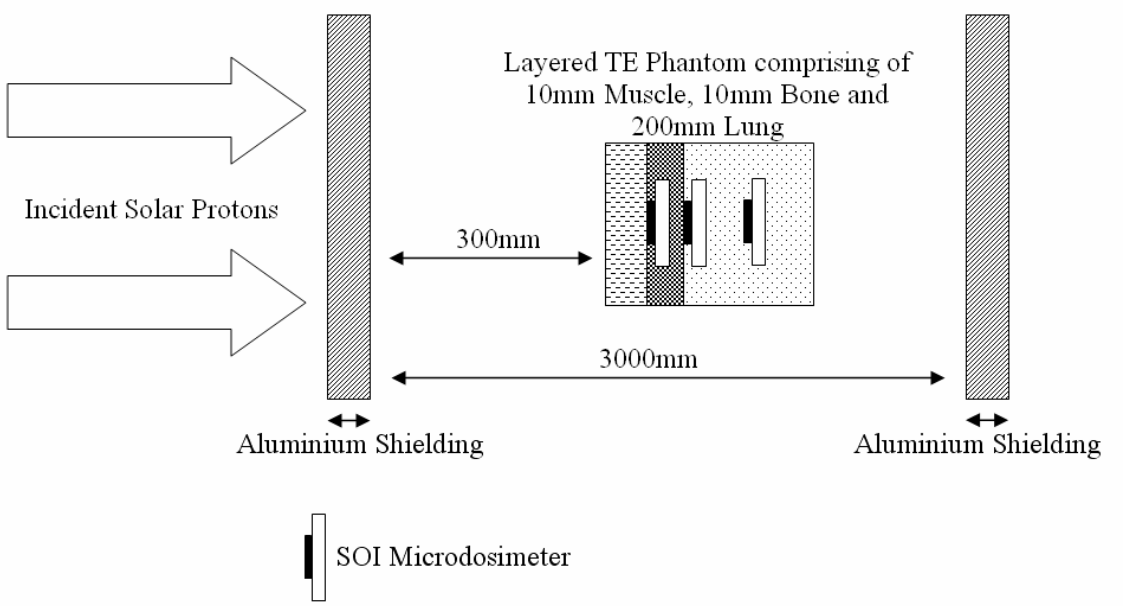

Figure 7-8: Schematic of simulation configuration determining the change in microdosimetry spectra as a function of position within a TE phantom. The microdosimeter was situated at the muscle/bone and bone/lung interfaces, whilst also at a depth of 100 mm within the lung portion of the phantom.

7.4.1.2 Physics Processes & Incident Particles

The main component of any Monte Carlo program is the physics processes that are to be employed in particle transport. In this case it was imperative that the process covered a wide energy range to account for the primary beam of protons having an energy range of 0.1-200MeV and also the secondaries produced by such particles. Low energy inelastic scattering (G4preCompound), low energy ionisation (ICRU-49) and multiple scattering models were employed for the transport of protons through the geometry of the simulation.

The physics of secondary particles also needed to be considered and accounted for. In the case of alpha particles, deuterons, tritons, and other generic charged ions produced as a result of inelastic proton interactions, the corresponding low energy inelastic scattering, low energy ionisation and multiple scattering models were utilised. The predominant particles generated within the simulation would be electrons resulting from proton ionisation interactions. Electron processes accounted for included low energy ionisation, low energy Bremsstrahlung and multiple scattering. In the event of photon generation, the physics processes included were low energy photoelectric effect, low energy

Compton scattering, low energy Rayleigh scattering, and low energy pair production. Neutron interactions were also accounted for using the appropriate models.

Incident protons whose energy was dictated by a random sampling of the JPL solar proton spectra (ignoring geomagnetic effects) were used in this simulation. An energy cut was applied in order to allow for realistic simulation times. For almost all simulations the entire JPL solar proton spectra was sampled for incident particle energy. However, in the case of the microdosimeter being imbedded in the TE phantom only protons with energies exceeding 30 MeV were considered, as those particles below such energies would not penetrate the 5 mm thick aluminium shield and contribute energy deposition events within the detector SV.

The position of the incident particles randomly covered the entire cross sectional area of RPP volume representing the spacecraft shield with an initial direction perpendicular to this shield. A separate simulation of 10^8 incident particles was carried out for each position of the SOI microdosimeter within the phantom structure

7.4.1.3 Tracking of Events

In this simulation all four arrays of the SOI microdosimeter were defined as the sensitive volumes within the DetectorConstruction class of the program and linked in series to provide improved statistics. All energy deposition events (whether from primary or secondary particles) within these volumes were tracked and the kinetic energy, charge and mass of the particle as well as the energy deposited within the SV was stored. Upon completion of the simulation within the RunAction class these events were then binned into a spectra of energy deposition events. A separate data analysis software program was then utilised to create the microdosimetry spectra from these results using the method outlined in [32, 33]. From this microdosimetry spectra the mean dose weighted lineal energy, average quality factor and dose equivalent was determined using the protocol outlined in [32, 33] and Section 2.5 As in Section 2.5 a mean chord length of 19.05 μm was used for microdosimetry spectra generation.

7.4.2 Shielding Results & Discussion

The shielding results are very interesting in understanding the proton radiation field outside the spacecraft and how this field is altered with differing levels of shielding.

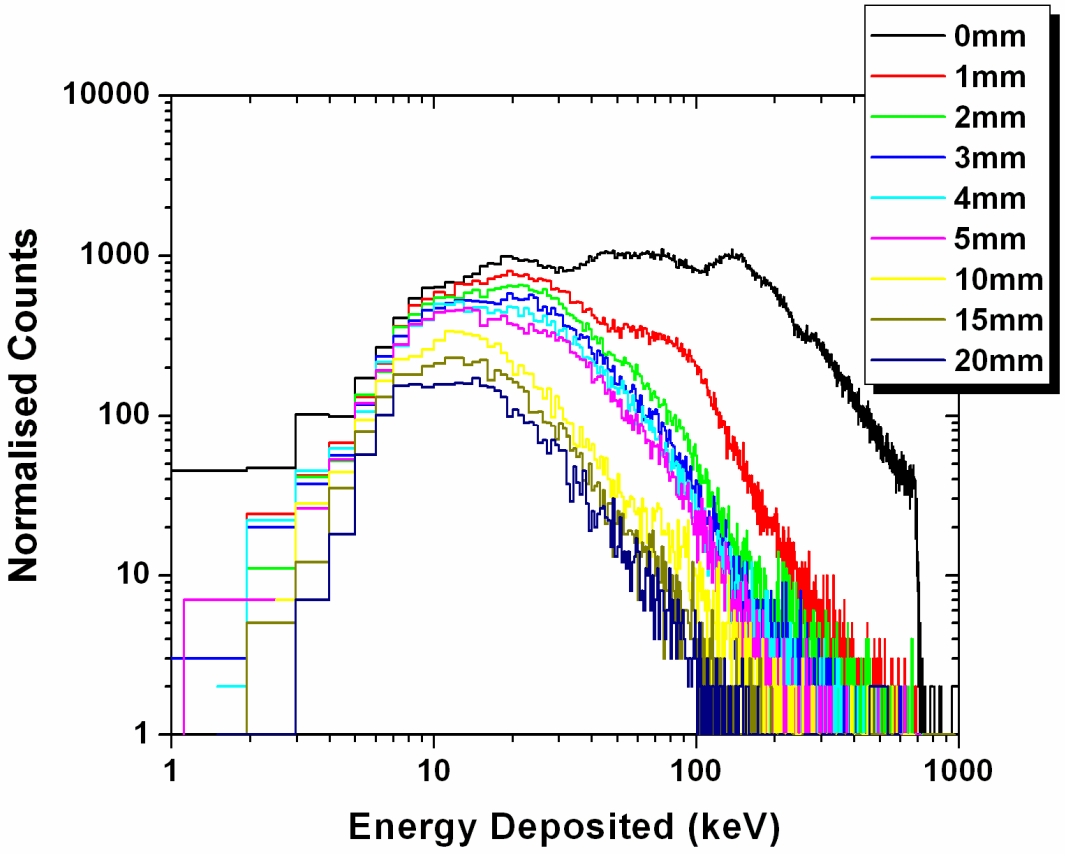

Figure 7-9: Energy deposition spectra from the simulated response of the SOI microdosimeter for varying thicknesses of Al shielding material.

It is clear from the results illustrated in Figure 7-9 that increasing levels of Al shielding result in decreased energy deposition events and energy pattern within the SOI microdosimeter. Clearly the external device experiences a far greater number of energy deposition events, with a significantly larger portion of higher energy events. The external device experiences energy deposition events of up to 700 keV. This corresponds to solar protons depositing their maximum energy within a 10 μm (thickness of the device) track within the SV and is known as the proton edge. Events below 700 keV correspond to protons crossing or stopping within the SV and only depositing a fraction of the possible proton energy. It is important to note that some energy deposition events exceeding 700 keV were detected, however these were statistically very rare in this case

(approximately 0.06% of energy deposition events exceeded 700 keV). Protons either obliquely striking the device, or experiencing scattering within the SV, have an increased path length resulting in higher energy depositions within the SV.

Figure 7-9 shows clearly the differences in energy deposition spectra for varying shielding thicknesses; however microdosimetry parameters may illustrate these changes more clearly. Calculating the mean dose weighted lineal energy, average quality factor and dose equivalent allows a more accurate estimation of the effect which increasing levels of Al shielding is having over the simulated radiation field. These parameters are contained within Table 7-1. Clearly, increasing the Al shielding causes subsequent decreases in the simulated dose equivalent, average quality factor and mean dose weighted lineal energy within the SOI microdosimeter.

Thickness Al (mm)	$\bar{y}_d\,(keV/\mu m)$	Dose Equivalent (mSv)	Average Quality Factor
0	38.87	4.33	14.77
1	1.30	1.98	6.87
2	0.57	1.90	6.59
3	0.31	1.47	5.13
4	0.24	1.43	5.00
5	0.20	1.38	4.80
10	0.10	1.64	5.71
15	0.04	1.04	3.64
20	0.02	1.00	3.51

Table 7-1: Mean dose weighted lineal energy, average quality factor and dose equivalent as determined from the simulated response of the SOI microdosimeter for varying thicknesses of Al.

Figure 7-10 provides the information contained within Table 7-1 graphically. Clearly, the dose equivalent sharply decreases with initial increases in Al shielding, with a greater than order of magnitude decrease observed for the addition of only 1 mm of Al. However, the dose equivalent plateaus with further increases in Al shield thickness. Correspondingly the average quality factor and mean dose weighted lineal energy values encounter sharp decreases with initial additions of Al shielding, but these also plateau as the shielding thickness is further increased. Thickening the Al shielding from 5 to 20 mm

decreases the frequency of energy deposition events substantially from 17000 to 4000, and correspondingly the dose equivalent decreases from 0.2 to 0.02 mSv. However, at the same time the average quality factor decreases only marginally from 1.38 to 1 and the mean dose weighted lineal energy decreases from 4.8 to 3.51 keV/μm, further illustrating this plateau effect.

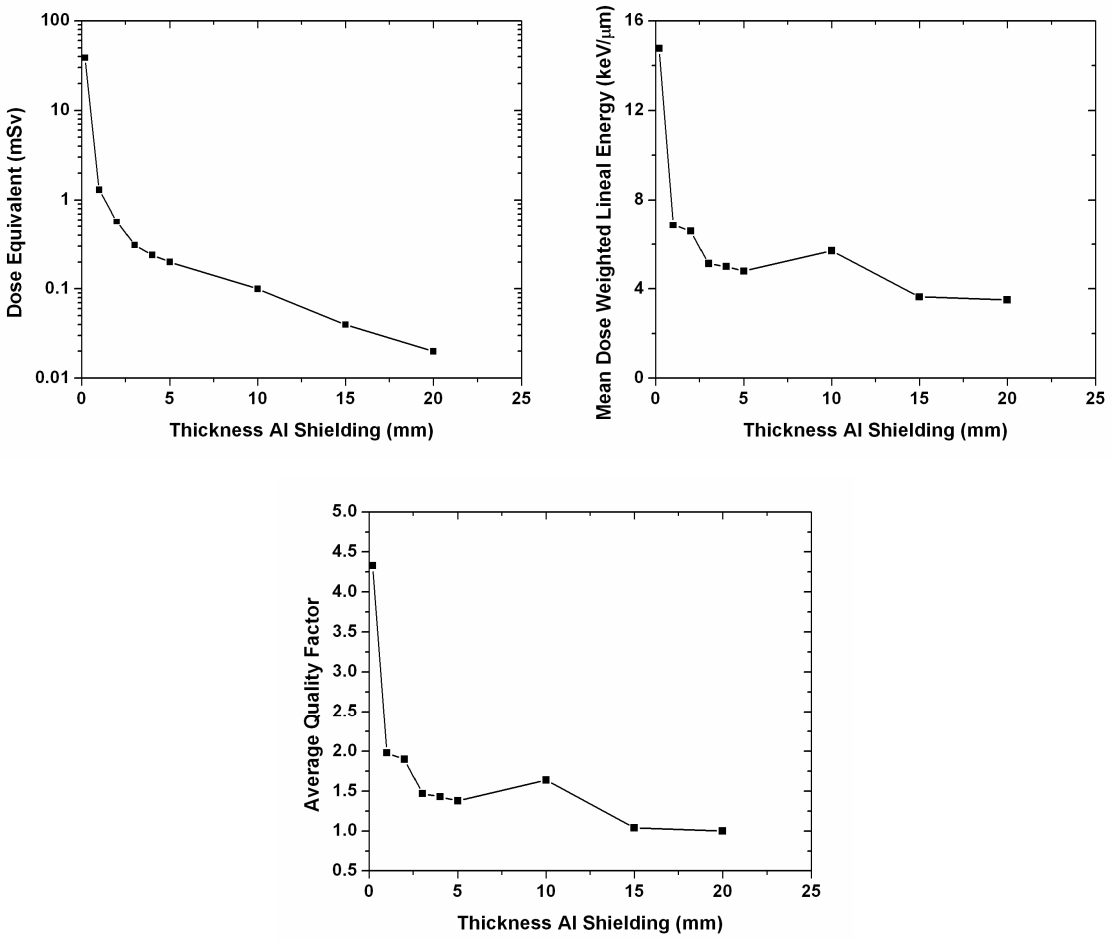

Figure 7-10: Graphical representation of the change in dose weighted lineal energy, average quality factor and dose equivalent with increasing Al shielding thickness for $1x10^8$ protons/$25cm^2$.

As mission payloads for space deployment have weight restrictions placed on them, shielding must be optimised to provide the best possible protection for astronauts and deployed electronics, whilst also maintaining the lowest weight possible. This simulation series has clearly shown that whilst the thickest shielding may provide an overall decrease in dose equivalent, this must be balanced against mean dose weighted lineal energy and average quality factor and collectively the benefits from increased shielding

thickness determined. So whilst the number of radiation events decreased through the addition of thicker shields, the nature of the radiation field may be changed so that corresponding decreases in radiation quality are not observed. In this instance Al shield thicknesses from 3-5 mm would be considered optimal as it provides filtering of low energy (and thus biologically damaging) protons whilst ensuring the mean dose weighted lineal energy and average quality factor is also kept low. It should be noted however, that in this case solar protons were the only incident radiation modality considered. For a more detailed assessment of the shielding structure required in such deployments, additional simulations of incident electrons, neutrons and heavy ions needs to be completed to develop optimised shielding parameters.

	Geomagnetic Effects Ignored	**Quiet Magnetosphere, Geomagnetic Effects Considered**
Total Mission Histories (cm^{-2})	1.20E+12	6.29E+10
Number of Histories Simulated (25 cm^2)	1.00E+08	1.00E+08
Fraction of Mission simulated	3.33E-06	6.36E-05
Collection time seconds	105	2006
Collection Time Minutes (All Arrays)	1.75	33.43
Collection Time Minutes (A4 Array)	8.17	156.12
Collection Time Minutes (A1 Array)	16.28	310.90

Table 7-2: Actual collection times of the SOI microdosimeter with respect to the mission duration.

These simulations also provide a means for assessing the time required for the SOI microdosimeter to acquire data. This has been calculated for the simulated results in both the case of geomagnetic effects ignored, and for the consideration of geomagnetic effects in a quiet magnetosphere (typical environment for the ISS and MidSTAR-1). SPENVIS provided the solar proton flux per cm^2 for a total 12 month mission duration. As the simulation was completed for $1x10^8$ particles incident on a 25 cm^2 RPP shielding structure it was possible to determine the time of simulation assuming a uniform (with respect to time) solar proton fluence. These values are contained within Table 7-2 and show the collection time in minutes for the case where all arrays are connected in series,

and also for Array 1 (120x120 μm with 150 detector elements) and Array 4 (30x30 μm with 4800 detector elements) [21] which are two arrays that will be used to collect data on the MiDN spacecraft.

From Table 7-2 it is clear that data can be acquired in minutes to hours depending on the radiation field present. When considering geomagnetic effects in a quiet magnetosphere Array 1 and Array 4 would theoretically collect this data in 311 and 156 minutes respectively, while all arrays in series would complete this in just over 30 minutes. While in the worst case scenario the collection of the above data theoretically would require only 1.75 to 16.3 minutes depending on the chosen array. This illustrates that in its current form the SOI microdosimeter would provide real time information on the radiation field allowing personnel to move to a safe shielded area of the spacecraft. Further improvements to not only the size of the arrays but also to the electronics would allow for faster acquisition times in space deployment.

Information on the time of simulation also allows for the rate of dose equivalent to be determined. Using the dose equivalent values from Table 7-1 and the theoretical time of simulation from Table 7-2 the rate of dose equivalent can be determined for varying levels of Al shielding both ignoring geomagnetic effects and considering geomagnetic effects in a quiet magnetosphere. It is clear from Table 7-3 that the rate of dose equivalent varies markedly for the worst case scenario of geomagnetic effects ignored and for the typical case of a quiet magnetosphere with geomagnetic effects considered. They also highlight the need for some shielding to be present in all cases to prevent damage to electronic and biological systems. Further work in this regard can be completed to simulate the dose equivalent from all components of the radiation field and compare this with actual measured data.

Thickness Al (mm)	Dose Rate (mSv/hr) Geomagnetic Effects Ignored	Dose Rate (mSv/hr) Quiet Magnetosphere, Geomagnetic Effects Considered
0	1332.604	69.752
1	44.667	2.338
2	19.707	1.032
3	10.570	0.553
4	8.364	0.438
5	6.692	0.350
10	3.407	0.178
15	1.204	0.063
20	0.825	0.043

Table 7-3: Actual dose rates for the ISS considering different shielding thicknesses as simulated by GEANT4 for the SOI microdosimeter when all arrays are connected in series.

7.4.3 Converter Results & Discussion

The energy deposition spectra from the simulated response of the SOI microdosimeter to varying thickness converter materials both outside the spacecraft shield and behind 3 and 10 mm of Al shielding material is presented in Figure 7-11, Figure 7-12 and Figure 7-13. For simulations of the SOI microdosimeter outside of the spacecraft shield it is immediately apparent that the addition of converter material causes a change in the energy deposition spectra. As the solar proton radiation field is comprised of a large percentage of low energy (less than 1 MeV) protons, the addition of any thickness of converter attenuates these particles, preventing them from depositing energy within the SV. Further increases in converter thickness produce additional incident particle attenuation resulting in a visible shift in the energy deposition spectra to lower energies. It would be recommended that in space applications, such as MidSTAR-I, two external sensors be utilised. One sensor with no converter to measure an un-attenuated incident proton radiation field, provide an accurate assessment of its microdosimetry properties and determine the probability for SEU and biological damage. A second sensor should then be employed with a converter in place to measure any neutron component present in the incident radiation field.

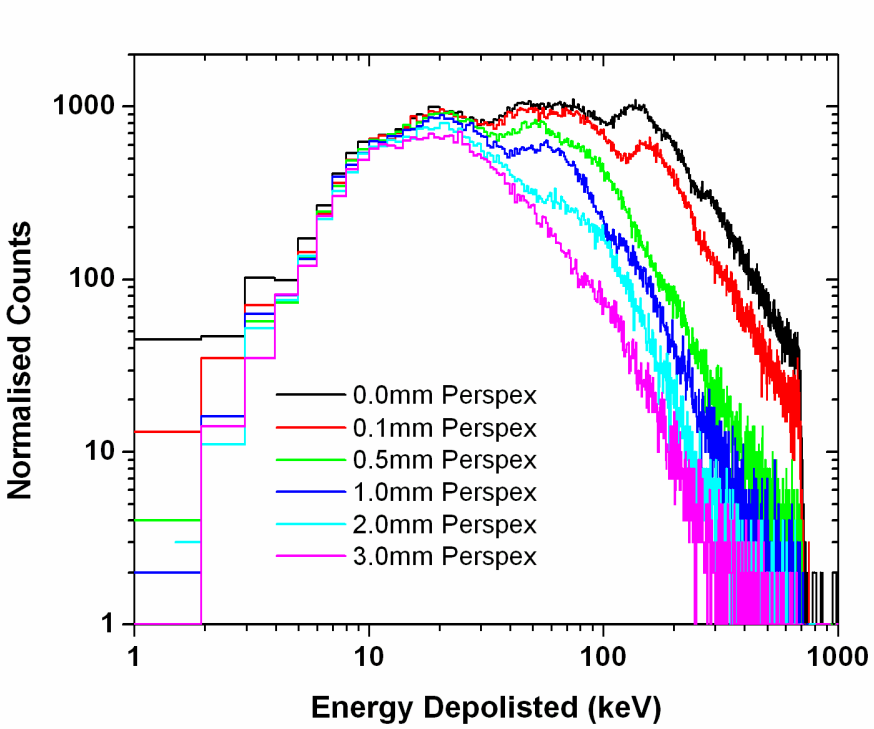

Figure 7-11: Energy deposition spectra from the simulated response of the SOI microdosimeter for varying thicknesses of converter material and no additional Al shielding.

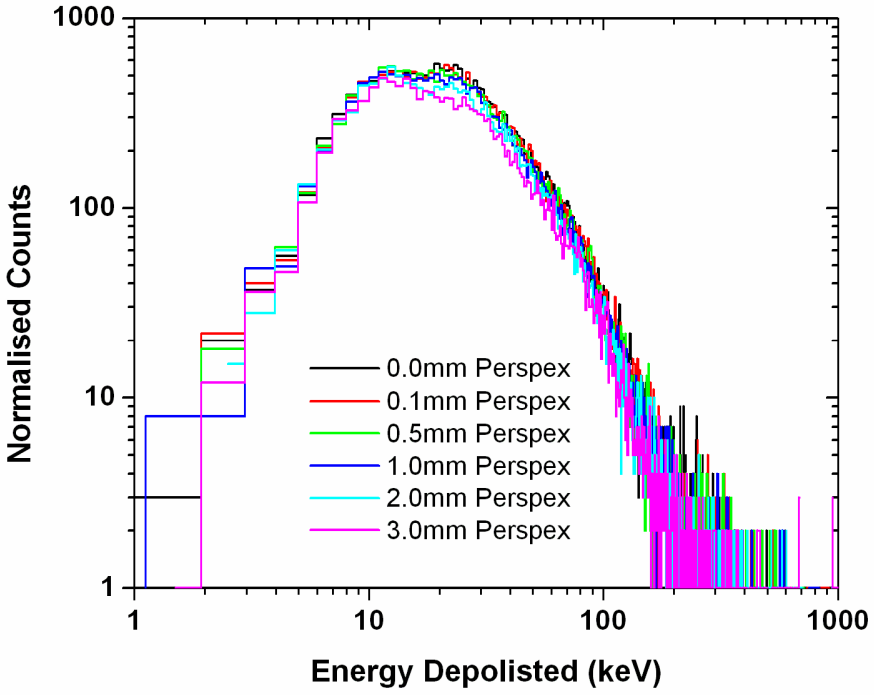

Figure 7-12: Energy deposition spectra from the simulated response of the SOI microdosimeter for varying thicknesses of converter material and 3 mm additional Al shielding.

Figure 7-12 and Figure 7-13 display the energy deposition spectra for a SOI microdosimeter behind an Al shield of 3 and 10 mm with varying additional converter thicknesses. What is immediately apparent is that for varying converter thickness there appears minimal visible change in the energy deposition spectra as the converter thickness increases. This is in contrast to the results obtained outside the spacecraft shield and is a direct consequence of the Al shield filtering almost all low energy protons. As such additional converter thickness results in minimal changes to the energy deposition spectra. Such results indicate that only a single sensor is required within the spacecraft and that this sensor should be coupled to a converter of suitable thickness. A device in this configuration would allow for accurate determination of the effect from the proton field (as evidenced by these simulated results), in addition to providing an assessment of the microdosimetric effect of any neutrons that are present. This device will save weight and power (through the requirement of a single in-cabin microdosimeter), whilst also providing an accurate assessment of the microdosimetric properties of the radiation field within the astronauts environment.

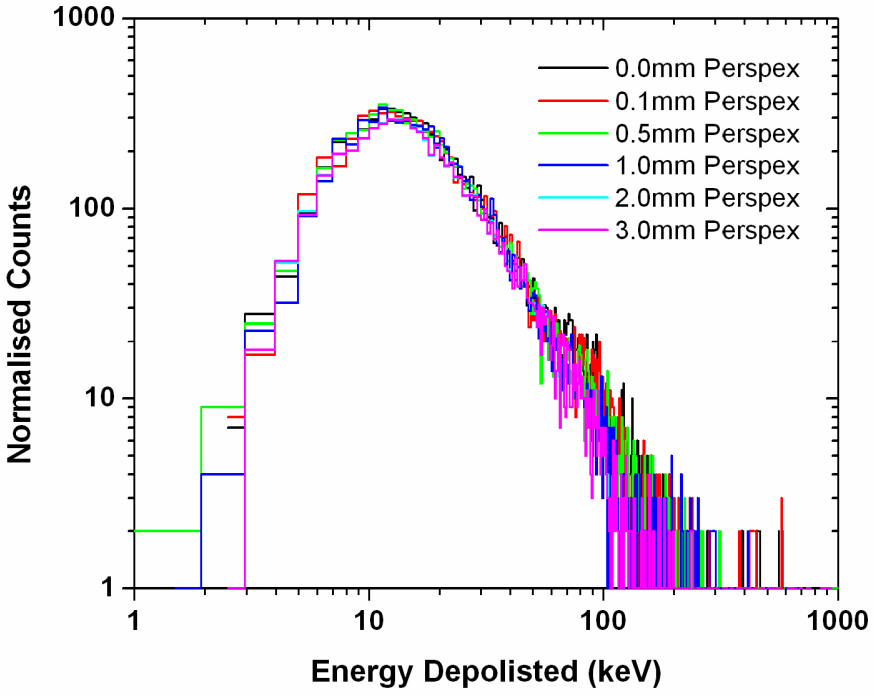

Figure 7-13: Energy deposition spectra from the simulated response of the SOI microdosimeter for varying thicknesses of converter material and 10 mm additional Al shielding.

To provide a more complete analysis of the effect which varying converter thickness had on the microdosimetry spectra both inside and outside the spacecraft shield, the dose equivalent, mean dose lineal weighted energy and average quality factor were determined and are contained in Figure 7-14. It is clear from these graphs that the conclusions made from the energy deposition spectra were accurate. The addition of up to 3 mm in Perspex converter to the SOI microdosimeter outside the spacecraft shield (i.e. 0 mm Al shielding) results in over an order of magnitude decrease in the dose equivalent, a 56% decrease in the mean dose weighted lineal energy and a 57% decrease in the average quality factor. These factors will provide an incorrect assessment of the external proton radiation field and supports the use of two separate devices to measure the radiation spectra outside the spacecraft separately from charged particles and neutrons.

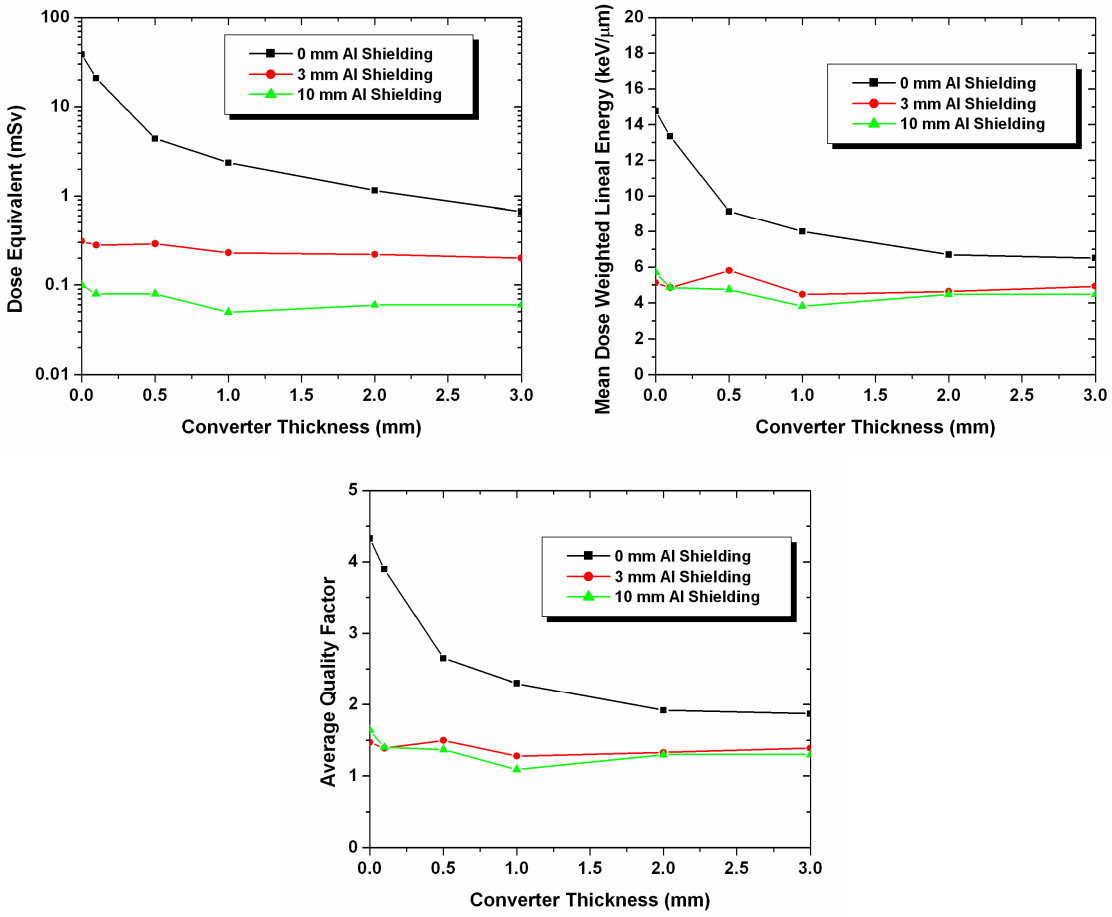

Figure 7-14: Graphical representation of the change in dose weighted lineal energy, average quality factor and dose equivalent both inside and outside the spacecraft shield with varying converter thickness.

Within the spacecraft (with a 3 or 10 mm Al shield) there is minimal variation in the dose equivalent, average quality factor and mean dose weighted lineal energy for increasing converter thickness. Some statistical variation is observed from low frequency high lineal energy events, which can be improved through larger simulation histories. This stable nature of the radiation field within the spacecraft is a direct result of the shielding filtering low range protons. This further supports the use of a single device within the astronaut's environment to minimise weight, and power consumption whilst retaining accurate radiation metrology data.

7.4.4 TE Phantom Results & Discussion

The simulated response of the SOI microdosimeter located within a layered TE phantom representing the chest of an astronaut is displayed in Figure 7-15. Clearly as the amount of material preceding the location of the SOI microdosimeter increases the incident radiation field is attenuated further. Hence, the total number of events and the number of high energy deposition events decreases. This results in a shift of the energy deposition spectra to lower energies, and a lowering of the peak amplitude.

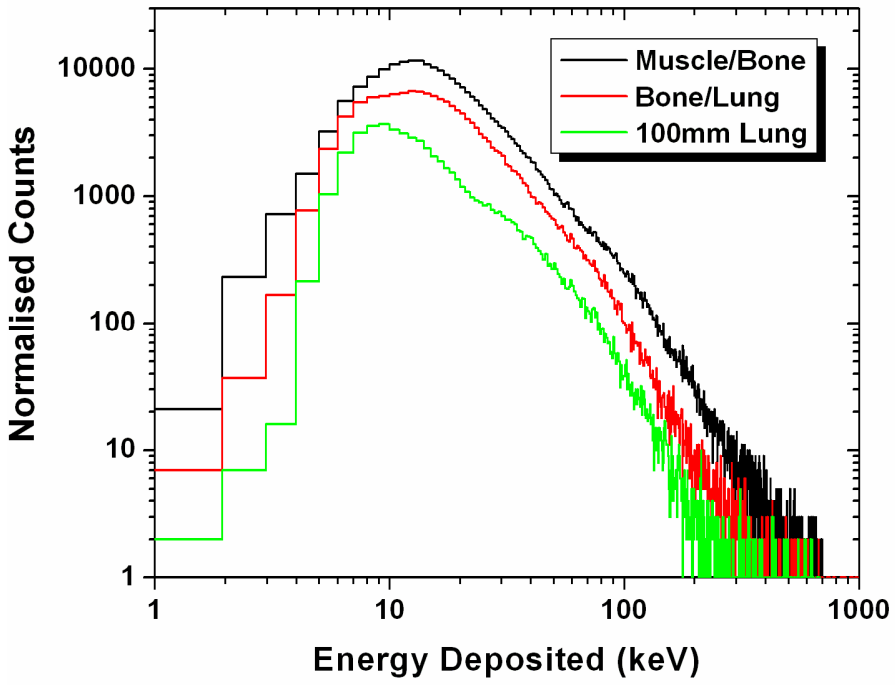

Figure 7-15: Simulated response of the SOI microdosimeter to solar protons within a layered TE phantom representing a human chest.

The microdosimetry properties of mean dose weighted lineal energy, dose equivalent and average quality factor for the radiation field have been determined for the three simulated measurement positions and are contained within Table 7-4. These results further support the conclusion that the more material interspaced between the device and the radiation field lowers the frequency of the total number of energy deposition events and also high energy deposition events. This was clearly indicated by the mean dose weighted lineal energy, average quality factor and dose equivalent decreasing with increasing depth in the TE phantom.

Thickness Al (mm)	$\bar{y}_d\,(keV/\mu m)$	**Dose Equivalent (mSv)**	**Average Quality Factor**
Muscle/Bone	4.92	2.49	1.37
Bone/Lung	3.90	1.02	1.09
100 mm Lung	3.63	0.36	1.02

Table 7-4: Mean dose weighted lineal energy, average quality factor and dose equivalent as determined from the simulated response of the SOI microdosimeter within a TE phantom representing a human chest.

Interestingly there is no increase in either of these parameters after the bone layer. This is most likely a direct result of the spectra of incident protons being of sufficiently low energy as to produce few nuclear interactions within this volume. This appears reasonable and in line with previous work which indicates that for high energy protons nuclear interactions can account for 10-20% of the protons energy loss [78]. The incident radiation field in this case was a spectra of protons with a maximum energy of 200 MeV and a great portion lower than 10 MeV, which must first traverse an Al shield of 5 mm before entering the phantom. It would be expected that protons reaching the TE phantom will not have a large cross section for nuclear interaction. Hence, no increase in measured spectra is obtained as a function of material. It would be interesting to repeat these measurements for heavy and more energetic hadrons experienced in a space environment to determine if the microdosimetric spectra changes within the astronaut further contributing to radiation risk assessments.

7.5 Solar Proton Simulation Conclusions

This GEANT4 study simulated the response of the SOI microdosimeter that has been produced by Fujitsu and developed at the Centre for Medical Radiation Physics, University of Wollongong. The device was irradiated by a spectra of solar protons that was sourced from the SPENVIS [86] website using the JPL model to a 95% confidence level for the International Space Station. The SOI microdosimeter was simulated to determine the effect of varying shield thickness, converter thickness and preceding tissue material on the microdosimetry spectra.

The simulation of solar protons has provided much needed information prior to the deployment of SOI microdosimeters into space on the MiDN project. Through simulating the response of the SOI microdosimeter to solar protons with different levels of shielding it has been possible to determine optimum levels of shielding to enhance astronaut protection and minimise SEU. In turn this has highlighted that such simulations and microdosimetry measurement parameters should be utilised in optimising shielding structures for future deployment. It was also possible to estimate the time of simulation and determine the effectiveness of the SOI microdosimeter in obtaining real time data, and in turn possibly provide an instrument for real time radiation protection applications.

Simulations of varying converter thickness allowed for the response of the SOI microdosimeter to solar protons to be evaluated both externally and behind spacecraft shielding. From this work it was clear that dual sensors should be utilised external to the spacecraft to provide an accurate assessment of both the solar proton radiation field and any neutron component that may be present. However, within the spacecraft, the addition of a converter produced minimal change in the measured radiation spectra. As such to minimise weight and power drain it is possible to have only one sensor located in-board which will provide an accurate assessment of the radiation field.

Finally simulations of a TE phantom provided information on the change in microdosimetric properties as solar protons traverse a human chest. It will be important to expand this work to other ions to determine changes in biological effect as a function

of position within the astronaut's structure, and if such changes can be countered through optimising shielding structures.

7.6 Heavy Ion Experimental Method

The SOI microdosimeter has been tested in neutron, proton, alpha and carbon radiation fields with excellent results [21, 25, 29, 30, 64-66]. However, as missions proceed further into space, interactions with heavier ions that comprise GCR (Figure 7-16) need to be considered and detection methods developed. Microdosimetry provides an adequate solution for measuring a wide range of particles and LET's, and in doing so can provide an assessment of the dose equivalent within a given radiation field. Solid-state devices such as SOI microdosimeters are ideal for space deployment however their response to heavy ion radiation fields is uncertain and needs to be benchmarked where possible against TEPC's, which are considered the standard microdosimetry measurement technique. Another issue which needs investigation is the radiation hardness of such detectors and the stability of performance in applied heavy ion radiation fields.

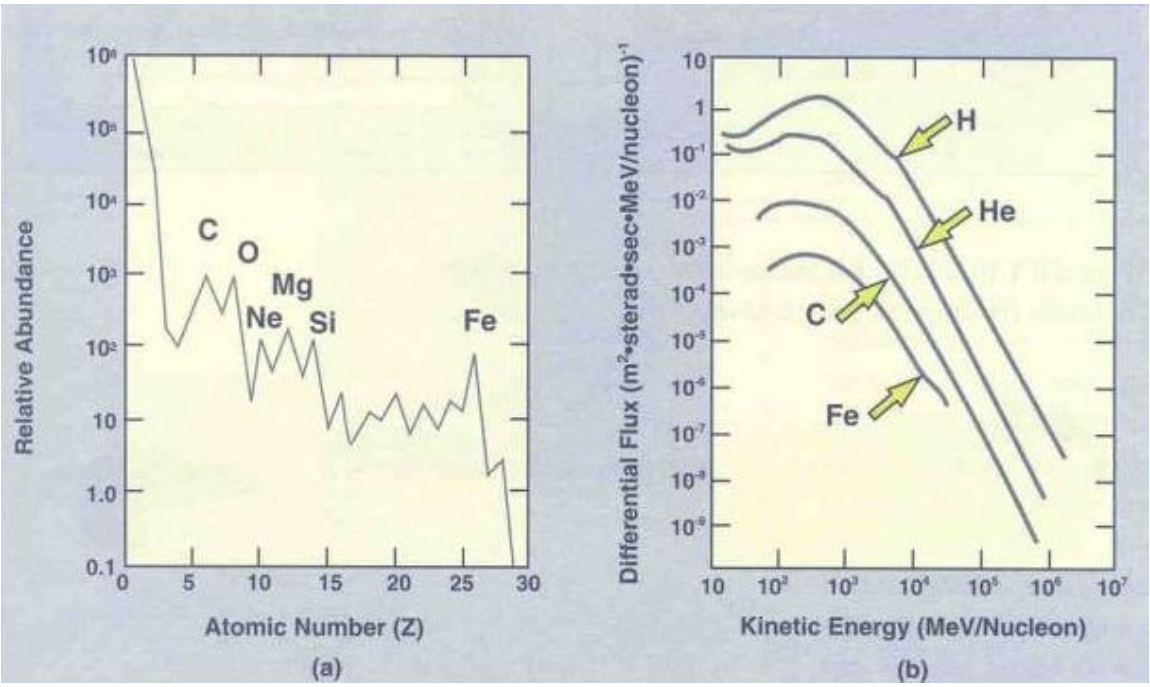

Figure 7-16: Abundances (a) and energy spectra (b) of GCR[88]. Note how the abundance of iron and carbon ions in GCR with peaks of abundance at approximately 0.6-1GeV/n.

The purpose of this work was to test the SOI microdosimeter under heavy ion radiation fields such as those experienced from GCR. Such radiation fields were provided at the NASA Space Radiation Laboratory (NSRL) at Brookhaven National Laboratory (BNL). The NSRL facility has been purpose built to study space radiation and its effects on biological and electronic systems. It utilises the existing Brookhaven MP-6 tandem accelerator and Booster synchrotron to accelerate the ions to the required energies [89]. This facility allows for a wide range of ions and energies to be accelerated providing a beam spill length of 300 ms, with a total spill duration of 3.8 s. The facility also allows for the production of uniform beam intensities of rectangular areas ranging in size from 1 to 20 cm. For this work the incident radiation field would consist of 0.6 GeV/n iron-56, 1 GeV/n titanium-48 and 1 GeV/n oxygen-16 ions all in a fully stripped state. The field size was approximately 3-4 cm in diameter at FWHM with a frequency of 1-5 kHz across field cross sectional area to avoid pile-up in the electronics.

A 5 μm thick SOI microdosimeter chip was chosen for this study. The array utilised comprises of 150 detector elements (30x5) with each cell having a physical size of 120x120 μm^2. The device was contained within a 0.9 mm thick probe holder of aluminium which would act as a Faraday cage. A 4 μm aluminium window was located immediately in front of the microdosimeter to allow the transport of secondary particles into the SV. To enable reproducible placement of the microdosimeter probe in the centre of the radiation field and at various points within the Perspex phantom, it was housed within a purpose built Perspex probe holder. This is the same system described in Section 3.5 and used in proton experiments (Section 5.2) and had no modifications prior to testing in heavy ion radiation fields. Alignment of the detector in relation to the incident beam was facilitated through the use of an adjustable table and alignment lasers as illustrated in Figure 7-17 and Figure 7-18. Measurements were completed along the central axis of the beam for varying depths in Perspex to sample along the Bragg peak of the heavy ion. Such measurements provided an assessment of the microdosimetry spectra of such ions as they traverse an astronaut. It also allows for the microdosimetry spectra for a range of ion energies to be determined given a single incident ion energy.

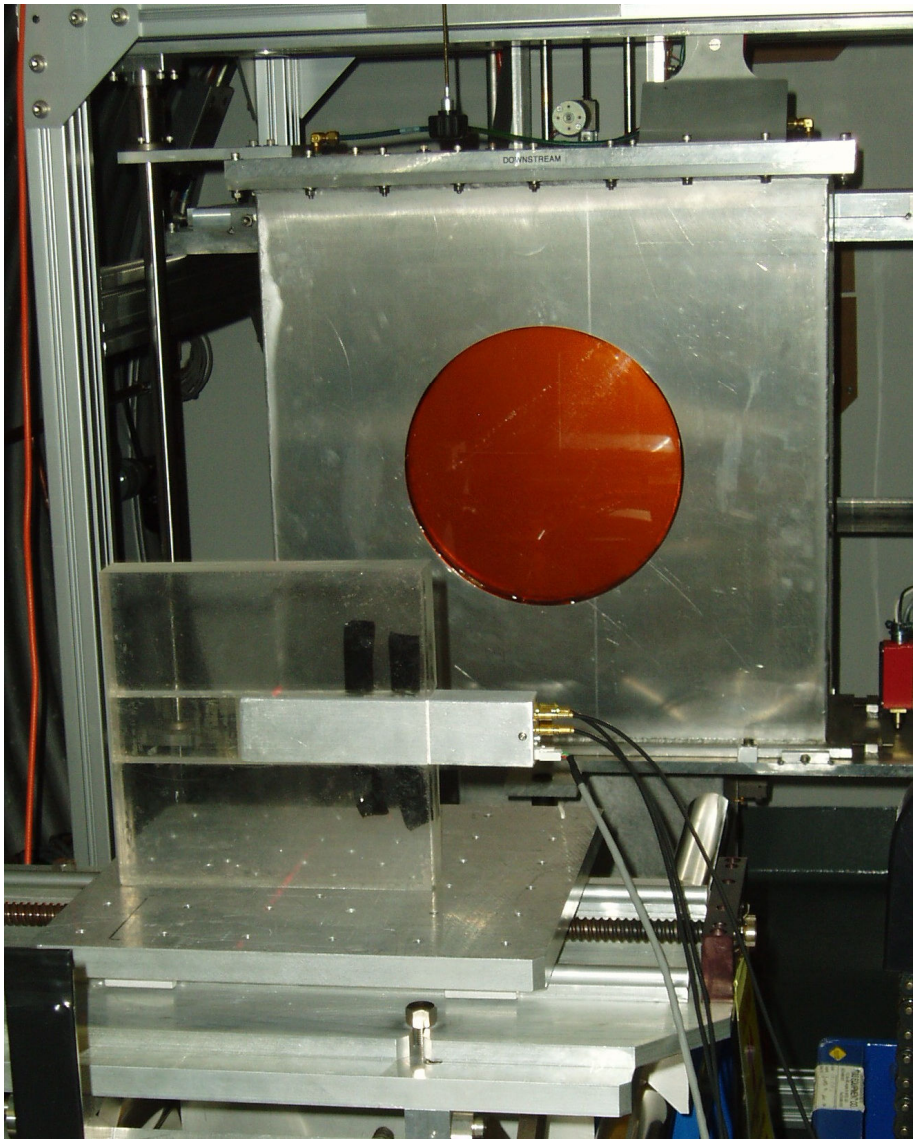

Figure 7-17: Picture of experimental setup for measurements of heavy ion spectra in free air. Note the beam exit window (orange) and the Perspex probe holder to ensure accurate placement of the SOI microdosimeter probe. Alignment to the beam exit window was made using alignment lasers and marks on the adjustable stage.

Located within the probe was the microdosimeter circuitry including an A-250 pre-amplifier, FET and buffer amplifier (x10), however, due to collimation of the beam these components received minimal radiation interaction. Bias to the SOI microdosimeter (10 V) and power to the A-250 (±6 V) was supplied via a purpose built battery supply which provided low noise. Data acquisition was completed using a Tennelec Model 244 main amplifier and an Amptek Pocket MCA (see Figure 3-9 for a picture of the experimental DAQ system). Regular noise level checks using a pulser were completed both pre, during

and post experiment. To minimise the effect of any secondaries following or preceding the beam the MCA was gated on a square logic pulse that surrounded the beam (i.e. 300 ms in length). Acquisitions were completed for 5-15 minutes and adjusted for adequate statistics.

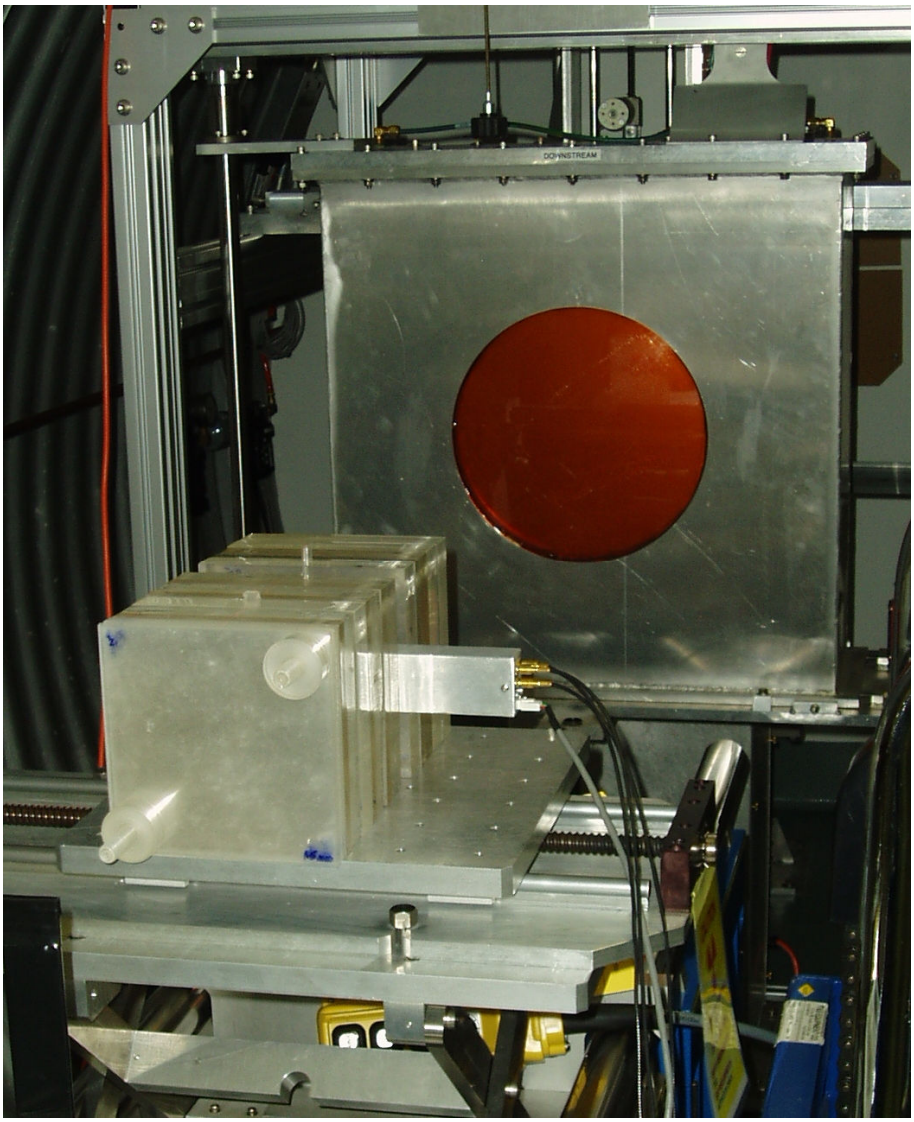

Figure 7-18: Picture of experimental setup for measurements of heavy ion spectra in a homogeneous Perspex phantom. Note the beam exit window (orange) and the layered homogeneous phantom structure to allow for measurement at any position along the Bragg peak. Alignment to the beam exit window was made using alignment lasers and marks on the adjustable stage.

Bragg curves in polyethylene were supplied by the staff at the NSRL facility and were completed using high density polyethylene (ρ=0.97 g/cm^3) foils and 2x32 cm diameter ion chambers (each consisting of 8 concentric rings at 2n cm radii where n is the ring

number). One chamber was situated upstream of the phantom (for normalisation) and the second situated downstream of a given thickness of phantom material. To obtain the Bragg Curve in Perspex the results were scaled according to phantom density (ρ=1.2g/cm^3). Such curves enabled accurate microdosimetry measurement positions to be determined and correlated with corresponding Bragg Peak position.

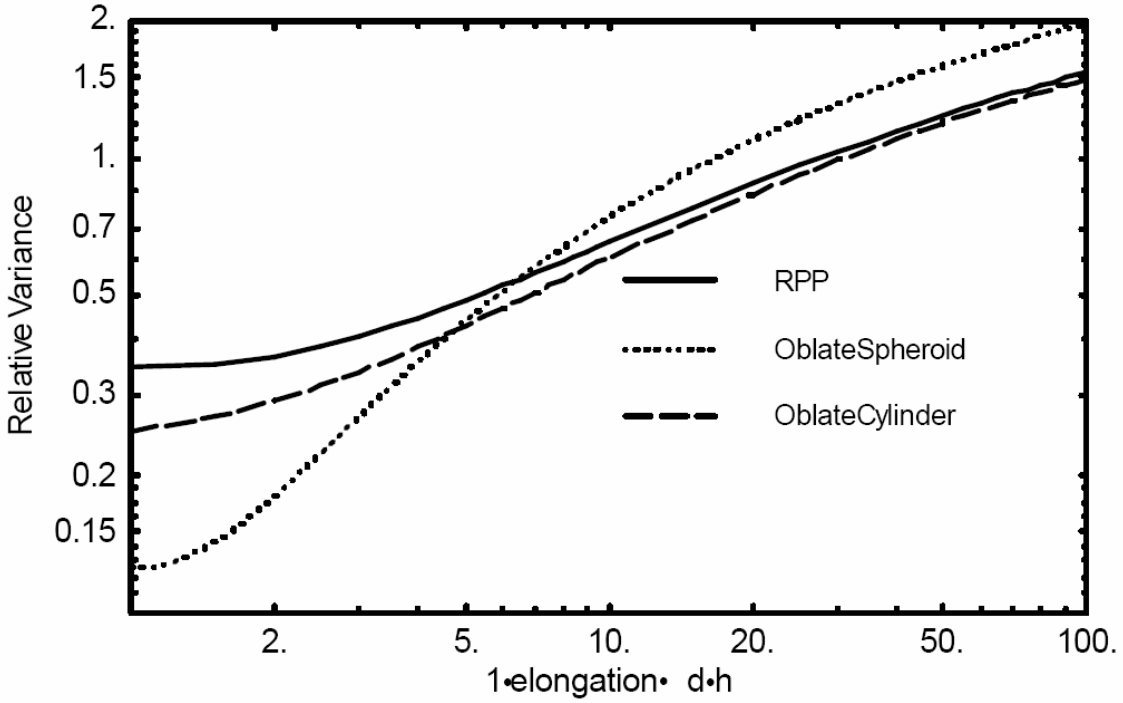

Figure 7-19: Relative variance of the chord length distribution as a function of elongation for oblate shapes [21].

Generation of microdosimetry spectra and mean dose weighted lineal energy was completed using the protocol outlined in [32, 33] and Section 2.5. In this study an array of 120x120x5 μm^3 SV elements was used and the choice of average chord length was important. In this instance because of the thin planar structure of the SV and the fact that the primary beam is predominantly normal to the detector, using the relationship stated in Equation 2-1 will greatly overestimate the average chord length. As all particles are predominantly normal to the surface of the phantom and will undergo minimal scattering due to their large size, the average chord length was set as the thickness of the SV or 5 μm. It is important to remember that by increasing the cross-sectional area of the SV from a cubic to planar structure there is a corresponding increase in the variance of the

average chord length (Figure 7-19). Scattered primary particles and associated secondaries have the potential to increase in chord length for a planar structure. For a cubic structure there is a variance of 0.345. In this case, the relative variance of the mean chord length increases by a factor of approximately 2 as there is a factor of 24 difference between the side length and thickness in the experimental SV. This increase will be largely offset and negated by a CCE of 0.8 which was determined in [26] for a range of ions and LET values from 20-820 keV/μm. As such the average chord length in tissue was 7.936 μm assuming a TE conversion factor of 0.63 which has been established through previous studies in other radiation fields [21, 25] and considered the CCE and the increased variance of the average chord length in a planar structure. This was compared with existing TEPC data to determine the validity of this assumption.

7.7 Heavy Ion Experimental Results

The results obtained using a 5 μm SOI microdosimeter at the NSRL irradiation facility are presented in the following sections.

7.7.1 Iron - 0.6 GeV/n

The iron beam was the first to undergo experimental measurements at the NSRL facility. Measurements were completed at the surface of the phantom and at varying depths along the Bragg peak to give an indication of changes in the microdosimetry spectra. In this instance four measurement positions were completed with the position along the Bragg peak illustrated in Figure 7-20. It should also be noted that from the depth dose measurement the actual energy of the Fe beam could be determined, as some energy is lost through interactions with beam modifying and monitoring devices. In this case the energy was determined to be 585.1 MeV/n.

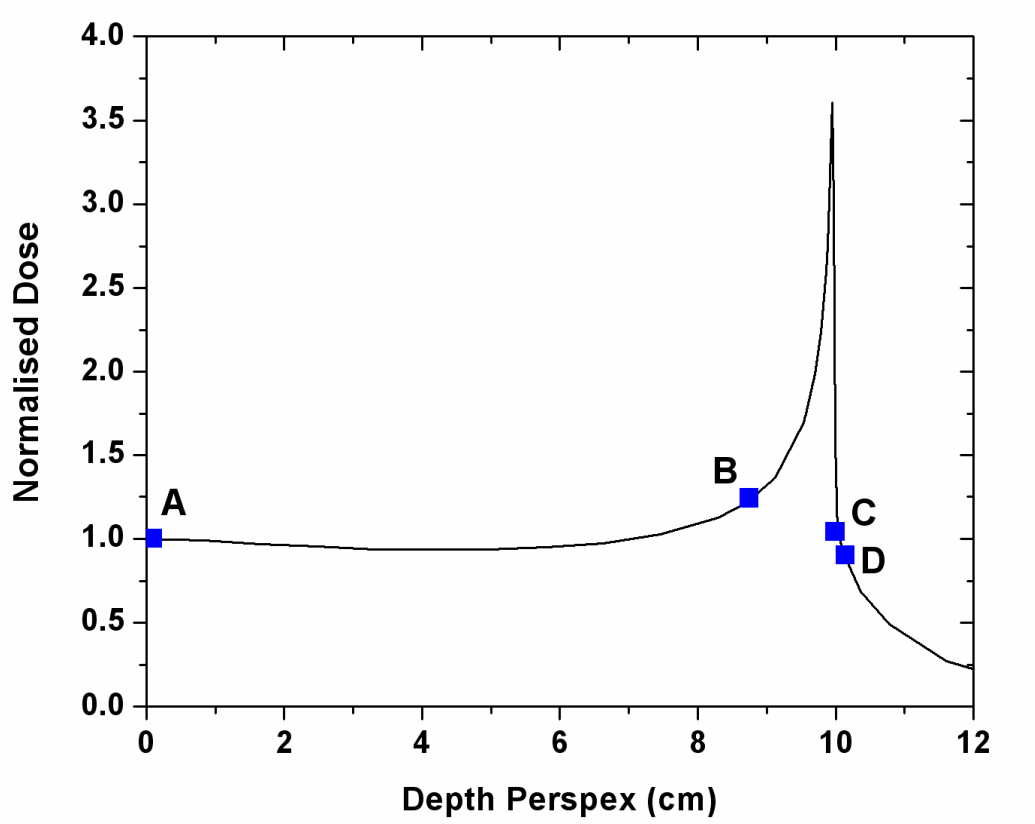

Figure 7-20: Measurement positions of the SOI microdosimeter along the 0.6GeV/n Fe Bragg Peak. Note that position A corresponds to a surface measurement, while positions B, C and D correspond to depths of 8.75, 10 and 10.15 cm respectively in Perspex.

Figure 7-21 illustrates the results obtained with a 5 μm SOI microdosimeter at varying depths in Perspex. It clearly displays how the iron peak moves to higher energies with increasing depth in Perspex from a mean peak energy of 1.75 MeV to almost 5.3 MeV on the distal edge of the Bragg peak. At the surface of the phantom some interaction is observed below 800 keV and this is most likely caused by lighter ions which are present in the radiation field produced through primary beam interactions with beam modifying and monitoring devices, and also through interaction of the Fe ions within the silicon SV. The presence of interactions below the Fe peak increases at depth due to the production of secondary particles through primary beam interaction with the phantom. Figure 7-21 also highlights a low energy peak which was continually detected at approximately one third the energy of the Fe-56 peak. The origins of this peak were investigated in collaboration with our team at ANSTO and the source explained in Section 7.8. It is important to note however that while this feature is visible on the

energy deposition spectra, it has a negligible effect on the microdosimetry spectra and the mean dose weighted lineal energy Figure 7-23.

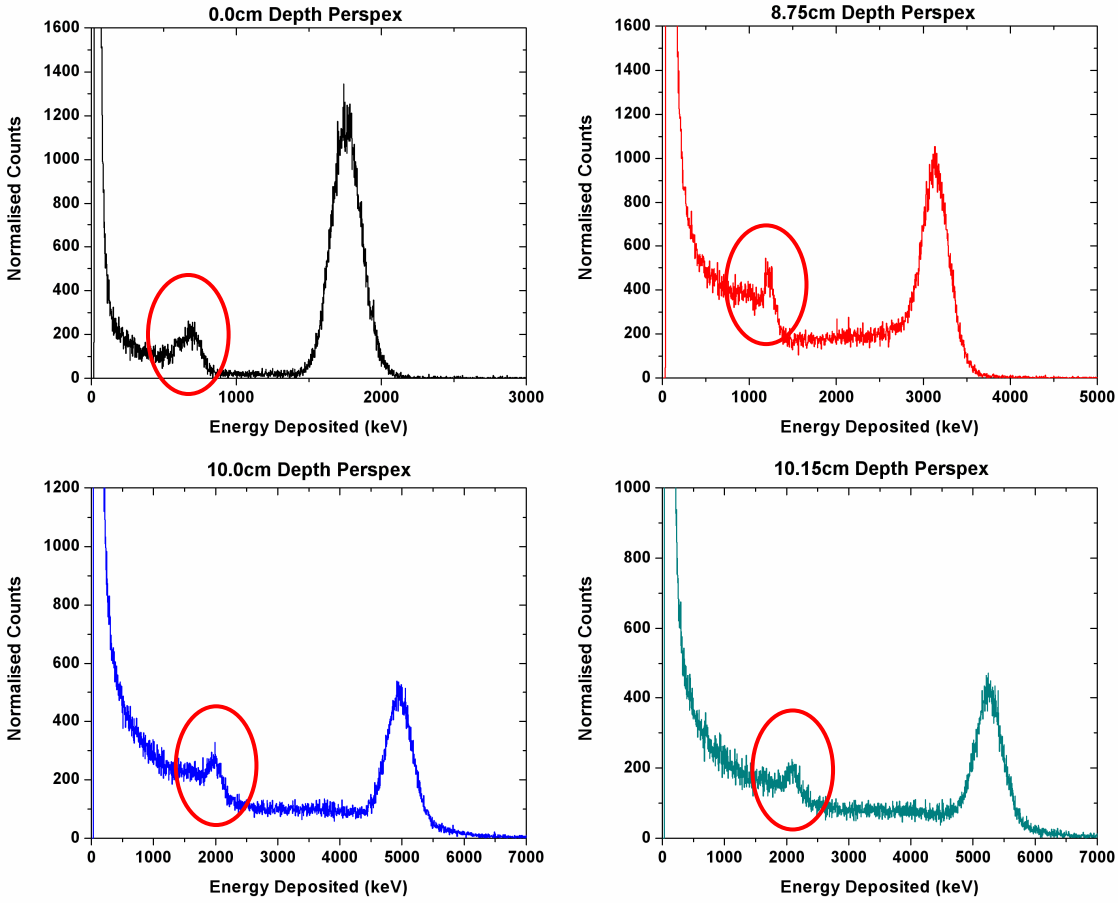

Figure 7-21: SOI microdosimeter results for the four measurement positions in the Perspex phantom when irradiated with 0.6 GeV/n Fe. Note the shift in the Fe peak to higher energies with increasing depth in Perspex. A low energy peak is highlighted in this series and is investigated in Section 7.8. Graphs are normalised to 100 s live time.

The change in spectra as a function of depth in Perspex can be more clearly seen in Figure 7-22. In this case all simulations were normalised to a 100 second live time or a total collection time of 5.5 minutes. It is also possible to see the effect of scattering on the measurement, which is evidenced by widening of the Fe peak FWHM with increasing depth in Perspex from straggling of the primary particle. Increased signal below the main Fe peak with increasing depth in Perspex also suggests the presence of fragments and secondaries produced through nuclear interactions. In Figure 7-22 a measurement position past the distal edge of the Bragg peak (11.5 cm depth in Perspex) is also

included. This measurement position, illustrates the production of neutrons and other nuclear fragments both within the beam modifying/monitoring devices and also within the phantom itself that travel to greater depths within the phantom than the primary beam. The same energy spectra measured at 11.5 cm depth in Perspex is also present within the background of all other measurement points (except those at the surface of the phantom) suggesting that this was caused by neutrons produced from primary beam interactions within the phantom.

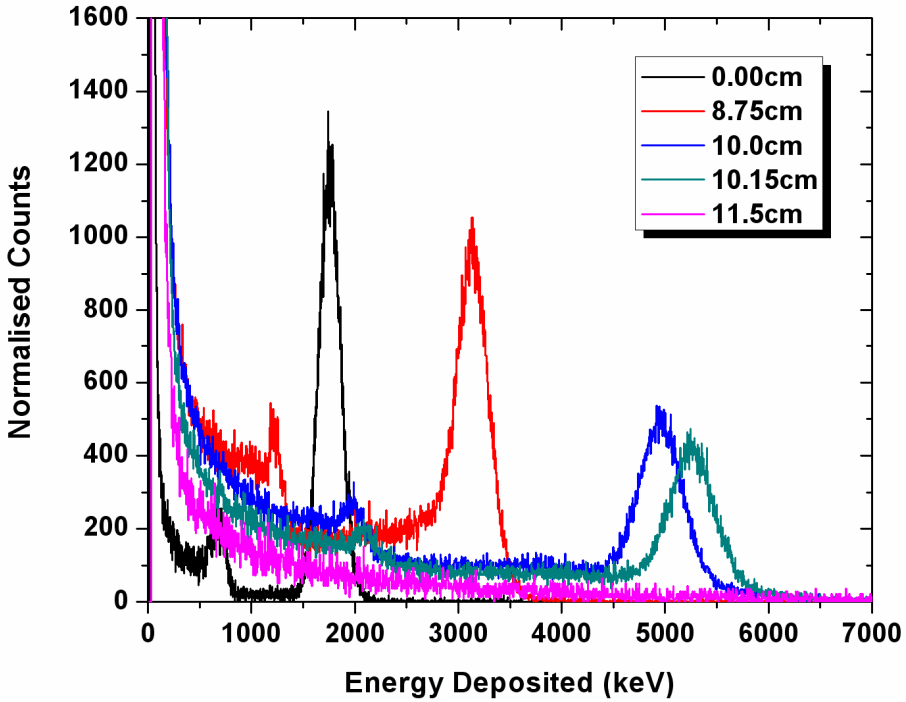

Figure 7-22: SOI microdosimeter results for the five measurement positions in the Perspex phantom when irradiated with 0.6 GeV/n Fe. Note the shift in the Fe peak to higher energies with increasing depth in Perspex which is clearly evident on a single graph. Spectra normalised to 100 s live time.

Converting the energy deposition spectra into a distribution of lineal energies (Figure 7-23) provides further information on the radiation field. These results provide a good indication on the change in lineal energy of a 0.6 GeV/n Fe beam with increasing depth in Perspex and can be overlaid with the Bragg Curve to illustrate this change in relation to the Bragg Peak (Figure 7-24). The measured lineal energy increases markedly near the Bragg Peak achieving maximum values at the distal edge. Such increases could indicate increased biological effect and single event upset (SEU) rate as the ionisation density increases.

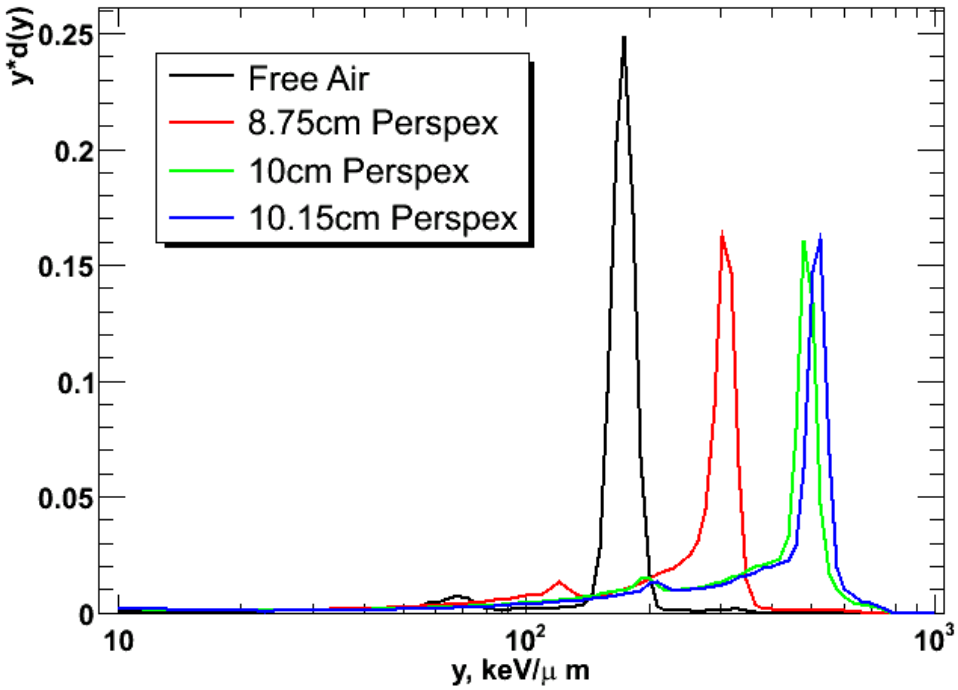

Figure 7-23: Dose weighted lineal energy spectra for different measurement positions in Perspex of 0.6GeV/n Fe. Spectra normalised to unity.

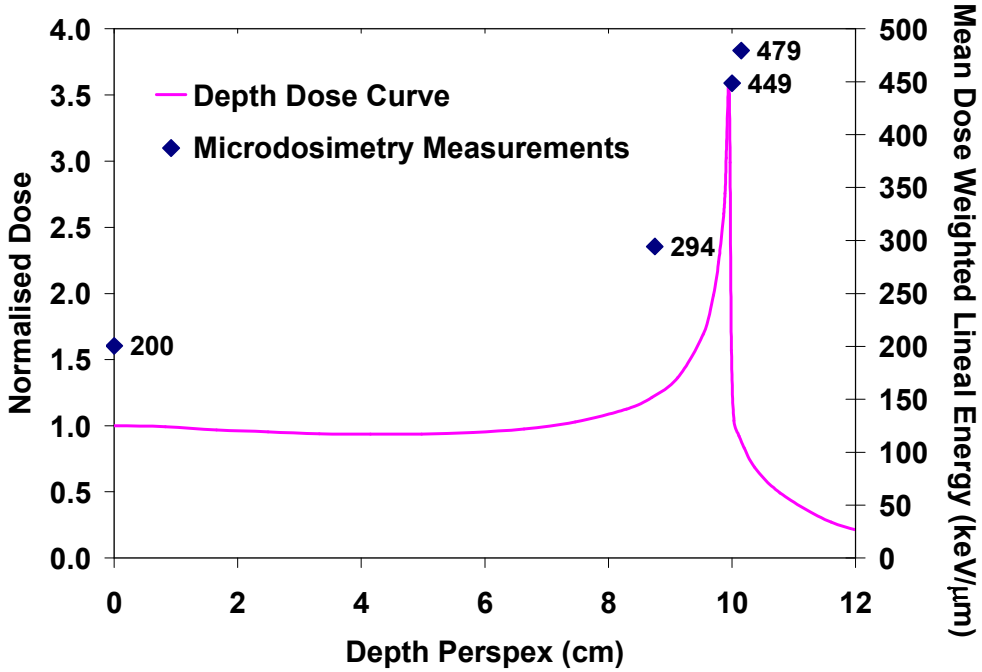

Figure 7-24: Measured depth dose distribution for 0.6GeV/n Fe in Perspex overlaid with measured dose weighted lineal energy values using the SOI microdosimeter.

What is especially encouraging about this work is that at the surface of the phantom the SOI microdosimeter measured a mean dose weighted lineal energy of 200 keV/μm for 0.585 GeV/n Fe using a TE correction factor of 0.63. This compares excellently with a TEPC measured value of 180 keV/μm for 0.535 GeV/n Fe [83]. Considering that these were world first measurements with SOI microdosimetry technology in heavy ion fields of this energy, to be within 10-12% of existing data supports the further use and testing of such a system for deep space deployment. The difference in this case is attributed to a number of factors concerning both the SOI microdosimeter measurement apparatus and the incident beam. Firstly the TEPC measurements were completed at the Bevalac Accelerator of the Lawrence Berkeley Laboratory CA, while SOI microdosimetry measurements were completed at the NSRL facility located at Brookhaven National Laboratory, NY. Different accelerator facilities utilize different ion sources, and have in place different beam monitoring/modifying devices which can contribute to a different spectrum of secondary particles. The spectra of secondary particles in such heavy ion experiments can be significant (as evidenced in Figure 7-25 and [90]) and can influence microdosimetry measurements. In the case of the SOI microdosimetry measurements, while Fe-56 was clearly the most abundant ion species, the beam contained up to 30% lighter ions which may have an impact on the measured lineal energy.

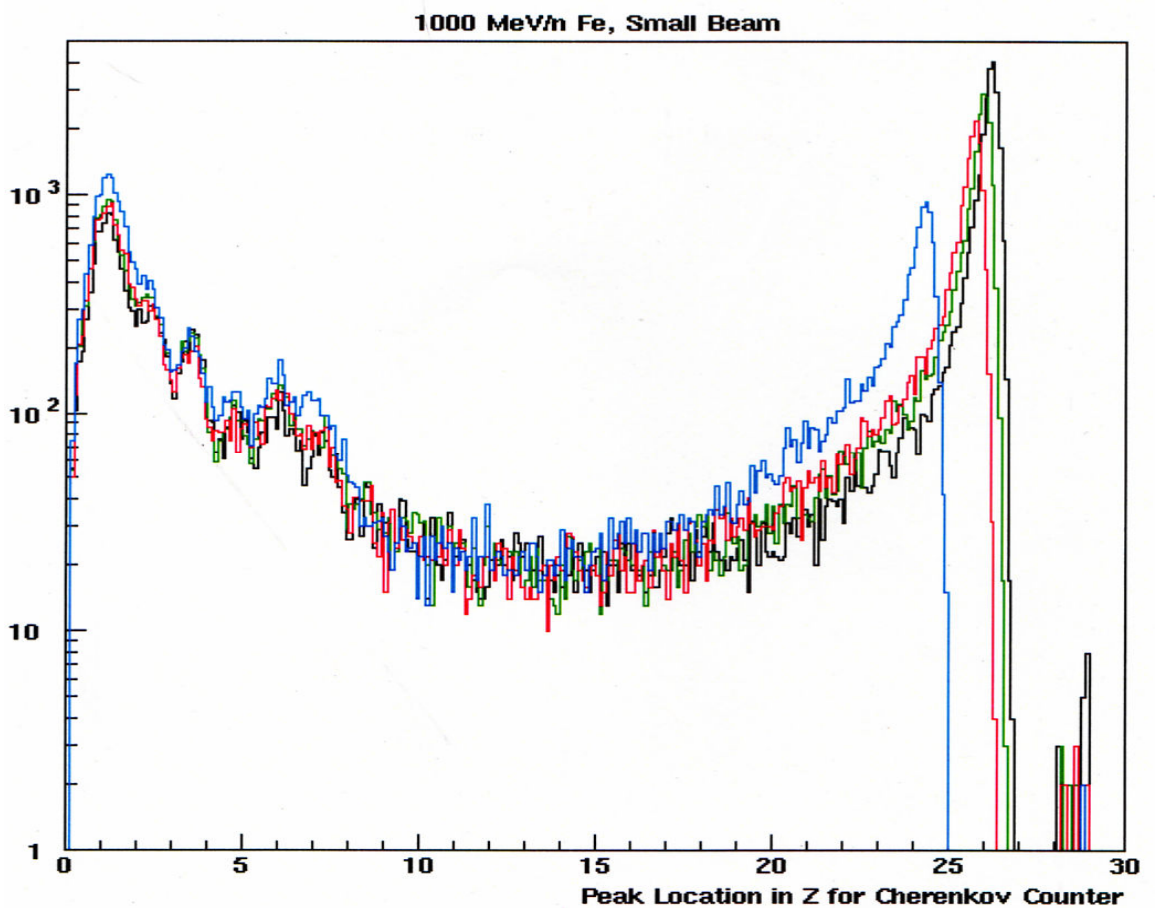

Figure 7-25: Measured spectra of incident 1 GeV/n Fe-56 at the NSRL facility using a Cherenkov Counter. Note the location and amplitude of the Fe-56 peak (located at 28 on the x-axis) and also the relative abundance of secondary particles present at the point of measurement. Provided and measured by Mike Sivertz.

In completing solid-state microdosimetry measurements in a heavy ion field certain assumptions needed to be made as these were world first measurements with SOI technology. These assumptions need to be considered when assessing differences to existing heavy ion data obtained using different measurement techniques (in this case a TEPC). The first assumption made was the average chord length. In this instance a relatively large planar microdosimeter was utilised that had a cross sectional area of 120x120 μm^2 with a SV thickness of 5 μm. While the variance of chord lengths with the planar structure was considered, variation in this response may be encountered at increasing depth in the phantom and with differing levels of primary fragmentation and variation in the secondary particle spectra. To determine the effect of this assumption, GEANT4 Monte Carlo simulations should be completed to assess the mean chord length

in such a field. Further, in the case of space deployment a more cubic structure would be more suitable, as in an omnidirectional field it will produce a more uniform response and be less dependant SV geometry.

The second assumption and possibly the main source of error in these measurements arise from the TE conversion factor. It has been shown in previous work with protons and alpha particles that the value of 0.63 gives good agreement to TEPC devices, however this has yet to be tested using heavy ions such as Fe-56. With agreement to established data being within 12% (which is in-line with previous estimations that the thickness of the SOI has a variation of ±10%) it can be assumed that this has been a fair assumption, and can be further proved through the use of Monte Carlo simulations. It should be noted however, that improvements to GEANT4 are currently underway to enable the simulation of high energy heavy ions and this should be considered when evaluating simulated data.

7.7.2 Oxygen - 1.0 GeV/n

1 GeV/n oxygen was the lightest ion to be tested at the NSRL facility. Measurements were completed at the surface of the phantom and at varying depths along the Bragg peak to give an indication of changes in the microdosimetry spectra. However, because of the large range of 1 GeV/n oxygen in Perspex (701.1 mm as calculated by SRIM [91]) depth dose curves were unable to be obtained. In this instance the measurement positions were determined from the SRIM range of 1 GeV/n oxygen in Perspex to be at the surface of the phantom and then at depths of 30, 53, 68 and 73 cm. Such a range of measurement positions provided a change in microdosimetry spectra along the Bragg curve, as localisation of measurement positions at the level of the Bragg peak were unobtainable due to the inability to generate a depth dose curve with the NSRL dosimetry system.

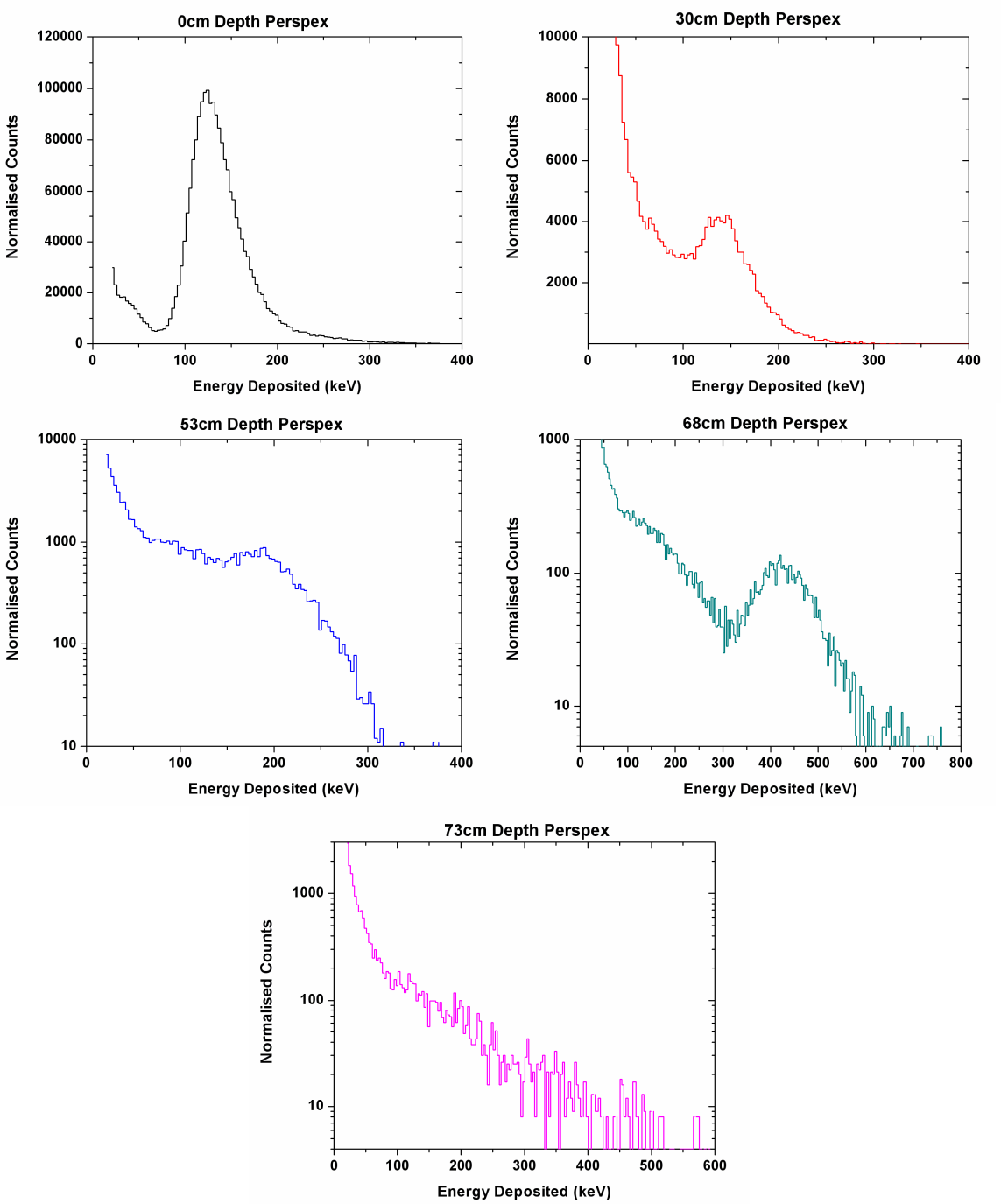

Figure 7-26: SOI microdosimeter results for the five measurement positions in the Perspex phantom when irradiated with 1.0 GeV/n oxygen. Note the shift in position and shape of the oxygen peak with increasing depth in Perspex. Also note the use of a linear y-axis for the first two measurement positions and the use of a logarithmic y-axis for the final three measurements to provide better peak definition. All spectra normalised to 100s live time.

Figure 7-26 illustrates the results obtained with a 5 μm SOI microdosimeter at varying depths in Perspex. Again all graphs have been normalised to a live collection time of 100 seconds to allow for accurate comparison between measurement points.

These figures clearly display how the main oxygen peak changes not only in energy but also in shape as a function of depth in Perspex. At the surface of the phantom the peak is sharp and clear denoting the near monoenergetic nature of the oxygen ions. Some interaction is observed below 50 keV and this is most likely caused by lighter ions which are present in the radiation field (produced through primary beam interactions with beam modifying and monitoring devices), and also through interaction of the oxygen ions within the silicon SV.

The presence of interactions below the main peak increases at depth for the first two measurement positions within the phantom (30 and 53 cm) due to the production of secondary particles through primary beam interaction with the phantom. However, events related to secondary particles below the main peak actually decrease at a depth of 68 cm in Perspex, with the oxygen peak becoming more defined. This is because the main peak moves to higher energies allowing for greater distinction between the main peak and energy depositions from secondary particles produced within the phantom. Further, with decreasing primary particle energy the cross section for generation of the secondary charged particles also decreases. This decrease in nuclear reaction cross section results in a decrease in the secondary particle fluence measured as energy deposition events below the main peak. A more detailed analysis of this is possible through GEANT4 simulations. However, care must be taken to ensure adequate simulation of nuclear cross sections for incident particles of this size and kinetic energy.

At 73 cm depth in Perspex, the measurement position is past the Bragg peak, however, this measurement provides information on the presence of secondary particles such as lighter ions and neutrons. Such particles can be produced both within the beam modifying/monitoring devices and the phantom itself, and have the potential to proceed to greater depths within Perspex than 1 GeV/n oxygen. It is important to note that this spectra is present as background in all measurement positions within Perspex and appears to increase in fluence with increasing depth in Perspex. This indicates that the secondary particle spectra is a result of secondaries (especially neutrons) produced within the phantom structure rather than upstream devices.

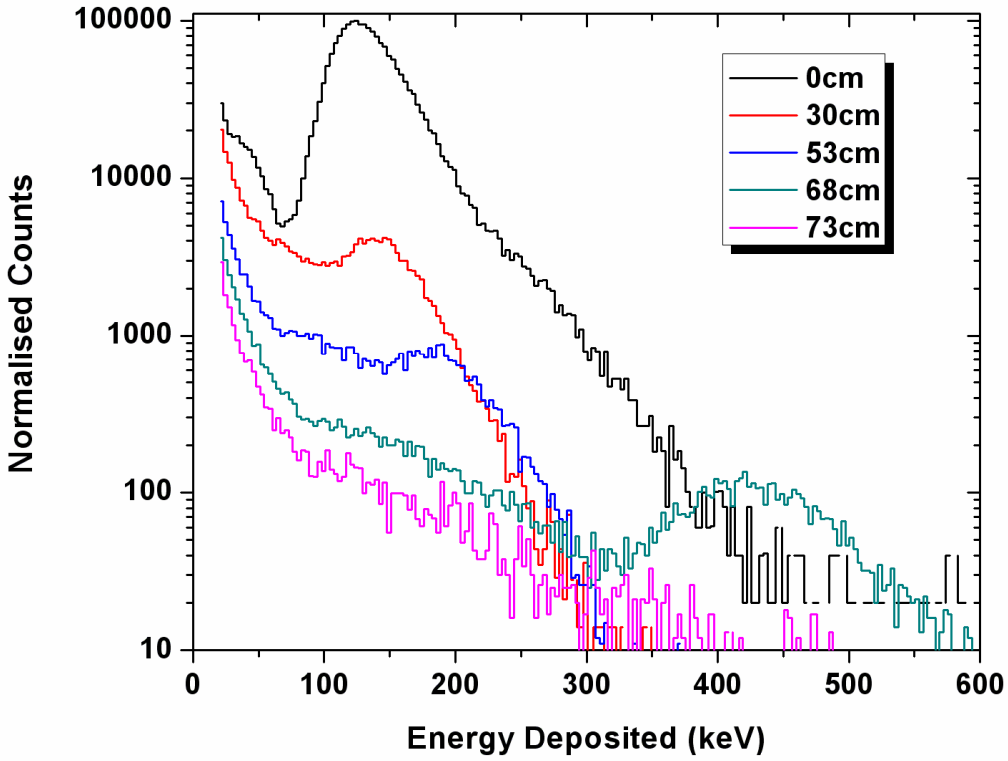

Figure 7-27: SOI microdosimeter results for the five measurement positions in the Perspex phantom when irradiated with 1.0 GeV/n oxygen. Note the shift in the oxygen peak to higher energies and its change in shape with increasing depth in Perspex which is clearly evident on a single graph. Spectra normalised to 100 s live time.

The change in spectra as a function of depth in Perspex can be more clearly seen in Figure 7-27. It is also possible to see the effect of scattering on the measurement of lighter ions. Not only does the mean peak energy move to higher energies with increasing depth in Perspex (as the particle slows and ionisation density increases), but the shape alters dramatically with significant broadening of the peak. Peak broadening from primary oxygen particle straggling is much more apparent than in the heavier ions, and is especially apparent at 30 and 53 cm depths in Perspex with the oxygen peak being almost obscured by the spectra of secondary particles below the main peak. At the surface of the phantom, the main energy peak appears to have a high energy tail associated with it that was not observed for measured data at depth within Perspex. This can be attributed to high LET low range secondaries produced within the beam modifying/monitoring devices upstream and that do not penetrate to depth within the

phantom. To support this conclusion, further work should be completed in obtaining Cherenkov detector data on the oxygen beam at NSRL.

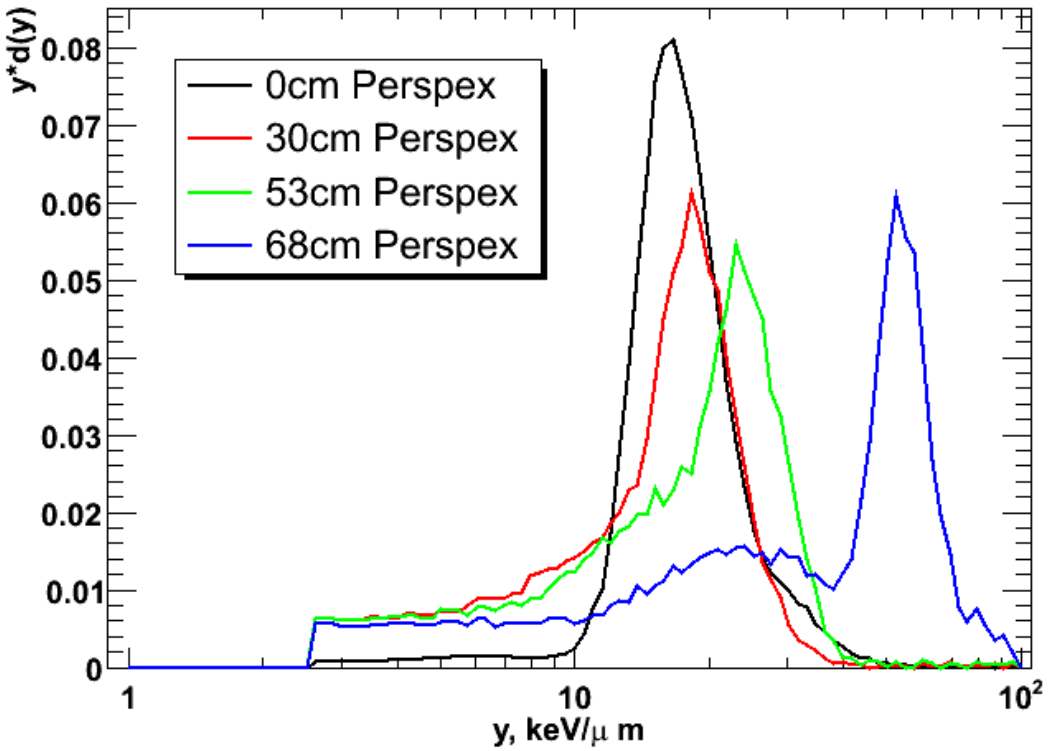

Figure 7-28: Dose weighted lineal energy spectra for different measurement positions in Perspex for 1GeV/n oxygen. Spectra normalised to unity.

The distribution of lineal energies for the measurement positions within Perspex are illustrated in Figure 7-28. These results provide a good indication of the change in lineal energy of a 1GeV/n O beam with the progression of the lineal energy peak to higher values with increasing depth in Perspex. The measured lineal energy increases markedly near the Bragg Peak (assuming a range of 701.1 mm as provided by SRIM) however the increase is not as dramatic as with heavier ions such as Fe and Ti.

7.7.3 Titanium - 1.0 GeV/n

The titanium beam was the last to undergo experimental measurements at the NSRL facility and was the most extensively tested due to advancements in the experimental protocol. Effort was made to complete measurements at the surface of the phantom and at varying depths along the Bragg peak to give an indication of changes in the

microdosimetry spectra. In this instance seven measurement positions were completed with the position of each along the Bragg peak illustrated in Figure 7-29. It should also be noted that from the depth dose measurement the actual energy of the Ti beam could be determined, as some energy is lost through interactions with beam modifying and monitoring devices. In this case the energy was determined to be 977.8 MeV/n.

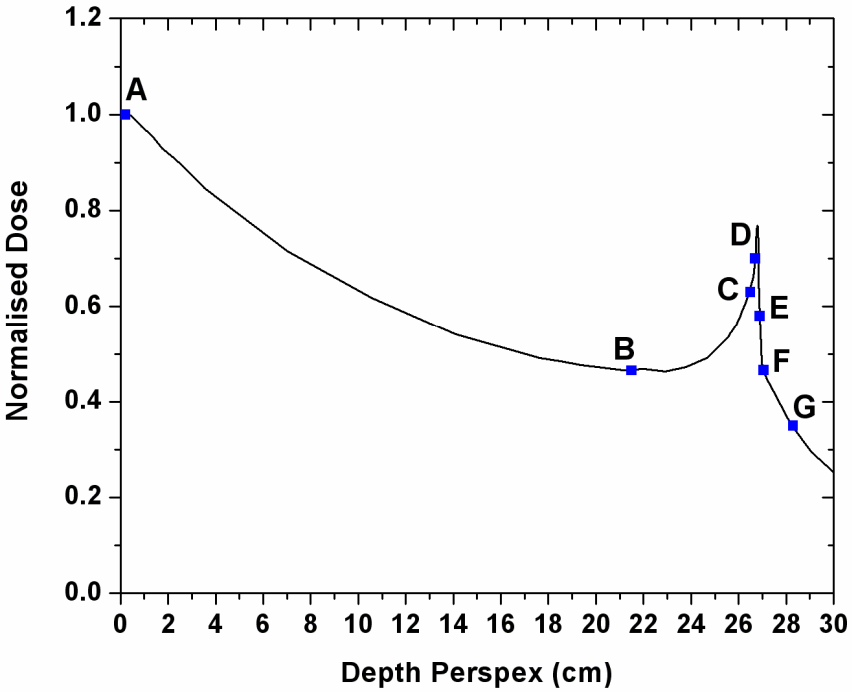

Figure 7-29: Measurement positions of the SOI microdosimeter along the 1GeV/n Ti Bragg Peak. Note that position A corresponds to a surface measurement, while positions B, C, D, E, F, and G correspond to depths of 21.5, 26.5, 26.7, 26.9, 27.05 and 28.3 cm respectively in Perspex.

Figure 7-30 illustrates the results obtained with a 5 μm SOI microdosimeter at varying depths in Perspex. It clearly displays how the titanium peak moves to higher energies with increasing depth in Perspex from a mean energy of 1.03 MeV to approximately 5 MeV on the distal edge of the Bragg peak. At the surface of the phantom some interaction is observed below 500 keV and this is most likely caused by lighter ions which are present in the radiation field (produced through primary beam interactions with beam modifying and monitoring devices), and also through interaction of the Ti ions within the silicon SV. The presence of interactions below the Ti peak increases at depth due to the production of secondary particles through primary beam interaction with the phantom. The surface measurement in Figure 7-30 also highlights a

low energy peak which is observed at approximately one third the energy of the titanium peak and was also noted during 0.6 GeV/n Fe experiments. The origins of this peak was investigated in collaboration with our team at ANSTO and the source is explained in Section 7.8

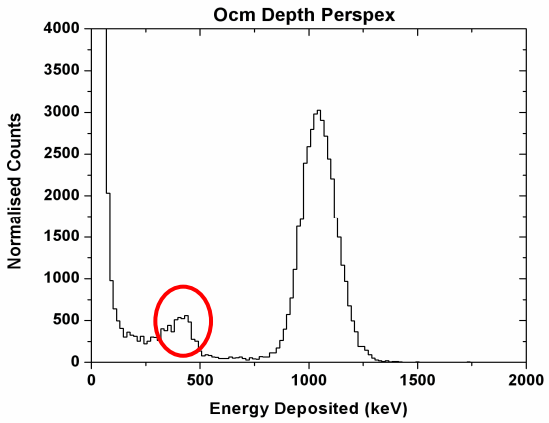

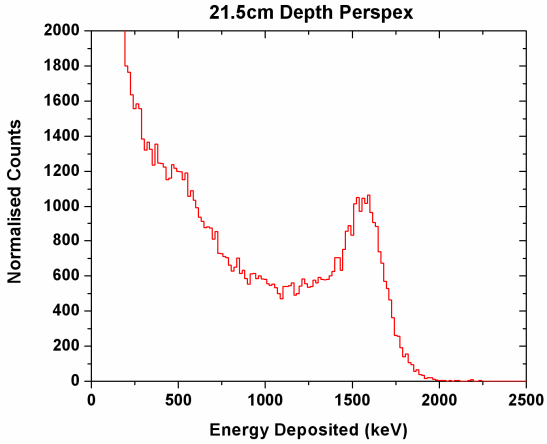

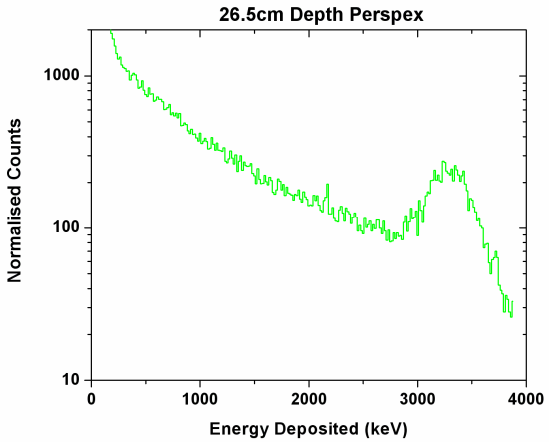

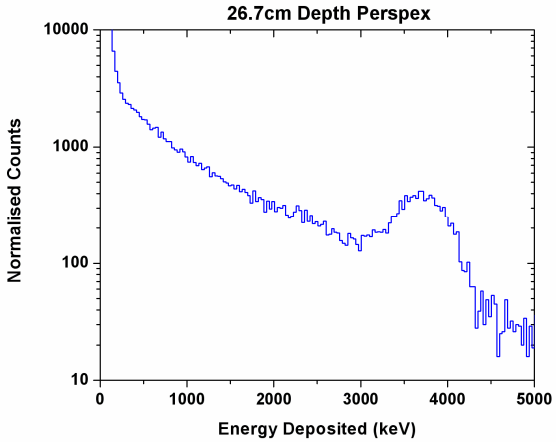

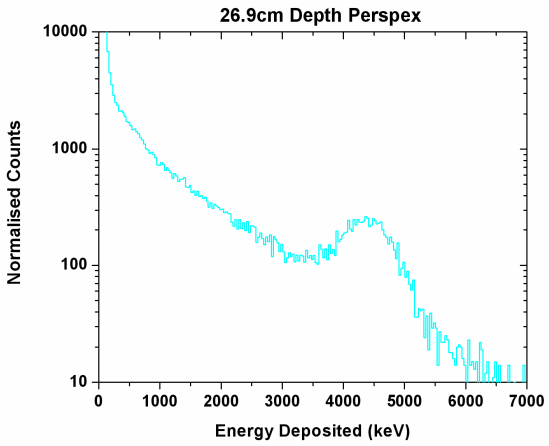

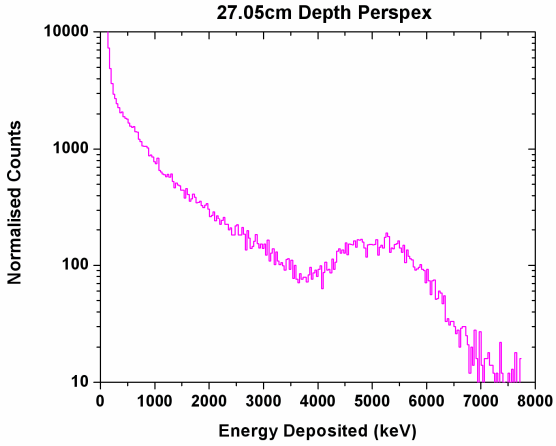

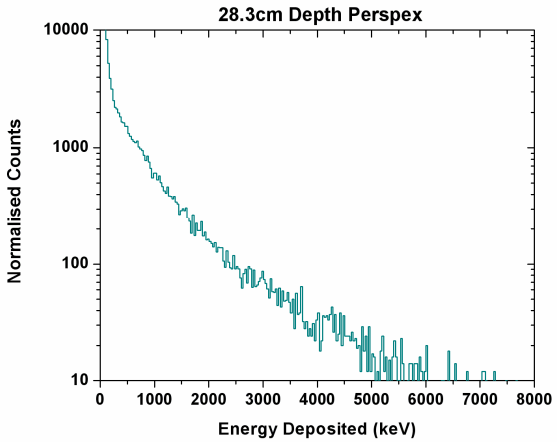

Figure 7-30: SOI microdosimeter results for the seven measurement positions in the Perspex phantom when irradiated with 1.0GeV/n Ti. Note the shift in the Ti peak to higher energies with increasing depth in Perspex. The low energy peak is circled in the surface measurement and was addressed in Section 7.8. Data normalised to 100s live time.

In this case all simulations were normalised to a 100 second live time as in previous experiments. At depth within the phantom even a large particle such as titanium undergoes some fragmentation and scattering. This is evidenced by the increase in signal below the peak (from fragmentation), and also in the widening of the Ti peak FWHM (from scattering). In Figure 7-30 a measurement position past the distal edge of the Bragg peak (28.3 cm depth in Perspex) was also completed. This measurement position, illustrates the production of neutrons and possibly other nuclear fragments both within the beam modifying/monitoring devices and phantom. This feature was observed in the background of all measurement positions within Perspex (i.e. not observed for the surface measurement), further supporting the theory that this was the result of an induced neutron field within the phantom.

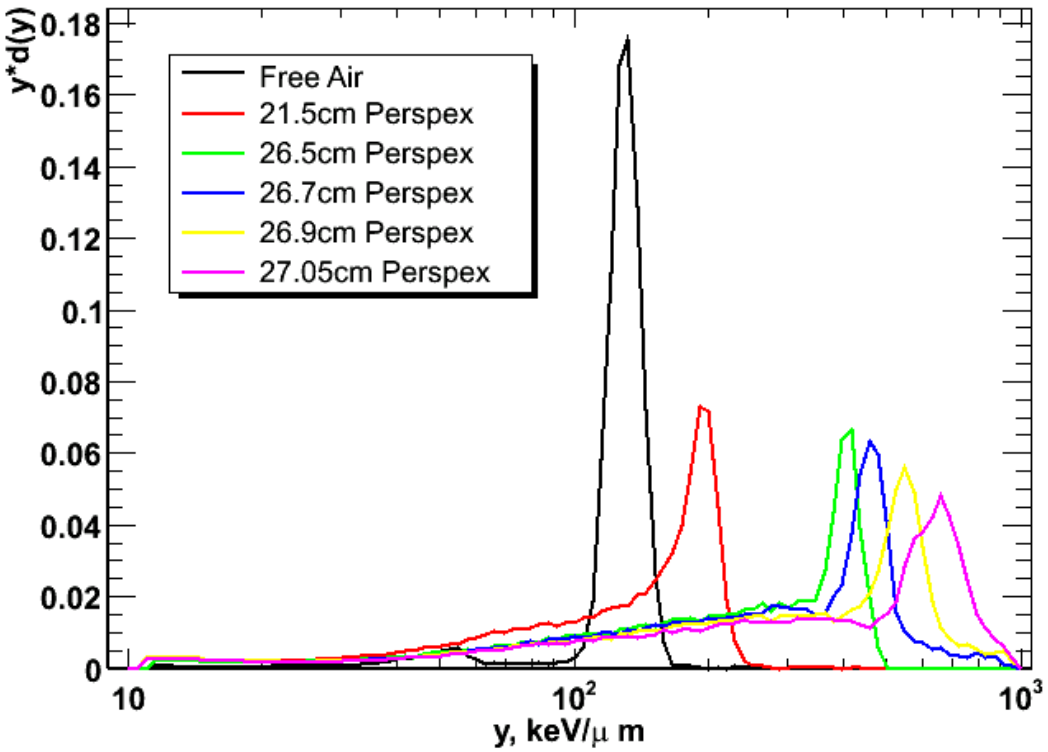

Figure 7-31: Dose weighted lineal energy spectra for different measurement positions in Perspex of 1GeV/n titanium. Spectra normalised to unity.

Converting the energy deposition spectra in to a distribution of lineal energies is illustrated in Figure 7-31 These results provide a good indication of the change in lineal energy of a 1.0 GeV/n Ti beam with depth in Perspex and can be overlaid with the Bragg curve to show this change in relation to the Bragg peak (Figure 7-32). The measured lineal energy increases markedly near the Bragg peak achieving maximum values at the distal edge. Such increases could indicate increased biological effect and single event upset (SEU) rate as the ionisation density increases in this region.

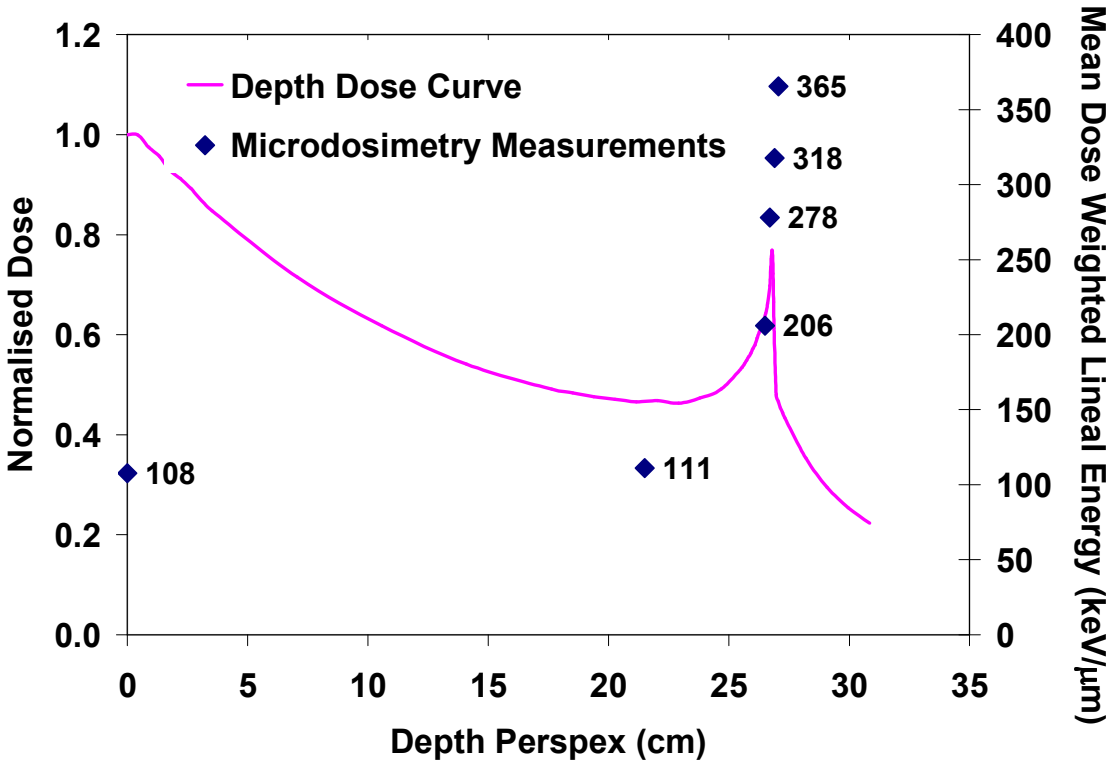

Figure 7-32: Measured depth dose distribution for 1GeV/n Ti overlaid with measured dose weighted lineal energy values using the SOI microdosimeter.

7.8 Low Energy Peak Analysis

SOI microdosimetry results obtained with heavy ions (Fe and Ti), showed the presence of a low energy peak at approximately one third the energy of the main peak. As the position of this peak was approximately reproducible for both Fe-56 (Figure 7-21) and Ti-48 (Figure 7-30) irradiations, and was also observed for alpha particle irradiation during device testing (Figure 3-6) it could be a feature of charge collection within the device. To determine if this was the case, Ion Beam Induced Charge Collection (IBICC) studies were conducted and analysed by our collaborators Dr Mark Reinhard at the Australian Nuclear Science and Technology Organisation, and Dr Iwan Cornelius from the University of Wollongong (Dr Cornelius had completed the original IBICC work on the SOI microdosimeters).

Ion Beam Induced Charge Collection (IBICC) utilizes monoenergetic ions that are focused onto a sample via X-Y raster scanning that is achieved using magnetic fields. The signal induced by each ion within a sample is collected using a charge sensitive pre-

amplifier system and provides information on the charge collected at a given time point. At the time of charge collection the magnet settings are recorded, providing information on the position of interaction. When combined in coincidence it is possible to obtain spatially resolved charge collection maps of the sample, which is useful in determining the charge collection properties of pixelated semiconductor radiation devices such as the SOI microdosimeter. This information can be provided in a number of forms both in one and two dimensions to allow for the analysis of different regions of charge collection.

In this study raster scans were completed covering a portion of Array 1 of a 5 μm SOI microdosimeter as this was the device and array used in heavy ion testing. The bias of the device was set to 10 V to reflect experimental conditions. The incident ions used in IBICC were 5.5 MeV helium ions and were delivered by the ANTARES accelerator situated at ANSTO. Initial measurements generated a pulse height spectra which allowed for the low energy peak to be identified (Figure 7-33) and marked with the appropriate channel number. Also, as the incident ions are monoenergetic low energy signal collection can be attributed to device charge collection characteristics (and not secondaries or other particles as in a mixed radiation field experiment) and as such charge collection can be overlaid with corresponding channel number in the pulse height spectra.

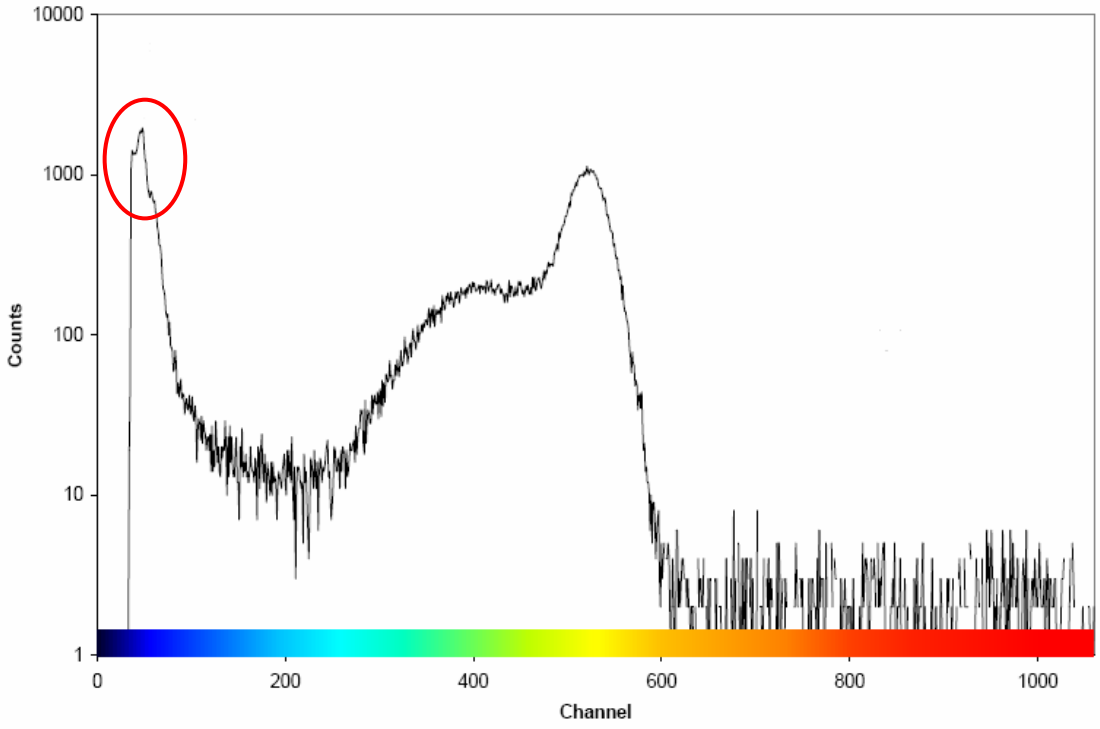

Figure 7-33: Pulse height spectra generated through 5.5 MeV helium particle irradiation of Array 1 of a 5 μm SOI microdosimeter. This provides information on the energy spectra collected from Array 1 as in a typical spectroscopy measurement, but can also be overlaid with a charge collection (coloured scale).

From Figure 7-33 it is clear yellow/orange corresponds to maximum charge collection (as denoted by the main helium peak in this region) with charge collection decreasing through green and blue to black which represents no charge collection. The low energy peak which is the source of this investigation is located at a region of dark blue or poor charge collection. The next step was to produce a 2D charge collection map to determine where on the array this region of poor charge collection was located. This is displayed in Figure 7-34.

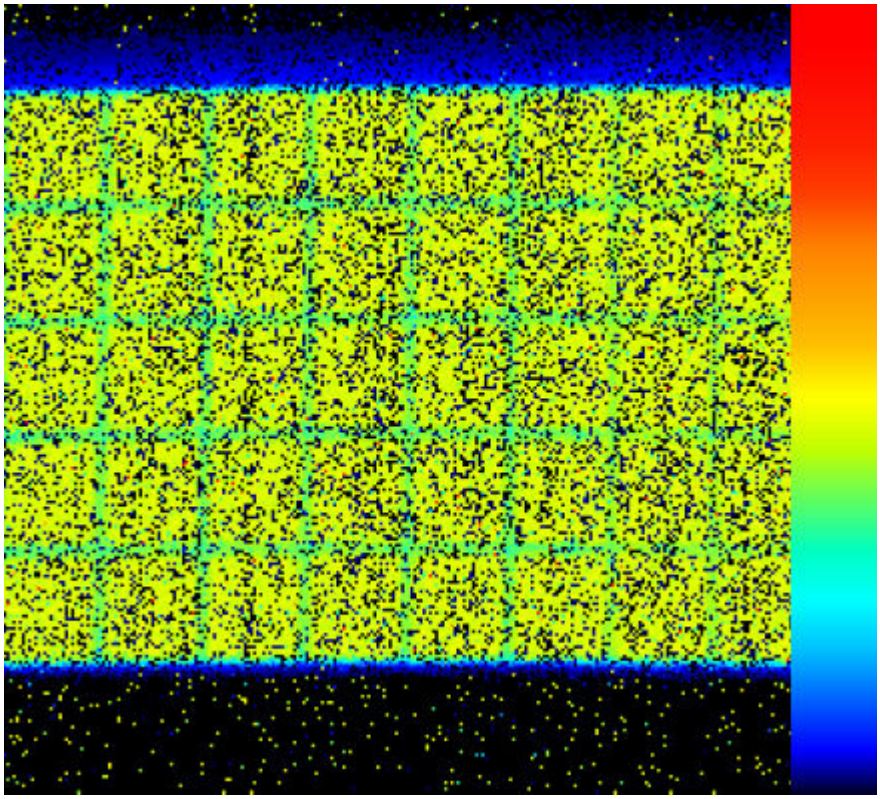

Figure 7-34: Charge collection map for Array 1 providing a spatially resolved map of charge collection efficiency across Array 1 (5x30 SV elements). The blue region of low charge collection, and of interest in this study, appears at the outer edge of the array.

It is clear in Figure 7-34 that the region of low charge collection lies outside the SV array on the periphery of the device. The region of reduced charge collection actually extends out from the edge of the array structure to a distance of approximately 80 μm. This "fringing" effect can be attributed to the formation of low energy events within the measured energy deposition spectra, and is considered bias voltage dependant. Further analysis of the charge collection properties of the SOI microdosimeter is currently being conducted, but is beyond the scope of this report which was to identify the cause of the low energy peak.

The low energy peak detected in heavy ion microdosimetry studies is clearly apparent in the energy deposition spectra collected using Fe-56 (Figure 7-21) and Ti-48 (Figure 7-30) ions. Charge collection or "fringing" outside the SV volume array may contribute in part to this formation. However, the fringing effect was observed at approximately 5% charge collection, or approximately 10% of the full energy peak for incident He particles

in IBICC. It would be reasonable to expect the same charge division effect in the same array of the SOI microdosimeter for Fe and Ti ions. Especially as the incident alpha particle used in IBICC studies were of a similar stopping power to ions studies at NSRL. However, in the case of Fe and Ti measurements, the secondary peak occurs at approximately 40% and 45% of the full energy deposition peak respectively. It was deemed that while the fringing effect may contribute to the low energy signal detected by the microdosimeter, it was possible that this effect may be caused by Si recoils generated through elastic nuclear interactions within the detector volume. The maximum energy delivered to a stationary particle, in this case a Si nucleus, from an incident ion is described in Equation 7-1.

$$E_{Si} = \frac{4 \times M_{Si} \times M_X}{\left(M_{Si} + M_X\right)^2} \times E_X$$

Equation 7-1: Relationship for maximum energy transfer between an incident ion of species X, and a Si nucleus via elastic nuclear interaction. E_{Si} and M_{Si} is the energy and mass of the recoil Si nucleus and E_X and M_X is the energy and mass of the incident ion of species X [1].

In this case the maximum energy of the Si recoil will be 0.88 the energy of an incident Fe ion and 0.93 the energy of an incident Ti ion. For the measurements at the surface of the phantom, where the incident particle has not undergone significant attenuation, the maximum energy of the Si recoil will be 29.57 and 44.64 GeV for incident 0.6 GeV/n Fe and 1.0 GeV/n Ti respectively. Using SRIM the relative stopping powers of the ions in Si were determined and are contained in Table 7-5.

Ion Species	Energy (GeV)	Stopping Power (keV/μm)
Fe	33.60	318.76
Ti	48.00	198.23
Si (generated by Fe)	29.57	80.67
Si (generated by Ti)	44.64	76.31

Table 7-5: Collection of information on the stopping power in Silicon provided by SRIM [91] for incident Fe and Ti particles used in heavy ion microdosimetry work and associated Si recoils.

From the experimentally measured data it was possible to determine the lineal energy in Silicon (using a chord length of 5 μm) for both the main ion peak and the secondary peak in question. This information is contained within Table 7-6. The stopping power information obtained from SRIM is in good agreement with the experimentally derived data for the primary ion energy deposition peak, further supporting the use of SOI microdosimeters in heavy ion measurements.

Incident Ion	Peak	Energy (keV)	Lineal Energy (keV/μm)
Iron	Primary	1750	350
Iron	Secondary	710	142
Titanium	Primary	1050	210
Titanium	Secondary	450	90

Table 7-6: Tabulated data on the energy and lineal energy of the main and secondary peaks contained within the experimentally measured SOI energy spectrum for incident Fe and Ti ions.

The lineal energy of the secondary peak closely reflects that of the stopping power for a Si recoil of maximum theoretical energy imparted by incident Fe and Ti ions used in this experiment and derived using Equation 7-1 and SRIM. There is some difference between the lineal energy value of the secondary peak in the experimental spectrum and the stopping power of the Si recoil of maximum energy. For Ti this is relatively small with a discrepancy of 18%, while for Fe generated Si recoils this error is approximately 75%. These discrepancies can be attributed to the Si recoil energy having a dependence on the angle of recoil, and also on the point of interaction within the SV. It is also important to remember that the energy imparted to a recoil nucleus is dependant on the relative charge states of the incident and target ions. In this case the incident ion whilst fully ionised in the vacuum tube does traverse a number of beam windows, monitoring chambers and air before entering the SV of the microdosimeter. The traversing of these materials may cause the charge state of the ion to change hence reducing the maximum energy which it can impart on the Si nucleus. The charge state of the ion as it enters the SOI microdosimeter can not be determined from current data and as such is a source of inaccuracy in this estimation.

The fact that the position of the peak is reflected in the stopping power of Si recoils with theoretical maximum energy supports the theory that this is the cause of the secondary peak in the heavy ion energy spectra. Energy depositions below this secondary peak can be attributed to:

- Si recoils being imparted energy less than the maximum transferable via an elastic collision with an incident particle.
- Other particles which make up the incident beam interacting within the SV. From Figure 7-25 and [90] it is clear that in the case of an incident Fe beam, ions other than Fe make up approximately 30% of the incident radiation field. Energy depositions below the secondary peak at the surface of the phantom can be attributed to such particles.
- The fringing effect of charge collection which is an inherent property of the current SOI technology.

Further investigations as to the source of this peak are recommended using other detectors (both gaseous and solid-state) and Monte Carlo calculations including GEANT4 or PHITS [92]. Further information on the elastic nuclear interaction cross sections would also be useful in determining the cause of this peak. It should be noted that the effect of this secondary peak on the measured microdosimetry spectra is minimal for heavy ion results (evident in Figure 7-23 and Figure 7-31) and is unobservable in lighter ions such as oxygen and therapeutic protons. It could be assumed that for lighted ions the cross section for the creation of Si recoils is low for lighter ion species, explaining its omission from the experimental spectra. Whilst this issue needs further investigation and should be considered in the development of next generation solid-state microdosimeters it does not preclude the deployment of the current device.

7.9 Heavy Ion Discussion & Conclusion

The SOI microdosimeter has been experimentally tested under Fe-56, Ti-48 and O-16 heavy ion radiation fields at the NSRL facility at Brookhaven National laboratory. These tests provided microdosimetry spectra utilising a 5 μm thick SOI microdosimeter for varying depths in Perspex along the central axis of the ions Bragg curve. From this work experimentally obtained mean dose weighted lineal energies as a function of depth were obtained and compared where possible to existing TEPC data. This comparison illustrated the accuracy of a solid-state microdosimeter in obtaining microdosimetry data with good agreement to existing data.

The real advantage of the solid-state system was that it allowed for spatially accurate measurements (due to the truly microscopic thickness of the device) near the Bragg curve hence providing an accurate assessment of mean dose weighted lineal energy with depth. This work showed that for Fe-56 the initial mean dose weighted lineal energy in tissue at the surface of the phantom was 200 keV/μm and this increased markedly near the Bragg Peak achieving maximum values of 479 keV/μm at the distal edge. Similarly for Ti-48, measurements at the surface of the phantom delivered mean dose weighted lineal energy values in tissue of 108 keV/μm which again increased markedly near the Bragg curve to 365 keV/μm.

It is the high lineal energies of such ions which make them important biologically as well as for the deployment of electronics in space and the consideration of SEU. This is despite their low abundance in space relative to lighter ions such as protons. Measurements along the Bragg curve have allowed for a number of heavy ion energies to be tested from the one single incident ion beam. This is important in space research as the ions experienced are of varying energy and are typically lower than 1 GeV/n (Figure 7-4). This information can then be compared to biological predictions to estimate cell death and mutation rates. In Figure 7-35 the calculation of the probability of excess cancer with varying LET is presented. This shows a peak at 100-200keV/μm which corresponds to Fe and Ti particles measured in this study. Such measured values further

highlight the need for more research in this area considering possible deep space deployments of both manned and unmanned missions.

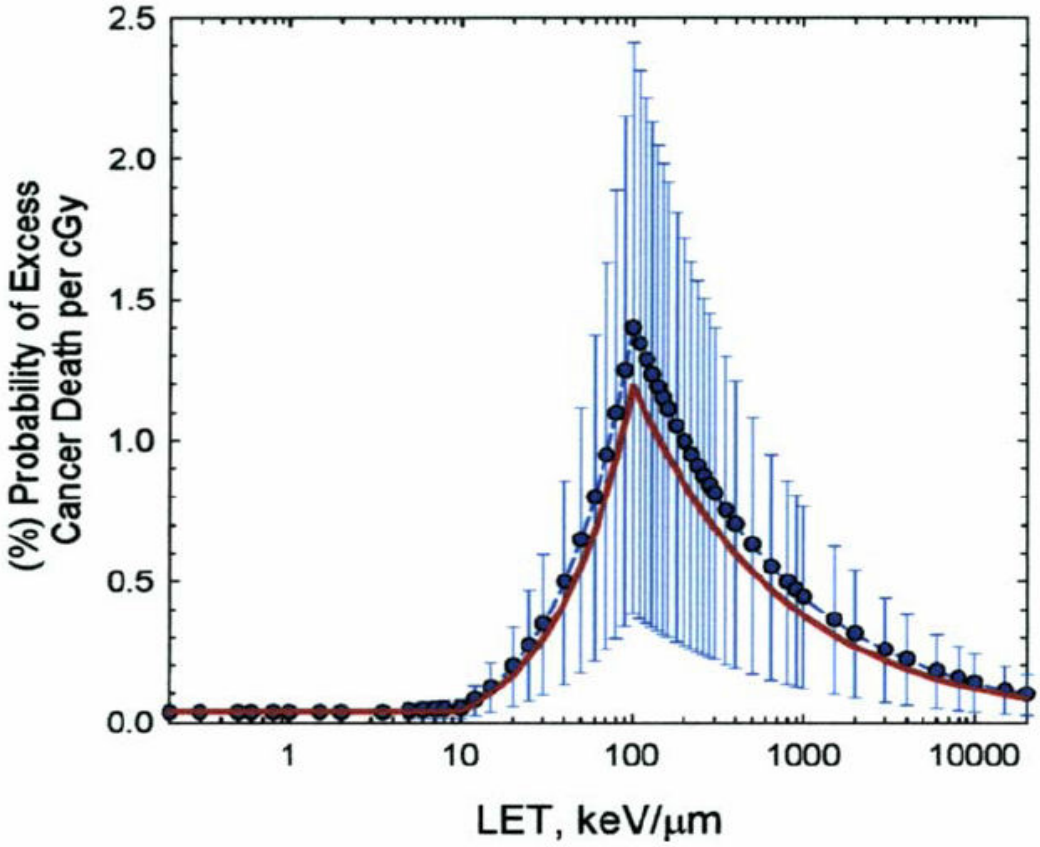

Figure 7-35: Calculation of the point estimate (symbols with dash line) and median values (solid lines) for the probability of excess fatal cancer per cGy versus LET and their subjective standard errors [88].

In this work the radiation hardness of the device was also looked at with regular checks of performance both pre and post measurement. During the course of irradiation with a number of different ion species only one device and array combination was used and no change in performance was detected. This was despite many hours of irradiation with various ion species and with varying energies (through modulation of the ion beam with Perspex). Such a result further supports the use of these devices in space deployments due to their radiation hardness in a high energy heavy ion radiation field and further supports SOI development for space and heavy ion therapy applications.

7.10 Single Si Cell Simulations

The results obtained experimentally utilising an SOI microdosimeter relied on measured energy deposition events within an array of microscopically small Si SV's. However, as the ion species size increases so does the density of the track structure and the range of the delta electrons produced. This is clearly evident in Figure 7-36 with the alpha particle producing delta electrons with a much greater range than those produced by primary protons. Heavy ions such as those tested at the NSRL facility produce delta rays, whose range can exceed the size of an individual SV cell.

Figure 7-36: Simulated track structure of a proton (top) and alpha particle (bottom) [93]. The track of the primary particle is represented by a solid line, while the tracks of the delta electrons are represented by broken lines. Sites of ionisation events are indicated by dots. It is clear that the heavier ion proceeds with minimal deviation and produces delta electrons with a much larger range.

To determine if there exists a limit of Si cell size which provides accurate data in heavy ion applications GEANT4.7.1p1 simulations of a single Si cell were completed. In these simulations the size of the Si cell was varied while a needle beam of various ion species was normally incident on the centre of the cell. The spectra of energy deposition events was determined for a given number of incident particles and through varying the cross sectional area of the cell it was possible to determine if there exists a size limitation at which results become inaccurate. Such simulations are of use especially as microdosimetry SV's become smaller with improvements in semiconductor manufacturing technology.

7.11 Simulation Parameters

7.11.1 Geometry

The GEANT4.7.1p1 Monte Carlo toolkit [52] was used for the basis of an application to evaluate the effect of delta ray transport from the SV thus affecting the energy signal detected by the device. A simple right-angled-parallelepiped (RPP) silicon cell was created within the application to represent the SV. The cross section dimensions of the volume were 2x2 μm^2, 5x5 μm^2, 10x10 μm^2 and 100x100 μm^2, with thicknesses of 2, 5 and 10μm.

7.11.2 Primary Beam

The primary beam utilised in this work had zero cross sectional dimension and was normally incident on the centre of the Si cell. Three heavy ion configurations were used that match the three heavy ion species tested experimentally at the NSRL facility. Monoenergetic Fe-56, O-16 and Ti-48 would constitute the incident ion species, each with an energy of 1.0GeV/n. The LET of 1GeV/n O, Ti and Fe is 26.47, 198.23 and 276.04 keV/μm respectively as provided by SRIM [91]. Each simulation was run for $1x10^6$ incident particle histories to ensure statistical accuracy. Simulations were carried out on the Loma Linda University Medical Center Cluster Computing Facility (LLUMC CCF) which is described in Section 6.2.

7.11.3 Physics Processes

The physics of simulating heavy ions is especially challenging because of the nuclear interactions and particle fragmentation which can occur as the ion traverses the geometry of the simulation. For each ion multiple scattering and ionisation was considered using the G4MultipleScattering and G4hLowEnergyIonisation models. Electrons produced via ionisation were transported down to 0.1 μm or 250eV (the lowest transportation limit of GEANT4.7.1p1) with low energy ionisation, low energy Bremsstrahlung and multiple scattering considered. Nuclear interactions were considered for incident oxygen ions using the G4BinaryLightIon model, however no nuclear interactions were considered for incident Ti and Fe ions. It was considered that this would not affect the results of the simulation as:

– Due to the thin film nature of the target (i.e. the thickest is 10μm) the probability for nuclear interaction is low.
– The predominant source for energy deposition within the SV is ionisation, which has been accounted for within the physics of the application.

In future simulations it would be recommended that the JQMD model be included to provide a more complete simulation of the energy deposition spectra within the SV.

7.11.4 Tracking of Events

For each incident ion, all energy deposition events (whether from a primary or secondary particles) was registered with the kinetic energy, charge and mass of the particle as well as the energy deposited within the SV stored. All energy deposition events per incident particle were summed and binned into an energy deposition spectra when the program was complete.

7.12 Results and Discussion

To provide an indication on the track density and delta electron range of the three different ion species, visual images of the ion track within a 10x10x10 μm^3 Si cell were constructed using GEANT4. These images are contained within Figure 7-37 and clearly illustrate how not only does the density of the ionisation track increase with increasing ion size, but also the number of long range delta rays that escape the SV. Oxygen generates comparatively few delta rays with only a single ionisation event escaping the SV. In comparison, the two heavier ions, Ti and Fe, have dense track structures with a large number of long range delta rays produced which escape the SV. It would be expected that this be identified in the energy deposition spectra measured within Si cells of varying cross sectional area.

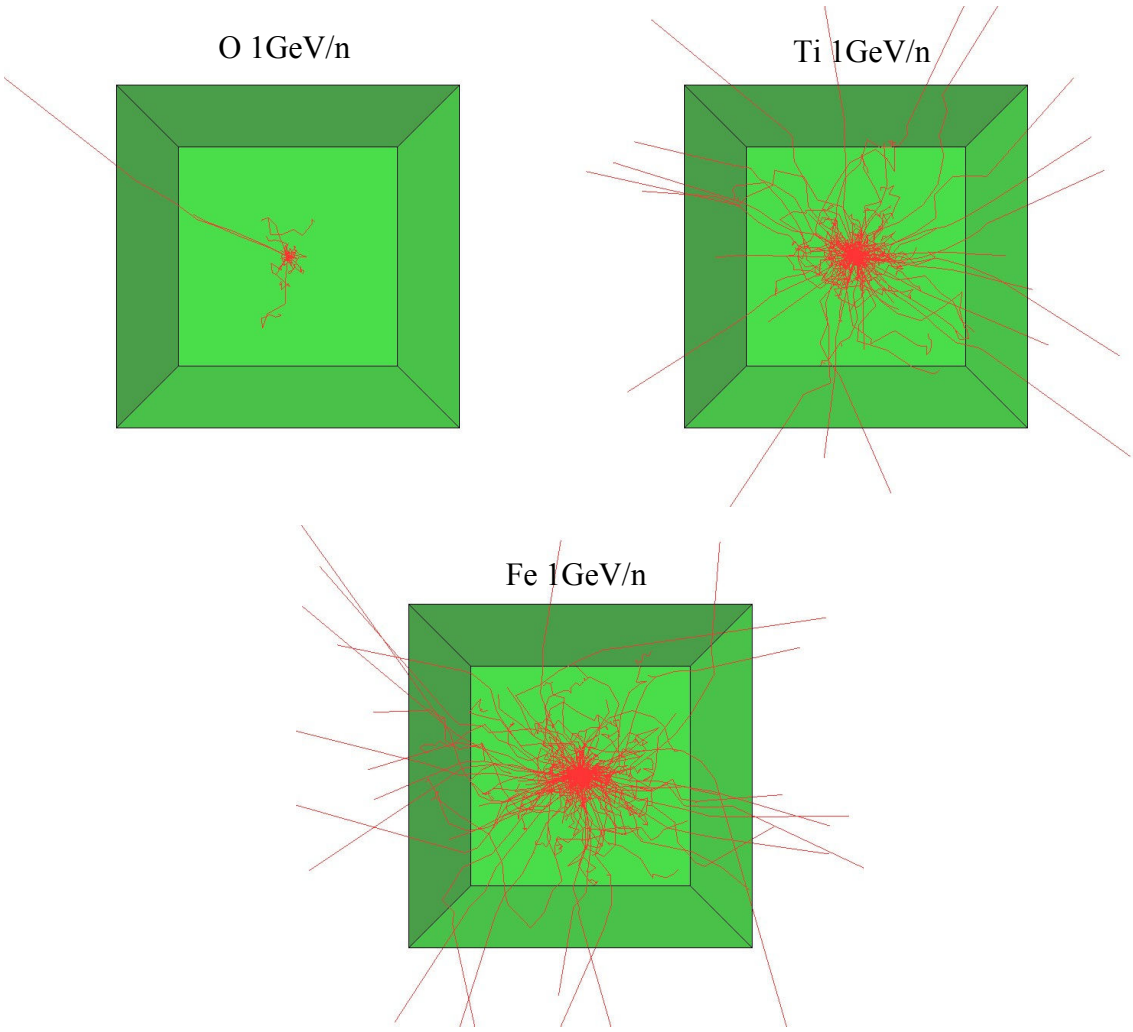

Figure 7-37: Visual representation of the track structure of the three ion species within a 10x10x10 μm^3 Si cell.

The energy deposition spectra results for the three separate ion species are located in Figure 7-38, Figure 7-39 and Figure 7-40, while further information on the energy deposition peak is located in Table 7-7, Table 7-8 and Table 7-9.

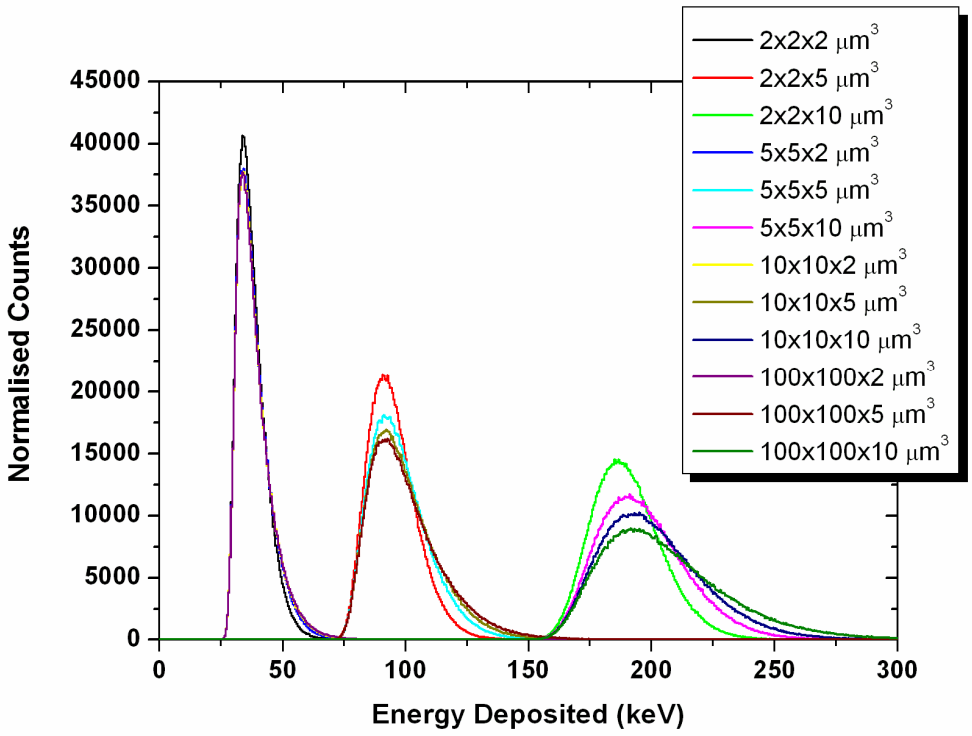

Figure 7-38: Energy deposition spectra obtained from irradiating Si cells of varying dimensions with 1GeV/n oxygen ions.

Cell Volume (μm^3)	Peak Energy (keV)	Variation from $100x100\mu m^3$ Result (keV)	% Variation from $100x100\mu m^3$ Result
2x2x2	34	0	0
5x5x2	34	0	0
10x10x2	34	0	0
100x100x2	34	-	-
2x2x5	92	-0.5	-0.54
5x5x5	92.5	0	0
10x10x5	92.5	0	0
100x100x5	92.5	-	-
2x2x10	187	-6	-3.11
5x5x10	191	-2	-1.04
10x10x10	192	-1	-0.52
100x100x10	193	-	-

Table 7-7: Information on the energy deposition peak from irradiating Si ells of varying dimensions with 1 GeV/n oxygen ions.

From these results it is clear that different thicknesses of silicon material produce different energy deposition regions based on the stopping power of the material and the LET of the incident particle. As was indicated in Figure 7-37 the lighter ions produce fewer long range delta rays which deposit energy outside the SV, hence producing a minimal shift in the energy deposition spectra for small cross sectional areas. This is clearly evident in the case of oxygen ion simulations with no variation in the peak position for 2 and 5 μm thick Si cells of varying cross sectional area from 2x2 μm^2 to 100x100 μm^2. Some variation 0.5-3% is observed ion the peak position as the cross sectional area is decreased from 100x100 μm^2 to 2x2 μm^2 in a 10 μm thick device. It is considered that this is a direct result of an increase in the probability of long range delta ray production within the thicker Si cell. Long range delta rays can transfer energy out of the cell causing the energy deposition spectra to shift to lower energies.

Titanium and iron results are similar because of the relatively close size and energy of the incident ion. As was observed in Figure 7-37 the heavier ions produce a much denser ionisation track with a higher portion of long range delta rays produced. This is reflected in the energy deposition spectra of both ions. Shifts in the energy deposition peak are detected for all three Si cell thicknesses. The shift is smallest in the case of 2 μm thick cells, with a maximum shift of 2 and 2.5% respectively for Ti and Fe. This shift increases as cell thickness increases to a maximum (from the simulated cell sizes) of approximately 7% for both ions when the SV thickness is 10 μm.

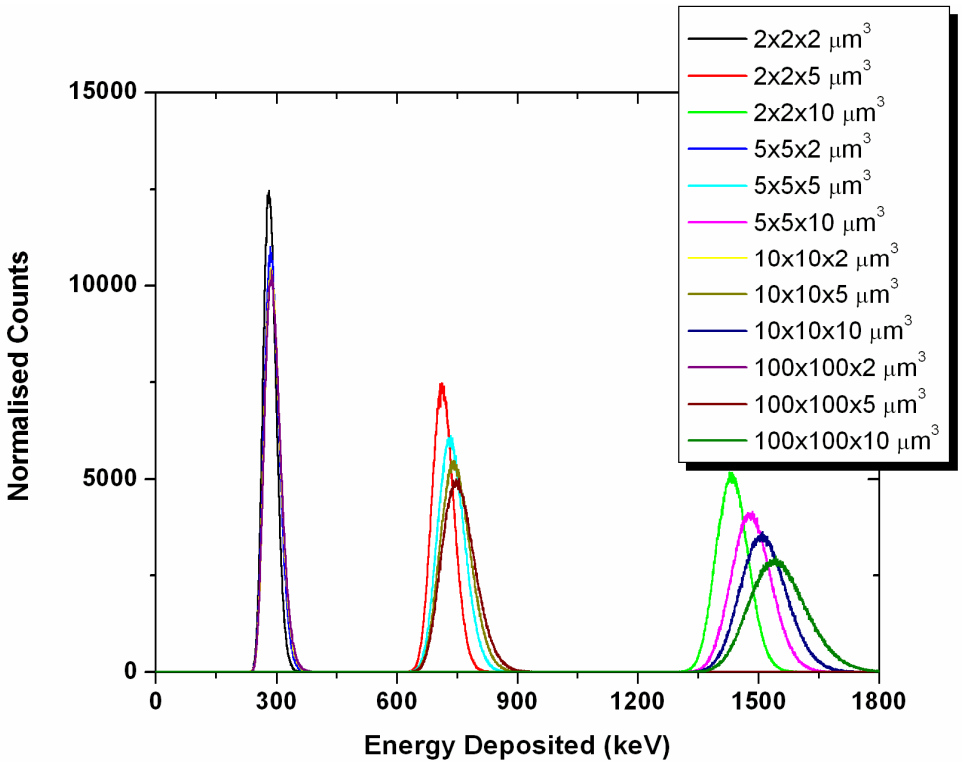

Figure 7-39: Energy deposition spectra obtained from irradiating Si cells of varying dimensions with 1GeV/n titanium ions.

Cell Volume (μm^3)	Peak Energy (keV)	Variation from $100x100\mu m^3$ Result (keV)	% Variation from $100x100\mu m^3$ Result
2x2x2	281	-6	-2.09
5x5x2	286	-1	-0.35
10x10x2	287	0	0.00
100x100x2	287	-	-
2x2x5	712	-34	-4.56
5x5x5	733	-13	-1.74
10x10x5	741	-5	-0.67
100x100x5	746	-	-
2x2x10	1434	-109	-7.06
5x5x10	1482	-61	-3.95
10x10x10	1509	-34	-2.20
100x100x10	1543	-	-

Table 7-8: Information on the energy deposition peak from irradiating Sic ells of varying dimensions with 1 GeV/n titanium ions.

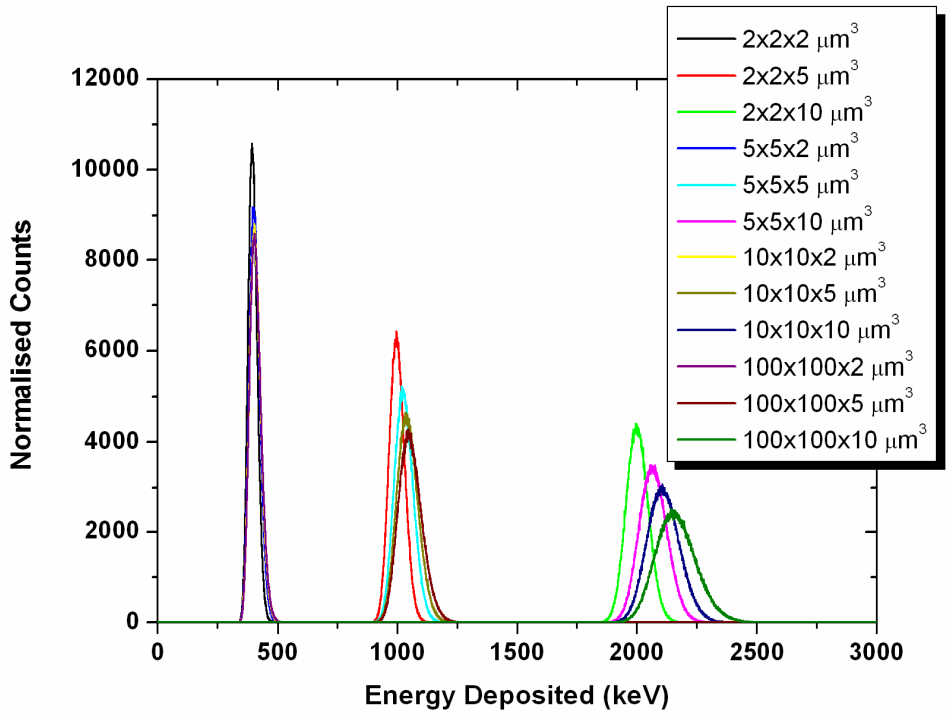

Figure 7-40: Energy deposition spectra obtained from irradiating Si cells of varying dimensions with 1GeV/n iron ions.

Cell Volume (μm^3)	Peak Energy (keV)	Variation from $100x100\mu m^3$ Result (keV)	% Variation from $100x100\mu m^3$ Result
2x2x2	394	-10	-2.48
5x5x2	400	-4	-0.99
10x10x2	404	0	0.00
100x100x2	404	-	-
2x2x5	995	-52	-4.97
5x5x5	1023	-24	-2.29
10x10x5	1038	-9	-0.86
100x100x5	1047	-	-
2x2x10	2002	-153	-7.10
5x5x10	2066	-89	-4.13
10x10x10	2106	-49	-2.27
100x100x10	2155	-	-

Table 7-9: Information on the energy deposition peak from irradiating Sic ells of varying dimensions with 1 GeV/n iron ions.

For heavier ions (such as Fe and Ti), the Gaussian shape of the spectra remains unchanged with varying cross sectional area despite changes in mean energy and FWHM. However, for the lighter oxygen ion as the SV thickness is increased, a high energy tail becomes more prominent on the energy deposition spectra. This is a direct result of scattering of these lighter ions within the volume, causing in a longer path length and hence higher energy deposition within the volume. As the cell thickness increases the probability that the ion will be scattered from its original path also increases, resulting in a longer high energy tail in the energy deposition spectra. Increasing the cross sectional area of the cell further increases the SV's ability to collect scattered particles further increasing the length of the high energy tail.

This work has also highlighted the applicability of current SOI technology to heavy ion radiation fields. Currently the smallest cross sectional area employed in SOI technology to microdosimetry is 30x30 μm^2. Based on the GEANT4 simulation results presented here such cross sectional areas will produce comparable results to the larger 120x120 μm^2 SV's for the three ion species studied.

Clearly this work has shown that the measured energy deposition spectra does depend on the size of the cell, especially as the size and energy of the ion increases and hence as the number of long range delta rays increases. As such the intended incident radiation field needs to be considered in new device design and fabrication to minimise charge sharing and loss. While this needs to be considered in current microdosimetry measurements, it is also important to remember that in practice the radiation field is not normally incident on the centre of the SV cell, but rather covers the entire cell. Long range delta rays in this instance can cause almost all the energy to be transported from the SV if the ion strikes near the cell edge. It should be remembered that this is also the case in actual human cells and biological systems. Radiation can strike the edge of the cell with delta rays transporting energy to other parts of the biological system without interaction with the cells nucleus or DNA. As such an array of cell sized SV's does reflect the conditions present in a larger biological system.

This work has raised an important point concerning the use of microdosimetry in heavy ion radiation fields. As SV's become smaller, there may exist a limit at which the microdosimetry model fails to deliver acceptable results as delta rays transport energy outside the SV, registering erroneous results. In this work it has been shown that shifts of up to 7% are observed in the peak position within the energy spectra when the cross sectional area of the cell is varied from 2x2 to 100x100 μm^2. Further reducing the cross sectional area of the Si cell will further increase this shift. At a point where the microdosimetry model breaks down, other methods need to be investigated such as ion counting and nanodosimetry methods. Further simulations should be completed to assess optimal SV size for application in heavy ion radiation fields.

7.13 Single Si Cell Simulation Conclusions

This simulation study has determined the effect of varying cross section area on energy spectra collected by a single Si cell irradiated with 1 GeV/n O, Ti and Fe ions. It is clear that heavier ions produce not only a denser track structure (which is evident through a high LET) but also longer range delta rays which can transfer energy out of the SV. The loss of energy through the escape of delta rays out of the SV can lead to a shift in the energy deposition spectra producing erroneous results. As such, the size and spacing of SV's should be considered in microdosimetry to minimise charge sharing and loss from Si cells.

Further work needs to be carried out that include nuclear interactions through incorporation of the JQMD model into the GEANT4 based application. Simulations incorporating a wide range of ion species and energies should be completed for future micro- and nanodosimetry applications to ascertain any limitations on future detector development.

7.14 Overall Recommendations & Future Work

This work has highlighted the applicability of SOI microdosimeters to space deployments in obtaining microdosimetry spectra from a range of different ion species and energies encountered in space. Initial simulations with GEANT4 have provided an assessment of the radiation field induced by solar protons at the orbit of the ISS. These results have provided useful information on shielding and converter thickness which can be utilised in the first space deployment of SOI microdosimeters aboard MidSTAR-I. Further simulation studies need to be completed to assess the impact of other particle species such as electrons, neutrons and heavier ions on the microdosimetry spectra for both near Earth and deep space deployments. These should be completed using the GEANT4 Monte Carlo Toolkit [52] and where possible cross referenced with existing experimental data.

SOI microdosimeters were deployed in MidSTAR-I, on 9th March 2007. This will provide experimental data for near Earth space radiation environments. The response, radiation hardness and microdosimetry spectra data provided by such instruments will be useful for future device development and also for planning future Earth based device testing. Such results should also be compared where possible to Monte Carlo studies allowing for further validation of this important resource.

Heavy ion irradiations with these SOI microdosimeters have provided useful information on the radiation field and microdosimetry spectra. When compared with existing TEPC data for Fe ions agreement was encouraging. Further inter-comparisons with TEPC's should be completed under the same experimental conditions. Further Monte Carlo calculations should be conducted to ascertain the correct chord length and TE conversion factor and validate assumptions made in this study. Further development of these devices for space deployment should utilise larger SV arrays with each SV cubic in shape to reduce geometrical effects in an omnidirectional field. Monte Carlo studies can also be utilised in this work to determine optimal SV shape and spacing.

Overall this work has shown that the SOI microdosimeter provides a system which can be used for measuring radiation fields of different particles over a range of energies and LET's. The small size of the device allows for measurements within phantoms and behind shielding structures. To better understand biological effects, microdosimetry results should be compared with biological cell survival and DNA plasmid data for the same radiation fields. Such work could lead to the development of useful biological and cancer induction models based on microdosimetry for space environments.

Further, the SOI microdosimeter and microdosimetry has shown its applicability to shielding optimisation for solar protons. In future shielding design and optimisation it would be recommended that preliminary Monte Carlo simulations be completed utilising microdosimetry methods including mean dose weighted lineal energy, dose equivalent and average quality factor as optimisation parameters. The SOI microdosimeter can then be used to experimentally test newly designed radiation shielding under a range of radiation fields and compare this with existing shielding structures. Such optimisation procedures could lead to improved radiation exposures to both astronauts and electronics.

Finally, the SOI microdosimeter has shown through theoretical simulations and experimental measurements that it is capable of measuring data over a wide range of ion species and LET's in real time. This would suggest that the development of this device for radiation protection and monitoring be undertaken for both space and Earth based applications. For space applications such a device may issue a warning to crew in the event of high radiation flux, allowing them to proceed to a safe shielded environment in the spacecraft, minimising exposure. It could also be used in conjunction with existing radiation detection apparatus to provide a better understanding of the radiation exposure to both astronauts and electronics allowing advancements to be made in order to minimise exposure.

8 Microdosimetry: ΔE-E Telescope

8.1 Introduction

This work has clearly illustrated the ability of microdosimetry techniques to obtain a wide range of information from various types of radiation. Such information includes the lineal energy, mean dose weighted lineal energy, average quality factor and dose equivalent, which can be used to determine radiation risk using the microdosimetry approach. However, while such quantities are useful in radiation therapy and radiation protection, the particle type and energy in combination with particle LET allows for a more detailed estimation of biological effect. Applications where knowledge on particle type and secondary particle production is beneficial are:

- Hadron therapy treatment planning, to ascertain the spectra of produced secondaries that may elevate the RBE in a certain region.
- Protective shielding construction in areas of radiation protection such as space. Knowledge of particle type after a shielding structure will allow for optimisation using a more complex layered construction to account for secondary production within the shielding structure.
- Risk assessments to occupationally exposed persons such as astronauts using the fluence based approach.
- Verification of Monte Carlo simulations in radiation therapy and radiation protection

Information on secondary particle type, energy, LET etc can be provided through the use of Monte Carlo codes such as GEANT4 [52]. However, such codes rely on accurate information of the primary radiation field in order to deliver accurate results. In an unknown radiation field such simulations are not feasible. Further, they do not provide an online experimental evaluation of a changing radiation field which is typical of a space environment. Identification of charged particles in mixed radiation fields is possible through the use of a series of two or more detectors, which combine to form a detector telescope. The first detector is a ΔE detector with thickness less than the range of the charged particle while the second detector, situated behind the ΔE detector, consists of a

SV thickness typically greater than the range of the particle. This second detector is aptly named the E detector as in combination with the ΔE detector it provides the total energy of the particle. The stoping power of charged particles can be presented using the relationship described in Equation 8-1. From Equation 8-1 it follows that two charged particles with the same energy but different MZ^2 product will produce different events on the two-dimensional plane of a ΔE and E detector coincidence event map.

$$\frac{dE}{dx} = A\left(\frac{MZ^2}{E}\right)\ln\left(\frac{E}{M}\right)$$

Equation 8-1: Relationship of charged particle stopping power where M is the mass, Z the charge and E the kinetic energy of the particle, while A is a proportionality coefficient [1, 2].

Telescope detector instrumentation is popular in nuclear physics research for the identification of nuclear reaction products and is generally comprised of two or more Si radiation detectors. For high energy charged particles the E-detector may be a scintillator detector such as the arrangement displayed in [94]. Detector telescopes have also been previously applied to space research for the identification of heavy ion radiation fields [95, 96]. The challenge in applying a telescope for the identification of high LET products is that it requires a very thin ΔE detector stage, with the thickness required less then several microns. The production of a freestanding ΔE detector of this size is difficult due to the fragility of Si. The thinnest commercially available ΔE Si detectors are typically 15 μm [97].

A monolithic ΔE-E silicon telescope overcomes the problems related to the limitation of freestanding ΔE detector thickness. It is possible to produce a ΔE detector within a monolithic telescope by epitaxial growth of Si above the E detector [98]. Another method of monolithic telescope formation is through high energy implantation of boron to a depth of 1-2 microns to produce a deep seated p-n junction within the E detector [99]. Recently, using technology as described in [99], a two stage ΔE-E solid-state telescope was produced with a $1mm^2$ active area at STMicroelectronics in collaboration with Politecnico di Milano. This device provides the ability to measure either the microdosimetric properties of the radiation field using the ΔE detector, or particle

identification and LET through the operation of the ΔE and E detectors in coincidence. The ability to measure both parameters can allow this detector to determine radiation risk using both the microdosimetry and fluence based approaches. This device has previously been tested under monoenergetic neutron radiation fields and the response simulated using Monte Carlo methods [100, 101]. Ion Beam Induced Charge Collection Imaging (IBICC) at the Australian Nuclear Science and Technology Organisation [102] has also been completed in collaboration between the CMRP and Politecnico di Milano to better understand the devices performance.

The characterization of a small area monolithic ΔE-E telescopes in hadron therapy applications was proposed at the CMRP. It is desirable to test the performance of this device in a charged hadron environment that is typically encountered in therapeutic applications. As such, both the SOI microdosimeter [25] and ΔE-E Silicon telescope were exposed to both modulated and non-modulated therapeutic proton beams. In both instances different positions along the Bragg Peak (BP) and Spread-Out Bragg Peak (SOBP) within a homogeneous polystyrene phantom was sampled. The data obtained from both detectors was complimentary with the SOI microdosimeter providing lineal energy spectra, while the ΔE-E telescope provided 2-dimensional information on particles detected and LET. The development of an associated two-dimensional in-vitro radiobiological matrix based on existing experimental data further enabled the ΔE-E telescope results to be linked directly to biological effect. This radiobiological matrix was applied to measured results and produced a plot of radiobiological effect (RBE) as a function of depth along the protons path. This was compared to published data to assess the accuracy of such a model. A variation of this matrix could be developed for a range of different cell lines and applied to treatment planning and radiation protection to provide a more accurate assessment of radiobiological effect.

8.2 ΔE-E Silicon Telescope

The ΔE-E Silicon telescope is a unique device in that is comprised of two separate detectors mounted on a single chip. The chip was manufactured at STMicroelectronics (Catania, Italy) where the ΔE detector is approximately 1 μm thick, while the E detector is constructed as 500 μm thick [100]. The cross sectional sensitive area of the detector is approximately 1 mm^2. The two separate detectors are formed on a single silicon substrate and share a common p+ anode which is created by high energy (1 MeV) boron implantation. The ultra-thin n+ cathode for the ΔE stage is formed through low energy As implantation while the electrical contact is constructed from a 0.2 μm thick Al/Si layer. The electrical properties of the device have been investigated and presented on previously [100, 101]. A schematic of the detector is contained within Figure 8-1.

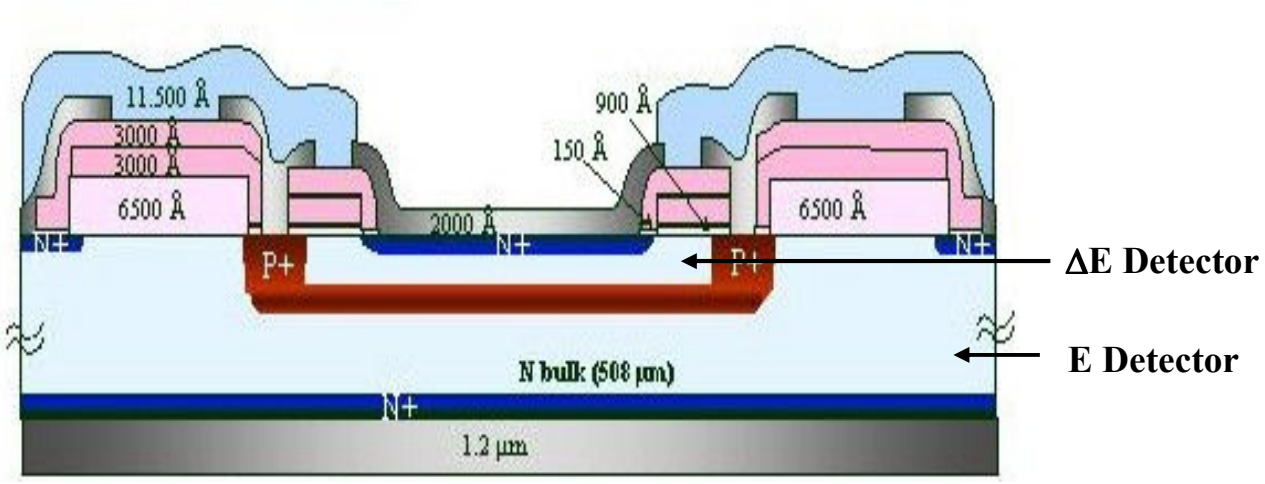

Figure 8-1: Schematic of the ΔE-E telescope [100].

This detector can be operated in a number of different ways utilising either of the detectors separately or together in coincidence. When operated separately the ΔE detector can operate as a planar microdosimeter, which could be useful in accelerator experiments where the beam is normal to the device, and hence the average chord length determined by the thickness of the detector. This was previously demonstrated in heavy ion irradiations of the SOI microdosimeter at the NSRL facility at BNL. However, in an omnidirectional radiation field the planar structure of the detector would exhibit a response that is dependant on the path of the incident particle. The E detector can also be operated separately as a 500 μm thick planar device which can be useful for

characterising and measuring the energy of charged particles that have a range smaller than that of the thickness of the device. However, the real advantage of such a device is when it is operated in coincidence mode where the ΔE stage provides the energy loss of the particle in 1 μm of Si (or the LET) while the ΔE+E stage provides the total energy of the particle (if its range is less than the thickness of the device). From such measured quantities it is possible to discern the type of particle as is described in Equation 8-1.

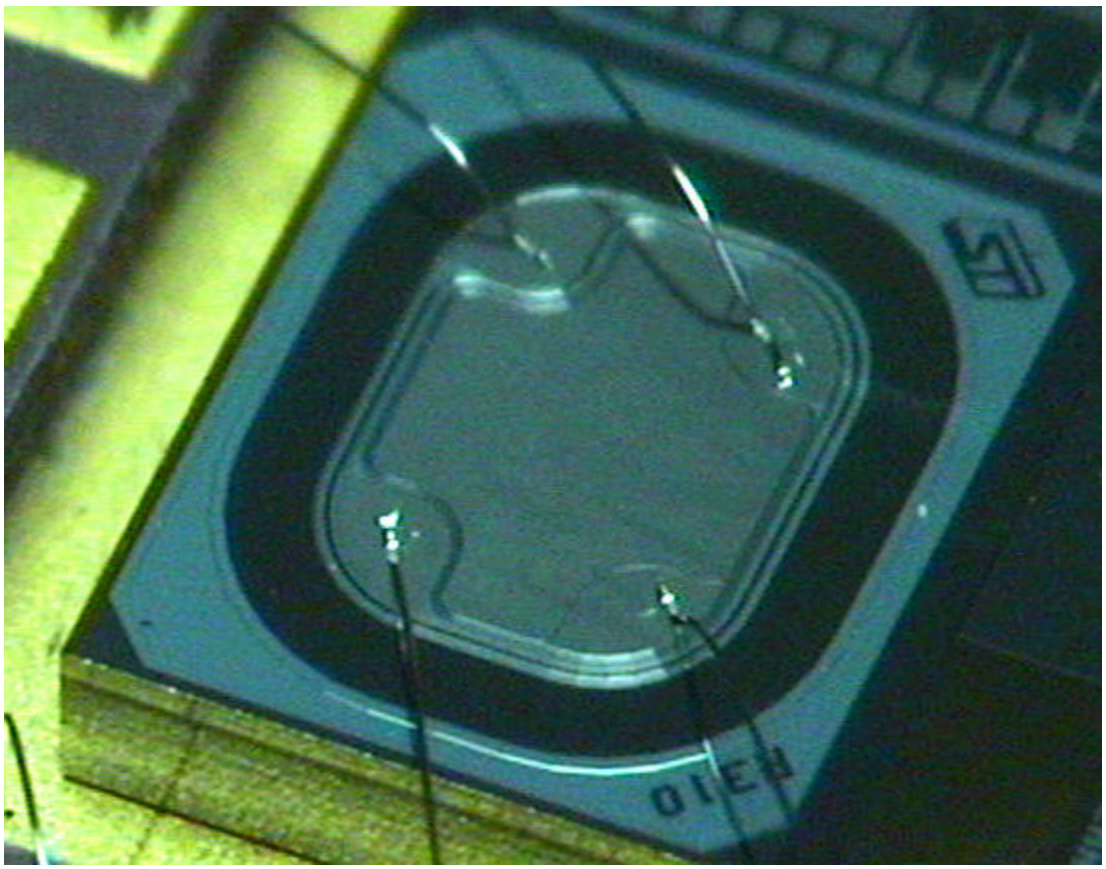

Figure 8-2: A picture of the SV area of the ΔE-E telescope chip.

In this work the primary radiation field comprised of high energy protons and the associated secondary particles. Clearly in this case the primary protons will traverse both stages of the device, in essence making this a ΔE-ΔE detector. However, the different thicknesses of the two stages provided information on the nature of the beam at different points along the primary particles path, and allowed for the identification of any recoil protons or other nuclear secondaries produced. Such particles would be observed as an individual locus based on particle type within the two-dimensional ΔE-E coincidence

map [94]. Further, it was interesting to observe the different characteristics of the un-modulated proton beam to the modulated protons used to create the SOBP.

8.3 Proton Beam Delivery & Dosimetry

Proton irradiation was completed at the Proton Therapy facility within Loma Linda University Medical Center in a specialised research irradiation hall which contains three separate research beam-lines. This work utilised the p-East research beam line and proton energy of 100 MeV. The advantage of using the P-East beam-line is that it comprises of no beam modifying devices other than a titanium exit window. This provided the opportunity to obtain an un-modulated 100 MeV proton beam (with little alteration from beam modifying devices that is typical on most treatment beam lines) and then create a modulated 100 MeV proton beam using ridge filters, scattering foils and a modulator wheel. Schematics of the two beam-line configurations are contained in Figure 8-3.

To monitor the instantaneous dose rate to the detector (to avoid pile-up) a custom-made circular parallel plate ionisation chamber (IC1) with a sensitive volume of 25.4 (diameter) × 1.57 mm^3 (SV thickness) (air mass 1.000+/-.005 mg at STP) was used [74]. Such a chamber resulted in minimal attenuation of the beam as the entrance and exit windows of this chamber were constructed with 12.7 μm Mylar and the chamber body was constructed of 1.57 mm Kapton. The IC was read out with a recycling integrator (RI) installed in close proximity to the LLUMC proton research beam lines. The ridge filters and 3 cm modulator wheel (rotated at 480 rpm) were the same as those used in therapeutic applications at Loma Linda, while the scattering foil was a 1 mm thick lead plate. The layered homogeneous polystyrene phantom was comprised of blocks used in routine QA applications. The variable thickness of the blocks down to a 1 mm minimal thickness allowed for a range of measurement positions along the Bragg Peak (BP) and SOBP. Throughout the course of the experiment the device was irradiated with 0.2-0.35 cGy per spill (accelerator delivered radiation pulse of approximately 0.3s duration with a total cycle time of 2 seconds in duration [9]) monitored using IC1. At the same time regular checks were made of the beam profile using radiochromic film to ensure adequate

coverage of the detector volume. Typically the beam profile was greater than 5 cm in diameter.

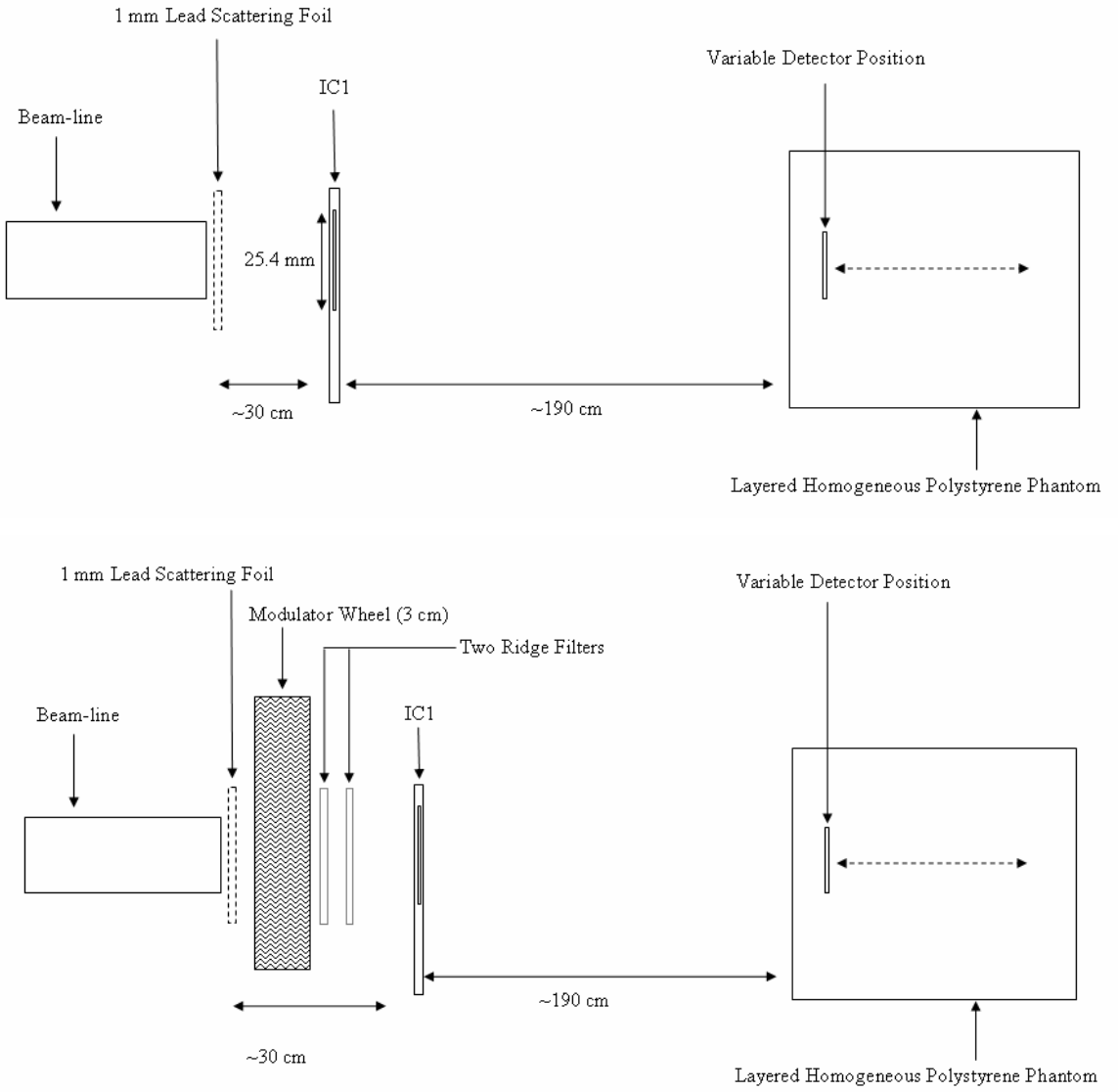

Figure 8-3: Schematic of the P-West beam-line configuration for an un-modulated 100 MeV proton beam (top) and a modulated proton beam with a 3 cm SOBP (bottom).

To determine SOI and ΔE-E measurement positions for adequate sampling the BP and SOBP, depth dose curves were obtained for the given proton energy and experimental setup. A Markus chamber was used to measure the charge collected at a given point within the phantom normalised to 100K IC1 counts or approximately 37 cGy (see detector calibration in Section 10.5). The beam spot at the entrance of the phantom was

also monitored and considered quasi-homogeneous (i.e. radius greater than 5 cm). The depth dose curves for both the modulated and un-modulated 100 MeV proton beams are displayed in Figure 8-4.

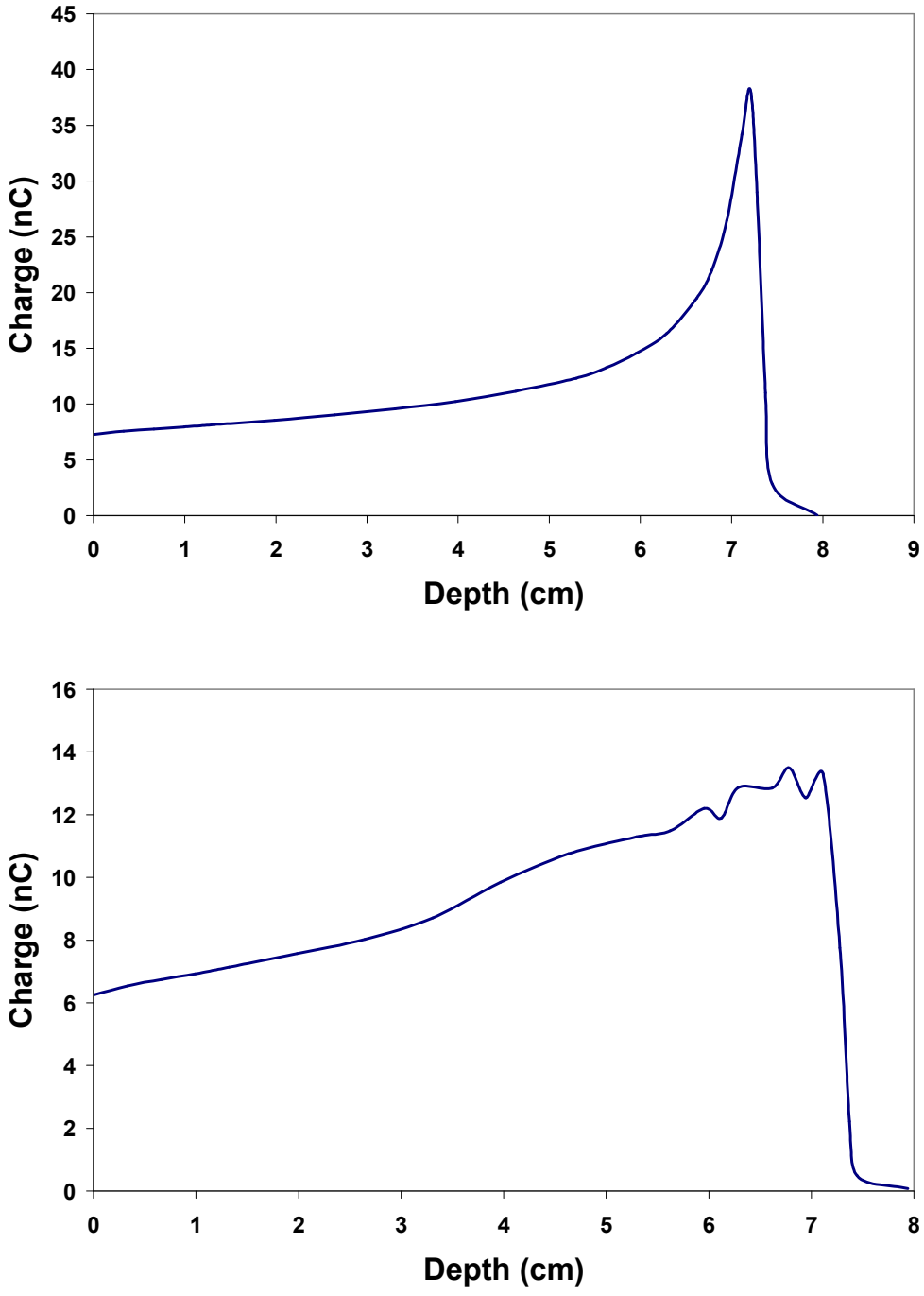

Figure 8-4: Depth dose profiles as obtained using a Markus chamber for the un-modulated (top) and modulated (bottom) 100 MeV proton beams.

The SOBP results do not show a uniform dose across the SOBP but rather the Bragg Peak components which make up the SOBP are clearly visible. The modulator wheel in this instance is optimised for 155 MeV protons and as such some increase in dose towards the distal edge of the SOBP and variation of dose across the SOBP region is expected. This however, does not effect microdosimetry measurements in this region, as it was interesting to observe the change in measured microdosimetry spectra and two-dimensional ΔE-E coincidence spectra across the SOBP where some protons will traverse the SV while others are stopping due to beam modulation.

8.4 ΔE-E Experimental Setup

To sample the radiation within the polystyrene phantom, the ΔE-E detector was attached to the end of a Perspex rod. Anterior to the device was affixed a 0.3 mm thick polyethylene converter while the whole assembly was contained within Al foil that acted as a Faraday cage. The probe was inserted at a given depth within the polystyrene phantom such that the device was parallel to the surface of the phantom (i.e. such that the incident field was normal to the device) and at the height of the central axis. At the opposite end of the probe was the pre-amplifier assembly, which was located in close proximity to the detector to minimise system noise. In this case the noise level for the ΔE and E stages of the detector were 12 and 10 keV respectively. A picture of the probe assembly is displayed in Figure 8-5, while a picture of the probe contained within the polystyrene phantom is displayed in Figure 8-6.

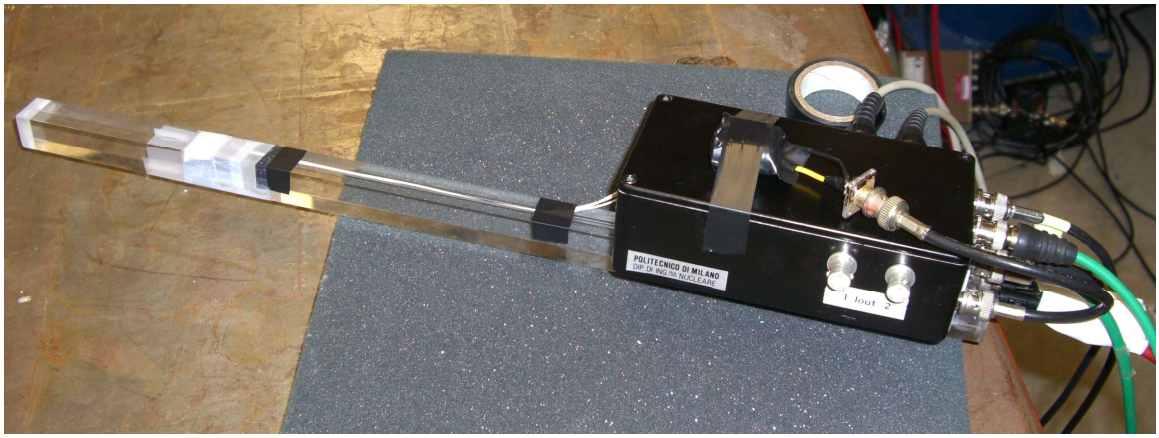

Figure 8-5: Picture of the ΔE-E probe assembly with attached pre-amplifier setup. Note the detector position approximately 10 cm from the end of the Perspex rod contained within the Al shielding.

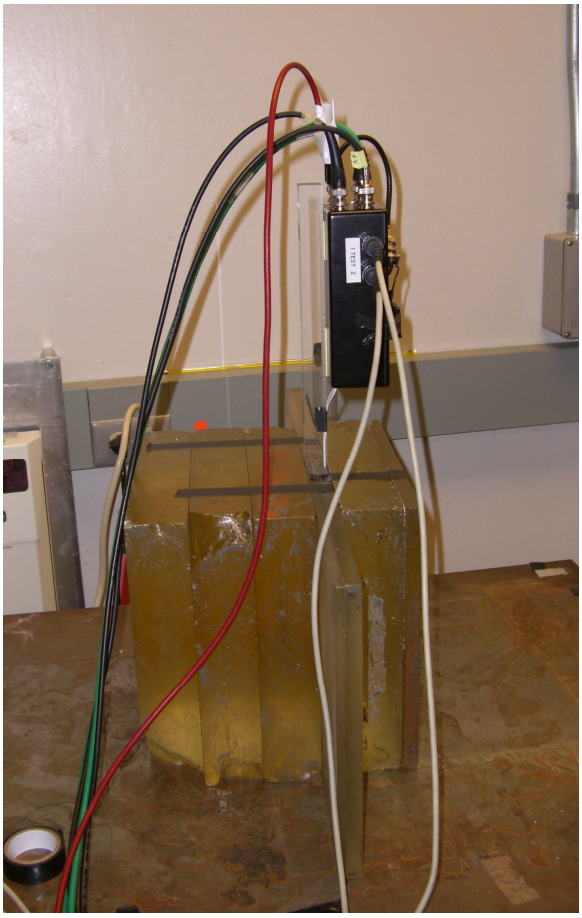

Figure 8-6: Picture of the experimental ΔE-E probe assembly contained within the polystyrene phantom. In this instance the radiation field moved from right to left and was normal to the surface of the phantom.

Detector bias to the E and ΔE stages was provided by a dedicated dual power supply. The E stage of the detector was operated with a bias of 100 V while the ΔE detector was operated with a bias of 6 V. The signal was passed from the detectors to a dedicated, purpose built, pre-amplifier assembly (powered by ±15 V) and then to a custom built multi-channel analyser (±15 V) for the collection of data from individual detector signal. The MCA was located outside the experimental hall approximately 20 m from the pre-amplifier, which was located as close as possible to the detector whilst remaining outside the radiation field. A USB interface from the MCA allowed for the connection of a computer or laptop and data was collected using a dedicated MathCAD program. This program allows for each individual detector element to collect data separately or in coincidence, allowing for particle identification. Readout electronics and software for the

DAQ system was produced by Politecnico di Milano. A schematic of the experimental setup is located in Figure 8-7.

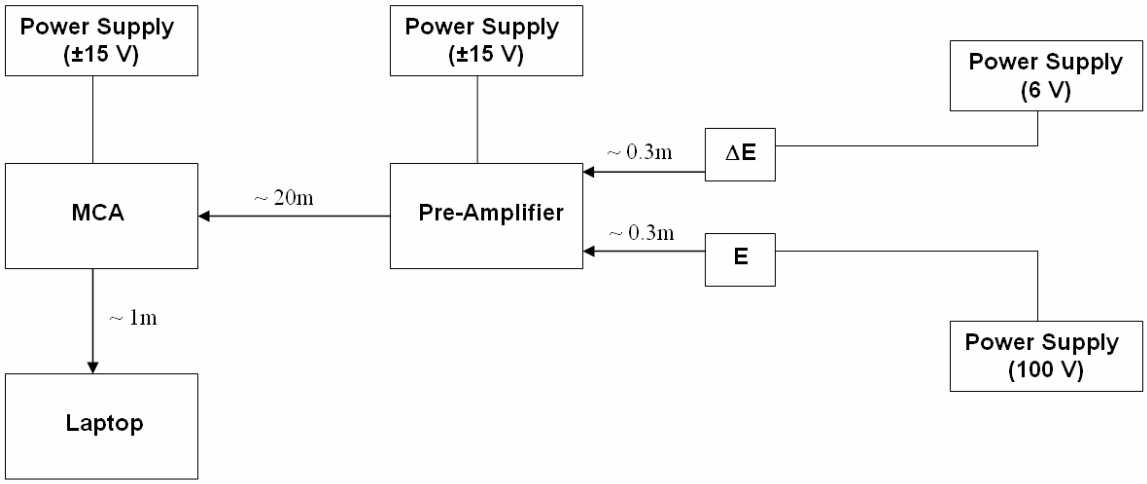

Figure 8-7: Schematic diagram of the complete ΔE-E experimental setup.

Calibration of the experimental system was completed at Politecnico di Milano using a calibrated pulser that was in turn calibrated through the use of multiple radioactive sources, similar to the method used in calibrating the SOI microdosimeter (Section 3.6). Separate calibrations for both the E and ΔE stages were completed, with the following calibration relationships used in this study:

$$Energy(E) = -2.29 + 3.86 \times Channel$$
$$Energy(\Delta E) = -0.02 + 0.28 \times Channel$$

Equation 8-2: Calibration relationships for the E and ΔE stages of the device used in this study.

8.5 SOI Experimental Setup

The experimental set-up utilised in this work was the same as that which was described in Section 5.2. A 10 μm thick SOI microdosimeter consisting of 4800 detector elements (40x120) with each cell having a physical size of 30x30 μm^2 was selected for this work. The calibration applied to this device is described in Section 3.6, while the method for determining the lineal energy spectra is described in Section 2.5. Using the methods described in [32] a tissue equivalent mean chord length of 19.05 μm was used in this work.

The device was contained within a 0.9 mm thick probe holder of aluminium which acted as a Faraday cage. A 4 μm thick aluminium window and 0.5 mm thick polyethylene converter was located immediately in front of the microdosimeter to allow the transport of secondary particles into the SV and detection of neutrons. The probe was placed at various points within a homogeneous polystyrene phantom at the central axis. The entire measurement system (i.e. power supply, main amplifier and MCA) was located within the experimental hall to minimise noise from extensively long cables. For all experimental measurements the dead time was kept stable at 10% with a low noise threshold set on the Multi-Channel Analyser (MCA) of 9 keV. The detector noise was approximately 15 keV or 0.8 TE keV/μm.

8.6 SOI Results & Discussion

SOI microdosimetry results were obtained for both an un-modulated and modulated 100 MeV proton beam within a homogeneous polystyrene phantom.

8.6.1 Un-Modulated 100 MeV Proton Beam

The measurement positions utilising SOI microdosimeter along an un-modulated 100 MeV Bragg Peak are illustrated in Figure 8-14. Positional (X-axis) error bars of ±1 mm are placed on these points to account for small variations in air gap and also some misalignment of the polystyrene phantom such that it was not perfectly normal to the incident radiation beam. A series of measurements was completed to assess the change in microdosimetry spectra as a function of position along the Bragg curve, with multiple measurements made around the Bragg peak where change in the microdosimetry properties of the incident radiation field is greatest.

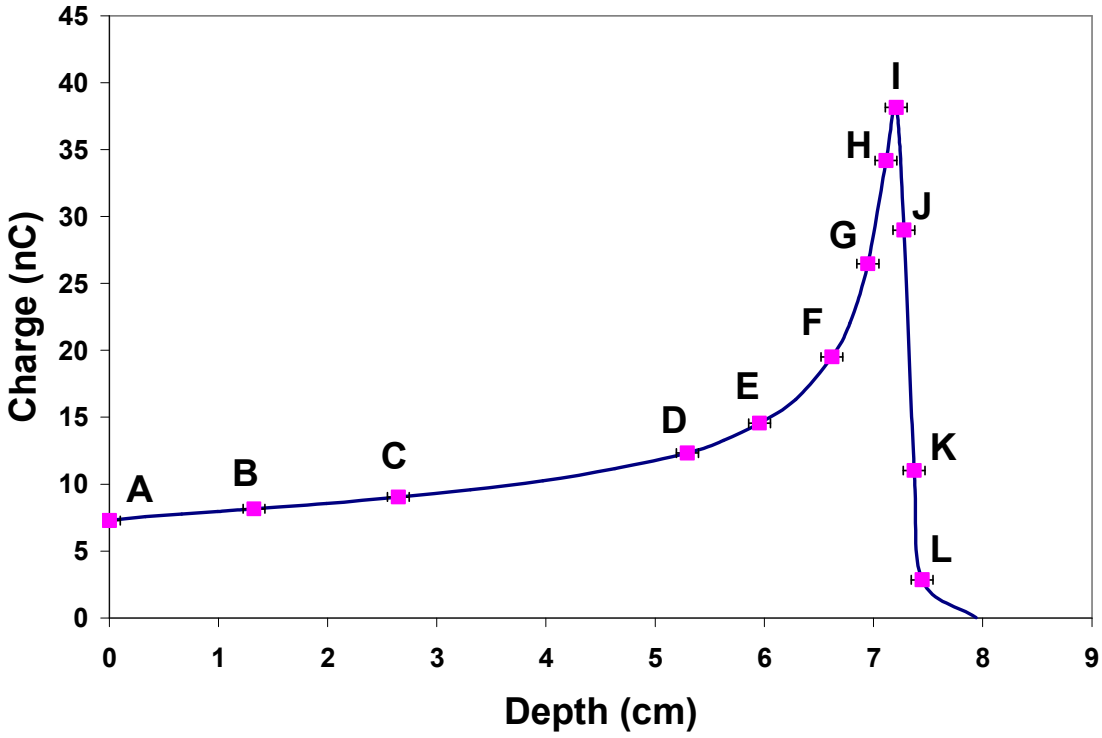

Figure 8-8: Measurement positions (A-L) along a 100 MeV un-modulated proton Bragg peak within a homogeneous polystyrene phantom.

Figure 8-9 shows the energy deposition spectra for the various measurement positions along the Bragg curve of a 100 MeV un-modulated proton beam. In this case the noise edge is approximately 15-20 keV or 0.8-1 keV/μm in tissue. As such, at the surface of the phantom and in the plateau region measurement of the proton peak is unobtainable because the LET of the incident proton beam (approximately 1.35 keV/μm [91]) ensures the primary proton peak lies below the noise threshold of the device [103]. However, near the Bragg peak and on the distal edge, the energy spectra moves to higher energy depositions which is indicative of a slowing proton. This has been observed previously both with TEPC's [18] and SOI microdosimeters [21]. In this spectra the maximum energy deposited is approximately 700 keV, which corresponds to the maximum energy deposition of a proton traversing 10 μm of Si, or normally incident on the SOI device [91]. Events (of frequency 10 or less) do occur at energy depositions higher than 700 keV and these are the direct result of protons scattering obliquely through the volume, being scattered within the SV, or from other nuclear secondaries (because of the low incident energy this is unlikely).

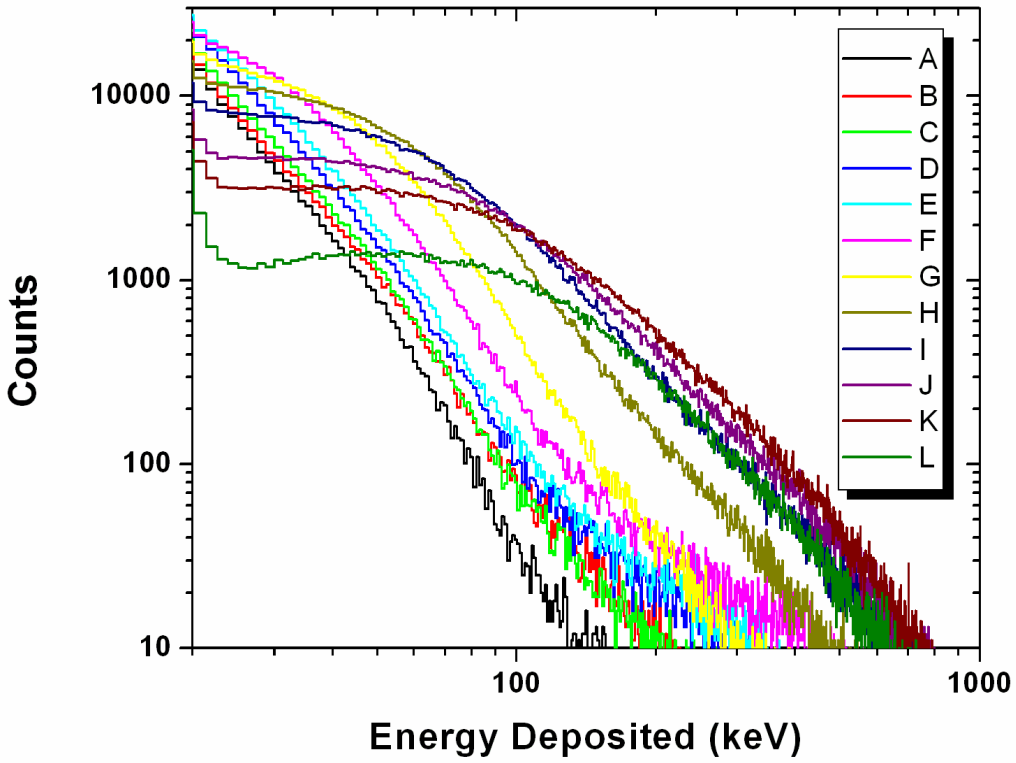

Figure 8-9: Energy deposition spectra for various points along an un-modulated proton Bragg curve as stipulated by Figure 8-8.

The energy deposition spectra was converted into a lineal energy spectra and is presented in Figure 8-10. This clearly illustrates how the system noise prevents detection of the main proton peak at the surface of the phantom and in the plateau region of the Bragg curve. For measurements around the Bragg curve the shift to higher lineal energies is clearly evident with the proton peak observable from position **F** onwards. This is not caused by pileup but rather slowing of the incident proton. Lineal energy events are detected up to 140 keV/μm, which correspond to stopping protons depositing maximum energy within the SOI SV along a chord length greater than the thickness of the device.

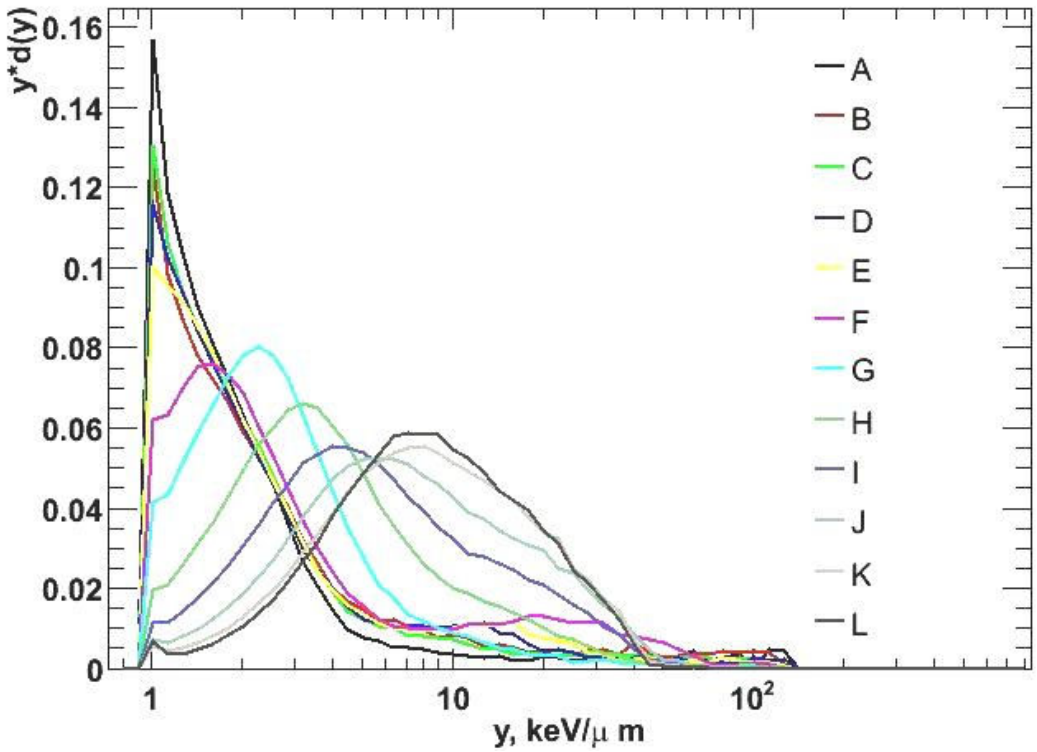

Figure 8-10: Microdosimetry spectra for various points along an un-modulated proton Bragg curve as stipulated by Figure 8-8.

These results clearly indicate that it is possible to discern the change in microdosimetry spectra of a therapeutic proton beam utilising an SOI microdosimeter. The results presented here are in excellent agreement with previously published data [18, 21]. Because of the devices small size, it was possible to complete measurements with a high degree of spatial resolution, especially around the Bragg peak, which is an improvement over larger TEPC chambers. Further improvements in chip design could be undertaken to improve the low noise level which currently prevents measurement of events below 0.8-1 TE keV/μm, and as a consequence the complete lineal energy spectra of primary protons is unobtainable. Regardless, this device provides a complete data set for measurements around the Bragg peak which is the area of interest in radiation therapy applications. Radiobiology would benefit from the use of such a device to measure the lineal energy spectra of the incident radiation fields and correlate changes in this spectra with radiobiological effect.

8.6.2 Modulated 100 MeV Proton Beam

The measurement positions utilising a SOI microdosimeter along a modulated 100 MeV Bragg Peak are illustrated in Figure 8-11. Positional (X-axis) error bars of ±1 mm are placed on these points to account for small variations in air gap and also some misalignment of the polystyrene phantom such that it was not perfectly normal to the incident radiation field. A complete series of measurements was completed to assess the change in microdosimetry spectra as a function of position along the SOBP, with multiple measurements made in the plateau region of the SOBP and distal edge where change in the microdosimetry properties of the incident radiation field is greatest and of most interest in radiation therapy.

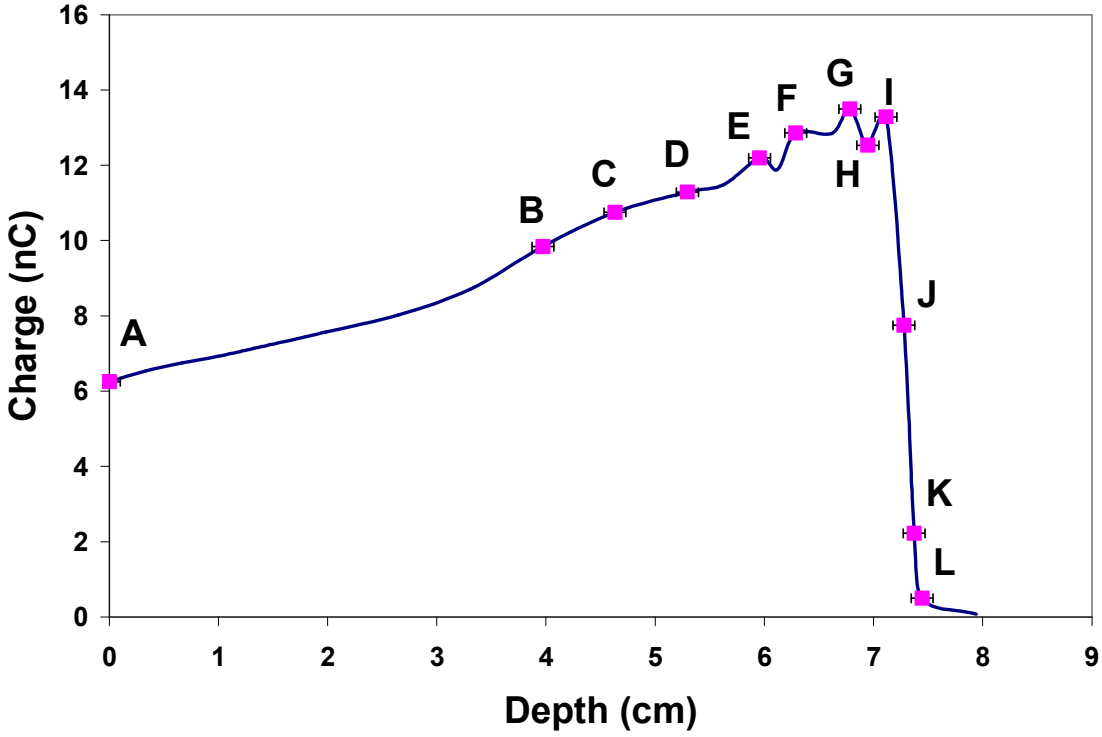

Figure 8-11: Measurement positions (A-L) along a 100 MeV modulated proton Bragg peak within a homogeneous polystyrene phantom.

The energy deposition spectra for the modulated 100 MeV proton beam is displayed in Figure 8-12. This is very similar to the spectra produced in the un-modulated case with a minimum detectable energy of 15-20 keV and a maximum energy detected (with a frequency of events larger than 10) of approximately 700 keV. Particles are detected

above 700 keV, as in the un-modulated case, whose cause has been previously discussed. It is clear that in the un-modulated case, the transfer from plateau region to sharp Bragg peak results in a rapid shift to higher energy deposition events. Conversely in the SOBP this shift is more gradual through the superposition of many individual Bragg curves to form the SOBP.

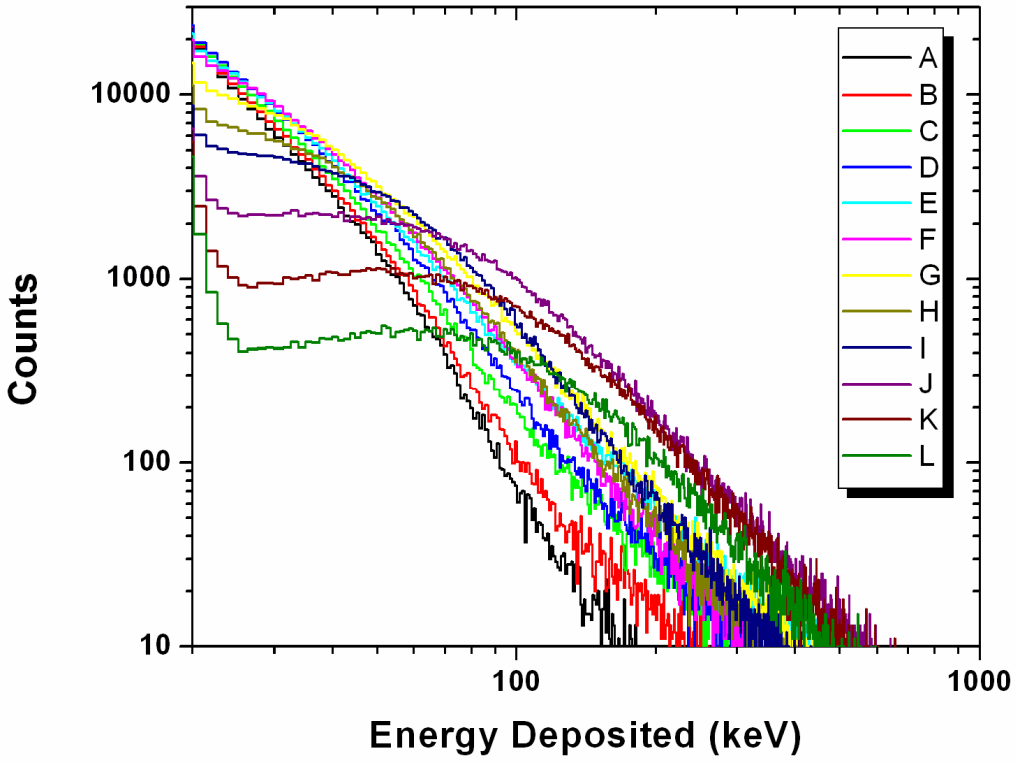

Figure 8-12: Energy deposition spectra for various points along a modulated proton Bragg curve as stipulated by Figure 8-11.

The measured energy deposition spectra was converted into a microdosimetry spectra and is displayed in Figure 8-13. As in the case of the un-modulated Bragg peak, noise prevents detection of the main proton peak at the surface of the phantom and proximal to the SOBP. Accurate measurements are possible in the distal third of the SOBP and the distal edge with the proton peak clearly discernable. Unlike the un-modulated case the shift to higher lineal energies is more gradual which is indicative of the SOBP. Further, such results would indicate a more gradual change in the radiobiological effect of protons when compared to an un-modulated proton beam. The distal portion of the SOBP is however very similar in all respects to the unmodulated case (although lower in fluence through modulation of the incident radiation field). As such, it could be assumed that the

biological effect in this region would be similar, however, this should be tested through further biological modelling and radiobiological experiments using thin-films (Section 10).

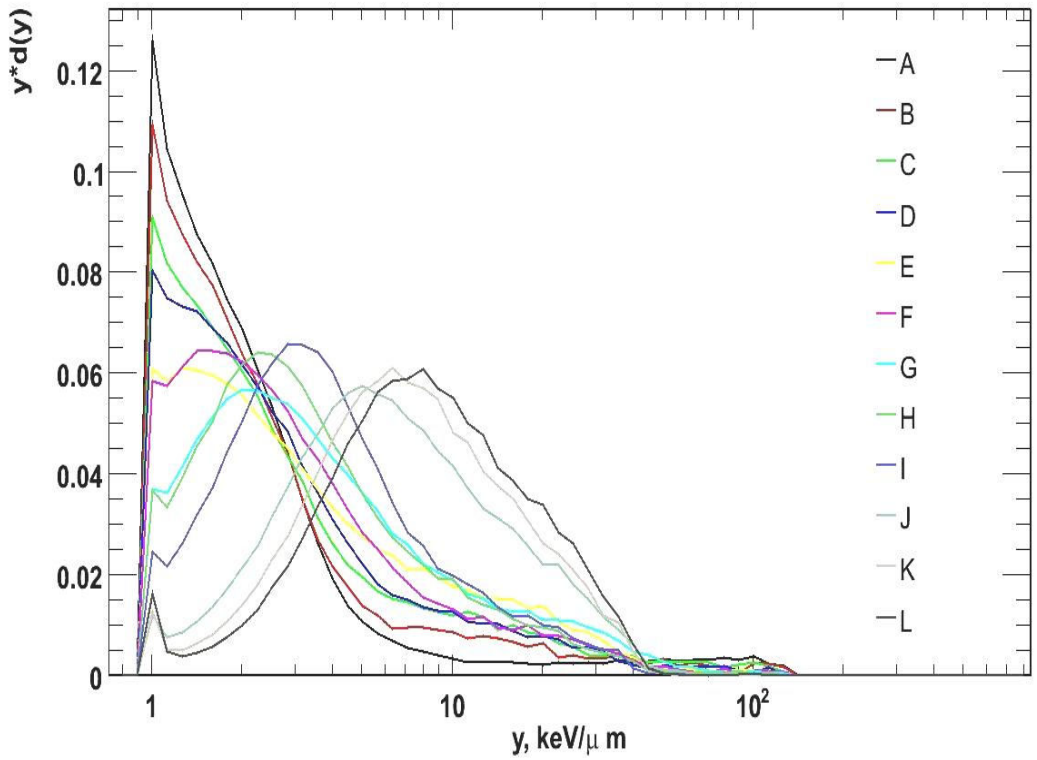

Figure 8-13: Microdosimetry spectra for various points along a modulated proton Bragg curve as stipulated by Figure 8-11.

The SOI microdosimeter has shown that it is a useful tool in measuring the microdosimetry spectra of therapeutic modulated and un-modulated proton beams and further supports previous experiments in this field [21]. The lower noise level prevents complete measurement of the incident radiation field and plateau region in both the modulated and un-modulated cases. Further improvements in the low noise threshold of the device would improve its performance in therapeutic primary beam applications. In its current form, the SOI microdosimeter is a useful tool in low energy proton and heavy ion radiation fields where the main energy peak has a value greater than 1 TE keV/μm. It is also a very useful tool in measuring the out of field dose equivalent (displayed in Section 4) where the energy of recoil protons is predominantly larger than 20 keV.

8.7 ΔE-E Results & Discussion

Coincidence and E detector results were obtained for a range of depths along a modulated and un-modulated 100 MeV proton Bragg Peak.

8.7.1 Un- Modulated 100 MeV Proton Beam

The measurement positions utilising the ΔE-E detector along an un-modulated 100 MeV Bragg Peak are illustrated in Figure 8-14. Positional (X-axis) error bars of ±1 mm are placed on these points to account for small variations in air gap and also some misalignment of the polystyrene phantom such that it was not perfectly normal to the incident radiation beam. Shallower coincidence measurement positions were not possible due to the noise level of the ΔE stage of the telescope.

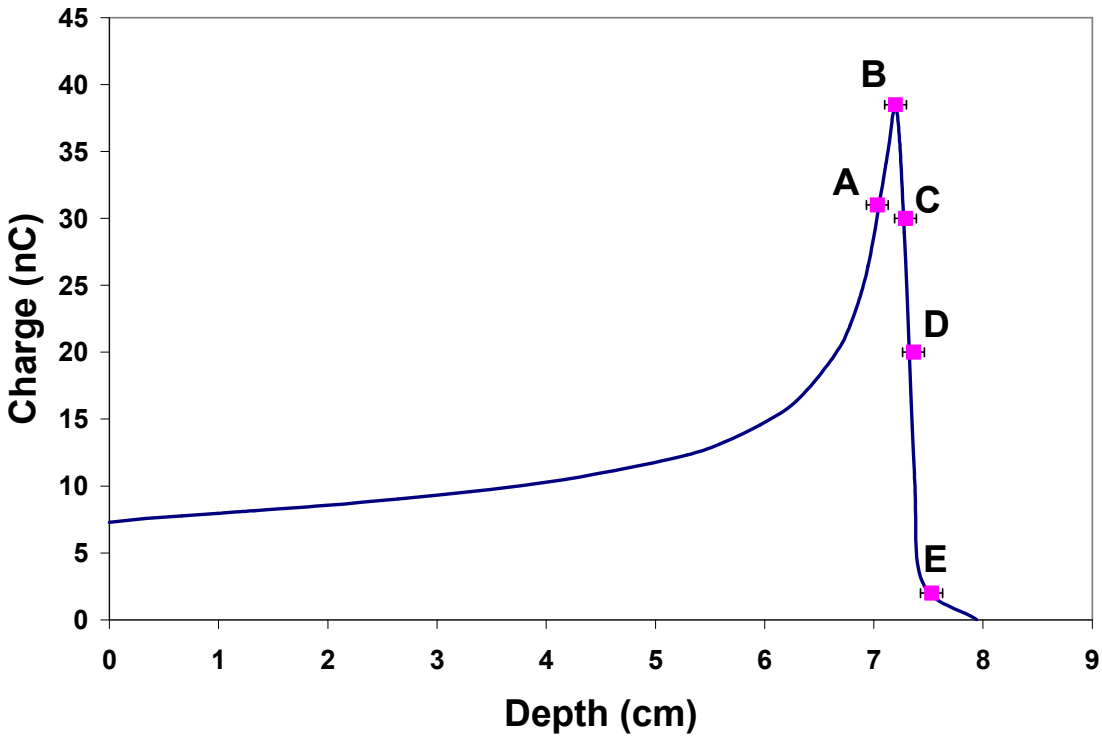

Figure 8-14: Unmodulated 100 MeV proton depth dose curve with associated ΔE-E device measurement positions (A-E)

Results obtained using the E detector only (i.e. energy deposition spectra within a 500 μm thick planar device) are displayed in Figure 8-15 for the 5 measurement positions outlined in Figure 8-14 in addition to a measured value at the phantoms surface. The surface measurement of the 100 MeV protons clearly indicates the LET of such particles

with a peak energy deposition of 600 keV in the 500 μm device or 1.2 keV/μm. This corresponds well with the theoretical value of 1.36 keV/μm provided by SRIM [91]. The LET of the particle clearly increases with depth as the peak moves to higher energy deposition values and begins to flatten as particles are scattered and deposit different amounts of energy within the SV from a maximum value of approximately 8 MeV (the proton edge).

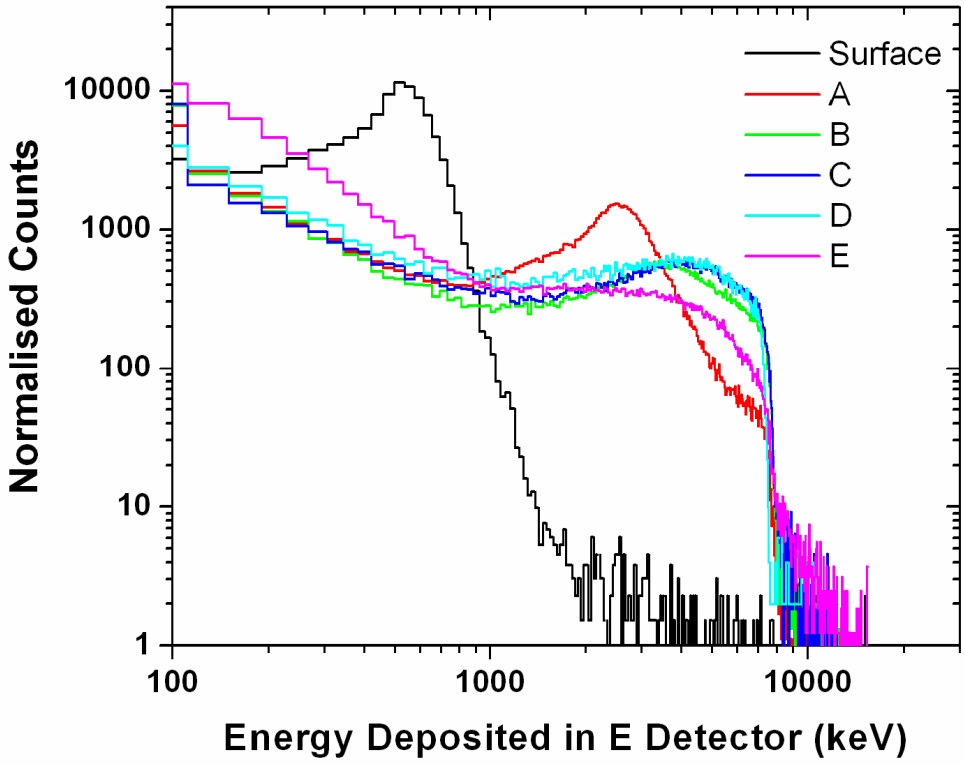

Figure 8-15: Spectra obtained with the 500 μm thick E stage for the 5 measurement positions described in Figure 8-14 and also at the surface of the phantom.

Maximum energy deposition within the E detector (8 MeV) corresponds to the range of the proton in 500 μm silicon (see Figure 8-16). Energy depositions larger than 8 MeV correspond to particles either obliquely striking the detector, scattering within the detector, stopping within the SV or interacting directly with the SV through nuclear interaction (less likely due to the relatively low energy of the primary beam). Such events are observed with increasing frequency at the distal edge of the Bragg peak. Further, as the acquisition times were much larger for distal edge measurements due to poor statistics in this region, it is possible that energy depositions above 8 MeV are

caused by neutrons that are statistically rare in this configuration with an incident proton energy of 100 MeV and minimal beam modifying devices.

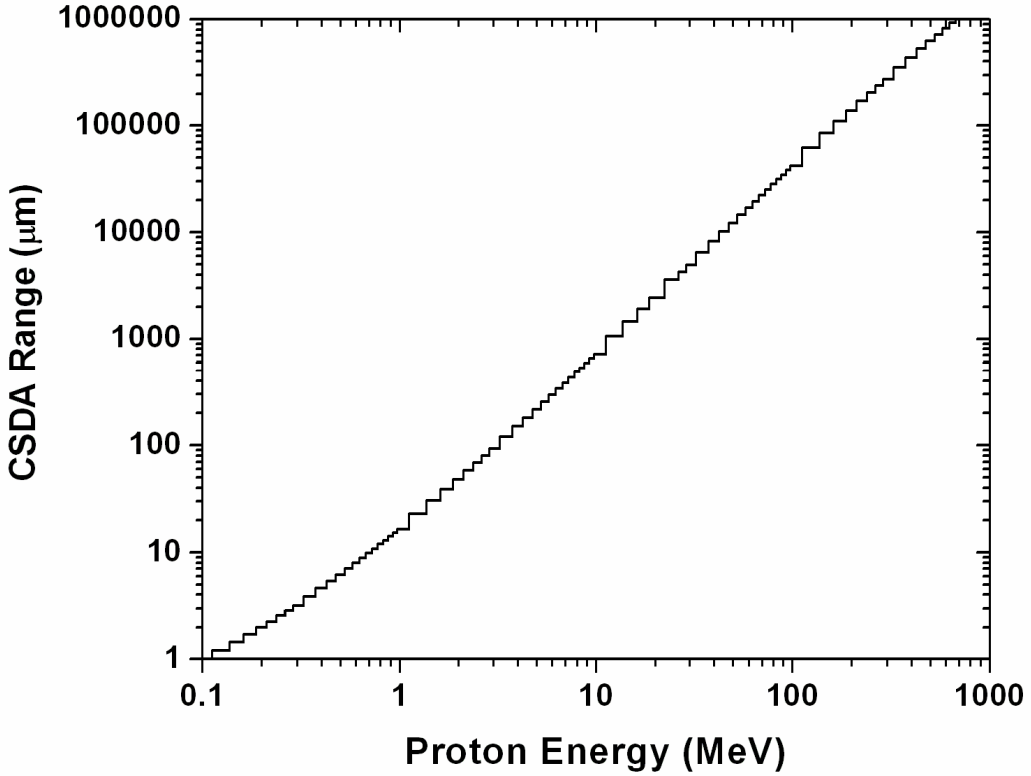

Figure 8-16: Relationship between proton range and energy as provided by NIST [35] and SRIM [91].

The main feature of the ΔE-E telescope is to collect signal from both detectors in coincidence and create a two-dimensional plot of ΔE detector response (or LET) against the total energy deposited within the ΔE+E detector. The five graphs contained within Figure 8-17 display the response of the ΔE-E telescope at various positions along the Bragg Peak as governed by the measurement positions displayed in Figure 8-14.

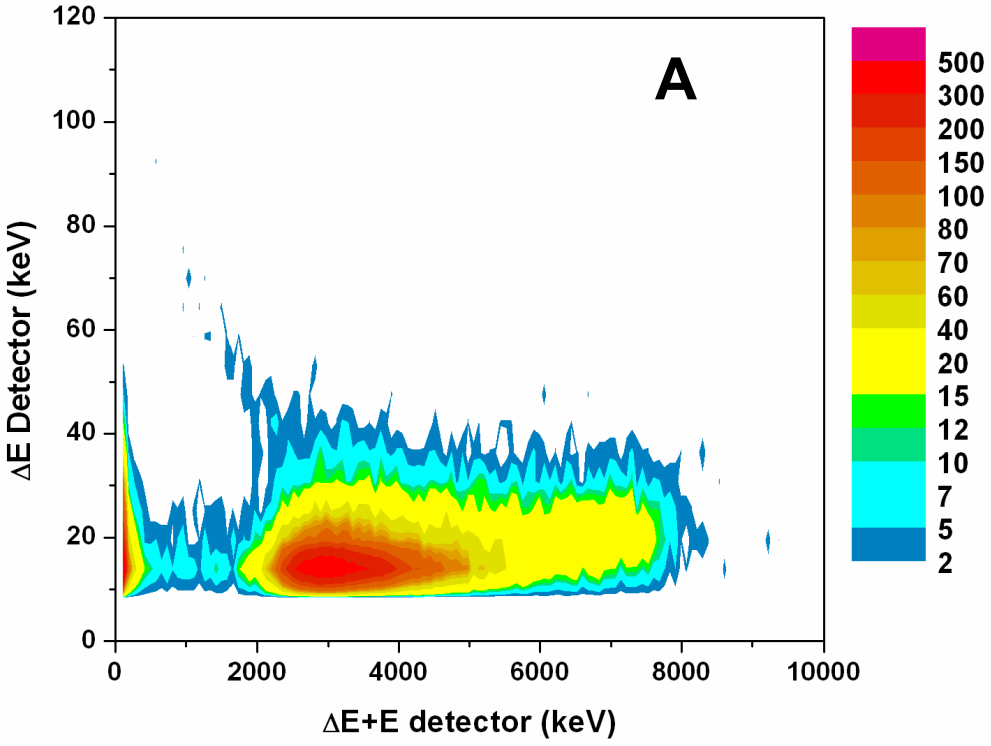
A
ΔE Detector (keV)
ΔE+E detector (keV)
0
20
40
60
80
100
120
0
2000
4000
6000
8000
10000
500
300
200
150
100
80
70
60
40
20
15
12
10
7
5
2

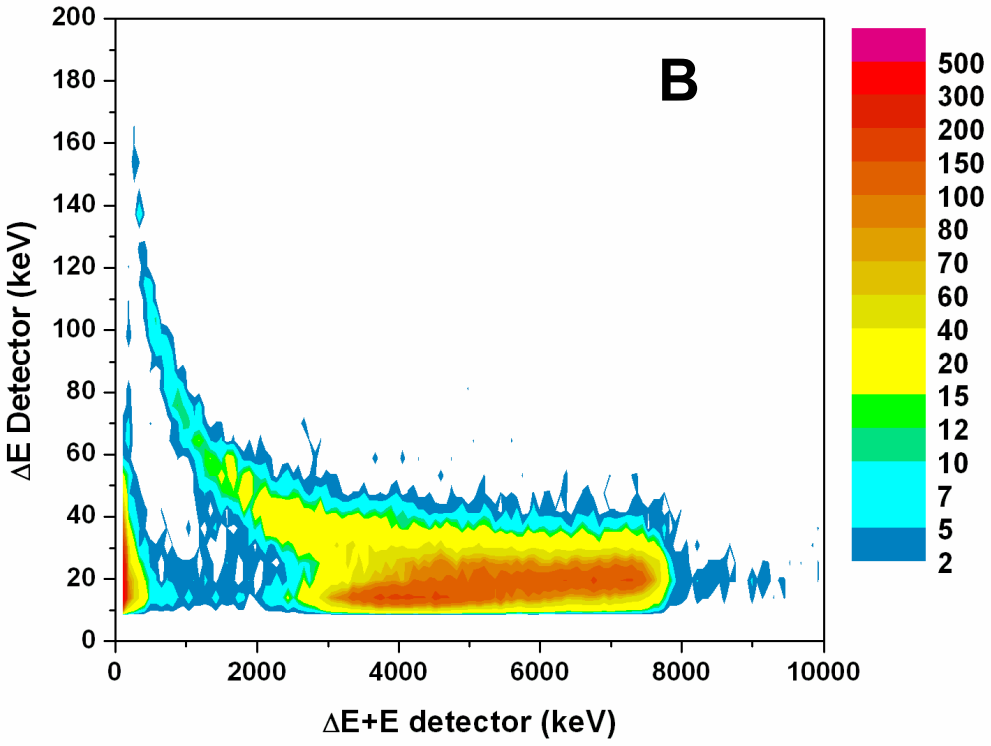
B
ΔE Detector (keV)
ΔE+E detector (keV)
0
20
40
60
80
100
120
140
160
180
200
0
2000
4000
6000
8000
10000
500
300
200
150
100
80
70
60
40
20
15
12
10
7
5
2

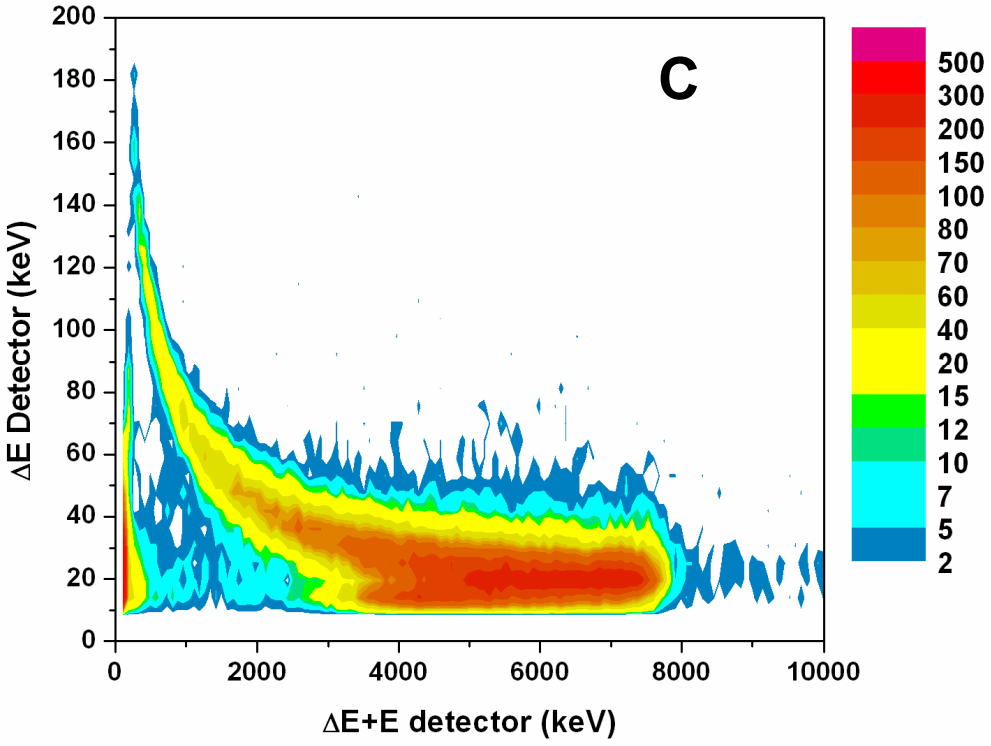
C
ΔE Detector (keV)
ΔE+E detector (keV)
0
20
40
60
80
100
120
140
160
180
200
0
2000
4000
6000
8000
10000
500
300
200
150
100
80
70
60
40
20
15
12
10
7
5
2

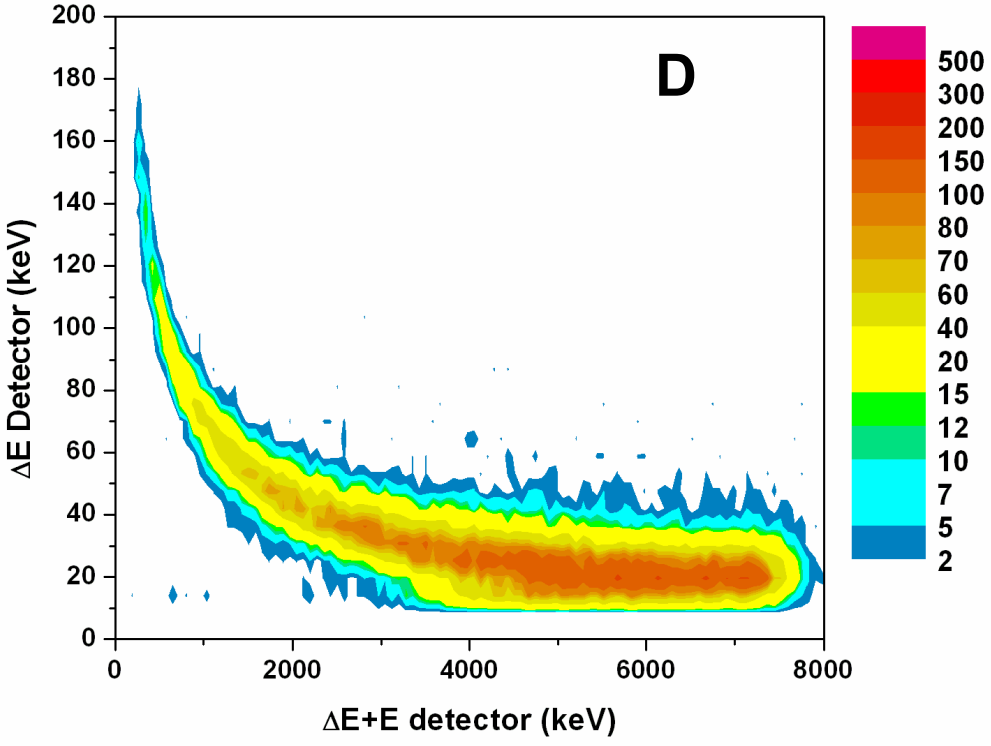
D
ΔE Detector (keV)
ΔE+E detector (keV)
0
20
40
60
80
100
120
140
160
180
200
0
2000
4000
6000
8000
500
300
200
150
100
80
70
60
40
20
15
12
10
7
5
2

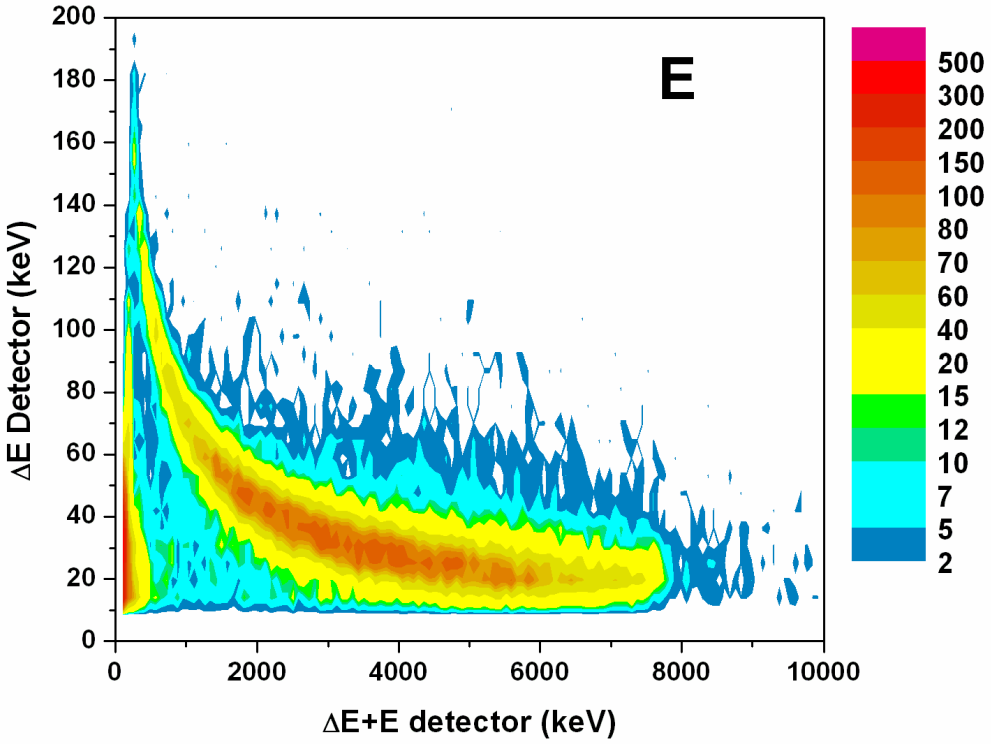

Figure 8-17: Results obtained with the ΔE-E telescope for an unmodulated 100 MeV proton beam. The labelled results (A-E) correspond to measurement positions outlined in Figure 8-14.

The coincidence results presented in Figure 8-17 deliver a great deal of information on the proton Bragg peak. The initial measurement position (**A**) which was proximal to the BP shows a band of events with an LET of approximately 15 keV/μm, and total energy deposition within the ΔE+E detector of 3 MeV. Proximal to the BP there are few high LET events. Measurement position **B**, which was at the maximum amplitude of the BP, shows a clear change in the profile of the radiation field which is reflected in the modification of the locus on the ΔE-E coincidence plane corresponding to proton events. The main component of energy deposition events is at an LET of 15 keV/μm, however total energy depositions within the ΔE+E detector shift from a peak at 3 MeV to a band from 3-7.5 MeV. This clearly indicates how the protons are slowing and depositing a larger amount of energy within the 500 μm E detector. High LET events were also measured at point **B** which were not present proximal to the BP.

Measurement positions **C** and **D** lie along the distal edge of the un-modulated BP. These measurements are characterised by a bulk of the events having an LET of 15

keV/μm, but with a higher portion of higher energy deposition events within the E detector. This trend is clearly evident in measurement position **D** with almost no events below 3 MeV for the ΔE+E detector response. The high LET "tail" on the locus also increases in strength in this region as more protons slow and stop within the detector volume.

Measurement position **E** was at the base of the distal edge of the Bragg Peak and displays increased levels of low energy deposition events within the E detector, and corresponding LET events from 10-100 keV/μm. This signal is produced by low energy protons depositing large amounts of energy in the ΔE stage and stopping with low energy deposition in the E stage. For example a 0.2 MeV particle with a range in Si of 2 μm will deposit approximately 90 keV in the ΔE stage with the balance of the energy deposited in the E stage [91]. The exact localisation of energy deposited in the ΔE+E stage is difficult to witness due to scale but is clearly observed in this region. These events were not observed at the previous measurement position which was only 1.7 mm shallower in the polystyrene phantom and is only discernible through the superior spatial resolution of the device. Such events should not be seen at shallower depths as protons are not of sufficiently low energy to produce such signal. This further highlights that small changes in position in this region produce dramatic changes in proton energy deposition spectra that will be linked to RBE the meaning of which will be discussed and introduced in the following section. Events produced of low LET and low energy depositions at this measurement position are thought to be caused by gamma events, i.e. Compton electrons. Further, a spectra of high LET events outside the locus is also observed. It is expected that these are caused by neutrons detected along the central axis of the beam which is impossible to identify using one-dimensional microdosimetry techniques. This one measurement position highlights how the two-dimensional collection of proton data provides superior information on the changing nature of the proton beam with minimal changes in phantom thickness.

The measurement technique and data presented here allow for observation of the changing radiation field which makes up an un-modulated proton BP as it provides

information on changing proton LET and energy as a function of depth within the phantom. Information on higher energy proton radiation fields (used in the treatment of deep seated tumours) is advisable as such proton fields exhibit a higher cross section for inelastic nuclear interactions [78]. The high LET secondaries produced by such interactions can be detected by this system (as loci which are dependant on the ion species) and their effect quantified. Within this work the cross section of inelastic interactions for 100 MeV protons is negligible, which is evident through the absence of multiple loci (representing different nuclear products) in the measured coincidence spectra. Correlation with in-vitro cell survival or animal biological data may allow for the determination of pseudo RBE which is relevant to beam quality at a given point within a proton radiation field, further enhancing the use of this system. Potentially, the most important application of ΔE-E detector system is particle identification for Monte Carlo verification, which provides a more robust verification of Monte Carlo codes than that which has been established with the SOI microdosimeter.

8.7.2 Modulated 100 MeV Proton Beam

The measurement positions utilising the ΔE-E detector along a modulated 100 MeV Bragg Peak are illustrated in Figure 8-18. Positional (X-axis) error bars of ±1 mm are placed on these points to account for small variations in air gap and also some misalignment of the polystyrene phantom such that it was not perfectly normal to the incident radiation beam.

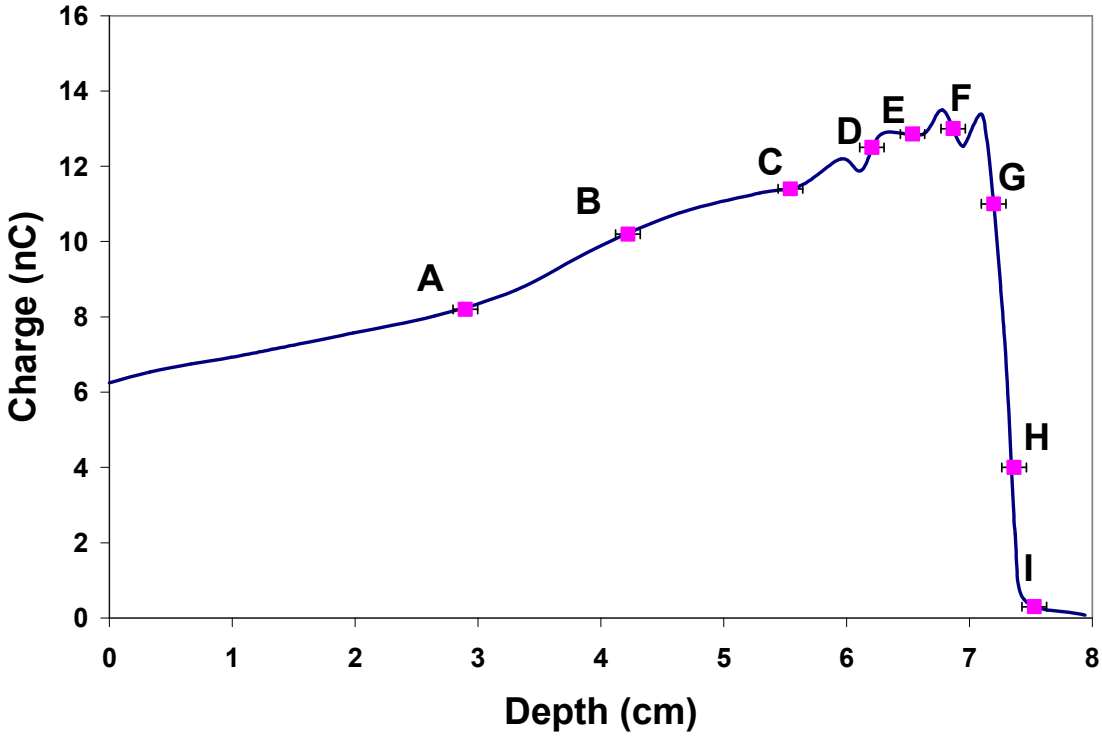

Figure 8-18: Modulated 100 MeV proton depth dose curve with associated ΔE-E device measurement positions (A-I)

Results obtained using the E detector only (i.e. energy deposition spectra within a 500 μm thick planar device) are displayed in Figure 8-19 for the nine measurement positions outlined in Figure 8-18 in addition to a measured value at the phantoms surface. As in the case of the un-modulated 100 MeV proton beam, the surface measurement has a peak energy deposition of approximately 600 keV. Again this correlates well with theoretical LET values provided by SRIM [91]. The LET of the particle clearly increases with depth as the peak moves to higher energy deposition values. The spectra begins to flatten at the distal edge of the SOBP as particles are scattered and deposit different amounts of energy within the SV from a maximum value of approximately 8 MeV, the significance of which has been discussed previously for the un-modulated proton case.

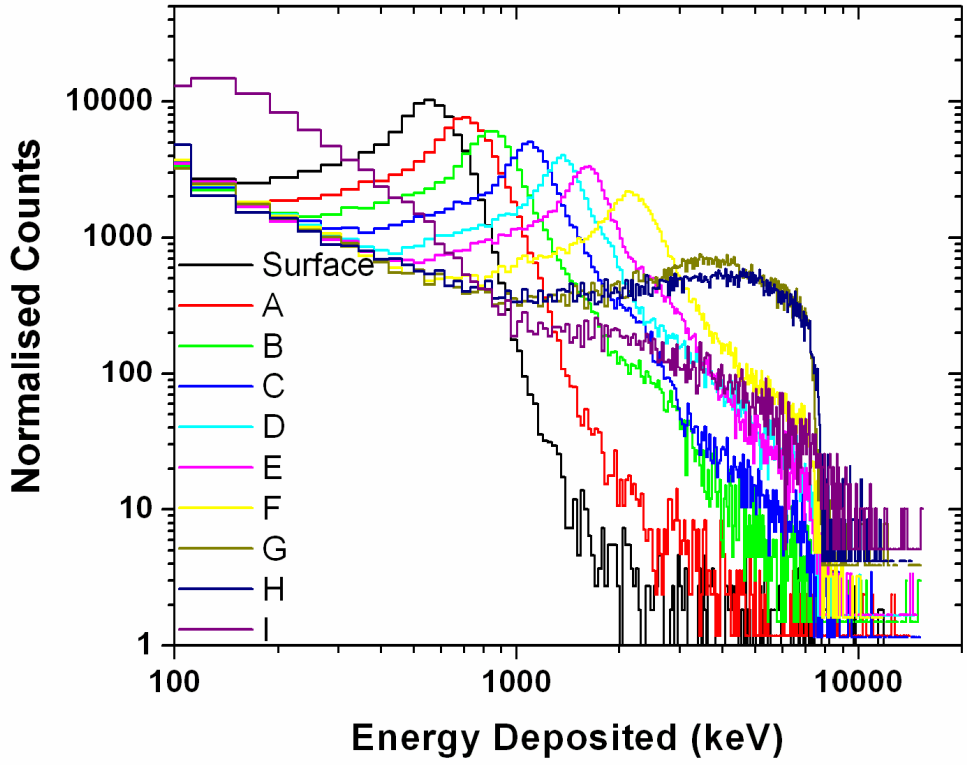

Figure 8-19: Spectra obtained with the 500 μm thick E stage for the nine measurement positions described in Figure 8-18 and also at the surface of the phantom.

The nine graphs contained within Figure 8-20 display the response of the ΔE-E telescope at various points along the SOBP as governed by the measurement positions displayed in Figure 8-18.

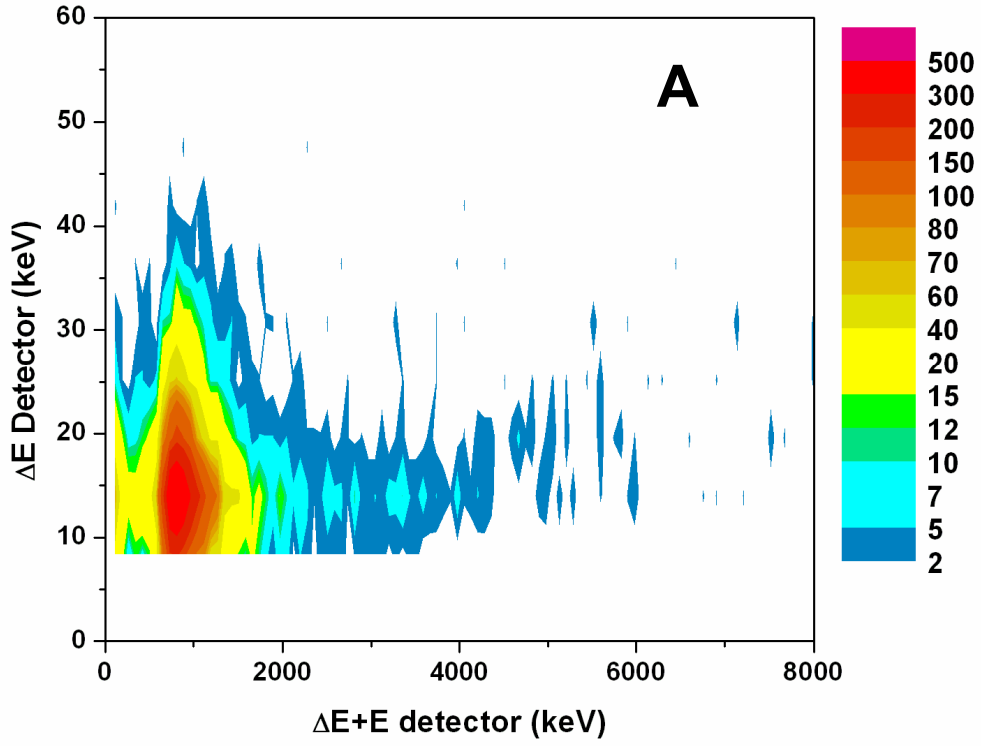
A
ΔE Detector (keV)
ΔE+E detector (keV)
0
10
20
30
40
50
60
0
2000
4000
6000
8000
500
300
200
150
100
80
70
60
40
20
15
12
10
7
5
2

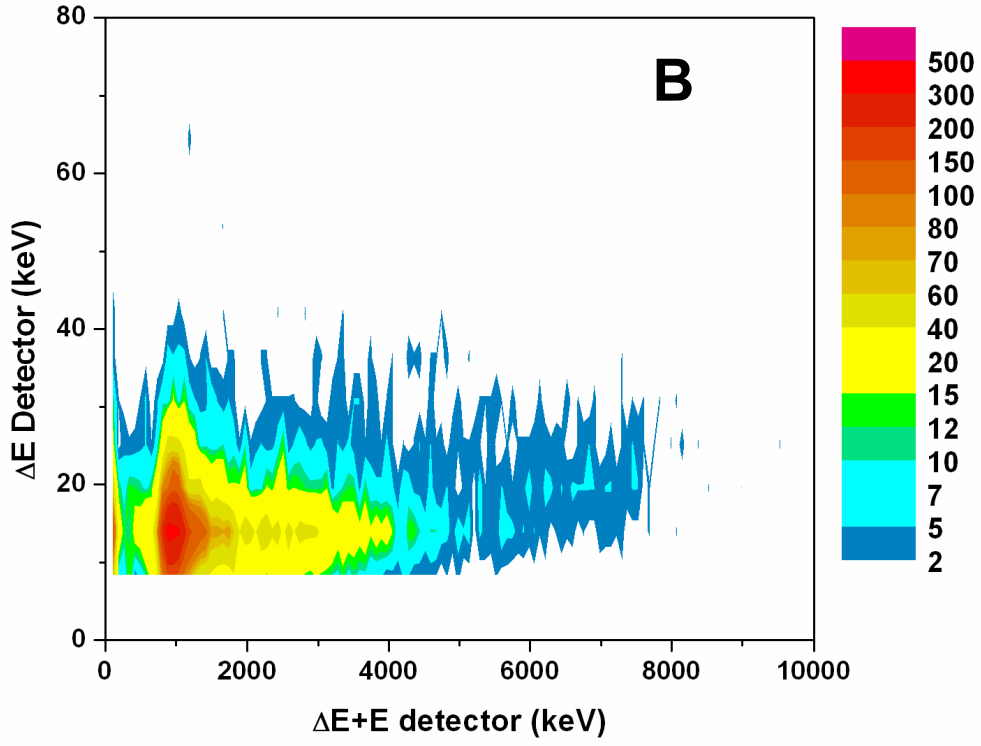
B
ΔE Detector (keV)
ΔE+E detector (keV)
0
20
40
60
80
0
2000
4000
6000
8000
10000
500
300
200
150
100
80
70
60
40
20
15
12
10
7
5
2

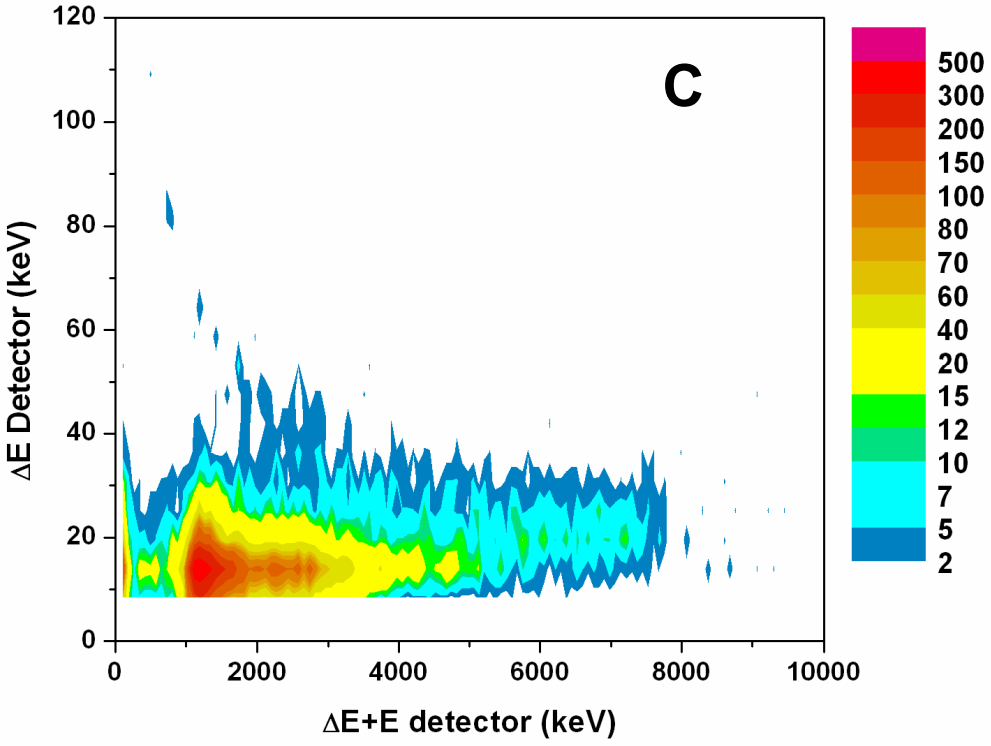
C
ΔE Detector (keV)
ΔE+E detector (keV)
0
20
40
60
80
100
120
0
2000
4000
6000
8000
10000
500
300
200
150
100
80
70
60
40
20
15
12
10
7
5
2

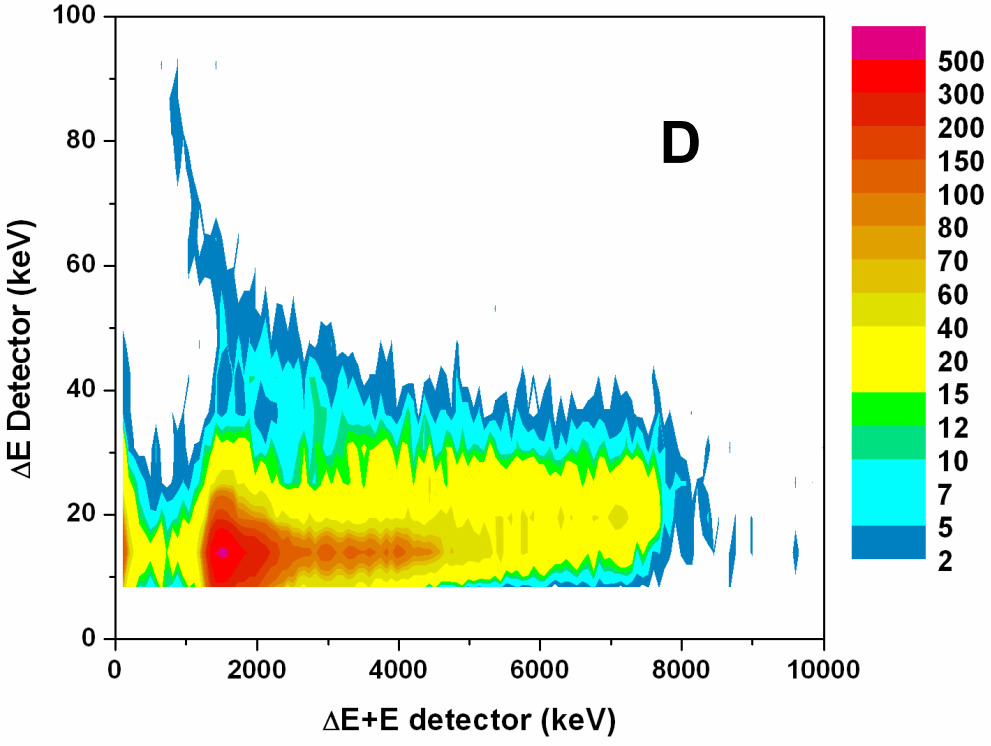
D
ΔE Detector (keV)
ΔE+E detector (keV)
0
20
40
60
80
100
0
2000
4000
6000
8000
10000
500
300
200
150
100
80
70
60
40
20
15
12
10
7
5
2

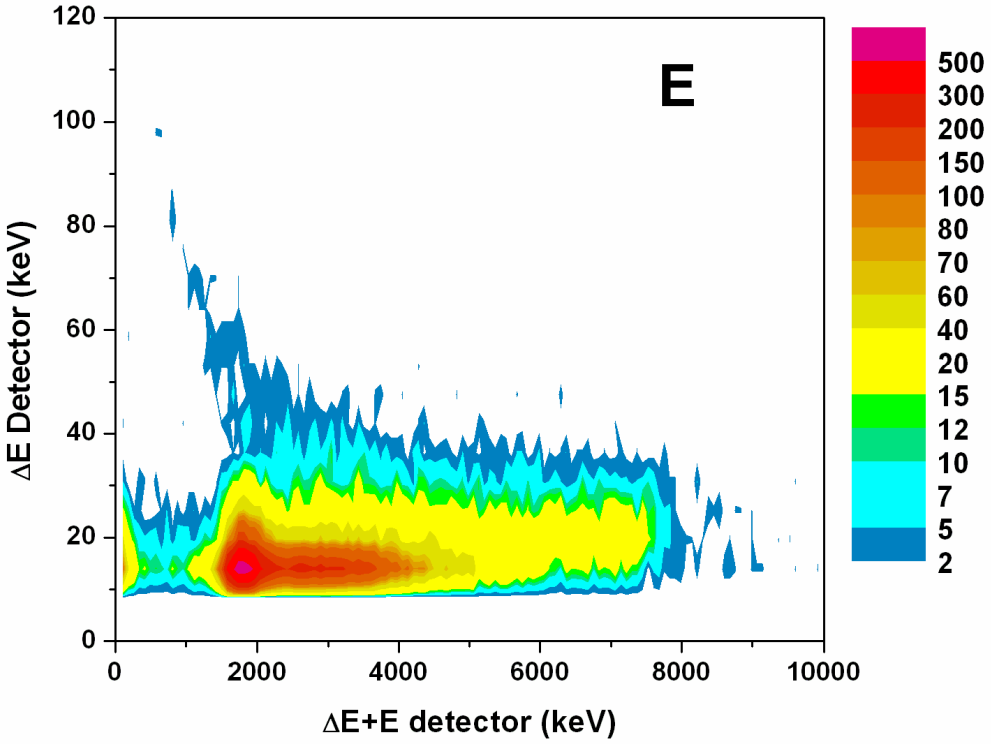
E
ΔE Detector (keV)
ΔE+E detector (keV)
0
20
40
60
80
100
120
0
2000
4000
6000
8000
10000
500
300
200
150
100
80
70
60
40
20
15
12
10
7
5
2

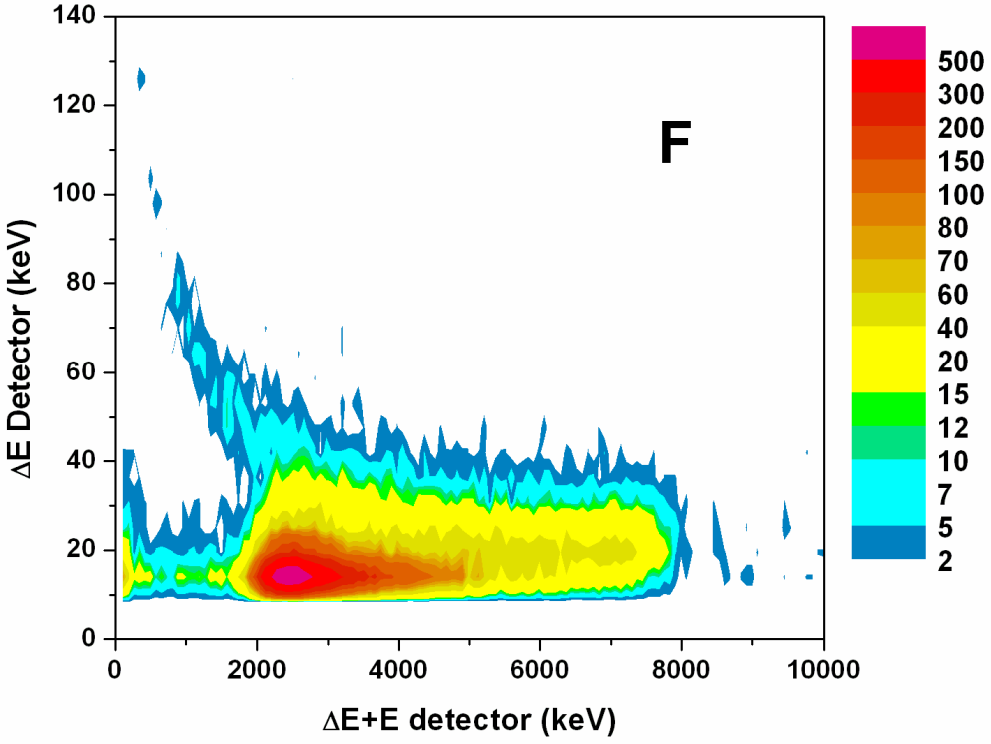
F
ΔE Detector (keV)
ΔE+E detector (keV)
0
20
40
60
80
100
120
140
0
2000
4000
6000
8000
10000
500
300
200
150
100
80
70
60
40
20
15
12
10
7
5
2

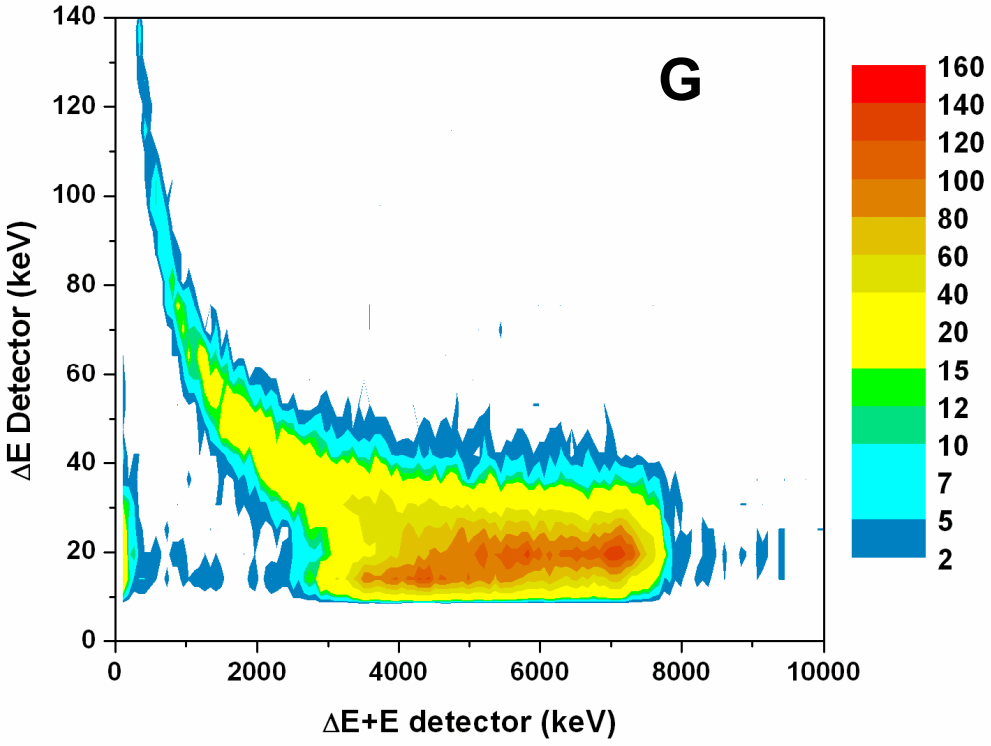
G
ΔE Detector (keV)
ΔE+E detector (keV)
0
20
40
60
80
100
120
140
0
2000
4000
6000
8000
10000
160
140
120
100
80
60
40
20
15
12
10
7
5
2

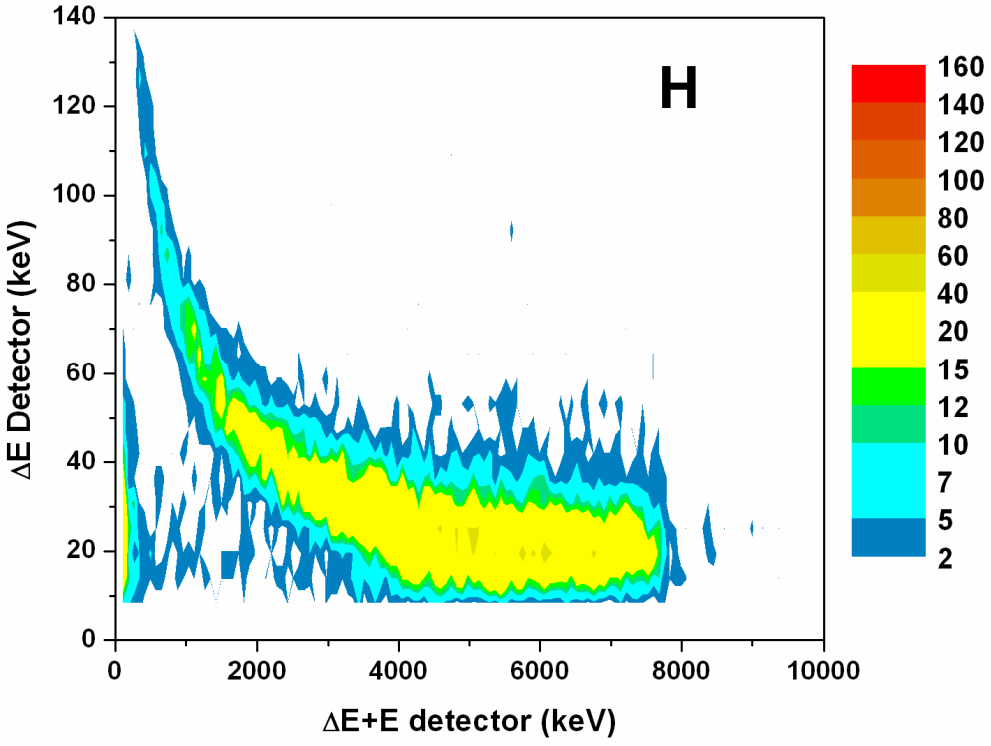
H
ΔE Detector (keV)
ΔE+E detector (keV)
0
20
40
60
80
100
120
140
0
2000
4000
6000
8000
10000
160
140
120
100
80
60
40
20
15
12
10
7
5
2

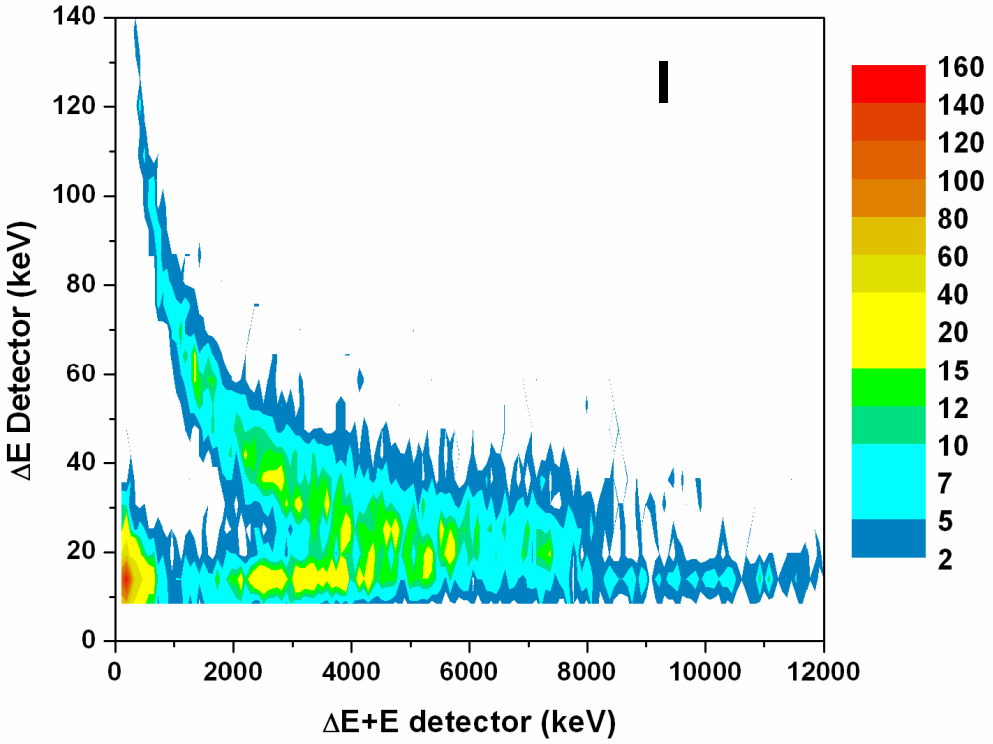

Figure 8-20: Results obtained with the ΔE-E telescope for a modulated 100 MeV proton beam. The labelled results (A-I) correspond to measurement positions outlined in Figure 8-18.

The results displayed in Figure 8-20 give an indication of the changing nature of the modulated proton beam as it traverses the polystyrene phantom. The nine measurement positions can be broken up into four subsections to allow for a more targeted discussion of the results. Positions **A** and **B** lie proximal to the SOBP, positions **C-F** lie on the SOBP, positions **G** and **H** lie on the distal edge, while position **I** lies at the base of the distal edge.

Firstly, the two measurement positions proximal to the SOBP (**A** and **B**) show no high LET component in the coincidence spectra. Such a result is expected as no slowing protons associated with a Bragg Peak are present in this region. Further, the incident proton energy is sufficiently low to have small cross sections for nuclear interactions. Almost all events have an LET value of 10-30 keV/μm with a spectra of energy deposition events in the ΔE+E detector from 0 to 4 MeV and 0 to 7 MeV respectively for the two measurement positions. The peak values detected corresponded to an LET of

approximately 15 keV/μm and 1 MeV energy deposition within the ΔE+E detector in both cases.

Measurement positions along the SOBP (**C-F**) exhibited the formation of a high LET tail and locus which is representative of the multiple Bragg Peaks used in the formation of the SOBP. The mix of crossing, slowing and stopping protons causes the detection of this high LET tail. However, as in the case of the proximal measurements most events were encountered in an LET band of 10-30 keV/μm with a total energy deposition within the ΔE+E detector of 0-8 MeV. As the measurement positions approach the distal edge of the SOBP the peak energy in the coincidence spectra increases from approximately 1 MeV at measurement point **C** to 2.5 MeV at measurement point **F**. This reflects the trend illustrated in Figure 8-19. These trends could indicate a continual increase in biological effect in this region which was investigated through the application of a matrix of radiobiological effect based on established in-vitro data to the measured data to determine average RBE.

Measurement positions **G** and **H** lie on the distal edge of the SOBP and as in this region all protons are slowing and/or stopping there are no events below 2-3 MeV energy deposition in the ΔE+E detector with low LET. Further, a greater portion of events lie in the high LET region of the proton locus. The high LET tail present in the coincidence spectra extends to a maximum value of 140 keV/μm. A majority of energy deposition events lie in the LET region of 20-40 keV/μm with energy depositions in the ΔE+E detector from 4-8 MeV. The increase in high LET events in this region, with an additional decrease of low LET events would further indicate increases in radiobiological effect.

Finally, position **I** lies at the base of the distal edge and displays increased levels of low energy deposition events within the E detector, and low LET events. These are most likely caused by photons present in the radiation field. Further, a spectra of low LET events with energy depositions larger than 8 MeV within the ΔE+E detector are noted. It is expected that these are caused by neutron induced recoil protons which traverse the E detector at and oblique angle, depositing energy greater than normally incident primary

protons (i.e. > 8 MeV). This provides information on the neutron spectra as it indicates that neutrons of high energy (i.e. 10+ MeV) are present in this region. Such events are observed at this position of measurement as the beam current and time of measurement was increased, thus increasing the detection probability of these particles which are not present in great abundance. The nature of this position of measurement at the base of the distal edge (i.e. primary particles stopping and secondaries crossing the device) leads to a breakdown in the spectra. Measurement positions past the distal edge would allow determination of the secondary particle spectra in this region and resultant radiobiological effect when correlated with established biological data. It would be expected that measurements of a more complex beam-line, with higher incident energy protons would produce increased signal collection in this region (due to the higher probability for neutron production). The identification and evaluation of which would make this system useful for measurement of dose equivalent external to the primary beam.

The data presented here is a unique perspective on the changing radiation field which makes up a modulated proton SOBP as it provides information on changing LET and particle energy (and type) with a two stage coincidence system. Further measurements past the distal edge and outside the primary field would be useful in further supporting data already collected using the SOI microdosimeter on the important issue of out-of-field dose equivalents.

8.8 Biological Interpretation of ΔE-E Measurements

The use of the term RBE in radiotherapy relates to a given biological endpoint in order to determine the success of treatment with particular radiation field or delivery technique. Clinical RBE is difficult or even impossible to predict by any physical measurements because it is very patient specific. In many situations RBE is associated with in-vitro cell survival experiments and determined by an absorbed dose ratio between the radiation field being studied and a standard radiation such as Co-60 or 250 kVp X-rays for the same endpoint (usually a level of cell survival). While this characteristic is not necessarily clinically specific, RBE defined in this way it is a good indication for comparison of beam qualities in radiation therapy and radiation protection. The use of RBE in this chapter refers to cell-RBE, which is related in-vitro cell survival. As such the RBE discussed here is similar to equivalent dose and is based on the response of a certain cell line for a certain endpoint to a particular spectra of charged particles. New RBE definitions may be introduced with appropriate changes in biological endpoint.

As has been discussed in Section 8.1, a two stage device which provides microdosimetry information and particle identification can be used to assess the quality of a radiation field through either microdosimetry or fluence based approaches. Such approaches can be used with the silicon ΔE-E telescope as it provides microdosimetry data utilising a 1 μm thick ΔE stage, and when utilised in coincidence with the 500 μm thick E stage can also provide particle identification which is required in the fluence based approach. However, both of these methods have limitations which would make the development of a conversion matrix, based on experimental biological data, to determine RBE directly from ΔE-E coincidence spectra advantageous.

The microdosimetry method is highly dependant on the lower energy limit of the device when measuring low-LET particles such as therapeutic protons. A relatively high noise level will result in the inability of the detector to measure the primary particle energy peak and hence discern accurate microdosimetry spectra. In this case the 1 μm thick ΔE stage of the ΔE-E telescope has a low energy threshold of 10-12 keV using this experimental set-up (measured as 30-40 keV using previous experimental configurations

[100]), making this an order of magnitude higher when compared to the 10 keV noise threshold of a 10 μm thick SOI device. Further, the large cross sectional area of the SV (1x1 mm^2) of the ΔE-E device makes it susceptible to variations in response that is dependant on higher chord variance (Figure 7-19). Such geometrical dependencies are not observed in spherical structure of the TEPC and are minimised by the cubic array structure of the SOI microdosimeter. It can be concluded that there are other devices better suited to measuring microdosimetry spectra rather than utilising the ΔE stage of the ΔE-E telescope as a dedicated microdosimeter. It should also be noted that the microdosimetry approach provides a one-dimensional dose deposition spectra that does not allow separate identification of events related to two different particles of the same LET, despite these particles potentially having a difference in radiobiological effect. This is a shortcoming of microdosimetry which can be addressed by a two stage ΔE-E system.

The fluence based approach requires the different components of the radiation field be determined and weighted accordingly to evaluate the overall effect of the radiation field. In this instance the ΔE-E telescope is extremely useful, as it provides particle identification for particles which stop in the 500 μm thick Si detector. A shortcoming of the fluence based approach is that it determines instance of cancer induction based on a theoretical determination of the radiation field induced at the time of exposure. Such identification is problematic experimentally and requires long term survival data based typically on radiation accidents or atomic bomb incidents in Japan.

As the ΔE-E telescope is unique in its ability to identify charged particles using coincidence data to link both particle LET and total particle energy (in the case of a stopping particle) or particle type in a two-dimensional matrix. It would be useful to develop a means for converting this information directly to biological effect for a given measured radiation field. This would make the ΔE-E telescope more useful for on-line assessments of radiation fields in radiation protection applications and for QA testing in hadron therapy. It could also be used for verification of Monte Carlo modelling techniques such as [47]. The use of such a system would not depend on particle identification, but rather total energy deposited in the ΔE and E stages of the device

(through the two-dimensional coincidence plane) and the correlation of this to induced RBE, making it suitable for use in high energy, long range radiation fields.

8.8.1 Radiobiological Matrix Development

The basis of the matrix development was chosen to be measured radiobiological effect (RBE) in-vitro for V79 Chinese Hamster cells. RBE was chosen as the model parameter as it allowed for correlation with the measured integral physical dose to determine the biological dose at a given point. Such a parameter is useful for biologically based treatment planning in hadron therapy. Further, in-vitro V79 data was chosen as it is the most prevalent and accessible data available. Information on the RBE for various particle types and varying LET were readily available to not only create a radiobiological interpretation of the two-dimensional ΔE-E coincidence map but also to test this interpretation with measured proton coincidence data. V79 has the added advantage of having a measurable response to increasing LET which is useful for radiobiological interpretation of the ΔE-E response.

The data used to develop the model is contained within Table 8-1. It was important to obtain data for not only a wide range of particle LET's, but also for a wide range of particles with differing track structure, as it is clear from past work that the cell response does depend on the incident particle, making the measurement of micro- and nanometric properties of the radiation field useful.

Energy	LET (Si)	RBE (α)	RBE (10%)	Particle	Author
3.66	17.02	2.49	1.25	Proton	Folkard
1.83	27.91	3.42	1.40	Proton	Folkard
1.07	42.24	5.63	1.91	Proton	Folkard
3.40	29.47	3.28	1.56	Deuteron	Folkard
2.14	42.24	5.77	1.97	Deuteron	Folkard
1.40	55.01	8.35	2.74	Deuteron	Folkard
0.93	68.74	9.32	3.04	Deuteron	Folkard
6.90	95.99	9.41	3.07	He3	Folkard
4.18	132.70	10.90	3.56	He3	Folkard
3.39	150.62	10.11	3.31	He3	Folkard
2.40	219.30	11.50	3.96	Alpha	Wang
3.80	167.14	13.20	4.55	Alpha	Wang
8.00	105.67	10.50	3.62	Alpha	Wang
132.00	270.44	9.78	3.42	Carbon	Weyrather
64.80	470.16	10.65	3.52	Carbon	Weyrather
50.40	558.73	6.87	2.56	Carbon	Weyrather
28.80	767.93	5.73	1.99	Carbon	Weyrather
208.60	294.04	6.22	3.12	Nitrogen	Tilly
0.57	55.44	4.50	1.06	Proton	Belli
0.64	52.10	5.06	1.33	Proton	Belli
0.76	47.54	5.59	1.60	Proton	Belli
1.41	32.91	3.64	1.82	Proton	Belli
3.20	18.84	2.88	1.65	Proton	Belli
5.01	13.61	2.22	1.46	Proton	Belli

Table 8-1: RBE data for various ion species and LET's. RBE data for protons, deuterons and He3 ions obtained from Folkard [104, 105], alpha data from Wang [106], Carbon data from Weyrather [107], Nitrogen data from Tilly [108] and proton data from Belli [109]. LET values in silicon were calculated using SRIM2006 [91].

Two RBE endpoints were used to develop two separate conversion matrices. The first used the quantity RBE(α), which is determined through the ratio of α parameters

(from fitting the linear-quadratic model) between the measured ion species and a low-LET gamma control. The second quantity is the RBE(10%) which is determined from the ratio of absorbed doses between the low-LET gamma control and the measured ion species to achieve 10% cell survival. The energy of the particle was determined and provided in the radiobiological study. The LET of the particle and range in silicon was determined using SRIM [91], where all particles tabulated had a range less than 500 μm in silicon and hence deposited all energy within the combined ΔE-E assembly. The LET range of the V79 biology results extended from 10-800 keV/μm and is illustrated in Figure 8-21 and Figure 8-22.

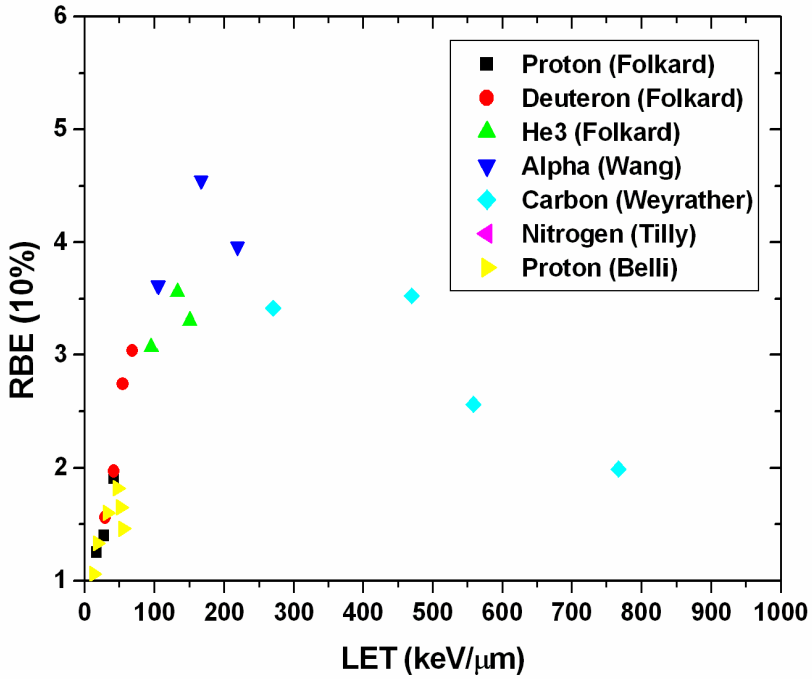

Figure 8-21: RBE(10%) versus LET distribution of V79 biology results used in the radiobiological interpretation of ΔE-E telescope response.

This data clearly shows how the RBE exhibits a peak at an LET of approximately 100-200 keV/μm. This dependence of radiobiological effect on LET is well known and has been published previously [62].

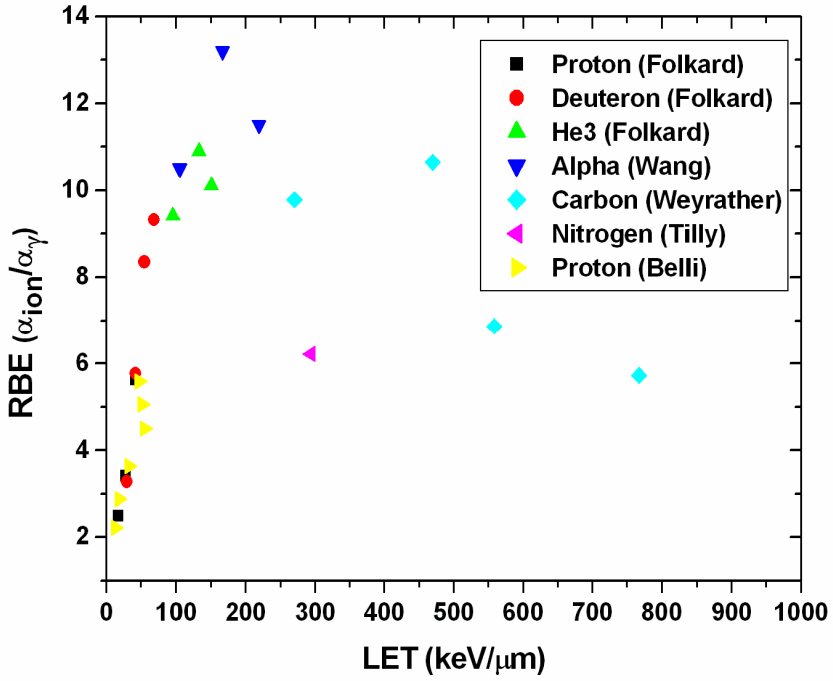

Figure 8-22: RBE(α) versus LET distribution of V79 biology results used in the radiobiological interpretation of ΔE-E telescope response.

This radiobiological data was tabulated and converted into a matrix using the correlation method within the Origin graphical analysis package [110]. The correlation method of generating a matrix from a random collection of points is based on the Kringing method [111]. This method generates a new value for each cell in the matrix from the points in the adjoining cells in the matrix that lie within the search radius. 1000x1000 cell matrices were generated using the correlation method with a search radius of 2 and a smoothing factor of 0.5. The X-dimension of the matrix represented the particle energy (i.e. total energy deposited in the ΔE and E stages of the telescope), the Y-dimension particle LET in silicon (i.e. the energy deposited in the ΔE stage of the telescope), while the cell value was a biological quality factor or RBE. The complete matrices for the V79 RBE(α) and RBE(10%) biological relationships are represented in the colour contour plots in Figure 8-23 and Figure 8-24.

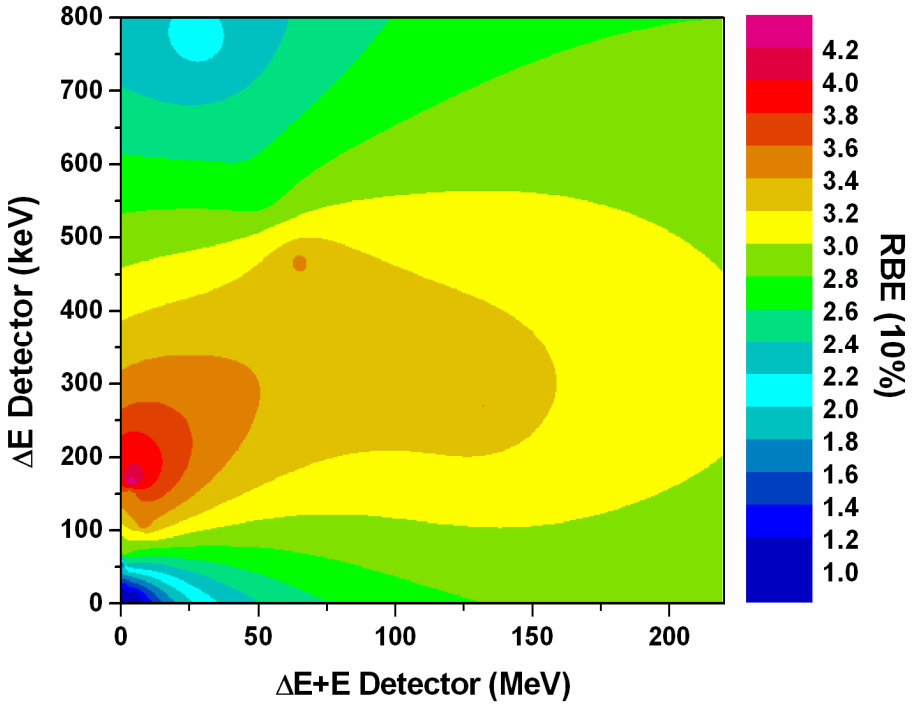

Figure 8-23: Interpretation of a two-dimensional matrix correlating RBE(10%) to ΔE signal (i.e. LET) and ΔE+E signal (i.e. particle energy deposited in 501 μm silicon).

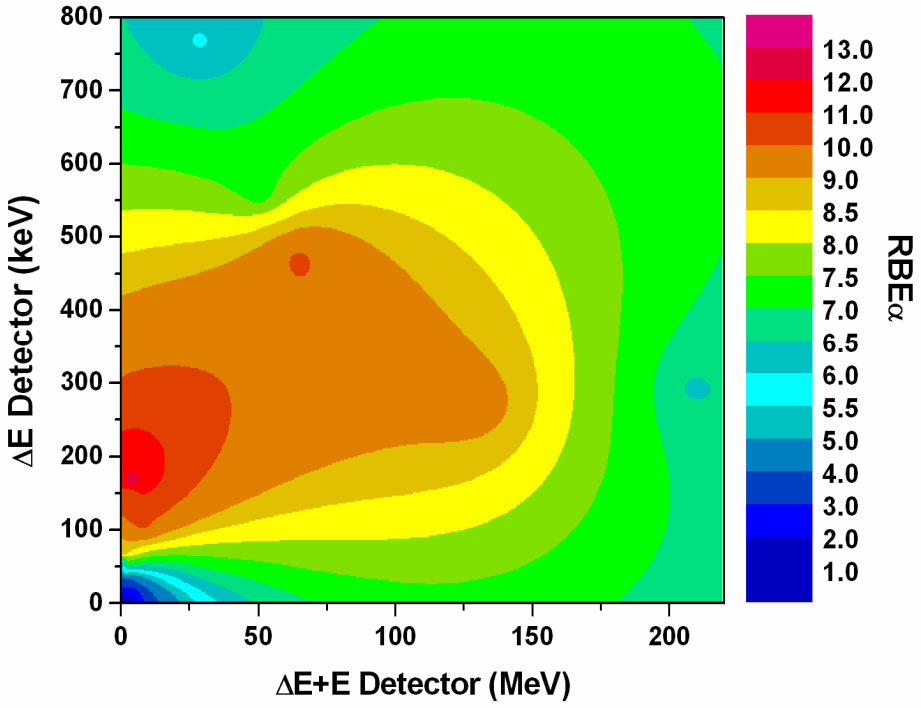

Figure 8-24: Interpretation of a two-dimensional matrix correlating RBE(α) to ΔE signal (i.e. LET) and ΔE+E signal (i.e. particle energy deposited in 501 μm silicon).

This method clearly shows a relationship in RBE that can be correlated with both ΔE signal (i.e. LET) and ΔE+E signal (i.e. particle energy deposited in 501 μm silicon). From the data used to develop the matrix, it was constructed to extend from $0 \leq \Delta E \leq 800$ keV/μm and $0 \leq E+\Delta E \leq 220$ MeV which covers almost all applications in both hadron therapy and radiation protection. It should be noted that it is not necessary for the particle to stop within the E detector and deposit its remaining energy. Particles of differing type will still produce clearly identifiable loci whose position is determined by particle type even when the second stage of the telescope has become a ΔE stage (Figure 8-25). Further, it is important to observe that this two-dimensional map of RBE indicates that particles of the same LET but differing species will produce a different radiobiological effect. Such particles produce different loci on two-dimensional ΔE-E plot which corresponds to identification of the particle (Figure 8-25) and with correlation to the RBE matrix, differing biological effect. A one-dimensional horizontal profile of the RBE matrix shows this effect clearly as particles of the same LET and differing ΔE+E signal (indication of different particle type) result in a different biological effect.

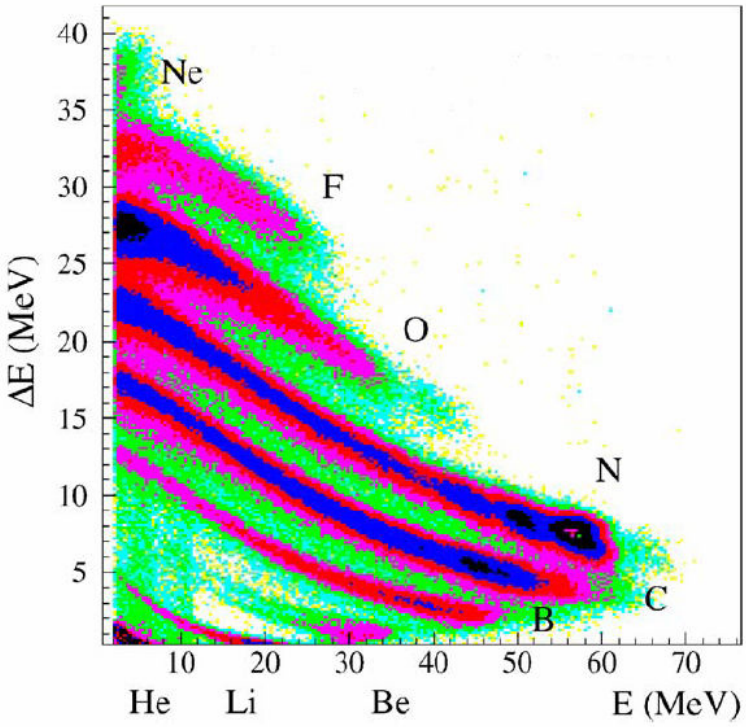

Figure 8-25: An example of different loci on a two-dimensional ΔE-E plot produced by different charged ion species [98], further indicating that such a system can provide information on particle species.

The data illustrated that maximum RBE was experienced at low particle energies with an LET of approximately 170 keV/μm. As both LET and deposited energy approach zero the RBE also approaches 1 which is indicative of the response from high energy protons and photons (i.e. low LET reference radiations). This indicates that while RBE is dependant on dose, endpoint, LET, dose rate and number of dose fractions, it is also dependant on the energy of the particle (which is in-turn defined by the particle type). Such a dependency supports the use of this technique as it will possibly allow for a more effective determination of radiobiological effect over a range of particles and LET values.

In measuring the response of the ΔE-E telescope to 100 MeV protons as they traverse a polystyrene phantom an LET range of $0 \leq \Delta E \leq 200$ keV/μm and an energy range $0 \leq E+\Delta E \leq 10$ MeV was employed. To allow for correlation between the radiobiological effect matrix and the experimental results, the radiobiological matrix needed to be altered such that each cell represented a corresponding point in the coincidence spectra obtained with the ΔE-E telescope. These magnified radiobiological effect relationships are presented in Figure 8-26 and Figure 8-27.

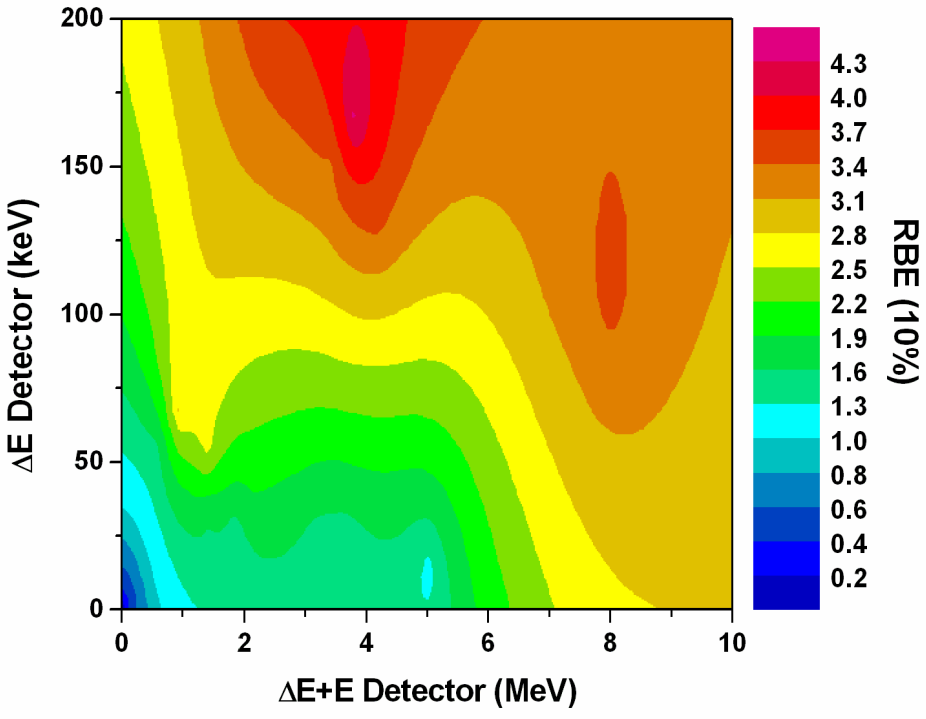

Figure 8-26: Magnified radiobiological effect matrix allowing for direct correlation between RBE(10%) and experimentally obtained coincidence data.

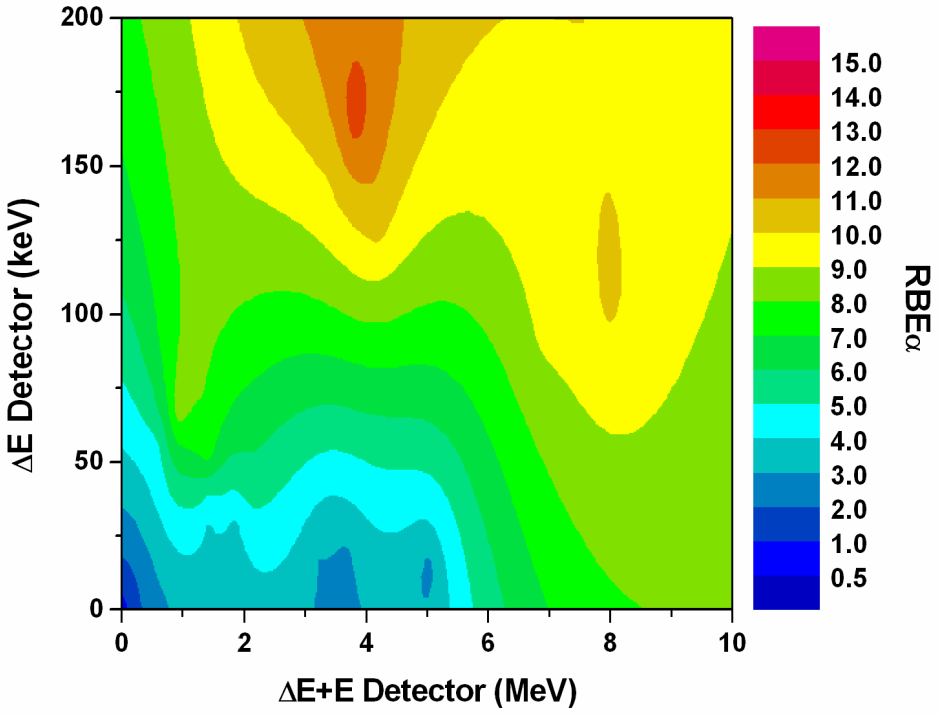

Figure 8-27: Magnified radiobiological effect matrix allowing for direct correlation between RBE(α) and experimentally obtained coincidence data.

The determination of the average RBE per particle was now easily obtainable through convolution of the radiobiological effect matrix and experimental ΔE-E coincidence data matrix of the same size. The resultant matrix was then summed and divided by the total number of incident particles to provide the average RBE per incident particle of a particular radiation field. This relationship is formalised in Equation 10-2, where $N_{i,j}$ is the experimentally measured frequency, $Q_{i,j}$ is the corresponding biological weighting function (which is determined from experimental in-vitro V79 data in this case) from the RBE matrix and N is the total number of energy deposition events.

$$RBE = \sum_{i,j} \frac{N_{i,j} Q_{i,j}}{N}$$

Equation 8-3: Method for determining RBE based on the convolution of radiobiological model matrix and experimental coincidence data matrix.

This method is extremely useful in both hadron therapy and radiation protection as it allows for instantaneous determination of RBE or dose equivalent for a wide range of

incident particles and their secondaries. Further, it allows for an accurate determination of RBE regardless of the secondary field present, which makes it extremely useful in heavy ion applications (such as those encountered in space and carbon therapy) as it can determine the overall effect of incident heavy ions, inelastic products and nuclear fragments. This is a large step forward in providing an online assessment of RBE in mixed radiation fields.

8.8.2 RBE Correlation: Testing & Discussion

The method for determining RBE based on coincidence data collected with the ΔE-E telescope was tested using data collected within a homogeneous polystyrene phantom when irradiated with both modulated and un-modulated 100 MeV protons. The results which were displayed in Section 8.7.1 and Section 8.7.2 have been convolved with the matrices displayed in Figure 8-26 and Figure 8-27 to create the average RBE(α) and RBE(10%) values per particle as a function of depth.

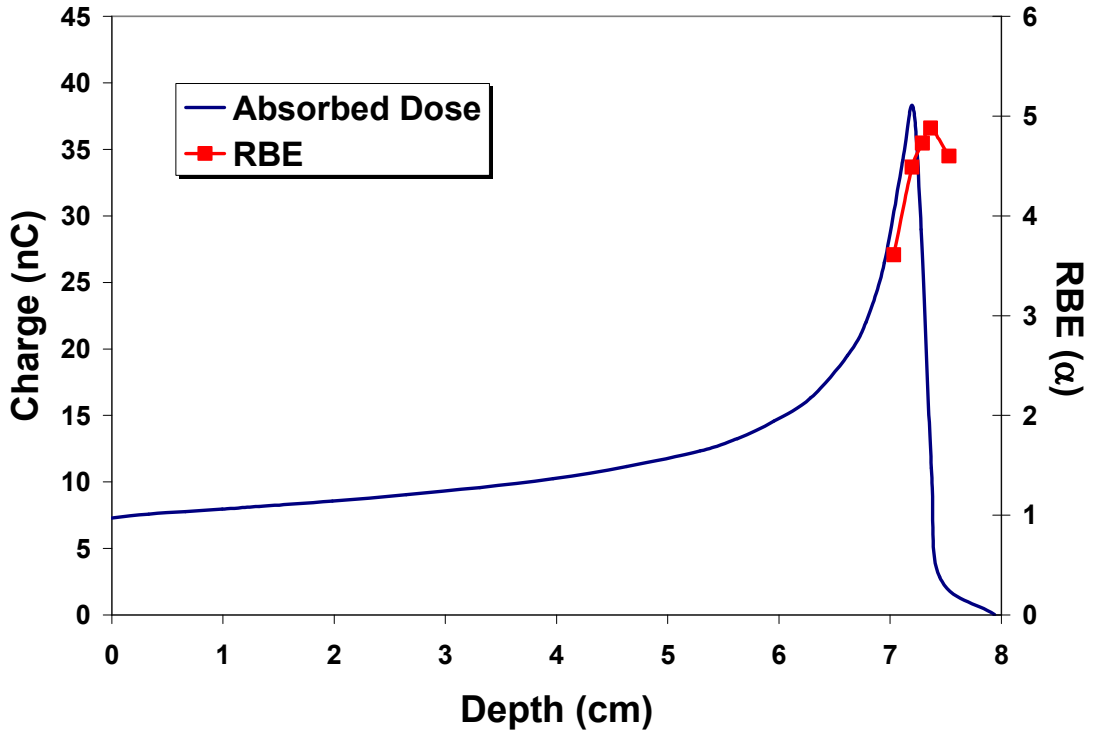

Figure 8-28: Average RBE(α) as a function of depth along an un-modulated 100 MeV proton depth dose curve (measured by ion chamber response in nC) as determined using the ΔE-E telescope and appropriate radiobiological effect matrix for in-vitro response of V79 cells.

In both cases the RBE peak for V79 cells is reached at the distal edge of the SOBP, which illustrates how stopping protons are more biologically damaging to cells. The maximum RBE(α) value is 4.88, while the RBE(10%) value is 1.85. The difference in the two maximum values is a direct result of the different RBE endpoints chosen. This illustrates how the absolute value of RBE is not unique, but depends on the level of biological damage and hence dose delivered to the cell volume.

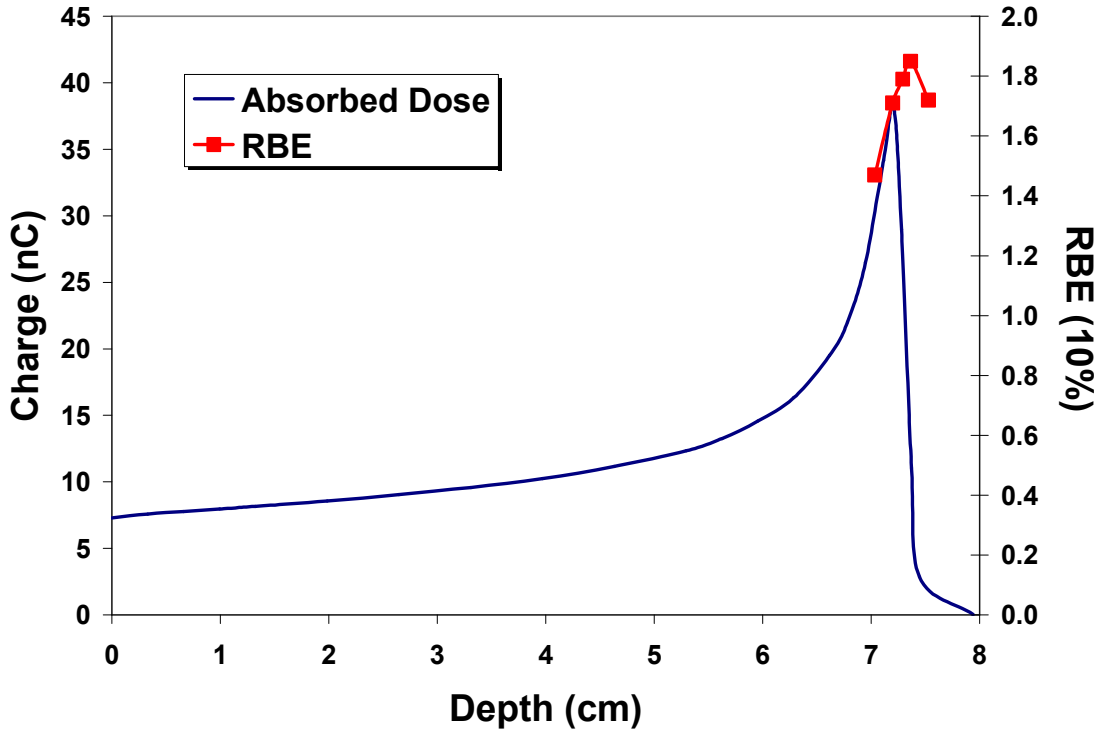

Figure 8-29: Average RBE(10%) as a function of depth along an un-modulated 100 MeV proton depth dose curve (measured by ion chamber response in nC) as determined using the ΔE-E and appropriate radiobiological effect matrix for in-vitro response of V79 cells.

When correlating the RBE and absorbed dose, the increase in RBE at the distal edge results in a distal edge shift in this case of approximately 1 mm between the absorbed dose and the biological dose profiles. Such shifts have been previously observed using radiobiological models in proton therapy applications [112]. In this instance shifts are observable experimentally due to the high spatial resolution of the detector system, making it valuable for in-phantom measurements QA applications. Such shifts would be more prevalent in higher energy proton fields and supports the use of radiobiological treatment planning algorithms to obtain maximum accuracy in not only Bragg peak

amplitude and position, but also distal edge placement. Further work should be completed to obtain a complete experimental RBE depth distribution for un-modulated proton beams of varying energy and hence varying ability to produce inelastic secondaries.

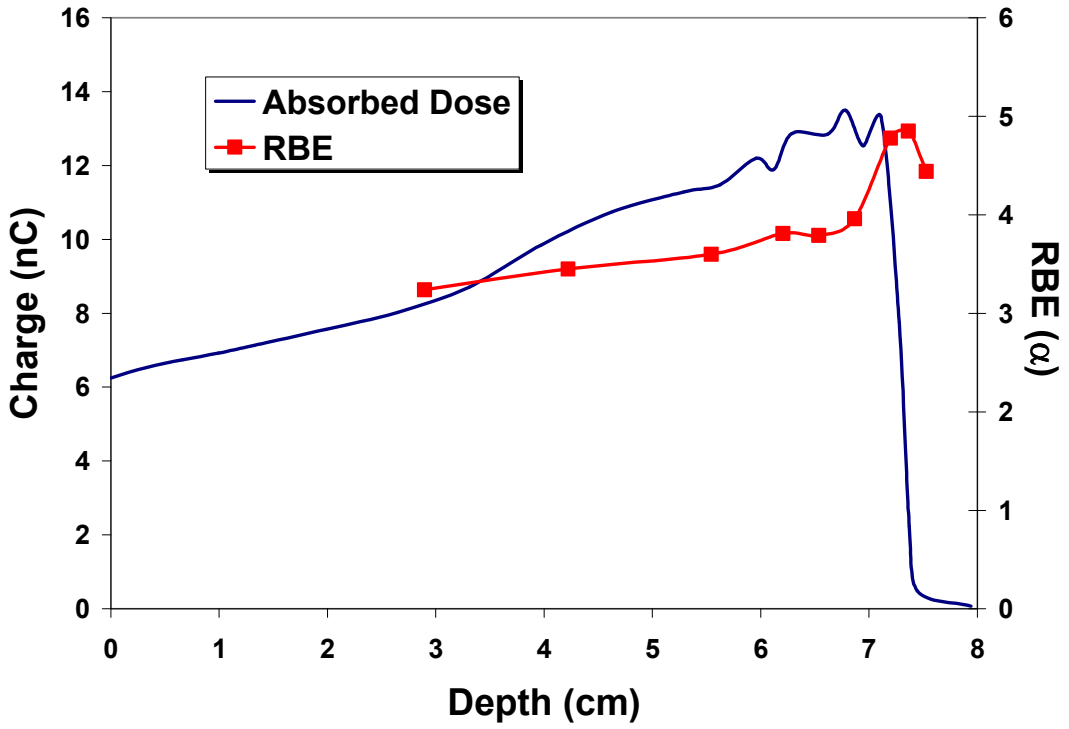

Figure 8-30: Average RBE(α) as a function of depth along a modulated 100 MeV proton depth dose curve (measured by ion chamber response in nC) as determined using the ΔE-E telescope and appropriate radiobiological effect matrix for in-vitro response of V79 cells.

More extensive ΔE-E telescope measurements of RBE were made across a modulated 100 MeV SOBP (Figure 8-30 and Figure 8-31). Both the RBE(α) and RBE(10%) profiles are similar in shape with the absolute value varying based on the endpoint. It is clear that the RBE is slightly elevated (10-20%) in the SOBP region and that the RBE increases slightly towards the distal portion of the SOBP. At the distal edge there is a sharp increase in RBE to a peak RBE(α) value of 4.85 and RBE(10%) value of 1.82. Again the increase in RBE towards the distal edge of the SOBP causes not only a change in the biological dose profile of the SOBP, with an elevation in biological dose from the proximal to the distal regions of the SOBP, but also may result in a shift in the distal edge

position. In this case the distal edge does shift by 1-2 mm which can result in the distal edge being positioned close to biologically important structures such as the brain stem.

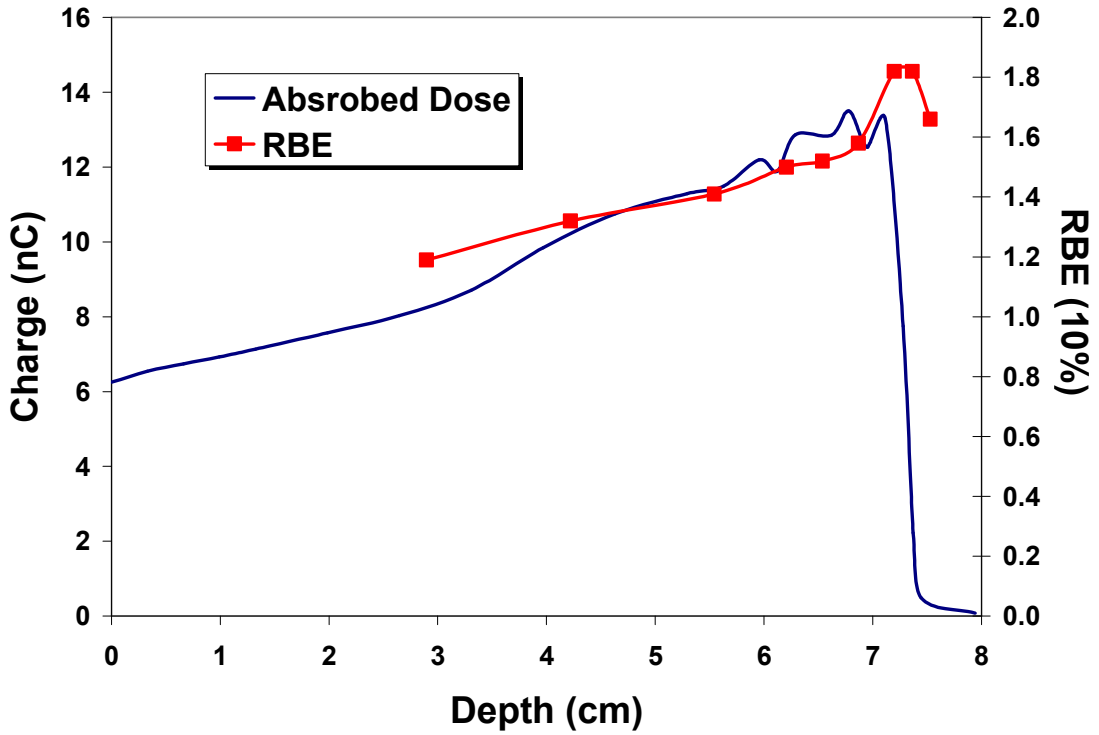

Figure 8-31: Average RBE(10%) as a function of depth along a modulated 100 MeV proton depth dose curve (measured by ion chamber response in nC) as determined using the ΔE-E telescope and appropriate radiobiological effect matrix for in-vitro response of V79 cells.

It should be noted that V79 cells deliver an elevated response to RBE [113] making them suitable to study such variations. Clearly in this instance a variation is seen in the distal edge of the BP and SOBP. However, the applicability of in-vitro V79 data to other cell lines or complete biological systems in-vivo is unclear. As the radiobiological effect matrix presented here is based on experimentally derived biological results it is possible to construct separate radiobiological effect matrices for all common cell lines encountered in radiation therapy. These matrices can be based on in-vitro data such as that which is presented here, or can be based on in-vivo data which may be obtained through mouse experiments. Direct implementation of such matrices into existing treatment planning would allow for tissue types (as determined by CT and/or MRI) to be tagged with a given RBE matrix and advanced treatment planning utilising biologically significant parameters would be possible.

It is important to benchmark the values obtained with the ΔE-E telescope against existing data. Data has previously been published on the RBE(10%) profile for a 70 and 160 MeV modulated proton beam [112] which was not used in model development, and as such is an independent source for verification. A comparison of this data with the 100 MeV data presented here is located in Table 8-2. It is clear that the 100 MeV data measured with the ΔE-E telescope and converted to RBE(10%) using the aforementioned radiobiological effect matrix is in excellent agreement with that published previously both proximal and distal to the SOBP. It is expected that because 100 MeV lies between 70 and 160 MeV, the RBE should do likewise and this is observed here. The exact trend of the RBE in this region, however, is unclear (i.e. is it a linear or non-linear relationship). Further work will be completed to measure proton beams of 70 and 160 MeV and ascertain with greater certainty the accuracy of this method.

Energy (MeV)	RBE Proximal	RBE Distal
70	1.24	1.93
100	1.19	1.82
160	1.11	1.60

Table 8-2: Information on the proximal and distal RBE(10%) values for a modulated 70 and 160 MeV proton beam [112] compared with the values obtained with the ΔE-E telescope for a 100 MeV modulated proton beam.

The radiobiological effect matrix for the ΔE-E telescope is based on actual experimental data, rather than solely on a mathematical relationship such as in the fluence-based approach or other LET based models. As a consequence, the results obtained with the ΔE-E telescope accurately reflect the radiation field present and when correlated with established experimental data, produce accurate RBE values for a given cell line. The proposed method of ΔE-E telescope correlation with RBE and results obtained using this method further support the use of this system in high energy radiation fields and development for radiation protection.

There exist two main limiting factors on this technique for determining RBE. Firstly, there is the limitation of the device itself which involves the lower energy threshold of the ΔE stage due to high capacitance. This feature makes it difficult to measure the ΔE-E coincidence spectra accurately for high energy proton fields, however does not impact

measurements around the BP or SOBP, which is the region of interest in radiation therapy. Further this does not impact the performance of the device in high energy heavy ion, low energy proton or neutron fields making it ideal for immediate application to space based radiation field studies and hadron therapy utilising protons and especially carbon ions. Certainly, improvements in the lower level noise threshold will improve the overall performance of the detector.

The radiobiological effect matrix relies on available cell survival data for a given cell line which means that ideally data should be obtained under the same radiation conditions as measured ΔE-E coincidence data. To facilitate this, a method for obtaining thin-film cell survival data is developed and presented in Section 10. However, it is possible to rely on published data from other sources, such as what has been completed here with good correlation with previously published data. Further, the advantage of this system is that is can be tailored and applied to many cell lines (both tumour and normal) as well as using in-vivo data obtained through mouse experiments. The basis of this approach on the interpolation of experimental biological data is its strength, and while this relies on rigorous biological experimentation to obtain such data, it results in a very accurate means for determining RBE.

8.8.3 RBE Correlation: Conclusion

The radiobiological interpretation of the ΔE-E telescope response in radiation therapy presented here provides a means for the determination of particle RBE for a particular radiation field which is based on experimentally derived cell survival values. Such a method is applicable over a range of particles and energies and allows for the influence of particle type to be considered along with particle LET. Using this method allows for determination of the radiobiological effect of a wide range of particles and associated secondaries with appropriate weighting values applied to various particles and LET values based on a matrix of cell response. Comparisons with existing data on varying proton RBE for V79 cells validated the use of this technique.

This technique can be further benchmarked and tested against other incident ion species utilised in both therapeutic and radiation protection applications. The wide range of particle energies and LET values makes it useful in a range of applications. Further, as the model is based on actual biologically derived data it can be applied to in-vitro and in-vivo results for a range of cell lines. Such expansion of the model allows it to be directly linked with advanced hadron therapy treatment planning using a biologically significant quantity as the planning parameter.

8.9 Conclusions

This research has described a new approach to radiobiological dosimetry of mixed radiation fields and applied this to determine the radiobiological properties of a therapeutic proton radiation field. The SOI microdosimeter presented here provides one-dimensional information on the lineal energy properties of the radiation field, the response of which was in good agreement with existing data. This information can be used to determine the dose equivalent or RBE of a given radiation field, as is described in Section 2.5. Further improvements to this device can be completed including a reduction in the current noise threshold, allowing for the complete microdosimetry spectra to be detected and displayed for high energy protons.

However, the one-dimensional spectra produced by the microdosimetry method does not consider the differing biological response induced by particles of the same LET (or lineal energy) but different particle type. A more accurate determination of RBE can be assessed through measurement of the particle track structure. The track structure of a given charged particle at a given energy is unique and can provide more accurate information on the properties of the applied radiation field. Track structure can be determined experimentally at the level of DNA using nanodosimetry measurement techniques (Section 9), and correlated to RBE through the development of appropriate radiobiological models (Section 9.8.2).

Presented and tested here is an approach to dosimetry that utilises a monolithic Si ΔE-E telescope to provide not only LET information, but also identification of both primary and secondary particles present in the radiation field. This device has a unique method of measuring the change in radiological properties of the radiation field using coincidence techniques and two stage detection methods that has never been completed previously in therapeutic radiation fields. The measured value produced by such a system is a two-dimensional chart linking in coincidence LET (or energy deposition in the ΔE stage) and particle energy deposited in both the E and ΔE stages (which provides information on particle type). Particles generate separate loci within two-dimensional map that is dependant on their associated charge and mass, allowing for clear distinction between particles of differing species, even if they have the same LET. This technology was applied to measuring the changing properties of both the modulated and un-modulated 100 MeV proton beam. Clear discernable data was obtained that not only provided further information on the applied radiation field, but also on the performance of this device in a hadron therapy application. The high spatial resolution of the device and the ability to make measurements within phantoms makes it useful for identifying changes in radiation spectra for small variations in position. An increase in the thickness of the E stage of the device will allow for increased energy deposition in this stage and further separation of particle loci in the two-dimensional coincidence chart, especially for high energy radiation fields. This may prove to be a new method of radiation measurement for QA in hadron therapy applications.

To compliment the measured ΔE-E telescope data a radiobiological effect matrix was developed using existing in-vitro V79 survival data. By correlating this matrix with measured coincidence data it was possible to determine the radiobiological effect of the radiation field at a given point. The data generated, indicated an elevation in RBE at the distal edge of both the modulated and un-modulated proton beam. Such results signify not only a potential difference in biological effect in this region, but also a possible shift in the distal edge of the biological dose profile. Comparisons with existing models and data proved successful in the case of proton radiation, with further validation work planned. The advantage of such a system is that is can be applied and expanded to any

cell line for which in-vitro or in-vivo data is available, and provides accurate results through an accurate determination of both LET and particle type, and correlation with experimental biological data.

The model and detector developed for this work provide a means for measuring directly the RBE of a therapeutic hadron field. This can be applied to treatment planning applications and the development of a treatment planning system with a biologically significant quantity as the planning parameter. Such a system may be a significant improvement over current planning technologies, while the detector apparatus can be utilised in the verification of Monte Carlo simulations for heterogeneous TE phantoms. This model enhances the use of the ΔE-E telescope in not only therapeutic applications but also radiation protection in evaluating the risk of mixed radiation fields.

8.10 Future Applications

The ΔE-E telescope has proven its ability to provide useful data in proton applications. It would be recommended that this be expanded to a more complete assessment of proton therapy for a range of treatment applications including various energies and modulation settings. Further, the ΔE-E telescope could provide a means of comparing the properties of passively and actively scanned proton beams in a clinical setting. Through the use of the radiobiological effect matrix, the ΔE-E telescope could provide an assessment of the RBE profile generated by comparative treatments and determine any variation between the two techniques that should be accounted for in the treatment planning process.

The ΔE-E telescope has a distinct advantage in that it can measure a wide range of particles and energies and through the use of the established radiobiological effect matrix provide an assessment of the biological effect of the radiation field. Such properties are of use in carbon therapy and would certainly be of use in treatment planning for hadron therapy. Further, it could provide useful data on heavy ion fields experienced in radiation protection applications such as space. It would be recommended that these fields be tested to ascertain the radiation hardness of the ΔE-E telescope, its ability to measure

densely ionising radiation fields, and to test the accuracy of the radiobiological effect matrix over a range of ions.

Finally, as the biophysical model is based on cell survival data for a single cell line, it is recommended that this be expanded to include a range of human normal and tumour cell lines. Once verified this data can be incorporated into an advanced hadron therapy treatment planning with a biologically significant quantity as the planning parameter and individual RBE's for different tumour and normal biological structures. Such a system may provide a more effective means for planning patient treatments and improve biological dose localisation to the tumour volume and hence the efficacy of the treatment.

9 Low-Pressure Gas Nanodosimetry

9.1 Introduction

This report has demonstrated the ability of microdosimetry to provide information on a radiation field at the micron or cellular level. The next logical step is to extend this work to measuring radiation interactions on the level of DNA, as it is radiation interactions with DNA producing base lesions, single strand breaks and double strand breaks which determines biological effect. Also as electronic circuits continue to advance and in turn decrease in size, measurements on the nanometre level will possibly provide a more accurate analysis of SEU rates, allowing for the incorporation of design features to extend deployment life-times. Experimental low-pressure gas nanodosimetry provides a means for measuring radiation interactions within a nanoscopic or DNA equivalent volume and will be investigated and presented upon.

The investigators at LLUMC, in collaboration with the Weizmann Institute of Science and the Santa Cruz Institute of Particle Physics, have built and optimized two ion counting nanodosimeters (ND). The operation of this device has been described previously in Section 2.6.2. One of these devices is currently installed on the PWEST research beam-line at Loma Linda University Medical Centre. This device is equipped with a Silicon Tracking Telescope (STT) [42] which allows for the analysis of incident particle track with respect to cluster formation within the Sensitive Volume (SV). This device was utilised to obtain the nanodosimetric spectra or ionisation cluster frequency distribution for a range of incident proton energies.

Experimental nanodosimetry would also benefit from the development and validation of Monte Carlo (MC) track structure simulations, accurately reflecting the experimental radiation conditions and response of the device. Once the Monte Carlo simulation system has been developed and verified it will be possible to include more complex homogeneous and heterogeneous structures into the theoretical model. This may then provide a means for better predicting radiation effects in radiation therapy or assess radiation risks in protection applications in cases where experimental data are not available.

This section work obtained experimental data utilising the low-pressure gas nanodosimeter for a range of incident proton energies. Using the STT it was possible to complete off-line data analysis and provide experimental data for varying SV length, and various incident ion positions relative to the SV. This experimental data was compared to the output from a specially designed Monte Carlo code that has been developed by Dr Bernd Grosswendt [114] to simulate proton interactions in water and low-pressure gases. However, such a program requires accurate assessment of the radiation field present in the experimental hall. As such GEANT4.7.1p1 was utilised to simulate the transport of the initial proton beam from the accelerator through the beam modifying devices of the experimental hall up to the SV of the ND. The output files of this program were then used as input files for the simulation of the ND's response. This study enabled an assessment of the accuracy of theoretical MC codes in simulating ionisation events on a nanometric level and identified areas of improvement that need to be addressed.

9.2 Experimental Method

Experimental data was collected for a range of incident proton energies and LET's. The proton accelerator at LLUMC provided incident protons of energy 250 and 30.7 MeV. These were transported along the experimental setup and into the ND. In this case a degrader was used to achieve three beam energies within the ND that closely resembled the incident proton energies utilised in cell survival work, described in Section 10.4.2. The three experimental assemblies are displayed in Figure 9-1, Figure 9-4 and Figure 9-5. These achieved approximate proton energies of 250, 17 and 5 MeV within the ND SV that were verified using GEANT4 and CsI calorimetry.

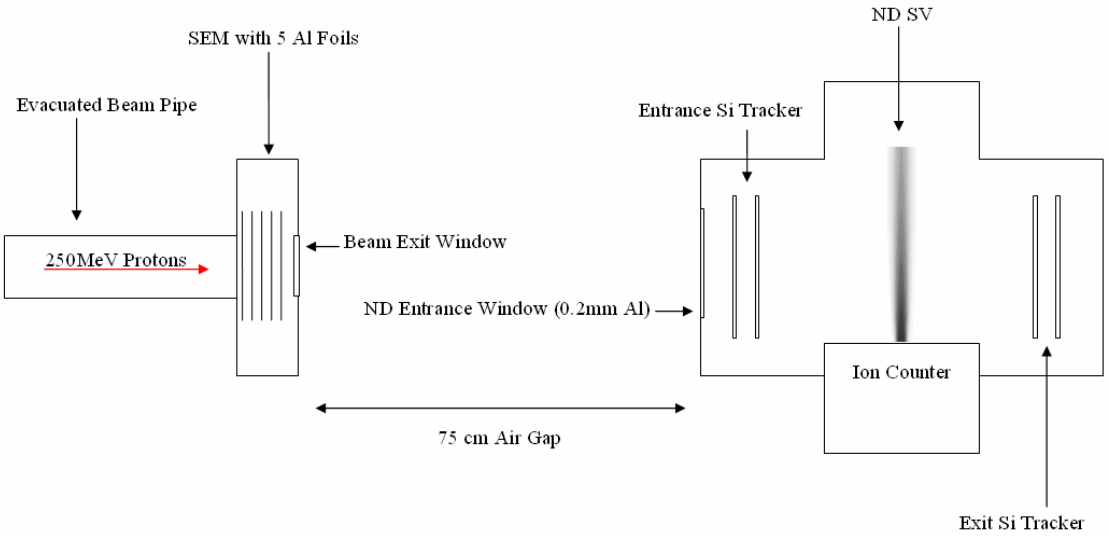

Figure 9-1: Schematic of the experimental set-up for acquisition of 250 MeV proton ND data (Setup A).

In the case of the 250 MeV acquisition no degrader or additional beam modifying/monitoring devices were utilised (Setup A). The STT registered the entrance and exit positions (both X and Y) of incident ions and allowed for correlation of the incident ion track with cluster formation. In this experimental setup the four separate planes of single-sided silicon strip detectors acted in coincidence as a trigger for ND acquisition. A single broad beam acquisition was completed for 250 MeV, with the Si tracker image of the beam profile displayed in Figure 9-2. Data was collected in all cases at an average rate of 2000 events per spill (accelerator cycle of approximately 2 seconds [9]). In the 250 MeV acquisition a total of $7x10^7$ particle events were collected for analysis. These events were then screened to reject pile-up events, events with more than one track or incomplete tracks, events with abnormally large energy depositions within the STT, and events with track orientation inconsistent with the beam direction. As such approximately $4x10^7$ events were available for further analysis.

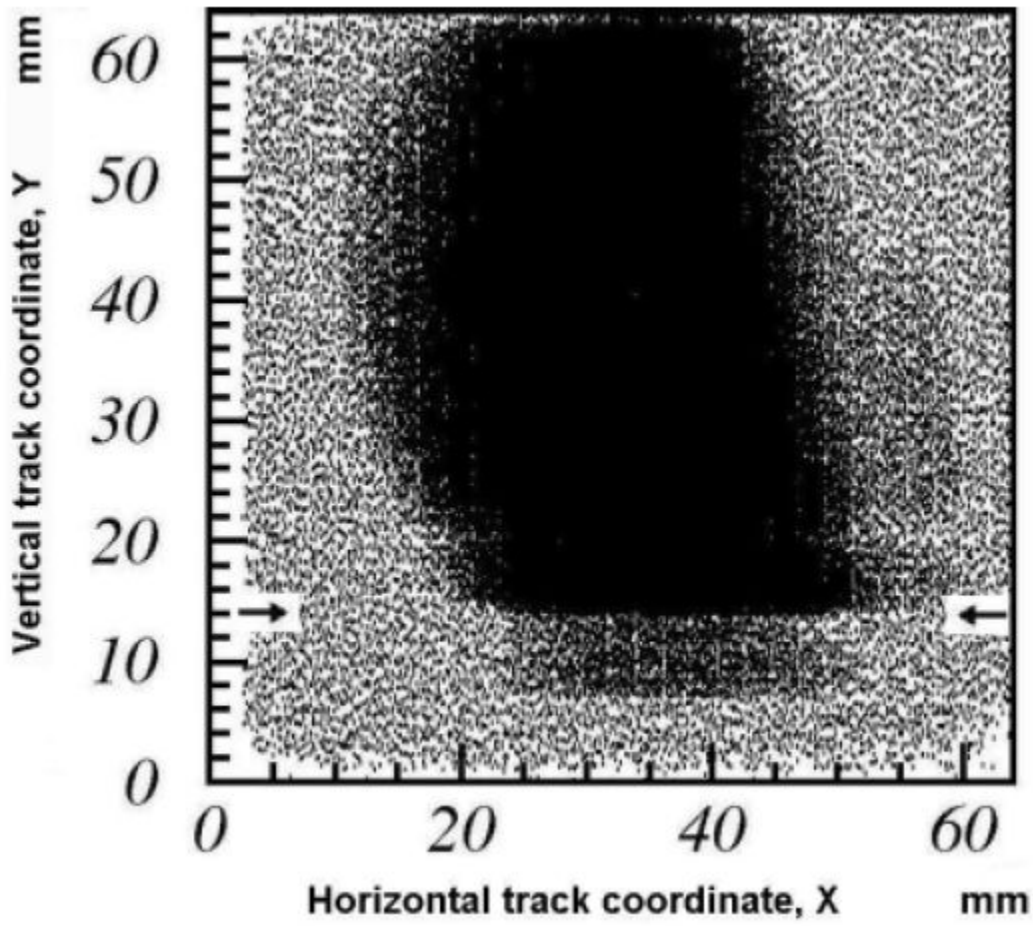

Figure 9-2: 250 MeV proton beam profile entering the ND as generated by the STT [115].

Using the STT and tracking information it was possible to complete off-line data cuts and analyse particles interacting with one portion of the ND SV. This is useful for comparisons with Monte Carlo simulations, and was used to generate the experimental ND spectra for incident proton tracks at three different lateral displacements from the central axis 0, 2, and 7 mm (corresponding to 0, 6 and 21 nm in tissue) at a height of 25 mm on the full SV (50 mm length total). A cross sectional profile of the ND SV and incident beam configuration (after off-line data analysis) to create the cluster size distribution (CSD) at three different distances from the SV is displayed in Figure 9-3. Further analysis of the ND performance for both a full and 7 nm long SV's was also completed with the 250 MeV broad beam for comparison with simulated results.

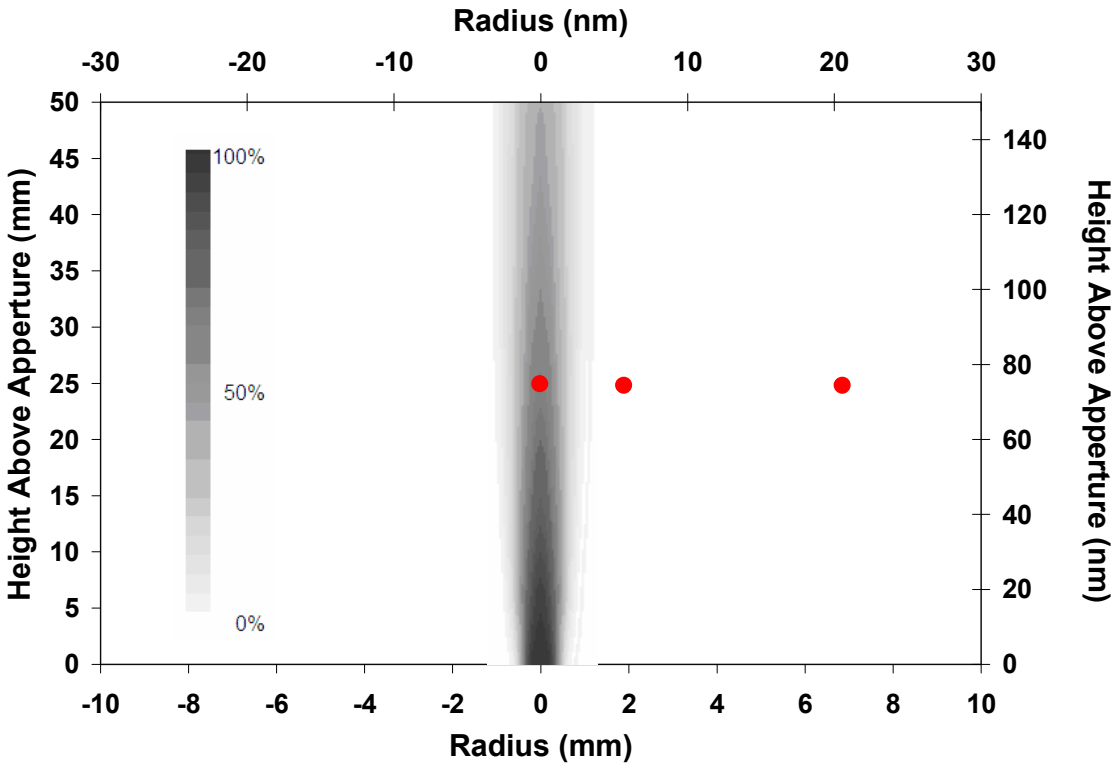

Figure 9-3: Cross sectional schematic of the ND SV and incident proton track positions for 0, 2 and 7 mm lateral displacement from the central axis at a height of 25 mm. In this case the red dot represents the proton path which is extending into the page. The greyscale of the SV represents ion collection efficiency. Three experimental data sets based on this analysis were created for all proton energies to be used in validating Monte Carlo simulations.

For a 17 MeV proton acquisition the beam was degraded from an incident energy of 30.7 MeV with the use of a 1.54 mm thick polystyrene degrader (Figure 9-4) and is designated as Setup B. The Si tracker efficiency for protons at this energy is very poor even at reduced bias voltages (recovery time up to few seconds depending on input charge). As such the Si tracker was suitable for providing positional information but the timing characteristics precluded its use as the ND trigger. A Bicron plastic scintillator BC-408 was employed immediately upstream from the ND to provide a trigger for the data acquisition system (DAQ) and allow for reconstruction of the proton track. In this case the scintillator was wrapped in 100 μm of Al and 100 μm of black polyethylene to avoid light contamination of the signal. As in the case of the 250 MeV results, offline analysis of the measured signal allowed for the experimental ND spectra to be obtained for 0, 6 and 21 nm lateral displacements from the SV at a height of 25 mm for further validation of the simulation program.

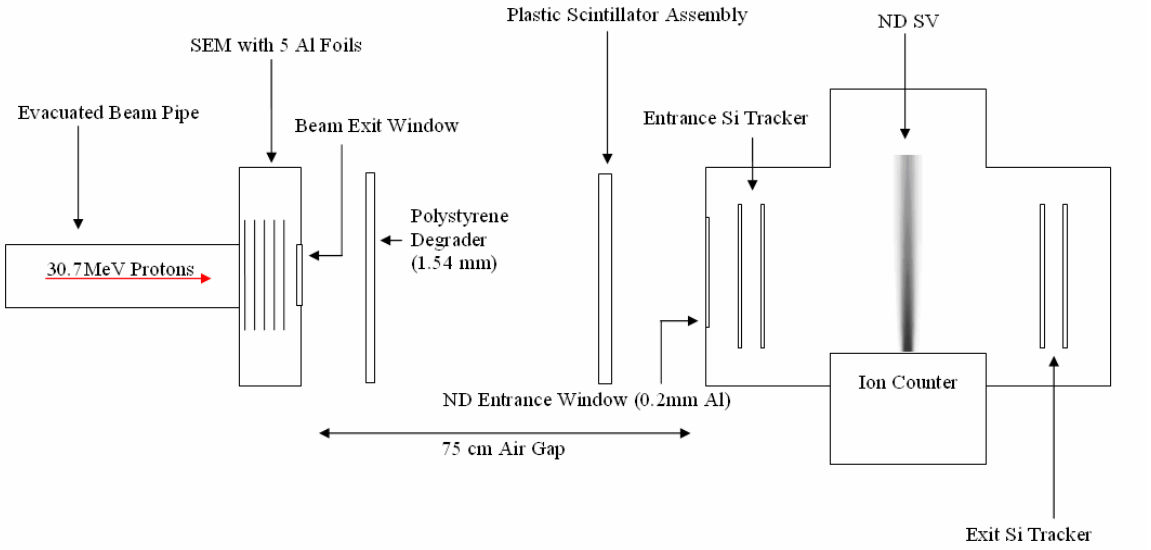

Figure 9-4: Schematic of the experimental set-up for the acquisition of 17 MeV proton ND data (Setup B).

For the collection of 5 MeV data, the experimental setup had to be changed significantly to compensate for the lower energy protons entering the ND (Figure 9-5) and is designated as Setup C. Firstly the STT could not provide viable data on particle position (entering and exiting the NS SV) due to poor efficiency and as such the entrance module (consisting of 2 single sided Si strip detectors) was removed. As in 17 MeV data collection, the plastic scintillator provided triggering for the ND. To minimise spurious triggering on particles that were scattered and did not enter the ND a lead collimator of 1.57 mm thickness was employed immediately upstream of the scintillator with a vertical slit of 1 x 0.2 mm^2. This was coupled with a 0.5 mm thick polystyrene collimator within the ND assembly (in place of the STT) that also had a vertical slit of 1 x 0.2 mm^2. The entrance window to the ND was also changed from 0.2 mm Al to 0.1 mm G10 to allow for the effective transport of low energy protons into the ND. The polystyrene degrader at the beam pipe exit was increased in thickness to 5.8 mm to obtain an energy of approximately 5 MeV in the ND (this was verified with GEANT4 simulations and CsI measurements).

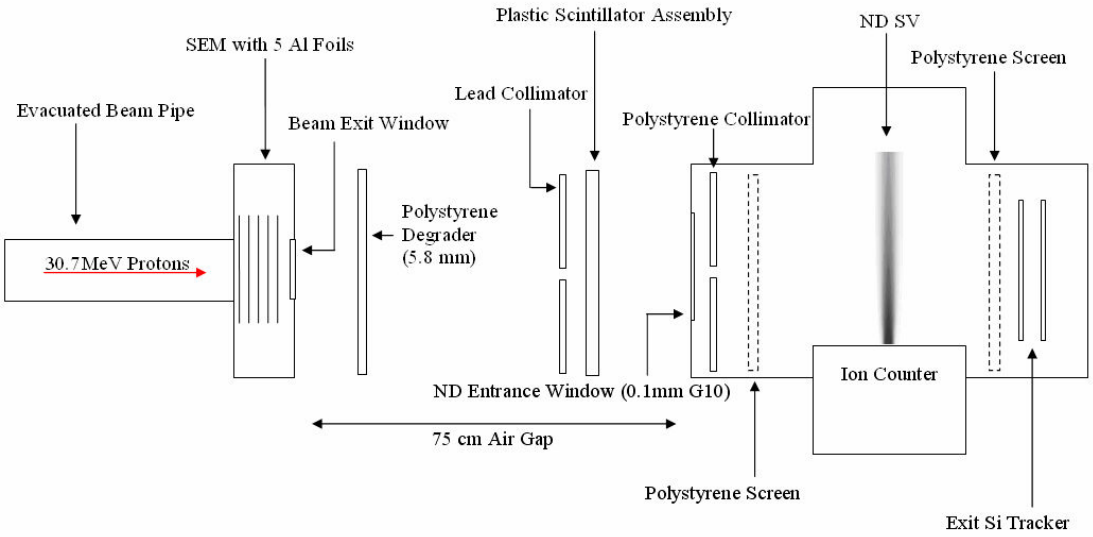

Figure 9-5: Schematic of the experimental setup used to obtain 5 MeV proton ND data (Setup C).

As experimental data was required for 3 lateral positions from the central axis (i.e. 0, 2 and 7 mm) at a height of 25 mm above the base of the SV the particle position needed to be isolated and determined for off-line analysis without the use of the front STT. To achieve this, two polystyrene screens were set up at the entrance and exit of the ND chamber. These screens had a horizontal slit measuring 1 x 50 mm^2 at a height of 25 mm. As such all particles crossing the ND SV would do so in a 1 mm thick horizontal band at 25 mm above the base of the SV. A single plane on the rear STT was then used to collect the X position of the particle crossing the SV. As the Y position was already known through collimation, off-line data analysis would allow for the determination of CSD with incident protons crossing the SV at a height of 25 mm and at a lateral distance of 0, 2 and 7 mm from the SV for comparison with Monte Carlo simulations.

In both the case of 17 and 5 MeV proton measurements the proton energy entering the ND SV was measured using a CsI calorimeter. This allowed for fine tuning of degrader thicknesses and checking of the experimental setup. The energy spectra produced through calorimeter measurements was compared to GEANT4 simulation results to further validate simulations of the experimental conditions.

9.3 Simulation of Experimental Beam Conditions

Monte Carlo codes provide a powerful tool to validate and improve experimental nanodosimetric systems and, once verified, could provide additional data without performing time-consuming and expensive accelerator experiments. For verification, it is important to accurately simulate the experimental conditions present whilst taking measurements with the nanodosimeter in order to obtain an accurate comparison.

For these simulations it was vital that accurate information on the beam incident on the nanodosimeter be obtained. To achieve this, the GEANT4.7.1p1 Toolkit [52] was used to simulate the research beam line at LLUMC and experimental ND set-up for the three configurations outlined in Section 9.2. The beam modifying devices and regions that were simulated within the geometry module of this program included the evacuated beam line, secondary emission module (SEM), entrance and exit windows, air gaps, STT, degraders, collimators and SV gas material. Dimensions and composition of these beam modifying devices are provided in Table 9-1. Elements making up materials utilised within the phantom geometry were defined by isotopic abundance. This provided the most accurate composition available and was obtained from an ICRU based program [35] and defined at standard temperature and pressure (except the SV gas which is given a pressure of 133.32Pa).

In addition to all materials defined in Table 9-1 the stainless steel casing of the beam pipe, SEM and ND were also constructed. It should be noted that in the case of the scintillator, it was wrapped within a layer of 0.1 mm Al and 0.1 mm cellulose, and as such the beam traversed these coverings twice (i.e. as it enters the scintillator and then as it exits). Further, all collimator aperture dimensions were constructed as described in Section 9.2.

Modifying Device	Thickness (mm)	Material
Beam-line	200.00	Vacuum
SEM Foils	1.27×10^{-2} (5 foils)	Aluminium
Beam-line exit Window	2.54×10^{-2}	Titanium
Degrader (17 MeV)	1.54	Polystyrene
Degrader (5 MeV)	5.80	Polystyrene
Collimator (5 MeV)	1.57	Lead
Scintillator	1.00	Bicron-B400
Scintillator Al Shield	0.10 (2 layers)	Aluminium
Scintillator Poly Wrap	0.10 (2 layers)	Cellulose
ND Entrance Window (250 & 17 MeV)	0.20	Aluminium
ND Entrance Window (5 MeV)	0.10	Kapton
Silicon Tracker (250 & 17 MeV)	0.40 (2 detectors)	Silicon
Collimator (5 MeV)	1.00	Polystyrene
Collimator Screens (5 MeV)	1.00	Polystyrene
ND Gas	N/A	Propane

Table 9-1: Composition and thickness of beam modifying devices comprising the proton-east research beam-line at LLUMC.

As in the microdosimetry simulations completed in this thesis, the physics processes were accounted for using a modular design based on the hadron therapy example released with the GEANT4.7.1p1 toolkit. Low energy inelastic scattering, low energy ionisation and multiple scattering models were employed for the transport of protons through the geometry of the simulation, while inelastic interactions were considered using the G4preCompound model. The physics of secondary particles also needed to be considered and accounted for. In the case of alpha particles, deuterons, tritons, and other generic charged ions produced as a result of inelastic proton interactions, the corresponding low energy inelastic scattering, low energy ionisation and multiple scattering models were utilised. The predominant particles generated within the simulation would be electrons resulting from proton ionisation interactions. Electron processes accounted for included low energy ionisation, low energy Bremsstrahlung and

multiple scattering. In the event of photon generation, the physics processes included were low energy photoelectric effect, low energy Compton scattering, low energy Rayleigh scattering, and low energy pair production. Neutron interactions were also accounted for using the appropriate models. As only incident protons could be considered by the ND simulation program the transport of secondaries was largely discounted through the use of a 20 mm range cut for photons, electrons and positrons. This had the added benefit of improving simulation times. For analysis of the secondary particle spectra entering the ND, selected simulations were completed with a 10 μm range cut employed for electrons and photons.

The incident radiation beam was defined in the GEANT4 application by energy, energy spread, cross sectional area, and divergence. In the case of 250 MeV incident proton simulations the beam was considered to have a σ=40keV and a beam radius of 10 mm with no divergence [116]. In the case of 30.7 MeV incident proton simulations the beam was approximated as monoenergetic with zero divergence and a beam radius of 5 mm.

The SV assigned within the GEANT4 based application was a 1 μm thick gas volume within the ND downstream of the STT or collimators. The cross sectional area and placement of the SV was dependant on whether broad beam data or information on the energy spectra at varying lateral displacements from the SV was required. In the case of broad beam data acquisition (completed for 250 MeV only), the SV within the application was considered as a 10 cm diameter cylinder covering the cross sectional area of the ND. All protons interacting within the volume (whether depositing energy or not) had their kinetic energy and position of interaction logged allowing for the generation of both spectral and fluence distributions. Broad beam simulations were completed for $5x10^6$ incident proton histories.

For simulations of the ND response for incident proton tracks at a given height and lateral displacement from the SV, three 1x1x0.001 mm^3 volumes at a height of 25 mm and lateral displacement from the central axis of 0, 2 and 7 mm were utilised. For protons interacting with these volumes, the kinetic energy was logged and a separate

proton kinetic energy distribution was created for each SV, as such each simulation output 3 separate energy spectra files. Due to the small cross sectional area of the SV's simulation times needed to be increased to $1.2x10^9$ incident histories to allow for sufficient statistics.

9.4 GEANT4 Simulation Results

The GEANT4 simulation of the beam modifying devices provided beam fluence (in the case of 250 MeV broad beam simulations) and energy spectra data that enabled an accurate assessment of the beam conditions entering the nanodosimeter.

In Figure 9-6, the energy spectrum of the incident proton beam before traversing the beam modifying devices is shown to have a mean energy of 250 MeV with σ=40 keV, as per the experimental beam conditions at LLUMC for experimental Setup A. After traversing the beam modifying devices, the beam has lost energy and undergone range straggling, resulting in a non-symmetrical peak with a low energy tail. The most probable proton energy is 248.9 MeV with a FWHM of approximately 0.3 MeV. Unfortunately, the CsI calorimeter used in proton energy validation is not of sufficient size to collect the entire proton energy for a 250 MeV beam and as such can not be used to verify the simulated energy spectra within the ND.

The GEANT4-based application provided not only accurate peak information but also information regarding low energy protons. These low energy protons are present below the peak energy and range down to energies of only 2MeV. Whilst not in any great abundance, these low energy protons have an elevated LET that could lead to increased cluster formation within the SV of the nanodosimeter. In order to accurately assess the impact of low energy protons, two files were output from this program. The first file gave the peak energy spectra between 247and 249.4 MeV while the second gave the low energy spectra of all proton energies below 247 MeV. The nanodosimetric cluster frequency distributions from both underwent a weighted summation based upon the relative number of histories in each input file to supply the total theoretical cluster distribution.

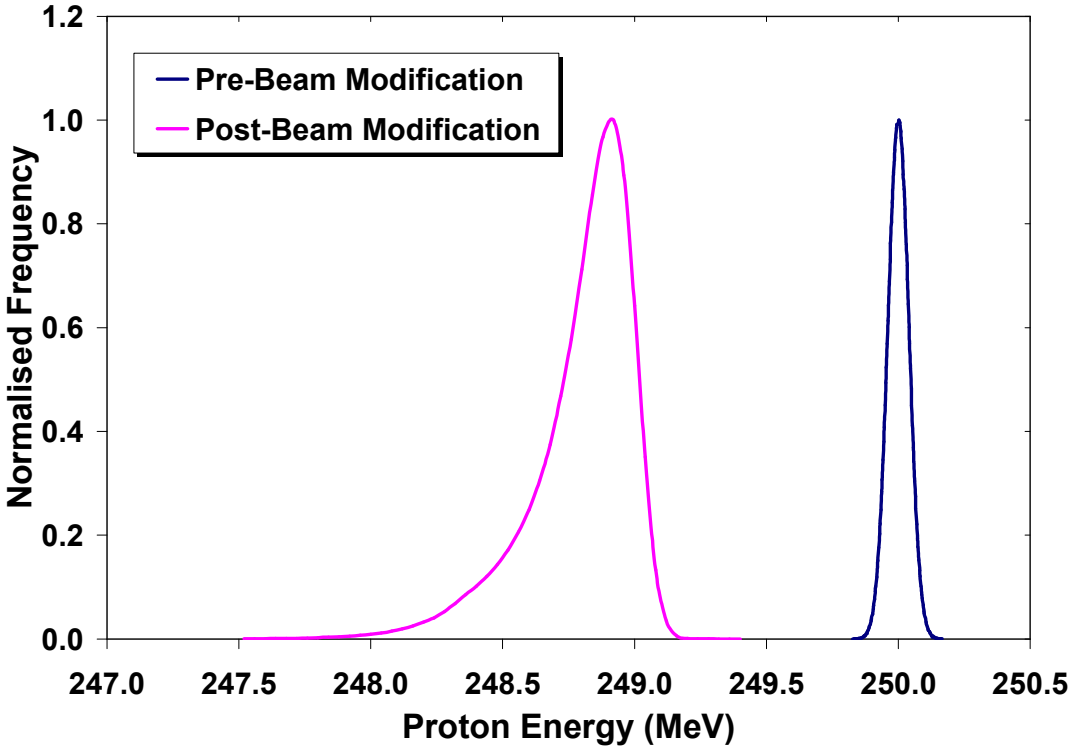

Figure 9-6: Simulated energy distributions of the LLUMC 250 MeV proton beam before and after proceeding through the beam modifying devices (Setup A). Distributions were normalised to peak frequency.

As per the experimental beam conditions, the incident beam prior to entering the beam modifying devices had a uniform profile and a radius of 1.0cm (Figure 9-7). Once passing through the beam modifying devices including SEM foils, air gap, nanodosimeter entrance window and Si strip detectors, the beam has spread significantly appearing Gaussian in shape and extends out to a radius of 1.0cm at FWHM. This fluence distribution was used as the input for 250 MeV broad beam simulations of nanodosimeter response.

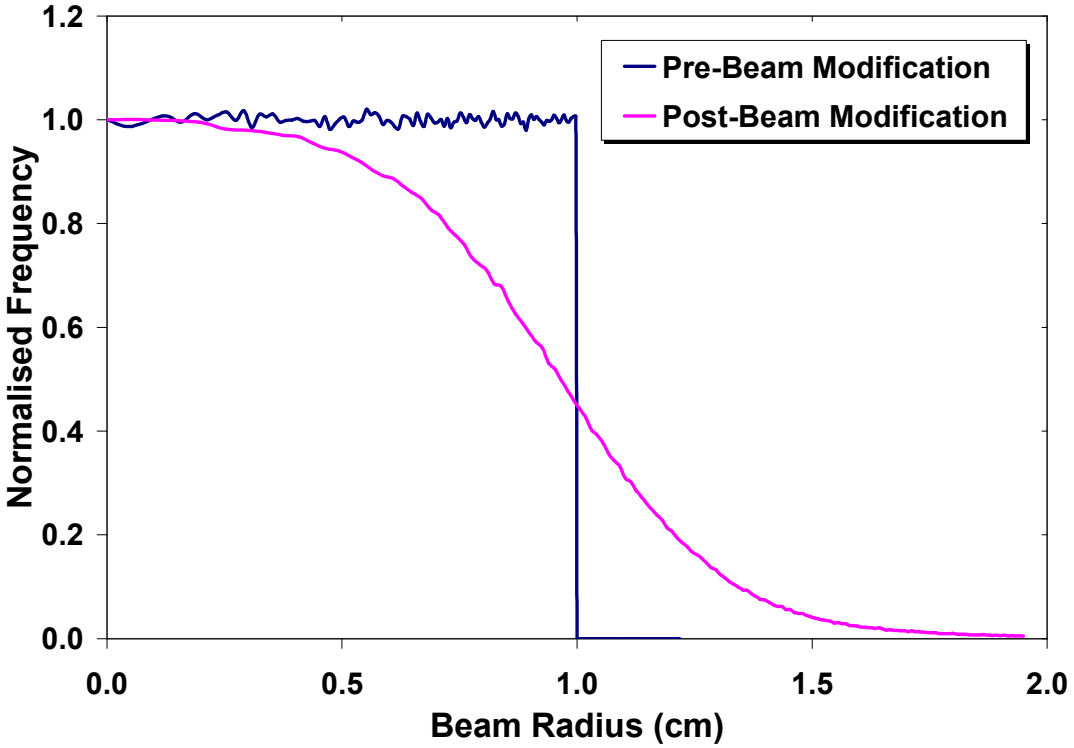

Figure 9-7: Simulated radial distributions of the LLUMC 250 MeV proton beam before and after proceeding through the beam modifying devices (Setup A). Distributions normalised to central bin frequency.

Using the geometry of the experimental setup used in the collection of ND data for 17 MeV protons (experimental Setup B) the energy spectra of the proton field entering the ND SV was simulated. This is compared with the experimentally measured value using a CsI calorimeter in Figure 9-8. The agreement between the experimental and simulated peak positions is excellent with values of 16.8 and 16.875 MeV respectively. The simulated spectra FWHM is not as broad as in the experimental case and this is a direct result of an assumption that the incident radiation field was monoenergetic. Future simulations can consider this, however, it must first be determined accurately within the accelerator transport system. Broadening of the experimental spectra can also be attributed to electronic noise in the experimental measurement system that was not considered in the simulated case.

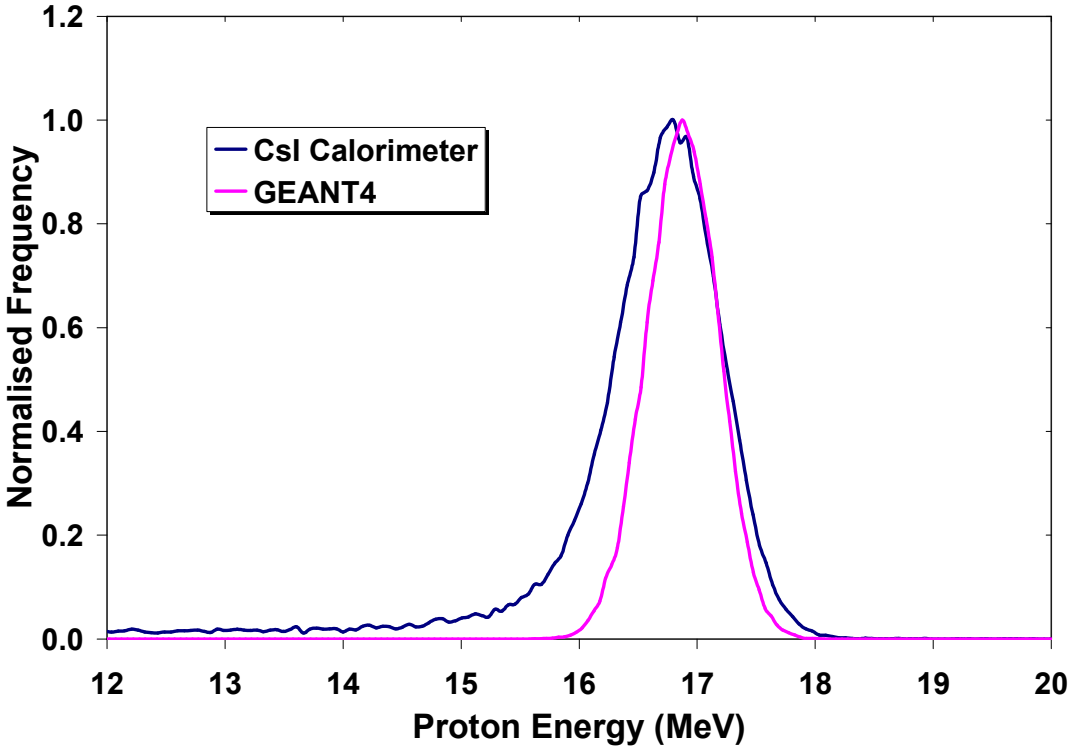

Figure 9-8: Comparison of simulated and experimentally measured energy distributions for incident protons entering the ND using experimental setup B (i.e. to achieve approximately 17 MeV protons within the ND).

The energy spectrum of the incident proton radiation field was also simulated using GEANT4 for the case of experimental setup C (to achieve 5 MeV protons within the ND). The simulated results are plotted against experimentally measured energy spectra using a CsI calorimeter and displayed in Figure 9-9. Agreement is excellent between the simulated and experimental cases with a 20 keV difference in mean peak position between the two spectra. Again the experimental case exhibits a larger FWHM which is attributed to spread in the initial beam energy and also in electronic noise of the calorimetry system.

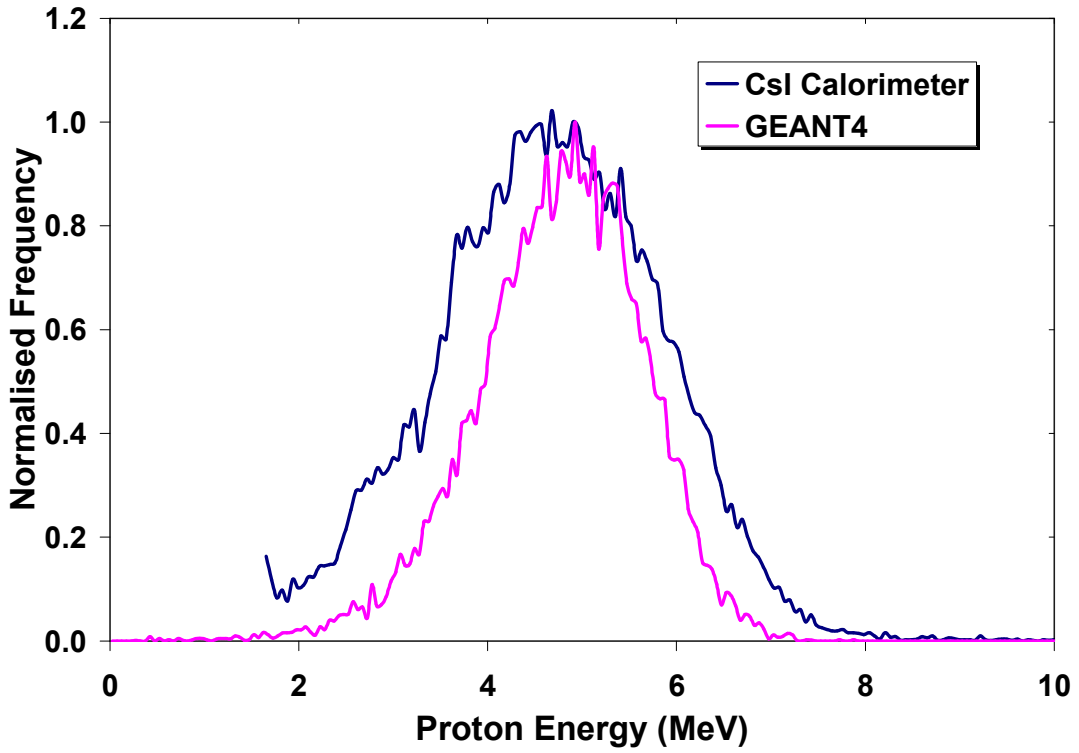

Figure 9-9: Comparison of simulated and experimentally measured energy distributions for incident protons entering the ND using experimental Setup C (i.e. to achieve approximately 5 MeV protons within the ND).

The simulated energy spectra (i.e. devoid of any experimental system noise and considered the ideal case) was used as input into a separate Monte Carlo program used to simulate the response of the ND. The use of such spectra will possibly allow for a more accurate simulated ND response as it will consider the incident radiation field.

9.5 ND Simulation Program

As ionisations within a nanoscopic volume were to be measured and cluster size determined, it was imperative that it be possible to simulate electrons down to the ionisation potential of the gas or 10 eV. Unfortunately GEANT4.7.1p1 can only transport electrons to an energy limit of 250 eV making it unsuitable for simulations of ND performance. In order to produce accurate simulations of the experimental conditions the GEANT4.7.1p1 based application provides the energy spectra and fluence (broad beam only) distribution of protons (both primary and secondary) incident into the ND SV as two separate output files. These output files were used as initial history input for a

special Monte Carlo code that has been developed by Dr. Bernd Grosswendt at Physikalisch-Technische Bundesanstalt (PTB), Braunschweig, Germany to simulate proton interactions in water and low-pressure gases [114]. A detailed description of this program can be found in the appendix of [37].

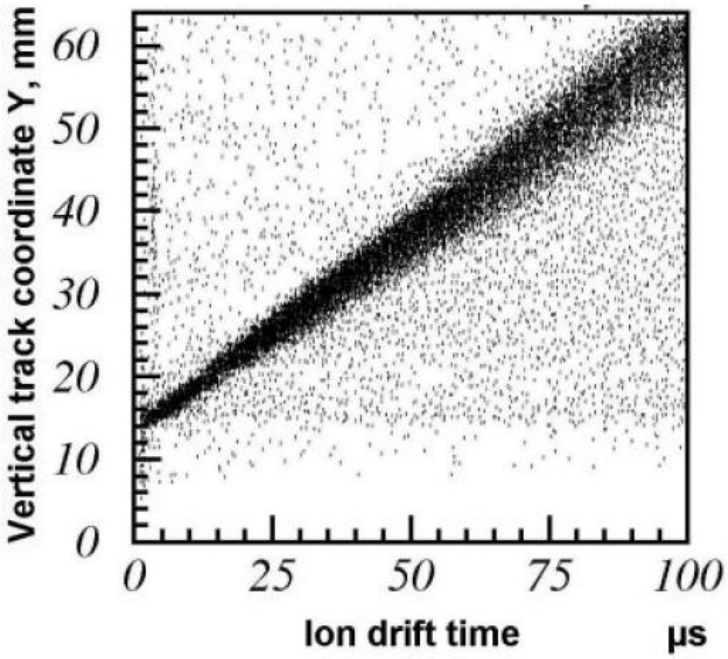

Figure 9-10: Correlation between measured ion drift time in Propane and vertical track co-ordinate [115].

The PTB Monte Carlo code was written in FORTRAN and utilises a compilation of experimental ionisation cross sections of protons and experimental electron interaction cross sections for elastic scattering, excitation and ionisation to transport high-energy protons and secondary electrons with energies down to 10 eV (the ionisation potential) in propane. The geometry utilised within this program, consisted of a wall-less homogeneous 1 Torr propane gas volume of 5x5x3 cm^3 embedded with the sensitive volume in which the position and number of ions was registered. The positions of the ions on a proton track segment in the SV were transformed into an ion-signal pulse train using a calculated three-dimensional efficiency map of the SV [37, 38] and the experimentally measured ion space–drift time relationship (Figure 9-10). Noise of the ND ion channel was accounted for by introducing random pulses corresponding to the frequency of those measured (i.e. 5 Hz). Simulations were completed for 10^7 incident proton histories to ensure adequate statistics.

9.6 ND Simulation Results & Discussion

Simulation of the response of the ND is presented in this section with direct comparison to experimentally measured ND response.

9.6.1 250 MeV Broad Beam

Simulations of the ND response to a 250 MeV broad beam utilised both the energy spectra and fluence distribution files generated by the GEANT4 based application as input for the ND simulation program. GEANT4 provided information regarding the entire proton energy spectrum entering the nanodosimeter from an incident 250 MeV proton beam, including recoil protons that are produced through nuclear scattering with the beam modifying devices upstream of the ND. The effect of these particles on ND spectra was determined by running separate simulations for the peak and lower energy spectra and summing these based on the relevant number of histories as provided by GEANT4 (Figure 9-11). It was assumed in these simulations that the fluence distribution (Figure 9-7) of particles making up the peak and lower energy spectra was identical.

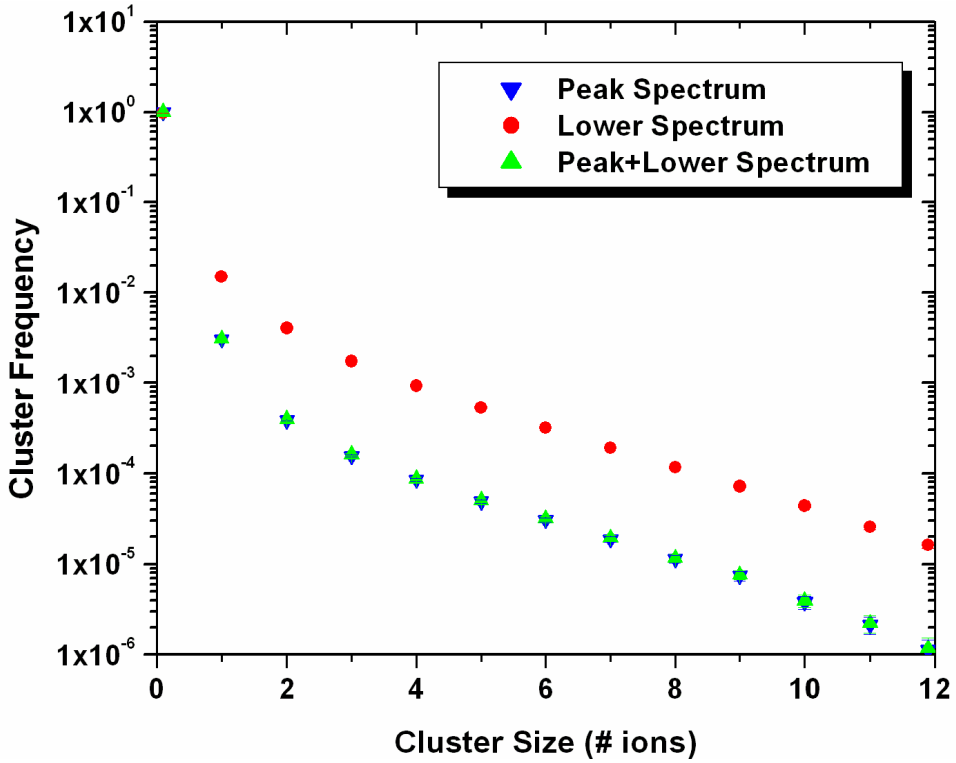

Figure 9-11: Cluster size distribution comparisons of peak, lower and summed simulation results normalised to the total number of events including zero events. Error bars contained within data points.

As could be expected for the same number of histories, the lower energy protons produce a higher probability of cluster formation (and hence ionisation or damage) within the DNA equivalent volume, which is indicative of their higher LET. However, in actual fact these lower energy protons comprised less than 0.5% of the total number of protons entering the nanodosimeter volume. When this weighting was applied and both results summed the effect from the lower energy protons is seen as negligible (Figure 9-11).

Figure 9-12a) illustrates a comparison between experimental and Monte Carlo cluster size distributions (transport of all low energy protons considered) *including* zero-events (proton events without any ion detection in the SV). Figure 9-12b) displays a comparison between experimental and Monte Carlo cluster size distributions *excluding* zero-events. The experimental cluster size distribution including zero events exhibits good agreement with the simulated results up to a cluster size of 8. In this region the simulation tends to over estimate the response of the ND with as much as a 30% increase over the experimental values. At cluster sizes greater than 8, the simulation under-estimates the response of the ND dramatically with as high as a factor of five variation in the frequency of cluster formation. The over-estimation of small cluster formation (less than 8 ions) and under estimation of large cluster formation by the Monte Carlo program is largely negated when using the mean cluster size (MCS) as an analysis parameter. In this case the experimental MCS is 5.68×10^{-3} compared to the theoretical MCS of 5.53×10^{-3}, which is a variation of approximately 2.5%.

For the cluster size distributions excluding zero events (Figure 9-12b) a similar trend is observed. For small cluster formations the Monte Carlo results exhibit an over-estimation of cluster formation (with the exception of a cluster size of 2), however such discrepancies are small and the simulation program exhibits good agreement with experimental values in this region. For large cluster formation (7 ions or larger) the experimental frequencies become progressively larger than the simulated frequencies as cluster size increases.

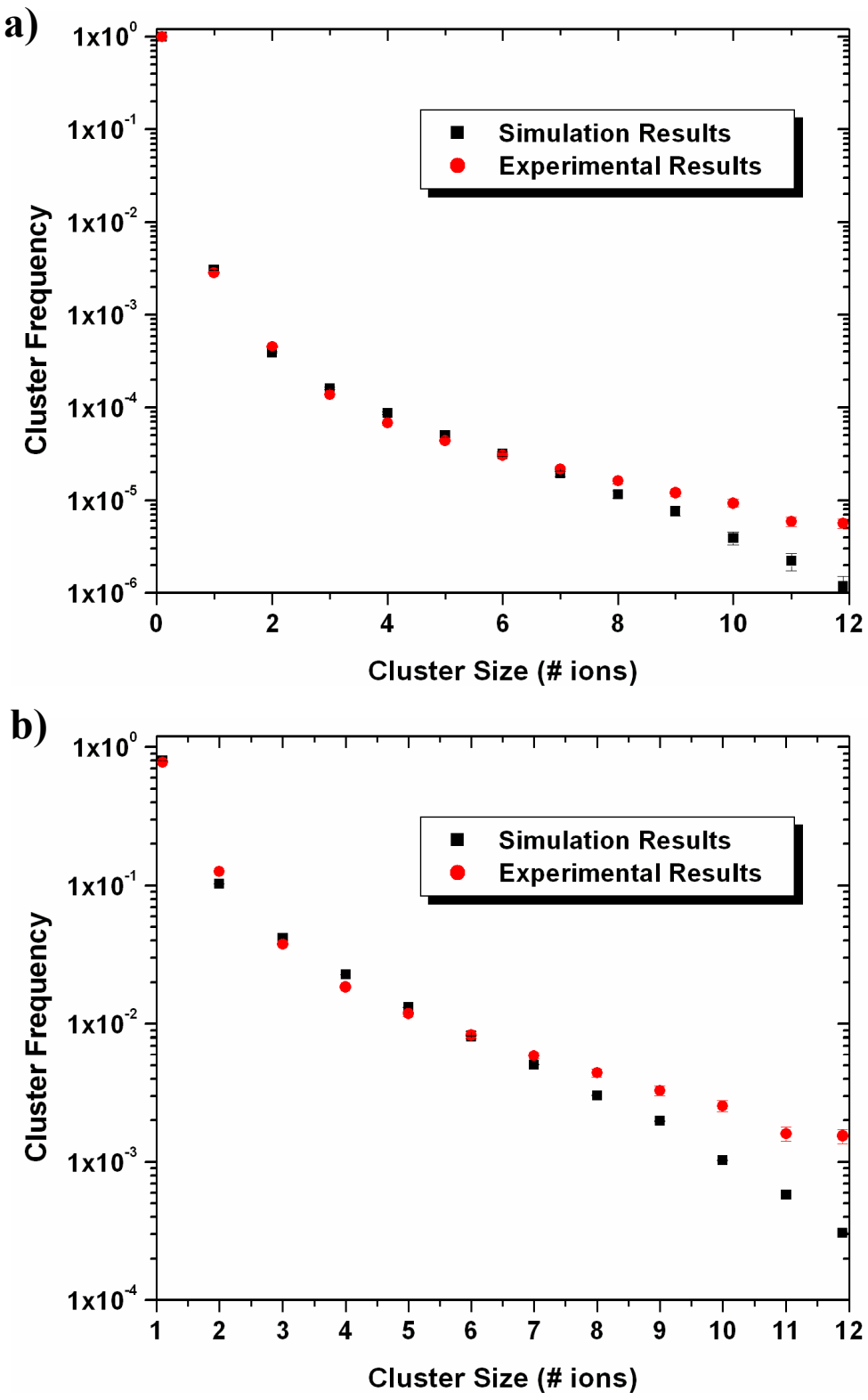

Figure 9-12: Cluster size distribution comparisons for theoretical and experimental results. a) Distribution normalised to the total number of events, including zero events; b) Distribution normalised to the total number of events with at least one ion (cluster size ≥1). Error bars are contained within data points.

The higher frequency of large clusters under experimental conditions could indicate that particles generating additional ionisation events are entering the ND gas volume that is not accounted for in the simulation. The simulation only accounts for protons entering the gas volume and as such the source of the additional clusters could be secondary electrons produced in the upstream silicon strip detectors as well as neutron contamination of the beam. To assess this, the spectrum of secondary electrons entering the ND was simulated using the GEANT4 based application.

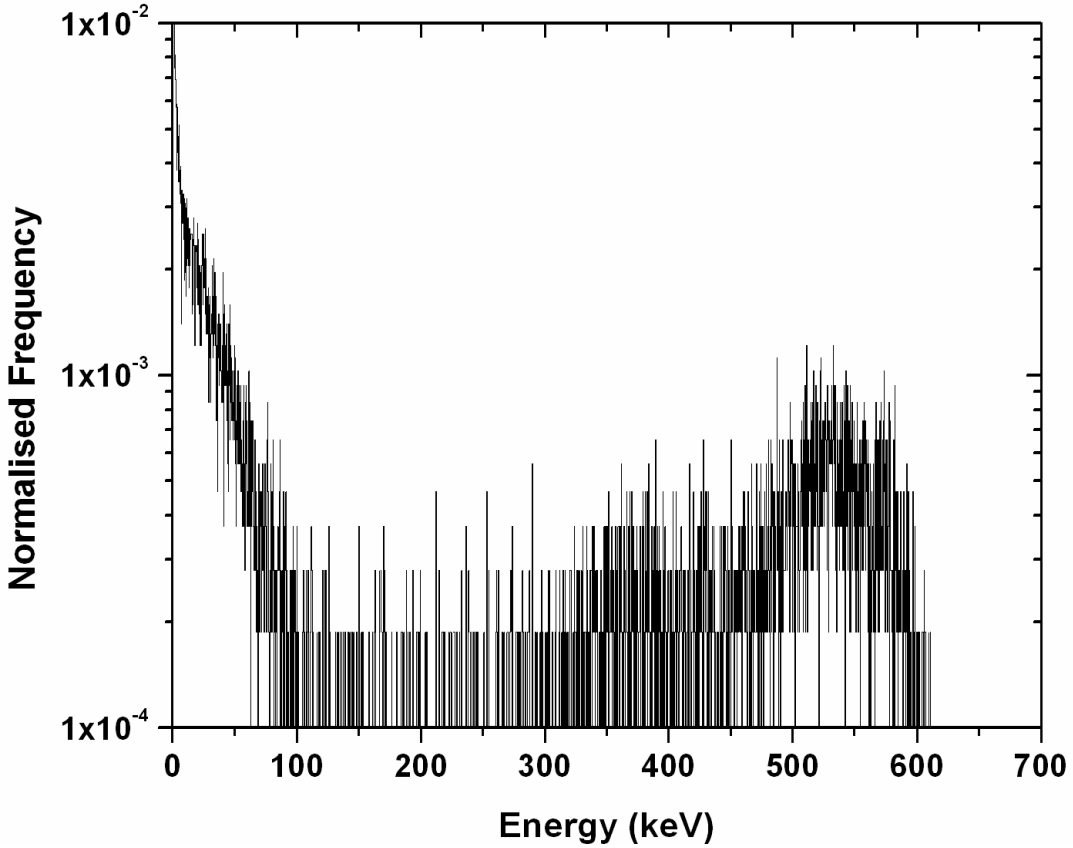

Figure 9-13: Energy spectra of electrons entering the nanodosimeter as simulated using the GEANT4 based application created for this study. The spectra was normalised to the total number of events.

It is clear from Figure 9-13 that electrons of a range of energies produced by the beam modifying devices are entering the nanodosimeter. Electrons ranging in energy from only a few hundred eV, which were most abundant, to just over 600 keV would go on to contribute to cluster formation within the SV. Low energy electrons could contribute to large cluster formation as they have the potential to stop within the SV. Indeed, there was approximately one electron for every 20 protons entering the nanodosimeter chamber. These secondary electrons could be the cause of the variation between the

experimental and simulated results. Increasing discrepancy of the conditional cluster size distributions for >8 ions may be due to stopping electrons or neutron contamination, since these would preferentially contribute large clusters. This effect could also be produced by a rare ion multiplication mechanism in the ion acceleration channel below the ND aperture as suggested by [37]. Further investigation of this is required and ideally it would be useful to complete simulations of ALL particles entering the ND under experimental conditions for comparison with experimental results.

9.6.2 Incident Track Validation

To further validate the combined Monte Carlo simulation system used to theoretically determine the response of the ND, experimental data was obtained for three separate proton energies 250, 17 and 5 MeV. Using the STT and off-line data analysis it was possible to isolate the experimental response of the ND to incident protons crossing at a height of 25 mm from the base aperture and at three different lateral displacements from the SV, 0, 2 and 7 mm in gas which corresponds to 0, 6 and 21 nm in tissue. Using the GEANT4 based application three separate energy distribution files were generated using the experimental conditions present during data collection (Section 9.4). These were used as input into the ND simulation program with the incident energy of the beam governed by the distributions generated by GEANT4 and the position of the beam localised to a co-ordinate corresponding to a height of 25 mm and a distance from the SV of 0, 2 or 7 mm. Separate simulations of 10^7 particles were run for each co-ordinate and the comparative results displayed in Figure 9-14, Figure 9-15 and Figure 9-16.

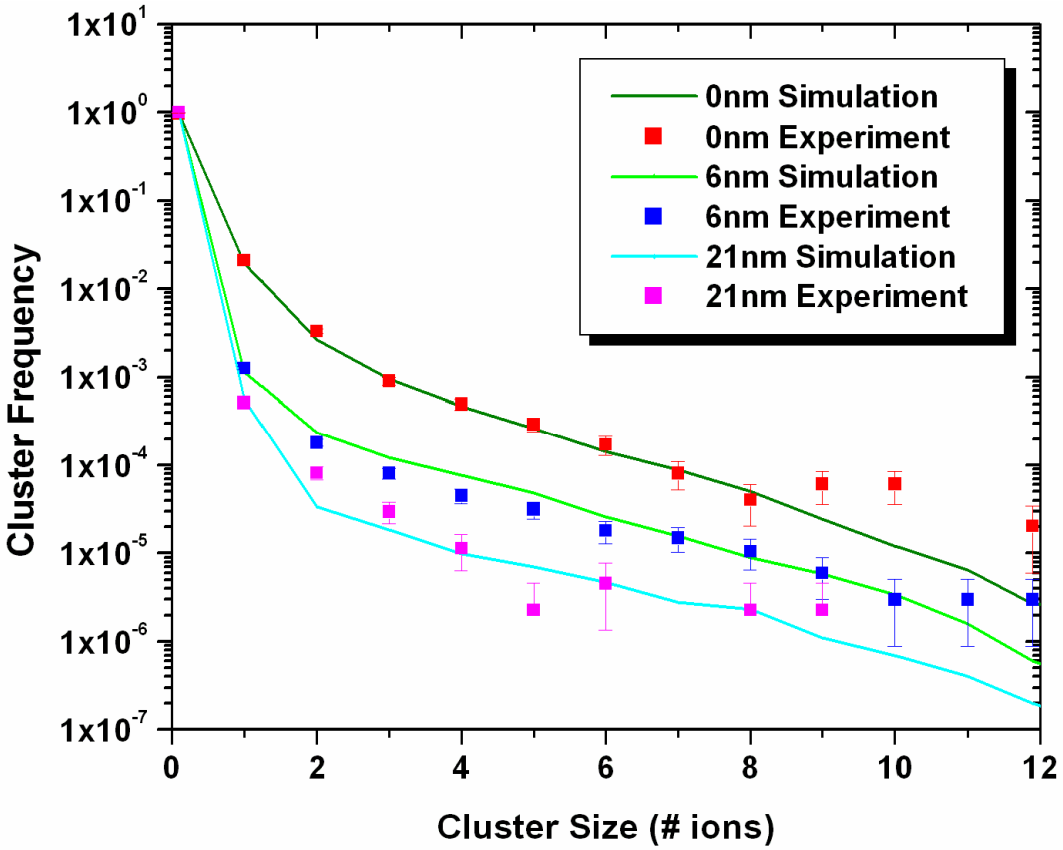

Figure 9-14: Cluster size distribution for ~250 MeV protons at a distance of 0, 6 and 21 nm from the SV generated experimentally and theoretically. Appropriate error bars are displayed for experimentally measured values.

The results generated for the 250 MeV beam are in good agreement across a range of generated cluster sizes. Some discrepancy is observed between the simulated and experimental cases for larger cluster sizes (>8 ions) which has been addressed previously in broad beam simulations. It is surmised that this discrepancy results from secondary particles entering the ND which are not considered in the simulation system, or possibly from a rare ion multiplication mechanism in the ion acceleration channel below the ND aperture as suggested by [37]. It is important to note that this discrepancy is most prevalent for 250 MeV at 0 mm lateral displacement from the SV yet is not observed in the 17 and 5 MeV cases (Figure 9-15 and Figure 9-16). As the neutron spectra present for experimental measurements is significantly reduced and almost non-existent for both of these energies (as the incident proton energy is only 30.7 MeV) it could be surmised that the increase in the frequency of large clusters for 250 MeV is a result of neutrons present in the radiation field that are not considered by the simulation program. This

supports the development of code that will account for these particles in cluster formation. Such results may also be useful in determining the effect of secondary neutrons in proton therapy treatment, especially when linked with a radiobiological model.

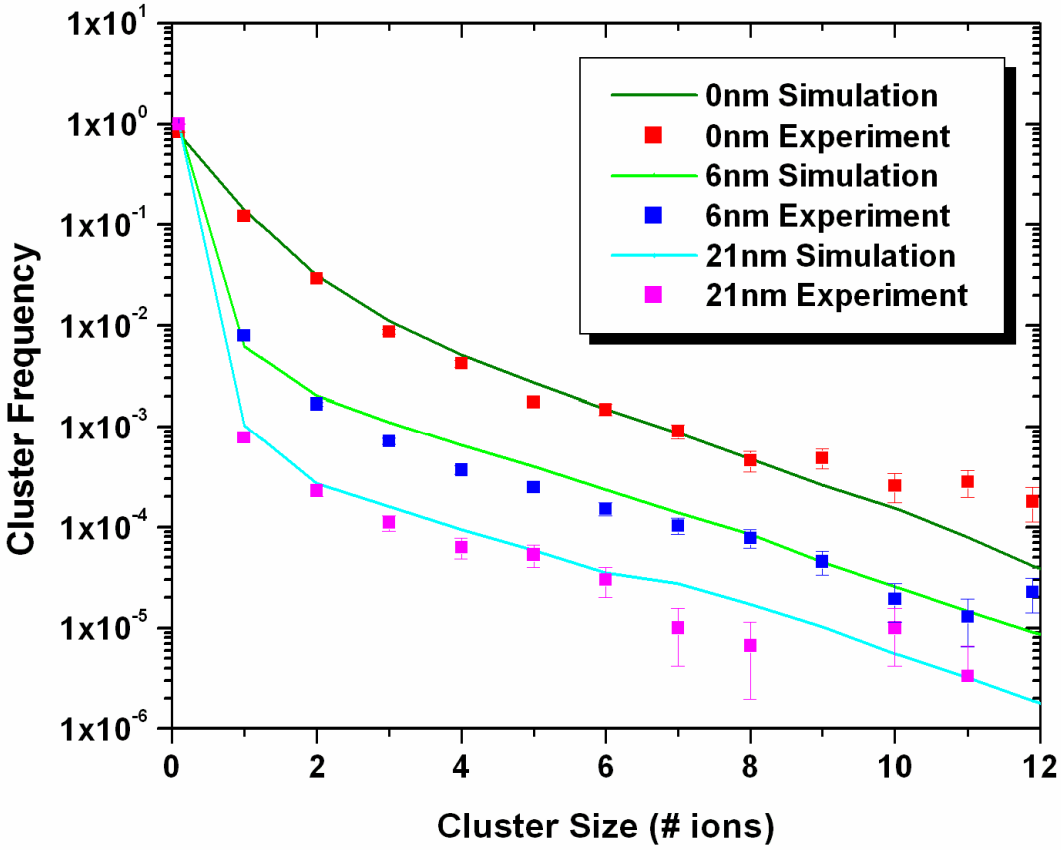

Figure 9-15: Cluster size distribution for ~17 MeV protons at a distance of 0, 6 and 21 nm from the SV generated experimentally and theoretically. Appropriate error bars are displayed for experimentally measured values.

For 17 and 5 MeV the comparative results are in good agreement with no significant deviations in the trends expressed by the experimental or theoretical results. It is apparent from Figure 9-15 and Figure 9-16 that at a lateral displacement of 21 nm (or 7 mm) from the SV, the experimental results do not exhibit a smooth trend. It is believed that this is a direct result of limited statistics in this region, as due to beam time constraints the number of histories collected for 17 and 5 MeV was only approximately 10% of those collected in 250 MeV experiments. Future work will be completed to

improve the number of collected histories for these energies and expand the results to other particles and proton energies.

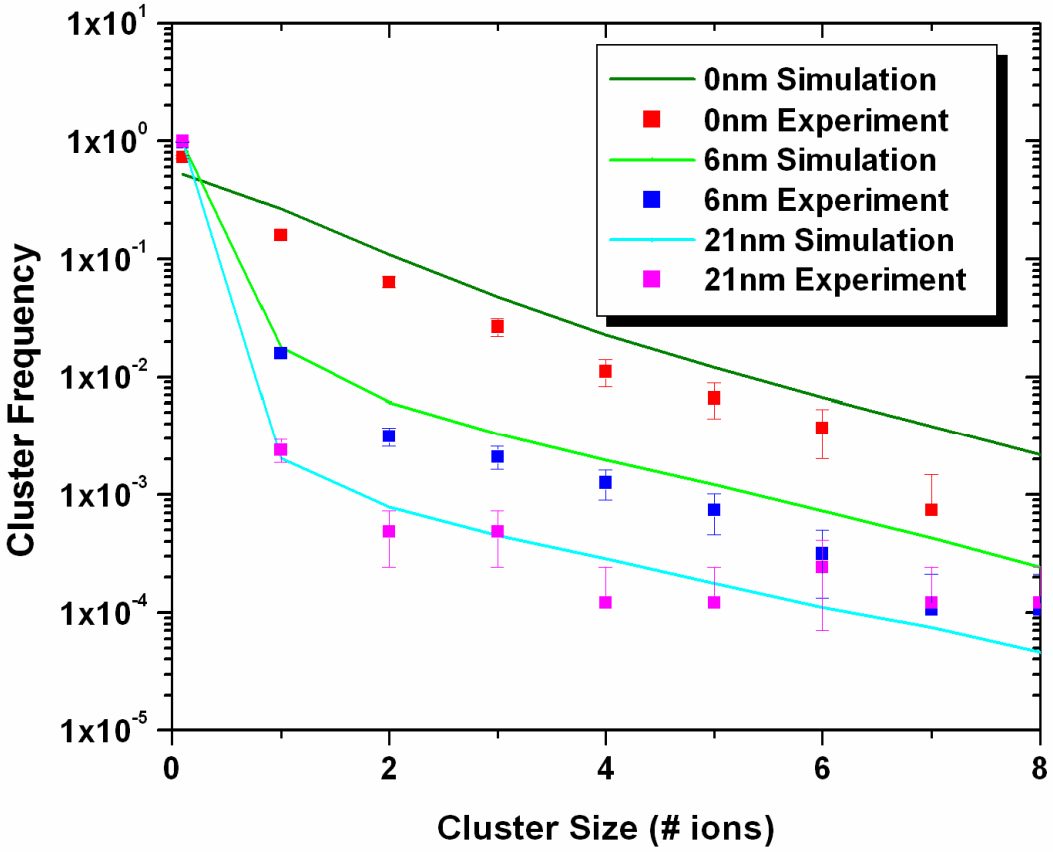

Figure 9-16: Cluster size distribution for ~5 MeV protons at a distance of 0, 6 and 21 nm from the SV generated experimentally and theoretically. Appropriate error bars are displayed for experimentally measured values.

In the case of 5 MeV protons, the simulations do reflect the experimental trends well, however in both the case of the 0 and 6 nm lateral displacements from the SV the theoretical results over-estimate the response of the ND. It is possible that this is a reflection of the discrepancies in the FWHM of the experimental (measured using a CsI calorimeter) and theoretical beam profile generated by GEANT4. Further work should be completed to incorporate accurate initial beam energy distributions and fluence maps into the GEANT4 application to obtain a more accurate spectrum of particles entering the ND. Such improvements should result in a more accurate theoretical response of the ND, especially at low energies where the beam has been degraded significantly from its incident energy.

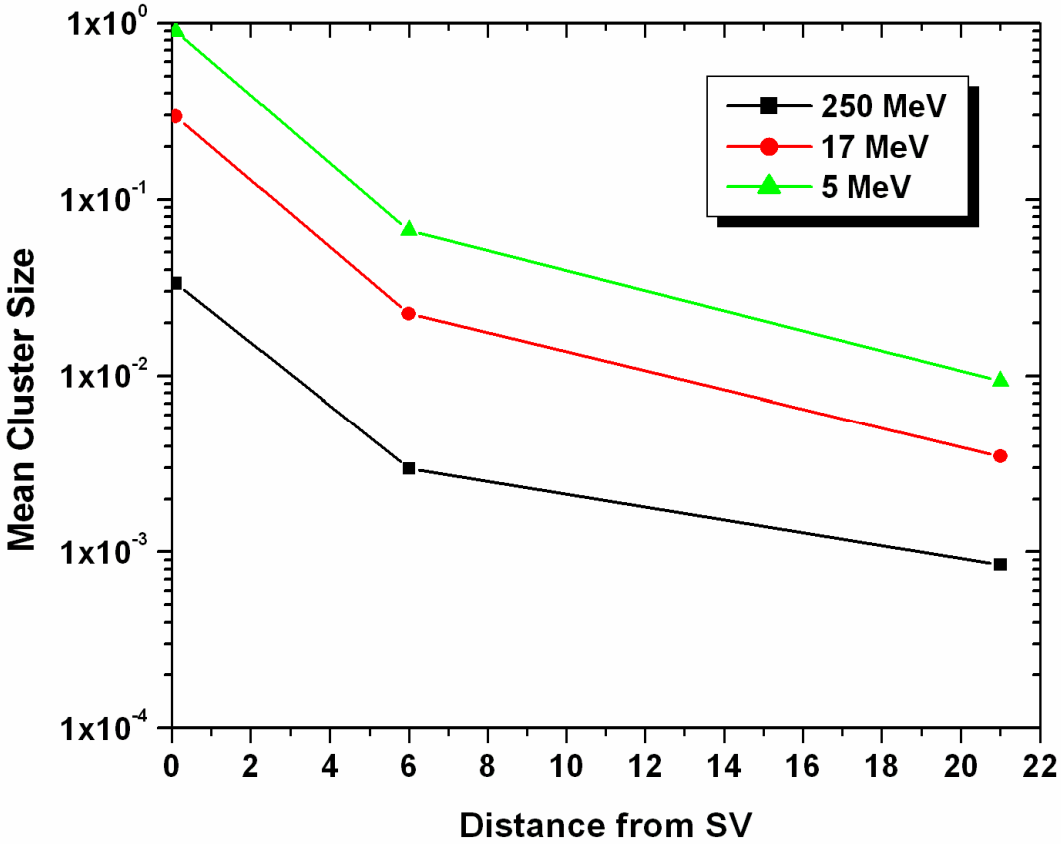

Figure 9-17: Mean cluster size as a function of lateral displacement from the SV at a height of 25 mm for 250, 17 and 5 MeV protons.

Figure 9-17 displays the MCS as a function of lateral displacement from the SV for the three proton energies tested. The results returned are interesting and provide information on the range of secondary electrons generated by the different incident radiations. Clearly the MCS increases as the incident particle LET and hence as the ionisation density increases. Further, it would be expected that the MCS also varies depending on particle type and associated track structure at the nanometre level which has been observed in previous work [37, 38]. At a height of 25 mm and with no lateral displacement there is a factor of 9 difference in MCS between 250 and 17 MeV protons while this increases dramatically to a factor of 27 difference when comparing 250 and 5 MeV protons. However, as the lateral displacement increases the difference in MCS between 250 MeV, 17 and 5 MeV protons decreases. Such that at a lateral displacement of 21 nm there is a factor of 4 difference in MCS between 250 and 17 MeV and a factor of 10 difference when comparing 250 and 5 MeV protons. As the lateral displacement

has increased from 0 to 21 nm the difference in MCS from 250 to 17 and 250 to 5 MeV protons has decreased by a factor of approximately 2. This illustrates that while 250 MeV protons may be sparsely ionising, electrons produced have potentially longer ranges than for lower energy protons. Long range delta rays can interact with DNA at distance from the incident particle track increasing biological damage. This data has further displayed how nanodosimetry provides information on particle track structure that is dependant on particle type and energy. Variations in either produce a measurable change in nanodosimeter response as observed in data presented above and in [40]. Such changes can in turn be correlated with biological effect (Section 9.8.2) and further supports the use of such quantities in treatment planning to better ascertain radiobiological effect from therapeutic radiation fields.

9.6.3 Effect of Electron Transport

The effect of secondary and Auger electron generation and transport in the gas volume was also investigated using a broad beam of 250 MeV protons and the results are displayed in Figure 9-18. It is clear that secondary electron interactions within the SV contribute significantly to cluster sizes larger than one ion, with only small cluster sizes deriving from direct proton ionisation within the SV. This is to be expected as a direct result of a high-energy proton's low LET producing a low-density ionisation track. Secondary electrons that are produced within the gas and traverse the SV can produce further ionisations within the DNA equivalent volume. It is the ionisations produced by these secondary electrons that create most of the clusters larger than 1-2 ions within the SV. Assuming that the ND SV simulates DNA, this means that secondary electrons are significantly enhancing the biological damage produced by the primary particles.

The effect of Auger electrons on cluster size was also studied by including or excluding these electrons from the simulation (Figure 9-18). It is clear that Auger electrons produced within the gas can cause further ionisations within the SV increasing the probability of larger clusters. However, this effect is quantitatively small when compared with the effect of all secondary electrons.

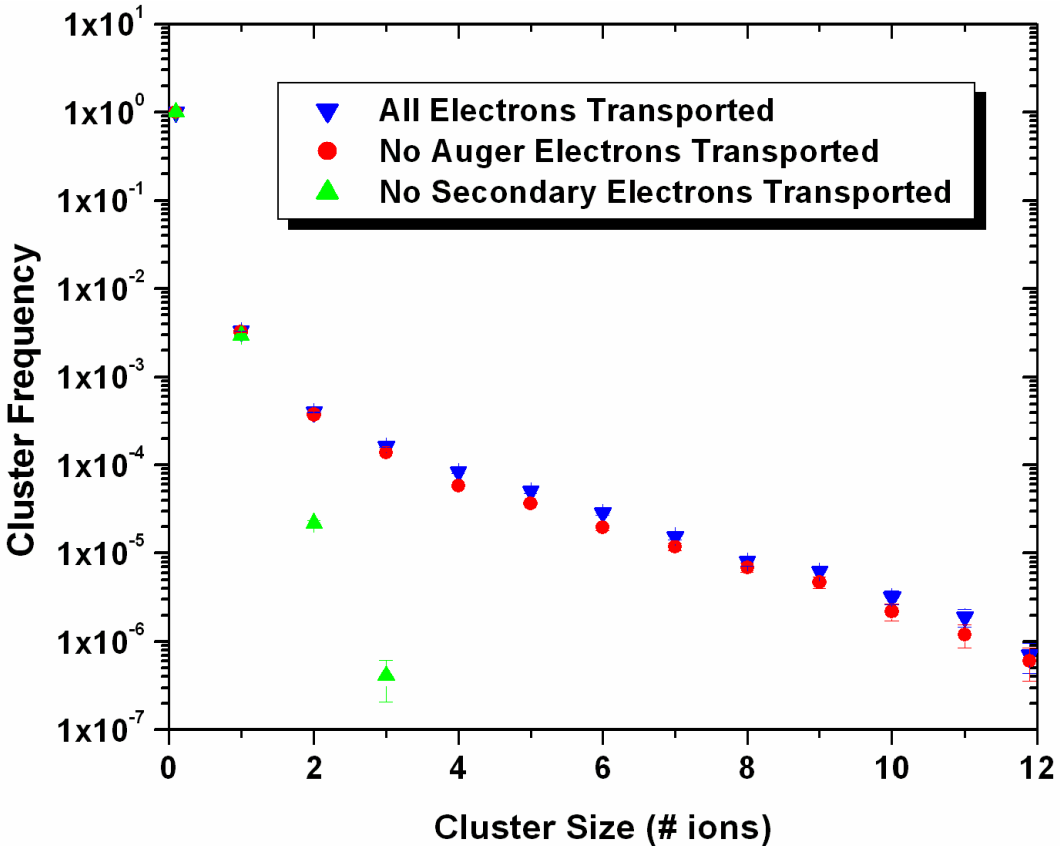

Figure 9-18: Cluster size distribution comparisons for simulations with different electron transport parameters. The different electron transport parameters provide information on the importance of secondary electrons to the cluster size distribution.

9.6.4 Dependence of CSD on SV Length

In all previous cases a full length (50 mm in gas) SV has been utilised in comparisons between experimental and simulated nanodosimetric CSD. However, it is also important to ascertain the accuracy of the simulation program for shorter SV's. To determine this, offline analysis of experimental data using appropriate cuts on ion drift time was conducted to achieve experimental data for an equivalent SV length of 7 nm (in tissue) irradiated with a 250 MeV broad proton beam (Setup A). These were then compared with simulated data for an equivalent 7nm SV within the nanodosimeter. As in previous cases the GEANT4 based application provided the energy and fluence spectra for a 250 MeV broad beam to the program that determines CSD within the nanodosimeter.

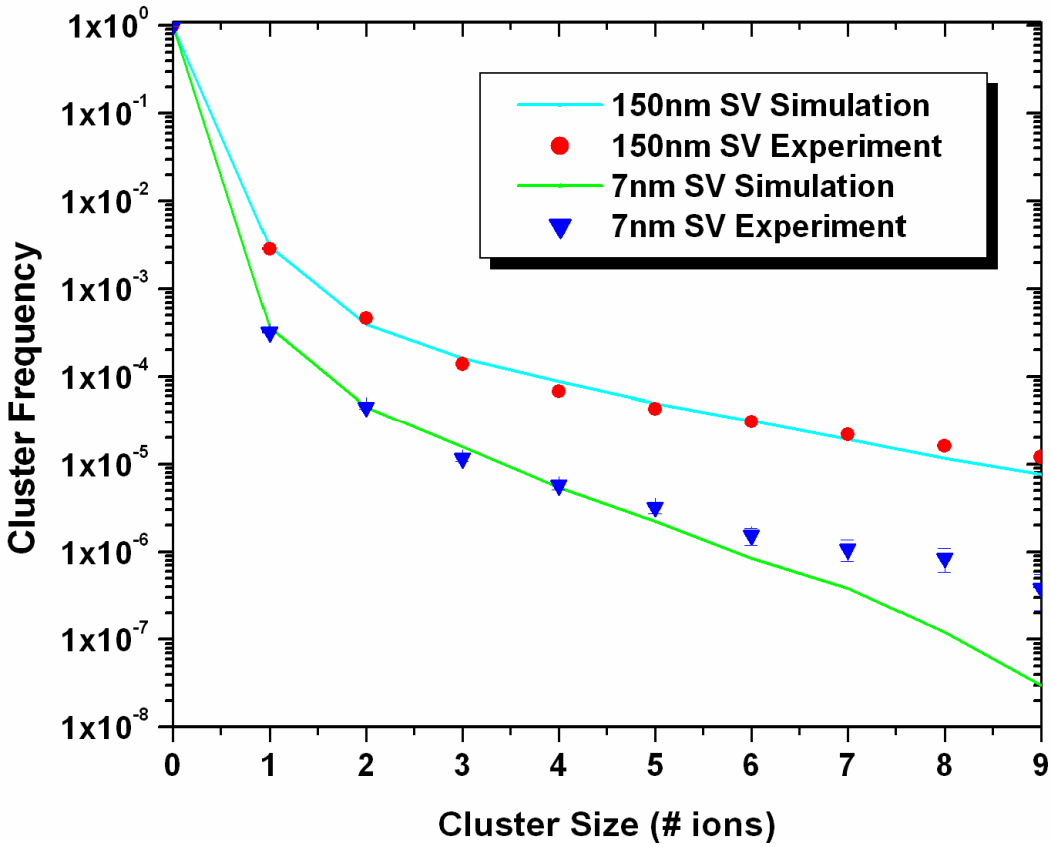

Figure 9-19: Cluster size distribution comparisons for theoretical and experimental results utilising both full and 7nm SV lengths. The distributions are normalised to the total number of events including zero events.

The simulated and measured CSD's for the 7 nm SV show good agreement for smaller cluster sizes and is similar to the results obtained for the full SV case. A discrepancy is observed between the theoretical and experimental results for large cluster sizes with the simulation under-estimating the response of the ND. It is important to note that both the simulated and measured frequency of clusters formed within the 7 nm SV is of an order of magnitude smaller than that for the full SV. For the simulated results this discrepancy between the two SV sizes increases as cluster size increases. The first observation is explained by the difference in the SV size, as the geometrical cross section of the primary beam and SV is about 10-times smaller for the 7 nm SV than for the full SV. The second observation can be explained by the fact that many of the larger clusters may not fit into a 7 nm volume and are therefore registered as smaller clusters with part of the cluster lying outside the SV.

The final observation from these results concerns the discrepancy between simulated and measured CSD for larger clusters. For the 7nm SV one observes that the measured cluster frequency departs from the simulated one at a cluster size of about 4-5 and then decreases with a similar slope as the measured CSD for the full SV (Figure 9-19). This result favours the already mentioned ion multiplication mechanism below the aperture [37], which would be independent of the selected SV size, as an explanation for the additional large clusters observed experimentally.

9.7 Conclusion

This work has investigated the effectiveness of the GEANT4 toolkit in obtaining incident beam data to achieve a simulated input for an independent ND simulation code. The GEANT4 based application created for this work provides a means for simulating the beam modifying devices that the radiation field must pass through before entering the nanodosimeter. The results obtained were compared where possible to CsI calorimeter measurements with good agreement in mean peak position observed. Further improvements including a more accurate estimation of the cross sectional area, divergence and energy spread of the delivered beam could be incorporated into future work to provide a more accurate assessment of the radiation field present during experimental measurements.

The output from GEANT4 was then processed by the PTB simulation code to compute theoretical nanodosimetric cluster size distributions. This two-stage simulation system allows for a more accurate assessment of the radiation field entering the nanodosimeter and provided better agreement between experimental and simulated cluster size distributions. The simulated response of the ND was compared to experimentally derived results over a range of energies and beam configurations.

Broad beam 250 MeV simulations were completed with the GEANT4 generated energy spectra and fluence distribution input into the ND simulation. In this case the GEANT4 based application provided the entire energy spectra of protons entering the SV including both the peak low energy recoil protons. Whilst the low energy protons make up less than 0.5% of all protons entering the SV, separate simulations of both the peak

and low energy proton spectra were conducted to ascertain their importance, or lack of, to CSD. Indeed the low number of recoil protons entering the nanodosimeter makes their contribution to CSD insignificant. Some discrepancy was observed in comparison between the simulated and experimental CSD especially for larger clusters where it appears that the simulation program under-estimates the response of the ND. It is believed this is caused by secondary electrons and neutrons produced in the up-stream beam modifying devices of the system. The ND simulation program in its present form is limited in that it can only account for one type of incident radiation, protons in this case. However, after passing through beam modification devices the radiation field will not only comprise of protons, but low-energy secondary electrons and also neutrons, both of which are likely to contribute to the additional clusters within the nanodosimeter observed experimentally. In order to improve the accuracy of the nanodosimeter simulation program, particles such as secondary electrons and neutrons produced in upstream devices and entering the gas volume also need to be accounted for. It is also possible that this discrepancy could also be caused by a rare ion multiplication mechanism in the ion acceleration channel below the ND aperture as suggested by [37].

Pencil beam simulations were also completed for 250, 17 and 5 MeV protons at a height of 25 mm on the SV and lateral displacements of 0, 2 and 7 mm in gas (or 0, 6, and 21 nm in tissue). These were compared with experimental data that was obtained through off-line analysis using the STT. The comparison between experimental and theoretically derived CSD's was good with discrepancies at larger cluster sizes observed as a result of secondary particles not accounted for in the simulation and limited statistical sampling. The trends of the experimental response were well reflected further validating the Monte Carlo simulation system employed in this work and identifying areas of future development. These measurements indicated the ability of the experimental and theoretical systems in measuring the change in track structure (nanometric radiation properties) of radiations of the same type but differing LET.

The importance of secondary electrons generated inside the nanodosimeter to cluster size was highlighted through simulations of the response of the ND to a broad beam of 250 MeV protons considering all electrons, discounting Auger electron formation and

discounting electron transport altogether. It was observed that secondary electrons are the main contributors to cluster sizes larger than two ions for 250 MeV proton irradiation of a nanometric volume, while Auger electrons make only a small contribution to cluster frequency.

Finally, the response of the ND to varying SV length was simulated for a 250MeV broad beam and compared with experimental data that was obtained using appropriate cuts on ion drift time for a 7 nm SV. The results indicated good agreement between the experimental and simulated cases for small cluster sizes. However, for both the 7 nm and full SV the simulation program tended to underestimate the response of the ND for large cluster sizes. The frequency of cluster formation for the 7 nm SV was approximately an order of magnitude lower than for the full SV, and this discrepancy increased with increasing cluster size. This later is most likely the direct result of larger clusters being unable to be contained within the smaller SV.

These results have presented both theoretical and experimental nanodosimetry data for a range of proton energies. The Monte Carlo system employed has been validated through these comparisons and areas of improvement have been identified for future work. The current ND system has demonstrated that it is useful in obtaining nanodosimetric data for laboratory conditions and supports the program we have implemented for the investigation of nanodosimetry and its importance to radiation therapy and radiation protection. Information on the nanometric cluster size distribution (or track structure) of an incident particle may provide a more accurate determination of radiation effects of mixed radiation fields, as the track structure of a given charged particle at a given energy is unique. Experimental measurements and theoretical simulations have shown that such measurements are possible using low-pressure gas nanodosimetry and associated Monte Carlo simulation systems. This may then be linked to an accurate prediction of RBE through the development of a biological model. Further work on detector development including improvements to portability, collection times, and ability for in-phantom measurements will also increase the application of nanodosimetry.

9.8 Future Work

Nanodosimetry is certainly an area in radiation metrology that will increase in its application for both radiation therapy and radiation protection. This work has benchmarked the performance of a low-pressure gas ion-counting nanodosimeter in proton radiation fields and compared this to a current Monte Carlo simulation system. There are three main areas of development that will be undertaken as a continuation of this work:

- Monte Carlo Simulations
- Radiobiological Modelling
- Detector Development

9.8.1 Monte Carlo Simulations

This work employed a two-stage Monte Carlo simulation system to provide the most accurate simulation of the ND response using current technologies. The first stage utilised a GEANT4 based application to simulate the primary radiation transport through beam modifying/monitoring devices and provide an accurate assessment of the radiation field entering the ND. However, GEANT4.7.1p1 can only transport electrons down to an energy of 250 eV which is insufficient for ND applications. In this field of endeavour, the electrons need to be transported down to the ionisation potential of the gas or approximately 10 eV in this case. To achieve this, a Monte Carlo simulation system developed at PTB incorporated the single particle (proton in this case) energy and fluence spectra from GEANT4 in simulating the ND response. The results obtained with such a system were satisfactory, however deficiencies were identified in the simulation system that need to be addressed in future work including:

- Assumptions in incident beam energy, profile and direction. In this case the incident beam was assumed to be monoenergetic, circular in profile and travelling normally down an evacuated beam pipe.
- Secondary particles of a different type to the primary could not be considered in the second stage of the simulation. As such neutrons and electrons were not considered in contributing to cluster formation in the experimental case.

- Particles entering the second stage of the simulation were considered to be entering normally with no angular divergence.
- Broad beam simulations simplified the particle fluence entering the ND as a radial profile, and discounted inhomogenaities in particle fluence.
- The second stage of the system can only consider ND cluster formation in a uniform propane or water volume and can not be expanded in its current state to simulate CSD's in other structures such as tissues for radiation therapy or silicon for SEU analysis.

These deficiencies have not contributed to significant errors in the current work which is evident through the good agreement with experimentally derived data. However, it provides a clear area of future development. Many of these issues can be addressed using a single Monte Carlo simulation system such as GEANT4 to simulate both the experimental setup and ND response. Such comparisons would validate GEANT4 and allow for an expansion of ND simulations to other geometries. Unfortunately the current status of GEANT4 precludes its use simulating the ND as electron transport does not extend down to 10 eV. Significant efforts are currently being invested into the development of numerical simulation codes modelling particle track structure on the nanometre scale including the GEANT4 DNA project [47]. The ion-counting nanodosimeter and current simulation system can be used in validating improvements made to GEANT4 low energy electron transport models. Further, once validated it may be possible to utilise GEANT4 in modelling the ND as a single stand-alone application.

9.8.2 Radiobiological Modelling

Nanodosimetry provides a means for determining experimentally (or theoretically through the use of Monte Carlo modelling) the number of ionisations within a DNA equivalent volume. To facilitate a useful analysis of the biological effectiveness of radiation fields, this output needs to be linked with a biological model. The endpoints for such a model may vary, but the quantity of most relevance to radiation therapy is colonogenic cell survival.

Radiation can interact with DNA and cause damage in a number of ways including single strand breaks (SSB), double strand breaks (DSB), modified or lost bases etc [62, 117]. Current radiobiological evidence points to the fact that DSB's are the most significant type of lesion in causing cell death [118]. A radiobiological model that correlates cluster frequency within a DNA volume to biological effect will hypothesize that the colonogenic cell survival is dependant on the difference in reparability of DSB's generated from radiations of differing LET.

DSB's can be repaired along two separate pathways, homologous and nonhomologous end-joining. In both cases nucleotides degrade the ends of the DNA and prepare it for repair post DSB formation. In homologous end–joining the DNA combines with a homologous (being equal in DNA sequence) undamaged counterpart using it as a template for repair. This form of repair is precise, however is less common and typically only occurs during S-phase in the cell cycle [119]. Nonhomologous end-joining does not require a non-damaged template but proceeds by simply rejoining the broken DNA strands. This is a fast and simple process that operates throughout the cell cycle. However, there is no guarantee that the DNA returns to its existing state and multiple DSB's in close proximity may result in misrejoining of the DNA strand. Despite this fact nonhomologous end-joining is the predominant DSB repair mechanism in human cells.

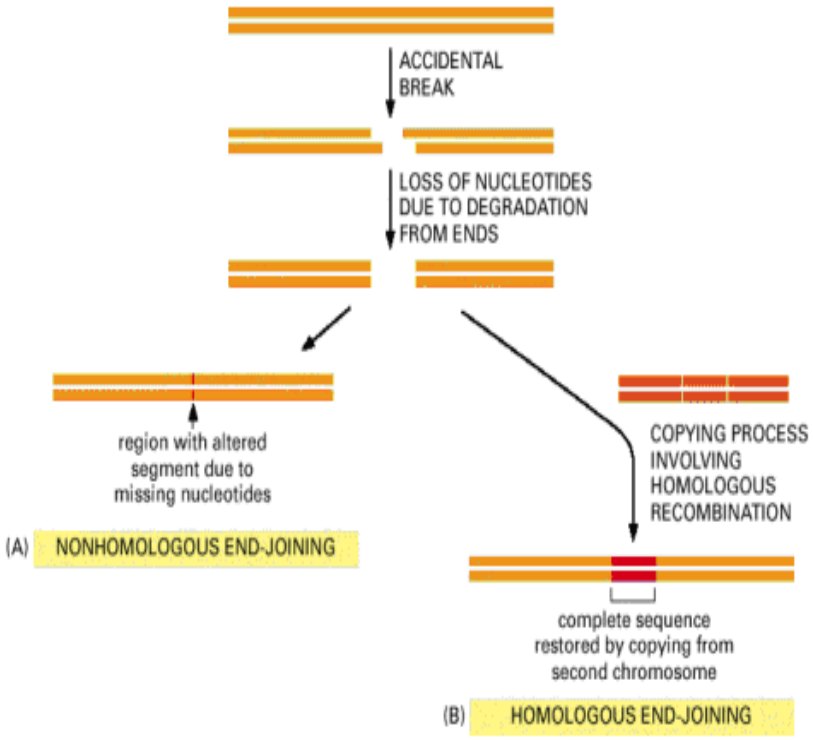

Figure 9-20: Schematic of the two pathways available for DSB repair in mammalian cells [119].

Generally, DSB's formed through low-LET radiation interaction with DNA are repaired correctly, particularly for lower doses or smaller numbers of DSB's (termed simple DSB's). As the dose delivered to the DNA or the LET of the incident radiation increases there may be increased levels of misrejoining in nonhomologous end-joining repair resulting in cell death or mutation. The fact that radiosensitivity is stable throughout the cell cycle indicates that repair by homologous end-joining is limited in repairing DSB's induced by high-LET radiation or high doses of low-LET radiation (termed complex DSB's). Such factors need to be considered in biological modelling.

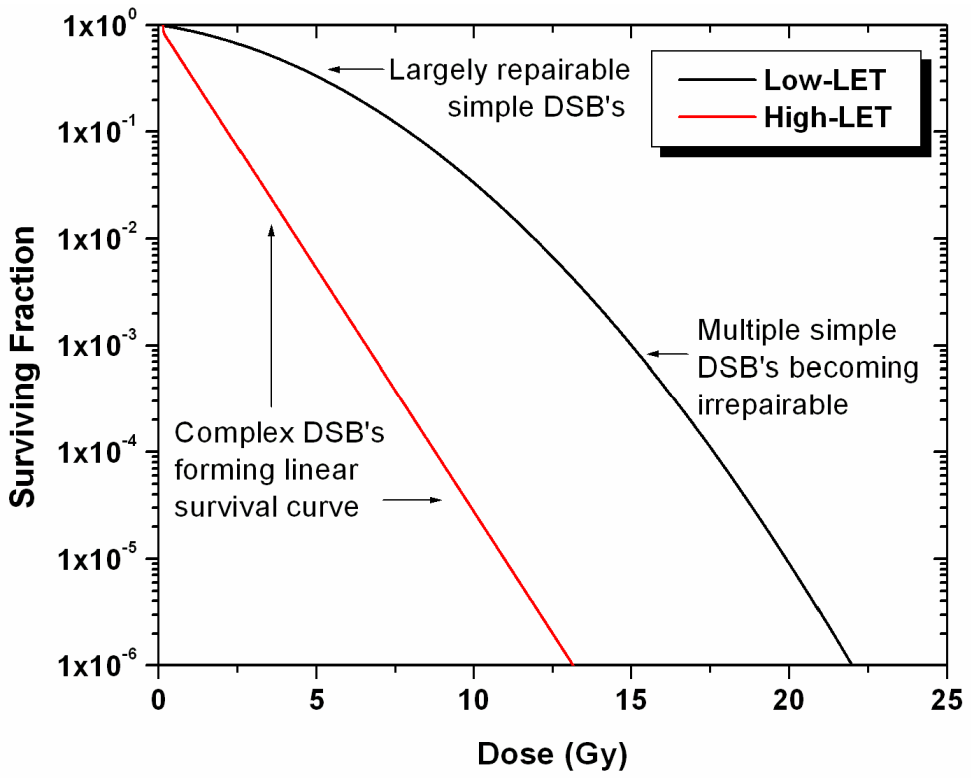

Figure 9-21: Example of a survival curve for high and low LET radiations. Note the differences in response produced by individual simple, multiple simple and complex DSB's.

Cell survival curves are generally described by a relationship between the surviving fraction of cells and the dose applied (Figure 9-21). The exponential response of the surviving fraction as a function dose is well explained by a Poisson model. The genome consists of a large number of independent DNA segments and only a small fraction of these will be affected by DSB's that lead to a lethal event. If the lethality of DSB's does not depend on the presence of other DSB's in the cell, a linear survival curve is the result when plotted in a semi-logarithmic graph. This is in fact the case for a typical high-LET cell survival curve. Survival curves generated by low-LET radiations show characteristic nonlinearities, the most universal one being a downward curvature of the cell survival curve with increasing dose. This can be explained by a linear-quadratic polynomial, where the linear part corresponds to the irreparable DNA damage and the quadratic part to damage that, in principle, can be repaired but is increasingly less likely to be repaired with increasing numbers of DSB's present per cell.

The model described here and that will be developed in future work uses experimental or Monte Carlo simulated data describing the frequency of event sizes in nanodosimetric volumes representing a segment of DNA as the basis to predict cell survival. The nanodosimetric data is used to predict the relative portion of high-LET type or complex DSB's and low-LET type or simple DSB's. Measured cell survival responses to a low-LET type radiation (e.g., Co-60 gamma rays) and to a high-LET type radiation (e.g., alpha particles) will provide the basis for the model. Combining these responses with the measured changes in the ND event size distribution, it is possible to predict the cell survival response to any monoenergetic or mixed radiation field for which ND data is available.

This model [120] assumes that the dose can be divided into two fractions *q1* and *q2*, where *q1* is the fraction of dose deposited in ion cluster events that lead to low-LET type DSB's and *q2* is the fraction of dose deposited in larger ion cluster events typically generating high-LET type DSB's. These properties are determined from the CSD as the ratio of frequencies over a certain range of cluster sizes corresponding to simple and complex DSB's respectively. It is hypothesised that cluster sizes of 2-5 produce low-LET type DSB's, while cluster sizes larger than 5 generating high-LET type DSB's. Note that *q1* and *q2* do not necessarily add up to 1 because a portion of dose is also deposited in single-ion events that do not lead to DSB's. According to this model, the surviving fraction from a delivered dose *D* is given by the relationship as described in Equation 9-1.

$$SF(D) = \exp\left(-\alpha_1\left(q_1 D\right) - \beta\left(q_1 D\right)^2 - \alpha_2\left(q_2 D\right)\right)$$

Equation 9-1: Model for deriving biological response from measured ND response. α_1 and β are simple DSB parameters produced by the low-LET radiation component, while α_2 is a complex DSB parameter produced by the high-LET radiation component.

The parameters α_1, β and α_2 are cell line dependant parameters that are determined through initial testing of the chosen cell line with a low-LET (e.g., Co-60 gamma rays) and high-LET (e.g., alpha particles) reference radiation. These parameters are established through initial benchmark testing of the cell line and remain unchanged

regardless of the beam conditions. From a measured (or simulated) CSD, beam quality factors *q1* and *q2* are derived that are dependant on particle mix and energy spectra but are considered to be independent of cell type.

Given proper benchmarking with a suitable low and high-LET reference radiation it is possible to predict in theory the colonogenic cell survival for any mammalian cell line using nanodosimetry. The key to successful modelling in this case will be a suitable radiobiological protocol which will allow for suitably accurate reference radiation experiments to be completed. To this end a radiobiological protocol has been developed and is tested in Section 10.

9.8.3 Detector Development

This investigation and previous studies [37-39, 116] have shown that a low-pressure gas nanodosimeter is capable of measuring ionisation clusters on a DNA equivalent volume. However, such a device has its limitations, the most prominent being its need for a dedicated beam-line, its lack of portability and slow collection times. If the realm of nanodosimetry is to be investigated further an improved nanodosimeter is required that will allow for deployments on space and aircraft, installation in radiation protection applications such as nuclear and military facilities and utilisation in radiation therapy and radiobiology. For this to take place the basic concept of the apparatus may need to be revisited.

Currently nanodosimetry is based on a low pressure gas instrument that measures the number of ions (cluster of ionisations) produced by a track of charged particles in a gas volume equivalent to the nanometric volume of a DNA segment. This was achieved using a low pressure (1 Torr) tissue equivalent gas (Propane) sensitive volume (SV) of millimetre size which is similar in mass to a DNA segment. The geometry of the gas SV is determined by configuration of the electric field which extracts the ions through a small aperture. A silicon tracking telescope allows for the position and track of incoming particles to be registered and correlated with cluster formation within the SV. The operational concept of such a device means that it is suited as a basic research device rather than for active deployment.

There are two developmental tracks which can be undertaken in order to further develop nanodosimetry. The first would involve keeping the gas concept and making it more portable, efficient and easier to use. The second would involve moving in a new direction and using current solid-state technologies in order to create nanometre sized sensitive volumes. Parallels can hence be drawn to microdosimetry and the development of tissue equivalent proportional counters (TEPC's) and solid-state microdosimeters to fulfil the criteria of collecting the energy deposited by ionising radiation in a micrometre volume.

Further development of the electronics, tracking and acquisition system of the current ion counting device can be considered. However, problems still remain that make such a device unsuitable for tasks other than research including:

- The materials surrounding the SV, including the housing, entrance window, exit windows and silicon tracking system are not TE. As such attenuation of the radiation field and the secondaries produced by such interaction will affect results.
- The differential pumping system is by nature complicated and large in size.
- The gas system does not measure interactions on a truly nanometre volume, but rather averages effects across a millimetre sized gas volume.
- The ND and STT is only suitable in a uni-directional radiation field.

Solid-state nanodosimeters of truly nanometre SV size should be investigated and developed in order to further this field of research. Attempts to develop solid-state radiation detectors sensitive to the track structure of charged particles was recently undertaken using the response of LiF Thermo-Luminescent Detectors (TLD-100) and based on recombination of electron hole pairs in spatially correlated trapping luminescent centres of LiF detectors [121]. It was observed that the shape of the glow peak produced by the TLD depends on the track structure. However, interpretation of this data is complicated and is unable to be applied in real time nanodosimetry.

Detector Performance Parameters	Low-Pressure Gas Nanodosimeter	Solid State Nanodosimeter
Efficiency of Data Collection	Poor	High
Efficiency of Ion Registration	Good	Moderate
Acquisition time for data points	Very High (20-40 hours)	Low (10-20 minutes)
Ability to measure neutrons	Very Poor	High
In-vivo measurement	Poor	High
Susceptibility to pile up	High (long collection time in gas)	Low (fast light emission and detection)
Other Parameters		
System Cost	High	Low
Portability	Poor (dedicated beam-line required)	Very High
System Complexity	Very High	Low
Integration into existing systems	Poor	High
Number of SV's	Single SV	Multiple
Tissue Equivalence	Good	Good

Table 9-2: Comparative advantages and disadvantages of current low-pressure gas nanodosimetry and proposed solid state analogue and digital nanodosimetry.

A more effective method for real time nanodosimetry utilising nanotechnology and quantum dots (QD's) is currently being explored by the CMRP under Professor Anatoly Rosenfeld. In contrast to gas nanodosimetry such a device would consider the track of a charged particle in a TE organic material. The subsequent detection of the cluster formation on this nanoscopic level would provide information on track structure with a specific signature of the δ-electron radial density distribution for a given induced radiation field. There are two methods which can be employed for solid state nanodosimetry utilising this technique, digital nanodosimetry (DND) and analogue nanodosimetry (AND). This mode of nanodosimetry has the potential for significant improvements over current technology which is outlined in Table 9-2. The development of such detectors would be useful across a range of therapeutic and radiation protection applications, however adequate testing and development needs to be conducted.

10 Radiobiology: Cell Survival Studies

10.1 Introduction

This work has shown the suitability of micro- and nanodosimetry in providing information on the cellular and DNA level for radiation protection and radiation therapy applications. Such information is useful in determining the quality of the radiation field and when linked with current risk assessments such as those presented in [122] can provide an estimation of induced fatal cancer risk. However, such assessments are uncertain [88, 123] and improvements are continually being undertaken in order to provide a better understanding of the biological effects of radiation (such as those presented in Section 8.8 and 9.8.2).

An area where an improved understanding of biological effects is required is in treatment planning for hadron therapy. Inelastic nuclear interactions and slowing of the incident hadron may have an influence on the relative biological effectiveness (RBE) of the treatment radiation [18]. It may be advisable to complete treatment planning using a radiobiological parameter rather than the macroscopic quantity of absorbed dose. The challenges in doing so are immense as they require:

- Understanding of the biological response of different tissues to different energies and types of radiation
- A detector capable of conducting routine quality assurance (QA) measurements of the therapeutic radiation field and return a biologically significant quantity.
- A biological model that can accurately assess biological response for a given measured quantity (such as cluster frequency, ΔE-E coincidence spectra or dose equivalent).

The development of such a system is a goal of this collaboration with micro- and/or nanodosimetry providing the means for a quantitative assessment of the radiation field and linking this back to biological data. For the development of a radiobiological model in proton therapy, biological studies as well as micro- and nanodosimetry measurements need to be completed for a range of ion energies under the same experimental conditions.

Such experiments will provide for a more accurate radiobiological model as the incident radiation field will remain consistent across biology studies and physics measurements.

The aim of this work was to develop and test an accurate cell survival protocol using a human cancer cell line. Irradiations were completed using Co-60 as a reference radiation with further experiments completed across a range of therapeutic proton energies allowing for the determination of the experimental cell survival curves and associated α/β ratios. The proton energies tested included 250 and 5 MeV. It was expected that this range of proton energies and LET's would provide a measurable difference in cell survival allowing for benchmark testing of this radiobiology protocol. This work provided an experimental technique and protocol for expanding such cell survival studies to other ions and cell lines. Such future studies will provide experimental radiobiological data for biophysical model development linking micro- and/or nanodosimetry to actual biological effects with protons and other charged hadrons.

10.2 Cell Line: U-251

U-251 is a human glioma cell line which has a mutated (inactivated) p53 suppressor gene. The role of the suppressor gene is to prevent uncontrolled cell reproduction. In the case of a cell line such as U-251 the inactivation of p53 results in uncontrolled cell division and tumour formation. Tumour formation occurs in the central nervous system and is most commonly found in the brain but can also be located in the spinal column or optic nerve. The standard treatment for such tumours is dependant on the location, size and grade, but can include surgery, radiation therapy and chemotherapy [124-126]. Current techniques have resulted in minimal success through the gliomas invasive growth patterns. Efforts are currently underway to use more highly conformal radiation therapy modalities such as proton and heavy ion therapy to treat such lesions. The conformal nature of the dose delivery as well as the additional advantage of increased RBE in the instance of carbon and other heavy ions [127] will possibly assist in the treatment of gliomas.

A radiobiological model determining glioma cell survival for a measured radiation quantity may assist in the clinical implementation of such techniques. As such the U-251 cell line was chosen to complete cell survival work with protons of varying energy and determine if it is feasible to develop a radiobiological model for this cell line utilising micro- and/or nanodosimetry.

10.3 Thin-Film Irradiation Techniques

The main challenge in this study was to provide a biological assessment of the radiation field with minimal variation in LET and hence minimal change in cell response across the sample. For high energy protons and Co-60 photons this poses no problem with comparatively large samples of suspended cell solution able to be irradiated with minimal change in LET across the sample. However, for low energy proton and alpha particle cell survival studies, sample thicknesses needs to be kept as thin as possible (i.e. order of microns) to avoid such variations in cell response. As this cell survival study was to utilise such radiation fields, a method for irradiating such samples needed to be established.

Thin-film irradiation techniques clearly provide an experimental means for limiting change in LET across the sample. Such techniques have been used in previous research with both cell suspensions and suspended plasmid irradiations [128, 129]. Other factors also need to be considered when developing the experimental protocol for use with cell suspensions. Firstly, the thickness of the fluid layer containing the cells and hence the thickness of the sample must be uniform. Further, this thickness must be reproducible from experiment to experiment. The cells must also be kept in a state of minimal stress which can be achieved through the adequate supply of oxygen and minimal changes in temperature or environmental pH. Sample evaporation at ambient temperatures is another factor which must be overcome.

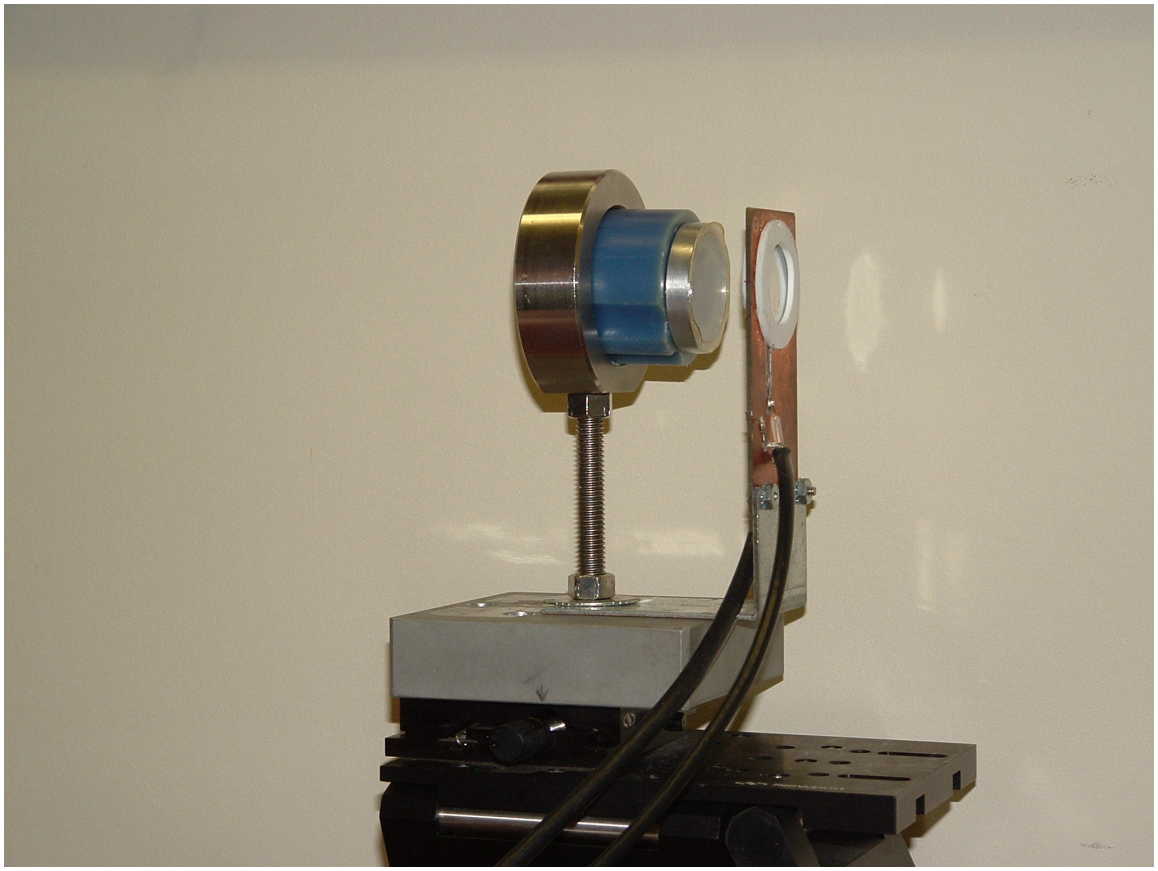

Figure 10-1: Picture of the biology sample mounted on its wax sample holder (blue) and IC1 which is used to monitor dose to the biology sample for proton irradiations.

The thin-film irradiation technique selected for this work is a variation of that presented in [74, 128, 129]. It consists of an Al ring approximately 35 mm in diameter with a window of 12 μm Mylar attached to one side. The cell suspension was applied as a drop (of 10 μL) on the Mylar window and a regular glass cover slip of 18 mm diameter was placed over the sample, to uniformly spread the sample and "sandwich" it between the Mylar and glass. Assuming that the sample is uniform thickness and further assuming that the cell suspension has the same density as water, this gives a sample thickness of approximately 40 μm. A sample thickness of this magnitude should encounter minimal LET variation across the sample and is approximately the same size as cell diameter. Further, the location of the sample between the glass cover-slip and Mylar window will provide a semi-closed environment which will minimise evaporation and contamination from outside sources.

In Co-60 photon experiments the ring (with the Mylar window facing the beam) was placed in a homogeneous radiation field and the sample irradiated. For proton irradiation the process was more complex. In this instance the sample ring was affixed to a wax sample holder and mounted with the Mylar window perpendicular to the radiation field (see Figure 10-1 and Figure 10-2).

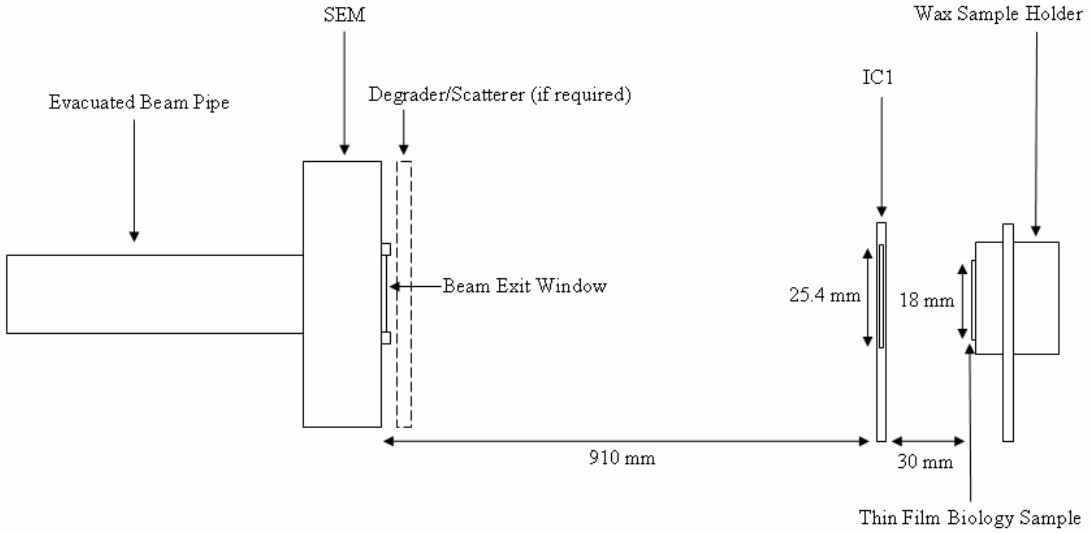

Figure 10-2: Schematic of complete experimental setup for proton irradiation of the cell suspension sample.

The sample was immediately located behind a thin walled ionisation chamber (IC1) that was used to monitor and regulate dose to the sample. This chamber is comprised of 12.7 μm Mylar entrance and exit windows, with a sensitive volume (air) of 1.57 mm thickness. Such an arrangement prevents attenuation of low energy proton beam, whilst also delivering accurate dosimetry (see Section 10.5). A more detailed schematic of the sample and its relation to IC1 is displayed in Figure 10-3, while a picture of the experimental setup is located in Figure 10-1.

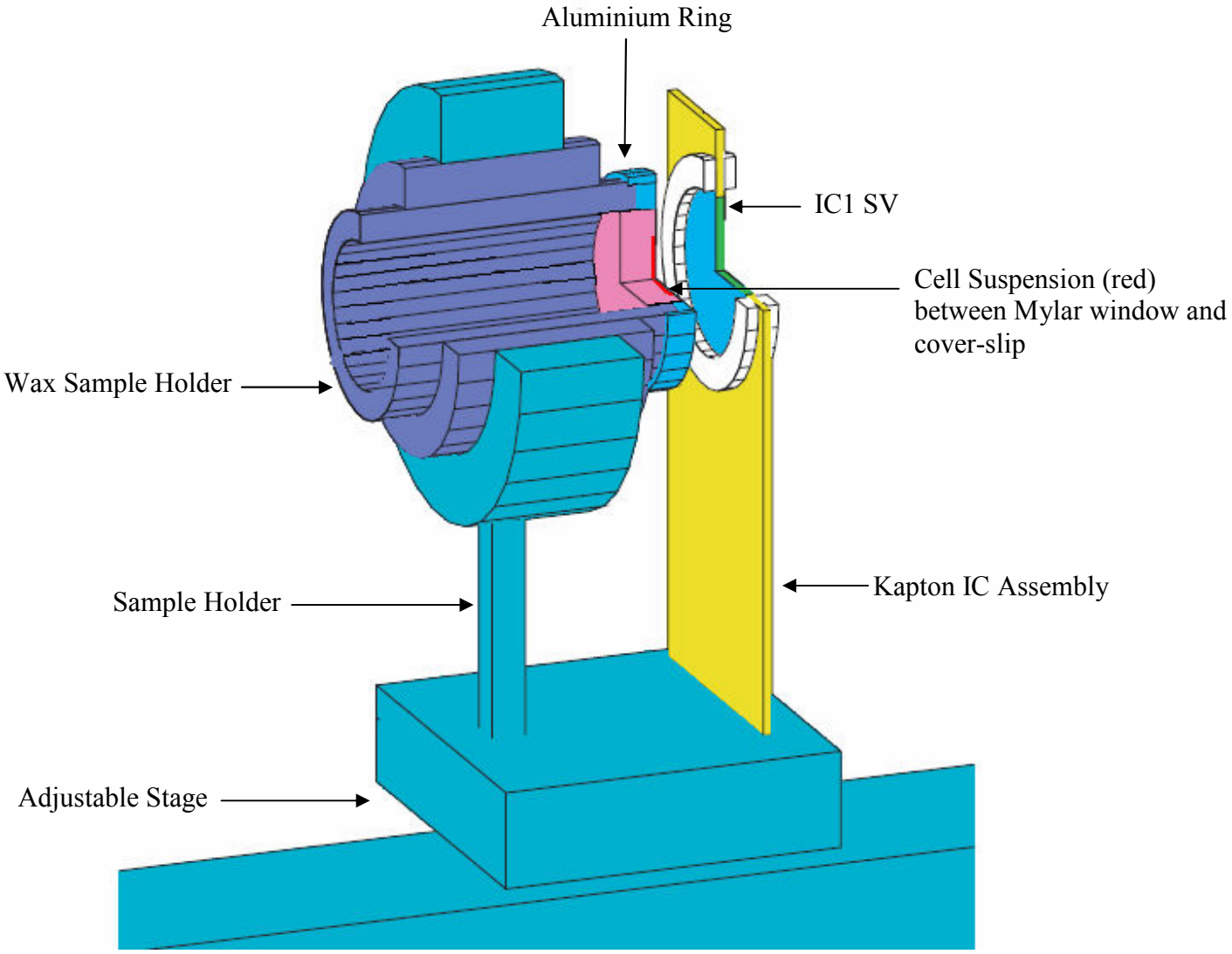

Figure 10-3: Schematic of sample and IC arrangement. Reproduced and altered from [74].

10.4 Radiation Delivery

In this experiment two radiation modalities were used to evaluate cell survival, photons and protons. Various proton energies were used to determine the effect of changing proton LET on cell survival. This section will cover the radiation environment and in the case of protons how this was optimised using GEANT4.7.1p1 Monte Carlo simulations.

10.4.1 Co-60 Irradiation

Photon irradiation was completed using a Co-60 therapeutic gamma irradiator located at Loma Linda University Medical Center which is dedicated to radiobiological work. A field size of 30x30 cm^2 and an SSD of 80 cm was used to allow for irradiation of multiple biological samples with a homogeneous radiation field. To provide D_{max} at the sample position a 0.5 cm water equivalent thickness build-up plate was placed anterior to the samples, as is illustrated in Figure 10-4. Dosimetry was controlled through a dose delivery program that was verified against calibrated ionisation chambers (see Section 10.7).

Figure 10-4: Picture of the experimental set-up for Co-60 irradiation. Note the four biological samples located in the Al rings, below a 0.5 cm water equivalent thickness build-up layer.

10.4.2 Proton Irradiation

Proton irradiation was completed at the Proton Therapy facility within Loma Linda University Medical Center. This facility routinely treats patients with therapeutic protons ranging in energy from 100-250 MeV. Irradiation was completed in a specialised research room which contains three separate research beam-lines. This work utilised the p-East and p-West research beam lines and required proton energies of 250, ~20 and ~5 MeV which needed to be checked and verified prior to all experiments. As this is a

therapeutic facility obtaining such low proton energies was difficult but achievable through beam tuning and optimisation of degraders/scatterers using GEANT4.

Two incident proton energies of 250 and 20 MeV were utilised in this study to obtain the three required energies at the sample. To achieve a uniform radiation field at the sample the 250MeV beam was broadened through the use of a scattering foil. On the other hand 20 MeV was used with no attenuator to achieve approximately 20 MeV at the sample, and with a polystyrene attenuator to achieve approximately 5 MeV at the sample. This was all simulated using GEANT4 and the proton energy at the centre of the sample determined.

10.4.2.1 Simulation Geometry

The simulation geometry was based on previous GEANT4 simulations of this research beam-line [116] while the geometry for the biology sample and dose monitoring chamber were obtained from [74]. All elements were defined using their isotopic composition, while materials were defined according to manufacturers specifications or those contained in the NIST database [35]. A schematic of the beam-line is illustrated in Figure 10-5, while component materials and thicknesses are defined in Table 10-1.

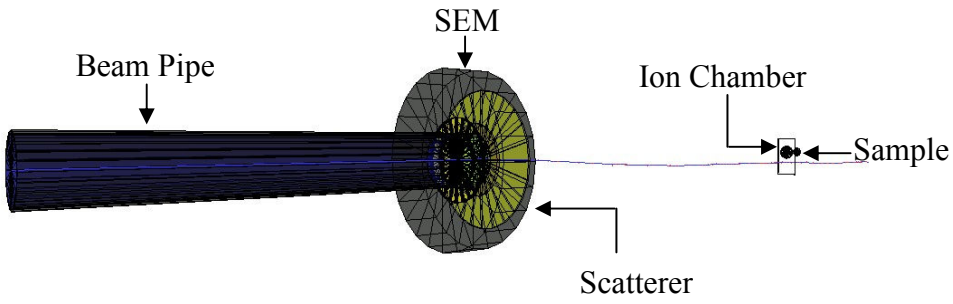

Figure 10-5: Schematic diagram of geometry used in GEANT4 Monte Carlo simulation. Note the track of a single incident proton (blue) as it traverses the experimental setup.

Component	Material	Thickness (mm)
SEM Foils	Aluminium	0.0127 x 5
Beam-line Exit Window	Titanium	0.0254
Scatterer (5 MeV)	Polystyrene	2.62
Scatterer (20 MeV)	N/A	N/A
Scatterer (250 MeV)	Lead	1.6
SSD	Air	910
IC Entrance/Exit Window	Mylar	0.012 x 2
IC Sensitive Volume	Air	1.6
IC Frame	Kapton	1.6
Biological Sample Cover	Mylar	0.012
Biology Sample	Water	0.04

Table 10-1: P-East beam-line components utilised within the GEANT4 simulation of proton kinetic energy at the centre of the biology sample to optimise beam conditions.

A scattered was employed immediately after the SEM to provide a uniform beam profile or the desired particle energy at the centre of the sample. The sample was approximated using water and was considered as 40 μm thick. This was derived assuming uniform dispersion of a 10 μL sample across the entire surface area of the 18 mm diameter glass cover slip. A sensitive region was defined as a 1 μm thick slice (with the same cross-sectional area of the sample) at the centre of the sample to obtain energy spectra information on the incident radiation field.

10.4.2.2 Incident Radiation Field

The incident radiation field was considered as a circular field 10 mm in diameter travelling normally along the evacuated beam pipe. The radiation field was considered as comprising of monoenergetic 250 or 20 MeV protons. Further enhancement of this program can be made by:

- Assigning a given energy spread to the incident beam. However, this must first be accurately determined.
- A beam spot of a given dimension can be assigned to the beam. However, this must first be accurately determined prior to traversing the beam modifying devices, yet

after the beam has traversed any bending magnets which may distort the beam profile. This would most effectively be completed by using the final MWIC before the calibration room. It should be noted that after traversing the Y-magnet some beam distortion may occur which can not be accounted for.

The assumptions made in incident field were not considered to affect the mean proton energy at the sample, but rather the spread of this energy and the beam profile, both of which are outside the scope of this investigation, which was to determine mean particle energy at the centre of the sample. In each case the simulation was conducted for 10^6 histories, which provided accurate information on the incident proton energy profile.

10.4.2.3 Tracking of Events

In this program incident protons and secondaries were tracked through the experimental setup. Interactions of both primary and secondary protons within the SV resulted in a sampling of the particles kinetic energy. This was binned to create an energy spectra of protons interacting with the SV (but not necessarily depositing energy). The number of bins in the spectra was determined by the operator to achieve adequate resolution of the proton energy peak.

10.4.2.4 Simulation Physics

In this case it was imperative that proton processes be considered to deliver an accurate proton energy spectra. The PhysicsList generated for this work was based on the modular design of that used in the hadron therapy example supplied with the GEANT4 distribution. Low energy inelastic scattering (G4preCompound model), low energy ionisation (using ICRU 49) and multiple scattering models were employed for the transport of protons through the geometry of the simulation. The physics of secondary particles was also considered and accounted for, despite these particles being neglected in the final energy spectra. In the case of alpha particles, deuterons, tritons, and other generic charged ions produced as a result of inelastic proton interactions, the corresponding low energy inelastic scattering, low energy ionisation and multiple scattering models were utilised. The predominant particles generated within the simulation would be electrons resulting from proton ionisation interactions. Electron

processes supported included low energy ionisation, low energy Bremsstrahlung, and multiple scattering. In the event of photon generation, the physics processes included were low energy photoelectric effect, low energy Compton scattering, low energy Rayleigh scattering, and low energy pair production. Neutron interactions were also accounted for using the appropriate models. To allow for realistic single processor simulation times the range cut for photons and electrons was set at 2 mm. This was considered appropriate as electrons were not considered in the final kinetic energy spectra.

10.4.2.5 Results & Discussion

The 3 experimental conditions considered in this simulation study were 250 MeV incident protons with a 1.6 mm thick lead scattering foil, 20 MeV incident protons with no addition absorber and 20 MeV incident protons with a polystyrene attenuator. The proton kinetic energy spectra for each experimental condition is contained within Figure 10-6, Figure 10-7 and Figure 10-8.

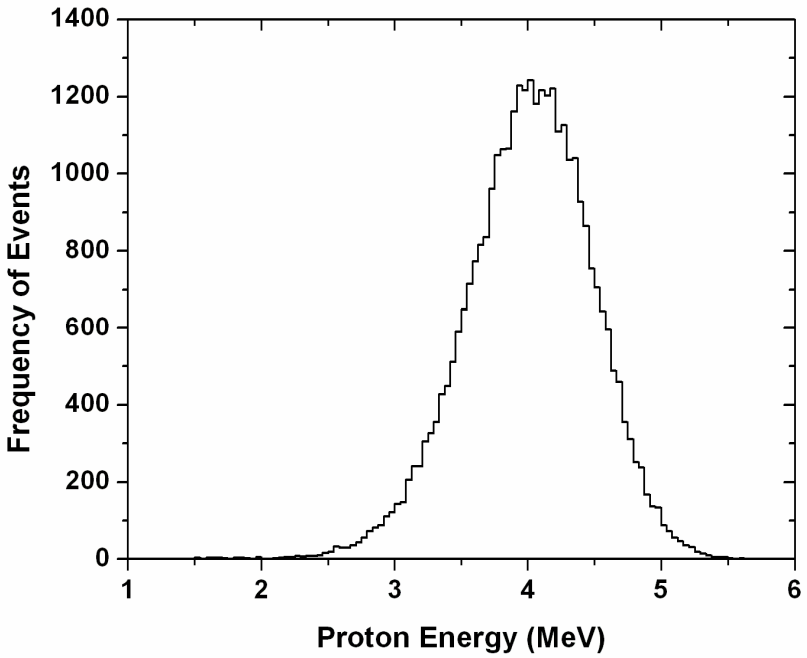

Figure 10-6: Energy spectra collected in the centre of the biology sample resulting from 20 MeV protons transported through a 2.62 mm thick polystyrene attenuator.

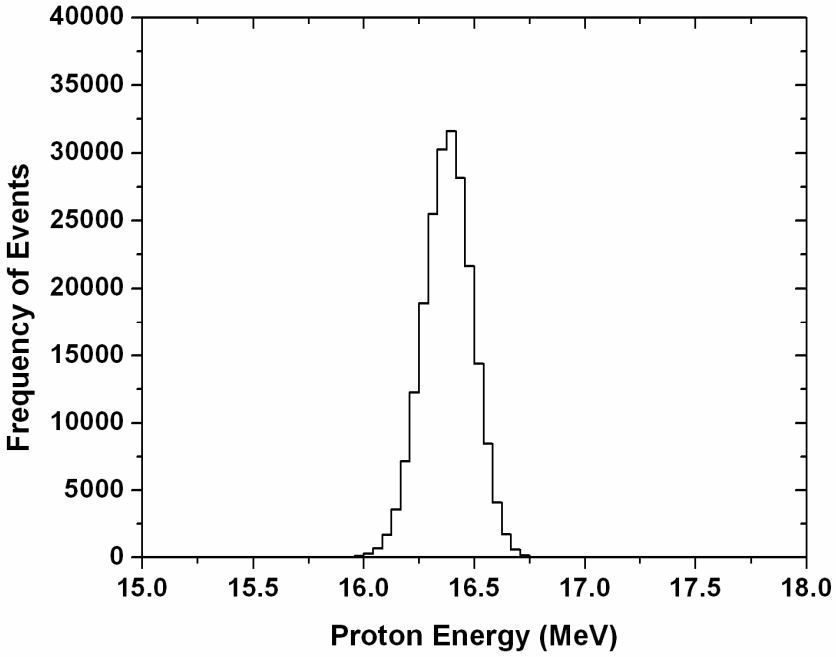

Figure 10-7: Energy spectra collected in the centre of the biology sample resulting from 20 MeV protons transported with no attenuator through the experimental setup.

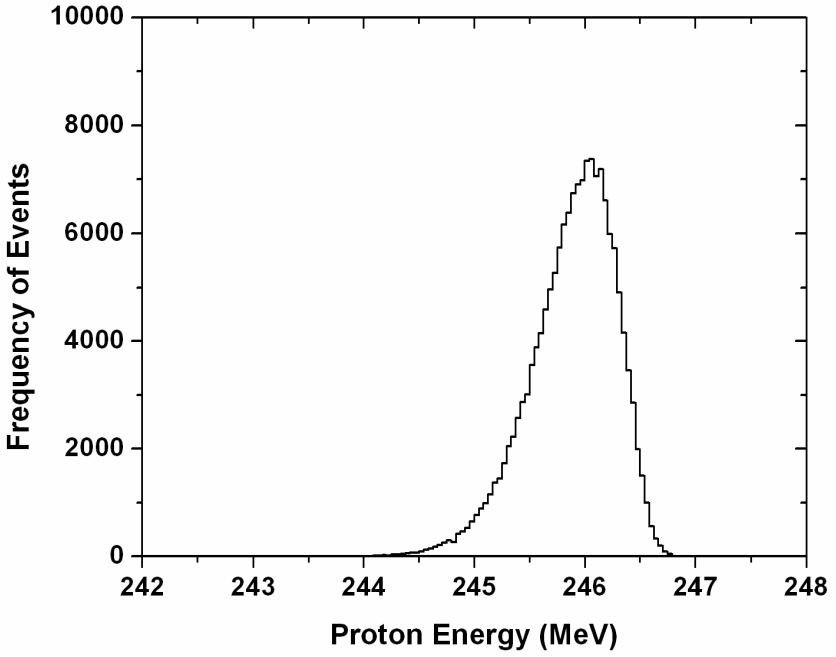

Figure 10-8: Energy spectra collected in the centre of the biology sample resulting from 250 MeV protons transported through a 1.6 mm thick lead scattering foil.

The results presented provide information on the proton energy expected at the centre of the biology sample given the above stated experimental conditions. From previous benchmarking work they were considered to provide accurate data on beam energy (Section 9.4). The simulation results also allow for the determination of the spread in proton energy (FWHM) and variation in proton LET within the proposed experimental setup. To achieve 4-5 MeV at the biology sample not only did the polystyrene degrader need to be optimised, but also compromises needed to be made given only certain QA polystyrene block thicknesses were available. The use of 2.62 mm of polystyrene provides a peak energy of 4.1 MeV (slightly lower than the desired 5 MeV), however the use of a slightly lower energy is advantageous in this case as it allowed for the determination of U-251 cell survival for a higher LET proton field.

Measurement Condition	Peak (MeV)	FWHM (MeV)	LET (keV/μm)
20 MeV + 2.62 mm Polystyrene	4.1	1.08	9.23
20 MeV	16.4	0.25	3.06
250 MeV + 1.6 mm Lead	246.0	0.90	0.395

Table 10-2: Peak energy, FWHM and LET information [35], for the three experimental proton radiation fields used in cell survival work.

The three experimental conditions provide a good spread in proton LET (Table 10-2) with values of 9.23, 3.06 and 0.395 keV/μm for incident proton energies of 4.1, 16.4 and 246 MeV respectively. Such a spread in LET values has the ability to provide a change in cell survival and also a variation in ND response allowing for the development and testing of a radiobiological model for U-251. The results of this simulation study indicated that the three experimental conditions tested should be (and were) used in experimental cell survival results as they provide a sufficient spread in LET and are achievable using available equipment.

10.5 Proton Dosimetry and Calibration

Biological experiments require accurate dosimetry to achieve reproducible and precise results. In this work thin samples of cell suspension were irradiated with a wide range of proton energies including 4, 16, and 250 MeV. To monitor the dose to the sample a custom-made circular parallel plate ionisation chamber (IC1) with a sensitive

volume of 25.4 mm (diameter) × 1.57 mm^3 (SV thickness) (air mass 1.000+/-.005 mg at STP) was used. To allow for minimum attenuation of the beam, especially with low energy protons, the entrance and exit windows of this chamber were constructed with 12.7 μm Mylar. The IC is read out with a recycling integrator (RI) installed in close proximity to the LLUMC proton research beam lines. The chamber was originally calibrated against a Faraday cup [74] and a calibration factor of 26.1 +/- 0.3 nC/Gy at standard temperature and pressure (STP, 298 K and 101.3 kPa) was determined.

For accurate determination of IC1's calibration factor and hence the dose delivered to the biology sample during proton irradiation, multiple measurement series were completed including:

- Cross calibration of IC1 with a PTW-76 and Markus ionisation chamber as reference with a uniform 250 MeV proton beam delivered along a therapeutic beam-line.
- Cross calibration with a Markus and PTW-76 ionisation chambers inside the research hall for incident proton energies of 4, 16 and 250 MeV.
- Cross check with a second ionisation chamber IC2 which has the same diameter as the biology sample (18 mm) and is located at the sample position (i.e. 30 mm behind IC1). This determined if there was any discrepancy in the measured dose and the dose delivered to the sample when the incident proton energy is varied.

10.5.1 IC1 Calibration: Therapeutic Proton Beam

Measurements with IC1 were completed in the horizontal fixed beam line (HBL) at LLUMC utilising a broad uniform beam of 250 MeV in free air then compared with reference measurements taken utilising a Markus TN 23343-3354 chamber and PTW-76 ionisation chamber resulting in a calibration factor of 2702 +/- 20 counts/Gy and 2715 +/- 10 counts/Gy at STP. These results are within 0.5% of each other and show excellent agreement. Previous published calibration data [74] for this IC was 2610 counts/Gy. The 4% difference between old and new calibration factors is within ~ 2 standard deviations of both measurements and therefore deemed acceptable. The calibration factor generated through these measurements with the PTW-76 ionisation chamber (2715 +/- 10 counts/Gy at STP) was used in cell survival work.

10.5.2 IC1 Calibration: Research Proton Beam

To exclude possible errors in the dose evaluation when using the proton research beam line, additional measurements were performed at proton energies of 250 MeV, ~16 MeV, and ~ 4 MeV on LLUMC's p-East research beam line. The response of IC1 was further established through comparisons against the reference chambers Marcus TN 23343-3354 for 16 MeV and 4 MeV and PTW 76 for 250 MeV. The 250, 16 and 4 MeV proton energies were obtained using the same methods as described in Section 10.4.2 so as to reflect the experimental conditions present in cell survival experiments.

In this work chambers were placed on the central beam axis at a distance of ~91cm from the exit window, which corresponded to the nominal position of IC1 during biology experiments. The central beam axis location and size of the beam was monitored by radiochromic film measurements. IC1 and reference chambers were irradiated to the same exposure level monitored by the SEM (about 10,000 SEM counts per exposure) with the charge collected read out by the RI. Measurements were repeated at least three times (typically 5 times) to get average and uncertainty estimates. The dose at STP per 10,000 SEM counts was calculated from the response of the reference chamber using its known calibration factor at STP. Results of these measurements are displayed in Table 10-3.

Proton Energy (MeV)	IC1 Response (Counts)	Reference Chamber Response (Gy)	σ (cm)
4	59007±300	21.87±0.03	>5
16	151715±1500	69.98±0.09	1.2
250	35635±30	14.32±0.05	2.2

Table 10-3: Response of IC1 and reference ionisation chambers to various proton energies per 10K SEM counts. The σ is also provided for the Gaussian beam and was obtained using radiochromic film.

The beam spot size (σ) was estimated from the FWHM of the spot on the radiochromic film at the position of the measurement except for 4 MeV protons where it was larger than 5 cm (quasi-uniform beam). As the beam spot size was of the same order of magnitude as the IC1 diameter (it was considerably larger than the reference chamber diameter), corrections had to be applied in order to determine the calibration factors for

IC1. The average dose measured by a circular parallel plate IC with a sensitive volume of radius R in a particle beam with Gaussian profile (assumed in this case) of divergence σ is described by Equation 10-1.

$$D = D_o \frac{2\sigma^2}{R^2}\left[1 - \exp\left(-\frac{R^2}{2\sigma^2}\right)\right]$$

Equation 10-1: Relationship between chamber radius (R) and Gaussian beam (σ) to determine a dose correction factor. D_o is the dose on the central beam axis.

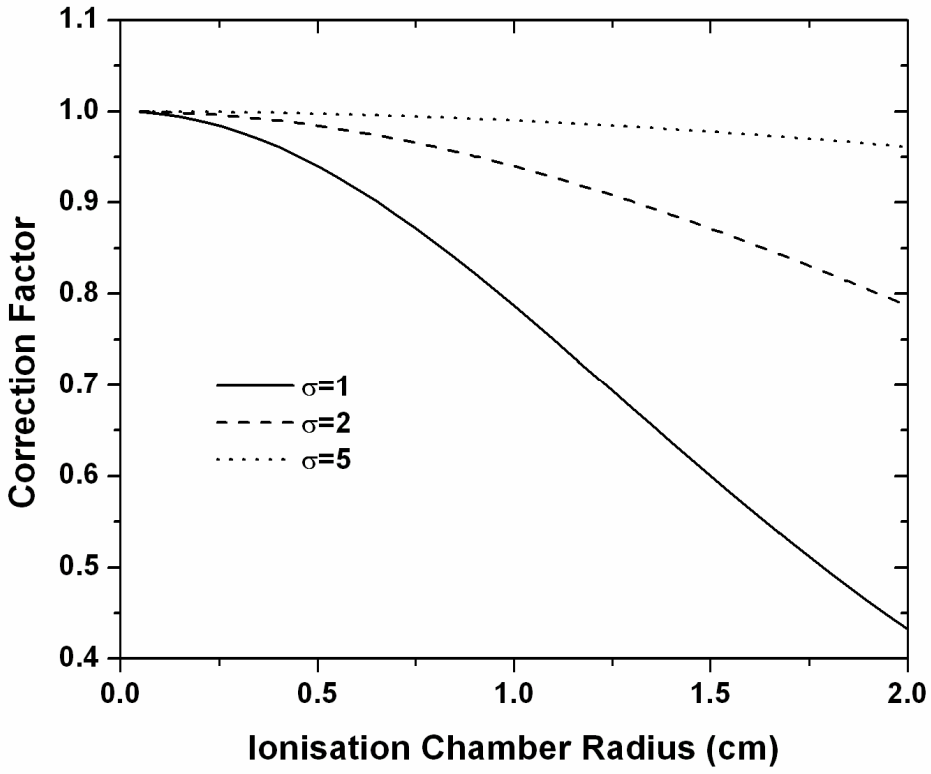

Figure 10-9: The relationship for σ = 1, 2, and 5 cm as a function of *R* (in cm).

Given that the radius of the collecting electrode of the reference chamber is 2.6 mm and the radii of IC1 is 12.7 mm it is possible to determine a correction factor for IC1. As the σ for the radiation field is larger than 5 cm in the case of 4 MeV protons, no correction factor was required. In the case of 16 and 250 MeV protons correction factors of 0.775 and 0.924 were applied to the calibration. The calibration and correction factors are outlined in Table 10-4. Errors estimations were calculated from standard errors in measurements, however it should also be noted that although the dose dependence on *R* is

rather shallow for a well scattered beam, such geometry correction can introduce an error of the order of a few % because of the uncertainty in σ. This is further compounded by the fact that the incident beam contains an elliptical deviation (as a result of bending magnets) from an exactly round shape, with an axis difference of 1-2 mm.

Proton Energy (MeV)	σ (cm)	Correction Factor	Calibration Factor (counts/Gy)
4	>5	1.000	2698±17
16	1.2	0.775	2798±32
250	2.2	0.924	2692±12

Table 10-4: Response of IC1 and reference ionisation chambers to various proton energies per 10K SEM counts. The σ is also provided for the Gaussian beam and was obtained using radiochromic film.

On the basis of the above measurements and taking into account all possible error sources, a calibration factor of 2700 (+/- 3%) RI counts/Gy for IC1 at STP has been established. This compares well with the value obtained in broad beam measurements on a therapeutic beam line. At the usual atmospheric pressure of 740 mm and 20 deg C temperature found in the research room, it would be recommended that the IC1 calibration factor becomes 2630 RI counts/Gy.

10.5.3 Dose Check at Sample

The stability of the dose monitoring chamber IC1 was evaluated across a number of different proton energies and calibrated against reference chambers. However, it was important to determine if the dose collected by this chamber was representative of the dose delivered to the biology sample. To achieve this, a second ionisation chamber IC2 was constructed with a smaller sensitive volume of 18 mm (diameter) × 1.57 mm^3 (height) (air mass 0.502 mg at STP) to match the diameter of biological sample. IC2 was calibrated using the same method outlined in Section 10.5.2 and was placed at the level of the biology sample behind IC1 (see Figure 10-10 and Figure 10-11).

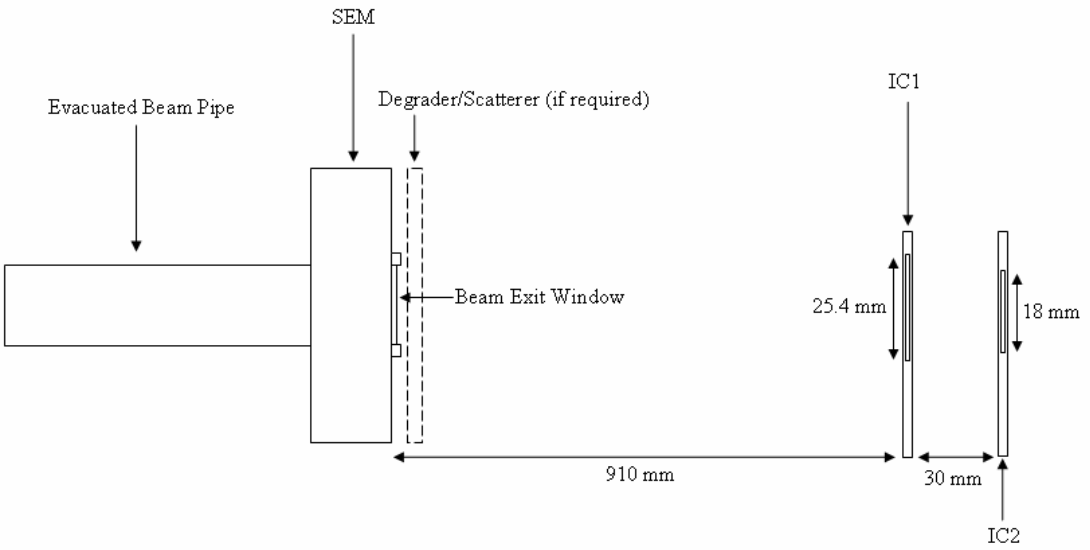

Figure 10-10: Schematic of experimental set-up with IC2 located behind IC1.

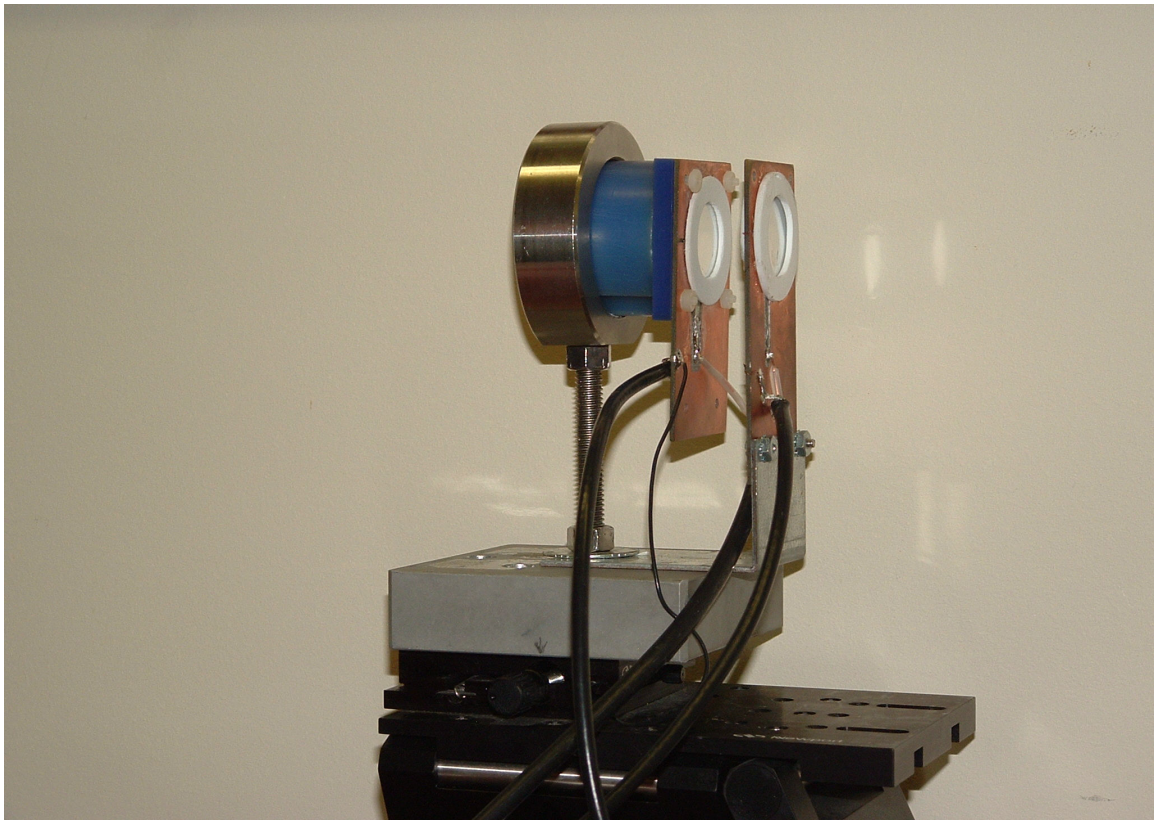

Figure 10-11: Picture of IC2 (left) and IC1 (right) set-up for verification measurements.

Data was obtained for all three experimental proton energies (250, 16 and 4 MeV), with the response of both IC1 and IC2 normalised to 10K SEM counts. The collection of simultaneous data from both IC's allowed for an assessment of the accuracy of IC1 in determining dose to the biology sample and determined if any correction factor was required. This data is contained within Table 10-5.

Proton Energy (MeV)	IC1 Response (Gy)	IC2 Response (Gy)	Correction Factor
4	23.4 ± 0.4	23.0 ± 0.4	0.98
16	59.3 ± 1.0	64.1 ± 1.0	1.09
250	13.5 ± 0.3	13.6 ± 0.3	1.01

Table 10-5: IC1 and IC2 comparison data with derived correction factor to determine more accurately the dose at the biology sample.

The results indicate that for 4 and 250 MeV variation in the dose delivered to IC1 and IC2 is minimal and can largely be discounted as it is within error estimations for both detectors. The 16 MeV beam was sensitive with respect to alignment of ICs and beam axis and this is reflected in the correction factor required for such measurements. For example, a lateral displacement of IC2 by 3 mm from the beam axis and IC1 resulted in a dose reduction of 10%. This highlights the need for accurate sample placement in the case of the 16 MeV irradiations.

10.5.4 Overall Proton Dosimetry Conclusions

This work provided a through assessment of the dose monitoring technique employed in this cell survival protocol for proton irradiations. Further, it provided a means for determining accurately the dose to the sample through accurate calibration of IC1 and determination of correction factors for incident beam profile, beam energy and experimental conditions. The calibration factor utilised in the experimental work was 2715 RI counts/Gy.

10.6 Recycling Integrator Calibration

The signal from IC1 is read out using an RI which is located in close proximity to the experimental setup. While the performance of the IC had been verified and benchmarked across a range of proton energies it was important to ensure that the RI exhibited a linear response to a range of input current values (that represents different beam intensities). This was completed using a Keithley Programmable Current Source Model 220. A constant current of a given value was input into the system for duration of 1 minute. Upon completion of the acquisition an average counts/second was output from the RI. This was repeated 5 times for each current setting to allow for a more accurate conversion from applied current to RI counts with appropriate error bars. From data obtained over a range of incident current values an evaluation of the linearity of response of the RI and hence a conversion of input current to counts could be determined.

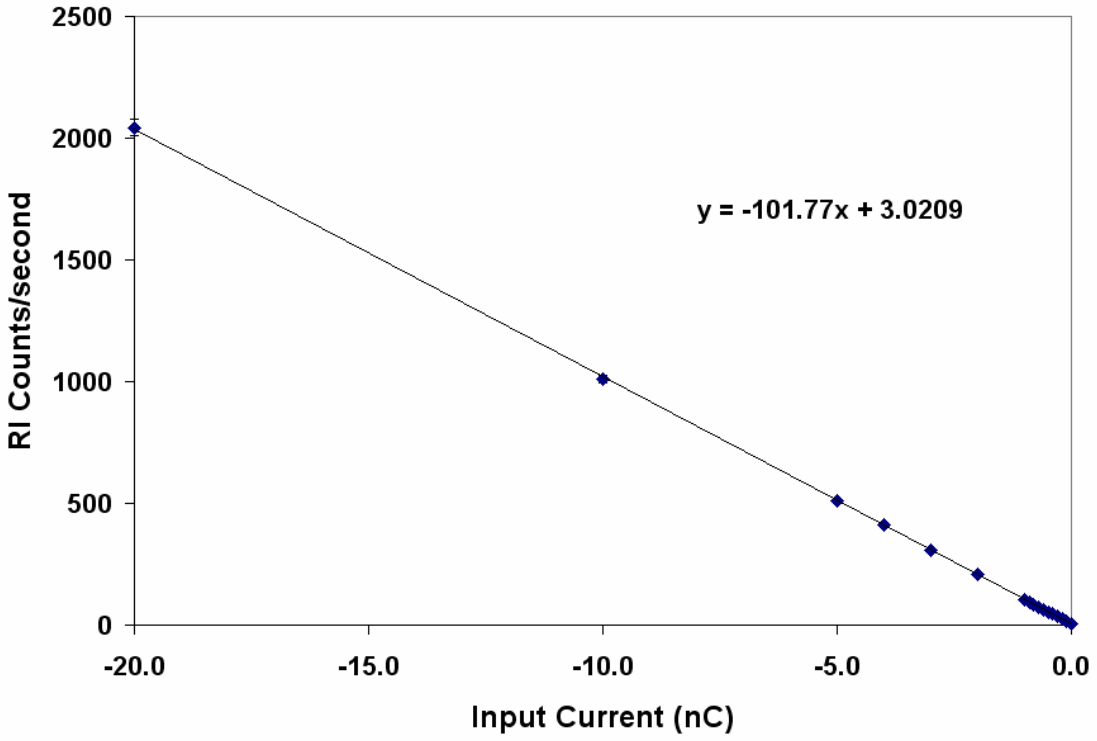

Figure 10-12: RI response to input current pulses from 0-20 nC. Note the linearity of the response over a range of current values, which is significantly larger than those experienced during cell survival work.

The results illustrated in Figure 10-12 and Figure 10-13 clearly indicates the linearity in response of the RI over a range of input currents. The error bars (so small in most cases they are obscured by the experimental point) indicate the reproducible nature and stable response of the RI. This work gave an RI readout of 1 count = 10.177 pC which corresponds very well with previously published values of 1 count = 10 pC +/- 1% [74] further illustrating the stability of the RI. Magnification of the RI response to the expected counts per second for cell survival work (Figure 10-13) further illustrates the linearity of the RI at low input currents associated with such radiation fields.

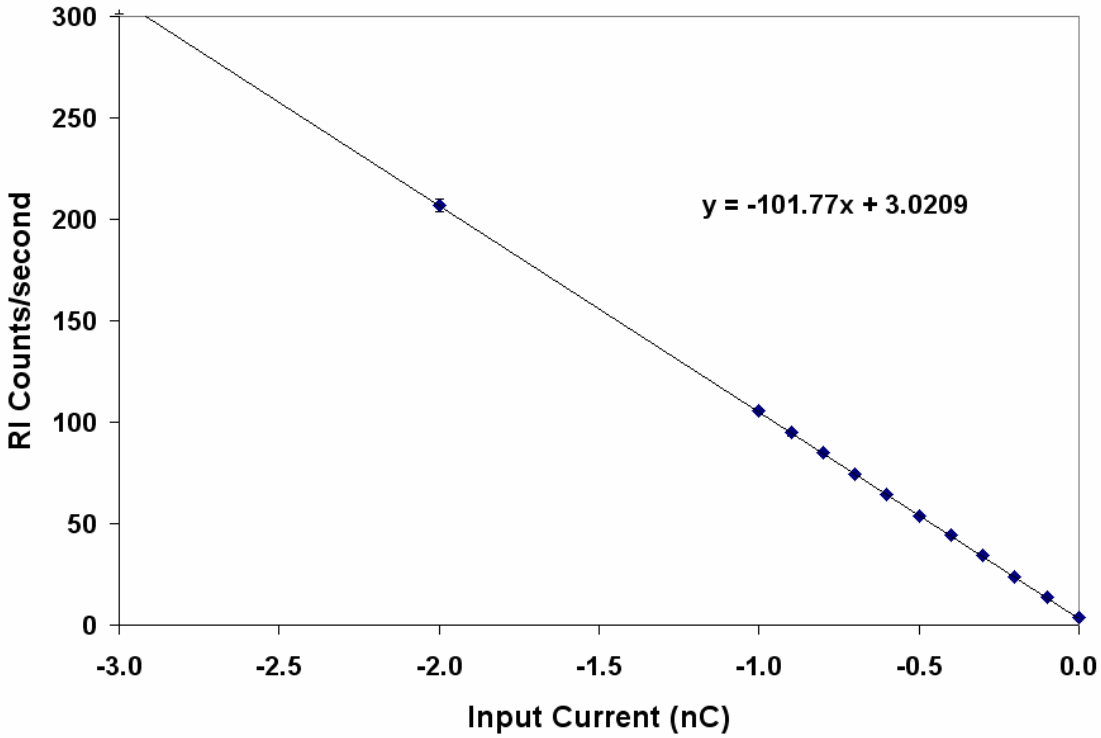

Figure 10-13: Magnified RI response to input current pulses from 0-3 nC. Note the linearity of the response over a range of current values, which are more representative of those experienced in cell survival work.

10.7 Co-60 Dosimetry and Calibration

Doses delivered by the Co-60 unit at LLUMC are governed by a program which calculates the time of irradiation for a given required dose based on known calibration factor and radioactive decay parameters for Co-60. To further cross check and verify this program a study was completed using three separate ionisation chambers and methods stipulated in [130]. Each chamber had a 0.5 cm water equivalent thickness build-up cap to measure the charge collected at the D_{max} position, which corresponded to the sample position in experiments. Using this technique the dose (in Gy) measured by the various ionisation chambers is given by Equation 10-2.

$$D(Gy) = Q \times KTP \times N_X \times A_{eq} \times F_{water} \times BS \times FF$$

Equation 10-2: Method for determining dose in water from a measured charge from a calibrated ionisation chamber as published in [130].

Where:

D = Absorbed dose in water (Gy)

Q = Charge collected by ionisation chamber in Coulombs

KTP = Temperature Pressure correction factor

N_x = Calibration factor for individual chamber (Gy/C) from Accredited Laboratory

A_{eq} = Chamber Collection Efficiency for Co-60

F_{water} = Conversion dose in air to dose in water

BS = Back Scatter factor

FF = Field factor when determining a dose for a 30x30 cm^2 field from a 10x10 cm^2 field

The BS has a value of 1.053 for a 30x30 cm^2 field, while the FF has a value of 1.07 [131]. The three chambers used in this experiment included a Capintec PRO-06G Farmer Chamber, a PTW Farmer Chamber and an Extradin T1 chamber. Measurements were completed in free air at 80 cm SSD for a 10x10 cm^2 field, hence the use of a field factor to convert to the dose in a 30x30 cm^2 field which is typically used in cell survival work to achieve a uniform coverage of all samples (and which is output by the dose calculation program). The measurements for the three ionisation chambers were compared to the

dose rate as determined by the biology control software, and the difference from the computer generated value established.

Dose Determinant	Dose Rate (cGy/min)	Difference from Software (%)
Software	67.32	N/A
Capintec	67.02	-0.45
PTW	67.21	-0.16
Extradin	67.57	0.37

Table 10-6: Dose validation of the Co-60 delivery software using three separate ionisation chambers.

The results contained within Table 10-6, show excellent agreement between the three separate ionisation chambers and the Co-60 dose delivery software. The dose rate returned by the dose delivery software was within 0.5% of measured values with two chambers reporting slightly lower values (up to 0.5% lower) and one chamber reporting a slightly higher value (0.4%). These results validate the use of such software in determining the dose delivered to biological samples in Co-60 experiments.

10.8 Experimental Cell Survival Protocol

In any instance of cell biology a clear and concise procedure is essential in order to:

- Clearly identify the steps needed for completion of a successful result
- To allow for effective delegation of responsibilities to other members of the team
- To allow for effective time management ensuring that all experiments were completed with the utmost efficiency (resulting in minimal stress to the cells) and to ensure that all experiments were completed with the utmost reproducibility.
- To enable to biology team to more easily identify areas of concern and address these, especially in the event of contaminated or outlying results.

So while the broad method of colonogenic cell survival with U-251 utilising thin-film irradiation techniques had been settled on, a more detailed procedure needed to be formulated and established. The protocol developed for this study will be discussed in this section.

10.8.1 Cell Preparation

Reproducible cell preparation is essential to have a stable experimental medium and thus reproducible experimental results. In this instance U-251 cells were prepared having a passage number between 10 and 35. Maintaining low passage numbers was desirable in ensuring a stable cell line from one experiment to the next. The cells were grown within a T75 flask in a medium comprising of Dulbecco's Modified Eagle's Medium (DMEM) with 10% Foetal Bovine Serum (FBS) and 1% Antibiotic-Antimycotic Agent which was prepared with 10,000 units/ml penicillin G sodium; 10,000 μg/ml streptomycin sulphate and 25 μg/ml amphotericin B as Fungizone in 0.85% saline. The cells were incubated at 37 degrees Celsius with 5.0% CO_2 until 70-90% confluence was reached. At these levels of confluence the cells were either passed, to maintain live cell stocks for experimental studies, or used in an experiment.

10.8.2 Sample Preparation

When preparing the cells for the experiment the media was first aspirated from the T75 flask and the cells washed with 5ml of Hanks Solution (HBSS). The HBSS was then aspirated and 1X Trypsin was added to make the cells detach from the flask and move into suspension. During this time the flask was incubated for 5-8 minutes with the status of the cells checked regularly under a microscope.

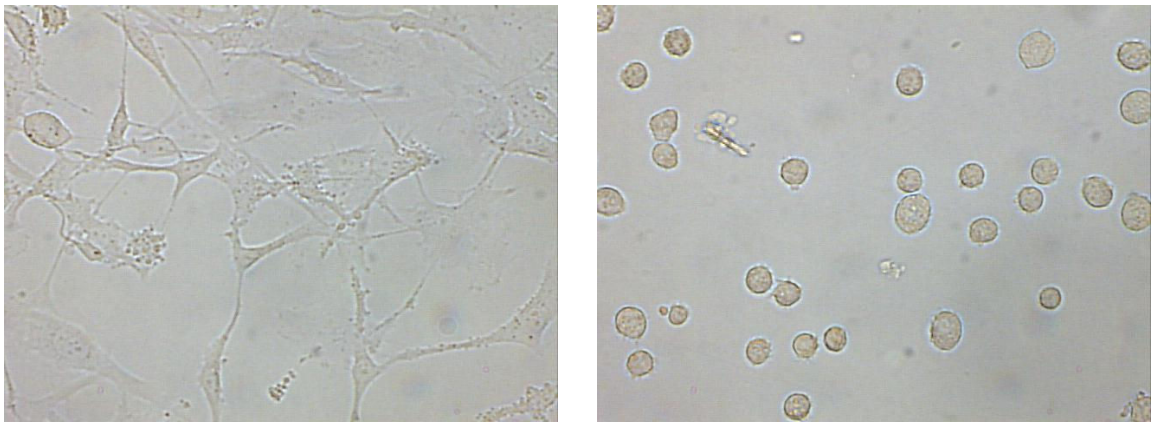

Figure 10-14: Images of U-251 cells attached to a surface (left), and in single cell suspension (right).

Once the cells are detached 5ml of complete DMEM media was added to the flask to inactivate the Trypsin. The cell suspension was then mixed using the pipette to ensure all

cells are detached from the flask and the cells no longer remain "clumped" but are in a true single cell suspension (Figure 10-14). The cells were then removed from the T75 flask and transferred to a 15 ml centrifuge tube. The suspension was then centrifuged at 1000rpm for 5 minutes. The media/Trypsin mixture was then aspirated, the pellet broken, new complete DMEM was added and centrifugation repeated. Following the second centrifugation the media was aspirated, the pellet broken and 300µl of media was added. This results in a cell suspension of $5x10^4$-$1x10^5$ cells per 10µl sample size to be irradiated.

To ensure that the suspension concentration was reproducible from experiment to experiment, a sample was checked in the coulter counter by diluting 10 µl of cell suspension (i.e. 1 experimental sample) into 2 ml of complete DMEM. From this sample of cell suspension, a 100 µl was then diluted into 9.9 ml of isotone contained within a cuvette (i.e. 1:100 dilution). This sample was then counted three times for statistical accuracy. If the sample had a concentration greater than $1x10^5$ cells then the original suspension was diluted further, while if the concentration was significantly lower than $5x10^4$ the cell suspension was removed and a new flask prepared.

10.8.3 Sample Irradiation

For cell suspension irradiation with either Co-60 photons or protons the thin-film irradiation technique was utilised. For each sample the suspension was vortexed for 5-10 seconds to ensure that the sample was well mixed and that the cells were uniformly distributed within the suspension. From this a 10 µL sample was pipetted and placed on the centre of the Mylar using a pre-prepared template. The 18 mm diameter glass cover slip was then placed on the suspension droplet to create a uniformly thin sample. The sample was then transported to the experimental room and placed on the wax sample holder (in the case of proton irradiation) and aligned normally to the incident radiation field. Irradiation times were monitored using pre-determined calibration curves and ionisation chambers.

Post-irradiation, the sample was removed from the experimental hall. The cover slip and Mylar window were washed using 2mL of complete media to remove all cells. The

2mL of cell suspension was removed and placed in a labelled test tube. The Al ring complete with Mylar window was sterilised using a 70% alcohol solution and UV light in preparation for the next experiment, while the cover slip was disposed of. 10-12 Al rings complete with Mylar windows allowed for a production line to be set-up allowing for the efficient preparation of samples for irradiation and collection.

This procedure was repeated for 8 dose points (0, 0.25, 0.5, 1, 2, 4, 8, 0 Gy) with 2 replicates per dose point for accuracy and to allow for any outlying or contaminated samples to be discounted without effecting the experiment as a whole. To allow for fast processing of samples and further economise the use of proton beam time, experiments were completed in two batches. The low dose batch used a dose rate of approximately 1.5-2 cGy/spill. These were completed (including a 0 Gy control sample) and sent for counting and seeding. The high dose batch consisting of 1, 2, 4, 8 Gy plus another 0 Gy control was then completed using a dose rate of approximately 8-10 cGy/spill. Completing the experiment in two batches with two separate dose rates allowed for the most efficient use of beam time, whilst also allowing for the samples to be processed effectively with minimal stress to the cells.

10.8.4 Plate Seeding

Once the samples had been irradiated it was important to get them back to the lab, counted, seeded and returned to the incubator as fast as possible to reduce stress to the cells. For each 2 mL irradiated sample, a 100 μL was removed and diluted in 9.9 mL of Isotone contained within a cuvette. This sample was then counted three times using the Beckman Z1 coulter counter to determine the concentration of the sample with the best possible accuracy. Given the concentration of the sample a known number of cells could be mixed with 12 mL of complete media and seeded into a labelled Petri dish. The cells were added to the media prior to seeding to ensure a uniform distribution across the dish and minimise “clumping” of colonies which would impede counting and increase errors. The plates were then storied in an incubator at 37^{o}C with 5% CO_2 for the duration of their incubation.

10.8.5 Plate Staining and Counting

The plates were incubated for 11-12 days as this was found to provide minimum overlap with clearly defined colonies. At this time the plates were removed from the incubator and the media aspirated. The plates were then "gently" rinsed twice in a solution of 0.5% NaCl solution. Each plate was then filled with a fixative comprising of 3 parts methanol and 1 part glacial acetic acid and allowed to stand for 15 minutes. The fixative was then removed and replaced with a 0.5% crystal violet stain solution and again the plates were left for 15 minutes. Finally the staining solution was removed and the plates rinsed and allowed to dry overnight.

In this study the number of viable colonies present was counted to determine the cell survival. A viable colony in this case was one consisting of 50+ cells which conforms to established radiobiological standards [63]. The number of colonies present was evaluated using an automatic colony counter, Colcount, produced by Oxford. This apparatus returned the number of colonies present in a given dish through light imaging technology, allowing for the determination of the plating efficiency and cell survival given the methods outlined in Section 2.9.

10.9 Biology Equipment Validation

It is essential that before utilising a piece of laboratory equipment its use and operation be carefully investigated to ensure that:

- It is suitable for the task at hand
- Proper procedures are in place for its use
- It returns reproducible results

Two major pieces of equipment used in this radiobiology study were the Coulter Counter and ColCount apparatus which was benchmarked prior to use.

10.9.1 Coulter Counter Validation

A Coulter Counter is an apparatus used to determine cell concentration in a given sample. This is achieved through measuring the change in electrical conductivity as the cell suspension is passed through an aperture. The electrolytic solution of the suspension is a good conductor, whilst cells passing through the aperture disrupt the conductivity of

the circuit and cause a voltage pulse. Integration of the voltage pulses for a given volume of cell suspension flowing through the aperture provides information on the cell concentration. In this work a Beckman Coulter Counter Model Z1 was used to determine the number of cells within a given volume of irradiated cell suspension to allow for a known number of cells to be seeded. This apparatus was chosen over the haemocytometer (generally seen as the standard for determining cell concentration in biology) because of the speed and accuracy of the counts returned by this apparatus. The counting limits of the device (i.e. the upper and lower particle radii to be counted) and the reproducibility of the coulter were investigated through a systematic study with a haemocytometer, before its use in survival experiments.

10.9.1.1 Haemocytometer Operation

The haemocytometer consists of a glass plate with a grid etched on either side. Counting the number of cells within a given grid allows for the concentration of cells/ml to be determined. Multiple counts using the haemocytometer allows for the standard deviation in results to be determined. The haemocytometer was operated using the following method:

- A single cell suspension of cells was prepared using the protocol developed for the experimental studies and which is outlined in Section 10.8.
- The haemocytometer and cover-slip were cleaned using water and 70% Alcohol and dried using kim-wipes. It is important to note that a special cover slip is utilised, as a regular cover slip does not have the specific weight in order to give the correct volume within the haemocytometer.
- The cell suspension was treated with Trypan blue and allowed to sit for 5 minutes.
- An inverted microscope (objectives under the stage and the light above the sample) was prepared to allow for the cells to be viewed and hence counted.
- The cell suspension was vortexed and two samples were aspirated using a Pasteur pipette and introduced into each side of the haemocytometer. Care was taken to ensure the cover slip did not shift and that the sample was not forced into the chamber but rather taken up via capillary action.

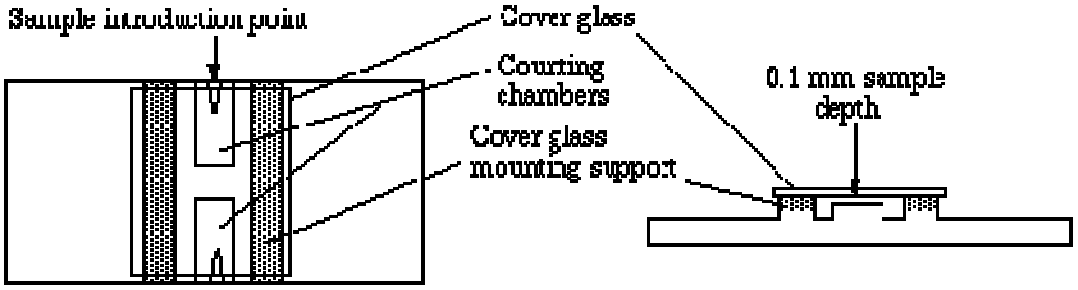

Figure 10-15: Schematic of the haemocytometer used in this study. Note the sample introduction points and channels under the cover slip to house the sample.

- Using the microscope 5 squares on each grid were counted, giving a total of 10 counted squares. The squares counted are highlighted in the below schematic. To ensure the accuracy of this technique 100+ cells need to be counted.
- The counted 10 squares gave the total number of cells in 1 μL ($1x10^{-6}$L). To obtain the total number of cells in 1 mL this value was multiplied by 1000.

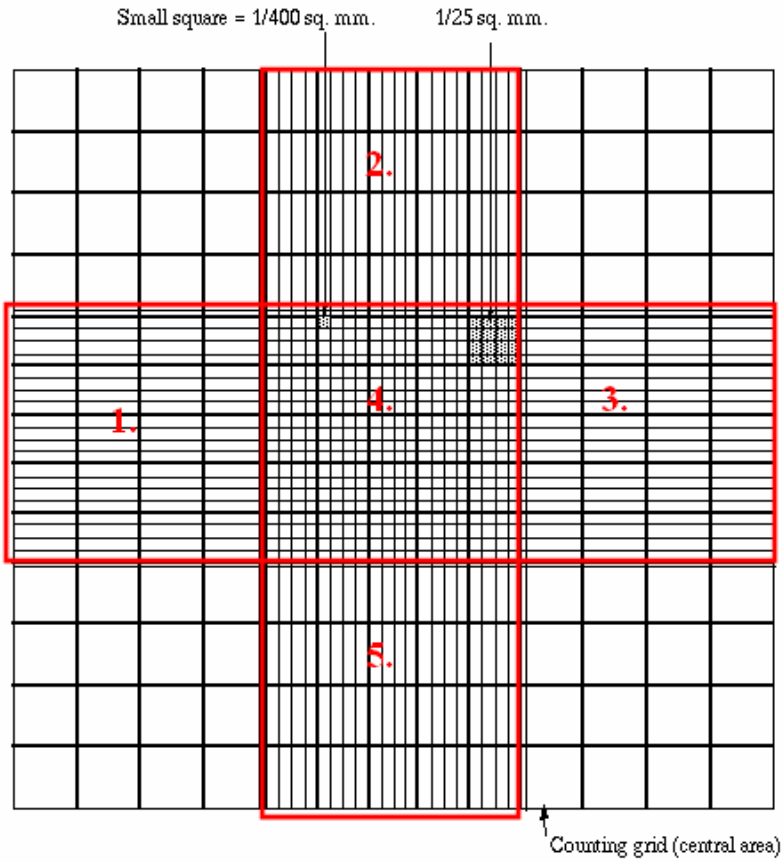

Figure 10-16: Schematic to illustrate the squares counted on each side of the haemocytometer (note that as the haemocytometer has 2 sides this gives a total of 10 large squares counted per experimental point).

Three separate counts were made using the haemocytometer to ensure accuracy and prevent a single outlier result from contaminating the study.

10.9.1.2 Coulter Counter Operation

In all uses of the coulter counter it is essential to ensure that the unit is properly prepared and cleaned. Background measurements were made with "clean" isotone for aperture counting limits of 7.5-15 μm and 7.5-30 μm, to evaluate the effect of aperture counting limits on background value and stability. A U-251 cell suspension was prepared with a concentration of cells typically used in thin-film irradiation experiments. Initially this was counted for aperture counting limits of 7.5-15 μm, 7.5-22 μm and 7.5-30 μm and compared with results from the haemocytometer. To evaluate the effect of either widening the counting window further or increasing the lower counting limit, experiments were also conducted for aperture counting limits of 7.5-10 and 30-55 μm.

10.9.1.3 Background Results

A total of 10 background measurements were completed for both counting limits of 7.5-15 and 7.5-30 μm respectively. The results of which are contained within Table 10-7.

Counting Limits	Average (Cells/mL)	σ (Cells/mL)
7.5-15 μm	370	240
7.5-30 μm	2820	363

Table 10-7: Background measurements made using "clean" isotone with the Z1 Coulter Counter for the counting limits of 7.5-15 and 7.5-30μm.

These results clearly show that the background does vary based on the counting limits selected. It is important that the background be measured prior to the experiment taking place and needs to be corrected for during the course of the experiment. This is especially true in the case of the 7.5-30 μm counting range as the background is almost a factor of 10 higher than the smaller counting limit. Despite the differences in average values the variation between adjacent measurements remains relatively stable regardless of the counting range selected.

10.9.1.4 Comparative Results

The comparative tests for various coulter counting limits and the haemocytometer are provided in Table 10-8.

Counting Limits	Average (Cells/mL)	σ (Cells/mL)
7.5-15 μm	224840	10663
7.5-22 μm	464533	27719
7.5-30 μm	486320	23024
Haemocytometer	479000	21517

Table 10-8: Results obtained utilising the coulter counter and haemocytometer for a representative solution of U-251 cells.

In each instance multiple (5-10) measurements were completed to ensure accuracy in counting. These results show that a counting limit of 7.5-30 μm is needed to obtain good agreement with the haemocytometer and hence count the cells correctly. The counting limit of 7.5-30 μm was within standard deviation of the haemocytometer results and provided a means for counting the cell samples accurately and quickly which was imperative in this experiment given the large number of samples to be processed.

Checks were then made to ensure the counting window on the coulter should not be widened further. Using a counting limit of 30-55 μm and the same U-251 cell suspension provided an average count of 1000 cells per mL. Such counts are of the order of background and are 2 orders of magnitude lower than counts within the window of 7.5-30 μm. This led to the conclusion that widening the counting window to 7.5-55 μm would provide no further accuracy in measurement.

10.9.1.5 Coulter Counter Conclusions & Recommendations

This work was essential in establishing the suitability and accuracy of the Beckman Z1 Coulter Counter in determining the concentration of cell suspensions. In comparisons with a haemocytometer, agreement was found with a counting window of 7.5-30 μm. The validation of such a device and use in this cell survival study would allow for fast processing of samples and seeding of a known number of cells in order to establish the surviving fraction.

10.9.2 Colcount Assessment

The Colcount unit utilises light imaging technology to count stained colonies on the Petri dish. This technology can be applied across a number of cell lines and it is important that the optimal counting settings for cell survival studies of U-251 be established and understood. These counting limits include the minimum radius (R_{min}) of colony to be counted to meet the 50 cell cut-off criteria, the maximum radius (R_{max}) of detection to ensure all colonies are counted whilst not counting closely packed colonies as a single event, and finally optical density (OD) which can vary based on the density of the colonies and staining procedures employed. The area of counting or shape mask also had to be established to ensure reproducible counting areas from sample to sample, and also to ensure that spurious counts from plate labelling were rejected.

To test the Colcount unit a number of U-251 plates were counted using the Colcount. The radius and optical density distributions were analysed to determine the appropriate values. The R_{min} limit was determined through identifying the smallest colonies and viewing under a microscope to determine if they met the 50+ cell limit.

10.9.2.1 Colcount Results & Discussion

From work benchmarking the survival of U-251 many plates were available for this study. A selection was made with 200 to 600 colonies per dish. The default settings for the Colcount unit were an OD of 0.1 and an R_{min} and R_{max} of 0.2 and 2 mm respectively. These are only a guideline and would provide an adequate starting point for this work. The initial setup was to create an appropriate shape mask allowing the entire surface area of the plate to be counted whilst discounting the edges which could introduce errors in counting. This is seen in Figure 10-17 as a red line surrounding the counting area. Once this was complete the R_{min} was set to 0.2 mm (the minimum value of the unit) and the R_{max} to 0.3 mm. This allowed the smallest colonies to be identified and studied with a microscope. The results indicated a minimum counted colony size of 80-100 cells with a number of smaller colonies not counted by the unit. As the R_{min} limit of the unit had been reached the OD needed to be lowered to enable counting of these smaller colonies. Incremental decreases of the OD allowed for colonies of 50 cells to be counted at an OD level of 0.05.

With an established R_{min} and OD, the R_{max} needed to be set. It is imperative that this value be set as close to the assumed largest colony size to limit the chance of counting multiple small colonies as a single entity. To establish the R_{max} limit, it was incrementally increased from 1.0 mm in 0.1 mm steps. It was found that the number of colonies increased until a plateau value was reached, further increases in R_{max} resulted in a decrease in the overall number of counted colonies as multiple small colonies were counted as single large colonies. It was deemed from this that the plateau region provided the best assessment of colonies counted and as such an R_{max} of 2.0 mm was selected.

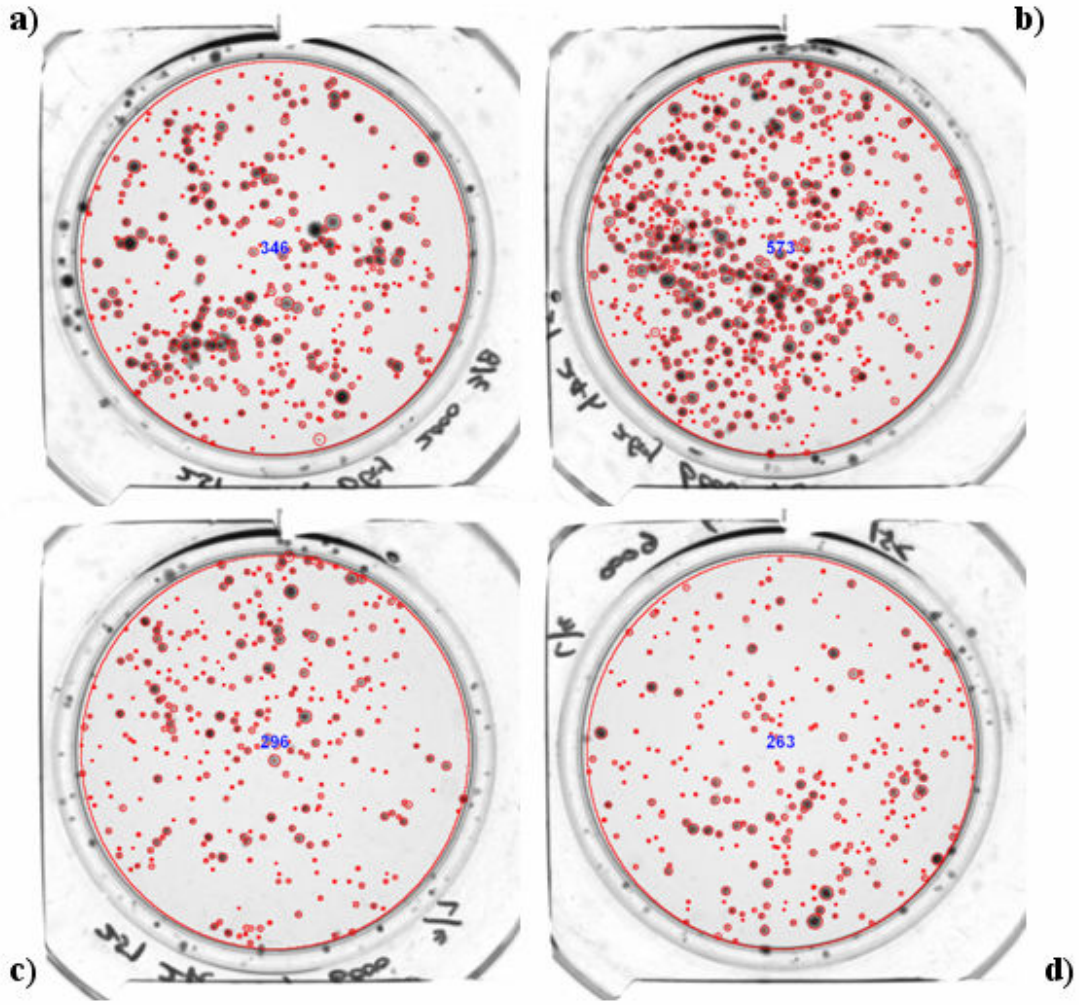

Figure 10-17: A selection of plates used in this study that were counted using Colcount. The counting area is clearly defined as a large red circle encompassing the base of the dish (so to avoid counting the black labelling on the edges of the dish), while each colony detected is surrounded by a red border. The labelling a-d will allow for correlation with radius and optical density data following in this section.

Using incremental increases in OD, R_{min} and R_{max} and comparing the colony size counted to the number of cells evaluated under a microscope it was possible to assign initial values of OD=0.05, R_{min}=0.2 mm and R_{max}=2.0 mm. These needed to be tested against experimentally obtained radius and optical density distributions to ensure colonies were not being overlooked. Colcount radius and OD distributions were generated for each plate with samples provided in Figure 10-18 and Figure 10-19.

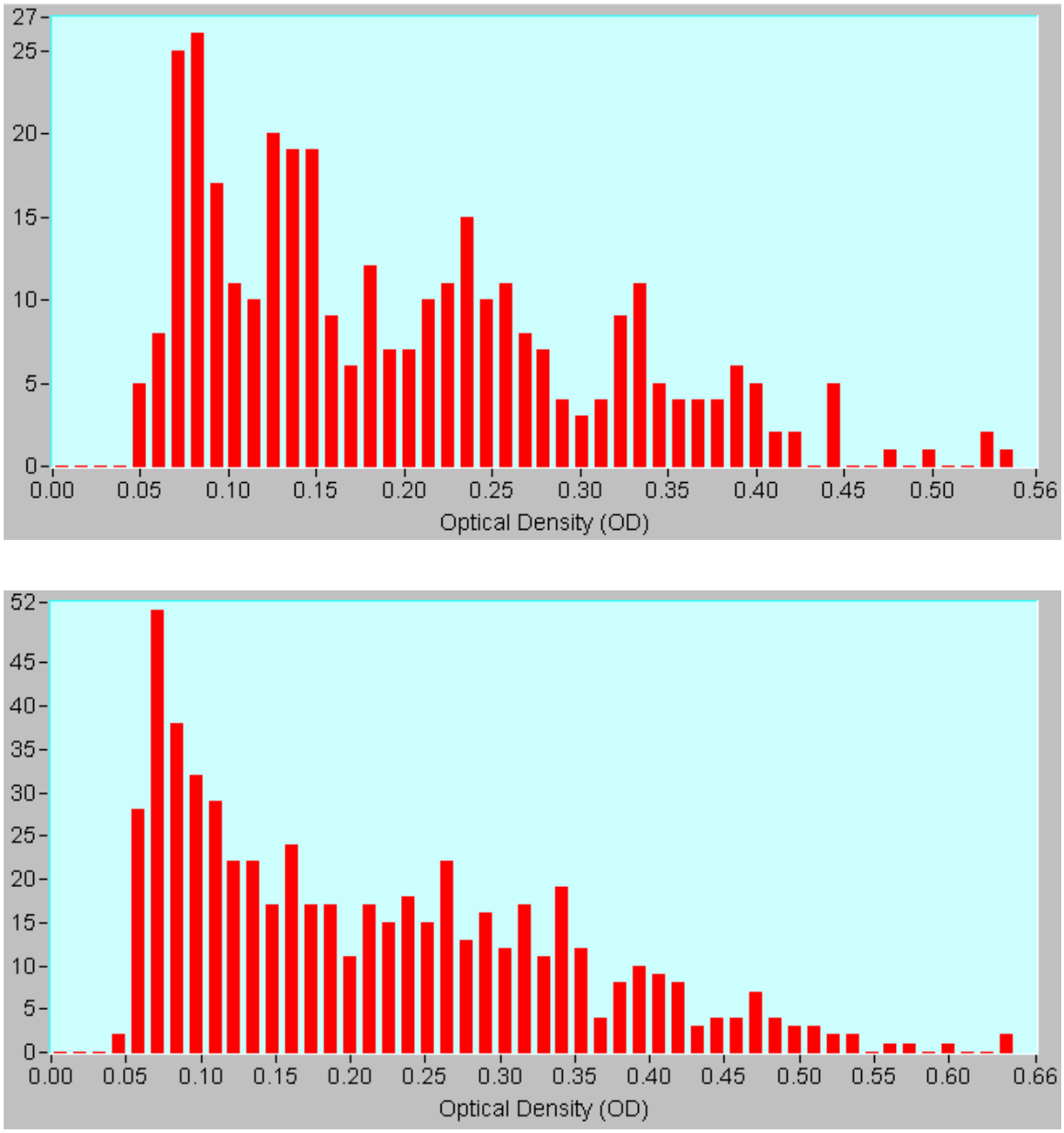

Figure 10-18: OD distributions for plate A (top) and plate B (bottom). It is clear that the default setting of 0.1 will discount many colonies from counting and that in the case of U-251 a OD limit of 0.05 is more appropriate.

Clearly the OD distributions in Figure 10-18 (that are representative of all distributions observed in this study), show a peak in colonies counted from 0.05-0.1 on the OD scale. Further, this peak does not lie below 0.05 and there is a decrease before the 0.05 cut-off suggesting we are not measuring "noise" which could be caused by dust or small unviable colonies. These results support the lower OD limit of 0.05 for use with U-251.

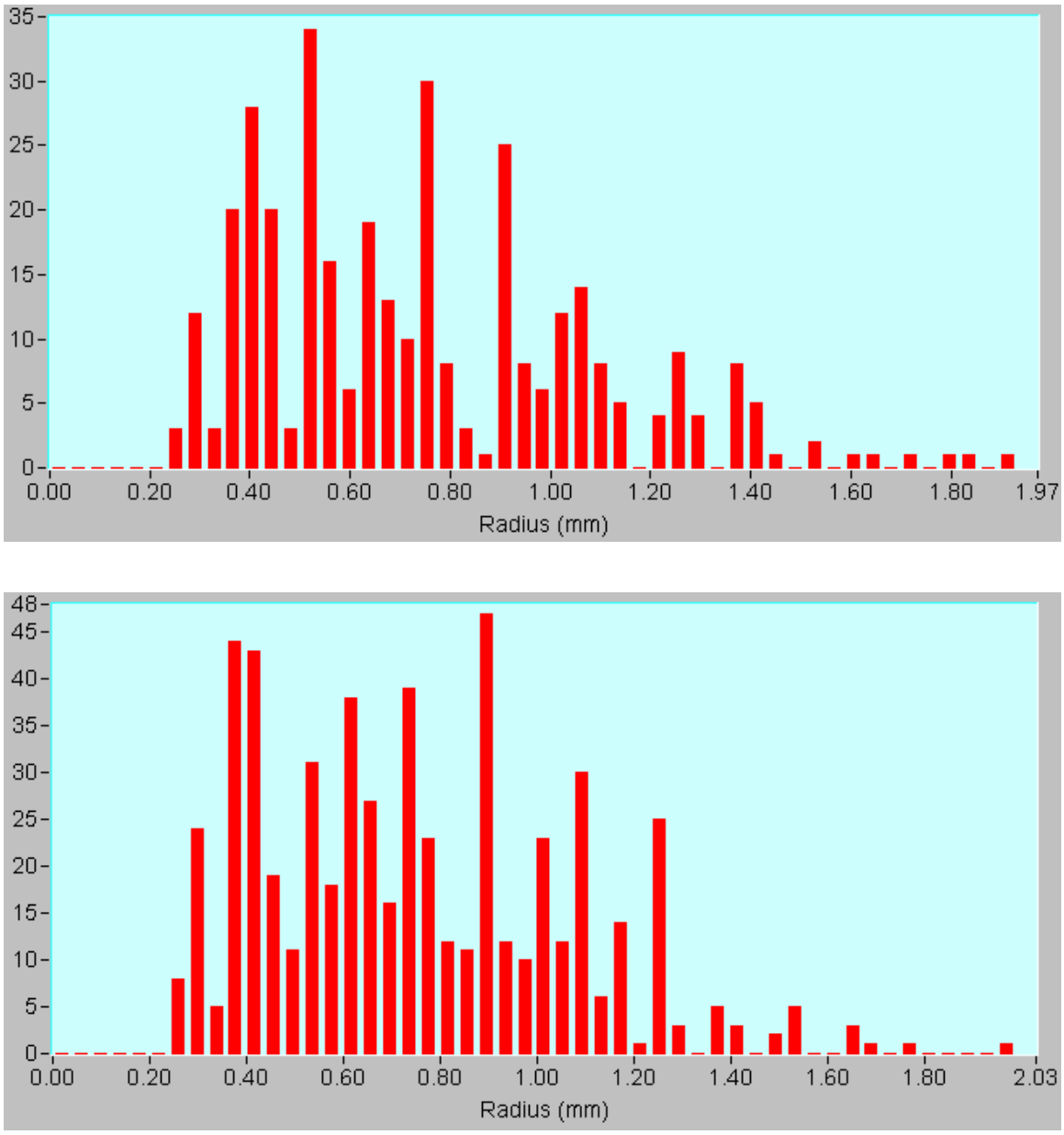

Figure 10-19: Radius distributions for plate A (top) and plate B (bottom). It is clear that the limits of R_{min}=0.2 mm and R_{max}=2.0 mm encompass the range of colony radii detected in U-251 experiments.

Clearly the distributions in Figure 10-19 (that are representative of all distributions observed in this study), show that the counted colonies lie between 0.2 and 2 mm in radius. Most colonies lie in the region of $0.2 \leq R \leq 1.4$ mm with some larger colonies having a radius greater than 1.4 mm. Colonies clearly have a radius greater than 0.2 mm with a decrease in counted colonies from 0.3 to 0.2 mm. These results support the radius limits of $0.2 \leq R \leq 2.0$ mm for use with U-251.

10.9.2.2 Colcount Conclusions & Recommendations

This work evaluated the Colcount unit and established operational parameters for use with U-251. From the results it is clear that the OD limit should be set at 0.05 while the R_{min} and R_{max} have values of 0.2 and 2.0 mm respectively. Such limits allowed for the counting of colonies down to 50 cells per colony whilst also minimising counting of multiple small colonies as single entity. Further, a shape mask was constructed to allow for the counting of the entire plate area while discounting the plate edges which could result in errors in counting.

10.10 Results & Discussion

This work has obtained cell survival results for U-251 cells exposed to Co-60 photons and protons of 250 and 4 MeV utilising a thin-film irradiation technique. Each experiment was completed 3-5 times with 2 samples and 2 replicates per dose point per experiment. As such, the cell survival at each dose value (and the corresponding error bars) is comprised of 12-20 data points. These results are contained in Figure 10-20, Figure 10-21 and Figure 10-22. Unfortunately, due to experimental difficulties, a 16 MeV proton cell survival series was not completed.

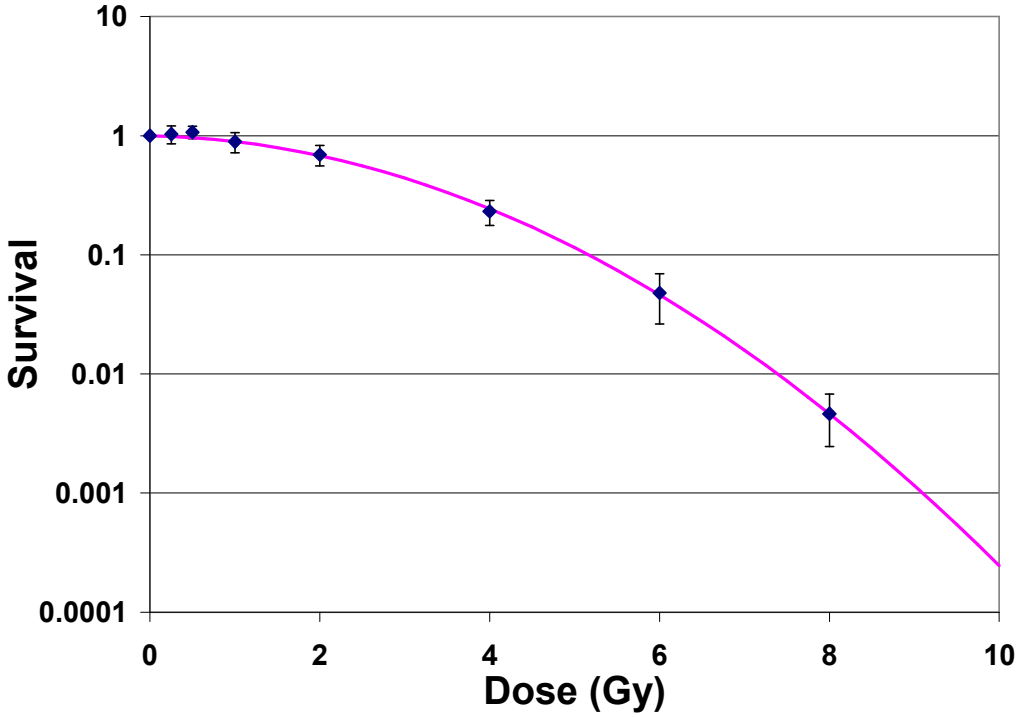

Figure 10-20: Co-60 U-251 cell survival results. Blue points represent experimental values with associated error bars, while the line is plotted from the derived α and β values.

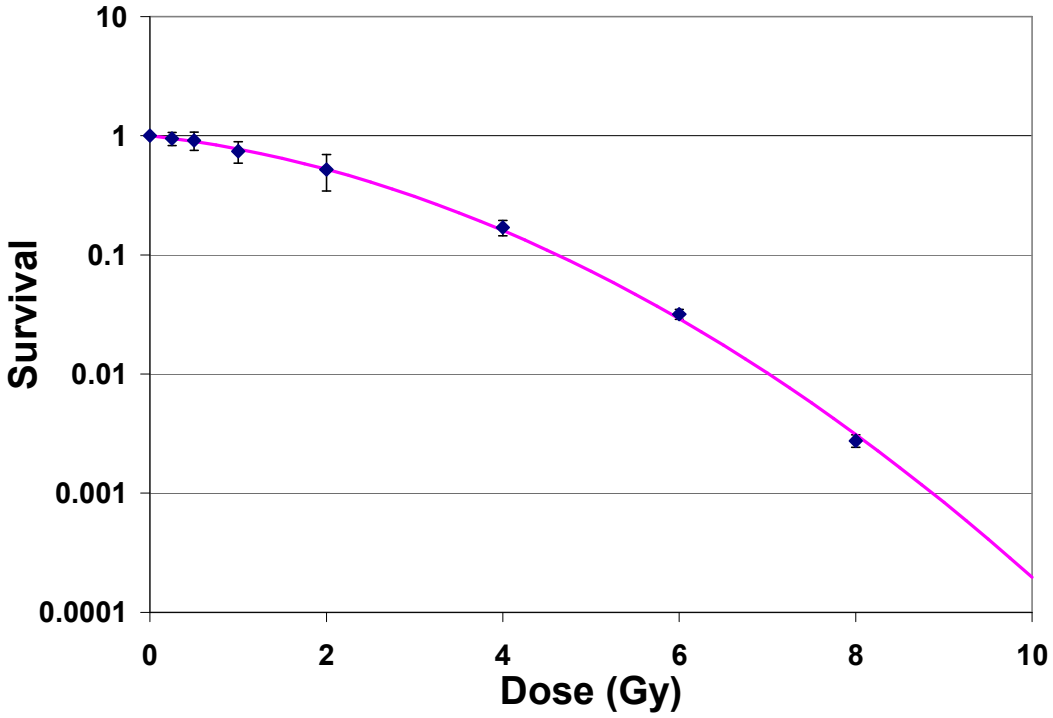

Figure 10-21: 4 MeV proton U-251 cell survival results. Blue points represent experimental values with associated error bars, while the line is plotted from the derived α and β values.

The results displayed for U-251 show a typical cell survival curve of a radio-resistant cell line with a large shoulder [62]. Further, the error bars on the experimental points are encouraging as their small nature indicates the reproducibility of the thin-film irradiation technique used in this study. Using the linear-quadratic model for cell survival as described in Section 2.9, the cell survival curve can be expressed using Equation 10-3.

$$S = \exp\left(-\alpha D - \beta D^2\right)$$

Equation 10-3: Expression for cell survival (S) using the linear-quadratic model. In this case α and β are constants, while D is the delivered dose.

By rearranging this relationship (Equation 10-4) it is possible to determine α and β from the experimental results as they represent the y-intercept and gradient respectively in a linear relationship. The α and β values were derived from the experimental results and the predicted cell survival using these values is plotted against experimental data points for comparison.

$$\frac{-\ln S}{D} = \alpha + \beta D$$

Equation 10-4: Rearrangement of the standard linear quadratic survival expression to obtain a linear relationship with α as the y-intercept and β as the gradient.

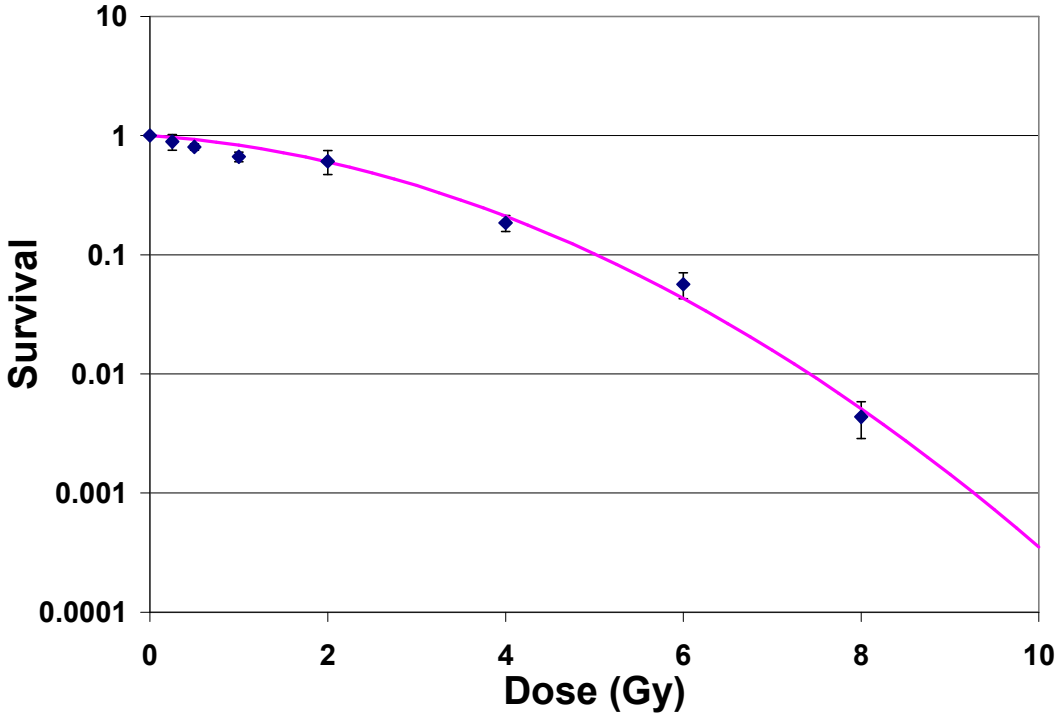

Figure 10-22: 250 MeV proton U-251 cell survival results. Blue points represent experimental values with associated error bars, while the line is plotted from the derived α and β values.

Co-60, 4 and 250 MeV proton results compare well with experimentally obtained α, β values and a linear-quadratic relationship. Clearly for Co-60 and 4 MeV proton irradiations, the linear quadratic expression follows the experimental values exactly, with all experimental points lying on the predicted curve. There is discrepancy with the 250 MeV results with some points lying outside the theoretical curve. In some cases this discrepancy is larger than experimental error bars. The reasons for this are unknown and may involve variations secondary particle spectra (such as neutrons) within the experimental hall or errors in dosimetry, Such results support further experiments with 250 MeV protons to determine more accurately the α, β parameters.

The α, β and α/β ratios for all experimental conditions evaluated in this study are contained within Table 10-9. From previously published data, the U-251 α/β ratio for γ irradiation (from Cs-137) is 0.56 [127] which is in agreement with the value of 0.44 found in this study. The variation in α/β for γ radiation can be attributed to the different energy in γ radiation used, Cs-137 in [127] and Co-60 in this study, and highlights how

the reference radiation type and energy needs to be carefully considered when making comparisons This agreement however demonstrates the suitability of thin-film irradiation techniques and the protocol developed.

Radiation	α	β	α/β
Co-60	0.0349	0.0796	0.4384
4 MeVp	0.1943	0.0659	2.9484
250 MeVp	0.1198	0.0675	1.7748

Table 10-9: α, β and α/β ratio date for U-251 irradiated with Co-60, 4 and 250 MeV proton radiation using thin-film irradiation techniques.

The α/β ratios (Table 10-9) and comparative plot of the 3 radiation conditions (Figure 10-23) illustrates some important factors concerning U-251. It has already been established that the Co-60 results are in agreement with previous work. What is surprising from these results is that 250 MeV protons produce a factor of four increase in the α/β ratio, which is attributed to an increase in α. As 250 MeV protons have a similar LET to Co-60 photons it could be expected that the response and hence the α/β parameters would be similar. This may be a result of neutrons present as a secondary particle through primary proton interactions with experimental beam modifying devices. This could affect the comparison between Co-60 and 250 MeV protons as neutrons are known to be more biologically damaging [67] and are not present during gamma irradiation. In future experiments the neutron component could be measured and its effect on the cell survival curve considered. It is important to note, however, when viewing the plot of 250 MeV proton results against those of Co-60 the variation in actual response is minimal and difficult to discern when considering errors in α/β determination. Overall, for two radiation modalities of similar LET, the agreement in survival as predicted by experimentally derived α/β ratios and the linear-quadratic model is quite accurate.

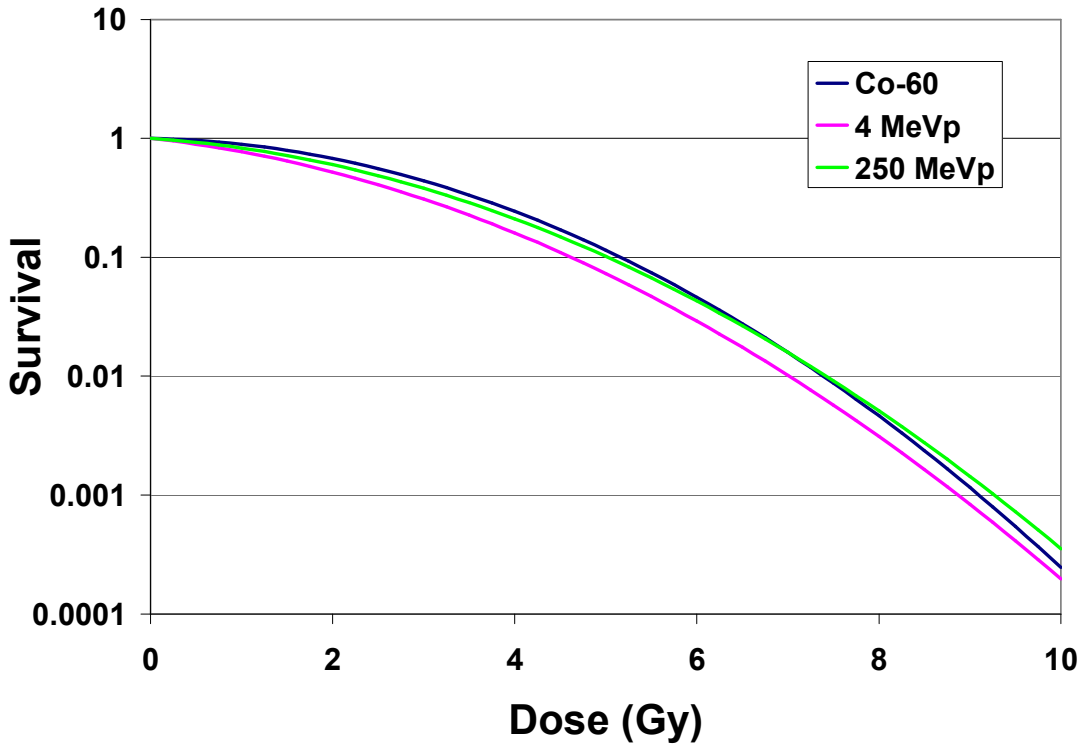

Figure 10-23: Comparative plot of the cell survival relationship as defined from the linear quadratic model for Co-60, 4 MeV protons and 250 MeV protons.

Figure 10-23 also illustrates how for U-251 cells a significant change in LET from 0.395-9.23 keV/μm in the case of 246 and 4.1 MeV protons produces minimal change in the cell survival curve. Published data on the response of U-251 to varying LET carbon ion beams from 20-105 keV/μm [127] suggests a definite change in response of U-251 to increasing LET. As the carbon LET increases a linear cell survival curve is observed which is indicative of a cells response to high LET radiation. This highlights how LET is not the only determinant in cell survival as particle type is also a factor. Such results have been previously observed in plasmid work [128] and illustrates how nanodosimetry and nanometric clustering (which has previously been established for carbon ions and protons [37, 38, 40, 128]) of ionisation events is a more accurate determinant of biological effect than LET. This further supports the use of the biophysical model developed in Section 8 which considers both particle type and LET in biological effect determination.

Figure 10-23 illustrates how the increase in proton LET has only a marginal effect on the cell survival. In a p53 mutant cell line such as U-251 the absence of apoptosis is highlighted by a broad shoulder on the cell survival curve and a small α component. This indicates that the cell must undergo reproductive or mitotic death for colony formation to not occur. Such mechanisms are obviously more prevalent and easier to induce using carbon ions than protons. The lack of response of U-251 to changing proton LET means that protons do not exhibit a radiobiological advantage in treating such tumours. Further, the development of a radiobiological model for proton irradiation with such a cell line is not required or useful as the response showed minimal variation with changing proton LET and measured micro- and nanodosimetric quantities.

10.11 Conclusions

This work has established a protocol for cell suspension irradiations using thin-film techniques. These protocols included the use of online dosimetry, acuate determination of cell concentration using coulter counter techniques and colony analysis using Colcount technology to study the response of U-251 glioma cells to Co-60 γ radiation, 4 and 250 MeV protons. The results for the photon control compared well with previous published data supporting the thin-film irradiation technique and associated protocol. There was a factor of four variation in the α/β ratio between Co-60 and 250 MeV proton results which was surprising considering that these are two low LET particles. However, when plotted in Figure 10-23 this difference produced little change in the cell survival curve.

The 4 MeV results for U-251 proved to have only minimal variation in the α/β ratio and change in the survival curve from 250 MeV protons. This indicates how p53 mutant cells such as U-251 do not undergo apoptosis as a consequence of their radioresistivity and as such, other pathways of cell kill such as mitotic cell death become predominant. Previous carbon ion survival data displays a marked difference in not only the α/β ratio, but also the shape of the cell survival curve with increasing LET. This supports the concept discussed in previous literature that cell survival is not only dependant on LET but rather the nanometric clustering of ionisation events (which is particle dependant) is a more accurate determinant of biological effect. This conclusion further supports the use

of the biological effect matrix developed in Section 8 which considers both particle type and LET in biological effect determination.

10.12 Future Recommendations & Developments

This work has demonstrated the effectiveness of the thin-film irradiation technique in obtaining cell survival curves for unsynchronised mammalian cell lines with proton and gamma radiation. However, this experimental study has also highlighted areas where improvements could be made and further work completed. It is recommended from the success of this work that this technique be applied to a number of different cell lines including other tumour cell lines and normal human fibroblasts as a control. This work could be extended from protons and photons to other heavier ions and neutrons to expand the applicability of this work to radiation protection and space applications.

In this work unsynchronised cells were used to study the effect of radiation on a glioma cell line. However, it may be more desirable to synchronise cells and provide an analysis of the cell response to radiation at different stages in the cell cycle. Cell synchronisation could be conducted using centrifugal elation, serum starvation or through the use of chemical inhibitors, with the choice being dependant on the cell line and previous experience with such synchronisation techniques. The information delivered by such studies may enhance our understanding of such radioresistant tumour cell lines such as glioma.

As has already been discussed, the irradiation of cell samples with light ions (protons and helium) of low energies requires very thin samples (100 μm or less) in order to limit the energy degradation and the resulting spread of linear energy transfer (LET) within the sample. The problem in such studies is to be able to reproducibly produce thin-films of cells for irradiations. If cells are allowed to attach to surfaces, they show a wide range of shapes and sizes. In addition, the thickness of the fluid layer surrounding the cell, needed to keep them viable, may vary from sample to sample and is subject to evaporation if the cells are kept at ambient temperatures.

In this study a technique for thin-sample cell irradiation was developed and utilised, however improvements are constantly being investigated to streamline the experimental process. Medical test strips that are commonly used in medical diagnostics provide a solution to this problem as they enable thin-films to be reproducibly obtained. In this design a chamber is formed between the base of the strip and a film covering it. The test strip is filled with a known sample volume by capillary action. Such a design may be more suitable to cell survival work and preliminary research has been completed on this concept and is presented below.

10.12.1 Test Strip Design

A conceptual design sketch of the test strip (courtesy of Dr Schulte) for thin sample irradiation is shown in Figure 10-24. The outer dimensions of the strip are 1" × 5/16". The strip base can be made of a common polyester material. It needs to be water-proof to avoid infiltration by the sample solution. It should be stiff enough to avoid accidental or gravitational bending of the strip. The base is covered by a thin-film (3/16" × 5/16") with a rectangular cut out (3/16" × 3/4"), forming the borders of the sample chamber. The material can be Mylar of 0.25 mil (6 μm) thickness provided by Lebow Company[1]. The height of the chamber is expected to exceed the side film thickness by 0.5 – 1.5 mil due to adhesion material used to attach it to the strip base. The top film, forming the roof of the chamber is a Teflon film of 0.5 mil thickness, also provided by Lebow. Teflon has the desired property of being impermeable to liquid water and permeable to gas (air, oxygen). This property is needed to prevent evaporation of the sample during long irradiation times and for replenishment of oxygen used by the cells during the irradiation process. Another important property of the Teflon film is its thickness uniformity, which should be better than ±10%. It may be necessary to apply some tension to the top film to avoid sagging and unwanted chamber height variations.

[1] Lebow Company, 5960 Mandarin Ave. Goleta, CA 93117, Phone (805) 964-7117, contact Ed Draper, www.lebow.company.com

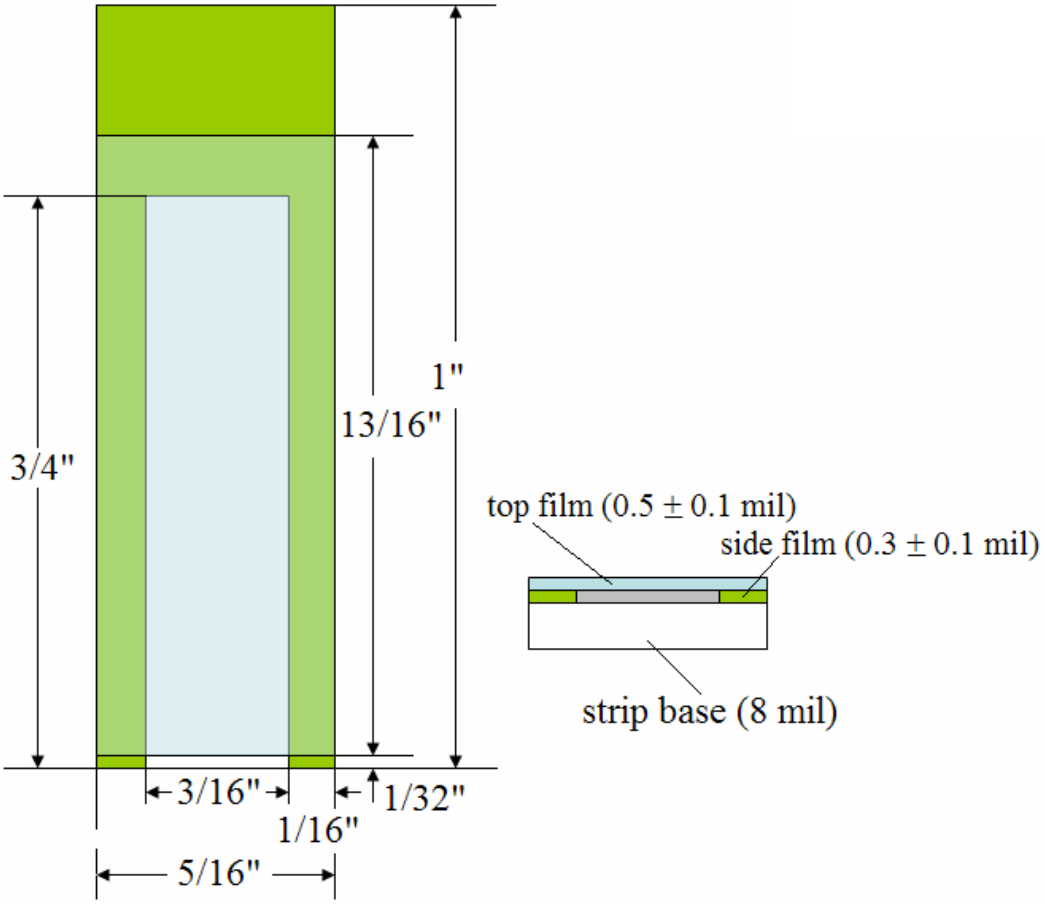

Figure 10-24: Schematic diagram of the radiobiological thin-film test strip.

10.12.2 GEANT4 Simulation

In order to assess the suitability of this device for low energy experiments Monte Carlo simulations have been conducted utilising the GEANT4.7.1p1 Monte Carlo toolkit. The test strip was recreated within the simulation program as per the above schematic diagram. The test strip was situated 10 cm from the exit window of the beam pipe as would be the case in an experimental situation. The sample was approximated as water which was assumed to uniformly fill the cavity. Simulations were conducted with the incident protons, deuterons, tritons and alpha particles of the same LET, as well as in addition to 5 MeV protons (the high LET proton radiation used in this cell survival work).

The PhysicsList generated for this work was based on the modular design of that used in the hadron therapy example supplied with the GEANT4 distribution. Low energy inelastic scattering (G4preCompound), low energy ionisation (using ICRU 49) and multiple scattering models were employed for the transport of protons and light ions through the geometry of the simulation. The physics of secondary ions was also considered and accounted for. The predominant particles generated within the simulation were electrons resulting from ionisation interactions. Electron processes supported included low energy ionisation, low energy Bremsstrahlung, and multiple scattering. In the event of photon generation, the physics processes included were low energy photoelectric effect, low energy Compton scattering, low energy Rayleigh scattering, and low energy pair production. Neutron interactions were also accounted for using the appropriate models. To ensure the accuracy of all calculations the program was forced to recalculate energy loss every 0.1 μm. This slowed simulations somewhat but ensured that all calculations were accurate.

The particle kinetic energy and LET was determined at 1 μm intervals within the sample and a corresponding LET and energy spectra files generated. This allowed for the variation in LET and particle kinetic energy to be determined as a function of sample thickness.

10.12.3 GEANT4 Results & Discussion

The graphs below show the simulation results for the test strip irradiated with different energies and particles. All results are normalised to the total number of hits on the test strip.

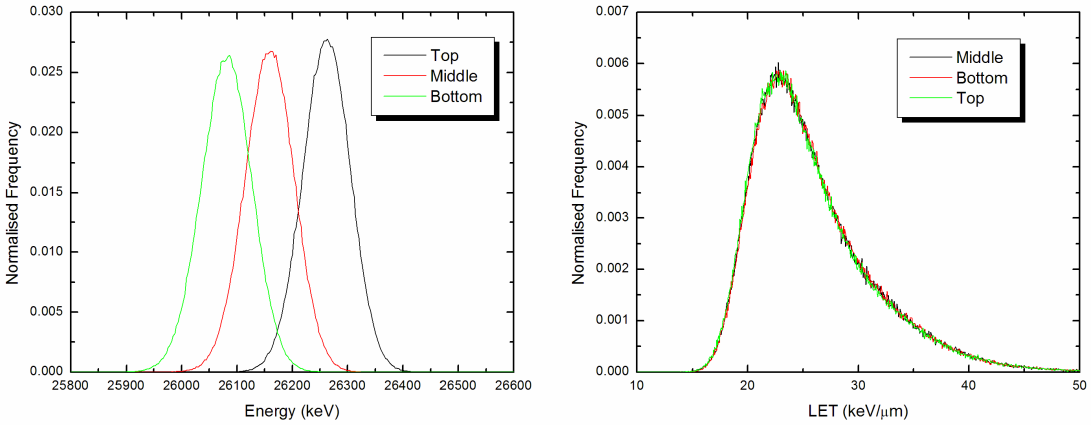

Figure 10-25: Particle kinetic energy and LET spectra results for the top, centre and bottom of the sample when irradiated with 27.5 MeV alpha particles.

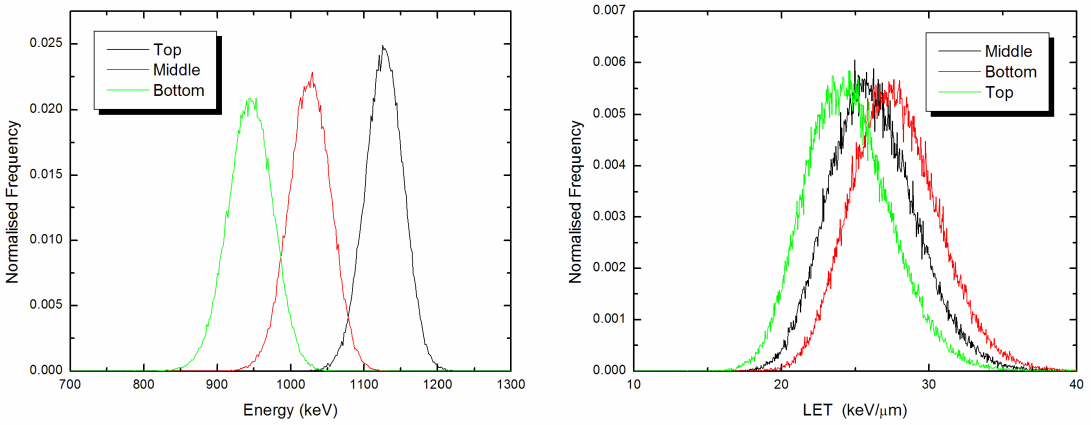

Figure 10-26: Particle kinetic energy and LET spectra results for the top, centre and bottom of the sample when irradiated with 2 MeV protons.

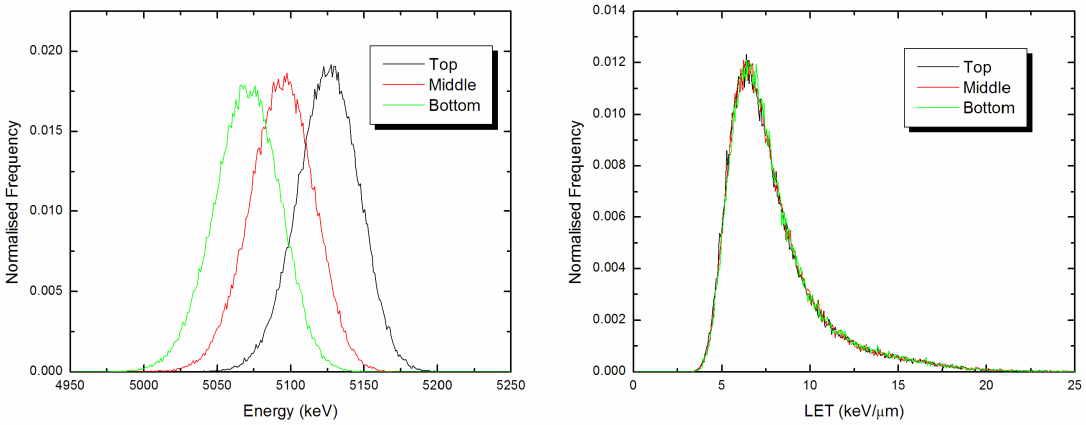

Figure 10-27: Particle kinetic energy and LET spectra results for the top, centre and bottom of the sample when irradiated with 5.5 MeV protons.

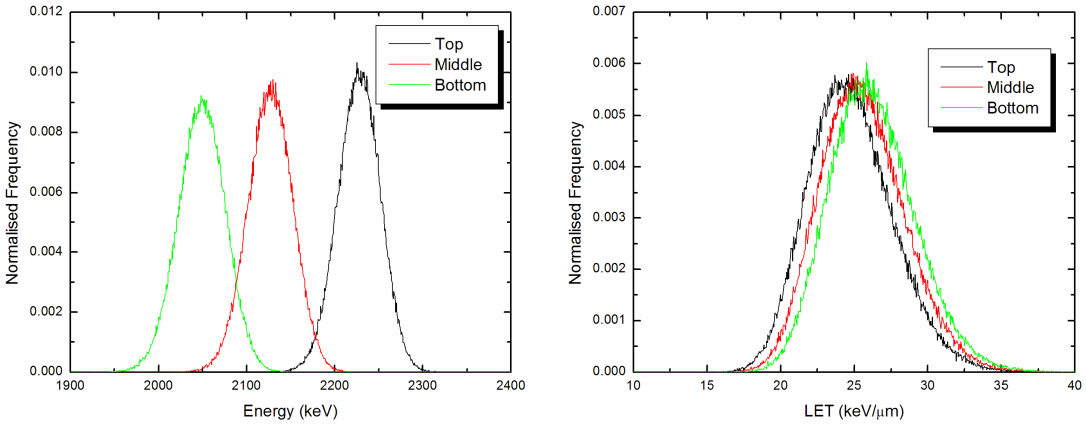

Figure 10-28: Particle kinetic energy and LET spectra results for the top, centre and bottom of the sample when irradiated with 3.25 MeV deuterons.

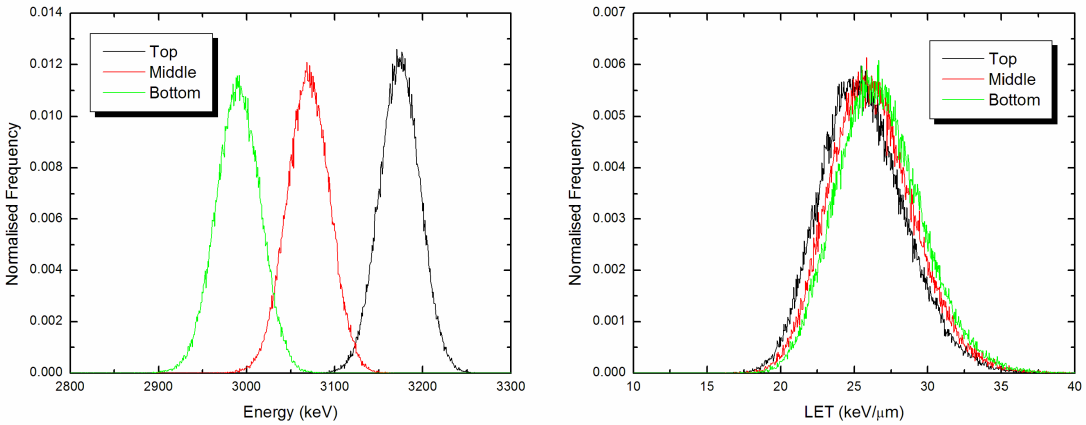

Figure 10-29: Particle kinetic energy and LET spectra results for the top, centre and bottom of the sample when irradiated with 4.25 MeV tritons.

These results provide the spectra of LET and kinetic energy of the particle at the top, centre and bottom of the sample when contained within the test strip assembly. It is clear from these results that the LET spread does not vary appreciably as a function of depth in the sample. Nor does the LET spectra develop a larger tail indicating fragmentation of the ion as it traverses the sample. To more clearly determine the effect of depth on LET the mean LET as a function of depth for the various ions is contained within Figure 10-30.

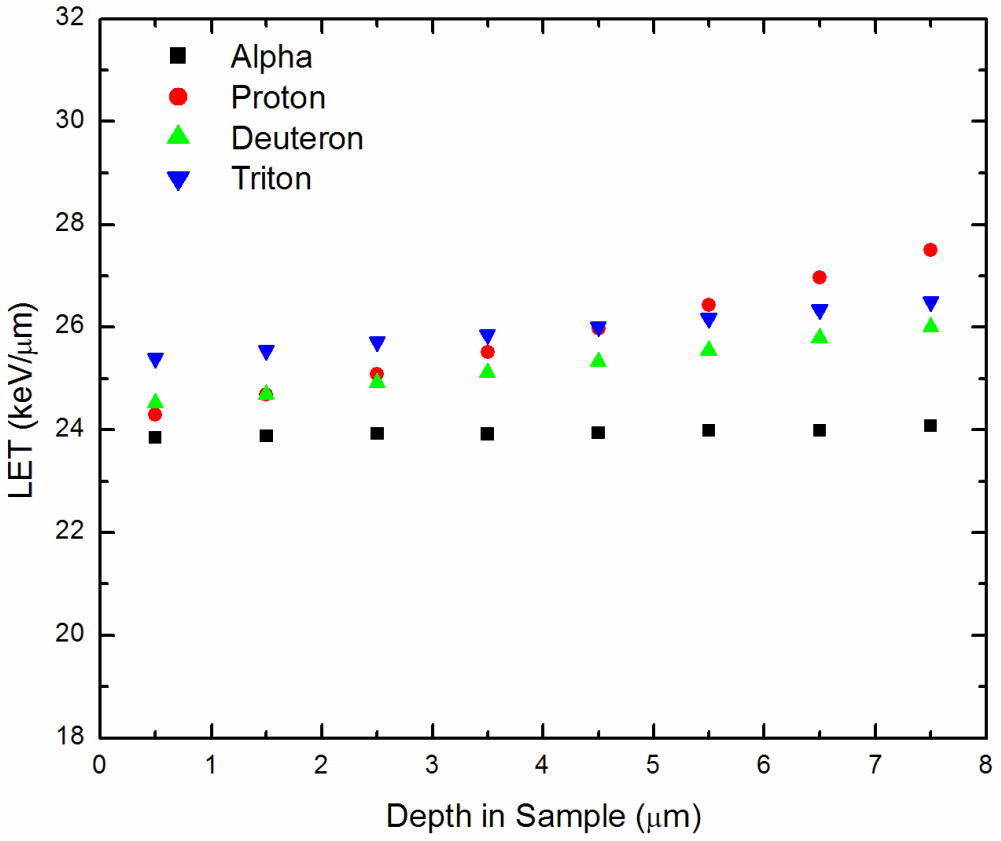

Figure 10-30: LET of the particle plotted as a function of depth in the sample for a) 2MeV protons, b) 3.25MeV deuterons, c) 4.25MeV tritons, d) 27.5MeV alphas incident on the test strip. Error bars are not included in this graph to improve readability.

It is clear from Figure 10-30 that the LET of the particle, especially for the heavier ions does not vary appreciably across the thickness of the sample. In the case of protons the LET variation is highest at approximately 15% with the LET variation for the other ions being less than 10% with almost no variation detected in the case of alpha particle radiation. It would thus be expected that such an irradiation technique would be useful

for work with heavier ions typical in space research. Further, when compared with the change in kinetic energy of the particle as a function of thickness in the sample (Figure 10-31) it is clear that a uniformly thin sample of the order to 10 μm is useful in such radiobiological experiments and that the test strip provides a means for reproducibly achieving thin-films for accurate radiobiological results.

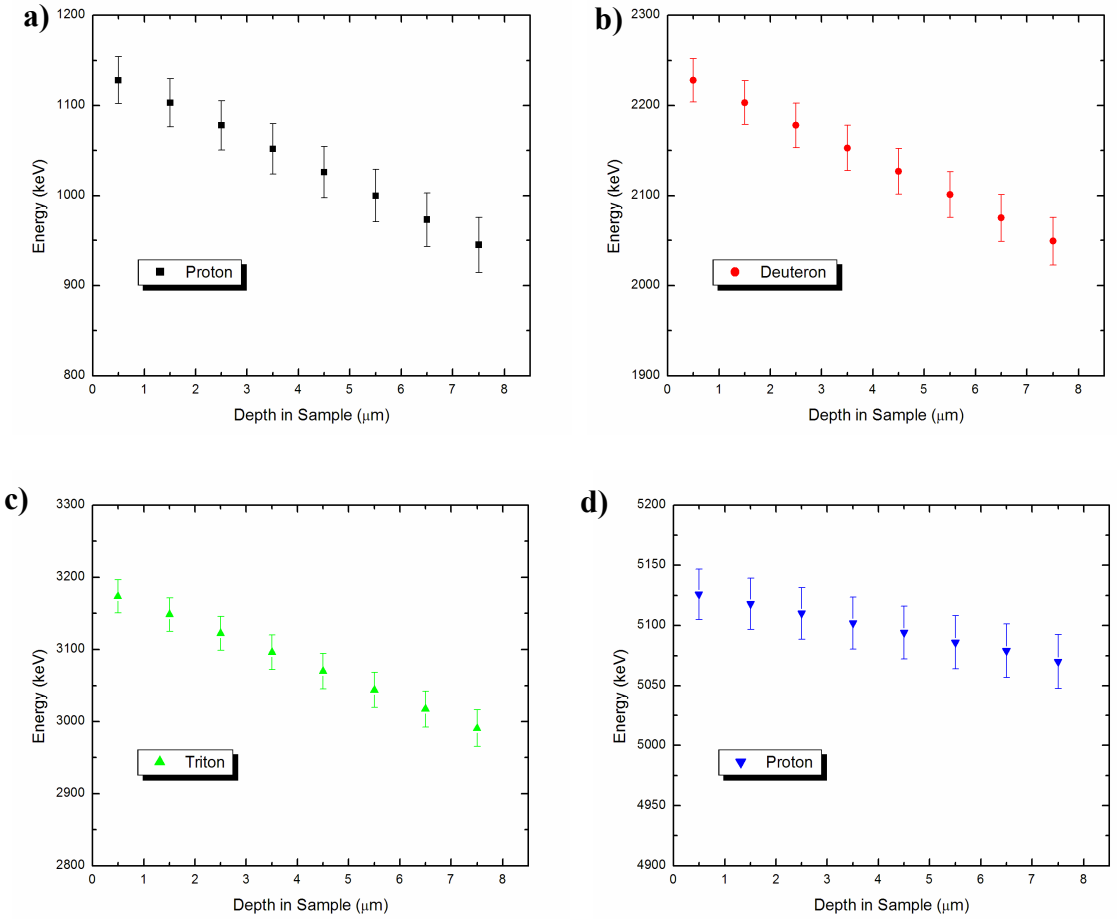

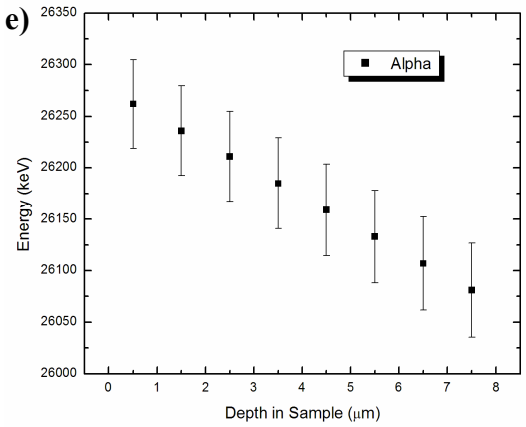

Figure 10-31: Kinetic energy of the particle plotted as a function of depth in the sample for a) 2MeV protons, b) 3.25MeV deuterons, c) 4.25MeV tritons, d) 5.5MeV protons, e) 27.5MeV alphas incident on the test strip. Error bars indicate the FWHM of the peak.

10.12.4 Test Strip Conclusions & Recommendations

Through GEANT4 Monte Carlo simulations of the proposed test strip design the suitability of such a device to thin-film radiobiology experiments has been established. The results indicated that the test strip could produce a radiation field across the sample that had a maximum variation of 15% in LET. Further, the design of the test strip, with minimal surrounding structures prevented attenuation or fragmentation of the ion beam. Hence, the energy spectra and corresponding LET spectra showed minimal tailing as a function of depth within the sample.

This work has also highlighted how GEANT4 and Monte Carlo studies are useful in biological work in providing an assessment of the radiation's quality through the sample. It would be recommended that such studies be expanded in radiobiological experiments to provide an assessment of parameters such as LET, energy spectra, dose and dose equivalent within the sample. Such simulations can highlight the presence of secondary particles and identify possible sources of such secondaries which can have an adverse effect on the response of biological systems.

Overall, the concept of a radiobiological test strip as a replacement to the current procedure for thin-film irradiation studies has some merit based on Monte Carlo transport studies. The results presented here have proved as the initial test of the concept, however

further investigation is required. Firstly, such a test strip needs to be built and tested experimentally to ensure that cells can be up-taken and removed easily with little stress to the cells. Such work may involve investigating combinations of hydrophilic and hydrophobic materials. This needs to be then incorporated into an experimental protocol and tested using a reference radiation such as Co-60 photons. Once such tests have been completed this technique could be utilised in accelerator experiments.

11 Overall Conclusions

This thesis further applies solid-state microdosimetry and low-pressure gas nanodosimetry to both radiation therapy and radiation protection. In doing so this research has further tested the current metrology devices under a range of different radiation fields, developed Monte Carlo simulation systems to investigate their performance, linked the output of such detectors to biological effect and put in place procedures and protocols to further the development and application of these technologies.

This study has shown the applicability of the SOI microdosimeter in measuring the dose equivalent outside proton treatment fields and has provided valuable information on the dose equivalent both at the surface and at depth experienced by prostate cancer patients treated with protons. SOI microdosimetry measurements compared favourably to those measured at other centres with Bonner spheres and bubble detectors further validating the use of the technique. However, close comparisons are difficult due to the different measurement conditions and apparatus used in each experimental data series. This in-turn limits the conclusions that can be made as to the accuracy of the SOI microdosimetry measurement technique in this application. Further studies utilising the SOI microdosimeter are currently being conducted with therapeutic proton fields generated with both passive and active beam delivery techniques under otherwise equivalent conditions at different facilities and for different clinical treatment scenarios including paediatric cancers. Comparative measurements will also be completed using existing metrology devices for validation. This work has opened a new direction for SOI microdosimetry in obtaining accurate dose equivalent data in mixed radiation fields. It is expected that this will have a positive impact on its use in both radiation therapy and radiation protection applications.

The research presented here has highlighted the ability of GEANT4 in simulating therapeutic proton radiation. In this work the response of a relatively complex radiation detection structure, the SOI microdosimeter, was simulated with acceptable accuracy considering the complex nature of the incident beam and heterogeneous phantom

structure. Some discrepancies were observed which can be reduced through further improvements to the simulation program. From the simulated response of the microdosimeter within commercially available TE phantoms it is clear that the quality of the proton radiation varies in different tissue substances. This has been established through the comparison of mean dose weighted lineal energy, dose equivalent and average quality factor obtained through the simulated response of an SOI microdosimeter situated at tissue boundaries within a head and chest phantom. Such variations in radiation quality were most prevalent immediately past the bone layer. While the biological effects of small variations in radiation quality and dose equivalent are unclear it would be advisable that they be considered over the entire course of treatment as the summation of these effects may be clinically relevant. Such changes in radiation quality are not accounted for in current treatment planning systems which rely on analytical simulation techniques and the macroscopic quantity of absorbed dose as a planning parameter. Future advances in treatment planning may utilise Monte Carlo methods, microdosimetry and dose equivalent their basis to accurately plan for changes in radiation field composition.

To determine the clinical relevance of SOI microdosimetry studies in commercially available TE phantoms, this work has tested the performance of commercially available and water equivalent phantom structures against ICRP compositions in therapeutic proton transport. It utilised the GEANT4.7.1p1 toolkit and assessed the performance of these different phantom configurations for adipose, brain, bone and muscle tissues utilising dose, range, lateral scatter, mean lineal energy and dose weighted mean lineal energy as the parameters for comparison. There is some possibility for improvement in the transport of therapeutic protons in water equivalent materials and commercially available phantoms to better reflect that of the ICRP case. Such improvements in radiation transport properties will enhance the accuracy of treatment planning and quality assurance measurements. Further work should be completed in assessing the response of these comparisons and the effect on two- and three-dimensional dose distributions and microdosimetry spectra in clinical situations.

To determine the suitability for space deployment of the SOI microdosimeter aboard MidSTAR-1 the GEANT4.7.1p1 toolkit was used to simulate the response of this device to solar protons as provided by SPENVIS for the International Space Station. The SOI microdosimeter was simulated to determine the effect of varying shield thickness, converter thickness and preceding tissue material on the microdosimetry spectra. Through simulating the response of the SOI microdosimeter to solar protons it has been possible to determine optimum levels of shielding to enhance astronaut protection and minimise SEU. In turn this has highlighted that such simulations and microdosimetry measurement parameters could be utilised in optimising shielding structures for future deployment. Simulations of varying converter thickness have enabled the effective configuration of microdosimeters for space deployment to be determined. It was also possible to estimate the time of simulation and determine the effectiveness of the SOI microdosimeter in obtaining real time data, and in turn possibly provide an instrument for real time radiation protection applications. It is expected that this deployment of the SOI microdosimeter may be the beginning of a long-term application for this device.

The ability of the SOI microdosimeter to be deployed in deep space applications and provide information on heavy ion interactions was experimentally tested under Fe-56, Ti-48 and O-16 heavy ion radiation fields at the NSRL facility at Brookhaven National laboratory. From this work experimentally obtained mean dose weighted lineal energies as a function of depth within a Perspex phantom were obtained and compared where possible to existing TEPC data with good agreement. The advantage of the SOI microdosimeter in this application was apparent through its ability to make accurate in-phantom measurements of such radiation fields. The high lineal energies of such ions make them important biologically as well as for the deployment of electronics in space and the consideration of SEU, despite their low abundance in space relative to lighter ions such as protons. Measurements along the Bragg curve have allowed for a number of heavy ion energies to be tested from the one single incident ion beam. This is important in space research as the ions experienced are of varying energy and are typically lower than 1 GeV/n. This information can then be compared to biological predictions to

estimate cell death and mutation rates. The radiation hardness of the device was also assessed with excellent results supporting their long term deployment.

The testing of a new ΔE-E monolithic silicon detector telescope in conjunction with corresponding SOI measurements of therapeutic proton beams has allowed for initial benchmarking of this new technology. This ΔE-E telescope has a unique method of measuring the change in radiological properties of the radiation field using coincidence techniques and two-stage detection methods that has never been completed previously in therapeutic radiation fields. The results from this work are a success with clear and discernable data obtained on the changing properties of both the modulated and un-modulated proton beam. To compliment the measured ΔE-E telescope data a radiobiological effect matrix was developed using existing V79 survival data. By correlating this matrix with the measured response of the ΔE-E telescope it was possible to determine the radiobiological effect of the radiation field at a given point. Comparisons with existing models and data proved successful in the case of therapeutic proton radiation and support the further application of this matrix to other radiation modalities. The matrix can further be expanded to other cell lines, both in-vitro and in-vivo, to increase its usefulness. The radiobiological effect matrix and monolithic Si ΔE-E telescope provide a complete detection system for measuring directly the RBE of mixed radiation fields which is exceptionally useful in radiation therapy and radiation protection applications for charged hadrons, protons and neutrons.

Nanodosimetry is a logical extension of microdosimetry to measure radiation effects on the nanometre or DNA level. Such measurements provide information on the particle track structure which is unique to particle type and energy, and may provide a more detailed and accurate predictor of biological effect and SEU rates. In this report both theoretical and experimental nanodosimetry data has been presented for a range of proton energies. The Monte Carlo system employed in theoretically determining the response of the nanodosimeter has been validated through these comparisons and areas of improvement have been identified for future work. The current low-pressure gas nanodosimetry system has shown it is useful in obtaining nanodosimetric data for

laboratory conditions and supports the program we have implemented for the investigation of nanodosimetry and its importance to radiation therapy and radiation protection. Further work on detector development and linking the measured output of nanodosimetry to biological effect will possibly increase the application of this area of radiation metrology.

To allow for continued development of radiobiological models for micro- and nanodosimetry adequate cell survival protocols need to be established and tested to provide accurate information for low energy ions. To achieve this, a protocol for cell suspension irradiations using thin-film techniques has been established and tested using human glioma cells. This protocol included the use of online dosimetry, acuate determination of cell concentration using coulter counter techniques and colony analysis using Colcount technology to study the response of cells, and can be applied to a wide range of radiation types and energies. Comparisons with existing data supported the accuracy of this technique and its further developments to assist in obtaining cell survival data for biological modelling.

It is envisaged that micro- and nanodosimetry will provide an ever expanding presence in the areas of radiation therapy and radiation protection. The work presented in this thesis is a step towards this goal, and will allow for the continued development of micro- and nanodosimetry and application of the current technologies to radiation therapy and radiation protection.

12 References

[1] J. E. Turner, *Atom, Radiation and Radiation Protection*. New York: Pergamon Press, 1986.

[2] G. F. Knoll, *Radiation Detection and Measurement*, 3rd ed: John Wiley & Sons, 1999.

[3] "American Cancer Society Statistics for 2004," *http://www.cancer.org/docroot/stt/stt_0.asp*, 2004.

[4] "Australian National Proton Facility Discussion Paper," *Australian National Proton Facility Steering Committee*, 2001.

[5] R. R. Wilson, "Radiological use of fast protons," *Radiology*, vol. 47, pp. 487-491, 1946.

[6] J. D. Slater, "Clinical applications of proton radiation treatment at Loma Linda University: Review of a fifteen-year experience," *Technology in Cancer Research & Treatment*, vol. 5, pp. 81-89, 2006.

[7] J. D. Slater, C. J. Rossi, L. T. Yonemoto, D. A. Bush, B. R. Jabola, R. P. Levy, R. I. Grove, W. Preston, and J. M. Slater, "Proton therapy for prostate cancer: The initial Loma Linda University experience," *International Journal of Radiation Oncology Biology Physics*, vol. 59, pp. 348-352, 2004.

[8] A. M. Koehler, R. J. Schneider, and J. M. Sisterson, "Flattening of proton dose distributions for large-field radiotherapy," *Medical Physics*, vol. 4, pp. 297-301, 1977.

[9] G. Coutrakon, M. Bauman, D. Lesyna, D. Miller, J. Nusbaum, J. Slater, J. Johanning, J. Miranda, P. M. Deluca, J. Siebers, and B. Ludewigt, "A Prototype Beam Delivery System for the Proton Medical Accelerator at Loma-Linda," *Medical Physics*, vol. 18, pp. 1093-1099, 1991.

[10] A. M. Koehler, R. J. Schneider, and J. M. Sisterson, "Range Modulators for Protons and Heavy-Ions," *Nuclear Instruments & Methods*, vol. 131, pp. 437-440, 1975.

[11] A. Lomax, F. Albertini, A. Bolsi, M. Steneker, T. Boehringer, A. Coray, S. Lin, E. Pedroni, H. P. Rutz, B. Timmermann, and G. Goitein, "Intensity Modulated Proton Therapy at PSI: Things we have learnt (and are still learning)," *Radiotherapy and Oncology*, vol. 76, pp. S54-S55, 2005.

[12] A. J. Lomax, F. Albertini, T. Boehringer, A. Bols, M. Bosshardt, A. Coray, G. Goitein, S. Lin, E. Pedroni, M. Stenecker, and J. Verwey, "Spot scanning proton

therapy: Treatment planning and treatment verification," *Radiotherapy and Oncology*, vol. 78, pp. S21-S21, 2006.

[13] E. Pedroni, "The new proton scanning gantry of PSI: A system designed for IMPT delivery in the whole body including moving targets," *Radiotherapy and Oncology*, vol. 78, pp. S71-S71, 2006.

[14] E. Pedroni, T. Bohringer, A. Coray, E. Egger, M. Grossmann, S. X. Lin, A. Lomax, G. Goitein, W. Roser, and B. Schaffner, "Initial experience of using an active beam delivery technique at PSI," *Strahlentherapie Und Onkologie*, vol. 175, pp. 18-20, 1999.

[15] "Paul Scherrer Institute Website," http://radmed.web.psi.ch/asm/gantry/gantry_master.html 2007.

[16] "Loma Linda University Medical Center Proton Website," http://www.llu.edu/proton/, 2007.

[17] J. Barak, "Analytical microdosimetry model for proton-induced SEU in modern devices," *IEEE Transactions on Nuclear Science*, vol. 48, pp. 1937-1945, 2001.

[18] G. Coutrakon, J. Cortese, A. Ghebremedhin, J. Hubbard, J. Johanning, P. Koss, G. Maudsley, C. R. Slater, C. Zuccarelli, and J. Robertson, "Microdosimetry spectra of the Loma Linda proton beam and relative biological effectiveness comparisons," *Medical Physics*, vol. 24, pp. 1499-1506, 1997.

[19] J. B. Robertson, J. M. Eaddy, J. O. Archambeau, G. B. Coutrakon, D. W. Miller, M. F. Moyers, J. V. Siebers, J. M. Slater, and J. F. Dicello, "Relative Biological Effectiveness and Microdosimetry of a Mixed Energy-Field of Protons up to 200 Mev," in *Life Sciences and Space Research Xxv(2)*, vol. 14, *Advances in Space Research*, 1994, pp. 271-275.

[20] J. F. Dicello, H. I. Amols, M. Zaider, and G. Tripard, "A Comparison of Microdosimetric Measurements with Spherical Proportional-Counters and Solid-State Detectors," *Radiation Research*, vol. 82, pp. 441-453, 1980.

[21] P. Bradley, "The Development of a Novel Silicon Microdosimeter for High LET Radiation Therapy," in *Engineering Physics*, vol. PhD Physics. Wollongong: University of Wollongong, 2000, pp. 333.

[22] P. J. McNulty, D. R. Roth, W. J. Beauvois, W. G. Abdel-Kader, and E. G. Stassinopoulos, "Microdosimetry in space using microelectronic circuits," *Presented at NATO-ASI on biological effects and physics of solar and galactic cosmic radiation: Conference Proceedings*, 1991.

[23] D. R. Roth, P. J. McNulty, W. J. Beauvais, R. A. Reed, and E. G. Stassinopoulos, "Solid-State Microdosimeter for Radiation Monitoring in Spacecraft and Avionics," *IEEE Transactions on Nuclear Science*, vol. 41, pp. 2118-2124, 1994.

[24] A. B. Rosenfeld, G. I. Kaplan, M. G. Carolan, B. J. Allen, R. Maughan, M. Yudelev, C. Kota, and J. Coderre, "Simultaneous macro and micro dosimetry with MOSFETs," *IEEE Transactions on Nuclear Science*, vol. 43, pp. 2693-2700, 1996.

[25] P. D. Bradley, A. B. Rosenfeld, and M. Zaider, "Solid state microdosimetry," *Nuclear Instruments & Methods in Physics Research Section B-Beam Interactions with Materials and Atoms*, vol. 184, pp. 135-157, 2001.

[26] I. Cornelius, "Towards silicon microdosimetry based verification of Monte Carlo calculations in hadron therapy," in *Engineering Physics*, vol. PhD. Wollongong: University of Wollongong, 2003, pp. 138.

[27] I. Cornelius, R. Siegele, A. B. Rosenfeld, and D. D. Cohen, "Ion beam induced charge characterisation of a silicon microdosimeter using a heavy ion microprobe," *Nuclear Instruments & Methods in Physics Research Section B-Beam Interactions with Materials and Atoms*, vol. 190, pp. 335-338, 2002.

[28] P. D. Bradley, A. B. Rosenfeld, K. K. Lee, D. N. Jamieson, G. Heiser, and S. Satoh, "Charge collection and radiation hardness of a SOI microdosimeter for medical and space applications," *IEEE Transactions on Nuclear Science*, vol. 45, pp. 2700-2710, 1998.

[29] A. B. Rosenfeld, P. D. Bradley, I. Cornelius, B. J. Allen, M. Zaider, R. L. Maughan, J. C. Yanch, J. Coderre, J. B. Flanz, and T. Kobayashi, "Solid state microdosimetry in hadron therapy," *Radiation Protection Dosimetry*, vol. 101, pp. 431-434, 2002.

[30] A. B. Rosenfeld, P. D. Bradley, I. Cornelius, G. I. Kaplan, B. J. Allen, J. B. Flanz, M. Goitein, A. Van Meerbeeck, J. Schubert, J. Bailey, Y. Takada, A. Maruhashi, and Y. Hayakawa, "A new silicon detector for microdosimetry applications in proton therapy," *IEEE Transactions on Nuclear Science*, vol. 47, pp. 1386-1394, 2000.

[31] P. D. Bradley, A. B. Rosenfeld, B. Allen, J. Coderre, and J. Capala, "Performance of silicon microdosimetry detectors in boron neutron capture therapy," *Radiation Research*, vol. 151, pp. 235-243, 1999.

[32] "Microdosimetry," *ICRU*, vol. 36, 1983.

[33] H. H. Rossi and M. Zaider, *Microdosimetry and Its Applications*. London: Springer, 1996.

[34] "International Commission on Radiation Units and Measurements - The quality factor in radiation protection," *Report ICRU-40*, 1986.

[35] NIST, "National Institute of Standards and Technology PSTAR Database Program," http://physics.nist.gov/cgi-bin/Star/compos.pl?ap.

[36] S. Shchemelinin, A. Breskin, R. Chechik, P. Colautti, and R. W. M. Schulte, "First measurements of ionisation clusters on the DNA scale in a wall-less sensitive volume," *Radiation Protection Dosimetry*, vol. 82, pp. 43-50, 1999.

[37] G. Garty, S. Shchemelinin, A. Breskin, R. Chechik, G. Assaf, I. Orion, V. Bashkirov, R. Schulte, and B. Grosswendt, "The performance of a novel ion-counting nanodosimeter," *Nuclear Instruments & Methods in Physics Research Section a-Accelerators Spectrometers Detectors and Associated Equipment*, vol. 492, pp. 212-235, 2002.

[38] G. Garty, S. Shchemelinin, A. Breskin, R. Chechik, I. Orion, G. P. Guedes, R. Schulte, V. Bashkirov, and B. Grosswendt, "Wall-less ion-counting nanodosimetry applied to protons," *Radiation Protection Dosimetry*, vol. 99, pp. 325-330, 2002.

[39] S. Shchemelinin, G. Garty, A. Breskin, R. Chechik, and R. W. M. Schulte, "Ion-counting nanodosimetry: A new method for assessing radiation damage to DNA," *Nuclear Instruments & Methods in Physics Research Section a-Accelerators Spectrometers Detectors and Associated Equipment*, vol. 477, pp. 527-530, 2002.

[40] G. Garty, "Development of ion-counting nanodosimetry and evaluation of its relevance to radiation biology," in *Physics*, vol. PhD. Rehovot: Weizmann Institute of Science, 2004, pp. 186.

[41] A. Breskin, R. Chechik, P. Colautti, V. Conte, L. Denardo, A. Pansky, S. Shchemelinin, G. Talpo, and G. Tornielli, "A Single-Electron Counter for Nanodosimetry," *Radiation Protection Dosimetry*, vol. 61, pp. 199-204, 1995.

[42] B. Keeney, V. Bashkirov, R. P. Johnson, W. Kroeger, H. Ohyama, H. F. W. Sadrozinski, R. W. M. Schulte, A. Seiden, and P. Spradlin, "A silicon telescope for applications in nanodosimetry," *IEEE Transactions on Nuclear Science*, vol. 49, pp. 1724-1727, 2002.

[43] S. Shchemelinin, S. Pszona, G. Garty, A. Breskin, and R. Chechik, "The absolute detection efficiency of vacuum electron multipliers, to keV protons and Ar+ ions," *Nuclear Instruments & Methods in Physics Research Section a-Accelerators Spectrometers Detectors and Associated Equipment*, vol. 438, pp. 447-451, 1999.

[44] M. A. Hill, "Radiation damage to DNA: The importance of track structure," *Radiation Measurements*, vol. 31, pp. 15-23, 1999.

[45] "GEANT4 Collaboration Website," http://geant4.web.cern.ch/geant4/, 2007.

[46] P. Rodrigues, R. Moura, C. Ortigao, L. Peralta, M. G. Pia, A. Trindade, and J. Varela, "Geant4 applications and developments for medical physics experiments," *IEEE Transactions on Nuclear Science*, vol. 51, pp. 1412-1419, 2004.

[47] S. Chauvie, Z. Francis, S. Guatelli, S. Incerti, B. Mascialino, G. Montarou, P. Moretto, P. Nieminen, and M. G. Pia, "Monte Carlo simulation of interactions of radiation with biological systems at the cellular and DNA levels: The Geant4-DNA project," *Radiation Research*, vol. 166, pp. 676-677, 2006.

[48] R. W. Schulte, V. Bashkirov, M. C. L. Klock, T. F. Li, A. J. Wroe, I. Evseev, D. C. Williams, and T. Satogata, "Density resolution of proton computed tomography," *Medical Physics*, vol. 32, pp. 1035-1046, 2005.

[49] J. Allison, K. Amako, J. Apostolakis, H. Araujo, P. A. Dubois, M. Asai, G. Barrand, R. Capra, S. Chauvie, R. Chytracek, G. A. P. Cirrone, G. Cooperman, G. Cosmo, G. Cuttone, G. G. Daquino, M. Donszelmann, M. Dressel, G. Folger, F. Foppiano, J. Generowicz, V. Grichine, S. Guatelli, P. Gumplinger, A. Heikkinen, I. Hrivnacova, A. Howard, S. Incerti, V. Ivanchenko, T. Johnson, F. Jones, T. Koi, R. Kokoulin, M. Kossov, H. Kurashige, V. Lara, S. Larsson, F. Lei, O. Link, F. Longo, M. Maire, A. Mantero, B. Mascialino, I. McLaren, P. M. Lorenzo, K. Minamimoto, K. Murakami, P. Nieminen, L. Pandola, S. Parlati, L. Peralta, J. Perl, A. Pfeiffer, M. G. Pia, A. Ribon, P. Rodrigues, G. Russo, S. Sadilov, G. Santin, T. Sasaki, D. Smith, N. Starkov, S. Tanaka, E. Tcherniaev, B. Tome, A. Trindade, P. Truscott, L. Urban, M. Verderi, A. Walkden, J. P. Wellisch, D. C. Williams, D. Wright, and H. Yoshida, "Geant4 developments and applications," *IEEE Transactions on Nuclear Science*, vol. 53, pp. 270-278, 2006.

[50] F. Lei, P. R. Truscott, C. S. Dyer, B. Quaghebeur, D. Heynderickx, P. Nieminen, H. Evans, and E. Daly, "MULASSIS: A Geant4-based multilayered shielding simulation tool," *IEEE Transactions on Nuclear Science*, vol. 49, pp. 2788-2793, 2002.

[51] G. Santin, P. Nieminen, H. Evans, E. Daly, F. Lei, P. R. Truscott, C. S. Dyer, B. Quaghebeur, and D. Heynderickx, "New Geant4 based simulation tools for space radiation shielding and effects analysis," *Nuclear Physics B-Proceedings Supplements*, vol. 125, pp. 69-74, 2003.

[52] S. Agostinelli, J. Allison, K. Amako, J. Apostolakis, H. Araujo, P. Arce, M. Asai, D. Axen, S. Banerjee, G. Barrand, F. Behner, L. Bellagamba, J. Boudreau, L. Broglia, A. Brunengo, H. Burkhardt, S. Chauvie, J. Chuma, R. Chytracek, G. Cooperman, G. Cosmo, P. Degtyarenko, A. Dell'Acqua, G. Depaola, D. Dietrich, R. Enami, A. Feliciello, C. Ferguson, H. Fesefeldt, G. Folger, F. Foppiano, A. Forti, S. Garelli, S. Giani, R. Giannitrapani, D. Gibin, J. J. G. Cadenas, I. Gonzalez, G. G. Abril, G. Greeniaus, W. Greiner, V. Grichine, A. Grossheim, S. Guatelli, P. Gumplinger, R. Hamatsu, K. Hashimoto, H. Hasui, A. Heikkinen, A. Howard, V. Ivanchenko, A. Johnson, F. W. Jones, J. Kallenbach, N. Kanaya, M. Kawabata, Y. Kawabata, M. Kawaguti, S. Kelner, P. Kent, A. Kimura, T. Kodama, R. Kokoulin, M. Kossov, H. Kurashige, E. Lamanna, T. Lampen, V. Lara, V. Lefebure, F. Lei, M. Liendl, W. Lockman, F. Longo, S. Magni, M. Maire, E. Medernach, K. Minamimoto, P. M. de Freitas, Y. Morita, K. Murakami, M. Nagamatu, R. Nartallo, P. Nieminen, T. Nishimura, K. Ohtsubo, M. Okamura,

S. O'Neale, Y. Oohata, K. Paech, J. Perl, A. Pfeiffer, M. G. Pia, F. Ranjard, A. Rybin, S. Sadilov, E. Di Salvo, G. Santin, T. Sasaki, N. Savvas, Y. Sawada, et al., "GEANT4-a simulation toolkit," *Nuclear Instruments & Methods in Physics Research Section a-Accelerators Spectrometers Detectors and Associated Equipment*, vol. 506, pp. 250-303, 2003.

[53] J. Baro, J. Sempau, J. M. Fernandezvarea, and F. Salvat, "Penelope - an Algorithm for Monte-Carlo Simulation of the Penetration and Energy-Loss of Electrons and Positrons in Matter," *Nuclear Instruments & Methods in Physics Research Section B-Beam Interactions with Materials and Atoms*, vol. 100, pp. 31-46, 1995.

[54] G. Santin, "Space Radiation Transport Models," *IEEE NSREC Short Course Notes*, 2006.

[55] A. J. Wroe, I. M. Cornelius, A. B. Rosenfeld, V. L. Pisacane, J. F. Ziegler, E. Nelson, F. Cucinotta, M. Zaider, and J. F. Dicello, "Microdosimetry simulations of solar protons within a spacecraft," *IEEE Transactions on Nuclear Science*, vol. 52, pp. 2591-2596, 2005.

[56] D. Visvikis, M. Bardies, S. Chiavassa, C. Danford, A. Kirov, F. Lamare, L. Maigne, S. Staelens, and R. Taschereau, "Use of the GATE Monte Carlo package for dosimetry applications," *Nuclear Instruments & Methods in Physics Research Section a-Accelerators Spectrometers Detectors and Associated Equipment*, vol. 569, pp. 335-340, 2006.

[57] P. Gonias, N. Bertsekas, N. Karakatsanis, G. Saatsakis, A. Gaitanis, D. Nikolopoulos, G. Loudos, L. Papaspyrou, N. Sakellios, X. Tsantilas, A. Daskalakis, P. Liaparinos, K. Nikita, A. Louizi, D. Cavouras, I. Kandarakis, and G. S. Panayiotakis, "Validation of a GATE model for the simulation of the Siemens biograph (TM) 6 PET scanner," *Nuclear Instruments & Methods in Physics Research Section a-Accelerators Spectrometers Detectors and Associated Equipment*, vol. 571, pp. 263-266, 2007.

[58] S. A. Kis, M. Emri, G. Opposits, T. Bukki, I. Valastyan, G. Hegyesi, J. Imrek, G. Kalinka, J. Molnar, D. Novak, J. Vegh, A. Kerek, L. Tron, and L. Balkay, "Comparison of Monte Carlo simulated and measured performance parameters of miniPET scanner," *Nuclear Instruments & Methods in Physics Research Section a-Accelerators Spectrometers Detectors and Associated Equipment*, vol. 571, pp. 449-452, 2007.

[59] H. Paganetti, H. Jiang, S. Y. Lee, and H. M. Kooy, "Accurate Monte Carlo simulations for nozzle design, commissioning and quality assurance for a proton radiation therapy facility," *Medical Physics*, vol. 31, pp. 2107-2118, 2004.

[60] H. Jiang and H. Paganetti, "Adaptation of GEANT4 to Monte Carlo dose calculations based on CT data," *Medical Physics*, vol. 31, pp. 2811-2818, 2004.

[61] H. Paganetti, H. Jiang, and A. Trofimov, "4D Monte Carlo simulation of proton beam scanning: modelling of variations in time and space to study the interplay between scanning pattern and time-dependent patient geometry," *Physics in Medicine and Biology*, vol. 50, pp. 983-990, 2005.

[62] E. J. Hall and A. J. Giaccia, *Radiobiology for the Radiologist*, Sixth Edition ed. Philadelphia: Lippincott Williams and Wilkins, 2006.

[63] T. T. Puck and P. I. Marcus, "Action of x-rays on mammalian cells," *Journal of Experimental Medicine*, vol. 103, pp. 653-666, 1956.

[64] A. Wroe, A. Rosenfeld, I. Cornelius, D. Prokopovich, M. Reinhard, R. Schulte, and V. Bashkirov, "Silicon microdosimetry in heterogeneous materials: Simulation and experiment," *IEEE Transactions on Nuclear Science*, vol. 53, pp. 3738-3744, 2006.

[65] A. Wroe, A. Rosenfeld, and R. Schulte, "Measured Out-Of-Field Dose Equivalents Delivered by Proton Therapy of Prostate Cancer," *Medical Physics*, 2007.

[66] M. I. Reinhard, I. Cornelius, D. A. Prokopovich, A. Wroe, A. B. Rosenfeld, V.Pisacane, J. F. Ziegler, M. E. Nelson, F. Cucinotta, M. Zaider, and J. F. Dicello, "Response of a SOI Microdosimeter to a 238PuBe Neutron Source," *IEEE Nuclear Science Symposium Conference Record*, pp. 68, 2005.

[67] E. J. Hall, "Intensity-modulated radiation therapy, protons, and the risk of second cancers," *International Journal of Radiation Oncology Biology Physics*, vol. 65, pp. 1-7, 2006.

[68] X. Yan, U. Titt, A. M. Koehler, and W. D. Newhauser, "Measurement of neutron dose equivalent to proton therapy patients outside of the proton radiation field," *Nuclear Instruments & Methods in Physics Research Section a-Accelerators Spectrometers Detectors and Associated Equipment*, vol. 476, pp. 429-434, 2002.

[69] G. Mesoloras, G. A. Sandison, R. D. Stewart, J. B. Farr, and W. C. Hsi, "Neutron scattered dose equivalent to a fetus from proton radiotherapy of the mother," *Medical Physics*, vol. 33, pp. 2479-2490, 2006.

[70] U. Schneider, S. Agosteo, E. Pedroni, and J. Besserer, "Secondary neutron dose during proton therapy using spot scanning," *International Journal of Radiation Oncology Biology Physics*, vol. 53, pp. 244-251, 2002.

[71] A. Rosenfeld, A. Wroe, M. Carolan, and I. Cornelius, "Method of Monte Carlo simulation verification in hadron therapy with non-tissue equivalent detectors," *Radiation Protection Dosimetry*, vol. 119, pp. 487-490, 2006.

[72] J. W. W. D. Letourneau, M. Oldham, M. Gulam, L. Watt, D.A. Jaffray, J.H. Siewerdsen, A.A. Martinez "Cone-beam-CT guided radiation therapy: technical implementation," *Radiotherapy and Oncology*, vol. 75, pp. 279-286, 2005.

[73] A. B. Rosenfeld, A. J. Wroe, L. M. Cornelius, M. Reinhard, and D. Alexiev, "Analysis of inelastic interactions for therapeutic proton beams using Monte Carlo simulation," *IEEE Transactions on Nuclear Science*, vol. 51, pp. 3019-3025, 2004.

[74] V. Bashkirov and R. W. Schulte, "Dosimetry system for the irradiation of thin biological samples with therapeutic proton beams," *Physics in Medicine and Biology*, vol. 47, pp. 409-420, 2002.

[75] P. G. A. Cirrone, G. Cuttone, F. D. Rosa, S. Guatelli, B. Mascialino, M. G. Pia, and G. Russo, "Validation of Geant4 Physics Models for the Simulation of the Proton Bragg Peak," presented at IEEE NSS & MIC, San Diego, USA, 2006.

[76] B. Mascialino, S. Guatelli, and M. G. Pia, "Geant4 Anthropomorphic Phantoms," presented at IEEE NSS & MIC, San Diego, USA, 2006.

[77] A. J. Wroe, L. M. Cornelius, and A. B. Rosenfeld, "The role of nonelastic reactions in absorbed dose distributions from therapeutic proton beams in different medium," *Medical Physics*, vol. 32, pp. 37-41, 2005.

[78] H. Paganetti, "Nuclear interactions in proton therapy: dose and relative biological effect distributions originating from primary and secondary particles," *Physics in Medicine and Biology*, vol. 47, pp. 747-764, 2002.

[79] J. A. Simpson, *Introduction to the Galactic Cosmic Radiation. Composition and Origin of Cosmic Rays*. Dordrecht: Reidel Publishing, 1983.

[80] G. D. Badhwar, "Shuttle radiation dose measurements in the international space station orbits," *Radiation Research*, vol. 157, pp. 69-75, 2002.

[81] P. D. Bradley and A. B. Rosenfeld, "Tissue equivalence correction for silicon microdosimetry detectors in boron neutron capture therapy," *Medical Physics*, vol. 25, pp. 2220-2225, 1998.

[82] "MIDSTAR Website," *http://web.ew.usna.edu/~midstar/*, 2007.

[83] J. F. Dicello, M. Wasiolek, and M. Zaider, "Measured Microdosimetric Spectra of Energetic Ion-Beams of Fe, Ar, Ne, and C - Limitations of Let Distributions and Quality Factors in Space Research and Radiation Effects," *IEEE Transactions on Nuclear Science*, vol. 38, pp. 1203-1209, 1991.

[84] V. L. Pisacane, Q. E. Dolecek, F. Maas, M. E. Nelson, P. J. Taddei, Z. Zhao, J. F. Ziegler, P. C. Acox, M. Bender, J. D. Brown, T. Garritsen, C. Gaughan, A. Hough, B. Kolb, J. Langlois, J. Ross, M. Sheggeby, D. Thomas, J. F. Dicello, F.

A. Cucinotta, M. Zaider, A. B. Rosenfeld, and A. Wroe, "MIcroDosimeter iNstrument (MIDN) on MidSTAR-I," *SAE Transactions Journal of Aerospace*, vol. 2006-01-2146, 2006.

[85] V. L. Pisacane, J. F. Ziegler, M. E. Nelson, M. Caylor, D. Flake, L. Heyen, E. Youngborg, A. B. Rosenfeld, F. Cucinotta, M. Zaider, and J. F. Dicello, "MIDN: A spacecraft microdosimeter mission," *Radiation Protection Dosimetry*, vol. 120, pp. 421-426, 2006.

[86] SPENVIS, *http://www.spenvis.oma.be/spenvis/*.

[87] CREME96, *https://creme96.nrl.navy.mil/]*.

[88] F. A. Cucinotta, W. Schimmerling, J. W. Wilson, L. E. Peterson, P. B. Saganti, and J. F. Dicello, "Uncertainties in estimates of the risks of late effects from space radiation," in *Space Life Sciences: Radiation Risk Assessment and Radiation Measurement in Low Earth Orbit*, vol. 34, *Advances in Space Research*, 2004, pp. 1383-1389.

[89] "NASA Space Radiation Facility," *http://server.c-ad.bnl.gov/esfd/nsrl/index.html*.

[90] C. Zeitlin, S. B. Guetersloh, L. H. Heilbronn, and J. Miller, "Measurements of materials shielding properties with 1 GeV/nuc Fe-56," *Nuclear Instruments & Methods in Physics Research Section B-Beam Interactions with Materials and Atoms*, vol. 252, pp. 308-318, 2006.

[91] J. F. Ziegler and J. P. Biersack, "SRIM," *http://www.srim.org/#SRIM*, 2003.

[92] D. Mancusi, L. Sihver, K. Gustafsson, C. La Tessa, S. B. Guetersloh, C. J. Zeitlin, J. Miller, L. H. Heilbronn, K. Niita, T. Sato, H. Nakashima, T. Murakami, and Y. Iwata, "PHITS - benchmark of partial charge-changing cross sections for intermediate-mass systems," *Nuclear Instruments & Methods in Physics Research Section B-Beam Interactions with Materials and Atoms*, vol. 254, pp. 30-38, 2007.

[93] C. Tsuruoka, M. Suzuki, T. Kanai, and K. Fujitaka, "LET and Ion Species Dependence for Cell Killing in Normal Human Skin Fibroblasts," *Radiation Research*, vol. 163, pp. 494–500 2005.

[94] "PSI Nuclear Physics Research Program," *http://www.src.wits.ac.za/groups/psi/nuc/particles.html*.

[95] H. Matsumoto, H. Koshiishi, T. Goka, M. Funjii, M. Hareyama, N. Kajiwara, S. Kodaira, K. Sakurai, and N. Hasebe, "Delta E x E silicon telescope of energetic heavy ions trapped in radiation belts," *Japanese Journal of Applied Physics Part 1-Regular Papers Brief Communications & Review Papers*, vol. 44, pp. 6870-6872, 2005.

[96] A. J. Kordyasz, E. Nossarzewska-Orlowska, E. Piasecki, D. Lipinski, A. Brzozowski, J. Kownacki, M. Kowalczyk, L. Swiderski, A. Syntfeld, L. Reissig, A. Pietrzak, A. Jakubowski, R. Pozorek, and R. Gasiorowski, "Response to heavy ions and fission fragments of the monolithic silicon E-Delta E telescopes produced by the Quasi-Selective Epitaxy," *Nuclear Instruments & Methods in Physics Research Section a-Accelerators Spectrometers Detectors and Associated Equipment*, vol. 530, pp. 87-91, 2004.

[97] "Ortec Website," *http://www.ortec-online.com/*.

[98] A. J. Kordyasz, E. Nossarzewska-Orlowska, E. Piasecki, D. Lipinski, A. Brzozowski, J. Kownacki, M. Kowalczyk, L. Swiderski, A. Syntfeld, L. Reissig, A. Pietrzak, A. Jakubowski, R. Pozorek, and R. Gasiorowski, "Monolithic silicon E-Delta E telescope produced by the quasi-selective epitaxy," *Nuclear Instruments & Methods in Physics Research Section a-Accelerators Spectrometers Detectors and Associated Equipment*, vol. 528, pp. 721-730, 2004.

[99] A. Musumarra, F. Amorini, M. Cabibbo, G. Cardella, G. DeGeronimo, A. DiPietro, P. G. Fallica, P. Figuera, M. Papa, G. Pappalardo, F. Rizzo, and S. Tudisco, "Implanted silicon detector telescope: New developments," *Nuclear Instruments & Methods in Physics Research Section a-Accelerators Spectrometers Detectors and Associated Equipment*, vol. 409, pp. 414-416, 1998.

[100] S. Agosteo, P. G. Fallica, A. Fazzi, A. Pola, G. Valvo, and P. Zotto, "A feasibility study of a solid-state microdosimeter," *Applied Radiation and Isotopes*, vol. 63, pp. 529-535, 2005.

[101] A. Fazzi, S. Agosteo, A. Pola, V. Varoli, and P. Zotto, "A micrometric thickness silicon diode proposed as a microdosimeter," *IEEE Transactions on Nuclear Science*, vol. 53, pp. 312-316, 2006.

[102] I. Cornelius, A. Rosenfeld, M. Reinhard, A. Fazzi, D. Prokopovich, A. Wroe, R. Siegele, A. Pola, and S. Agosteo, "Charge collection imaging of a monolithic ΔE-E telescope for radiation protection applications," *Radiation Protection Dosimetry*, vol. 122, pp. 387 - 389, 2006.

[103] Z. Palajova, F. Spurny, and M. Davidkova, "Microdosimetry distributions for 40-200 MeV protons," *Radiation Protection Dosimetry*, vol. 121, pp. 376-381, 2006.

[104] M. Folkard, K. M. Prise, B. Vojnovic, H. C. Newman, M. J. Roper, and B. D. Michael, "Inactivation of V79 cells by low-energy protons, deuterons and helium-3 ions," *International Journal of Radiation Biology*, vol. 69, pp. 729-738, 1996.

[105] P. Kundrat, "Detailed analysis of the cell-inactivation mechanism by accelerated protons and light ions," *Physics in Medicine and Biology*, vol. 51, pp. 1185-1199, 2006.

[106] C. K. C. Wang and X. Zhang, "A nanodosimetry-based linear-quadratic model of cell survival for mixed-LET radiations," *Physics in Medicine and Biology*, vol. 51, pp. 6087-6098, 2006.

[107] W. K. Weyrather, S. Ritter, M. Scholz, and G. Kraft, "RBE for carbon track-segment irradiation in cell lines of differing repair capacity," *International Journal of Radiation Biology*, vol. 75, pp. 1357-1364, 1999.

[108] N. Tilly, A. Brahme, J. Carlsson, and B. Glimelius, "Comparison of cell survival models for mixed LET radiation," *International Journal of Radiation Biology*, vol. 75, pp. 233-243, 1999.

[109] M. Belli, F. Cera, R. Cherubini, M. Dalla Vecchia, A. M. I. Haque, F. Ianzini, G. Moschini, O. Sapora, G. Simone, M. A. Tabocchini, and P. Tiveron, "RBE-LET relationships for cell inactivation and mutation induced by low energy protons in V79 cells: further results at the LNL facility," *International Journal of Radiation Biology*, vol. 74, pp. 501-509, 1998.

[110] "OriginLab Website," *http://www.originlab.com*.

[111] J. C. Davis, *Statistics and Data Analysis in Geology*, 2nd ed: John Wiley & Sons, 1986.

[112] J. J. Wilkens and U. Oelfke, "A phenomenological model for the relative biological effectiveness in therapeutic proton beams," *Physics in Medicine and Biology*, vol. 49, pp. 2811-2825, 2004.

[113] H. Paganetti, A. Niemierko, M. Ancukiewicz, L. E. Gerweck, M. Goitein, J. S. Loeffler, and H. D. Suit, "Relative biological effectiveness (RBE) values for proton beam therapy," *International Journal of Radiation Oncology Biology Physics*, vol. 53, pp. 407-421, 2002.

[114] B. Grosswendt, L. De Nardo, P. Colautti, S. Pszona, V. Conte, and G. Tornielli, "Experimental equivalent cluster-size distributions in nanometric volumes of liquid water," *Radiation Protection Dosimetry*, vol. 110, pp. 851-857, 2004.

[115] V. Bashkirov, R. Schulte, A. Breskin, R. Chechik, S. Schemelinin, G. Garty, A. Wroe, H. Sadrozinski, and B. Grosswendt, "Ion-counting nanodosemeter with particle tracking capabilities," *Radiation Protection Dosimetry*, vol. 122, pp. 415 - 419, 2006.

[116] A. J. Wroe, R. Schulte, V. Bashkirov, A. B. Rosenfeld, B. Keeney, P. Spradlin, H. F. W. Sadrozinski, and B. Grosswendt, "Nanodosimetric cluster size distributions of therapeutic proton beams," *IEEE Transactions on Nuclear Science*, vol. 53, pp. 532-538, 2006.

[117] C. V. Sonntag, *Free-radical-induced DNA Damage And Its Repair: A Chemical Perspective.*, 1st ed. New York: Springer Verlag, 2006.

[118] P. Pfeiffer, W. Goedecke, S. Kuhfittig-Kulle, and G. Obe, "Pathways of DNA double-strand break repair and their impact on the prevention and formation of chromosomal aberrations," *Cytogenetic and Genome Research*, vol. 104, pp. 7-13, 2004.

[119] B. Alberts, A. Johnson, J. Lewis, M. Raff, K. Roberts, and P. Walter, *Molecular Biology of the Cell*, 4th ed. New York and London: Garland Science, 2002.

[120] R. Schulte, V. Bashkirov, S. Shchemelinin, G. Garty, R. Chechik, and A. Breskin, "Modeling of radiation action based on nanodosimetric event spectra," *Physica Medica*, vol. 17, pp. 177-180, 2001.

[121] Y. S. Horowitz, D. Satinger, and O. Avila, "Track structure approach to the calculation of peak 5a to peak 5 (TLD-100) relative intensities following heavy charged particle irradiation," *Radiation Protection Dosimetry*, vol. 119, pp. 45-48, 2006.

[122] "National Council on Radiation Protection and Measurement : Limitation of exposure to ionizing radiation," *NCRP Report - 116*, 1993.

[123] F. A. Cucinotta, W. Schimmerling, J. W. Wilson, L. E. Peterson, G. D. Badhwar, P. B. Saganti, and J. F. Dicello, "Space radiation cancer risks and uncertainties for Mars missions," *Radiation Research*, vol. 156, pp. 682-688, 2001.

[124] M. D. Walker, S. B. Green, D. P. Byar, E. Alexander, U. Batzdorf, W. H. Brooks, W. E. Hunt, C. S. Maccarty, M. S. Mahaley, J. Mealey, G. Owens, J. Ransohoff, J. T. Robertson, W. R. Shapiro, K. R. Smith, C. B. Wilson, and T. A. Strike, "Randomized Comparisons of Radiotherapy and Nitrosoureas for the Treatment of Malignant Glioma after Surgery," *New England Journal of Medicine*, vol. 303, pp. 1323-1329, 1980.

[125] W. R. Shapiro, S. B. Green, P. C. Burger, M. S. Mahaley, R. G. Selker, J. C. Vangilder, J. T. Robertson, J. Ransohoff, J. Mealey, T. A. Strike, and D. A. Pistenmaa, "Randomized Trial of 3 Chemotherapy Regimens and 2 Radiotherapy Regimens in Postoperative Treatment of Malignant Glioma - Brain-Tumor Cooperative Group Trial-8001," *Journal of Neurosurgery*, vol. 71, pp. 1-9, 1989.

[126] K. Takakura, H. Abe, R. Tanaka, K. Kitamura, T. Miwa, K. Takeuchi, S. Yamamoto, N. Kageyama, H. Handa, H. Mogami, A. Nishimoto, T. Uozumi, M. Matsutani, and K. Nomura, "Effects of Acnu and Radiotherapy on Malignant Glioma," *Journal of Neurosurgery*, vol. 64, pp. 53-57, 1986.

[127] K. Tsuboi, Y. Tsuchida, T. Nose, and K. Ando, "Cytotoxic effect of accelerated carbon beams on glioblastoma cell lines with p53 mutation: clonogenic survival and cell-cycle analysis," *International Journal of Radiation Biology*, vol. 74, pp. 71-79, 1998.

[128] C. Leloup, G. Garty, G. Assaf, A. Cristovao, A. Breskin, R. Chechik, S. Shchemelinin, T. Paz-Elizur, Z. Livneh, R. W. Schulte, V. Bashkirov, J. R. Milligan, and B. Grosswendt, "Evaluation of lesion clustering in irradiated plasmid DNA," *International Journal of Radiation Biology*, vol. 81, pp. 41-54, 2005.

[129] G. D. D. Jones, J. R. Milligan, J. F. Ward, P. M. Calabrojones, and J. A. Aguilera, "Yield of Strand Breaks as a Function of Scavenger Concentration and Let for Sv40 Irradiated with He-4 Ions," *Radiation Research*, vol. 136, pp. 190-196, 1993.

[130] "A Protocol for the Determination of Absorbed Dose from High-Energy Photon and Electron-Beams," *Medical Physics*, vol. 10, pp. 741-771, 1983.

[131] "Central axis depth dose and related data measured in water or equivalent media," *British Journal of Radiology*, vol. Supplement 25, 1996.